

Methods in
Molecular Biology 1695

Springer Protocols

Tatjana C. Jakobs *Editor*

Glaucoma

Methods and Protocols

 Humana Press

METHODS IN MOLECULAR BIOLOGY

Series Editor

John M. Walker

School of Life and Medical Sciences

University of Hertfordshire

Hatfield, Hertfordshire, AL10 9AB, UK

For further volumes:

<http://www.springer.com/series/7651>

Glaucoma

Methods and Protocols

Edited by

Tatjana C. Jakobs

*Department of Ophthalmology, Massachusetts Eye and Ear Infirmary/Schepens Eye
Research Institute, Harvard Medical School, Boston, MA, USA*

Editor

Tatjana C. Jakobs
Department of Ophthalmology
Massachusetts Eye and Ear Infirmary/Schepens Eye
Research Institute
Harvard Medical School
Boston, MA, USA

ISSN 1064-3745 ISSN 1940-6029 (electronic)
Methods in Molecular Biology
ISBN 978-1-4939-7406-1 ISBN 978-1-4939-7407-8 (eBook)
<https://doi.org/10.1007/978-1-4939-7407-8>

Library of Congress Control Number: 2017952425

© Springer Science+Business Media LLC 2018

This work is subject to copyright. All rights are reserved by the Publisher, whether the whole or part of the material is concerned, specifically the rights of translation, reprinting, reuse of illustrations, recitation, broadcasting, reproduction on microfilms or in any other physical way, and transmission or information storage and retrieval, electronic adaptation, computer software, or by similar or dissimilar methodology now known or hereafter developed.

The use of general descriptive names, registered names, trademarks, service marks, etc. in this publication does not imply, even in the absence of a specific statement, that such names are exempt from the relevant protective laws and regulations and therefore free for general use.

The publisher, the authors and the editors are safe to assume that the advice and information in this book are believed to be true and accurate at the date of publication. Neither the publisher nor the authors or the editors give a warranty, express or implied, with respect to the material contained herein or for any errors or omissions that may have been made. The publisher remains neutral with regard to jurisdictional claims in published maps and institutional affiliations.

Printed on acid-free paper

This Humana Press imprint is published by Springer Nature
The registered company is Springer Science+Business Media, LLC
The registered company address is: 233 Spring Street, New York, NY 10013, U.S.A.

Preface

Glaucoma is a common eye disease that affects 1 in 40 people over the age of 40. It is estimated that this translates to 60 million people suffering from glaucoma worldwide, with over eight million bilaterally blind from the disease. In all forms of glaucoma, the retinal ganglion cells, the retina's only projection neurons, degenerate and eventually die. An elevation of the intraocular pressure is among the most common risk factors, and indeed all current glaucoma therapies aim at lowering pressure. Yet, the mechanisms that connect intraocular pressure and ganglion cell pathology are far from clear. It is also known that, in some cases, the disease progresses in spite of successful lowering of the intraocular pressure. Once lost, ganglion cells cannot regenerate, and the visual field defects caused by ganglion cell dropout are permanent. Clearly, new therapeutic approaches that protect ganglion cells directly would be welcome.

The aim of the present volume is to introduce the reader to current methods in glaucoma research, in particular those that make use of animal disease models. We hope that both ophthalmologists in clinical practice and researchers will find the volume useful.

Boston, MA, USA

Tatjana C. Jakobs

Contents

1	Use of Animal Models and Techniques in Glaucoma Research: Introduction	1
	<i>Harry A. Quigley</i>	
2	Hypertonic Saline Injection Model of Experimental Glaucoma in Rats	11
	<i>John C. Morrison, Elaine C. Johnson, and William O. Cepurna</i>	
3	The Microbead Occlusion Model of Ocular Hypertension in Mice	23
	<i>David J. Calkins, Wendi S. Lambert, Cathryn R. Formichella, William M. McLaughlin, and Rebecca M. Sappington</i>	
4	Ocular Hypertension/Glaucoma in Minipigs: Episcleral Veins Cauterization and Microbead Occlusion Methods	41
	<i>Elena Vecino, Haritz Urcola, Alejandro Bayon, and Sansar C. Sharma</i>	
5	Noninvasive Intraocular Pressure Measurement in Animals Models of Glaucoma	49
	<i>Yan Hu and John Danias</i>	
6	High-Throughput Binocular Pattern Electroretinograms in the Mouse	63
	<i>Tsung-Han Chou, Jonathon Toft-Nielsen, and Vittorio Porciatti</i>	
7	Visual Evoked Potentials in Glaucoma and Alzheimer’s Disease	69
	<i>Elisa Cerri, Carlotta Fabiani, Chiara Criscuolo, and Luciano Domenici</i>	
8	Investigation of the Functional Retinal Output Using Microelectrode Arrays	81
	<i>Günther Zeck</i>	
9	Quantitative Proteomic Analysis of Human Aqueous Humor Using iTRAQ 4plex Labeling	89
	<i>Anna Trzeciecka, Padmanabhan Pattabiraman, Maria Carmen Piqueras, Carol Toris, and Sanjoy K. Bhattacharya</i>	
10	Shotgun Sphingolipid Analysis of Human Aqueous Humor	97
	<i>Anna Trzeciecka, Ulises Arbelo, Arturo Barron, Genea Edwards, Sruthi Sampathkumar, Carol Toris, and Sanjoy K. Bhattacharya</i>	
11	Assessment of Aqueous Humor Dynamics in the Rodent by Constant Flow Infusion	109
	<i>J. Cameron Millar, Tien N. Phan, and Iok-Hou Pang</i>	
12	Methods for Analyzing Endoplasmic Reticulum Stress in the Trabecular Meshwork of Glaucoma Models	121
	<i>Prabhavathi Maddineni, Ramesh B. Kasetti, and Gulab S. Zode</i>	
13	Quantification of Scleral Biomechanics and Collagen Fiber Alignment	135
	<i>Ian C. Campbell, Joseph M. Sherwood, Darryl R. Overby, Bailey G. Hannon, A. Thomas Read, Julia Raykin, and C. Ross Ethier</i>	

14 Biolistic Labeling of Retinal Ganglion Cells 161
Luca Della Santina and Yvonne Ou

15 Anterograde Tract Tracing for Assaying Axonopathy and Transport
Deficits in Glaucoma 171
Samuel D. Crish and Brett R. Schofield

16 In Vitro and In Vivo Methods for Studying Retinal Ganglion
Cell Survival and Optic Nerve Regeneration 187
Yujin Yin and Larry I. Benowitz

17 3D Histomorphometric Reconstruction and Quantification
of the Optic Nerve Head Connective Tissues..... 207
*Hongli Yang, Juan Reynaud, Howard Lockwood, Galen Williams,
Christy Hardin, Luke Reyes, Stuart K. Gardiner,
and Claude F. Burgoyne*

18 Visualizing Astrocytes of the Optic Nerve..... 269
Daniel Sun

19 Investigation of MicroRNA Expression in Experimental Glaucoma 287
*Hari Jayaram, Diana C. Lozano, Elaine C. Johnson,
and John C. Morrison*

20 Utilizing RNA-Seq to Identify Differentially Expressed Genes
in Glaucoma Model Tissues, Such as the Rodent Optic Nerve Head 299
*Diana C. Lozano, Dongseok Choi, Hari Jayaram, John C. Morrison,
and Elaine C. Johnson*

21 Single-Cell Dissociation and Characterization in the Murine Retina
and Optic Nerve 311
Hee Joo Choi, Rui Wang, and Tatjana C. Jakobs

Index 335

Contributors

- ULISES ARBELO • *Bascom Palmer Eye Institute, University of Miami, Miami, FL, USA*
- ARTURO BARRON • *Bascom Palmer Eye Institute, University of Miami, Miami, FL, USA*
- ALEJANDO BAYON • *Department of Veterinary Ophthalmology, Murcia University, Murcia, Spain*
- LARRY I. BENOWITZ • *Department of Neurosurgery, F.M. Kirby Neurobiology Center, Boston Children's Hospital, Boston, MA, USA; Department of Neurosurgery, Harvard Medical School, Boston, MA, USA; Department of Ophthalmology, Harvard Medical School, Boston, MA, USA*
- SANJOY K. BHATTACHARYA • *Bascom Palmer Eye Institute, McKnight Vision Research Center, University of Miami, Miami, FL, USA*
- CLAUDE F. BURGOYNE • *Optic Nerve Head Research Laboratory, Legacy Research Institute, Devers Eye Institute, Portland, OR, USA; Discoveries in Sight Research Laboratories, Legacy Research Institute, Devers Eye Institute, Portland, OR, USA*
- DAVID J. CALKINS • *The Vanderbilt Eye Institute, Vanderbilt University Medical Center, Nashville, TN, USA; Department of Ophthalmology and Visual Sciences, Vanderbilt University School of Medicine, Nashville, TN, USA*
- IAN C. CAMPBELL • *Wallace H. Coulter Department of Biomedical Engineering, Georgia Institute of Technology and Emory University, Atlanta, GA, USA; Rehabilitation Research and Development, Atlanta VA Medical Center, Decatur, GA, USA*
- WILLIAM O. CEPURNA • *Casey Eye Institute, Oregon Health and Science University, Portland, OR, USA*
- ELISA CERRI • *Neuroscience Institute of the National Council of Research (CNR), Pisa, Italy*
- DONGSEOK CHOI • *Casey Eye Institute, Oregon Health and Science University, Portland, OR, USA; School of Public Health, Oregon Health and Science University, Portland, OR, USA*
- HEE JOO CHOI • *Department of Ophthalmology, Massachusetts Eye and Ear Infirmary/Schepens Eye Research Institute, Harvard Medical School, Boston, MA, USA*
- TSUNG-HAN CHOU • *Bascom Palmer Eye Institute, McKnight Vision Research Center, University of Miami Miller School of Medicine, Miami, FL, USA*
- CHIARA CRISCUOLO • *Neuroscience Institute of the National Council of Research (CNR), Pisa, Italy*
- SAMUEL D. CRISH • *Department of Pharmaceutical Sciences, Northeast Ohio Medical University, Rootstown, OH, USA*
- JOHN DANIAS • *Department of Cell Biology, SUNY Downstate, Brooklyn, NY, USA; Department of Ophthalmology, SUNY Downstate, Brooklyn, NY, USA*
- LUCIANO DOMENICI • *Neuroscience Institute of the National Council of Research (CNR), Pisa, Italy; Department of Applied Clinical Sciences and Biotechnology (DISCAB), University of L'Aquila, L'Aquila, Coppito AQ, Italy*
- GENEA EDWARDS • *Bascom Palmer Eye Institute, University of Miami, Miami, FL, USA*
- C. ROSS ETHIER • *Wallace H. Coulter Department of Biomedical Engineering, Georgia Institute of Technology and Emory University, Atlanta, GA, USA; Rehabilitation Research and Development, Atlanta VA Medical Center, Decatur, GA, USA; George W. Woodruff School of Mechanical Engineering, Georgia Institute of Technology, Atlanta, GA, USA*

- CARLOTTA FABIANI • *Neuroscience Institute of the National Council of Research (CNR), Pisa, Italy*
- CATHRYN R. FORMICHELLA • *The Vanderbilt Eye Institute, Vanderbilt University Medical Center, Nashville, TN, USA*
- STUART K. GARDINER • *Discoveries in Sight Research Laboratories, Legacy Research Institute, Devers Eye Institute, Portland, OR, USA*
- BAILEY G. HANNON • *Wallace H. Coulter Department of Biomedical Engineering, Georgia Institute of Technology and Emory University, Atlanta, GA, USA; George W. Woodruff School of Mechanical Engineering, Georgia Institute of Technology, Atlanta, GA, USA*
- CHRISTY HARDIN • *Optic Nerve Head Research Laboratory, Legacy Research Institute, Devers Eye Institute, Portland, OR, USA; Discoveries in Sight Research Laboratories, Legacy Research Institute, Devers Eye Institute, Portland, OR, USA*
- YAN HU • *Department of Cell Biology, SUNY Downstate, Brooklyn, NY, USA*
- TATJANA C. JAKOBS • *Department of Ophthalmology, Massachusetts Eye and Ear Infirmary/Schepens Eye Research Institute, Harvard Medical School, Boston, MA, USA*
- HARI JAYARAM • *Glaucoma Service, NIHR Biomedical Research Centre for Ophthalmology, UCL Institute of Ophthalmology and Moorfields Eye Hospital, London, UK*
- ELAINE C. JOHNSON • *Casey Eye Institute, Oregon Health and Science University, Portland, OR, USA*
- RAMESH B. KASETTI • *The North Texas Eye Research Institute, CBH-413, University of North Texas Health Science Center, Fort Worth, TX, USA*
- WENDI S. LAMBERT • *The Vanderbilt Eye Institute, Vanderbilt University Medical Center, Nashville, TN, USA*
- HOWARD LOCKWOOD • *Optic Nerve Head Research Laboratory, Legacy Research Institute, Devers Eye Institute, Portland, OR, USA; Discoveries in Sight Research Laboratories, Legacy Research Institute, Devers Eye Institute, Portland, OR, USA*
- DIANA C. LOZANO • *Casey Eye Institute, Oregon Health and Science University, Portland, OR, USA*
- PRABHAVATHI MADDINENI • *The North Texas Eye Research Institute, CBH-413, University of North Texas Health Science Center, Fort Worth, TX, USA*
- WILLIAM M. McLAUGHLIN • *The Vanderbilt Eye Institute, Vanderbilt University Medical Center, Nashville, TN, USA*
- J. CAMERON MILLAR • *North Texas Eye Research Institute, University of North Texas Health Science Center, Fort Worth, TX, USA*
- JOHN C. MORRISON • *Casey Eye Institute, Oregon Health and Science University, Portland, OR, USA*
- YVONNE OU • *Department of Ophthalmology, University of California, San Francisco, CA, USA*
- DARRYL R. OVERBY • *Department of Bioengineering, Imperial College London, London, UK*
- IOK-HOU PANG • *North Texas Eye Research Institute, University of North Texas Health Science Center, Fort Worth, TX, USA; Department of Pharmaceutical Sciences, College of Pharmacy, University of North Texas Health Science Center, Fort Worth, TX, USA*
- PADMANABHAN PATTABIRAMAN • *Department of Ophthalmology, Case Western Reserve University, Cleveland, OH, USA*
- TIEN N. PHAN • *North Texas Eye Research Institute, University of North Texas Health Science Center, Fort Worth, TX, USA*
- MARIA CARMEN PIQUERAS • *Bascom Palmer Eye Institute, McKnight Vision Research Center, University of Miami, Miami, FL, USA*

- VITTORIO PORCIATTI • *Bascom Palmer Eye Institute, McKnight Vision Research Center, University of Miami Miller School of Medicine, Miami, FL, USA*
- HARRY A. QUIGLEY • *Glaucoma Center of Excellence, Wilmer Eye Institute, Johns Hopkins School of Medicine, Johns Hopkins Hospital, Baltimore, MD, USA*
- JULIA RAYKIN • *Wallace H. Coulter Department of Biomedical Engineering, Georgia Institute of Technology and Emory University, Atlanta, GA, USA*
- A. THOMAS READ • *Wallace H. Coulter Department of Biomedical Engineering, Georgia Institute of Technology and Emory University, Atlanta, GA, USA*
- LUKE REYES • *Optic Nerve Head Research Laboratory, Legacy Research Institute, Devers Eye Institute, Portland, OR, USA; Discoveries in Sight Research Laboratories, Legacy Research Institute, Devers Eye Institute, Portland, OR, USA*
- JUAN REYNAUD • *Optic Nerve Head Research Laboratory, Legacy Research Institute, Devers Eye Institute, Portland, OR, USA; Discoveries in Sight Research Laboratories, Legacy Research Institute, Devers Eye Institute, Portland, OR, USA*
- SRUTHI SAMPATHKUMAR • *Department of Ophthalmology, Case Western Reserve University, Cleveland, OH, USA*
- LUCA DELLA SANTINA • *Department of Ophthalmology, University of California, San Francisco, CA, USA*
- REBECCA M. SAPPINGTON • *The Vanderbilt Eye Institute, Vanderbilt University Medical Center, Nashville, TN, USA; Department of Ophthalmology and Visual Sciences, Vanderbilt University School of Medicine, Nashville, TN, USA; Department of Pharmacology, Vanderbilt University School of Medicine, Nashville, TN, USA*
- BRETT R. SCHOFIELD • *Department of Anatomy and Neurobiology, Northeast Ohio Medical University, Rootstown, OH, USA*
- SANSAR C. SHARMA • *Department of Anatomy and Cell Biology, New York Medical College, Valhalla, NY, USA*
- JOSEPH M. SHERWOOD • *Department of Bioengineering, Imperial College London, London, UK*
- DANIEL SUN • *Department of Ophthalmology, Massachusetts Eye and Ear Infirmary/Schepens Eye Research Institute, Harvard Medical School, Boston, MA, USA*
- JONATHON TOFT-NIELSEN • *Jorvec Corporation, Miami, FL, USA*
- CAROL TORIS • *Department of Ophthalmology, Case Western Reserve University, Cleveland, OH, USA*
- ANNA TRZECIECKA • *Bascom Palmer Eye Institute, McKnight Vision Research Center, University of Miami, Miami, FL, USA*
- HARITZ URCOLA • *Experimental Ophthalmology-Biology Group, Department Cell Biology and Histology, University of the Basque Country, Leioa, Vizcaya, Spain; Ophthalmology Section, Hospital Universitario Araba, Vitoria, Spain*
- ELENA VECINO • *Experimental Ophthalmology-Biology Group, Department Cell Biology and Histology, University of the Basque Country, Leioa, Vizcaya, Spain*
- RUI WANG • *Department of Ophthalmology, Massachusetts Eye and Ear Infirmary/Schepens Eye Research Institute, Harvard Medical School, Boston, MA, USA; Department of Ophthalmology, The First Hospital of Xi'an, Xi'an, Shaanxi, China*
- GALEN WILLIAMS • *Optic Nerve Head Research Laboratory, Legacy Research Institute, Devers Eye Institute, Portland, OR, USA; Discoveries in Sight Research Laboratories, Legacy Research Institute, Devers Eye Institute, Portland, OR, USA*

HONGLI YANG • *Optic Nerve Head Research Laboratory, Legacy Research Institute, Devers Eye Institute, Portland, OR, USA; Discoveries in Sight Research Laboratories, Legacy Research Institute, Devers Eye Institute, Portland, OR, USA*

YUQIN YIN • *Department of Neurosurgery, F.M. Kirby Neurobiology Center, Boston Children's Hospital, Boston, MA, USA; Department of Neurosurgery, Harvard Medical School, Boston, MA, USA*

GÜNTHER ZECK • *Neurophysics, NMI at the University Tübingen, Reutlingen, Germany*

GULAB S. ZODE • *The North Texas Eye Research Institute, CBH-413, University of North Texas Health Science Center, Fort Worth, TX, USA*

Chapter 1

Use of Animal Models and Techniques in Glaucoma Research: Introduction

Harry A. Quigley

Abstract

This chapter provides an overview over the use of animal models in glaucoma research from a historical perspective. Strengths and limitations of various models are considered, and the challenges of translating results in animal experiments to successful clinical trials in humans are discussed.

Key words Glaucoma, Animal models, Retinal ganglion cells, Axons, Intraocular pressure, Lamina cribrosa, Tonometry, Inflammation, Neuroprotection

1 Definition of Glaucoma

Glaucoma refers to a group of clinical diseases that share a common phenotype, consisting of a deepening or excavation of the optic nerve head viewed ophthalmoscopically and a loss of visual sensitivity in the sequence beginning in the mid-peripheral visual field [1]. The main forms of glaucoma in humans are open angle, angle closure, glaucoma due to another disease, and childhood onset glaucoma. Together, the glaucomas are the second leading cause of blindness worldwide after cataract [2]. The disease in the majority of persons is slowly progressive, but its course is improved by the lowering of intraocular pressure (IOP), accomplished by daily eye drop administration, laser treatment to the eye, or ocular surgery [3]. The clinical and histological features of glaucoma show that the cardinal event in the disease is injury to the axons of retinal ganglion cells (RGCs) as these fibers exit the eye within the optic nerve head [4]. Since mammalian eyes are not typically capable of RGC regeneration after substantial injury, there is subsequent RGC death by apoptosis [5] and Wallerian degeneration of the axon between the eye and its central nervous system (CNS) targets. Death of RGC in glaucoma is not accompanied by loss of its upstream partners in the retina, nor even synaptically linked

amacrine cells [6]. However, consecutive degeneration of the CNS targets occurs secondarily (lateral geniculate nucleus neurons in monkeys and humans, superior colliculus neurons in rodents) [7, 8].

Thus, the primary features of an appropriate animal model for duplicating the key features of human glaucoma are: (1) axonal injury at the optic nerve head, and (2) loss of RGC, but not other retinal neurons. Since glaucoma in humans is related to the level of IOP, it has been most typical to produce animal models by artificial IOP elevation above the normal range. In human open angle glaucoma, a sizable minority of persons suffer from glaucomatous RGC loss at levels of IOP that are within the range found in persons without the disease. Yet, lowering their IOP therapeutically reduces the rate of RGC loss; hence, the most consistent risk factor for the disease is IOP level, regardless of whether it is above the statistical normal or not.

2 History of Glaucoma Model Research

Until the 1960s, the pathophysiology of glaucoma was known only from human eyes that were surgically removed as blind and painful. This limited (and selective) view of its pathology has been substantially updated by the study of more typical glaucoma eyes donated to eye banks or obtained at autopsy [9]. Excavation of the optic nerve head is now understood to consist of the combination of RGC axon loss and remodeling of the supporting connective tissue of the lamina cribrosa. Non-glaucoma forms of RGC disease, called optic atrophies, cause axon loss, but do not exhibit optic nerve head deepening, since there is no connective tissue remodeling as occurs in glaucoma. While this difference can be appreciated in clinical imaging studies that show excavation in glaucoma but not ischemic optic neuropathy [10]. The lack of lamina remodeling is seen in monkeys that undergo optic nerve transection, while remodeling is dramatic in experimental monkey glaucoma [11]. The vital role of lamina cribrosa regional structure and its remodeling in glaucoma injury is shown by the greater loss of RGC passing through the weaker upper and lower zones of the nerve head [12].

Initial animal glaucoma models used obstruction of the outflow of aqueous humor from the anterior chamber to increase IOP. Such methods included α -chymotrypsin injection in small monkeys [13] and cotton fiber injection in rabbits [14], for the first time producing histological changes that simulated aspects of human glaucoma pathology, including axon damage at the nerve head and specific RGC death. The use of animal glaucoma models was greatly enhanced by the development of tonometric devices that accurately measured IOP in both humans and animals. Goldman's tonometer [15] revolutionized the science of IOP assessment, and a hand-held

version was soon developed for easier use in animals with eyes similar to human dimensions [16]. Unfortunately, the most common animal used in ophthalmic research in the twentieth century, the rabbit, has retinal and nerve head structure quite different from the human. In addition, rabbits proved highly resistant to undergoing RGC loss in the manner typical for glaucoma [17, 18].

Gaasterland and Kupfer [19] elevated IOP in monkey eyes by laser treatment of the trabecular meshwork, and, after definition of useful laser parameters [20], this approach continues to be used as a glaucoma model. The rhesus monkey eye is similar in many key aspects to human eyes, though only 2/3 the size; in many experiments, the use of young monkeys makes the features more similar to those of glaucoma in children or young adults. The optics of large monkey eyes are similar enough to the human that standard clinical imaging devices can be utilized.

The cost of monkeys and the desire to perform experiments with sufficient numerical power to test treatment hypotheses led to a search for small animal glaucoma models. After substantial trial and error, Morrison showed that hypertonic saline injection into small outflow channels in the rat would not only cause extended IOP elevation, but produce axon injury at the nerve head and selective RGC loss [21]. There was resistance to use of rodent glaucoma models, since the key injury site, the lamina cribrosa, was devoid of connective tissue and this was thought to preclude typical axon injury. However, in rats and mice the astrocytes of the nerve head are configured in a pattern similar to that of the astrocyte-covered laminar connective tissue beams in the primate eye. The IOP-related stress and strain on axons and other tissues of the nerve head therefore seem to duplicate in a sufficiently valid way the transmission of damage to RGC axons. Seemingly, this derives from the proportionately smaller stress in such small eyes which is, nonetheless, delivered at the same location. A group of additional methods to raise the IOP in rats were then reported, including laser angle treatment [22] and injections of viscoelastic substances [23].

It was hoped that mouse glaucoma models could be developed to utilize the power of murine genetics and gene alteration techniques, but two obstacles slowed its progress. First, methods that succeeded in rats were more challenging in mice (hypertonic saline and laser). The development of the Tonolab (rebound) tonometer [24] solved this problem and replaced the cumbersome puncturing of the mouse eye with needles connected to a transducer. Second, the Tonopen that was at least usable to assess IOP in rats was useless in mice. The suggestion that microbead obstruction of the outflow might be effective by Sappington and coworkers [25] has led to refinements of this approach with high rates of chronic IOP elevation [26].

Spontaneous glaucoma in animals has also been exploited effectively. Animal strains with a glaucoma-like phenotype occur in dogs,

chickens, and rabbits [17, 27, 28], but it was the recognition of the DBA/2J mouse strain at the Jackson Labs by John and colleagues that has been used most often to study IOP-related damage [29]. Genetically based glaucoma models avoid interventions that introduce the additional variables of induced inflammation and foreign body immune reaction. The DBA-2J mouse develops typical glaucoma damage slowly, which is both a strength and a weakness, as experiments are inevitably year-long. Further, there is substantial variability in the amount of RGC damage (even between two eyes of the same mouse). By contrast, the microbead injection method produces damage in 6 weeks, which raises the interesting question: how fast is too fast? While human acute angle closure glaucoma exhibits sudden very high IOP, it is a small minority of prevalent glaucoma. Injury should occur and evolve over at least weeks to months to be similar to open angle glaucoma.

3 Important Features of Glaucoma Models

As described above, the key features of glaucoma that must be present in a model are axonal injury at the nerve head as an initial feature of damage, and, selective RGC loss with sparing of other retinal neurons. There are subtle distinctions becoming evident among models that share even these features. Optic nerve transection or crushing in the orbit (in which the major vascular supply is spared) has both key features. RGC death after these insults is within 10 days in rodents. Interestingly, we have become aware that the mechanisms leading to RGC death may be both shared and different between crush and elevated IOP models. Welsbie et al. found that dual leucine kinase inhibitor, tozacertib, prolongs RGC life after both crush and experimental glaucoma in rodents—indicating a benefit by inhibiting the same pathological pathway [30]. But, another neuroprotective strategy, oral delivery of the transforming growth factor β inhibitor, losartan, is protective in glaucoma, but not after optic nerve crush [31].

The laser-induced ischemic optic neuropathy model in rat and monkey features RGC injury at the nerve head and selective RGC loss is present, but is not a glaucoma model, as the injury produces acute vascular and tissue damage with nerve head bleeding and swelling. Studies in which IOP is raised high enough to cut off blood flow to the retina have been called “acute IOP models,” as if they are related to glaucoma, but ischemia—reperfusion causes massive retinal damage to much more than RGC and has little in common with glaucoma. Further afield, reports have claimed to be “glaucoma” models when NMDA is injected into the vitreous, on the theory that there was evidence (now largely discredited) that glutamate toxicity is an important feature of glaucoma damage. The production of RGC damage by a mechanism that injures or

kills RGC bodies in the retina is not a glaucoma a model—it is a model of optic neuropathy. There have been some reports of animal models that are said to be “low tension” glaucoma models. In general, these reports show RGC loss, but none has yet shown that the model has an initiating axonal injury detectable at the nerve head. As such, they are more similar to human Leber’s optic atrophy rather than glaucoma. Humans differ greatly in their susceptibility to the effects of IOP and other risk factors in producing glaucoma injury. It is relevant to this feature of glaucoma that some mouse strains are more or less sensitive to IOP-induced stress than others [26].

Among the glaucoma models, both spontaneous (genetic) and induced, the degree of RGC loss has varied substantially. When a model induces loss of only a small proportion of RGC, the number of animals in a group must be very large to determine if there has been an effect. If most RGC die, again it may be difficult to produce a protective effect without a truly huge protective power. Glaucoma models that generate loss of 25-50% of RGC in months of follow-up seem most useful. It is equally important that the variability among animals in damage be low, since sample size is driven by the variance about the mean level of RGC loss.

Every animal, IOP-elevation glaucoma model yet studied produces an enlargement of the axial globe length [32]. In part, this is an effect of the thinner and younger animal sclera. IOP-generated stress delivered to the nerve head through the sclera is a key feature of glaucoma pathogenesis. If globe enlargement were unknown in human eyes, this would be an important difference in the models. It is well known, however, that the eyes of children with glaucoma enlarge (buphthalmos) and the pattern of visual field loss that is produced in their larger eyes are similar to that in adult glaucoma [33]. Nonetheless, it is increasingly clear that older age both potentiates and modifies the rate of glaucoma injury in both human and animal eyes. Strains of mice differ among each other in whether older mice are more or less susceptible to induced glaucoma injury [34]. There have been some attempts to study the effect of age on mice and even to exploit a free-living colony of monkeys that has been reported to develop spontaneous glaucoma in older age [35].

The number and distribution of RGC differs among mammalian species, with 40,000 RGC per eye in mice to 1–2 million in humans. The human RGC population is dominated by midget cells synapsing nearly one to one with cones in the foveal zone, while a broad diversity of RGC types in mice lacks this type or any fovea at all. It is only recently that selectively fluorescent RGC of various types in mice have been available to study how differently each RGC phenotype responds to IOP damage [36]. There is a known pattern of human glaucoma loss of RGC, affecting those with axons passing through the upper and lower poles of the optic nerve head

[9]. There is also evidence strongly supporting greater death among larger RGC in human and monkey eyes [37], and more recently in mice as well. But, the “hourglass” pattern of RGC loss at the optic nerve level is not shared by rat or mouse glaucoma models [38], perhaps due to the many anatomic differences in both RGC and ocular features. Species-related differences in anatomy and physiology are not necessarily detrimental in glaucoma models. We may learn what features and risk factors are operative by utilizing the effects of such differences on RGC injury. For example, if the thinner sclera of mice were found to produce similar strain from a given IOP level compared with the monkey, and RGC damage was similar in magnitude, it implies that physiological strain, not anatomical scleral thickness, is the operative factor.

Some rodent models of glaucoma have been criticized due to the potential influence of secondary effects produced by their induction of IOP elevation. For example, it has been claimed that some models are less useful because they induce “inflammation.” Every animal model in which IOP is increased sufficiently to kill RGC produces secondary effects that are, while undesirable, largely unavoidable. These include globe enlargement, corneal ectasia and vascularization, sclera shrinkage and internal hemorrhage from laser delivery, and microscopic or macroscopic infiltration by immune system cells. Immune-mediated mechanisms are often cited as participating in some parts of glaucoma pathogenesis [39]. Thus, it is not whether “inflammation” is present, but which aspects and how severe are its influences that are relevant.

4 Outcome Measures in Glaucoma Models

Since RGC loss is glaucoma’s primary pathology, counts of RGC body and/or axon loss are the most important measures to assess effects in glaucoma models. Sampling of at least 10% of somas or axons is needed due to normal variability in number of RGC and variation in damage levels in any model. RGC loss can proceed at slightly different rates and through different mechanisms in the soma and axon [40], so evaluation of both zones is useful. Specific genetic alterations in mice can produce loss of soma with axon preservation [41], or vice versa [42]. Of the neurons in the RGC layer of the retina, approximately half are amacrine cells, so that simple nuclear (DAPI, NeuN) counting is inadequate. Either backfilling from the axon with dye, or specific RGC labels are needed, and whole mounted retina is the ideal sampling frame, rather than sectioned retina. Backfilling has a high rate of RGC identification early after dye injection, but with RGC death, macrophages engulf fluorescent material and must be manually differentiated for accurate counts [43]. Furthermore, attempts at backfilling after IOP elevation is established may give unpredictable labeling due to

axonal transport obstruction. Many epitopes are characteristic of normal RGC and are easily labeled (e.g., Brn3, Thy1), avoiding the backfilling procedure. However, many RGC genes downregulate rapidly after IOP elevation. The more robust candidates used at present to avoid this problem are RBPMs [44] and β -tubulin [45]. Random sample axon counting remains the standard to assess RGC fiber loss [26]. Qualitative grading is inadequate for the measurement of important outcomes. Automated methods to count RGC bodies [46] or axons [47] have been proposed and seem adequate to count normal tissue, but, with degeneration, these methods require considerable manual intervention to avoid misidentification. In models where IOP elevation is the primary insult, cumulative exposure to IOP over time during the experiment should be taken into account statistically in evaluating RGC loss [48].

5 Translation of Animal Model Data into Human Clinical Trials

There has been critical commentary attempting to explain why apparently neuroprotective effects seen in animal models do not translate into successful human clinical trial outcomes [49]. This seems to be an apt question for brain-centered diseases (stroke, Alzheimer) for which many attempted clinical studies have not succeeded. In glaucoma, there are only two known human clinical trials. The first, using memantine orally, was concluded without any published reported finding. The second, involving brimonidine eye drops [50], did not actually duplicate any animal experimental result, and had a variety of weaknesses that have suggested the need for more investigation. In a longer review, the issue of how to perform neuroprotective glaucoma trials successfully in patients was discussed [51]. It is reasonable to consider what factors might lead to non-confirmation of animal glaucoma model results in humans. Clearly, many ocular and systemic features separate rodents (and even monkeys) from humans. The animal models thus far all occur in months, while the human disease moves generally more slowly over years. Protection of RGC for days to weeks is therefore inherently easier than doing so for longer periods. Slowing of RGC death must be profound if it is not complete protection. Much animal research is performed with young animals, while glaucoma in general has increasing incidence with older age. In many animal experiments a full dose-response evaluation is not performed, or, the beneficial effect is only seen with exposures that are toxic or generate unreasonable side effects. In model systems, treatment is often simultaneous with IOP elevation, while in humans the disease can be established and ongoing. Only recently have functional endpoints been added to animal glaucoma studies, which are needed to supplement simple RGC counting,

which may enumerate cell bodies or axons that are no longer useful. To avoid some of these problems, it may be prudent to carry out therapeutic studies in more than one animal model prior to initiating human trials.

References

1. Foster PJ, Buhmann R, Quigley HA, Johnson GJ (2002) The definition and classification of glaucoma in prevalence surveys. *Br J Ophthalmol* 86:238–242
2. Tham YC, Li X, Wong TY, Quigley HA, Aung T, Cheng CY (2014) Global prevalence of glaucoma and projections of glaucoma burden through 2040: a systematic review and meta-analysis. *Ophthalmology* 121:2081–2090
3. Leske MC, Heijl A, Hussein M, Bengtsson B, Hyman L, Komaroff E, Early Manifest Glaucoma Trial Group (2003) Factors for glaucoma progression and the effect of treatment: the early manifest glaucoma trial. *Arch Ophthalmol* 121:48–56
4. Quigley HA, Addicks EM, Green WR, Mautner AE (1981) Optic nerve damage in human glaucoma. II. The site of injury and susceptibility to damage. *Arch Ophthalmol* 99:635–649
5. Quigley HA, Nickells RW, Kerrigan LA, Pease ME, Thibault DJ, Zack DJ (1995) Retinal ganglion cell death in experimental glaucoma and after axotomy occurs by apoptosis. *Invest Ophthalmol Vis Sci* 36:774–786
6. Kielczewski JL, Pease ME, Quigley HA (2005) The effect of experimental glaucoma and optic nerve transection on amacrine cells in the rat retina. *Invest Ophthalmol Vis Sci* 46:3188–3196
7. Yücel YH, Zhang Q, Gupta N, Kaufman PL, Weinreb RN (2000) Loss of neurons in magnocellular and parvocellular layers of the lateral geniculate nucleus in glaucoma. *Arch Ophthalmol* 118:378–384
8. Chaturvedi N, Hedley-Whyte ET, Dreyer EB (1993) Lateral geniculate nucleus in glaucoma. *Am J Ophthalmol* 116:182–188
9. Quigley HA, Addicks EM, Green WR (1982) Optic nerve damage in human glaucoma. III. Quantitative correlation of nerve fiber loss and visual field defect in glaucoma, ischemic neuropathy, disc edema, and toxic neuropathy. *Arch Ophthalmol* 100:135–146
10. Danesh-Meyer HV, Boland MV, Savino PJ, Miller NR, Subramanian PS, Girkin CA, Quigley HA (2010) Optic disc morphology in open angle glaucoma compared with anterior ischemic optic neuropathies. *Invest Ophthalmol Vis Sci* 51:2003–2010
11. Morrison JC, Dorman-Pease ME, Dunkelberger GR, Quigley HA (1990) Optic nerve head extracellular matrix in primary optic atrophy and experimental glaucoma. *Arch Ophthalmol* 108:1020–1024
12. Quigley HA, Addicks EM (1981) Regional differences in the structure of the lamina cribrosa and their relation to glaucomatous optic nerve damage. *Arch Ophthalmol* 99:137–143
13. Kalvin NH, Hamasaki DI, Gass JD (1966) Experimental glaucoma in monkeys. I. Relationship between intraocular pressure and cupping of the optic disc and cavernous atrophy of the optic nerve. *Arch Ophthalmol* 76:82–93
14. de Carvalho CA (1962) Histopathology of retina and optic nerve with experimental glaucoma. *Arch Ophthalmol* 67:483–487
15. Goldmann H (1954) A new applanation tonometer. *Bull Mem Soc Fr Ophthalmol* 67:474–477
16. Kaufman PL, Davis GE (1980) “Minified” Goldmann applanating prism for tonometry in monkeys and humans. *Arch Ophthalmol* 98:542–546
17. Greaves DP, Perkins ES (1951) Buphthalmos in rabbit. *Br J Ophthalmol* 35:232
18. Quigley HA, Addicks EM (1980) Chronic experimental glaucoma in primates. I. Production of elevated intraocular pressure by injection of autologous red blood cells. *Invest Ophthalmol Vis Sci* 19:126–136
19. Gaasterland D, Kupfer C (1974) Experimental glaucoma in the rhesus monkey. *Investig Ophthalmol* 13:455–457
20. Quigley HA, Hohman RM (1983) Laser energy levels for trabecular meshwork damage in the primate eye. *Invest Ophthalmol Vis Sci* 24:1305–1307
21. Morrison JC, Moore CG, Deppmeier LM, Gold BG, Meshul CK, Johnson EC (1997) A rat model of chronic pressure-induced optic nerve damage. *Exp Eye Res* 64:85–96
22. Levkovitch-Verbin H, Quigley HA, Martin KRG, Valenta D, Kerrigan-Baumrind LA, Pease ME (2002) Translimbal laser

- photocoagulation to the trabecular meshwork as a model of glaucoma in rats. *Invest Ophthalmol Vis Sci* 43:402–410
23. Moreno MC, Marcos HJ, Oscar Croxatto J, Sande PH, Campanelli J, Jaliffa CO, Benozzi J, Rosenstein RE (2005) A new experimental model of glaucoma in rats through intracameral injections of hyaluronic acid. *Exp Eye Res* 81:71–80
 24. Pease ME, Hammond JC, Quigley HA (2006) Manometric calibration and comparison of TonoLab and TonoPen tonometers in rats with experimental glaucoma and in normal mice. *J Glaucoma* 15:512–519
 25. Sappington RM, Carlson BJ, Crish SD, Calkins DJ (2010) The microbead occlusion model: a paradigm for induced ocular hypertension in rats and mice. *Invest Ophthalmol Vis Sci* 51:207–216
 26. Cone FE, Gelman SE, Son JL, Pease ME, Quigley HA (2010) Differential susceptibility to experimental glaucoma among 3 mouse strains using bead and viscoelastic injection. *Exp Eye Res* 91:415–424
 27. Gelatt KN, Peiffer RL Jr, Gwin RM, Sauk JJ Jr (1976) Glaucoma in the beagle. *Trans Sect Ophthalmol Am Acad Ophthalmol Otolaryngol* 81:OP636–OP644
 28. Albrecht May C (2008) Comparative anatomy of the optic nerve head and inner retina in non-primate animal models used for glaucoma research. *Open Ophthalmol J* 2:94–101
 29. John SW, Smith RS, Savinova OV, Hawes NL, Chang B, Turnbull D, Davissin M, Roderick TH, Heckenlively JR (1998) Essential iris atrophy, pigment dispersion, and glaucoma in DBA/2J mice. *Invest Ophthalmol Vis Sci* 39:951–962
 30. Welsbie DS, Yang Z, Ge Y et al (2013) Functional genomic screening identifies dual leucine zipper kinase as a key mediator of retinal ganglion cell death. *Proc Natl Acad Sci U S A* 110:4045–4050
 31. Quigley HA, Pitha IF, Welsbie DS, Nguyen C, Steinhart MR, Nguyen TD, Pease ME, Oglesby EN, Berlinicke CA, Mitchell KL, Kim J, Jefferys JJ, Kimball EC (2015) Losartan treatment protects retinal ganglion cells and alters scleral remodeling in experimental glaucoma. *PLoS One* 10:e0141137
 32. Nguyen C, Cone FE, Nguyen TD, Coudrillier B, Pease ME, Steinhart MR, Oglesby EN, Quigley HA (2013) Studies of scleral biomechanical behavior related to susceptibility for retinal ganglion cell loss in experimental mouse glaucoma. *Invest Ophthalmol Vis Sci* 54:1767–1780
 33. Robin AL, Quigley HA, Pollack IP et al (1979) An analysis of visual acuity, visual fields, and disk cupping in childhood glaucoma. *Am J Ophthalmol* 88:847–858
 34. Steinhart MR, Cone-Kimball E, Nguyen C, Nguyen TD, Pease ME, Chakravarti S, Oglesby EN, Quigley HA (2014) Susceptibility to glaucoma damage related to age and connective tissue mutations in mice. *Exp Eye Res* 119:54–60
 35. Dawson WW, Brooks DE, Dawson JC, Sherwood MB, Kessler MJ, Garcia A (1998) Signs of glaucoma in rhesus monkeys from a restricted gene pool. *J Glaucoma* 7:343–348
 36. El-Danaf RN, Huberman AD (2015) Characteristic patterns of dendritic remodeling in early-stage glaucoma: evidence from genetically identified retinal ganglion cell types. *J Neurosci* 35:2329–2343
 37. Quigley HA, Sanchez RM, Dunkelberger GR, L'Hernault NL, Baginski TA (1987) Chronic glaucoma selectively damages large optic nerve fibers. *Invest Ophthalmol Vis Sci* 28:913–920
 38. Nguyen C, Midgett D, Kimball EC, Steinhart MR, Nguyen TD, Pease ME, Oglesby EN, Quigley HA (2017) Measuring deformation in the mouse optic nerve head and peripapillary sclera. *Invest Ophthalmol Vis Sci* 58(2):721–733
 39. Wax MB, Tezel G (2009) Immunoregulation of retinal ganglion cell fate in glaucoma. *Exp Eye Res* 88:825–830
 40. Levkovitch-Verbin H, Makarovskiy D, Vander S (2013) Comparison between axonal and retinal ganglion cell gene expression in various optic nerve injuries including glaucoma. *Mol Vis* 19:2526–2541
 41. Bull ND, Chidlow G, Wood JP, Martin KR, Casson RJ (2012) The mechanism of axonal degeneration after perikaryal excitotoxic injury to the retina. *Exp Neurol* 236:34–45
 42. Libby RT, Li Y, Savinova OV, Barter J, Smith RS, Nickells RW, John SW (2005) Susceptibility to neurodegeneration in a glaucoma is modified by Bax gene dosage. *PLoS Genet* 1:17–26
 43. Blair M, Pease ME, Hammond J, Valenta D, Kielczewski J, Levkovitch-Verbin H, Quigley H (2005) Effect of glatiramer acetate on primary and secondary degeneration of retinal ganglion cells in the rat. *Invest Ophthalmol Vis Sci* 46:884–890
 44. Kwong JM, Quan A, Kyung H, Piri N, Caprioli J (2011) Quantitative analysis of retinal ganglion cell survival with Rbpm immunolabeling in animal models of optic neuropathies. *Invest Ophthalmol Vis Sci* 52:9694–9702

45. Chen H, Wei X, Cho KS, Chen G, Sappington R, Calkins DJ, Chen DF (2011) Optic neuropathy due to microbead-induced elevated intraocular pressure in the mouse. *Invest Ophthalmol Vis Sci* 52:36–44
46. Danias J, Shen F, Goldblum D, Chen B, Ramos-Esteban J, Podos SM, Mittag T (2002) Cytoarchitecture of the retinal ganglion cells in the rat. *Invest Ophthalmol Vis Sci* 43:587–594
47. Marina N, Bull ND, Martin KR (2010) A semi-automated targeted sampling method to assess optic nerve axonal loss in a rat model of glaucoma. *Nat Protoc* 5:1642–1651
48. McKinnon SJ, Lehman DM, Kerrigan-Baumrind LA, Merges CA, Pease ME, Kerrigan DF, Ransom NL, Tahzib NG, Reitsamer HA, Levkovitch-Verbin H, Quigley HA, Zack DJ (2002) Caspase activation and amyloid precursor protein cleavage in rat ocular hypertension. *Invest Ophthalmol Vis Sci* 43:1077–1087
49. Levin LA, Danesh-Meyer HV (2010) Lost in translation: bumps in the road between bench and bedside. *JAMA* 303:1533–1534
50. Krupin T, Liebmann JM, Greenfield DS, Ritch R, Gardiner S, Low-Pressure Glaucoma Study Group (2011) A randomized trial of brimonidine versus timolol in preserving visual function: results from the low-pressure glaucoma treatment study. *Am J Ophthalmol* 151:671–681
51. Quigley HA (2012) Clinical trials for glaucoma neuroprotection are not impossible. *Curr Opin Ophthalmol* 23:144–154

Chapter 2

Hypertonic Saline Injection Model of Experimental Glaucoma in Rats

John C. Morrison, Elaine C. Johnson, and William O. Cepurna

Abstract

A reliable method of creating chronic elevation of intraocular pressure (IOP) in rodents is an important tool in reproducing and studying the mechanisms of optic nerve injury that occur in glaucoma. In addition, such a model could provide a valuable method for testing potential neuroprotective treatments. This paper outlines the basic methods for producing obstruction of aqueous humor outflow and IOP elevation by injecting hypertonic saline (a sclerosant) into the aqueous outflow pathway. This is one of several rodent glaucoma models in use today. In this method, a plastic ring is placed around the equator of the eye to restrict injected saline to the limbus. By inserting a small glass microneedle in an aqueous outflow vein in the episclera and injecting hypertonic saline toward the limbus, the saline is forced into Schlemm's canal and across the trabecular meshwork. The resultant inflammation and scarring of the anterior chamber angle occurs gradually, resulting in a rise in IOP after approximately 1 week. This article will describe the equipment necessary for producing this model and the steps of the technique itself.

Key words Hypertonic saline, Brown Norway rat, Intraocular pressure, Glaucoma, Aqueous humor, Episcleral veins, Optic nerve, Chronic angle closure

1 Introduction

In the eye, the balance between the rate of aqueous humor formation and the rate of aqueous outflow through the anterior chamber angle governs intraocular pressure (IOP). Obstruction of aqueous outflow is the primary mechanism of IOP elevation in glaucoma and most experimental models of IOP elevation rely on creating this situation. Increasing resistance to aqueous outflow can be achieved by scarring these pathways in the angle using a laser [1–6], by injecting microspheres or other substances in the anterior chamber [7–10], and, as described in this article, by producing scarring through injection of hypertonic saline, a sclerosing agent, via aqueous humor-containing veins located in the episclera [11, 12]. This article describes the materials and steps used in producing this model. This technique relies on excellent,

high-power magnification and illumination, preferably using a surgical microscope with a foot-powered focus, and meticulous, steady surgical technique. A plastic ring that constricts all episcleral veins draining the angle (other than that being injected) is critical. This is followed by careful exposure of the vein and insertion of a fine glass microneedle, through which the saline is injected, either manually or with a syringe pump. Elevation of IOP generally occurs gradually and depends on recovery of normal aqueous outflow in conjunction with scarring of the anterior chamber angle. When carefully monitored through measurement of IOP in awake animals, the pressure response, although variable, can show excellent correlation with histologic evidence of optic nerve damage [13], functional abnormalities [14], and effects on gene expression responses within the optic nerve head and retina [15–18]. Methods for measuring IOP in rodents and evaluating subsequent optic nerve damage are described in several other articles and general summaries present in the literature [13, 19–26].

2 Materials

1. Microscope. This must provide excellent magnification and clarity, ranging up to 40 \times . A non-manual focusing capability is essential, leaving both hands free for surgery (*see Note 1*).
2. Fine jewelers forceps for grasping tissue and vein (Dumont #5SF Forceps, Fine Science Tools 11252-00, Foster City, CA, USA) (*see Note 2*).
3. Curved, reverse-action jewelers forceps for holding needle. (Dumont Self-Closing #7 Curved Forceps, Fine Science Tools). These should be grooved on the inside to provide adequate needle fixation (*see Note 3*).
4. A plastic ring (5.5 mm inner diameter and 1.8 mm width) to provide annular compression of episcleral vessels. A gap in the ring allows it to be spread apart and then placed around the equator of the eye. An inner groove allows the ring to sit stably on the eye in this position (Fig. 1.) (*see Note 4*).
5. Microneedle. This consists of a glass microneedle (approximately 50–80 μm outer diameter) constructed from a pulled glass micropipette, and P-50 polyethylene tubing (Intramedic™ Polyethylene Tubing, PE 50, 427411, Becton, Dickinson and Company, Franklin Lakes, New Jersey, USA) that has been heated and pulled to a fine taper. A portion of the needle is placed inside the tubing and then the two are joined by a drop of hard-drying epoxy cement.

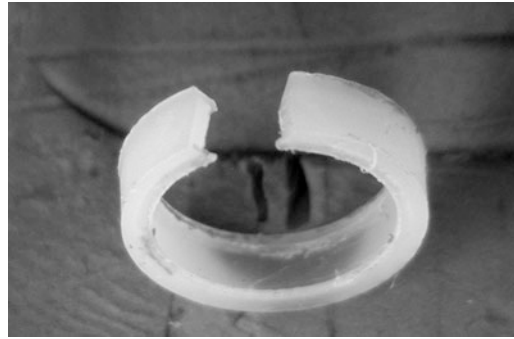


Fig. 1 Plastic ring used to constrict episcleral vessels at the equator and confine hypertonic saline injection to the limbal vasculature, Schlemm's canal, and the trabecular meshwork. Note inner groove to allow stable contact with the globe equator and gap cut out to allow ring to straddle the vein to be injected

6. Fine-tipped Vannas Capsulotomy Scissors Curved Storz E3387 Bausch and Lomb Surgical, Inc. (Rancho Cucamonga, CA) (*see Note 5*).
7. Hypertonic saline: 1.5 M–2.0 M NaCl in distilled water. The final solution is then filtered through a millipore filter into 1 cc syringe (*see Note 6*).
8. Rat cocktail anesthetic: 25 mg/mL ketamine, 5 mg/mL xylazine, 1 mg/mL acepromazine in sterile water.

3 Methods

1. Anesthesia. Intraperitoneal injection of a rat cocktail anesthetic (1.5 mL/kg). This provides excellent anesthesia and immobilization (*see Note 7*).
2. The choice of which eye to inject will depend on the anatomy of the episcleral vasculature. This is dominated by a circular, limbal plexus that consists of a single arteriole (fed by anterior ciliary arterioles that may be difficult to identify in some eyes) and an interconnected plexus of veins that are responsible for aqueous humor drainage [11]. Several radially oriented veins emerge from this plexus to flow posteriorly (Fig. 2). The goal is to isolate one of these for injection. Ideally, the best vessel to choose is the one that is relatively large and has few branches, so that it will be possible to occlude all vessels draining the limbal plexus with the plastic ring, sparing the target vein (*see Note 8*).
3. Placing the ring around the equator is best performed prior to positioning the animal under the microscope. The plastic ring should have a gap cut out, which allows the ring to “straddle” the vein to be injected and makes it possible to spread the ring

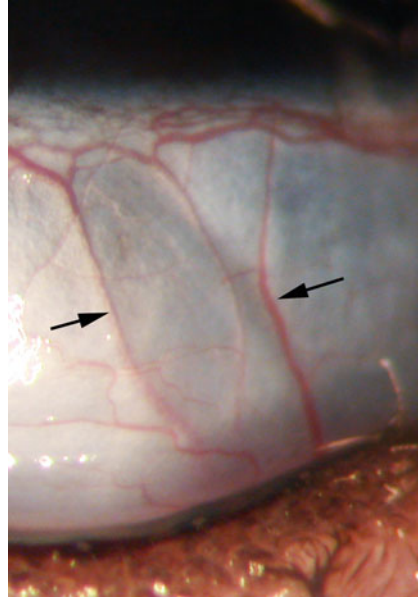


Fig. 2 Normal rat limbus showing 2 radial episcleral vessels (*arrows*) draining blood (and aqueous) from the limbal venous plexus (*top*). Either of these vessels could be cannulated for hypertonic saline injection. The more visible one on the right is closely adherent to the conjunctival surface, and requires more careful dissection before inserting the microneedle, as discussed in **Note 13**

slightly (using a small hemostat) and slip it around the eye. With the ring at the equator of the globe, it is then slipped off the hemostat and allowed to hug the eye. In an ideal situation, placing the gap in the ring over the vein to be injected will allow access to the vein, with the ring compressing all other radial vessels against the globe. In this manner, hypertonic saline injected toward the limbus will be forced into the limbal vascular plexus and then into Schlemm's canal via collector channels.

4. The animal should be positioned under the microscope so that the surgeon can orient the microneedle toward the limbus, with the tip pointed away from the surgeon. This is best accomplished by laying the animal prone (on its stomach) with the nose pointed either to the right or left. Since most injections are performed superiorly (*see Note 9*), this means that for injecting the right eye the animal's nose should be pointed to the left, and for a left eye the animal should be oriented to the right (*see also Note 10* for additional points on hand positioning).
5. The eye should be rotated down, or away from the surgeon, to allow the best access. This can be performed by an assistant who grasps the inferior limbus with a fine-toothed forceps. The upper lid is held up by the surgeon while performing the

conjunctival dissection. The disadvantage of this approach is that it is sometimes difficult for the assistant to provide steady fixation if the dissection is unusually tedious. This also takes the assistant away from performing other tasks (*see Note 11*).

6. Conjunctival dissection. The conjunctival incision is performed radially, parallel to the vein, using the Vannas microscissors. The jeweler's forceps provides precise tissue control (*see Note 12*).
7. Exposing the vein. Because of the precision necessary to insert the needle into these extremely small veins, all connective tissue must be dissected off the vein wall to avoid making a false passage outside the vessel lumen. Grasping a small amount of tissue adjacent to the vein with the jeweler's forceps and pulling it to the side will indicate if all of this tissue has successfully been removed. If not, remaining bands can then be incised with the microscissors placed adjacent to and parallel to the vessel (*see Note 13*).
8. Insertion of microneedle. Once the vessels are properly exposed and occluded by the ring and accessory clips (if needed), the goal is to stabilize the vessel with the jeweler's forceps and insert the microneedle into the vein. To minimize tremor, the hands should be well supported, which allows them to relax. Keeping the backs of the right and left thumbs in contact will help the hands to work together. By orienting the needle shaft, with bevel up, parallel to and immediately on the top of the vessel, the tip of the needle should engage the vessel wall first and can then be advanced into the lumen. To avoid accidentally going entirely through the vessel, the heel of the needle can be lowered slightly once the tip enters the vessel, which will help guide it inside the lumen (*see Note 14*).
9. Injecting hypertonic saline. Once the needle is safely in the lumen, the injection can begin. This may be done manually by the assistant using a 1 cc syringe. However, the injection force is hard to standardize. We have found that a syringe pump, adjusted to deliver 50 μl of fluid over 10 s, is a good alternative, and this can even be activated by the surgeon using a foot switch if necessary (*see Note 15*).

Typically, a good injection will produce immediate blanching of the perilimbal vascular plexus. In addition to this, the anterior chamber will deepen, indicating that the hypertonic saline is being forced into Schlemm's canal and across the trabecular meshwork, into the eye. Finally, a lens opacity, which is generally asymmetric, develops. This is most likely secondary to the hypertonicity of the saline, and clears during the first few hours following surgery.

10. After injection, the vein is occluded by the jeweler's forceps for 30 s, to help keep the saline in the limbal veins. Erythromycin

ointment is then instilled in the conjunctival sac and the animal is allowed to recover. A mild amount of conjunctival injection (redness) during the first few days after surgery is not uncommon, and the intraocular pressure may be lower than normal, indicating a mild inflammatory reaction. Typically, the IOP will begin to increase above normal by 7–10 days after surgery, as aqueous humor formation recovers and the scarring of the anterior chamber angle (and increased outflow resistance) develop (*see Note 16*).

In animals housed in light:dark conditions, elevated IOP may first be detected at night, due to the marked diurnal fluctuation of IOP in the rat [13, 27]. These pressures alone may be sufficient to produce significant optic nerve damage. Simply assessing IOP during the day (or light phase of the cycle) could therefore miss important pressure elevations. Looking at injury only in eyes with elevated “day time” IOPs may likely reveal extensive injury, and may lead to the false impression that nerve injury from elevated IOP in these animals is an “all or none” phenomenon.

4 Notes

1. A standard, bench-top dissecting microscope with a fiber-optic light source may be adequate, as long as the focus range is appropriate and a remote, most likely foot-operated, focusing capability is added. This also must allow enough free bench space to allow proper animal positioning and room for the assistant, if needed. An ophthalmic surgical microscope, often available as surplus from a dedicated operating room, is a better alternative. These are floor-mounted, which frees up bench space, and have the appropriate magnification and illumination, which is essential for working at high magnification.
2. It is essential to use forceps with the finest tips available. Jewelers, which have smooth tips, allow accurate grasping of the conjunctiva and the episcleral vein. A toothed forceps will be too crude for accurate handling of these delicate tissues.
3. The curved nature of this forceps allows access to the superior aspect of eye. This is because the surgeon needs to reach over the head to achieve this access and at the same time point the needle toward the limbus. This forceps needs to be customized, by placing a groove along the inner aspect of each face of the forceps. With this, it is possible to grasp the glue-joint between the needle and tubing with 4-point contact. This prevents rocking of the needle that would occur if each face was flat, providing only 2-point contact.

4. This ring can be made of any flexible plastic with good memory characteristics. We primarily use Delrin (DuPont, Wilmington, DE). While these can be entirely machined on a lathe, we generally make them by heating the delrin and forcing it into a brass injection mold. We then machine the outer dimensions to final specifications on a lathe (Fig. 1.).
5. The finest tip micro scissors are essential. We have found that Storz provides the best of these. The fine tips are essential to allow accurate dissection and removal of fibrous tissue from the wall of the vessel.
6. Filtering the hypertonic saline removes impurities that might obstruct the very fine needle lumen.
7. Anesthesia with rat cocktail allows unrestricted animal positioning. While anesthesia with inhalational isoflurane is adequate, this requires a stationary nose cone that restricts the ability to position the animal correctly for hypertonic saline injection and also limits bench-top space, which interferes with surgery and the assistant's access to the eye.
8. Typically, one eye will always have a more favorable vasculature than the other. Generally, the superior vessels are larger. This, combined with the fact that there is better access to the superior bulbar conjunctiva (beneath the upper lid), dictates that the majority of injections will be performed superiorly.
9. With the animal on its stomach in this position, the surgeon must effectively reach over the fellow eye and top of the animal's head to gain access to the eye to be injected. The curved nature of the self-closing forceps, which holds the microneedle, allows the surgeon to do this, with the tip pointing away from the surgeon.
10. The extremely fine surgical control required to insert the needle into the vein also means that any source of tremor should be eliminated. This is accomplished by placing a small platform (approximately 0.5 in. high) against the side of the animal's head on the side of the surgeon. This serves as a convenient hand and wrist rest, and allows the hands to be fully relaxed. As the forceps self closes on the needle, the surgeon does not need to actively "pinch" or hold the forceps shut, which eliminates another source of tremor.
11. An alternative is a self-retaining wire speculum (Fig. 3). Constructed from a paper clip or similar gauge wire, this is placed into the inferior fornix, with the feet of the retainer on the table. Placing a weight on this depresses the wire into the inferior fornix and rotates the eye down. This will free up the assistant to concentrate on anesthetic injection and preparation of the next animal, while the surgeon performs the conjunctival dissection.



Fig. 3 Wire lid retainer shaped to fit into the inferior fornix. Lead weight (foreground) creates downward pressure and rotates eye down for dissection and injection, eliminating the need for an assistant to actively rotate and stabilize the eye

12. The microvasculature of many eyes is not ideal and simple positioning of the ring will not always occlude all vessels adequately. If not corrected, injected hypertonic saline will simply escape via the non-occluded vessel and will not be forced into Schlemm's canal and the trabecular meshwork. This is a common cause of injection "failure." In this situation, we have found that vascular microclips modified to a point can be used to occlude specific vessels during this dissection (S&T Vascular Clamps, Fine Science Tools 00396-01, Foster City, CA) [22].
13. In some instances, the vessel wall and the conjunctiva are closely adherent, and very careful microdissection is required to expose the vessel wall. To avoid cutting into the vessel, it is best to open the scissors as little as possible before each cut. This prevents the vessel wall from getting between the scissors blades. This same technique can be used whenever precise microdissection is performed with these scissors. For this to be effective, it is essential that the scissors be as sharp as possible and cut cleanly to their absolute tip. As these delicate instruments are easily damaged and wear out quickly, even with normal use, it is important to plan on a certain rate of attrition and always have at least one back-up pair in reserve.
14. This is the most demanding step in the procedure. The problem is to first get the tip of the needle engaged in the vessel

wall. If any adventitial tissue still adheres to the vessel, the tip will engage this, in which case advancing the needle forward will create a false passage outside the vessel lumen. Once the vessel is adequately exposed, the needle tip tends to push the vessel away, rather than engage it. This can be counteracted by delicate coordination between the hands. While trying to engage the vessel wall, the jeweler's forceps are pulled slightly toward the surgeon. This will stretch the vessel and help stabilize it. However, this also makes the vessel thinner and the lumen smaller. So, once the tip is in the vessel wall, relaxing tension on the vessel will allow the lumen to fill with blood, making it easier to insert the needle. Again, dropping the back of the needle slightly, and lifting up its tip, will make it easier to advance the needle down the lumen. This entire procedure is made easier with high magnification and good illumination, and fine control of the focus, best accomplished by the surgeon using a foot control mechanism.

15. Generally, because of the extremely delicate surgery, the surgeon will rarely get a second chance at a vein once it is entered. Because the needle sometimes gets obstructed, it is best to have a specific routine prior to the injection. This consists of initially flushing the needle just after grasping the vein, ensuring that it is patent. Then, once the needle is in the vein, it is best to use one-word signals (e.g., "Go" to start the injection, followed by "Count" once the surgeon sees that the injection is correct and timing can begin), as even talking can be enough to interfere with needle control. Injection timing can be done by the assistant, allowing the surgeon to concentrate on the needle and vein.
16. The concentration of hypertonic saline can range from 1.5 M to 2.5 M. Concentrations less than 1.5 M generally will not produce a significant scarring reaction and IOP elevation will not occur. Concentrations above 2.5 M may produce too much inflammation. This can produce ocular responses extraneous to those produced by elevated IOP. In addition, too much inflammation may result in long-term aqueous hyposecretion and failure to develop elevated IOP.

Acknowledgments

The National Institutes of Health Grants: R01EY010145 (JCM), P30EY010572 (OHSU Core Grant) and an unrestricted grant from Research to Prevent Blindness (RPB), Inc. JCM is a past RPB Senior Investigator.

References

1. Ueda J, Sawaguchi S, Hanyu T, Yaoeda K, Fukuchi T, Abe H, Ozawa H (1998) Experimental glaucoma model in the rat induced by laser trabecular photocoagulation after an intracameral injection of India ink. *Jpn J Ophthalmol* 42(5):337–344
2. Salinas-Navarro M, Alarcon-Martinez L, Valiente-Soriano FJ, Ortin-Martinez A, Jimenez-Lopez M, Aviles-Trigueros M, Villegas-Perez MP, de la Villa P, Vidal-Sanz M (2009) Functional and morphological effects of laser-induced ocular hypertension in retinas of adult albino Swiss mice. *Mol Vis* 15:2578–2598
3. Park KH, Cozier F, Ong OC, Caprioli J (2001) Induction of heat shock protein 72 protects retinal ganglion cells in a rat glaucoma model. *Invest Ophthalmol Vis Sci* 42(7):1522–1530
4. Levkovitch-Verbin H, Quigley HA, Martin KR, Valenta D, Baumrind LA, Pease ME (2002) Translimbal laser photocoagulation to the trabecular meshwork as a model of glaucoma in rats. *Invest Ophthalmol Vis Sci* 43(2):402–410
5. Gross RL, Ji J, Chang P, Pennesi ME, Yang Z, Zhang J, Wu SM (2003) A mouse model of elevated intraocular pressure: retina and optic nerve findings. *Trans Am Ophthalmol Soc* 101:163–169. discussion 169–171
6. Aihara M, Lindsey JD, Weinreb RN (2003) Experimental mouse ocular hypertension: establishment of the model. *Invest Ophthalmol Vis Sci* 44(10):4314–4320
7. Weber AJ, Zelenak D (2001) Experimental glaucoma in the primate induced by latex microspheres. *J Neurosci Methods* 111(1):39–48
8. Cone FE, Gelman SE, Son JL, Pease ME, Quigley HA (2010) Differential susceptibility to experimental glaucoma among 3 mouse strains using bead and viscoelastic injection. *Exp Eye Res* 91(3):415–424. <https://doi.org/10.1016/j.exer.2010.06.018>
9. Samsel PA, Kisiswa L, Erichsen JT, Cross SD, Morgan JE (2011) A novel method for the induction of experimental glaucoma using magnetic microspheres. *Invest Ophthalmol Vis Sci* 52(3):1671–1675. <https://doi.org/10.1167/iovs.09-3921>
10. Sappington RM, Carlson BJ, Crish SD, Calkins DJ (2010) The microbead occlusion model: a paradigm for induced ocular hypertension in rats and mice. *Invest Ophthalmol Vis Sci* 51(1):207–216. <https://doi.org/10.1167/iovs.09-3947>
11. Morrison JC, Fraunfelder FW, Milne ST, Moore CG (1995) Limbal microvasculature of the rat eye. *Invest Ophthalmol Vis Sci* 36(3):751–756
12. Morrison JC, Moore CG, Deppmeier LM, Gold BG, Meshul CK, Johnson EC (1997) A rat model of chronic pressure-induced optic nerve damage. *Exp Eye Res* 64(1):85–96. <https://doi.org/10.1006/exer.1996.0184>
13. Jia L, Cepurna WO, Johnson EC, Morrison JC (2000) Patterns of intraocular pressure elevation after aqueous humor outflow obstruction in rats. *Invest Ophthalmol Vis Sci* 41(6):1380–1385
14. Fortune B, Bui BV, Morrison JC, Johnson EC, Dong J, Cepurna WO, Jia L, Barber S, Cioffi GA (2004) Selective loss of the electroretinogram scotopic threshold response (STR) at low levels of elevated intraocular pressure in a rat model of experimental glaucoma. *Invest Ophthalmol Vis Sci* 45(supplement 2):U146
15. Guo Y, Cepurna WO, Dyck JA, Doser TA, Johnson EC, Morrison JC (2010) Retinal cell responses to elevated intraocular pressure: a gene array comparison between the whole retina and retinal ganglion cell layer. *Invest Ophthalmol Vis Sci* 51(6):3003–3018. <https://doi.org/10.1167/iovs.09-4663>
16. Guo Y, Johnson EC, Cepurna WO, Dyck JA, Doser T, Morrison JC (2011) Early gene expression changes in the retinal ganglion cell layer of a rat glaucoma model. *Invest Ophthalmol Vis Sci* 52(3):1460–1473. <https://doi.org/10.1167/iovs.10-5930>
17. Johnson EC, Doser TA, Cepurna WO, Dyck JA, Jia L, Guo Y, Lambert WS, Morrison JC (2011) Cell proliferation and interleukin-6-type cytokine signaling are implicated by gene expression responses in early optic nerve head injury in rat glaucoma. *Invest Ophthalmol Vis Sci* 52(1):504–518. <https://doi.org/10.1167/iovs.10-5317>
18. Johnson EC, Jia L, Cepurna WO, Doser TA, Morrison JC (2007) Global changes in optic nerve head gene expression after exposure to elevated intraocular pressure in a rat glaucoma model. *Invest Ophthalmol Vis Sci* 48(7):3161–3177. <https://doi.org/10.1167/iovs.06-1282>
19. Morrison JC, Cepurna Ying Guo WO, Johnson EC (2011) Pathophysiology of human glaucomatous optic nerve damage: insights from rodent models of glaucoma. *Exp Eye Res* 93(2):156–164. <https://doi.org/10.1016/j.exer.2010.08.005>

20. Morrison JC, Johnson E, Cepurna WO (2008) Rat models for glaucoma research. *Prog Brain Res* 173:285–301. [https://doi.org/10.1016/S0079-6123\(08\)01121-7](https://doi.org/10.1016/S0079-6123(08)01121-7)
21. Morrison JC, Johnson EC, Cepurna W, Jia L (2005) Understanding mechanisms of pressure-induced optic nerve damage. *Prog Retin Eye Res* 24(2):217–240. <https://doi.org/10.1016/j.preteyeres.2004.08.003>
22. Morrison JC, Cepurna WO, Johnson EC (2015) Modeling glaucoma in rats by sclerosing aqueous outflow pathways to elevate intraocular pressure. *Exp Eye Res* 141:23–32. <https://doi.org/10.1016/j.exer.2015.05.012>
23. Pang IH, Clark AF (2007) Rodent models for glaucoma retinopathy and optic neuropathy. *J Glaucoma* 16(5):483–505. <https://doi.org/10.1097/IJG.0b013e3181405d4f>
24. Wang WH, Millar JC, Pang IH, Wax MB, Clark AF (2005) Noninvasive measurement of rodent intraocular pressure with a rebound tonometer. *Invest Ophthalmol Vis Sci* 46(12):4617–4621. <https://doi.org/10.1167/iovs.05-0781>
25. Chauhan BC, Levatte TL, Garnier KL, Tremblay F, Pang IH, Clark AF, Archibald ML (2006) Semiquantitative optic nerve grading scheme for determining axonal loss in experimental optic neuropathy. *Invest Ophthalmol Vis Sci* 47(2):634–640. <https://doi.org/10.1167/iovs.05-1206>
26. Morrison JC, Jia L, Cepurna W, Guo Y, Johnson E (2009) Reliability and sensitivity of the TonoLab rebound tonometer in awake Brown Norway rats. *Invest Ophthalmol Vis Sci* 50(6):2802–2808. <https://doi.org/10.1167/iovs.08-2465>
27. Moore CG, Johnson EC, Morrison JC (1996) Circadian rhythm of intraocular pressure in the rat. *Curr Eye Res* 15(2):185–191

The Microbead Occlusion Model of Ocular Hypertension in Mice

David J. Calkins, Wendi S. Lambert, Cathryn R. Formichella,
William M. McLaughlin, and Rebecca M. Sappington

Abstract

Glaucoma is a common optic neuropathy that leads to vision loss through the degeneration of retinal ganglion cells (RGCs) and their axons. RGC degeneration in glaucoma is associated with sensitivity to intraocular pressure (IOP) and elevated IOP (also known as ocular hypertension) is the primary modifiable risk factor. Ocular hypertension is the primary characteristic of rodent models for glaucoma research. Intracameral injection of microbeads has evolved as a preferred method of IOP elevation in rodents, particularly in mice. Here, we outline the protocol and method for the Microbead Occlusion Model in mice. We highlight the importance of anesthesia choice and the utilization of glass micropipettes in combination with a micromanipulator and microsyringe pump for the successful execution of the model.

Key words Intraocular pressure, Glaucoma, Mouse model, Ocular hypertension, Rodent, Microbead

1 Introduction

Glaucoma is a common optic neuropathy that leads to vision loss through the degeneration of retinal ganglion cells (RGCs) and their axons. RGC degeneration in glaucoma is associated with sensitivity to intraocular pressure (IOP) and elevated IOP (also known as ocular hypertension) is the primary modifiable risk factor. Although ocular hypertension is not synonymous with glaucoma, therapeutics that lower IOP slow glaucoma progression and are the standard clinical intervention. Similarly, ocular hypertension is the primary characteristic of rodent models for glaucoma research. In these models, ocular hypertension results from reduced aqueous outflow from the anterior chamber of the eye and is achieved by either inherent or inducible means. Inherent ocular hypertension is typically associated with genetic mutations, like those in *gpnmb* and *tyrp1* genes of the DBA/2 mouse strain [1]. Inducible ocular hypertension is achieved by surgical intervention that impedes aqueous drainage through the trabecular meshwork in the anterior

chamber. This can be achieved by disruption of episcleral veins [2–7], or physical blockade of the trabecular meshwork [2, 8, 9].

As in all animal research, inherent and inducible models of glaucoma possess significant advantages and disadvantages. These have been reviewed in detail over the past 10 years [10–14]. In summary, inherent models, like the DBA/2 mouse, exhibit sustained elevations in IOP that are comparable to those observed in glaucoma patients (23 mmHg–35 mmHg). However, the onset and prevalence of the phenotype can vary widely among individuals, requiring large experimental cohorts that are maintained over a long period of time. For all inducible models, the onset of ocular hypertension is precise and controllable. Similarly, all offer the potential to readily utilize transgenic strains for mechanistic studies. Inducible models utilizing laser photocoagulation or hypertonic saline injection result in dramatic elevation of IOP (35 mmHg–70 mmHg) that is often not stable over time and can vary widely between individuals in both duration and magnitude. Depending on the method of IOP elevation, there is also the potential for confounds from ocular trauma, secondary inflammation, and altered venous pressure. For these models, surgical skill of the experimenter is a key element in model success and determines the relative significance of the aforementioned disadvantages. As such, these models lend themselves best to experimentation in rats, for which transgenic manipulations have been slow to develop.

Here, we provide detailed methodology to induce ocular hypertension by intracameral injection of microbeads. In this model, inert microbeads are injected into the anterior chamber and are distributed throughout the drainage canals to impede flow of aqueous humor and elevate IOP (Fig. 1). The use of microbeads for the induction of ocular hypertension was first described in primates [15] and later was applied to rats [8] and rabbits [16]. The approach was systematically revised and optimized for the application to both rats and mice by Sappington et al. in 2010 [9]. The Microbead Occlusion Model of ocular hypertension has significant advantages over other inducible models. Specifically, it: (1) is less technically challenging, (2) produces highly reliable elevations in IOP similar to those in inherent models and humans, (3) possesses far less risk of confounds from surgery, (4) possesses a true internal control, and (5) can be temporally controlled. Although this approach can be applied to any species, we will focus on induction of ocular hypertension with microbeads in mice, which maximize utility of the model by providing vast transgenic options.

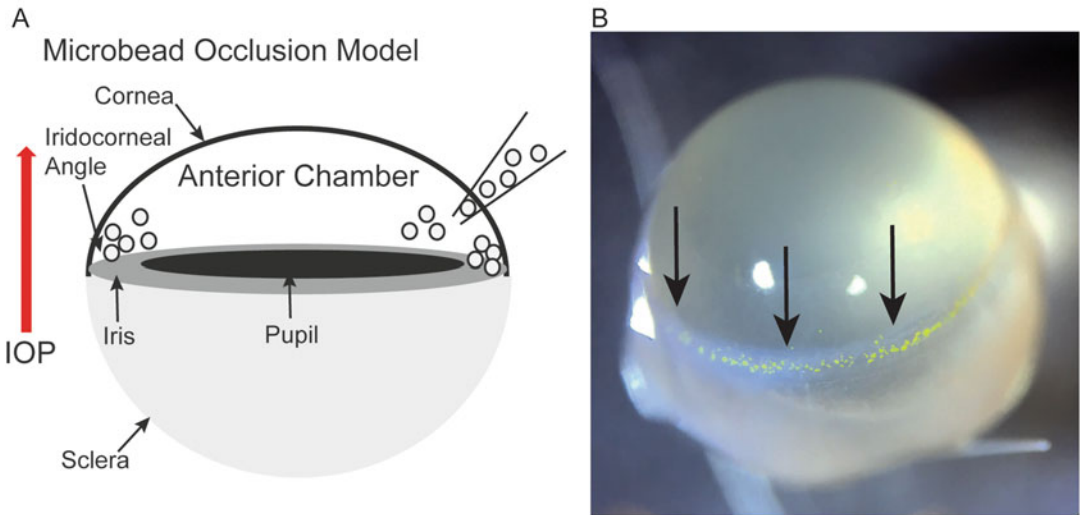


Fig. 1 The microbead occlusion model of rodent ocular hypertension. **(a)** Schematic of the principle basis for elevation of intraocular pressure by intracameral injection of microbeads. **(b)** Photograph of fluorescent microbeads (15 μm) throughout the iridocorneal angle (*arrows*) of a fixed eye (4% paraformaldehyde) from an albino mouse (Balb/c) 4 weeks after a single intracameral injection of microbeads

2 Materials

Since this is a survival surgery, the aseptic technique applies to mixing of all reagents and all equipment and materials should be either sterile, single-use, or appropriately sanitized, i.e., autoclave or ethanol wash. Solutions should be prepared as single-use or stored as stated. This procedure requires approval by an Institutional Animal Care and Use Committee and its practice should adhere to the applicable animal welfare codes and regulations.

2.1 Equipment

1. Micropipette puller (Sutter Instruments).
2. Microcentrifuge.
3. Tabletop Laboratory Animal Inhalation Anesthesia System (isoflurane administration).
4. CO₂/O₂ Mixture Single Stage 0–100 Adjustable Pressure Regulator (for gas cylinder).
5. Manual manipulator (World Precision Instruments).
6. Magnetic base for manual manipulator (World Precision Instruments).
7. Manual Microsyringe Pump, recommend digital display (World Precision Instruments—kit for pump includes tubing, gaskets, and glass needle holder).

8. Metal stand—minimum 8 in. tall. We utilize a 9-in. metal bookend.
9. Large lab jack support system (8 × 8 in.; Fisher Scientific).
10. Focal light source for surgery, recommend dual gooseneck LED.
11. No. 5 forceps for trimming micropipettes.
12. Non-serrated, flat end, or curved (approximately 2 mm) for eye positioning. The use of curved or flat forceps is a matter of individual preference and comfort.

2.2 Consumable Materials

1. 2 Charcoal canisters (isoflurane waste container).
2. 4-in. thin-wall glass capillaries with filament (1.5 OD/1.12 ID).
3. 0.6 ml Microcentrifuge tubes, autoclaved.
4. Glass scintillation vials with screw caps.
5. Sterile vacuum filter units (250 ml, pore size = 0.22 μm) for sterilization of solutions.
6. 5 cc disposable syringe.
7. Disposable dry wipes, i.e., Kimwipes.
8. Surgical gloves, sterile—single use.

2.3 Reagents

1. 100% ethanol (for sterilization).
2. 95% O₂/5% CO₂-EM Compressed Gas (in cylinder).
3. Isoflurane.
4. Mineral Oil, Light (NF/FCC).
5. Polystyrene Microspheres, 15 μm (1 × 10⁶ beads/ml stock solution). We utilize yellow-green fluorescent polystyrene microspheres (ThermoFisher Scientific) engineered for blood-flow determination (*see Note 1*). Store at 4 °C.
6. Phosphate-buffered saline without sodium azide.
7. 1% tropicamide ophthalmic solution (dilation drops).
8. 0.5% proparacaine hydrochloride ophthalmic solution (anesthetic drops). Store at 4 °C.
9. 0.5% moxifloxacin hydrochloride ophthalmic solution (antibiotic drops).

2.4 Injection and Anesthesia Assembly

1. Figure 2 depicts the complete anesthesia and injection assemblies. Follow the manufacturer's instructions for the assembly of anesthesia and injection apparatus. Assembly of both occurs only once at initial procurement of the equipment.
2. In general, the anesthesia assembly should include an isoflurane canister connected to a cylinder of O₂ gas for mixing. The

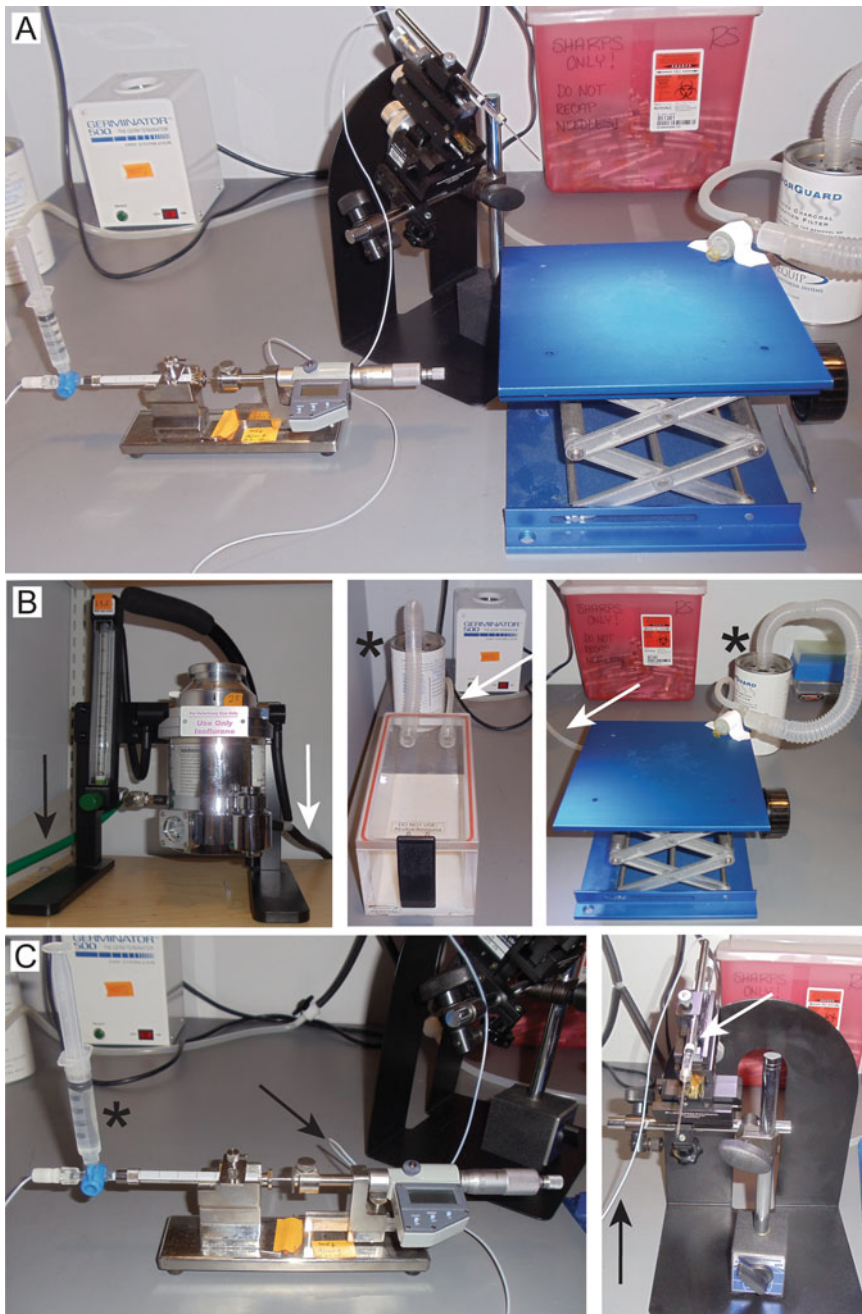


Fig. 2 Anesthesia and injection assemblies. (a) Photograph of complete injection system assembly. (b) Photographs of isoflurane regulator (left), anesthesia chamber (middle), and nose-cone (right). The *black arrow* indicates gas supply line running from O₂/CO₂ cylinder to the isoflurane regulator. *White arrows* indicate anesthesia supply line running to a diverter that will switch flow of isoflurane between the anesthesia chamber and the nose-cone. Asterisks indicate isoflurane waste lines that feed into charcoal filter canisters. (c) Photographs of microsyringe pump (right) and micromanipulator (right) assemblies. *Black arrows* indicate plastic tubing filled with mineral oil that connects the microsyringe pump to the glass needle. *White arrow* indicates glass needle seated in the micromanipulator. Asterisk indicates 5 cc syringe that supplies mineral oil to the assembly

canister should have two hoses with diverters, one for a gas chamber (initial anesthesia) and one for the nose cone (anesthesia maintenance during the procedure). Both the lines should be connected to charcoal waste filters.

3. The injection assembly consists of the pump connected by plastic tubing to the microsyringe, which is placed in a manual micromanipulator. The plastic tubing and microsyringe are filled with mineral oil supplied via a valve connected to a 5 cc plastic syringe. The micromanipulator is attached to a stand for stability.

2.5 Reagent Preparation

1. Using aseptic technique, aliquot polystyrene microbeads into a 0.6 ml microcentrifuge tube. Aliquot volume should be slightly more than the typical volume utilized per experiment. Solution remaining in the aliquot at the end of the surgical day should be discarded (*see Note 2*).
2. Sterilize phosphate-buffered saline, using vacuum sterilization filter units. Sterile solution can be stored at 4 °C for 1 month. Using aseptic technique, transfer 300 ml of sterilized phosphate-buffered saline to a 0.6 ml microcentrifuge tube.
3. Transfer approximately 5 ml of 100% ethanol to a scintillation vial.
4. Use a glass micropipette puller to create micropipettes for microbead and saline injection (*see Note 3*). Two micropipettes are created from a single glass capillary (Fig. 3). For the P-97 model from Sutter Instruments, the program settings should be as follows (*see Note 4*):

$P = 500$ units

Heat = 490 units

Pull = 30 units

Velocity = 120 units

Time = 200 units

Insert a glass capillary into the holder and secure with screws. Press the “pull” button. The filament will heat and separate the glass electrode into two micropipettes, as dictated by the above settings. Loosen screws and remove.

5. Trim the micropipette tip half-way between the very tip and the appreciable v-shaped taper (approximately 1 mm from tip) with No. 5 forceps by “pinching” the glass (Fig. 4).

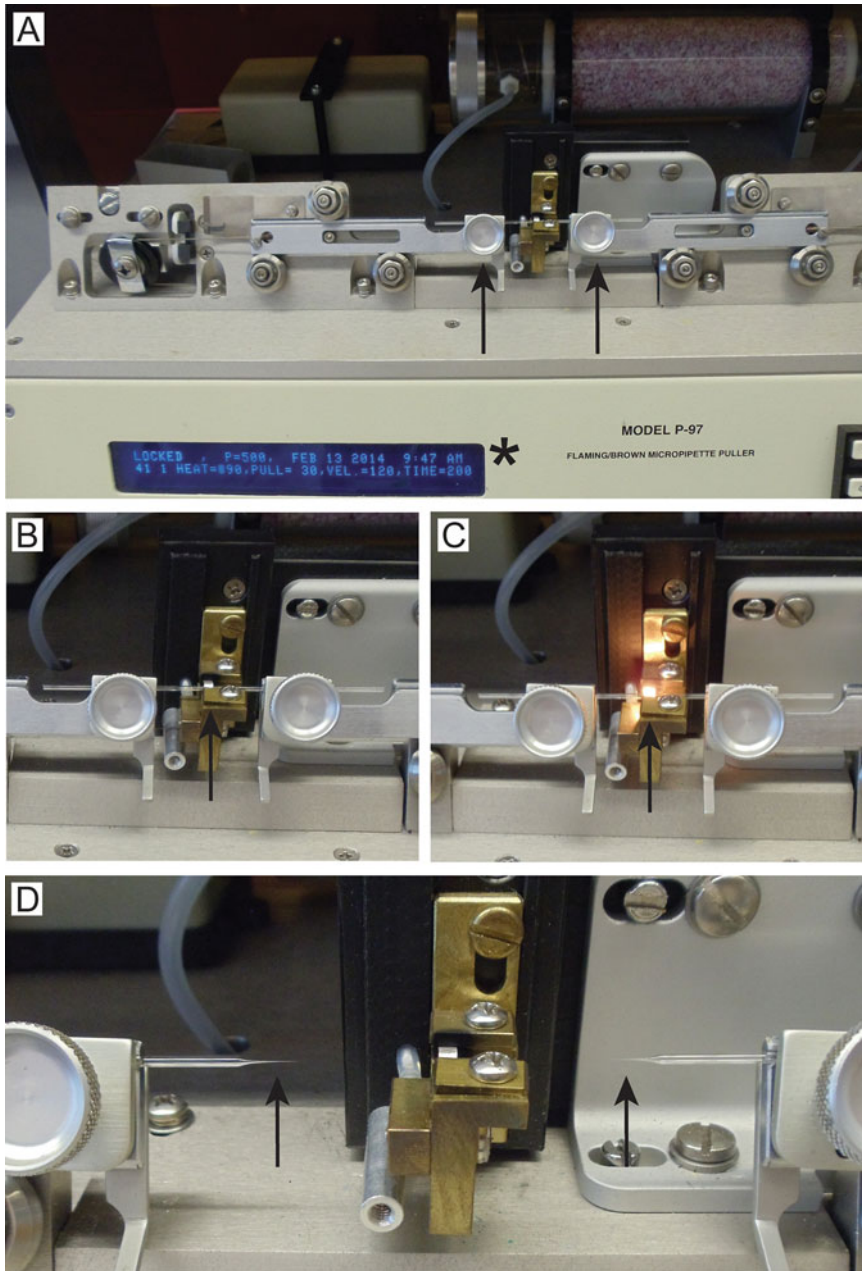


Fig. 3 Production of glass micropipettes. (a) Photograph of microelectrode puller. *Black arrows* indicate the seat and screws for placement of glass capillaries. Asterisks indicate settings for glass pulling. (b) Photograph of a glass capillary secured in the puller. *Black arrow* indicated location of the heating element. (c) Photograph of a glass capillary pulling. *Black arrow* indicates engaged heating element. (d) Photograph of the two micropipettes (*black arrows*) produced by the puller

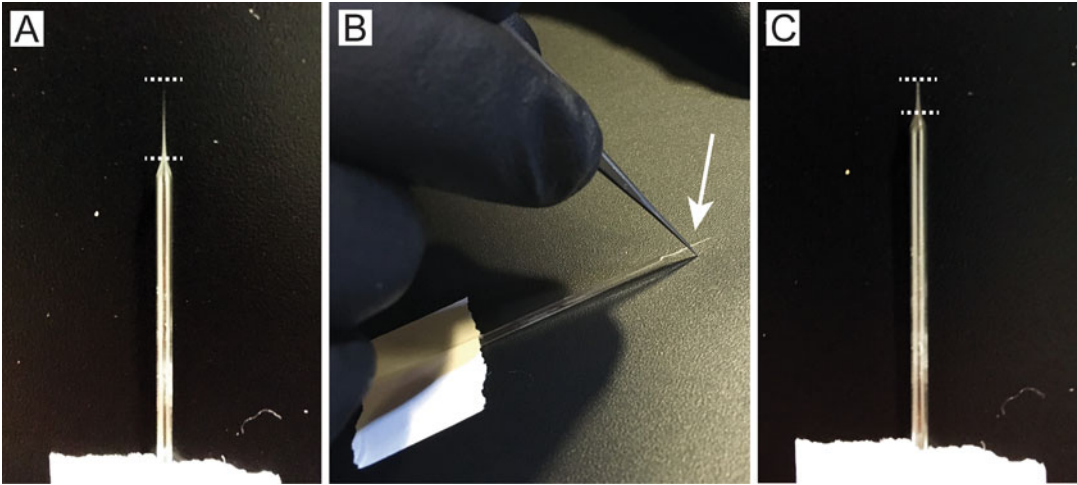


Fig. 4 Micropipette trimming. **(a)** Photograph of untrimmed micropipette. *Dotted lines* indicate the distance between the initial taper and the tip of the micropipette. **(b)** Photograph of method for trimming the micropipette. *Arrow* indicates the proper point of trimming. **(c)** Photograph of trimmed micropipette. *Dotted lines* indicate the distance between the initial taper and the tip of the micropipette

3 Methods

This procedure requires two persons—one to operate the microsyringe pump and micromanipulator and one to position the eye during injections. Baseline measurements of IOP should be obtained for all study animals (*see Note 5*).

1. Insert the trimmed micropipette into the glass needle mounted in the micromanipulator. Tighten the ring to secure the micropipette (Fig. 5a).
2. Fill the micropipette with mineral oil by depressing the plunger of the 5 cc syringe attached to the microsyringe pump. Depress plunger until mineral oil beads on the tip of the micropipette. Use a Kimwipe to remove the bead of mineral oil (*see Note 6*). Sterilize the micropipette by submerging it in 100% ETOH (Fig. 5b).
3. Place mouse in the isoflurane chamber to anesthetize (*see Note 7*). Once the mouse is sufficiently anesthetized, divert isoflurane flow to the nose cone and place mouse on the surgical platform with nose securely situated in the cone (*see Note 8*).
4. Initiate iris dilation by topical administration of 1% tropicamide ophthalmic solution (one drop/eye; Fig. 5c). While waiting for dilation, adjust platform height to ensure there is sufficient room to advance and retract the micropipette. The tip of the micropipette should reach the eye and still have room to advance further.

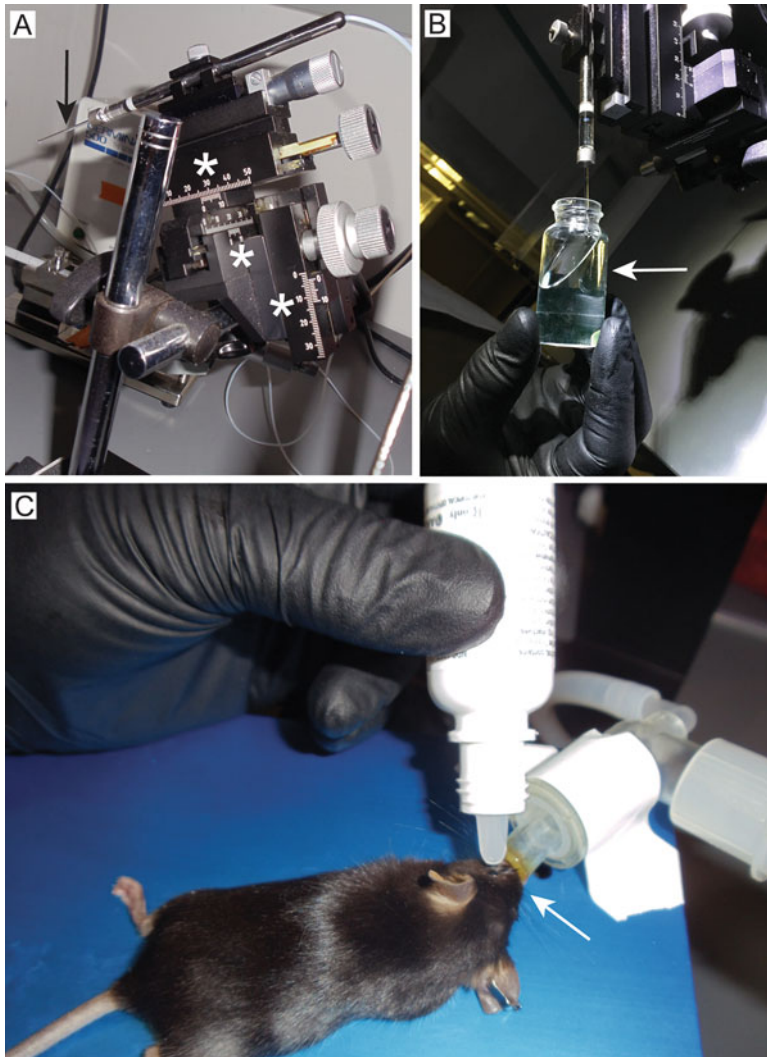


Fig. 5 Pre-injection preparations. **(a)** Photograph of glass micropipette secured in the micromanipulator (*arrow*). *Asterisks* indicate dials and settings for adjustment and movement. **(b)** Photograph of method for sterilization of micropipette with 100% ETOH. *Arrow* indicates location of micropipette. **(c)** Photograph of procedure for the placement of the mouse on the surgical platform (*arrow*) as well as the application of topical solutions to the eye

5. Set syringe pump to zero (zero out).
6. Re-sterilize the tip of the micropipette by submerging in scintillation vial with 100% ETOH.
7. If performing unilateral microbead and saline injections in the same animal, always inject saline first (*see Note 9*). If performing bilateral or unilateral injection of microbeads only, you must still pull saline into the syringe first. This “wets” the needle and prevents microbeads from sticking to

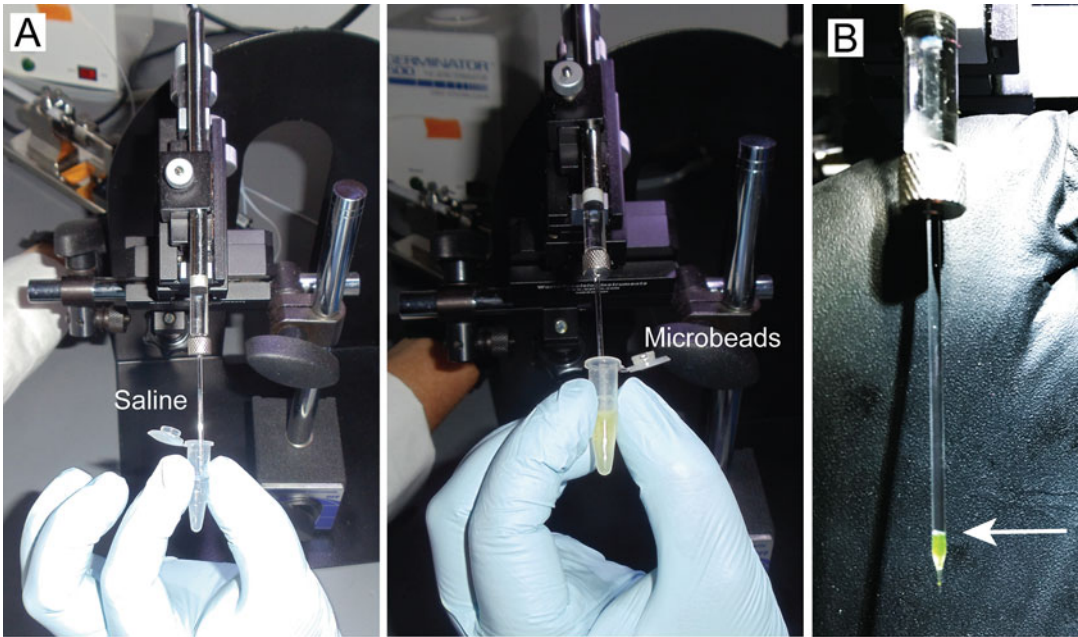


Fig. 6 Micropipette loading. (a) Photographs of micropipette loading with saline (left) and microbead (right) solutions. (b) Photograph of micropipette loaded with microbead solution. *Arrow* indicates location of the meniscus formed between the microbead solution and mineral oil

the mineral oil and sides of the micropipette. If saline will not be used in an injection, discard it into a Kimwipe by depressing the 5 cc syringe. Re-sterilize the micropipette with 100% ETOH and load microbeads as detailed below.

8. To fill the micropipette with saline or microbeads, one person holds the tube of injectable solution, while the other operates the microsyringe pump (Fig. 6a). Each microsyringe pump will be calibrated differently and the calibration scale will be delineated in the manual. According to the calibration scale of the microsyringe pump, pull up two times the desired injection volume (*see Note 10*). For example, our typical injection volume of 1.5 μl (*see Note 11*) equals 0.9 units on our microsyringe pump. We pull up 1.9 units of saline. Load microbead solution slowly allowing beads to enter the tip and fill the micropipette without air or clogging of the tip. Saline may be drawn up at a faster rate, but air bubbles must still be avoided (*see Note 12*). Keep the tip of the micropipette submerged in the solution until the proper volume of the solution is loaded. Check the location of the meniscus where the injectable solution interfaces with the mineral oil to ensure that the proper volume is loaded (Fig. 6b).
9. Upon sufficient dilation of the eye (Fig. 7a *insert*), apply local anesthesia (0.5% proparacaine hydrochloride ophthalmic solution; one drop) directly to the eye.

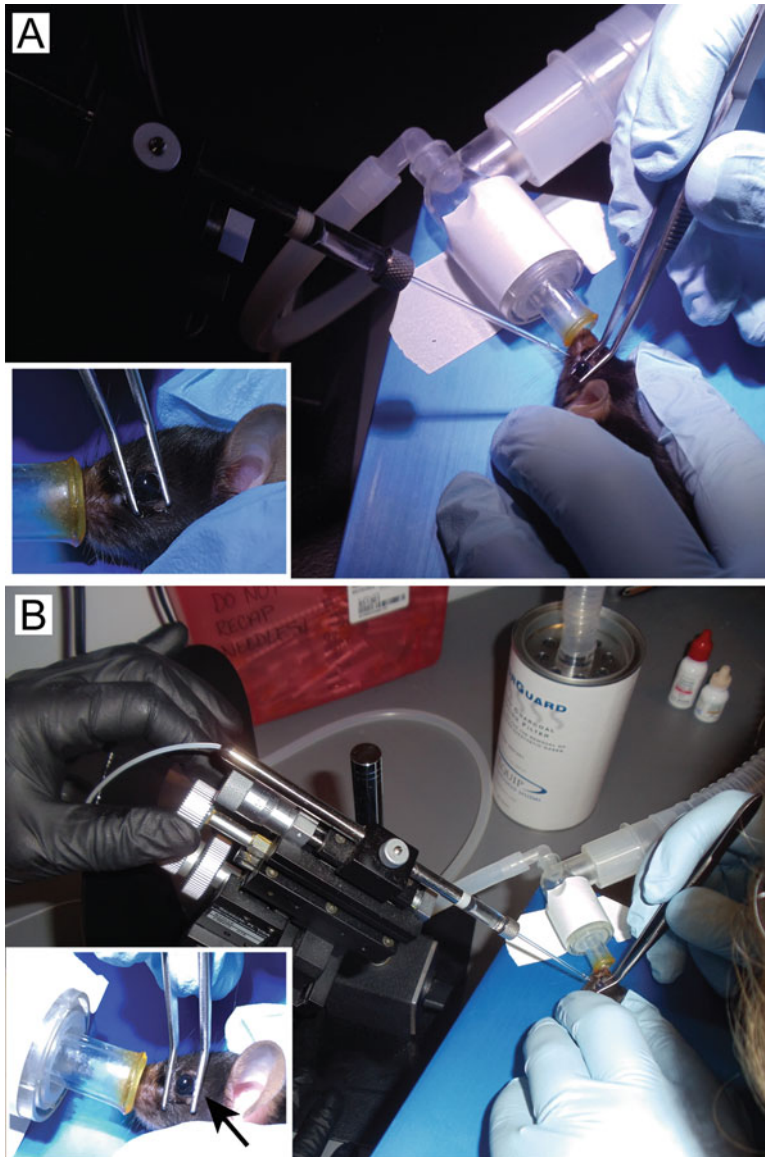


Fig. 7 Eye proptosis, operator configuration, and placement of forceps. (a) Photograph of eye proptosis with forceps. *Insert:* Magnified view illustrating both placement of forceps for initial proptosis and proper eye dilation (*arrow*). (b) Photograph of operator configuration during intracameral injection. *Insert:* Magnified view of proper placement of the forceps during injection. *Arrow* indicates the “brace” position held by the back arm of the forceps

10. Proptose eye by applying slight, downward pressure to the eyelids on either side of the eye with curve or flat-edge forceps (Fig. 7a). It is important not to squeeze the eye, as this can result in various ocular injuries and impede aqueous flow in the anterior chamber.
11. Line up micropipette with the eye so that the tip is right over the far edge of the dilated iris (*see Note 13*).

12. One person advances the micropipette toward the cornea, using the micromanipulator (Fig. 7b). The other person continues to proptose the eye with the back arm of the forceps (opposite the micromanipulator) aligned parallel to the eye. The back arm of the forceps serves as a brace to prevent backward rotation of the eye (*see Note 14*; Fig. 7b *insert*). Advance the micropipette until the cornea is breached (Fig. 8a). This should be done in as fluid of a motion as possible (*see Note 15*).
13. With the eye still proptosed, inject the desired volume, according to the calibration scale of the microsyringe pump, over a period of approximately 5–7 s (Fig. 8a; *see Note 16*). Eye

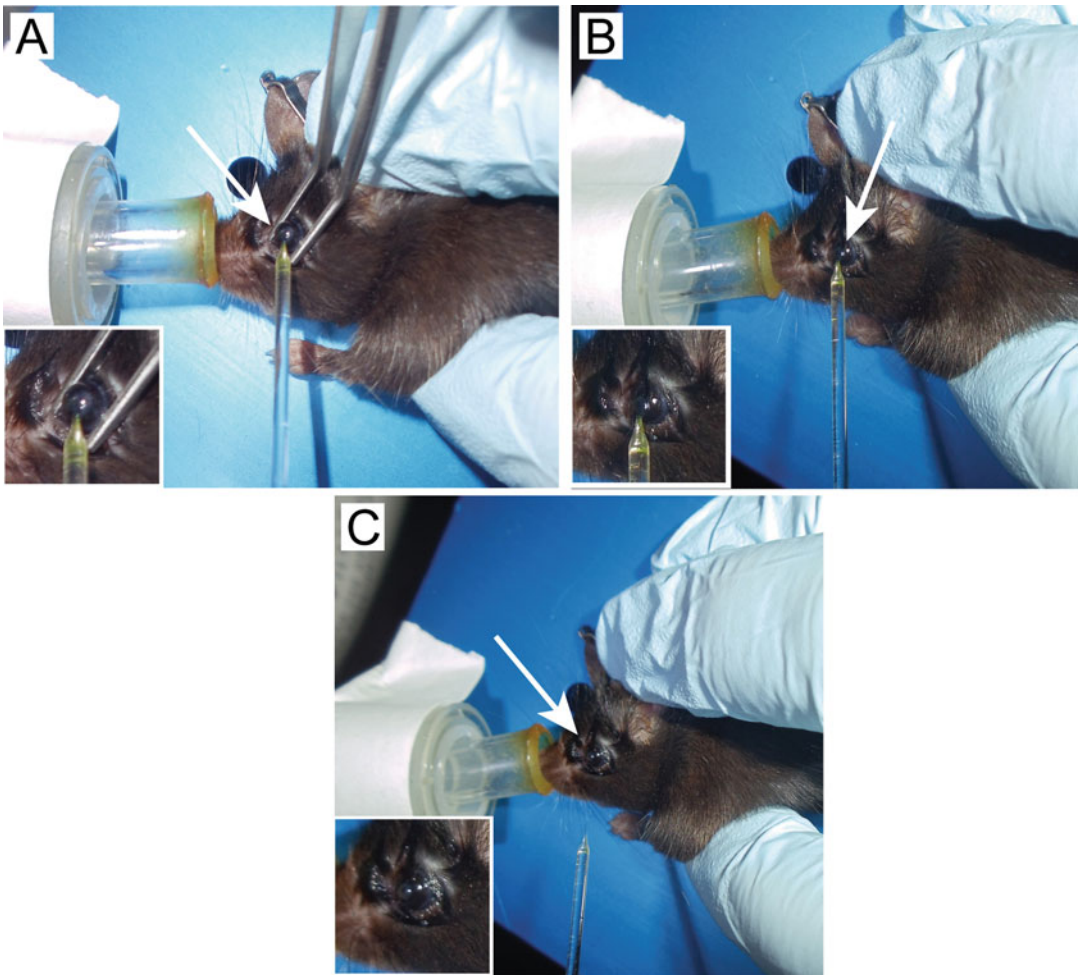


Fig. 8 Microbead injection. (a) Photograph of the first 5–7 s of microbead injection. The eye is braced by forceps until the desired volume of microbead solution is delivered (*arrow*). (b) Photograph of the second 10–15 s of microbead injection. Forceps are withdrawn and the micropipette remains until microbeads disperse (*arrow*). (c) Photograph of completed microbead injection following micropipette retraction (*arrow*)

should remain protruded until the desired injection volume is actually released into the anterior chamber (*see Note 17*). This will take 10–15 s, with microbeads taking longer to inject than saline.

14. Carefully move the forceps away from the eyelids and allow the eye to resume its normal position. The micropipette should still be in the cornea. Wait another 15 s to ensure dispersion of the microbeads (*see Note 18*; Fig. 8b).
15. Slowly retract microinjector to remove the micropipette from the cornea (Fig. 8c).
16. Apply another drop of 0.5% proparacaine hydrochloride ophthalmic solution directly to the cornea followed by a drop of 0.5% moxifloxacin hydrochloride ophthalmic solution (antibiotic).
17. If performing bilateral injections, flip animal over to the other side and repeat **steps 4–15** with the desired injectable solution.
18. Upon completion of all injections, remove the animal from the nose-cone and place in a clean cage for recovery. With isoflurane anesthesia, the animal will awake within minutes.
19. Monitor the animal for signs of distress, as per the approved IACUC protocol. Clouding of the cornea in the first 24 h after surgery is an indicator of good microbead injection. This clouding is temporary, typically resolving within 36–48 h. After this point, there should be no visible distinction between saline and microbead-injected eyes beyond the difference in IOP. To ensure that the microbead-induced IOP elevation was successful, we recommend measuring IOP for 3 consecutive days beginning 24 h post-surgery (*see Note 16*). IOP measurements can then be reduced to two to three times weekly for the duration of the experiment. Duration of IOP elevation can be extended by re-injection prior to decline of IOP elevation [9].

4 Notes

1. The use of fluorescent-tagged microbeads aids tremendously in visualization during injection. Microbeads made of latex and ferromagnetic polystyrene have also been utilized in primates, rats, and mice [8, 15, 17, 18]. In mice, smaller diameter microspheres have also been utilized for IOP elevation (1 μm and 6 μm), including a combination of smaller diameter microspheres [17, 19].
2. Microbeads have a tendency to aggregate and stick to the sides of plastic centrifuge tubes. Always ensure that microbeads are frequently mixed by tapping to prevent aggregation and sticking before use.

3. Others have utilized a modified approach to deliver microbeads, namely 30–33 gauge needles or glass electrodes attached to handheld syringes. We find that the use of metal needles and glass electrodes attached to handheld syringes produces a larger and “rougher” opening in the cornea that does not seal quickly. This results in significant and variable efflux of aqueous humor and microbeads/saline from the injection site. Most of these variations also employ additional treatments to successfully access the anterior chamber and to retain microbeads post-injection, including pre-puncture of the cornea, viscoelastic substances, and magnets [17–21]. In our hands, the combined use of glass micropipettes with a micromanipulator and a micro-syringe pump produces a smooth and seamless puncture that seals with no further intervention. Based on our testing during model development, this approach exceeded handheld injectors and metal needles in terms of simplicity of execution, penetrance of successful IOP elevation, consistency in IOP elevations between individuals, and the incidence of adverse reactions at the injection site.
4. The settings provided above refer to those on the P-97 Model from Sutter Instruments. To ease translation to other brands of micropipette puller: Pull = arbitrary scale of 0–999; Heat = arbitrary scale of 0–999 with maximum current of 65 Amps; Velocity = 10 ms/unit, Time = 0.5 ms/unit. Micropipettes may be pulled in advance and stored in a petri dish with modeling clay (to immobilize and separate).
5. We strongly recommend measuring IOP by tonometry in awake, behaving mice. If mice are acclimated to scruffing via behavioral training, they will tolerate IOP measurements well. This approach avoids the myriad of confounds introduced by anesthetic agents and significantly reduces the amount of time necessary to perform IOP measurements in animal cohorts.
6. If a drop of mineral oil appears repeatedly at the end of micropipette, the tip of the micropipette is too sharp/narrow. Use No. 5 forceps to break the tip of the micropipette and widen the opening further. Care must be taken not to shorten the tip too far, as this impedes cornea puncture and introduces the risk of producing a large hole in the injection site for beads to efflux. With settings defined above for the pipette puller, the opening in the pipette after trimming should be approximately 100 μm in diameter.
7. The use of injectable anesthetics, i.e., ketamine, reduces flow in an anterior chamber and impedes dispersion of beads to trabecular meshwork. This results in greater efflux of beads following the removal of micropipette, as beads remain close to injection site in a clump rather than dispersing immediately

throughout the anterior chamber. The use of isoflurane as the anesthetic is essential for incidence of model success, post-surgery survival rates, and maximization of model outcomes, including magnitude of IOP elevation and ganglion cell pathology.

8. Place the mouse slightly on its side rather than lying flat. This improves access to the eye and assists in establishing the proper angle for injection. To achieve the proper angle for injection, we recommend adjusting the position of the mouse on the platform rather than the angle of injection on the micromanipulator. To inject the other eye, flip the mouse over to the other side.
9. We use one micropipette per animal. When a single animal is injected with both saline and microbeads, the saline injection always precedes microbead injections. Otherwise, microbeads that stick to the sides of the micropipette will be introduced into the saline injection.
10. Pulling twice the required volume into the micropipette ensures that mineral oil is not inadvertently injected into the anterior chamber and allows room to “flush” a clogged micropipette during microbead injection.
11. We prefer an injection of 1.5 μl for mouse eyes. Others have used anywhere between 1 and 4 μl of microbeads [17, 19, 20]. We find that 1.5 μl produces the most robust IOP elevation without the increased variability in efflux and risk of corneal damage associated with larger injection volumes.
12. If an air bubble occurs, depress the 5 cc syringe to clear the air bubble from the tip. Re-load solution and re-sterilize the micropipette with 100% ETOH, if necessary.
13. We find that the micromanipulator should be situated perpendicular to the animal.
14. Force should never be applied to the forceps in a closing or squeezing motion, as this can cause tremendous efflux, corneal damage, and potentially, retinal detachment. Force applied to the forceps should remain downward to proptose the eye. Slight inward pressure on the back arm of the forceps only (opposite the micromanipulator) is applied at the time of cornea puncture to prevent backward rotation of the eye. The only force on the eye should come from the corneal puncture.
15. There will be some resistance when the micropipette reaches the cornea. Do not stop at this point, but continue slow and steady advancement. Stopping or jarring motions can cause breakage of the glass micropipette or failed puncture that can wound the cornea. A slight “pop” will be felt when the micropipette breaches the cornea and advancement should stop at this time.

16. We find that the tempo of injection can reduce the likelihood of clog formation in the micropipette. We recommend operating the manual pump in the following rhythm—turn, turn, quick turn. . .turn, turn, quick turn—until the desired volume is reached.
17. If a clog is observed or suspected, the eye can be very subtly shifted backward and forward in an attempt to promote flow of the solution. Again, be careful not to squeeze with the forceps, but rather push the eye with one arm of the forceps or the other. A more severe clog can be cleared by pulling a minute volume of solution back up into the pipette (1/2 turn of syringe pump) and then back down in a flushing motion. However, great care must be taken not to disrupt the injection site (movement will enlarge the corneal opening) or to move too much fluid in either direction, which creates excess suction.
18. At this point in time, a majority of the microbeads should be visible throughout the circumference of the anterior chamber. Most will be concentrated in and around the corneo-irido angle. If microbeads remain near the injection site for longer than 30 s, this indicates a significant reduction in flow of aqueous humor. The most common causes for decreased perfusion of the anterior chamber are the use of injectable anesthetics and “squeezing” of the eye with forceps.

References

1. John SW et al (1998) Essential iris atrophy, pigment dispersion, and glaucoma in DBA/2J mice. *Invest Ophthalmol Vis Sci* 39(6):951–962
2. Levkovitch-Verbin H et al (2002) Translimbal laser photocoagulation to the trabecular meshwork as a model of glaucoma in rats. *Invest Ophthalmol Vis Sci* 43(2):402–410
3. Morrison JC et al (1997) A rat model of chronic pressure-induced optic nerve damage. *Exp Eye Res* 64(1):85–96
4. Sawada A, Neufeld AH (1999) Confirmation of the rat model of chronic, moderately elevated intraocular pressure. *Exp Eye Res* 69(5):525–531
5. Bayer AU et al (2001) Electroretinographic abnormalities in a rat glaucoma model with chronic elevated intraocular pressure. *Exp Eye Res* 72(6):667–677
6. Shareef SR et al (1995) Chronic ocular hypertension following episcleral venous occlusion in rats. *Exp Eye Res* 61(3):379–382
7. Mittag TW et al (2000) Retinal damage after 3 to 4 months of elevated intraocular pressure in a rat glaucoma model. *Invest Ophthalmol Vis Sci* 41(11):3451–3459
8. Urcola JH, Hernandez M, Vecino E (2006) Three experimental glaucoma models in rats: comparison of the effects of intraocular pressure elevation on retinal ganglion cell size and death. *Exp Eye Res* 83(2):429–437
9. Sappington RM et al (2010) The microbead occlusion model: a paradigm for induced ocular hypertension in rats and mice. *Invest Ophthalmol Vis Sci* 51(1):207–216
10. Goldblum D, Mittag T (2002) Prospects for relevant glaucoma models with retinal ganglion cell damage in the rodent eye. *Vis Res* 42(4):471–478
11. Pang IH, Clark AF (2007) Rodent models for glaucoma retinopathy and optic neuropathy. *J Glaucoma* 16(5):483–505
12. Morrison JC, Johnson E, Cepurna WO (2008) Rat models for glaucoma research. *Prog Brain Res* 173:285–301
13. Vecino E, Sharma SC (2001) Glaucoma animal models. In: Rumelt S (ed) *Glaucoma basic and clinical concepts*. intechopen.com: InTech, pp 319–334
14. Morgan JE, Tribble JR (2015) Microbead models in glaucoma. *Exp Eye Res* 141:9–14

15. Weber AJ, Zelenak D (2001) Experimental glaucoma in the primate induced by latex microspheres. *J Neurosci Methods* 111 (1):39–48
16. Ngumah QC, Buchthal SD, Dacheux RF (2006) Longitudinal non-invasive proton NMR spectroscopy measurement of vitreous lactate in a rabbit model of ocular hypertension. *Exp Eye Res* 83(2):390–400
17. Cone FE et al (2010) Differential susceptibility to experimental glaucoma among 3 mouse strains using bead and viscoelastic injection. *Exp Eye Res* 91(3):415–424
18. Samsel PA et al (2011) A novel method for the induction of experimental glaucoma using magnetic microspheres. *Invest Ophthalmol Vis Sci* 52(3):1671–1675
19. Frankfort BJ et al (2013) Elevated intraocular pressure causes inner retinal dysfunction before cell loss in a mouse model of experimental glaucoma. *Invest Ophthalmol Vis Sci* 54 (1):762–770
20. Chen H et al (2011) Optic neuropathy due to microbead-induced elevated intraocular pressure in the mouse. *Invest Ophthalmol Vis Sci* 52(1):36–44
21. Smedowski A et al (2014) A rat experimental model of glaucoma incorporating rapid-onset elevation of intraocular pressure. *Sci Rep* 4:5910

Chapter 4

Ocular Hypertension/Glaucoma in Minipigs: Episcleral Veins Cauterization and Microbead Occlusion Methods

Elena Vecino, Haritz Urcola, Alejandro Bayon, and Sansar C. Sharma

Abstract

Two methods to induce elevation of the intraocular pressure (experimental glaucoma) are described in the present chapter. The first method is based on increasing the post-trabecular resistance to aqueous outflow by cauterizing the episcleral veins (EVC). This method allows the observation of ultrastructural changes in the trabecular meshwork (TM) without interfering with any structure within the eye such as TM, ciliary body, and/or the Retina. The second method is the multiple injection of microbeads into the anterior chamber, as a pre and intra-trabecular method that induce secondary effects on the TM cells. Both methods lead to an increase in IOP.

Key words Glaucoma, Episcleral veins, Retina, Trabecular, Minipigs, Pigs, Microbead

1 Introduction

Increased resistance to aqueous humor outflow is generally considered the predominant risk factor for increased intraocular pressure (IOP) in glaucomatous eyes. Thus, elevation of IOP is the main objective to induce experimental glaucoma and different methods have been developed for that purpose [1].

The minipig as an experimental animal is very interesting as it is more accessible than non-human primates. In addition to being phylogenetically closer to humans than other species, it is very easy to handle and its body grows rather slowly. The Göttingen minipig eye has a system with multiple vessels of the angular aqueous plexus contrasting with the unique Schelmm's canal in human eyes [2, 3]. The retinal morphology and distribution of the retinal ganglion cells (RGC) and glia is well established and is very similar between pig and Minipig [4–8]. We have demonstrated that a moderate increase of IOP in pig eyes induced retinal ganglion cell death following a pattern similar to that described in human glaucoma [9]. We have also induced experimental glaucoma in Göttingen minipigs and have described changes in the vasculature of

the optic disk, which were similar to those observed in human POAG [10].

Two methods to induce elevation of the intraocular pressure are described in the present protocols. The first one is based on increasing the post-trabecular resistance to aqueous humor outflow by cauterizing the episcleral veins (EVC). This method allows the preservation of the trabecular meshwork (TM) ultrastructure and in addition the changes induced in the retina by the elevation of IOP can be studied. The second method pertains to the multiple injection of microbeads into the anterior chamber, as a pre-and intra trabecular method that has a secondary effect on TM cells. Both the methods have been used in our group to compare the impact on the IOP in the TM as well as in the retinal ganglion cell survival in rats and pigs [1, 11, 12].

The episcleral veins cauterization (EVC) was developed by Sharma's group [13] in rats and then adapted to pigs and is the method most used in a larger number of studies of experimental glaucoma. The microbead method was first used in monkey by [14] and was further improved in our group by combining the beads with viscoelastic substances such as hydroxypropylmethylcellulose (HPM) in order to induce higher IOP elevation spikes and for longer period time [12]. At present this multiple microbeads injection method is used in different animal species and is the main method used in mice. Through this procedure conjunctival dissection is avoided and it is not necessary to recognize the anatomical landmarks of the EVC method, it converts to an easier method with a short learning curve. On the other hand, the main limitation of this surgery is the invasive approach into the anterior chamber and therefore has a higher risk of inducing postsurgical endophthalmitis. Besides, this method requires multiple injections for at least 9 weeks to induce permanent IOP elevation and the penetration of these microbeads into the TM could limit the physiology of TM and alter the study of experimental glaucoma within the retina.

The best experimental glaucoma method in minipig in our hands has been EVC. The advantages are the elevated values of the pressure for longer period of time (months) and using this method has allowed us to propose some mechanisms on the initiation and progression of glaucoma.

1. The elevation of IOP in pigs and minipigs induces the expression of endothelial leukocyte adhesion molecule 1 (ELAM-1) at the anterior chamber level of the outflow pathway system as a response to cellular stress [15]. This molecule has been identified as the first molecular marker for glaucomatous trabecular meshwork cells in humans [16]. The finding that ELAM-1 is upregulated in the outflow pathway in pig and human experimental glaucoma models will promote further studies related to the development of glaucoma treatments.

2. Ultrastructural changes in the Minipig trabecular meshwork secondary to the increase of IOP were found. A greater amount of fibrillar material and elastic-like fibers in the TM in eyes with elevated IOP allowed us to suggest that the origin of the primary open glaucoma (POG) may initially be associated with an increase in the post-trabecular resistance to aqueous humor outflow and, subsequently, the increase in the IOP may cause changes in the trabecular meshwork obstructing the evacuation of the aqueous humor. We cannot rule out that the changes originated at the trabecular level in susceptible individuals, (in whom peaks in lifelong physiological variations in IOP occur), are sufficient to cause secondary changes in the trabecular meshwork. We propose that the obstruction of the trabecular could sometimes be the effect and not the cause, thereby initiating a vicious cycle that culminates in chronic disease of glaucoma [2, 8].

Depending on the interest of the study, one can use one or the other method to experimentally induce ocular hypertension and if it is maintained for weeks or months, only then, we can call it “experimental glaucoma.”

2 Materials

2.1 Animals

Göttingen minipigs are the preferred animals since they are very social and are very easy to handle. The average age of the animals at the beginning of the experimental period should be around 5 months. Minipigs become sexually mature at 3–4 month of age in males, weighing 7–9 kg, and 4–5 month of age in females, weighing 9–11 kg.

All animals used should be of the same age and considered young adults. In our experience no significant differences were found between male and female, but to avoid any possible differences, the same sex should be used.

Animals should be kept in the animal house under a 12:12 h light: dark cycle, fed twice a day and should have ad libitum access to water.

2.2 Anesthesia and Analgesic

1. Ketamine hydrochloride (Ketolar) + xylazine (Diazepan), 20 mg/kg inject intramuscularly.
2. 5% povidone iodine for the application in the area to be operated.
3. Tetracaine hydrochloride + oxibuprocaine (Double anesthetic), apply one drop per eye.
4. Intravenous Propofol 10 ml/h.

5. Intravenous 1 g of Metamizole as an analgesic treatment after EVC operation.
6. Use Steroid-antibiotic ointment containing chloramphenicol and dexamethasone.

2.3 Surgical Material

1. Speculum.
2. Scissors different sizes.
3. Tweezers different sizes.
4. Surgical thread.
5. Cautery.
6. Surgical sponges.
7. Sterile 30-gauge needle.

2.4 Microbeads

1. Latex microspheres 10 μm in diameter (FluoSpheres™; Molecular Probes, Eugene, OR).
2. 0,15 M NaCl in 0.02% Tween-20 (Sigma) pH 7.4 (vehicle).
3. 2% Hydroxypropylmethylcellulose (Methocel; Novartis).

2.5 Tonometry

1. TonoLab rebound tonometer (*Icare Tonolab*, Finland).

3 Methods

3.1 Induction of Experimental Glaucoma

1. The minipigs are deeply anesthetized with an intramuscular injection of ketamine hydrochloride (Ketolar) + xylazine (Diazepan), at 20 mg/kg each. An intravenous cannula is applied to the ear vein in order to provide the animal with additional anesthesia (10 ml Propofol/hour), maintaining deep anesthesia throughout the operation.
2. The IOP is measured after the administration of 1 drop of topical anesthesia (tetracain 0,1% and oxibuprocain 0,4%). The surgical interventions are carried out under general anesthesia with propofol. Mechanical ventilation and monitoring of vital signs are maintained in every moment of the surgery.
3. Two drops of 5% povidone iodine are topically applied to the eye before surgery to prevent potential infection. The surgical area is disinfected and protected with surgical drapes.
4. Briefly, two dorsal episcleral veins, located near the superior rectus muscle, and one temporal episcleral vein, near the lateral rectus muscle are isolated from the surrounding tissues. A cautery is specifically and precisely applied to the selected veins with care taken to avoid thermal damage to the rest of the neighboring tissues. After each procedure, steroid-antibiotic ointment containing chloramphenicol and

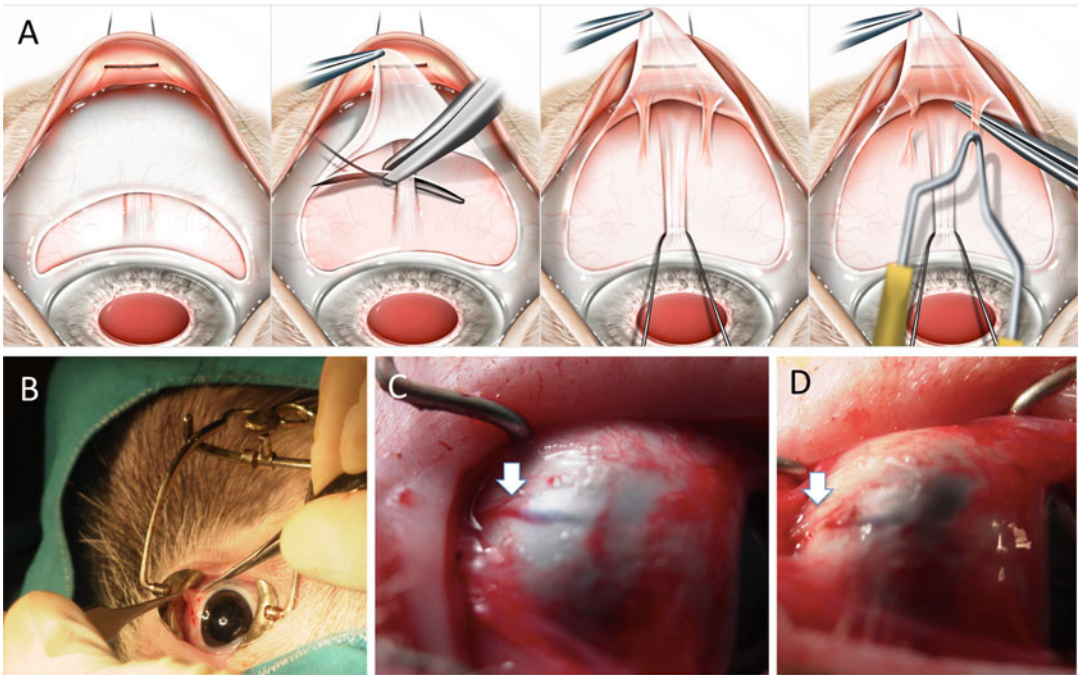


Fig. 1 Episcleral vein cauterization protocol. (a) Drawings of the sequence of the episcleral vein cauterization (EVC) protocol from left to right. Limbal peritomy (a strip of conjunctiva is incised and exposed to reveal the superior rectus muscle), resection of the superior rectus muscle, episcleral veins exposure, and cauterization. (b) Photograph of the limbal peritomy. (c) Photograph of the dorsal episcleral vein exposure (*arrow*). (d) Photography of the episcleral vein after cauterization, the *arrow point* to the cauterized vein

dexamethasone is applied to the eye surface. In control animals sham surgery is performed in the left eye while the right eye undergoes a similar surgical procedure except for the cauterization of episcleral veins.

5. After the operation and before the animal wakes up, 1 g of intravenous metamizole is injected as an analgesic treatment. The animals are kept alive for 21 weeks after episcleral vein occlusion and the IOP is measured weekly.
6. Several months after the first surgery, in some animals the IOP declines to control values, in this case, a second operation is carried out on the previously operated eyes, with further cauterization of two ventral episcleral veins to ensure continuation of elevation of IOP (Fig. 1).

3.2 Microbeads/ Microspheres/ Fluospheres

1. The animals are anesthetized as described in the previous section.
2. Injections into the anterior chamber are made using a sterile 30-gauge needle, which is initially oriented tangential to the corneal surface and then redirected posteriorly, so it enters into the anterior chamber parallel to the iris. This manoeuver,

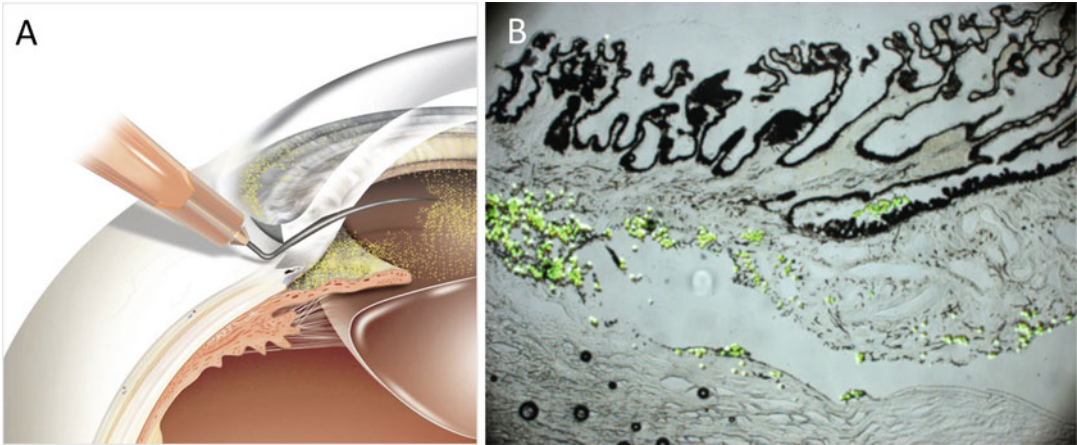


Fig. 2 Microbeads method. (a) Drawing of fluorospheres injection. (b) Histological section of the anterior chamber after the injection. Note the *green* fluorescent microbeads have accumulated in between the trabecular meshwork cells and episcleral channels

introduced for cataract surgery [17], allows the creation of a self-sealing corneal tunnel and avoids the continuous leaking of beads through the incision. A total volume of 100 μl is injected. In the right (control eye) only the vehicle is injected while in the left eye a total of $2\text{--}4 \times 10^5$ fluorospheres are injected.

3. Injections of microspheres are performed weekly until a maintained IOP elevation is observed in the left eye. A sustained elevation is usually achieved after nine injections.
4. **To induce faster IOP elevation with less number of injections, fluorospheres can be mixed with 50 μl of 2% HPM (Methocel) dissolved in the NaCl plus Tween-20 (Fig. 2).**

3.3 Intraocular Pressure Measurements

1. Intraocular pressure (IOP) is measured with a rebound tonometer in awake animals with only a drop of topical anesthesia previous to the measurement (Fig. 3). The tonometer is applied perpendicularly to the apical side of the cornea, until at least five or six independent measurements are obtained (each of these values is the average of four readings). The results of the IOP reading are accepted if the confidence interval is greater than or equal to 95% (*see Note 1*). IOP is analyzed before surgery in both eyes in order to obtain the baseline values, 1 week after operations, and then weekly until the end of the experimental period. Overall, the IOP monitoring includes a mean follow-up period of 14 months, with one weekly measurement.
2. 48 h after the EVC procedure the IOP typically increases and remains elevated during the following months (*see Note 2*).



Fig. 3 Tonometry in the minipig

4 Notes

1. IOP measurements should always be taken at the same hour of day in order to avoid circadian IOP variation.
2. Normal IOP for minipigs is about $22.43 + 4.46$ mmHg. IOPs of about $26.04 + 5.01$ mmHg are typically achieved after cauterization of the episcleral veins.

Acknowledgments

We want to specially thank Francisco Martin for his suggestions to improve the method and handling of animals. During the development of the methods a grant from The Glaucoma Foundation (TGF) supported the research.

References

1. Vecino E, Sharma SC (2011) Glaucoma animal models. In: Rumelt S (ed) Glaucoma-basic and clinical concepts. InTech, Rijeka, Croatia, pp 319–334
2. Galdos M, Vecino E (2011) Ultrastructural changes in the trabecular meshwork and increased IOP. Which came first, the chicken or the egg? Arch Soc Esp Oftalmol 86(8):241–242. <https://doi.org/10.1016/j.ofal.2011.06.001>
3. Vecino E, Galdos M, Bayon A, Rodriguez FD, Mico C, Sharma SC (2015) Elevated intraocular pressure induces ultrastructural changes in the trabecular meshwork. J Cytol Histol S3:007. <https://doi.org/10.4172/2157-7099.S3-007>
4. Garca M, Ruiz-Ederra J, Hernandez-Barbachano H, Vecino E (2005) Topography of pig retinal ganglion cells. J Comp Neurol 486(4):361–372. <https://doi.org/10.1002/cne.20516>
5. Ruiz-Ederra J, Garcia M, Hicks D, Vecino E (2004) Comparative study of the three neurofilament subunits within pig and human retinal ganglion cells. Mol Vis 10:83–92
6. Ruiz-Ederra J, Hitchcock PF, Vecino E (2003) Two classes of astrocytes in the adult human and pig retina in terms of their expression of high affinity NGF receptor (TrkA). Neurosci Lett 337(3):127–130
7. Veiga-Crespo P, del Rio P, Blindert M, Ueffing M, Hauck SM, Vecino E (2013) Phenotypic map of porcine retinal ganglion cells. Mol Vis 19:904–916

8. Vecino E, Rodriguez FD, Ruzafa N, Pereiro X, Sharma SC (2016) Glia-neuron interactions in the mammalian retina. *Prog Retin Eye Res* 51:1–40. <https://doi.org/10.1016/j.preteyeres.2015.06.003>
9. Ruiz-Ederra J, Garcia M, Hernandez M, Urcola H, Hernandez-Barbachano E, Araiz J, Vecino E (2005) The pig eye as a novel model of glaucoma. *Exp Eye Res* 81(5):561–569. <https://doi.org/10.1016/j.exer.2005.03.014>
10. Galdos M, Bayon A, Rodriguez FD, Mico C, Sharma SC, Vecino E (2012) Morphology of retinal vessels in the optic disk in a Gottingen minipig experimental glaucoma model. *Vet Ophthalmol* 15(Suppl 1):36–46. <https://doi.org/10.1111/j.1463-5224.2011.00937.x>
11. Ruiz-Ederra J, Garcia M, Martin F, Urcola H, Hernandez M, Araiz J, Duran J, Vecino E (2005) Comparison of three methods of inducing chronic elevation of intraocular pressure in the pig (experimental glaucoma). *Arch Soc Esp Oftalmol* 80(10):571–579
12. Urcola JH, Hernandez M, Vecino E (2006) Three experimental glaucoma models in rats: comparison of the effects of intraocular pressure elevation on retinal ganglion cell size and death. *Exp Eye Res* 83(2):429–437. <https://doi.org/10.1016/j.exer.2006.01.025>
13. Shareef SR, Garcia-Valenzuela E, Salierno A, Walsh J, Sharma SC (1995) Chronic ocular hypertension following episcleral venous occlusion in rats. *Exp Eye Res* 61(3):379–382
14. Weber AJ, Zelenak D (2001) Experimental glaucoma in the primate induced by latex microspheres. *J Neurosci Methods* 111(1):39–48
15. Suarez T, Vecino E (2006) Expression of endothelial leukocyte adhesion molecule 1 in the aqueous outflow pathway of porcine eyes with induced glaucoma. *Mol Vis* 12:1467–1472
16. Wang ZX, Cai SP, Xu J (2001) Study on expression of ELAM-1 and ICAM-1 mRNA on microvascular endothelial cells during focal cerebral ischemia/reperfusion. *Zhongguo Ying Yong Sheng Li Xue Za Zhi* 17(3):236–239
17. Langerman DW (1994) Architectural design of a self-sealing corneal tunnel, single-hinge incision. *J Cataract Refract Surg* 20(1):84–88

Noninvasive Intraocular Pressure Measurement in Animals Models of Glaucoma

Yan Hu and John Danias

Abstract

Intraocular pressure (IOP) elevation is a critical risk factor for development and progression of glaucoma. As such, measuring IOP in animal models of the disease is important for any research work trying to understand the pathophysiologic mechanisms of glaucoma. Noninvasive IOP measurement in animals uses methods that have been adapted from use on humans. Calibration of the instruments used for the specific animal and even strain used is critically important for allowing meaningful comparisons of results. We describe below the methods used for noninvasive IOP measurement in animals that are relevant to glaucoma research.

Key words Intraocular pressure, Glaucoma, Model, Applanation tonometry, Pneumotonometry, Electronic tonometry, Rebound tonometry, Methods

1 Introduction

Intraocular pressure IOP measurement is a critical method for glaucoma research as elevated IOP is a known risk factor for the development and progression of the disease [1–4]. In addition, IOP is the only modifiable parameter, reduction of which can prevent visual loss from glaucoma [1]. Although specific animal models for glaucoma may not necessarily rely on IOP elevation (if for example they only recapitulate the neurodegenerative aspects of the disease), recording IOP during experimental work related to glaucoma is a good practice.

For experiments of relatively short duration, IOP can be monitored by direct cannulation of the eye (e.g., *see* refs. [5–8]). However, for chronic experiments direct, cannulation for continuous IOP recording is not practical except under special circumstances [9]. Repeated cannulations introduce a significant risk for infection or other complications and are generally not practical as well. Thus, for the majority of experimental work, IOP measurement relies on a number of noninvasive methods that indirectly estimate its true

value through the wall of the eye. Most of these methods have been adapted from methods used on humans and have specific limitations that one has to keep in mind. Eye characteristics including corneal thickness and elasticity affect almost all of the noninvasive methods for measuring IOP [10–12].

Selection of the most appropriate method for IOP measurement depends on the size of the animal eye, availability of equipment, and experimental design. In general, because of diurnal variation, IOP measurements should be performed at approximately the same time of the day. For mice, IOP exhibits an increase at night [13], making differences between groups easier to detect. Maintaining the animals in a reverse light cycle (e.g., lights off at 8 AM, on at 8 PM) and measurement of IOP under dim light (or using night vision equipment) may be helpful if such a setup is available. For rats, constant light exposure also seems to elevate IOP making detection of IOP differences easier [14].

The five main methods for measuring IOP noninvasively are: applanation, indentation, pneumotometry, electronic tonometry, and rebound tonometry. Indentation tonometry has been largely abandoned for both human and animal work as it depends to a large degree on scleral rigidity and it causes a significant change in IOP over time. Indentation is used in a separate glaucoma research method which is called tonography and is infrequently used to measure trabecular outflow.

Of the four remaining methods, *applanation tonometry* relies on the principle of applying a variable force on the corneal surface to make it flat (plane). At that point the force exerted to the outside of the eye is equal in magnitude to the force exerted by IOP. A clever split prism optical system coupled with the use of fluorescein on the corneal surface allows the determination of the end-point of measurement (corneal flattening), while the force applied (and by consequence the IOP) can be read off a dial and is expressed in mmHg. Applanation tonometry can be performed in all animal species, but for mice and rats special prism tips are needed [15, 16], which are not commercially available at this time. For larger species, applanation tips used in human tonometry can be used. However, it should be pointed out that tips for human tonometry have been designed so that the capillary force exerted by the tear meniscus counteracts the spring force of the cornea as it is being applanated. The latter force differs in other species. This causes a deviation of applanation IOP readings from true IOP that increases with increasing IOP. Typically for animals with larger eyes than humans (e.g., bovine) IOP is significantly lower when measured by applanation and the range of IOPs is dramatically compressed.

In addition for applanation tonometry, the amount of fluorescein applied to the cornea affects the accuracy of measurements. Consistency is important.

Finally, because the visual end-point of these measurements is subjective, when used in research work, applanation tonometry should always be performed in a masked fashion.

Pneumotonometry relies on the principle of applanation but uses pressure generated by a compressed gas (usually air) to flatten the cornea. The pressure is recorded continuously and graphed. Although pneumotonometry is probably the most accurate method for measuring IOP in humans, it is not extensively used because it is not integrated with the rest of the ophthalmic examination. The archetypical pneumotonometry instrument is the Mentor 30 tonometer which was introduced in the 1960s. A number of these instruments are still available. Unfortunately newer versions of this instrument, because of FDA regulations, have eliminated the ability to change the gain and offset of the instrument and do not allow recalibration for use on experimental animals. Such recalibration is needed as pneumotonometry suffers similar problems with applanation when it comes to measuring IOP of species with significantly larger eyes. Adjusting the gain of the instrument can significantly expand the scale of the measurements providing expanded IOP resolution. Pneumotonometry typically requires access to electrical power.

Electronic tonometry detects a characteristic change in force applied as the cornea gets pressed by a 1 mm diameter plunger, in order to determine IOP. The Tonopen[®] is the instrument used clinically to perform electronic tonometry. Use of electronic tonometry has been reported for all animal species including the mice [17], rats [18], rabbits [19], cattle [20], dogs [21], and cats [22]. However, for tonometry in mice, the authors recommended the use of the instrument without the protective latex cover. This results in tear fluid entering between the central plunger and the surrounding collar which necessitates frequent disassembly of the instrument for cleaning and may result in significant variation between readings. For electronic tonometry application of the instrument along the visual axis is critical for obtaining accurate measurements.

Rebound tonometry relies on the analysis of the deceleration speed of a probe that impacts the cornea in order to estimate IOP [23]. To optimize the detection characteristics two versions of the instrument are available for research work (Tonolab[®] and Tonovet[®] for smaller and larger animals respectively) and an additional version is available for human use (iCare tonometer). One of the advantages of rebound tonometry is that it can be performed without the application of topical anesthesia as the contact time of the probe with the eye is in the range of milliseconds (and faster than the blink reflex). In addition, rebound tonometry is fairly insensitive to small off axis deviations in the positioning of the probe in respect to the visual axis [23].

It is important prior to initiation of any experimental work using any of the above methods, to establish the relationship between the true IOP and the IOP measured by the tonometer. Although many of the instruments used to measure IOP provide values in mmHg and can be used without knowing the exact relationship with *true* IOP (for example in comparative studies), calibrating the instrument for the specific animal species and strain used is important for the following reasons:

1. To detect small differences in IOP that may be masked by a compressed scale.
2. To accurately estimate the magnitude of IOP difference between groups or over time.
3. To compare IOP values across species or strains.

For longitudinal studies (especially when the experimental intervention may affect the ocular characteristics), it is also important to establish the relationship between instrument readings and *true* IOP at both the beginning and the end of the study (and at any point when ocular characteristics change).

We will describe below details of the IOP measurement methods that are used for glaucoma research in various species.

2 Materials

For all tonometry methods except rebound tonometry, topical anesthesia (using either proparacaine 0.5%, tetracaine 1%, or benoxinate 0.25%) should be used. Although rebound tonometry can be performed without topical anesthesia, it is often easier to perform under topical anesthesia. General anesthesia is not required for any species (or methods) if animals can be restrained adequately. However, it is important to avoid compression of the animal neck and thoracic and abdominal cavities while obtaining IOP measurements, as such compression will affect IOP readings. Specific restraining holders have been described for a number of animal species [11, 24, 25]. It is also important to allow the animals to relax before initiating IOP measurements. Measuring IOP in rats without the use of general anesthesia can be challenging, unless a prolonged period of acclimation is allowed where the animals get used to being handled over a period of many days. When general anesthesia is required (or elected) it is preferable to use inhalational anesthesia as it seems to affect IOP less than anesthesia involving the use of ketamine (at least in some species) [26]. If ketamine is used, IOP measurements should be obtained immediately after induction, as ketamine significantly reduces IOP in a time-dependent manner [27].

For IOP measurements the following equipment are needed:

1. Applanation tonometry: Perkins handheld tonometer.
2. Pneumotonometry: Mentor 30 pneumotonometer.
3. Electronic tonometry: Tonopen tonometer.
4. Rebound tonometry: Tonolab or Tonovet tonometers (depending on species).

Instrument tips should be cleaned after each use with 70% alcohol and dried. For instruments with disposable tips (or covers), a new tip (or cover) should be used for measurements of each animal.

For establishing the relationship between measured and true IOP, tubing (various diameters), syringes, plastic three way valves, needles ranging from 26G to 18G and phosphate-buffered saline (or ideally balanced salt solution) are needed. Epoxy glue (5 min setting) is useful for ensuring lack of leaks.

In-line pressure sensing is preferable to allow confirmation of the intraocular pressure and ensure lack of occlusion of the needle but can be dispensable if the open stopcock method (described below) is used.

3 Methods

3.1 Calibration (Establishing the Relationship Between Measured IOP and True IOP)

1. Connect tubing, syringes, and pressure sensor as shown in Fig. 1. Ensure that no air-bubbles are trapped in the system (*see Notes 1 and 2*).
2. Open the three-way valve 1 and raise the fluid reservoir so that the free fluid level is ~5 cm above the plane of the eye to obtain a very slow fluid flow through the needle.
3. Cannulate the eye with the needle at approximately 90 degrees to the visual axis through the peripheral cornea (*see Notes 3 and 4*).
4. Dry the cornea around the area of the needle entry using a rolled up kimwipe[®] (weck[®] cell sponges can also be used).
5. Observe under an operating microscope to ensure lack of leaks.
6. For mice or rat eyes, apply epoxy glue around the needle entry site after mixing components and wait until the epoxy hardens.
7. Raise fluid reservoir so that the free fluid surface level is 10 cm above the plane of the eye.
8. Record pressure through the pressure transducer (if the pressure transducer is not available proceed to **step 17**).
9. Close three-way valve 1, isolating the reservoir from the eye/-sensor circuit.

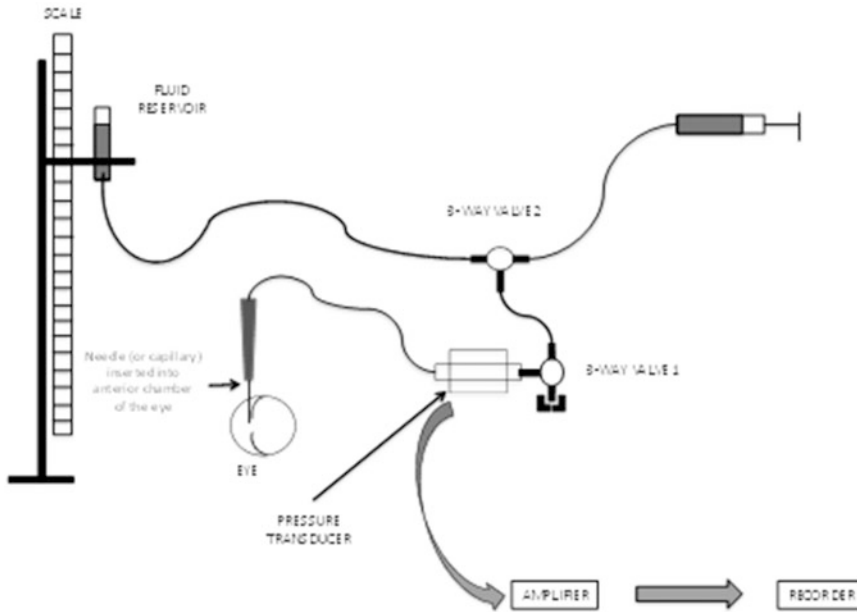


Fig. 1 Schematic setup for tonometer calibration. A similar setup can be used for direct IOP measurement. Two 3-way valves are used: 3-way valve 1 has one port permanently closed and allows at will connection between the column of fluid and the eye. 3-way valve 2 allows replenishment of the fluid in the system using a syringe. The port connecting to the syringe is closed during measurements. Pressure transducer is optional if the open stopcock method is used. (Components and eye are not to scale)

10. Record pressure through the pressure transducer to ensure that it has not changed.
11. Measure IOP using the appropriate instrument and record (*see below for details*) (*see Notes 5 and 6*).
12. Record pressure through the pressure transducer to ensure that it has not changed.
13. Open the three-way valve 1 allowing flow from the fluid reservoir to the eye/sensor circuit.
14. Raise reservoir so that free fluid surface level is 5 cm higher than before.
15. Repeat **steps 8–14** until you have reached a free fluid surface level that is 60 cm above the eye plane.
16. Graph the recorded IOP values against the recorded pressure values from the pressure transducer at which each IOP reading was obtained. Use this relationship to appropriately adjust IOP reading when reporting for publication (*see Note 7*).
17. Measure IOP using the appropriate instrument and record (do so without closing the three-way valve—this is the open stopcock method). Note on the record the distance between the free fluid surface level and the eye (*see Note 8*).

18. Raise reservoir so that free fluid surface level is 5 cm higher than before.
19. Repeat **steps 17–18** until you have reached a free fluid surface level that is 60 cm above the eye plane.
20. Graph the recorded IOP values against the recorded distance between the free fluid surface level and the eye at which each IOP reading was obtained. Use this relationship to appropriately adjust IOP reading when reporting for publication (*see Note 7*).

3.2 Applanation Tonometry

1. Wear a face mask and head cover. Your face will come very close to the animal head while measuring IOP.
2. Instill the local anesthetic drops and then the fluorescein. A small amount of fluorescein is needed. Be consistent (*see Note 9*).
3. Wipe the tip with an alcohol swab and dry with a kimwipe.
4. Turn the Perkins tonometer on and hold it with your dominant hand.
5. Make sure that the tonometer head is perpendicular to the surface of the eye and that the long axis of the prism tip is along the visual axis.
6. Move the tonometer forward slowly until the prism rests gently on the center of the cornea while observing through the viewfinder of the Perkins tonometer. Use one or two fingers from the other hand to keep the eyelids of the animal open (*see Note 10*).
7. With your thumb and index finger turn the calibrated dial on the tonometer clockwise until the two fluorescein semicircles in the prism head are seen through the viewfinder to touch and form a horizontal “S” shape. The correct end point is when the inner edges of the two fluorescein semicircle images just touch.
8. Withdraw the prism from the corneal surface, note the reading on the dial and record it.
9. Wipe the tip, turn the dial to zero, and repeat the measurement at least once more (preferably obtain three to five readings for averaging).
10. Repeat the procedure for the other eye.
11. Wipe the prism tip with alcohol, dry and proceed to measure other animals.
12. After completion of measurements, remove the tip, wipe with a clean, dry swab, and place it in a receptacle containing disinfectant (*see Note 11*).
13. Turn Perkins tonometer off and store in case.

3.3 Pneumotonometry

1. Instill the local anesthetic drops.
2. Wipe the tip of the pneumotonometer with an alcohol swab. Ensure that the silicone membrane at the tip is present and has no rips.
3. Turn the Mentor Model 30 tonometer on. Press on the “Zero” button to record the electrical zero baseline. Offset this reading (by turning the “Offset” knob) so that the tracing falls within the marked (graduated) area of the recording paper strip.
4. Hold the probe with your dominant hand and make sure that the tonometer head is perpendicular to the surface of the eye along the visual axis.
5. Move the tonometer probe forward slowly while depressing the foot-pedal until the tip of the probe touches the center of the cornea. Use one or two fingers from the other hand to keep the eyelids of the animal open (*see Note 10*).
6. Continue to advance the probe until the black line on the central tube of the probe disappears. The red line on the same tube should remain visible at all times. Notice the pitch of the noise as you are recording. It should be stable.
7. Continue recording for 20–30 s.
8. Withdraw the probe and repeat at least once more.
9. Review recordings to ensure stable readings and mark the eye and the periods where the actual reading was performed (*see Note 12*).
10. Wipe the tip and repeat the procedure for the other eye.
11. Wipe the prism with alcohol, dry and proceed to measure other animals.
12. After completion of measurements turn the instrument off and wipe the tip after cleaning with alcohol.
13. To calculate IOP subtract from the measurement value the electrical zero value. Use the calibration curve created during the instrument calibration (*see Note 13*) to convert these numbers to IOP in mmHg.

3.4 Electronic Tonometry

1. Instill the local anesthetic drops.
2. Turn the Tonopen on and perform the recommended testing by the manufacturer to ensure proper operation (*see Note 14*).
3. Place a disposable latex cover over the instrument tip.
4. Hold the probe with your dominant hand and make sure that the tonometer head is perpendicular to the surface of the eye and the tonometer is along the visual axis.
5. Move the tonometer forward decisively at moderate speed and touch the cornea. Use one or two fingers from the other hand

to keep the eyelids of the animal open (*see Note 10*). Make sure you hear the characteristic chirp indicating that a reading has been obtained.

6. Repeat **step 5** until the tonometer has accumulated enough readings and has calculated an IOP value that is within acceptable confidence limits. Record that value displayed on the instrument screen.
7. Repeat measurements at least five times per eye (*see Note 15*) and then measure the contralateral eye.
8. Change tip cover and proceed to measure other animals.
9. After the completion of measurements turn the instrument off and cover the tip with a new cover for storage.

3.5 Rebound Tonometry

1. Instill the local anesthetic drops (this step is optional).
2. Turn the instrument on and insert a new probe into the instrument head. Trigger the instrument to ensure that the probe moves freely forward and then is pulled back.
3. Bring the instrument close to the eye and trigger the device. Ensure that the probe axis is on the visual axis (*see Notes 16 and 17*).
4. Record the reading and repeat measurement at least twice more.
5. Remove the probe from the instrument wipe and replace. Repeat the procedure for measuring IOP in the other eye.
6. Wipe the probe with alcohol, dry and proceed to measure other animals.
7. After the completion of measurements turn the instrument off remove the probe and wipe the instrument head (*see Note 18*).

4 Notes

1. Intravenous (IV) tubing can be used for cannulation of large eyes or when using the open stopcock method. However, it does have significant compliance and should be avoided when using the closed stopcock method. Polyethylene tubing (PE) is excellent for this method. When cannulating smaller eyes the tubing can cause significant torqueing which makes positioning often difficult or unstable. Small diameter PE tubing can be used and can be stretched while heated to make it much more pliable.
2. Air bubbles can occlude tubing and can make measurements unreliable. Ensure that no bubbles are introduced during tube connections (especially when using luer connections). To avoid

trapping bubbles fill all tubing with fluid prior to assembling. Fill female luer connectors with fluid using a syringe with a 30G needle to inject the fluid in the bottom of the hub prior to assembling male with female luer portions. Ideally, use degassed fluid (fluid can be easily degassed by applying house vacuum while stirring in a beaker). Be meticulous about inspecting the tubing after assembly and removing any bubbles (even the tiniest ones).

3. Ideally eyes to be cannulated should not be removed from the orbit and the animal should be deeply anesthetized (but alive) during the procedure. In practice using animals immediately after death is also acceptable. Removal of the eye from the orbit may facilitate positioning but eliminates the cushioning effect of the periorbital fat. Thus for methods that depend on dynamic phenomena (rebound and electronic tonometry) measurements may be affected. Keep that in mind when interpreting data obtained in vivo. For large animals (like bovine) usually only the eye is available when calibrating the instrument. The effect of fat cushioning is less in these eyes.
4. When cannulating larger eyes use a larger bore needle. For bovine eyes use 18–21G needles, for rabbit eyes 21–23G needles, and for smaller eyes 25–26G needles. For mice a 26G needle with a short bevel is preferable. Enter the eye with the bevel toward the lens to decrease the risk of penetrating the lens capsule. Once in the eye rotate the needle so that the bevel faces anteriorly to avoid occlusion by the iris. In mouse eyes avoid inserting the needle too deeply (across the anterior chamber) as it will affect IOP measurements. Needles can be substituted with pulled capillaries. Pull capillaries in a capillary puller. Ensure that the pulled capillaries have at least 100 μm diameter. Pulled capillaries may be preferable to needles when cannulating small eyes (especially mouse eyes).
5. A minimum of three to five measurements should be obtained at each pressure level when performing calibration and the measurements averaged.
6. It is critically important to keep the surface of the eye moist while obtaining readings. Re-wet the cornea with PBS and remove excessive fluid prior to obtaining readings at a new pressure level.
7. Please remember that $1 \text{ mmHg} = 1.33 \text{ mbar}$ or $\sim 1.34 \text{ cmH}_2\text{O}$. Please ensure that all readings are in the correct units when reporting results.
8. Selection of the open vs closed stopcock methods depends on the availability of equipment. In general, when possible, the closed stopcock method is preferable. However, for methods

that depend on dynamic phenomena, the open stopcock method is almost equivalent and can be used.

9. A fixed combination of anesthetic and fluorescein is also commercially available. However the amount of fluorescein included is too much. If you use this preparation allow 3–5 min for the tears to flush out the majority of fluorescein before measuring IOP.
10. Do not apply pressure to the eye itself as this will raise IOP. Hold the upper and if needed lower eyelids against the superior and inferior edges of the orbit to avoid exerting such pressure.
11. Chlorhexidine can be used for disinfectant. Alternatively, a solution of dilute bleach (10% dilution) can be used. Do not leave the tip in disinfectant overnight. Remove after 30 min, wash with water, dry and store.
12. Notice that tracings fluctuate with heart cycle and with breathing, but the average should remain stable. As the instrument continuously records while the foot-pedal is pressed you will need to mark clearly the portions of the tracing that should be used for IOP calculation.
13. As mentioned earlier, the Mentor 30 instrument is the only pneumotonometer that allows changes in the gain and offset. Changes are made by adjusting two screws in the back of the instrument during the calibration process. Adjusting the gain will expand the scale allowing for finer IOP readings. However, excessive increase in the gain will result in noise. Once set during the calibration process do not change the gain during the actual IOP measurements. Although Mentor 30 tonometers are preferable for experimental work, newer pneumotonometers can be used. However, it will be harder to detect small IOP differences using these instruments as the scale will be significantly compressed. Newer instruments automatically provide a single IOP value. Do not rely on these values. Instead obtain and inspect the tracings.
14. If you get a “Bad” reading turn off and try again. It is not unusual to need to turn on and off for a few times before you can get the tonometer to give a “Good” reading.
15. Tonopen readings are often highly variable. Ensure that the instrument is touching the apex of the cornea at the right angle and that the application of the instrument on the cornea is performed in a consistent way. You may need to collect up to 10 readings per eye and use statistical methods to remove outliers.
16. For small eyes (e.g., mouse eyes) alignment can be difficult. It can be facilitated by securing the instrument and moving it with the use of a micromanipulator. Using such an approach will also ensure that triggering the device does not

inadvertently cause the probe track to change. Alignment should be performed under an operating microscope and verified in the Z-axis through inspection from the side. That is part of the reason that although rebound tonometry can be performed on non-sedated mice many investigators prefer to perform under sedation. Modifications to the instrument to create a detached probe housing and a foot-switch operated triggering mechanism circumvent such problems. For larger animals (using the Tonovet) positioning is less critical in obtaining accurate readings.

17. For large animals, it is not usually necessary to hold the eyelids while recording. If needed use one or two fingers from the other hand to keep the eyelids of the animal open (*see Note 10* above). For mice and rats, make sure that you apply minimal pressure.
18. Animal dander and tears often tend to accumulate in the probe shaft or on the probe itself. In addition the probe may become magnetized. If needed demagnetize the probe using a demagnetizer. Also avoid using the instrument next to instruments that can cause strong magnetic interference (including cell phones). Use the manufacturer's suggestions for keeping the probe shaft clean of debris. Canned compressed air is often useful for cleaning the instrument. Check for the possibility that the probe is bent by rolling the probe on a flat surface. Discard bent probes.

Acknowledgments

Grant support: NEI R01 EY025543.

References

1. The Advanced Glaucoma Intervention Study (AGIS) (2000) 7. The relationship between control of intraocular pressure and visual field deterioration. The AGIS investigators. *Am J Ophthalmol* 130(4):429–440
2. Gordon MO, Beiser JA, Brandt JD, Heuer DK, Higginbotham EJ, Johnson CA, Keltner JL, Miller JP, Parrish RK 2nd, Wilson MR, Kass MA (2002) The ocular hypertension treatment study: baseline factors that predict the onset of primary open-angle glaucoma. *Arch Ophthalmol* 120(6):714–720. discussion 829–730
3. Nemesure B, Honkanen R, Hennis A, Wu SY, Leske MC, Barbados Eye Studies G (2007) Incident open-angle glaucoma and intraocular pressure. *Ophthalmology* 114(10):1810–1815. <https://doi.org/10.1016/j.ophtha.2007.04.003>
4. Sommer A, Tielsch JM, Katz J, Quigley HA, Gottsch JD, Javitt J, Singh K (1991) Relationship between intraocular pressure and primary open angle glaucoma among white and black Americans. The Baltimore eye survey. *Arch Ophthalmol* 109(8):1090–1095
5. Avila MY, Carre DA, Stone RA, Civan MM (2001) Reliable measurement of mouse intraocular pressure by a servo-null micropipette system. *Invest Ophthalmol Vis Sci* 42(8):1841–1846
6. Kiel JW, Reitsamer HA, Walker JS, Kiel FW (2001) Effects of nitric oxide synthase inhibition on ciliary blood flow, aqueous production and intraocular pressure. *Exp Eye Res* 73(3):355–364. <https://doi.org/10.1006/exer.2001.1050>

7. Huang W, Fileta JB, Filippopoulos T, Ray A, Dobberfuhr A, Grosskreutz CL (2007) Hsp27 phosphorylation in experimental glaucoma. *Invest Ophthalmol Vis Sci* 48(9):4129–4135. <https://doi.org/10.1167/iovs.06-0606>
8. John SW, Smith RS, Savinova OV, Hawes NL, Chang B, Turnbull D, Davisson M, Roderick TH, Heckenlively JR (1998) Essential iris atrophy, pigment dispersion, and glaucoma in DBA/2J mice. *Invest Ophthalmol Vis Sci* 39(6):951–962
9. Downs JC (2015) IOP telemetry in the non-human primate. *Exp Eye Res* 141:91–98. <https://doi.org/10.1016/j.exer.2015.07.015>
10. Chihara E (2008) Assessment of true intraocular pressure: the gap between theory and practical data. *Surv Ophthalmol* 53(3):203–218. <https://doi.org/10.1016/j.survophthal.2008.02.005>
11. Nissirios N, Goldblum D, Rohrer K, Mittag T, Danias J (2007) Noninvasive determination of intraocular pressure (IOP) in nonsedated mice of 5 different inbred strains. *J Glaucoma* 16(1):57–61. <https://doi.org/10.1097/IJG.0b013e31802b3547>
12. Doughty MJ, Zaman ML (2000) Human corneal thickness and its impact on intraocular pressure measures: a review and meta-analysis approach. *Surv Ophthalmol* 44(5):367–408
13. Sacki T, Aihara M, Ohashi M, Araie M (2008) The efficacy of TonoLab in detecting physiological and pharmacological changes of mouse intraocular pressure—comparison with TonoPen and microneedle manometry. *Curr Eye Res* 33(3):247–252. <https://doi.org/10.1080/02713680801919716>
14. Moore CG, Johnson EC, Morrison JC (1996) Circadian rhythm of intraocular pressure in the rat. *Curr Eye Res* 15(2):185–191
15. Cohan BE, Bohr DF (2001) Goldmann applanation tonometry in the conscious rat. *Invest Ophthalmol Vis Sci* 42(2):340–342
16. Cohan BE, Bohr DF (2001) Measurement of intraocular pressure in awake mice. *Invest Ophthalmol Vis Sci* 42(11):2560–2562
17. Reitsamer HA, Kiel JW, Harrison JM, Ransom NL, McKinnon SJ (2004) Tonopen measurement of intraocular pressure in mice. *Exp Eye Res* 78(4):799–804. <https://doi.org/10.1016/j.exer.2003.11.018>
18. Moore CG, Milne ST, Morrison JC (1993) Noninvasive measurement of rat intraocular pressure with the Tono-Pen. *Invest Ophthalmol Vis Sci* 34(2):363–369
19. Lim KS, Wickremasinghe SS, Cordeiro MF, Bunce C, Khaw PT (2005) Accuracy of intraocular pressure measurements in new zealand white rabbits. *Invest Ophthalmol Vis Sci* 46(7):2419–2423. <https://doi.org/10.1167/iovs.04-0610>
20. Gum GG, Gelatt KN, Miller DN, MacKay EO (1998) Intraocular pressure in normal dairy cattle. *Vet Ophthalmol* 1(2-3):159–161
21. Gelatt KN, MacKay EO (1998) Distribution of intraocular pressure in dogs. *Vet Ophthalmol* 1(2-3):109–114
22. Rusanen E, Florin M, Hassig M, Spiess BM (2010) Evaluation of a rebound tonometer (Tonovet) in clinically normal cat eyes. *Vet Ophthalmol* 13(1):31–36. <https://doi.org/10.1111/j.1463-5224.2009.00752.x>
23. Kontiola AI, Goldblum D, Mittag T, Danias J (2001) The induction/impact tonometer: a new instrument to measure intraocular pressure in the rat. *Exp Eye Res* 73(6):781–785. <https://doi.org/10.1006/exer.2001.1088>
24. Wang WH, Millar JC, Pang IH, Wax MB, Clark AF (2005) Noninvasive measurement of rodent intraocular pressure with a rebound tonometer. *Invest Ophthalmol Vis Sci* 46(12):4617–4621. <https://doi.org/10.1167/iovs.05-0781>
25. Gerometta R, Podos SM, Candia OA, Wu B, Malgor LA, Mittag T, Danias J (2004) Steroid-induced ocular hypertension in normal cattle. *Arch Ophthalmol* 122(10):1492–1497. <https://doi.org/10.1001/archophth.122.10.1492>
26. Cone FE, Steinhart MR, Oglesby EN, Kalesnykas G, Pease ME, Quigley HA (2012) The effects of anesthesia, mouse strain and age on intraocular pressure and an improved murine model of experimental glaucoma. *Exp Eye Res* 99:27–35. <https://doi.org/10.1016/j.exer.2012.04.006>
27. Jia L, Cepurna WO, Johnson EC, Morrison JC (2000) Effect of general anesthetics on IOP in rats with experimental aqueous outflow obstruction. *Invest Ophthalmol Vis Sci* 41(11):3415–3419

High-Throughput Binocular Pattern Electroretinograms in the Mouse

Tsung-Han Chou, Jonathon Toft-Nielsen, and Vittorio Porciatti

Abstract

We describe a new method for obtaining user-friendly, robust pattern electroretinograms (PERG) simultaneously from each eye using asynchronous binocular stimulation and one-channel acquisition of signals recorded from a subcutaneous needle in the snout.

Key words Pattern electroretinogram, PERG, Retinal ganglion cell, Mouse

1 Introduction

The Pattern Electroretinogram (PERG) in response to contrast reversing patterns selectively depends on the presence of functional retinal ganglion cells [1]. Thus, the PERG has become an important outcome measure in the investigation of optic nerve disorders such as glaucoma [2]. Typically, the PERG amplitude is severely reduced in the early stages of the disease, even before evidence of retinal ganglion cell death while the latency may be modestly delayed. All the components of the PERG waveform appear equally affected. Here, we describe a technique that allows high-throughput, robust assessment of PERG in mice from both eyes simultaneously that does not require dark adaptation and pupil dilation. The technique exploits the physiological property of the PERG generators in mice, which differently from those of the standard ERG generate a widespread bioelectrical field. Thus, the PERG can be recorded from the snout with an amplitude similar to that recorded for the cornea. Both the eyes are stimulated simultaneously using patterned visual stimuli generated on LED displays that are presented to each eye with a slightly difference in the frequency of pattern reversal. Responses from each eye are obtained by deconvolution of the signal recorded from a common snout electrode. Details of this technique have been previously published [3–5].

2 Materials

1. The mouse holder consists of a thermostatic plate (TCAT-2LV, Physitemp Inc., Clifton NJ) inserted in a recording stage (Jorvec Corp, Miami, FL) including a bite bar and head holders bars that allow for an unobstructed view of the stimuli (Fig. 1).
2. Visual stimuli consisting of horizontal gratings (95% contrast, 0.06 cycles/degree spatial frequency, 700 cd/m² mean luminance) are generated on two (15 × 15 cm) LED tablet displays (Jorvec Corp, Miami, FL, USA) and presented at each eye separately at a distance of 10 cm (Fig. 2). Gratings reverse in contrast at slightly different temporal frequency (OD, 0.984 Hz; OS, 0.992 Hz) to allow deconvolution of the signal and retrieval of PERG from each eye [5].
3. PERG signals are recorded from a common subcutaneous needle (Grass Technologies, West Warwick, RI) placed in the snout and referenced to a similar electrode placed in the back of the head. A third subcutaneous electrode placed at the root of the tail serves as a ground.
4. PERG signals are fed to an Opti-Amp bioamplifier (Intelligent Hearing Systems Inc., Miami, FL) amplified (10,000 fold), filtered (1–300 Hz, 6 dB/oct), and averaged (OD, 372 epochs of 492 ms; OS, 372 epochs of 496 ms) [5] using a Universal Smart Box acquisition system (Intelligent Hearing Systems Inc., Miami, FL).
5. PERG waveforms and corresponding noise waveforms, obtained using a plus/minus reference [6], are displayed on a general purpose laptop computer (Fig. 3).

3 Methods

All the procedures are performed in compliance with the Association for Research in Vision and Ophthalmology (ARVO) Statement for Use of Animals in Ophthalmic and Vision Research.

1. As the PERG is a light-adapted response, dark adaptation is not necessary. All the procedures are performed in a moderately lit room. Mice are weighed and anesthetized with intraperitoneal injections (0.5–0.7 mL/kg) of a mixture of ketamine (42.8 mg/mL) and xylazine (8.6 mg/mL). Care needs to be used in order not to stress the mouse. The typical duration of the anesthesia is 30–40 min, and the occurrence of lens opacity is extremely rare (*see* **Notes 1** and **2**).
2. The mouse superior incisor teeth are hooked to the bite bar and the head is gently restrained by the head holder bars. A

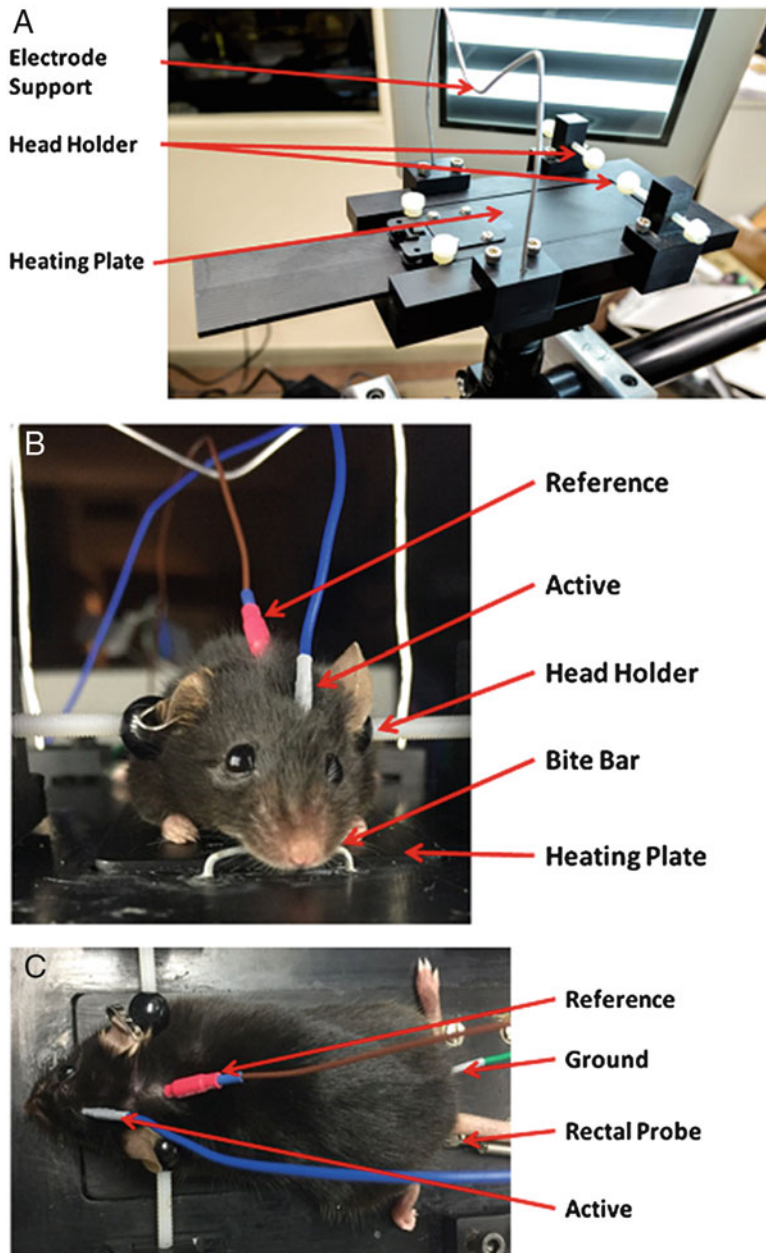


Fig. 1 Mouse stage. (a) Base with heating plate, head holders, and support for electrode wires. (b) The anesthetized mouse is gently restrained by a head-holder and its superior incisor teeth are hooked to a bite bar. The active electrode is a subcutaneous needle inserted in the snout. The reference electrode is a subcutaneous needle inserted in the back of the head. (c) The ground electrode is a subcutaneous needle inserted at the root of the tail. The body temperature is monitored with a rectal probe and controlled via a feedback-controlled heating plate

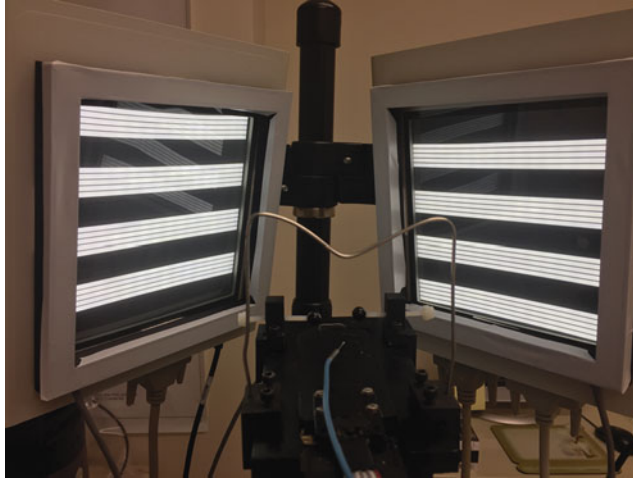


Fig. 2 Pattern stimuli are generated on two identical LED displays. These displays are situated around the animal stage (Fig. 1a) and are positioned to present stimuli separately to each eye of the mouse. The bioamplifier is positioned behind the stage and away from the stimulus displays to ease positioning of electrodes and reduce stimulus artifact pick up

temperature probe is inserted in the rectum to keep the body temperature at 37.0 °C using a feedback-controlled heating pad (TCAT-2LV, Physitemp Inc., Clifton NJ, *see Note 3*). One small drop of balanced saline solution (BSS) is instilled in each eye using a 30-gauge cannula to prevent corneal dryness (*see Note 4*). Pupil dilation is not necessary as the small pupil size maximizes the depth-of-field and keeps the stimulus focused on the retina.

3. The active electrode is a subcutaneous stainless steel needle (Grass, West Warwick, RI, USA) placed in the snout. Similar electrodes are placed medially on the back of the head (reference) and at the root of the tail (ground). Refer to Fig. 1b,c for electrode placement. Active, reference, and ground electrode leads are leaned on a metal support bridge and inserted into the Opti-Amp bioamplifier (Intelligent Hearing Systems INC, Miami, FL). The bioamplifier is then connected to the Universal Smart Box acquisition system (Intelligent Hearing Systems Inc., Miami, FL) via a fiber optic cable.
4. Generation of visual stimuli and signals acquisition/processing to retrieve PERG waveforms from each eye simultaneously is operated with proprietary software (Jorvec Corp, FL) on a general-purpose laptop. Three consecutive PERG responses are recorded, superimposed to check consistency, and averaged. Identification of the major positive (P1) and negative waves (N2), as well as the measurement of their amplitude and latency, is automated (Fig. 3).

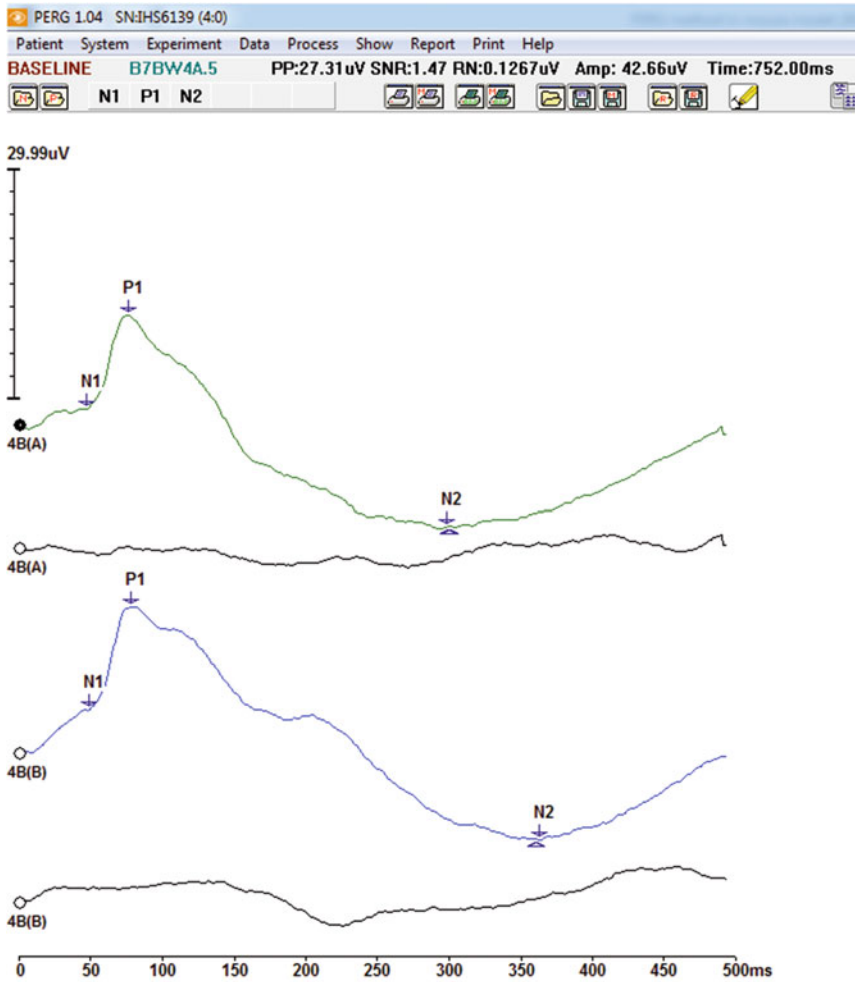


Fig. 3 Examples of PERG and noise waveforms recorded simultaneously from each eye of a young C57BL/6J mouse. PERG waveforms are characterized by a small negativity peaking at approximately 50 ms (N1), a major positive wave peaking at approximately 80 ms (P1), and a late negative wave peaking at approximately 350 ms (N2). Response amplitude is calculated from P1 to N2, and response latency as the time-to-peak of P1. Noise waveforms are simultaneously obtained by averaging odd and even sweeps in counterphase to have an index of uncorrelated background activity

4 Notes

1. PERG recording should not be performed if any opacity of the eyes is apparent prior to recording. Optical opacities deteriorate the contrast of the pattern stimulus resulting in an abnormal PERG.
2. Additional anesthesia may be required if mouse whiskers start moving during recording.

3. The mouse body temperature should be kept at 37 °C all the time during PERG recording. Body temperature drop causes significant reduction of PERG amplitude.
4. When applying BSS eye drops, care should be taken not to wet the eyelids, which may result in an electrical shunt between the electrodes and inability of record any response.

Acknowledgments

Grant support. NEI R43 EY023460 (JTN), NEI EY019077 (VP), NEI P30EY14801 (VP).

References

1. Porciatti V (2015) Electrophysiological assessment of retinal ganglion cell function. *Exp Eye Res* 141:164–170. <https://doi.org/10.1016/j.exer.2015.05.008>
2. Porciatti V, Saleh M, Nagaraju M (2007) The pattern electroretinogram as a tool to monitor progressive retinal ganglion cell dysfunction in the DBA/2J mouse model of glaucoma. *Invest Ophthalmol Vis Sci* 48(2):745–751. <https://doi.org/10.1167/iovs.06-0733>
3. Chou TH, Porciatti V (2012) The bioelectric field of the pattern electroretinogram in the mouse. *Invest Ophthalmol Vis Sci* 53(13):8086–8092. <https://doi.org/10.1167/iovs.12-10720>
4. Chou TH (2011) Age-related structural and functional changes of the mouse eye: role of intraocular pressure and genotype. *Biomedical engineering*, vol 2011. University of Miami, Scholarly repository, Miami, FL, p 94
5. Chou TH, Bohorquez J, Toft-Nielsen J, Ozdamar O, Porciatti V (2014) Robust mouse pattern electroretinograms derived simultaneously from each eye using a common snout electrode. *Invest Ophthalmol Vis Sci* 55(4):2469–2475. <https://doi.org/10.1167/iovs.14-13943>
6. Schimmel H (1967) The (+) reference: accuracy of estimated mean components in average response studies. *Science* 157(3784):92–94

Visual Evoked Potentials in Glaucoma and Alzheimer's Disease

Elisa Cerri, Carlotta Fabiani, Chiara Criscuolo, and Luciano Domenici

Abstract

Visual responses to gratings alternating in contrast have been studied in humans and several mammalian species. Previous evidence from human patients and animal models of neurodegeneration has highlighted the importance to record simultaneously the pattern electroretinogram (P-ERG) and visual evoked cortical potentials (VEPs) to investigate retinal and post-retinal sites of neurodegeneration.

In view of the increasing importance of research on experimental models of neurodegenerative diseases, we present here the parametric properties of visual evoked responses in animal models of glaucoma and Alzheimer's disease. Glaucoma and Alzheimer's disease (AD) are two distinct multifactorial neurodegenerative and progressive diseases, primarily affecting the elderly.

Key words Visual cortical evoked potentials (VEPs), Pattern electroretinogram (P-ERG), Visual system, Neurodegenerations, Biomarkers

1 Introduction

Visually evoked potentials (VEPs) in the electric field domain were elicited by strobe flash in the early years (1930s) of clinical encephalography (EEG); VEP waveforms were extracted from the EEG by signal averaging. Riggs and colleagues have recorded visual responses [1, 2] to a grating alternating in phase without change in mean luminance (pattern reversal); this commonly used pattern reversal method for ERG and VEP was popularized from the early 1960s [3]. One of its points of popularity is that the pattern reversal was revealed to be more sensitive to inner retina injury and lesions, optic nerve lesions and primary visual cortex impairment than flash evoked responses [4–6]. Indeed, this method of stimulation is more appropriate than flashes of diffuse light for stimulating neurons with center-surround organization of the receptive field such as the retinal ganglion cells and visual cortical neurons. The simultaneous recording of pattern ERG (P-ERG) and VEPs provided a useful tool for assessing the functional retinal and cortex and the

state of visual pathways from the retina to the cortex [7]. Gratings alternated in contrast at different Hz have been widely used to generate VEPs the amplitude of which is related to the psychophysical contrast sensitivity [8, 9]. In rodents sinusoidal gratings alternated in contrast at 1 Hz or less evokes transient P-ERG and VEPs. Sinusoidal gratings alternated in contrast at 2–8 Hz generate steady-state P-ERG and VEPs with a sine-wave signal. Recording steady-state VEPs as well as P-ERG is much speedier. On the other hand, transient responses generate complex waveform characterized by components with specific amplitude and latency.

Glaucoma is a group of eye disorders, currently recognized to be multifactorial, progressive, leading to reduction in vision and eventual blindness. The primary open angle glaucoma (POAG) is the most prevalent form of glaucoma [10]. Glaucoma is characterized by the progressive degeneration of retinal ganglion cells (RGCs) till cell death, optic nerve (ON) atrophy, impairment of visual function with visual field defects, and finally loss of neurons in the lateral geniculate nucleus and visual cortex [11]. POAG occurs with an intraocular pressure (IOP) higher than normal in 60–70% of patients. In the presence of ocular hypertension, there is no obvious damage to the RGC and ON. However, in a recent paper, we showed that retinal responses (P-ERG) and VEPs are altered during ocular hypertension in a murine model of glaucoma [12]. Our results suggest that an early phase characterized by alteration of inner retina circuitry caused by ocular hypertension precedes RGC degeneration and ON atrophy. Thus, P-ERG and VEPs (*see* the examples in Fig. 1) contribute to characterize the progression of glaucoma.

Alzheimer's Disease (AD) is a neurodegenerative progressive disease leading to dementia. The neuropathological changes of an AD brain include classical hallmarks such as the senile plaques formed by beta amyloid, neurofibrillary tangles, and dystrophic neurites containing hyperphosphorylated tau [13–15]. Entorhinal cortex and hippocampus are affected early in AD [15]. However, recent studies have highlighted that more than 60% of AD patients have a decline in one or more visual function(s). AD causes vision impairment by affecting the eye [16] and by deterioration of visual functions, from retina to visual cortex. In particular, clinical studies support a link between cognitive performance and visual dysfunction [17]. The gradual loss of memory is frequently accompanied by alteration of visuospatial function in animal models and AD patients [18, 19], suggesting that early AD is a synaptic dysfunction in several brain areas [20]. In Fig. 2, we reported P-ERG and VEPs in a murine model of AD showing that visual responses are affected. The simultaneous use of transient P-ERG and VEPs in AD patients revealed an impairment of the visual responses arising from the magnocellular streams of visual processing without an impairment of the retino-cortical time [21]; we suggested that large RGCs are

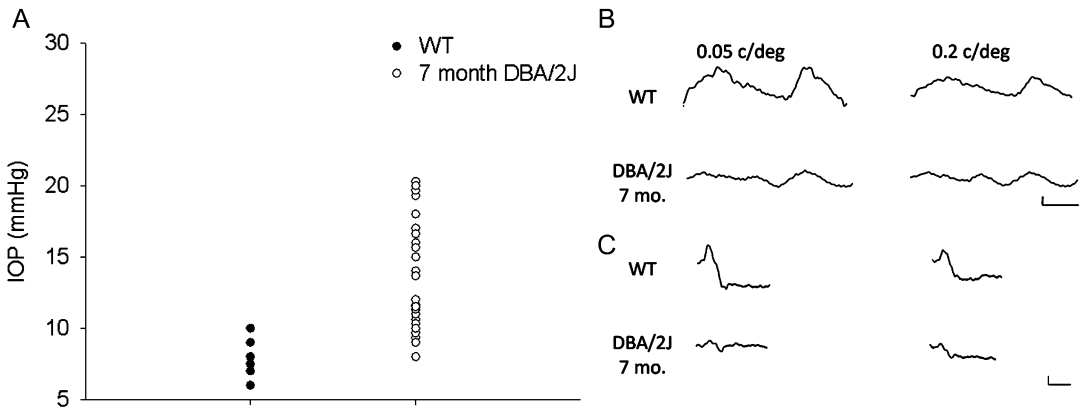


Fig. 1 Visual evoked responses in a murine model of glaucoma with ocular hypertension. **(a)** IOP values in C57BL/6J (wild type, WT) and DBA/2J (glaucoma model) mice. As a model of spontaneously arising glaucoma we used the DBA/2J mouse, which develops ocular hypertension at 6–7 months of age [12]. IOP (mmHg) measured by TonoLab tonometer (Icare, Finland) was already elevated in 7 month-old-DBA/2J mice ($N = 23$) as compared with WT mice (C57BL/6J, $N = 23$). **(b)** P-ERG waves in C57BL/6J (WT, controls) and DBA/2J mice. Typical examples of steady-state P-ERG evoked by gratings at spatial frequencies (measured in cycles/degree, c/deg) of 0.05 c/deg (left column) and 0.2 c/deg (right column) in WT control mice (top row) and 7 month DBA/2J mouse with ocular hypertension (bottom row). P-ERG was elicited by gratings (90% contrast) sinusoidally alternated in phase at 4 Hz. The amplitude of P-ERG was clearly reduced in DBA/2J mouse with ocular hypertension. Horizontal calibration bar = 50 ms, vertical calibration bar = 2 μ V. **(c)** VEP waves in C57BL/6J (WT, controls) and DBA/2J mice. Typical examples of transient VEP evoked by gratings at 0.05 c/deg (left column) and 0.2 c/deg (right column) in WT control mice (top row) and 7 month DBA/2J mouse with ocular hypertension (bottom row). VEPs were elicited by gratings (90% contrast) sinusoidally alternated in phase at 1 Hz. VEPs show prominent positive components characterized by latency around 100 ms. VEPs were recorded through a screw placed on the top of the cranial occipital bone contralateral to the stimulated eye. The amplitude of VEPs was clearly reduced in DBA/2J mouse with ocular hypertension. Horizontal calibration bar = 200 ms, vertical calibration bar = 10 μ V

primarily affected in AD. Altogether, the results in murine models and patients converge to the idea that visual impairment has a clear impact on the pathogenesis of AD.

2 Materials

Prepare rodents (rats and mice), including models of glaucoma and Alzheimer's disease, using common anesthetics for electrophysiological recordings. Following anesthesia, rodents should be mounted on a stereotaxic holder or an animal restraining apparatus starting the monitoring of body temperature and heart function. Follow diligently the procedure for anesthesia, animal handling, and care.

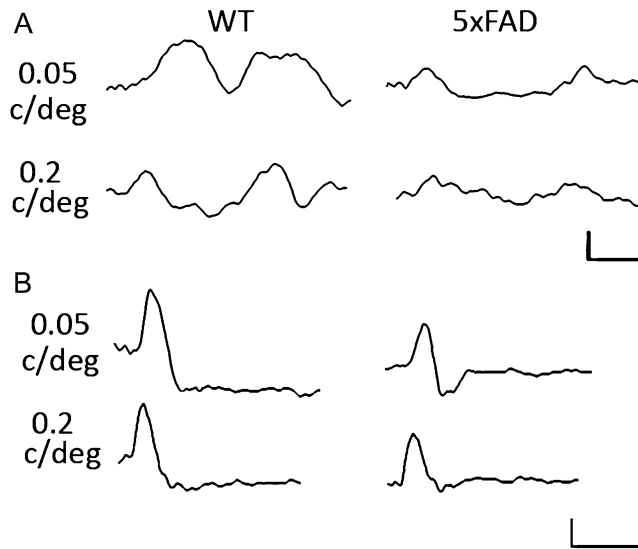


Fig. 2 Visual evoked responses in a murine model of Alzheimer's disease (AD). **(a)** P-ERG waves in C57BL/6J mouse (WT, controls) and a murine model of AD ($5 \times$ FAD transgenic mouse). Typical examples of steady-state P-ERG evoked by gratings at 0.05 c/deg (top row) and 0.2 c/deg (bottom row) in C57BL/6J mouse (WT, left column) and $5 \times$ FAD transgenic mouse (murine model of AD; right column) characterized by beta amyloid accumulation. P-ERG was elicited by gratings (90% contrast) sinusoidally alternated in phase at 4 Hz. The amplitude of P-ERG was reduced in $5 \times$ FAD mouse. Horizontal calibration bar = 50 ms, vertical calibration bar = 2 μ V. **(b)** VEP waves in C57BL/6J mouse (WT, control) and $5 \times$ FAD transgenic mouse (model of AD). Typical examples of transient VEP at 0.05 c/deg (top row) and 0.2 c/deg (bottom row) in WT (C57BL/6J, left column) and $5 \times$ FAD mouse (right column). VEPs were elicited by gratings (90% contrast) sinusoidally alternated in phase at 1 Hz. VEPs show prominent positive components characterized by latency around 100 ms. VEPs were recorded through a screw placed on the top of the cranial occipital bone contralateral to the stimulated eye. The amplitude of VEPs was reduced in $5 \times$ FAD mouse. Horizontal calibration bar = 200 ms, vertical calibration bar = 10 μ V

2.1 Recording Electrodes

1. P-ERG. The electrode used to record P-ERG is a small silver filament isolated on one surface to decrease the electromagnetic interference and inserted between the lateral eyelid and the eye ball.
2. VEPs. VEPs are usually recorded through external electrodes placed on the occipital scalp or chronically implanted electrodes such as a screw (stainless steel, 1 mm in diameter) on the top of the cranial occipital bone, in the correspondence of the primary visual cortex (binocular area Oc1b in rodents) contralateral to the stimulated eye [22]. Chronically implanted electrodes show high signal reliability within a single session and intersessions. Single electrodes (electrolyte-filled glass micropipettes as well as metal extracellular recording electrodes) can be used to record VEPs after the insertion into the primary visual cortex perpendicularly to the stereotaxic plane. The advantage of using microelectrodes is that VEPs can be recorded at different occipital positions in accordance with the retinotopy and ocularity [22, 23].

2.2 Visual Stimuli

1. Visual stimuli. Commonly used visual stimuli are pattern reversal and pattern onset/offset. Pattern reversal is a preferred stimulus because there is more inter-subject VEP reliability than with pattern onset stimuli. Several laboratories developed pattern reversal visual stimuli; originally the authors back-projected a checkerboard pattern onto a translucent screen with two projectors that each projected reversed checkerboard images. Other authors projected alternating vertical stripes using a reversing mirror system. Commercially produced, visual evoked potential systems, simulating these pattern reversals, now largely use video monitors.
2. Video monitors. In rodents the mean luminance of cathode ray tube monitors (CRT) should be set at 15–30 cd/m²; high mean luminance of the screen should be avoided. Different spatial frequencies (checkerboard or gratings of different orientation; at least three cycles should be contained in the screen) are generated on the screen. The contrast of square/sinusoidal wave gratings of various spatial frequencies is alternated in phase (counterphase) at 2–8 Hz for steady-state responses and 1 Hz or less for transient responses (*see* Subheadings 3.1 and 3.2) without change in mean luminance.

2.3 Amplifiers and Filters

The electrical signals are usually amplified several thousand-fold (5000–10000), band-pass filtered (0.3–200 Hz), digitized and averaged.

2.4 Restraining Device and Stereotaxic Holder

A compliant holder device for restraining the rodent's head is necessary to reduce the noise generated by breath cycle and heart rate. We recommend mounting anesthetized rats and mice in a stereotaxic holder if single microelectrodes should be inserted into specific occipital positions to record VEPs as a function of retinotopy and ocularity (*see* Subheading 2.1).

2.5 Body Temperature Control and Heart Monitoring

Thermoregulatory support devices are used to maintain temperature in anesthetized rodents around 37–38 °C. The measurement of heart rate by surface electrodes is central to understanding cardiovascular control under anesthesia.

2.6 Averaging

1. Averaging. VEPs are extracted from the EEG by a simple program (signal averaging), which adds the electrical activity for set time periods [24]. The computer programs save a defined time period of EEG activity following a visual stimulus, which is repeated over and over adding the signals together (usually 100–200 responses in blocks of ten events each). The random EEG activity (noise) is averaged, leaving the visually evoked potential.

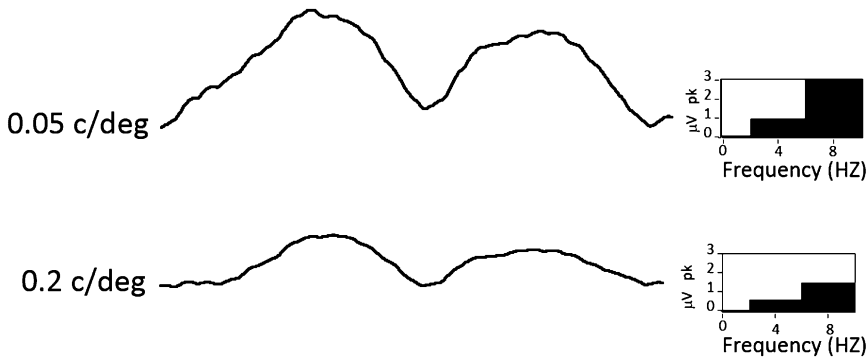


Fig. 3 Steady-state evoked responses. Typical examples of steady-state P-ERG (left column) elicited by square gratings (90% contrast; 0.05 c/deg, top row and 0.2 c/deg, bottom row) sinusoidally alternated in phase (counterphase) at 4 Hz with the relative power percentage of single harmonics (right column) in adult C57BL/6J mouse. The second harmonic (8 Hz, right column; μV at peak) is largely prevalent

2. Fast Fourier transform. Gratings sinusoidally alternated in phase (counterphase) at 1 Hz or less generate a complex waveform while at frequency of 2–8 Hz these generate steady-state P-ERG and VEPs with a sine-wave signal that can be split into a number of harmonic frequency components whose phase, amplitude, and relative power can be separated by a Fourier analyzer. In this condition, the analysis program saves the averaging of responses time-locked to 2–8 Hz. Frequency domain analysis of the steady-state responses with amplitude, phase, and relative power of different harmonics derives from fast Fourier transform (the relative power of the second harmonic should be higher than 50% while other harmonics representing noise are less represented; *see* Fig. 3). The phase is a function of the stimulus frequency and the time delay between stimulus and brain response (*see* Subheadings 3.2 and 3.3). The amplitude indicates the total magnitude of the steady-state responses and/or the relative magnitude of a given harmonic of the response measured in microvolts [9, 25].

2.7 Anesthesia

VEPs and P-ERG are usually examined under anesthesia. Unfortunately, some anesthetics can affect the VEP, mainly when deep anesthesia is induced. Usually, in our laboratory, we use 2,2,2-Tribromoethanol (avertin; 200 mg/kg injected intraperitoneally) for short-term anesthesia (2 h or less) and a mixture of zoletil-xilor (100–200 mg/kg body weight for Ketamine and 5–16 mg/kg body weight for Xylazine injected intraperitoneally) for long-term anesthesia.

2.8 Antibodies Recognizing Beta Amyloid

Several commercially available antisera and monoclonal antibodies produced against oligomeric and fibrillar forms of beta amyloid are directed against conformation-specific epitopes that are associated

with the aggregated state and are absent in normal proteins. Antibodies recognizing beta amyloid are typically specific for a particular part of the beta amyloid sequence or a particular amyloid conformation.

3 Methods

Carry out the recording sessions following the illustrated methods.

3.1 *Electrophysiological Recordings*

In anesthetized rodents, VEPs are usually recorded through a chronically implanted screws placed on the top of the cranial occipital bone or external electrodes in the correspondence of the primary visual cortex (binocular area Oc1b) contralateral to the stimulated eye. Screws are placed on the top of the cranial occipital bone, in a superficial hole of the occipital bone made by a cranial drill in the correspondence of area Oc1b contralateral to the stimulated eye. Screws are usually fixed using dentist cement on the top of the cranial bone and connected through isolated wires to filters and amplifiers [12]. A reference electrode is usually placed on the earlobe, on the midline on the top of the head. A ground electrode can be placed at any location, scalp, or earlobe. The time period analyzed is usually 200 and 500 ms following onset of each visual stimulus in accordance with the reversal frequency. The electrical signals are usually amplified several thousand-fold, band-pass filtered, digitized, and averaged. Start the recording session when the signal-to-noise ratio is high (*see Note 1*). During the recording session check the pupil size and direction. The P-ERG and VEP amplitudes evoked by gratings alternating in phase (counterphase) can be analyzed as a function of spatial frequency and contrast (*see Subheadings 3.2, 3.3 and Note 2*). Recording steady-state responses is much speedier and can be accomplished for low amplitude signal. This represents a clear advantage when P-ERG and VEPs are recorded in animal models of injury and diseases quite often characterized by a low signal-to-noise ratio due to neurodegenerative processes affecting retina and/or post-retinal sites. Usually, in our laboratory, we use steady-state responses in different animal models of neurodegeneration such as the glaucoma and Alzheimer's disease. During the recording session, the body temperature of rodents should be maintained around 37–38 °C and the heart monitored (*see Notes 3–5*).

3.2 *Visual Evoked Responses and Temporal Frequencies*

The dependence of P-ERG and VEP response upon the temporal frequency should be investigated by modulating the contrast sinusoidally in time (counterphase). In rodents VEPs have a complex waveform at frequencies lower than 1 Hz: when recordings are performed through external electrodes there is a prominent positive amplitude component at about 100 ms (Figs. 1 and 2) followed

by a more variable negative component. The amplitude of P100 decreases as a function of increasing spatial frequencies. Using single microelectrodes inserted into the primary visual cortex perpendicularly to the stereotaxic plane, VEPs are usually formed by a prominent wave characterized by a negative amplitude according to the depth of the microelectrode through the cortical layers [22]. At frequencies higher than 2 Hz, the waveform of P-ERG and VEP in rodents is approximately a sinewave corresponding to the second harmonic of the contrast modulation as it appears in Fig. 3.

3.3 Dependency of VEPs and P-ERG on Contrast and Phase

1. Contrast. The amplitudes of P-ERG and VEPs in response to alternating gratings of different spatial frequencies increase with stimulus contrast (low-moderate contrast), showing a difference between P-ERG and VEPs. The VEP amplitude is a linear function of log contrast while the P-ERG amplitude increases monotonically with stimulus contrast.
2. Phase. The temporal phase of the steady-state responses (counterphase gratings) increases linearly with the temporal frequencies. The variation of the temporal phase with the temporal frequency permits us to estimate the latency of retinal and cortical responses to single stimulus. The delay is proportional to the slope of the regression line, relating response phase to stimulus frequency [9].

3.4 Cortical Spatial Resolution Limit

Cortical spatial resolution limit is an electrophysiological correlate of the behavioral visual acuity. This can be easily measured using VEPs evoked by increasing spatial frequencies. The cortical spatial resolution limit in each eye can be calculated by means of linear extrapolation of data points to the noise level as in the examples reported in Fig. 4 for the mouse eye.

3.5 Retino-Cortical Time

Retino-cortical time is the difference between P-ERG and VEPs prominent components when transient responses are evoked. The retino-cortical time is a useful tool for assessing the state of visual pathways, retina, and post-retinal sites. The temporal delay of P-ERG and VEPs can also be measured looking at the response phase of the steady-state responses (*see* Subheading 3.3).

3.6 Measurement of IOP in Animal Models of Glaucoma

Repeated measures of IOP should be obtained using common tonometers in unanesthetized rodents trained to take position in partial restrainers without invasive handling (Fig. 1a). At least six measurements from each eye should be collected.

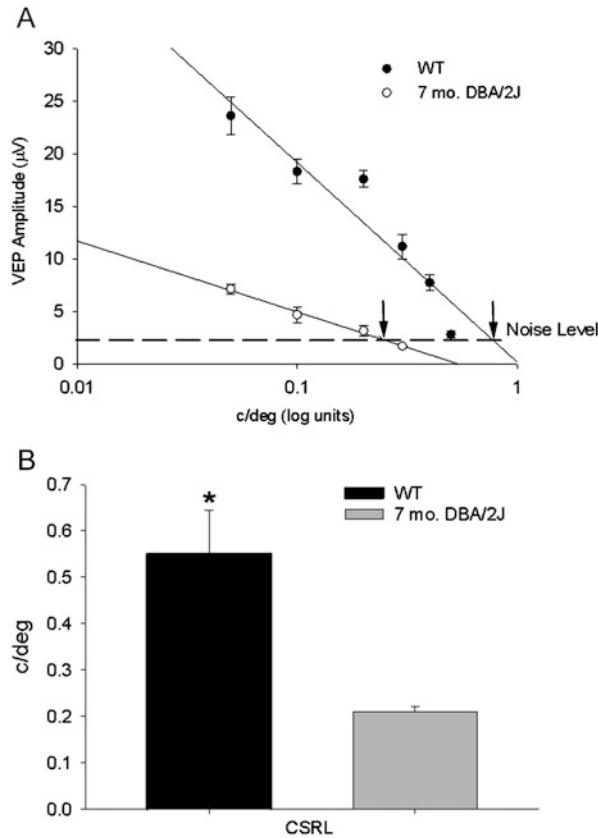


Fig. 4 Cortical resolution limit in a murine model of glaucoma. **(a)** The cortical spatial resolution limit (measured in cycles/degree, c/deg) was calculated by linear extrapolation to noise level as in the reported examples. VEP amplitudes were plotted as a function of spatial frequencies, semi-logarithmic scale, for the eye of a C57BL/6J mouse (WT; *black circles, solid line* indicates the linear fit) and the eye of a DBA/2J mouse with ocular hypertension (*empty circles, dashed line* indicates the linear fit); cortical spatial resolution limit for each eye is indicated by an arrow. **(b)** The averaged cortical spatial resolution limit (CSRL) in DBA/2J mice with ocular hypertension ($n = 4$ eyes, mean = 0.21 c/deg, SEM = 0.01) was significantly lower than in WT control mice ($n = 4$ eyes, mean = 0.55 c/deg, SEM = 0.09); $*p < 0.05$, Student's *t* test. Error bars indicate SEM

3.7 Assessment of Beta Amyloid Accumulation in the Visual System of Animal Models of AD

The accumulation of beta amyloid is usually observed in the brain tissues of AD rodent models. With the aim of characterizing the temporal and spatial expression pattern of beta amyloid accumulation in the retina and visual cortex, the immunoblot technique can be used. Retinas are dissected from eyes and tissue blocks from the visual cortex region, based on anatomical landmarks. The tissue homogenates can be processed using western blot or dot blot. Briefly, in western blot analysis an equal amount of proteins (μg) is resolved electrophoretically on a 7.5–12% SDS-PAGE Bis-TRIS gel. Proteins are transferred on a nitrocellulose or polyvinylidene fluoride (PVDF) membrane, followed by a first incubation in blocking solution and a second one with anti-beta amyloid primary

antibodies at 4 °C overnight. Following washes, the membranes are incubated with a secondary anti-IgG antibody, HRP-linked for 1 h at room temperature. Proteins can be detected through chemiluminescence detection systems. Bands and dots can be quantified using dedicated software.

4 Notes

1. Signal-to-noise ratio. Using cathode ray tube monitors (CRT) nearly everyone with close to normal visual function produces similar evoked potential using pattern reversal stimuli. A challenge is represented by the presence of environmental electromagnetic interference, noise generated by monitor and biological internal noise. The electromagnetic noise can be easily calculated recording responses evoked by pattern reversal with zero contrast. The electromagnetic noise can be contrasted by using an isolated ground and/or a small faraday cage surrounding the recording device. Monitor generated noise and internal biological noise can be reduced changing the frequency of grating alternation and/or improving the recording conditions, including anesthesia.
2. Spatial frequency and contrast. VEPs show longer delay when evoked by higher spatial frequencies [25]. We'd like to emphasize one more time that amplitudes of evoked responses increase with contrast.
3. Body temperature and thermoregulation. Both P-ERG and VEP latencies are strongly influenced by temperature and become progressively longer as body temperature is lowered under 37 °C. VEP amplitudes show a marked decline as temperatures of rodents fall below approximately 30 °C [12, 23].
4. Anesthetic agents. Evoked responses that travel via polysynaptic pathways, such as the VEPs, are susceptible to the anesthesia. In general, inhalational anesthetics are more potent suppressants of VEPs than intravenous and intraperitoneal agents [26]. Anesthetics used for intravenous anesthesia, with a few exceptions, produce a dose-dependent suppressive effect on VEPs. Opioids, in general, do not affect the quality of VEP unless infused at high doses. Benzodiazepines moderately suppress the VEPs [26], and their use should be avoided. Beyond the used anesthetics, monitoring of VEPs at different time periods following anesthesia induction is recommended. General anesthesia affects thermoregulation.
5. Pupil. Changes of pupil size and direction during the recording session affect evoked responses. Usually, the size of the pupil is maintained around 1 mm (this is a pupil size ensuring good

contrast at low spatial frequencies) for several hours following the induction of anesthesia; the pupil direction and size should be checked through the recording session to avoid potential artifacts [12, 23].

Acknowledgments

The present chapter is dedicated to the memory of Dr. Adriana Fiorentini. This work is supported by the Department of Applied Clinical Sciences and Biotechnology (DISCAB), University of L'Aquila, L'Aquila, Italy and the consortium IN-BDNF. We thank Ms. S. Wilson for revising the English style.

References

1. Riggs LA, Johnson EP, Schick AM (1964) Electrical responses of the human eye to moving stimulus patterns. *Science* 144 (3618):567. <https://doi.org/10.1126/science.144.3618.567>
2. Sokol S, Riggs LA (1971) Electrical and psychophysical responses of the human visual system to periodic variation of luminance. *Investig Ophthalmol* 10(3):171–180
3. Sokol S (1986) Visual evoked potentials. In: Aminoff MJ (ed) *Electrodiagnosis in clinical neurology*, 2nd edn. Churchill Livingstone, New York
4. Wildberger HG, Van Lith GH, Wijngaarde R, Mak GT (1976) Visually evoked cortical potentials in the evaluation of homonymous and bitemporal visual field defects. *Br J Ophthalmol* 60(4):273–278
5. Milner BA, Regan D, Heron JR (1974) Differential diagnosis of multiple sclerosis by visual evoked potential recording. *Brain* 97 (4):755–772
6. Fiorentini A, Maffei L, Pirchio M, Spinelli D, Porciatti V (1981) The ERG in response to alternating gratings in patients with diseases of the peripheral visual pathway. *Invest Ophthalmol Vis Sci* 21(3):490–493
7. Armington JC, Corwin TR, Marsetta R (1971) Simultaneously recorded retinal and cortical responses to patterned stimuli. *J Opt Soc Am* 61(11):1514–1521
8. Chen SA, Wu LZ, Wu DZ (1990) Objective measurement of contrast sensitivity using the steady-state visual evoked potential. *Doc Ophthalmol* 75(2):145–153
9. Fiorentini A, Porciatti V, Morrone MC, Burr DC (1996) Visual ageing: unspecific decline of the responses to luminance and colour. *Vis Res* 36(21):3557–3566
10. Quigley HA, Broman AT (2006) The number of people with glaucoma worldwide in 2010 and 2020. *Br J Ophthalmol* 90 (3):262–267. <https://doi.org/10.1136/bjo.2005.081224>
11. Quigley HA (2011) Glaucoma. *Lancet* 377 (9774):1367–1377. [https://doi.org/10.1016/S0140-6736\(10\)61423-7](https://doi.org/10.1016/S0140-6736(10)61423-7)
12. Domenici L, Origlia N, Falsini B, Cerri E, Barloscio D, Fabiani C, Sanso M, Giovannini L (2014) Rescue of retinal function by BDNF in a mouse model of glaucoma. *PLoS One* 9 (12):e115579. <https://doi.org/10.1371/journal.pone.0115579>
13. Serrano-Pozo A, Frosch MP, Masliah E, Hyman BT (2011) Neuropathological alterations in Alzheimer disease. *Cold Spring Harb Perspect Med* 1(1):a006189. <https://doi.org/10.1101/cshperspect.a006189>
14. Braak H, Braak E (1991) Demonstration of amyloid deposits and neurofibrillary changes in whole brain sections. *Brain Pathol* 1 (3):213–216
15. Braak H, Braak E (1993) Entorhinal-hippocampal interaction in mnemonic disorders. *Hippocampus* 3 Spec No:239–246
16. Graw J (2017) From eyeless to neurological diseases. *Exp Eye Res.* <https://doi.org/10.1016/j.exer.2015.11.006>
17. Hof PR, Morrison JH (1990) Quantitative analysis of a vulnerable subset of pyramidal neurons in Alzheimer's disease: II. Primary and secondary visual cortex. *J Comp Neurol* 301(1):55–64. <https://doi.org/10.1002/cne.903010106>

18. Rizzo JF 3rd, Cronin-Golomb A, Growdon JH, Corkin S, Rosen TJ, Sandberg MA, Chiappa KH, Lessell S (1992) Retinocalcarine function in Alzheimer's disease. A clinical and electrophysiological study. *Arch Neurol* 49 (1):93–101
19. Crow RW, Levin LB, LaBree L, Rubin R, Feldon SE (2003) Sweep visual evoked potential evaluation of contrast sensitivity in Alzheimer's dementia. *Invest Ophthalmol Vis Sci* 44 (2):875–878
20. Selkoe DJ (2002) Alzheimer's disease is a synaptic failure. *Science* 298:789–791
21. Sartucci F, Borghetti D, Bocci T, Murri L, Orsini P, Porciatti V, Origlia N, Domenici L (2010) Dysfunction of the magnocellular stream in Alzheimer's disease evaluated by pattern electroretinograms and visual evoked potentials. *Brain Res Bull* 82(3-4):169–176. <https://doi.org/10.1016/j.brainresbull.2010.04.001>
22. Origlia N, Valenzano DR, Moretti M, Gotti C, Domenici L (2012) Visual acuity is reduced in alpha 7 nicotinic receptor knockout mice. *Invest Ophthalmol Vis Sci* 53(3):1211–1218. <https://doi.org/10.1167/iovs.11-8007>
23. Porciatti V, Pizzorusso T, Maffei L (1999) The visual physiology of the wild type mouse determined with pattern VEPs. *Vis Res* 39 (18):3071–3081
24. Dawson GD (1951) A summation technique for detecting small signals in a large irregular background. *J Physiol* 115(1):2p–3p
25. Fiorentini A, Pirchio M, Spinelli D (1983) Electrophysiological evidence for spatial frequency selective mechanisms in adults and infants. *Vis Res* 23(2):119–127
26. Banoub M, Tetzlaff JE, Schubert A (2003) Pharmacologic and physiologic influences affecting sensory evoked potentials: implications for perioperative monitoring. *Anesthesiology* 99(3):716–737

Investigation of the Functional Retinal Output Using Microelectrode Arrays

Günther Zeck

Abstract

Microelectrode array (MEA) recordings of the ex vivo flat-mounted retina enable the functional analysis of the retinal output. The electrical activity of a large portion of retinal ganglion cells (RGCs) is recorded simultaneously in response to various light stimuli. Analysis of the recorded time series of action potentials reveals physiological parameters such as firing rate, time latency, receptive field size, axonal conduction velocity. These parameters change during retinal diseases.

Key words Extracellular recording, Microelectrode array, Ex vivo retina, Ganglion cell

1 Introduction

Microelectrode array (MEAs) recordings offer a wide range of electrophysiological parameters for the functional characterization of retinal ganglion cell (RGC) activity. The functional readout using MEAs is performed at a single-cell level in large populations of simultaneously recorded RGC types. The activity of many RGCs of different functional subtypes (i.e., ON, ON-OFF, OFF, direction selective, intrinsically photosensitive types) is recorded simultaneously and identified through offline data analysis in a retinal portion (typical size $\sim 2 \times 2 \text{ mm}^2$) [1, 2]. The following (non-exhaustive) parameter set can be extracted from such recordings. These parameters are then used to compare the RGC functionality in control retinas to the functionality in disease models.

1. Bias index, i.e., the preferred response to incremental (ON) light stimuli versus decremental (OFF) stimuli.
2. DS index, an index indicating the preferred sensitivity for light stimuli moving in different directions.

3. *Response latency*, a parameter quantifying how fast the first burst of action potentials is recorded after light stimulus onset [3].
4. Size of the receptive field center. The receptive field center of a RGC roughly corresponds to the size of its dendritic arbour and can be estimated using so-called binary white noise flicker stimuli [4]. Changes of the receptive field center indicate changes of the dendritic field diameter. Smaller receptive fields have been reported in α -type OFF RGCs in a mouse model of transiently elevated intraocular pressure [5, 6].
5. Axonal conduction velocity. Using high-density MEAs with electrode spacing in the order of 10 μm , the electrical signal along single RGC axons can be electrically imaged [7, 8]. This allows extraction of an additional physiological parameter, the axon conduction velocity of RGCs [3]. Typical values are 1–1.5 m/s.

In the following, we describe how such functional characterization can be performed in practice.

2 Materials

Animal handling, animal euthanasia, and dissection of the retina must follow the Institutional Animal Care and Use Committee protocols. In the following, a protocol for the preparation of mouse retina is provided. The preparation of other retinæ (rat, guinea pig, rabbit) is almost equivalent.

2.1 Dissection of the Ex Vivo Retina

1. Preparation of the Ringer solution for dissection and measurement. We used carbogenated Ames' medium (Sigma). About 30 min prior to the start of the experiment supplement the Ames' powder with sodium bicarbonate and add carbogen (95% oxygen + 5% CO₂) [3]. As an alternative oxygenated artificial cerebrospinal fluid (ACSF) [5] may be used.
2. Dark—adapt the mouse for at least 30 min. The isolation of the retina should be performed in dim red light. Rodents retina show little sensitivity to red light (wavelength above 650 nm), thus the photoreceptors in the ex vivo retina will not be bleached.
3. Following decapitation briefly transfer the eyeballs into a beaker containing carbogenated Ames' medium.
4. Grab the eyeball with one forceps (Dumont #5) and make a small incision above the ora serrata using another forceps or eyes scissors.

5. Cut the eyeball into two pieces. Gently remove the lens and the vitreous without damaging the retina (*see Note 1*).
6. Invert the remaining eyecup, peel the retina of the RPE, and cut the connection between retina and sclera at the optic nerve disc. Transfer the free floating ex vivo retina to a new beaker containing carbogenated Ames' medium (*see Note 2*).

2.2 Interfacing of the Retina onto the MEA

1. Prior to the placement of the retina clean the microelectrode array (MEA) using recommended treatment solution [3]. It is of great importance to have a hydrophilic MEA surface (*see Note 3*). Optional step: Add about 200 μL of poly-L-lysine solution (1 mg/mL) to the MEA surface for at least 30 min [3]. Right before placing a piece of retina onto the MEA rinse the MEA chamber three times with carbogenated Ames' medium.
2. Cut a portion of the isolated retina using either eye scissors or a scalpel. Trim the edges of the retinal portion. Transfer the prepared retina using a pipette with large opening into the MEA chamber containing Ames' medium. Avoid touching the retina during the transfer.
3. Once the retinal portion is transferred to the MEA chamber, grab it at the border using fine forceps and place it ganglion cell layer down onto the MEA surface. We recommend doing the placement under a stereomicroscope illuminated by a cold light source. The correct placement (ganglion-cell-side in close proximity to the extracellular electrodes) can be easily determined considering the retinal curvature.
4. Using different pipettes (first 1 mL, than 100 μL) remove all Ames' medium from the MEA chamber. The retinal piece will flatten such that the electrodes become visible. Gently tilt the MEA to ensure that the retina is tightly interfaced. Prior to the placement in the MEA amplifier add fresh Ames' medium (*see Note 4*).
5. *Optional step:* Several labs use a customized plunger-system to ensure tight adherence. Della Santina et al. [18] state: "The retina was covered by a 25–50 mm² square piece of tissue culture membrane (Corning Life Sciences), held in place by a platinum ring" (*see Note 5*).

2.3 Selection of the Appropriate Recording Hardware

The experimental setup to investigate the functional retinal output is shown in Fig. 1. At its heart a microelectrode array interfaces to a flat-mount retina (Fig. 1b). During recording of RGC activity the MEA chamber is continuously perfused by appropriate Ames' solution. Light activation of the retina is achieved by microdisplays mounted on the microscope's camera port. In the following, we discuss the individual hardware in detail.

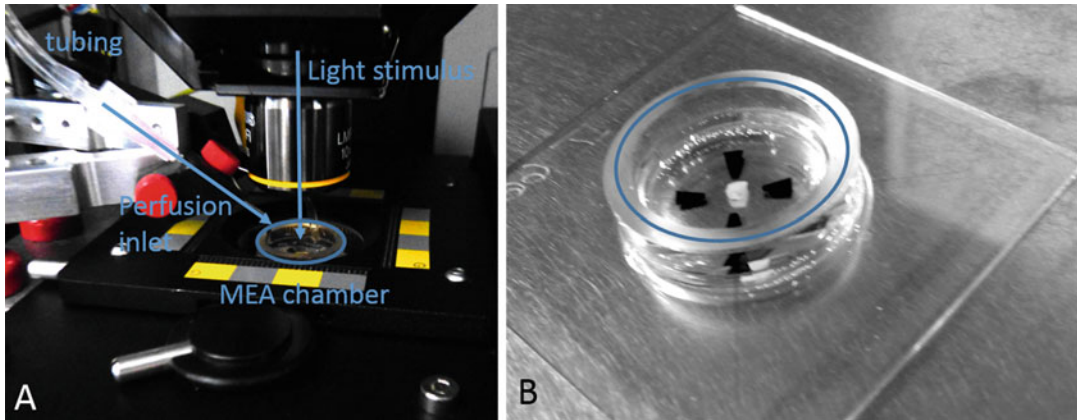


Fig. 1 Photographs of the experimental setup for MEA recording (a) and a glass-based MEA with metal electrodes with interfaced ex vivo retina (b). In (a) the MEA is placed in an extracellular amplifier (*black stage*). The MEA chamber (2 cm in diameter) is shown in the center. Light stimuli are projected through an objective. The retina on the MEA is continuously perfused (Perfusion inlet is shown). (b) A retinal portion is interfaced to the electrode array of a glass-based MEA. The electrodes cover an area of 1–4 mm² (depending on the MEA type)

2.3.1 Microelectrode Arrays

Several companies offer MEA recording setups, including amplifier, recording, and analysis software (www.multichannelsystems.com, www.axionbiosystems.com, www.med64.com). With respect to MEA design, electrode diameters in the range of 10–30 μm are most commonly used. The spacing between the electrodes ranges between 30 and 300 μm . MEAs with a small spacing are suggested for retinal recordings, given that the ganglion cells are tightly packed at a density up to 3000 cells/mm². On high-density MEAs the activity of each ganglion cell is picked up by several electrodes, enabling unequivocal cell signal identification. Toward even smaller spacing, high-density arrays with an electrode pitch of less than 20 μm are now being offered (www.multichannelsystems.com; www.3brain.com/home; <http://www.mxwbio.com/>). An alternative perforated MEA has been reported recently, where the adhesion of the interfaced retinal portion is improved by pressure [9].

2.3.2 Light Stimulation Hardware and Software

The simplest light stimuli are generated using single LEDs, which are turned ON and OFF at high temporal precision. Spatially structured stimuli are presented using commercial microdisplays [7]. These can be mounted at the camera port of upright microscopes, thus illuminating the back-plane of an objective (Fig. 1a). The image is then easily focused onto the MEA plane. Alternatively, the microdisplay and objective may be mounted in the place of the condenser in an inverting microscope, thus illuminating the retina through the transparent MEAs. High light intensities may be achieved using customized digital-light-processing chips. Light stimuli can be programmed using a wide range of software (*see Note 6*). The

following list may help the user in selecting the most appropriate tool: (1) Psychtoolbox for Matlab (<http://psychtoolbox.org/>), (2) Vision-Egg (<http://visionegg.org/>), (3) Psychopy (<http://www.psychopy.org/>) or the GPU-based software GEARS (<http://gears.vision/>).

2.3.3 Auxiliary Equipment

The electrical RGC activity will be recorded at about 33 °C. A temperature controller, which heats the perfusion and also the bottom of the MEA chamber, may be used. The intensity and the spectrum of the projected light onto the retina can be measured using a commercial photometer.

3 Methods

3.1 Measurement Procedure

During the recording retinal tissue is perfused continuously with carbogenated Ames' medium (or ACSF) at a rate of 2–4 mL/min. The temperature in the MEA chamber should be maintained at ~33 °C by heating the bottom of the recording chamber and the incoming solution using a temperature controller. Retinas are left on the array for at least 10 min before recording, because the amplitude of the recorded spikes usually improved during this period. Extracellular recordings may last for several hours (*see Note 7*).

Extracellular recording can be performed over a wide frequency range (1 Hz–10 kHz) or may be band-pass filtered to reveal action potentials only [10]. In my lab recordings are performed with little filtering. We reason that more global information about the retinal functionality is revealed in the low-frequency range while the spiking of individual ganglion cells is revealed in the high-frequency range (*see Fig. 2*).

Band-pass filtered extracellular signals of somatic RGC spikes have a biphasic waveform, with a larger initial negative phase [7]. The positive second phase of the extracellular trace is in most cases attributed to low pass filtering. In contrast, axonal signals picked up by the electrodes display a biphasic peak with a larger initial positive phase [7]. Therefore, negative triggers are used to detect somatic spikes. Conversely, if axonal spikes are of interest a positive trigger for threshold detection may be set.

3.2 Data Analysis

MEAs record continuously the extracellular voltage above each electrode. The most contributions to the recorded electrode signal originate within a hemisphere with a radius of five times the electrode radius [11]. Within the recorded trace on each electrode within few tens of milliseconds following a light stimulus “spiky” voltage deflections occur. These spikes reflect action potentials elicited by ganglion cells in response to the applied light stimulus.

To reveal action potentials (spikes) the recorded voltage traces may be bandpass filtered between 100 and 3000 Hz. (This option

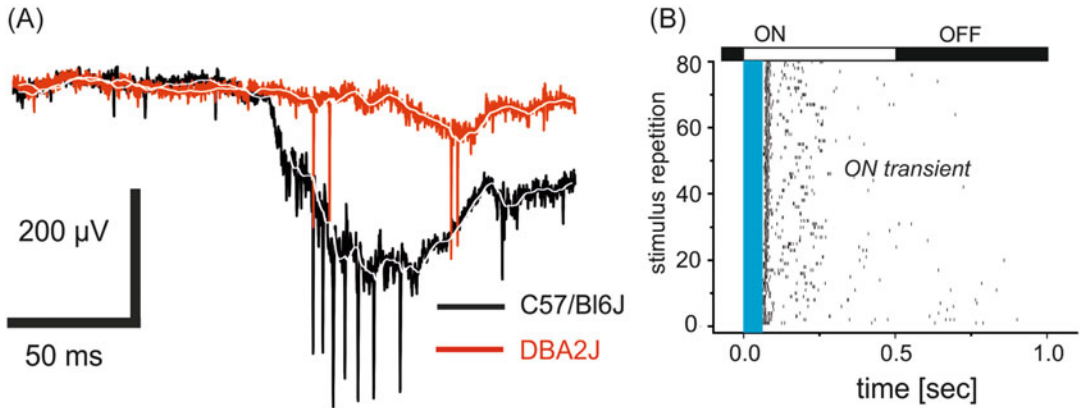


Fig. 2 Exemplary MEA recordings from adult glaucoma mouse model (DBA/2J, *red traces*) and a pigmented wild-type mouse retina (C57/Bl6J, *black traces*). (a) Extracellular voltage signal in the ganglion cell layer recorded by one electrode reveal differences between the DBA/2J and pigmented WT retina in the scotopic (night-vision) regime. Spiking activity is visible as sharp peaks in the fluctuating voltage trace. (b) Rasterplots of the activity of one RGC (On transient type). The light stimulus is presented 80 times at a frequency of 1 Hz (duty cycle 0.5). At each stimulus presentation spiking is detected and represented as a raster. Note the response latency of ~50 ms (marked by the *blue box*)

can be set during the recording as well, without saving the data in this range only). To identify spikes a threshold detection of the extracellular voltage is performed. The noise level for spike detection is commonly set to five times standard deviation. For recordings with high activity the noise standard deviation may be calculated as suggested (http://www.scholarpedia.org/article/Spike_sorting).

To assign spikes to one corresponding cell the following steps are required: (1) cutout of the voltage waveform within a short time window around the threshold detection time; (2) Sorting of waveforms with similar statistical properties to one cluster, corresponding to one cell, (3) Cross-correlation between all recorded clusters and removal of duplicates. This procedure is called “spike sorting”—with many open-source software packages available [12–15]. The quality of the spike sorting has to be controlled. In a first control the so-called refractory periods of the sorted trains are estimated. Only cells with a low percentage of interspike intervals smaller than 2 ms should be used for analysis. The quality of the spike sorting may also be assessed using artificial ground truth spike trains.

Following spike sorting, the RGC time stamps are saved on hard disc. Offline analysis of the spike trains is commonly performed using published [16, 17] or customized Matlab routines. The quantitative electrophysiological measures of these routines are—as mentioned above—mean firing rate (i.e., average number of spikes within a predefined time interval), light-induced firing rate, latency of the response to light onset or offset, estimation of the direction selectivity index, receptive field size, or estimation of the axonal conduction velocity [3].

3.3 Anticipated Results

MEA recordings have been performed in experimental mouse model for glaucoma [18]. Functional changes, revealed by MEA, include the maintained spiking activity, the spike latency to brief light flashes, and shrinkage of receptive field size of various RGC types or a preferential loss of so-called OFF-RGCs [6]. An important conclusion from the MEA study was that functional changes can be detected at a stage at which the structural changes have not occurred yet, or were only minor, so that the changes are possibly reversible.

4 Notes

1. It is of great importance to remove the vitreous body for subsequent MEA recording. We recommend checking for remaining fine vitreous fibers emerging from the ora serrata and carefully remove them. This should be done prior to removing the retina from the eyecup.
2. While keeping the ex vivo retina in the carbogenated Ames' medium (or ringer solution) pay attention that the floating retina does not trap any gas bubbles. This can be achieved by placing a filter in front of the carbogen inlet.
3. A hydrophilic MEA surface ensures that the adhesive coating (poly-lysine or CellTak) adheres onto the electrode surface. The hydrophilic nature can be easily tested by adding a drop of water. The water drop should spread onto the surface and in no case form a hemisphere.
4. Tight interfacing between retina and MEA surface can be tested by tilting the MEA by about 90 degrees. The retina should by no means slip along the surface.
5. In my lab plungers are not very popular as they may damage the photoreceptor layer.
6. The selected light stimulation software should support synchronization with the recording software as well as the option to trigger the recording hardware via USB ports.
7. Appropriate grounding is necessary to eliminate measurement noise. Most MEAs contain an internal reference electrode. Without the perfusion connected to the filled MEA chamber the recording system should be noise free. In many cases the perfusion inlet is made of a metal. This metal piece needs to be grounded to the amplifier ground.

References

1. Farrow K, Masland RH (2011) Physiological clustering of visual channels in the mouse retina. *J Neurophysiol* 105(4):1516–1530
2. Zeck GM, Masland RH (2007) Spike train signatures of retinal ganglion cell types. *Eur J Neurosci* 26(2):367–380
3. Stutzki H et al (2014) Inflammatory stimulation preserves physiological properties of retinal ganglion cells after optic nerve injury. *Front Cell Neurosci* 8:38
4. Chichilnisky EJ (2001) A simple white noise analysis of neuronal light responses. *Network* 12(2):199–213
5. Ou Y et al (2016) Selective vulnerability of specific retinal ganglion cell types and synapses after transient ocular hypertension. *J Neurosci* 36(35):9240–9252
6. El-Danaf RN, Huberman AD (2015) Characteristic patterns of dendritic remodeling in early-stage glaucoma: evidence from genetically identified retinal ganglion cell types. *J Neurosci* 35(6):2329–2343
7. Zeck G, Lambacher A, Fromherz P (2011) Axonal transmission in the retina introduces a small dispersion of relative timing in the ganglion cell population response. *PLoS One* 6(6): e20810
8. Bakkum DJ et al (2013) Tracking axonal action potential propagation on a high-density microelectrode array across hundreds of sites. *Nat Commun* 4:2181
9. Reinhard K et al (2014) Step-by-step instructions for retina recordings with perforated multi electrode arrays. *PLoS One* 9(8): e106148
10. Menzler J, Channappa L, Zeck G (2014) Rhythmic ganglion cell activity in bleached and blind adult mouse retinas. *PLoS One* 9(8):e106047
11. Zeitler R, Fromherz P, Zeck G (2011) Extracellular voltage noise probes the interface between retina and silicon chip. *Appl Phys Lett* 99(26):263702
12. Yger P et al (2016) Fast and accurate spike sorting in vitro and in vivo for up to thousands of electrodes. *bioRxiv:067843*
13. Rossant C et al (2016) Spike sorting for large, dense electrode arrays. *Nat Neurosci* 19(4):634–641
14. Franke F et al (2010) An online spike detection and spike classification algorithm capable of instantaneous resolution of overlapping spikes. *J Comput Neurosci* 29(1–2):127–148
15. Leibig C, Wachtler T, Zeck G (2016) Unsupervised neural spike sorting for high-density microelectrode arrays with convolutive independent component analysis. *J Neurosci Methods* 271:1–13
16. Meier R et al (2008) FIND—a unified framework for neural data analysis. *Neural Netw* 21(8):1085–1093
17. Egert U et al (2002) MEA-Tools: an open source toolbox for the analysis of multi-electrode data with MATLAB. *J Neurosci Methods* 117(1):33–42
18. Della Santina L et al (2013) Differential progression of structural and functional alterations in distinct retinal ganglion cell types in a mouse model of glaucoma. *J Neurosci* 33(44):17444–17457

Quantitative Proteomic Analysis of Human Aqueous Humor Using iTRAQ 4plex Labeling

Anna Trzeciecka, Padmanabhan Pattabiraman, Maria Carmen Piqueras, Carol Toris, and Sanjoy K. Bhattacharya

Abstract

iTRAQ 4plex method enables multiplexing of up to four samples for simultaneous quantitation to improve sensitivity and scope of proteomic analysis. Here, we describe iTRAQ 4plex labeling of human aqueous humor specimens followed by ultra-high performance liquid chromatography-tandem mass spectrometry (UHPLC-MS/MS) and data analysis for peptide identification and quantitation using Proteome Discoverer software. The protocol can be applied for other animals as well; however, pooling of specimens may be required to obtain sufficient amount of protein for labeling.

Key words Human, Aqueous humor, Proteins, Proteome, Relative quantitation, iTRAQ 4plex, Ultra-high performance liquid chromatography-tandem mass spectrometry

1 Introduction

Determining the proteome of human aqueous humor may be a challenging task due to a low protein concentration: 0.02% as compared to 7% in plasma and small volume of the specimen that can be aspirated without complete flattening of anterior chamber: 0.05–0.15 mL. But since there is accumulating evidence of aqueous humor proteins being differentially expressed in various eye diseases of both the anterior and posterior segments [1–7], a highly sensitive method for accurate proteome quantitation is needed.

Isobaric tags for relative and absolute quantitation (iTRAQ)—one of the most important technologies in modern proteomic research, shows promise in this regard. It allows multiplexing of two to eight samples in a single-mass spectrometry experiment to improve sensitivity and scope of analysis [8, 9], and has proven to be a successful tool for detecting relative changes in abundance of peptides and proteins in a variety of settings including aqueous humor studies [1, 2, 5, 6, 10, 11].

The iTRAQ 4plex labeling, described here, employs four isobaric (145 kDa) reagents. iTRAQ tag consist of an N-methyl piperazine reporter group (114 kDa or 115 kDa or 116 kDa or 117 kDa), a balance group, and an N-hydroxy succinimide ester peptide reacting group. Following preparation (denaturation, reduction, alkylation, and digestion), each sample is labeled using one of the iTRAQ tags and then all iTRAQ labeled samples are pooled together. The peptide mixture is subjected to UHPLC-MS/MS analysis. Spectra are searched against UniProtKB/Swiss-Prot human database using Proteome Discoverer software. Relative quantitation of peptides is determined based on the relative intensities of reporter ions released from iTRAQ-tagged peptides by fragmentation during tandem mass spectrometry (MS/MS) [8, 9].

In this protocol, we describe quantitative proteomic analysis using iTRAQ 4plex labeling for human aqueous humor applications. It can be also implemented for other animal specimens. However, regarding total volumes of aqueous humor, e.g., mouse: 4.4 μL [12], rat: 13.6 μL [13] versus human: 260 μL [14], pooling of specimens may be required to obtain sufficient amount of protein for labeling and analysis. While it is a potentially valuable approach, risk of bias due to biological averaging of the samples needs to be considered [15, 16].

2 Materials

2.1 iTRAQ 4plex Labeling

1. Protein quantitation assay of choice (*see Note 3*).
2. Dissolution Buffer: 0.5 M triethylammonium bicarbonate (TEAB) pH 8.5 in Milli-Q water.
3. Denaturant Solution: 2% sodium dodecyl sulfate (SDS) in Milli-Q water.
4. Reducing Reagent: 110 mM tris(2-carboxyethyl)phosphine (TCEP) in Milli-Q water (stored at $-20\text{ }^{\circ}\text{C}$).
5. Iodoacetamide Solution: 84 mM iodoacetamide in 100 mM ammonium bicarbonate (freshly prepared and stored at $4\text{ }^{\circ}\text{C}$).
6. Trypsin Solution: sequencing grade modified trypsin reconstituted with supplied suspension buffer to a concentration of $0.1\text{ }\mu\text{g}/\mu\text{L}$ (use freshly prepared or prepared and stored at $-20\text{ }^{\circ}\text{C}$ for up to 3 days).
7. iTRAQ Reagents (AB Sciex Pte. Ltd., Framingham, MA).
 - (a) iTRAQ Reagent—4plex—114.
 - (b) iTRAQ Reagent—4plex—115.
 - (c) iTRAQ Reagent—4plex—116.
 - (d) iTRAQ Reagent—4plex—117.

8. Vortexer.
9. Centrifuge.
10. ThermoMixer/water bath: set at 60 °C.
11. ThermoMixer/water bath/cell culture incubator: set at 37 °C.
12. Centrifugal vacuum concentrator.
13. Freezer: –80 °C.
14. Ethanol: absolute, HPLC-grade or better.
15. Milli-Q water.
16. pH test strips.
17. Aluminum foil.

2.2 UHPLC and Mass Spectrometric Analysis

1. Solvent A: water, suitable for UHPLC.
2. Solvent B: acetonitrile, suitable for UHPLC.
3. Column: Acclaim PepMap RSLC C18, 2 μm , 100 \AA , 75 μm i.d. \times 15 cm, nanoViper (Thermo Fisher Scientific Inc., Weston, FL).
4. Precolumn: Acclaim PepMap100 C18, 3 μm , 100 \AA , 75 μm i.d. \times 25 cm, nanoViper (Thermo Fisher Scientific Inc., Weston, FL).
5. Nanoflow Liquid Chromatograph: EASY-nLC 1000 (Thermo Fisher Scientific Inc., Weston, FL).
6. Mass Spectrometer: Q Exactive Hybrid Quadrupole-Orbitrap Mass Spectrometer (Thermo Fisher Scientific Inc., Weston, FL).

2.3 Data Analysis

1. Proteome Discoverer 1.4 (Thermo Fisher Scientific Inc., Weston, FL) software, designed to identify and quantitate proteins in complex biological samples. It supports multiple database search algorithms: SEQUEST, Z-Core, Mascot, etc.
2. UniProtKB/Swiss-Prot: a manually annotated, nonredundant protein sequence database.
3. Sample spectra data.

3 Methods

For specimen handling and total protein quantitation *see* **Notes 1–4**.

3.1 iTRAQ 4plex Labeling

1. Sample preparation (denaturation, reduction, alkylation).
 - (a) To each sample containing 5–140 μg of protein (almost completely dried in a centrifugal vacuum concentrator—volume of up to 10 μL) add 30 μL Dissolution Buffer.

- (b) Add 1 μL of the Denaturant Solution to each sample and vortex for 1 min to mix.
 - (c) Add 2 μL of Reducing Reagent (110 mM TCEP stock) for a final TCEP concentration of 5 mM in each sample.
 - (d) Vortex for 1 min to mix, then spin to bring the solution to the bottom of the tube.
 - (e) Incubate the tubes at 60 °C for 1 h.
 - (f) Spin the samples to bring the solution to the bottom of the tube.
 - (g) Add 1 μL of freshly prepared Iodoacetamide Solution (*see Note 5*).
 - (h) Vortex and spin as in **step (d)**.
 - (i) Incubate the tubes in the dark at room temperature for 30 min (wrap tubes in aluminum foil) (*see Note 5*).
 - (j) Vortex and spin as in **step (d)**.
2. Protein digestion
- (a) Add 10 μL of the Trypsin Solution to each sample.
 - (b) Vortex and spin as in **step 1(d)**.
 - (c) Incubate samples at 37 °C for 3 h.
 - (d) Add 1 μL more of Trypsin Solution and incubate at 37 °C overnight (12–16 h).
 - (e) Vortex and spin as in **step 1(d)**. (*see Note 6*).
3. Labeling the samples with iTRAQ Reagents
- (a) Bring vials of iTRAQ Reagents to room temperature.
 - (b) Add 70 μL of Ethanol to each iTRAQ Reagent vial being used.
 - (c) Vortex and spin as in **step 1(d)**.
 - (d) Check the pH of each reconstituted iTRAQ Reagent. If it is not at least 7.8 then add Dissolution Buffer to bring pH up to pH 7.8–8.5 (*see Note 7*).
 - (e) Transfer the contents of one iTRAQ Reagent vial to one sample tube.
 - (f) Vortex and spin as in **step 1(d)**.
 - (g) Incubate the tubes at room temperature for 1 h.
 - (h) Add 100 μL of Milli-Q water to each tube to quench the iTRAQ reaction.
 - (i) Incubate the tubes at room temperature for 30 min.
4. Pooling of the iTRAQ Reagent-labeled samples
- (a) Spin each iTRAQ Reagent-labeled sample tube to bring the solution to the bottom of the tube.

- (b) Combine the contents of all tubes into one tube.
- (c) Vortex and spin as in **step 1(d)**.
- (d) Dry the sample containing all the iTRAQ mixes combined in a centrifugal vacuum concentrator.
- (e) Add 100 μL of Milli-Q water to the tube.
- (f) Vortex and spin as in **step 1(d)**.
- (g) Dry the sample completely in a centrifugal vacuum concentrator.
- (h) Repeat **step 1(e)–(g)**. 2 more times to a total of three times.
- (i) Pooled vacuum-dried iTRAQ-labeled sample from four human aqueous humor specimens can be stored at $-80\text{ }^{\circ}\text{C}$ or used directly for UHPLC-MS/MS.

3.2 UHPLC and Mass Spectrometric Analysis

1. Reconstitute sample obtained in Subheading 3.1, **step 4(i)**, in 98% Solvent A/2% Solvent B.
2. Load reconstituted sample onto Column coupled with Pre-column and both connected in-line to Nanoflow Liquid Chromatograph (*see Note 8*).
3. Elute using a 75-min gradient from 2% to 98% of Solvent B.
4. For mass spectrometric analysis, run the eluted samples in a data-dependent acquisition (DDA) mode, with an automatic gain control (AGC) target value of 1e^6 for full MS and 2e^5 for dd-MS². Specify the isolation window to 1.3 m/z with normalized collision energy (NCE) of 28 eV. Set first mass to 103 m/z and runtime to 75 min.

3.3 Data Analysis

We process proteomic data using Proteome Discoverer 1.4. The MS/MS spectra are searched against UniProtKB/Swiss-Prot human database with the following settings: trypsin cleavage specificity with up to 2 missed cleavages, and N-terminal and dynamic iTRAQ modifications. Mass tolerance is specified to 10 ppm for precursor ions and 0.02 Da for fragment ions. Relaxed false discovery rate (FDR) is set to 0.05 and strict FDR is set to 0.01. Relative quantitation of peptides is determined based on the relative intensities of reporter ions released from iTRAQ-tagged peptides (*see Note 9*).

4 Notes

1. Aqueous humor aspirate should be immediately placed into sterile tubes and centrifuged (e.g., $11,000 \times g$ for 10 min at $4\text{ }^{\circ}\text{C}$) to remove debris. Supernatant collected into new sterile

tubes can be stored at $-80\text{ }^{\circ}\text{C}$ until further analysis. Discard any samples contaminated with blood or iris pigment.

2. Since aqueous humor contains several abundant proteins (albumin, transferrin, antitrypsin, haptoglobin, fibrinogen, IgG, and IgA), consider performing immunodepletion to ensure identification of less abundant proteins [2, 17].
3. The relative quantitation method is based on the assumption that each iTRAQ Reagent-labeled sample contains equal amounts of total protein. Therefore, it is essential to measure total protein content of specimens with, e.g., BCA [18] or Bradford [19] assay, and adequately adjust the volume to have the same amount of total protein in each sample before drying those in a centrifugal vacuum concentrator. You can additionally run and silver stain the gel to verify equal protein content of samples.
4. Overall protein content of aqueous humor is low, between 100 and 500 ng/ μL of protein for human samples [17, 20]. It is critical to use the amount of protein within the range 5–140 μg *per* sample. Higher amounts (within given range) of protein *per* sample enable a more diverse set of potentially low abundant peptides to be identified.
5. Iodoacetamide is unstable and light-sensitive.
6. In order to maximize labeling efficiency, the volume of the sample digest must be less than 50 μL . If the volume of the sample digest is greater than 50 μL , dry the sample in a centrifugal vacuum concentrator, then reconstitute with 30 μL Dissolution Buffer.
7. Ensure to check (using pH test strips) and adjust pH of reconstituted iTRAQ Reagents. If the pH is less than 7.8 labeling efficiency can be significantly reduced.
8. Equilibrate and wash Column and Precolumn according to the manufacturer's instructions.
9. To compare the abundance of peptides across multiple iTRAQ experiments, standardize peptide quantity values by subtracting the mean peak area of all four samples within each experiment. These standardized peptide quantity values can be used to calculate mean protein quantity values across different analyses.

References

1. Ji Y, Rong X, Ye H, Zhang K, Lu Y (2015) Proteomic analysis of aqueous humor proteins associated with cataract development. *Clin Biochem* 48(18):1304–1309. <https://doi.org/10.1016/j.clinbiochem.2015.08.006>
2. Kim TW, Kang JW, Ahn J, Lee EK, Cho KC, Han BN, Hong NY, Park J, Kim KP (2012) Proteomic analysis of the aqueous humor in age-related macular degeneration (AMD)

- patients. *J Proteome Res* 11(8):4034–4043. <https://doi.org/10.1021/pr300080s>
3. Saccà SC, Centofanti M, Izzotti A (2012) New proteins as vascular biomarkers in primary open angle glaucomatous aqueous humor vascular biomarkers in glaucomatous aqueous humor. *Invest Ophthalmol Vis Sci* 53(7):4242–4253. <https://doi.org/10.1167/iovs.11-8902>
 4. Izzotti A, Longobardi M, Cartiglia C, Sacca SC (2010) Proteome alterations in primary open angle glaucoma aqueous humor. *J Proteome Res* 9(9):4831–4838. <https://doi.org/10.1021/pr1005372>
 5. Yang Q, Lu H, Song X, Li S, Wei W (2016) iTRAQ-based proteomics investigation of aqueous humor from patients with coats' disease. *PLoS One* 11(7):e0158611. <https://doi.org/10.1371/journal.pone.0158611>
 6. Yao J, Chen Z, Yang Q, Liu X, Chen X, Zhuang M, Liu Q (2013) Proteomic analysis of aqueous humor from patients with branch retinal vein occlusion-induced macular edema. *Int J Mol Med* 32(6):1421–1434. <https://doi.org/10.3892/ijmm.2013.1509>
 7. Chiang SY, Tsai ML, Wang CY, Chen A, Chou YC, Hsia CW, Wu YF, Chen HM, Huang TH, Chen PH, Liu HT, Shui HA (2012) Proteomic analysis and identification of aqueous humor proteins with a pathophysiological role in diabetic retinopathy. *J Proteome Res* 11(10):2950–2959. <https://doi.org/10.1021/jpr.2011.12.006>
 8. Ross PL, Huang YN, Marchese JN, Williamson B, Parker K, Hattan S, Khainovski N, Pillai S, Dey S, Daniels S, Purkayastha S, Juhasz P, Martin S, Bartlett-Jones M, He F, Jacobson A, Pappin DJ (2004) Multiplexed protein quantitation in *Saccharomyces cerevisiae* using amine-reactive isobaric tagging reagents. *Mol Cell Proteomics* 3(12):1154–1169. <https://doi.org/10.1074/mcp.M400129-MCP200>
 9. Aebersold RH, Bottari PQ, Gelb MH, Turecek F (2004) Chemical reagents and methods for detection and quantification of proteins in complex mixtures. Google Patents
 10. Bennett KL, Funk M, Tschernutter M, Breitwieser FP, Planyavsky M, Ubaida Mohien C, Muller A, Trajanoski Z, Colinge J, Superti-Furga G, Schmidt-Erfurth U (2011) Proteomic analysis of human cataract aqueous humour: comparison of one-dimensional gel LCMS with two-dimensional LCMS of unlabelled and iTRAQ(R)-labelled specimens. *J Proteome Res* 10(2):151–166. <https://doi.org/10.1021/jpr.2010.10.002>
 11. Kliuchnikova AA, Samokhina NI, Ilina IY, Karpov DS, Pyatnitskiy MA, Kuznetsova KG, Toropygin IY, Kochergin SA, Alekseev IB, Zgodva VG, Archakov AI, Moshkovskii SA (2016) Human aqueous humor proteome in cataract, glaucoma, and pseudoexfoliation syndrome. *Proteomics* 16(13):1938–1946. <https://doi.org/10.1002/pmic.201500423>
 12. Remtulla S, Hallett PE (1985) A schematic eye for the mouse, and comparisons with the rat. *Vis Res* 25(1):21–31
 13. Hughes A (1979) A schematic eye for the rat. *Vis Res* 19(5):569–588
 14. Ruskell G (2000) The human eye, structure and function Clyde W. Oyster; Sinauer associates, Sunderland, MA, 1999, 766 pages, hardback, ISBN 0-87893-645-9, £49.95. *Ophthalmic Physiol Opt* 20(4):349–350. <https://doi.org/10.1046/j.1475-1313.2000.00552.x>
 15. Escoffier P, Paris L, Bodaghi B, Danis M, Mazier D, Marinach-Patrice C (2010) Pooling aqueous humor samples: bias in 2D-LC-MS/MS strategy? *J Proteome Res* 9(2):789–797. <https://doi.org/10.1021/pr9006602>
 16. Diz AP, Truebano M, Skibinski DO (2009) The consequences of sample pooling in proteomics: an empirical study. *Electrophoresis* 30(17):2967–2975. <https://doi.org/10.1002/elps.200900210>
 17. Chowdhury UR, Madden BJ, Charlesworth MC, Fautsch MP (2010) Proteome analysis of human aqueous humor. *Invest Ophthalmol Vis Sci* 51(10):4921–4931. <https://doi.org/10.1167/iovs.10-5531>
 18. Smith PK, Krohn RI, Hermanson GT, Mallia AK, Gartner FH, Provenzano MD, Fujimoto EK, Goeke NM, Olson BJ, Klenk DC (1985) Measurement of protein using bicinchoninic acid. *Anal Biochem* 150(1):76–85
 19. Bradford MM (1976) A rapid and sensitive method for the quantitation of microgram quantities of protein utilizing the principle of protein-dye binding. *Anal Biochem* 72:248–254
 20. Tripathi RC, Millard CB, Tripathi BJ (1989) Protein composition of human aqueous humor: SDS-PAGE analysis of surgical and post-mortem samples. *Exp Eye Res* 48(1):117–130

Chapter 10

Shotgun Sphingolipid Analysis of Human Aqueous Humor

Anna Trzeciecka, Ulises Arbelo, Arturo Barron, Genea Edwards,
Sruthi Sampathkumar, Carol Toris, and Sanjoy K. Bhattacharya

Abstract

This protocol provides a step-by-step guide to shotgun sphingolipid analysis of aqueous humor. We describe the Bligh and Dyer crude lipid extraction method and electrospray ionization tandem mass spectrometry (ESI-MS/MS) coupled with MZmine 2.21 data processing for identification and ratiometric quantitation of sphingosine, sphingosine-1-phosphate, sphingomyelin, and ceramide.

Key words Aqueous humor, Sphingolipids, Sphingosine, Sphingosine-1-phosphate, Sphingomyelin, Ceramide, Shotgun lipidomics, Electrospray ionization-tandem mass spectrometry (ESI-MS/MS), MZmine 2.21

1 Introduction

Being once attributed to structural roles only, it is now known that many sphingolipid species are biologically active and play a role in development and progression of neurodegenerative diseases [1–5]. Due to many similarities with the central nervous system, the eye has become an object of sphingolipid research as well. However, until recently, the functions of sphingolipids in the eye [6–10], including the aqueous humor [11, 12], have been explored rarely.

Here, we describe techniques for shotgun sphingolipid analyses to be used for human aqueous humor, and with modifications for other selected classes of lipids and/or other eye tissues. The procedure is simpler, easier and faster to perform in comparison to many others reported for sphingolipids. Nevertheless, the readers should be aware of its limitations, i.e., Bligh and Dyer extraction method is not specific to sphingolipids, resulting in the complexity of the sample and potential matrix effect. This method also does not ensure total sphingolipid recovery, especially of more polar species,

e.g., sphingosine-1-phosphate. We recommend the use of both internal and external standards to improve the precision and accuracy of the method.

2 Materials

2.1 Lipid Extraction (See Note 1)

1. Methanol–chloroform: LC-MS grade methanol and LC-MS grade chloroform in 2:1 ratio (freshly prepared in an amber glass bottle at room temperature).
2. Chloroform: LC-MS grade (stored in an amber glass bottle at room temperature).
3. Internal lipid standards (Avanti Polar Lipids Inc., Alabaster, AL, USA) (*see* Table 1).
4. Glassware: Teflon-capped tubes, homogenizers, and pipette tips (*see* Note 2).
5. Argon gas: compressed, ultrahigh purity grade.
6. Protein quantitation assay kit of choice.
7. Others:
 - (a) Freezer: -80°C .
 - (b) Ice bucket or Styrofoam container with ice.
 - (c) Vortexer.
 - (d) Centrifuge.
 - (e) Centrifugal vacuum concentrator.
8. Optional:
 - (a) Antioxidant: butylated hydroxytoluene (BHT).
 - (b) Water: LC-MS grade.

2.2 Mass Spectrometric Analysis

1. Acetonitrile–isopropanol: LC-MS grade acetonitrile and LC-MS grade 2-propanol in 1:1 ratio (stored in an amber glass bottle at room temperature).
2. Lithiated chloroform–methanol: 5 mM LiCl in LC-MS grade methanol and LC-MS grade chloroform in 1:1 ratio (freshly prepared).
3. Internal and external lipid standards (Avanti Polar Lipids Inc., Alabaster, AL, USA; *see* Table 1).
4. Mass spectrometry:
 - (a) TSQ Quantum Access Max Triple Quadrupole Mass Spectrometer (Thermo Fisher Scientific Inc., Pittsburgh, PA, USA) controlled by Xcalibur 2.3 Software.
 - (b) TriVersa NanoMate (Advion Bioscience Ltd., Ithaca, NY, USA): chip-based electrospray ionization technology with Chipsoft 8.3.3 software for direct infusion of samples and standards.

Table 1
Parameters for analyses of different spingolipid classes. Internal standards are indicated with *. They are also available as parts of Spingolipid Mix I/II (LM-6002/6005)

Class	Lipid standard (Avanti number)	Collision energy [V]	Ionization mode	Q2 CID gas pressure [psi]	Daughter mass [m/z]	Scan type	Mass range [m/z]
Sphingosine [13]	D-erythro-sphingosine (860490) Heptadeca-sphing-4-enine (LM-2000)*	18	Positive	0.5	48	NLS	200–1000
Sphingosine-1-phosphate [14]	D-erythro-sphingosine-1-phosphate (860492) Heptadeca-sphing-4-enine-1-phosphate (LM-2144)*	24	Negative	1.5	79.1	PIS	200–1000
Sphingomyelin [15]	N-oleoyl-D-erythro-sphingosylphosphorylcholine (860587) N-(dodecanoyl)-sphing-4-enine-1-phosphocholine (LM-2312)*	50	Positive	1.0	213.2	NLS	350–1000
Ceramide [16]	N-oleoyl-D-erythro-sphingosine (860519) N-(dodecanoyl)-sphing-4-enine (LM-2212)*	32	Negative	1.5	256.2	NLS	300–1000

5. Other:
 - (a) Argon gas: compressed, ultrahigh purity grade.
 - (b) Nitrogen: compressed, ultrahigh purity grade.
 - (c) Vortexer.
 - (d) Ice bucket or Styrofoam container with ice.

2.3 Data Analysis

1. MZmine 2.21: an open source software designed specifically for mass spectrometry data analysis. It allows for spectra processing, building of chromatograms for identification and export of a variety of vendor specific formats.
2. Sample spectra data.
3. Custom database (optional).

3 Methods

3.1 Lipid Extraction (See Notes 1–5)

Before starting lipid extraction, transfer an aliquot of each sample to a new tube for determination of total protein content using bicinchoninic acid (BCA) [17] or Bradford method [18]. For lower protein concentrations not measurable using BCA or Bradford method, we recommend the use of the PhastGel system and densitometry using a bovine serum albumin (BSA) standard for protein quantitation [19–21].

1. Add the same amount of each internal standard (e.g., 250 pmol) to each of your sample.
2. Add methanol–chloroform in a solvent–sample ratio of 3:1 depending on the volume of the aqueous humor specimen (*see Note 6*):
e.g., add 300 μL of methanol–chloroform to 100 μL of aqueous humor sample.
3. Homogenize for 2 min using a glass homogenizer (*see Note 2*).
4. Add chloroform in a chloroform–sample ratio 2–1:1 depending on the volume of aqueous humor specimen in Subheading 3.1, step 2:
e.g., add 100–200 μL of chloroform if the volume of aqueous humor sample in Subheading 3.1, step 2 was 100 μL .
5. Homogenize as in Subheading 3.1, step 3.
6. Vortex for 30 s.
7. Centrifuge samples at $20,000 \times g$ for 15 min at 4 °C.
8. You should have obtained phase separation into (*see Notes 7 and 8*):
 - (a) Superior aqueous layer (aqueous-soluble compounds in methanol–water).

- (b) Inferior organic layer (lipids in chloroform).
- 9. Place the lipid fractions into new tubes. To prevent contamination by proteins due to repeated pipetting through the aqueous phase, use a new tip each time.
- 10. Aliquot each lipid fraction into four parts.
- 11. To remove chloroform dry lipid extracts in a centrifugal vacuum concentrator for 90 min or longer if needed (*see Note 9*).
- 12. Dried lipids can be stored at -80°C until mass spectrometric analysis (*see Note 10*).

3.2 Mass Spectrometric Analysis

1. To prepare lipid samples and external standard calibrators (*see Notes 10 and 11*):
 - (a) Reconstitute dried lipid samples obtained in Subheading 3.1, **step 12** with acetonitrile–isopropanol, except for samples dedicated to analysis of sphingomyelin that should be reconstituted in lithiated chloroform–methanol. Vortex for 1 min.
 - (b) Create each external standard calibration curve (e.g., 6-point from 0 to 300 pmol) in acetonitrile–isopropanol except for sphingomyelin standard that should be diluted in lithiated chloroform–methanol. To each calibrator add the same amount of matching internal standard as added to samples in Subheading 3.1, **step 1**.
2. For different sphingolipids set the following parameters: *see Table 1*, in Thermo Scientific Xcalibur and Tunes Software.
3. Set the following parameters for ESI:
 - (a) Flow rate infusion: 10 $\mu\text{L}/\text{min}$.
 - (b) Spectrum recording: 2 min.
 - (c) Scan: 0.5 s.
 - (d) Ionization voltage: 1.55 kV for Positive ion mode or 1.3 kV for Negative ion mode.
 - (e) Gas pressure: 0.45 psi for Positive ion mode or 0.6 psi for Negative ion mode.
4. For quality control: run lipid standards separately before and after running the samples. Moreover, a blank (acetonitrile–isopropanol) can be run before and after each sample to exclude carryover.

3.3 Data Analysis

3.3.1 Raw Data Import

1. Raw Data Methods > Raw Data Import. The software supports such vendor-specific formats as mzXML, NetCDF, Waters Raw, Agilent CSV, and Thermo CSV.
2. Select and open the desired spectra. The spectra selected should appear in the left half of the interface (Raw Data Files) once successfully imported.

3.3.2 *Mass Detection*

The purpose of this step is to create a list of masses for each raw file. The settings depend on how the data were acquired and the scan quality. For centroided data, the Centroid Mass Detector is applied and assumes that every signal above the specified noise level is a peak.

1. Raw Data Methods > Peak Detection > Mass Detection.
2. Adjust the parameters according to data resolution and precision:
 - (a) MS level: depends on type of scan. 2 for NLS and 1 for PIS or full MSI scans.
 - (b) Polarity: depends on type of ionization.
 - (c) Mass Detector: Centroid.
 - (d) Noise level = 0.
 - (e) Mass list name: masses.
3. Other mass detectors may be used as the exact mass detector: local maxima, recursive threshold or wavelength transform mass detectors.

3.3.3 *Chromatogram Builder (See Note 12)*

After running the mass detection, the chromatogram builder makes a constant chromatogram across the scans for each mass. While ideal setting for each chromatogram may change depending on the data set, common baseline settings for several classes are given.

The min time span parameter specifies the minimum time during which a peak must be detected to be included in the chromatogram. Min height is determined by the least possible intensity of the highest data point. Any chromatogram found below the set level is rejected as noise. The m/z tolerance is the greatest allowed m/z difference between data points to be grouped into the same chromatogram.

1. Raw Data Methods > Peak Detection > Chromatogram Builder.
2. Parameters:
 - (a) Mass list: masses.
 - (b) Set filters (MS level and polarity should be the same as the parameters for mass detection):
 - Positive ion mode species.
Min time span: 0.
Min height: 5.00E3.
 m/z tolerance 0.3.
 - Negative ion mode species.
Min time span: 0.
Min height: 5.00E2.
 m/z tolerance 0.3.

3. The completed chromatograms now should appear under the Peak List column on the right side of the interface. Clicking on a completed chromatogram should display a window with the ID, average m/z , retention time, peak shape, height, and area in table form.
4. Troubleshooting
 - (a) If the chromatogram table appears blank, the parameters may have been set too high, causing all data to be discounted as noise. Manually inspect the spectra to adjust the parameters for noise level.

3.3.4 Isotopic Peak Correction

The isotopic peaks grouper leaves one representative peak for a group of isotopes.

1. Peak List Methods > Isotopes > Isotopic Peak Grouper.
 - (a) m/z tolerance: 0.05.
 - (b) RT tolerance: entire duration of analysis.
 - (c) Monotopic shape: checked.
 - (d) Maximum charge: 2.
 - (e) Representative isotope: Lowest m/z .

3.3.5 Identification

Identification of the generated peaks is done using either custom databases or those provided by the software. Below are the instructions for identifying lipids from a custom database. If no custom database is available, the software provides an adduct ion search, a peak complex search, and an online database search. Note that a custom database may be created by the user (*see* Subheading 3.3.7).

1. Peak list methods > Identification > Custom Database Search > Select the correct database.
2. Parameters:
 - (a) Field separator: , (comma).
 - (b) Field order: ID, m/z , Retention time, Identity, Formula.
 - (c) Ignore First List: Checked.
 - (d) m/z tolerance: 0.3 (*see* **Note 13**).
 - (e) RT tolerance: the entire duration of the direct infusion analysis.

3.3.6 Export of CSV File

1. Select file (individually) > Peak list methods > Export/Import > Export to CSV.
2. Parameters:
 - (a) Filename.
 - (b) Field separator: , (comma).
 - (c) Export common elements: *Export row m/z only*.

- (d) Export identity elements: *Name* only.
 - (e) Export data file elements: *Export peak area* only.
3. After the files are exported, they can be combined and further analyzed and quantified outside of MZmine if needed (*see* Subheading 3.3.8). However, MZmine offers several analysis and visual representation methods. Other export formats can be selected—such as MzTAB, XML, and SQL which may open alternatives for later analysis.

3.3.7 Creating a Class-Specific Database (See Note 14)

Each lipid class will require a corresponding database which contains the attributes to each species. These databases can be obtained from a variety of Internet sources—such as the NIH’s LIPIDMAPS. Guidelines for using LIPIDMAPS are given.

1. Visit LIPIDMAPS website > Resources > Classification.
2. Open the desired main class from the eight categories.
3. At the bottom of the list find the *Download results* tab, choose CSV format and all pages.
4. Open the file in Excel and place the columns in the order of ID, *m/z*, Retention Time, Identity (Common name), Formula.
5. Save as .csv.
6. The new custom database can now be selected in the custom database search interface for identification.

3.3.8 Post-MZmine Analysis

For experimental purposes it is often useful to organize and analyze the data as presented in the MZmine-exported file. Further manipulation is often required to analyze data from large experiments or for selecting species for detailed study.

1. **Ratiometric Quantification:** The quantitation of different sphingolipid species is obtained by the use of constant amount of nonnaturally occurring internal standard together with calibration curves obtained with different amounts of naturally occurring species. To compensate for some limitations of the method, e.g., matrix effect or machine instabilities, instead of analyte or external standard calibrator areas, their ratios to respective internal standard areas are used.
 - (a) Construct external standard calibration plots of concentration of external (C_{ES}) standard (x -axis values) versus area ratio of external (A_{ES}) and internal (A_{IS}) standard (A_{ES}/A_{IS}) (y -axis values).
 - (b) For each external standard calculate linear regression curves.
 - (c) To determine analyte concentration from obtained linear regression equation ($y = ax + by$), substitute y with area ratio of analyte (A_A) and internal standard (A_A/A_{IS}) in the sample of interest (*see* Note 15).

- (d) The amount of lipid species obtained from the ratiometric quantification analyses above is then divided by the total amount of protein in the sample for normalization. The final amount of lipid is expressed in pmol of lipid/ μg protein.
2. Multisample analysis: The nature of experimentation often requires manipulations of parameters across different sheets to obtain a single data point. For lipidomics this may include selecting the lowest m/z and manually averaging the associated peak areas for a single species in many data sheets in tandem, quickly becoming a very time-consuming task. Third-party software exists but may be difficult to locate and secure. As such, it can be necessary to design simple programs (e.g., in Excel's VBA language). Some useful program schematics follow:
 - (a) Programs which will average the m/z and peak area values for each occurrence of a certain named species, assigning results to a new sheet.
 - (b) Programs which can indicate the frequency of occurrence of identified peaks across multiple sheets from different replicates.
 - (c) Programs which conduct a search comparison between data sheets, indicating the species which are unique to a set or present in both sets.
 - (d) Programs which can carry out other statistical analyses.

4 Notes

1. Lipids are extracted using solvents that are potentially hazardous to personnel working in the laboratory. Study Material Safety Data Sheets (MSDS) of reagents being used before you start working with the material.
2. To avoid any source of contamination, lipid extraction should be carried out using glassware: Teflon capped tubes, homogenizers and pipette tips. Except for Teflon, all plastics must be avoided because they leach contaminants into the sample.
3. Since lipids are particularly sensitive to oxidation and degradation, it is critical that one strictly adheres to the protocol and storage conditions to obtain accurate spectra.
4. It is important to keep samples on ice at all times.
5. Flush samples with argon gas frequently to prevent lipid oxidation—as a rule of thumb—every time you open a tube. To avoid spillage, direct a gentle stream of argon gas down into the tube for few seconds, then cap it tightly.

6. Optionally, to prevent lipid oxidation, you can add antioxidant (butylated hydroxytoluene) to a final concentration of 10 μM .
7. For aqueous humor, as for other body fluids, i.e., cerebrospinal fluid or tears, the layers after centrifugation may not be very apparent. We advise to collect less of the organic layer rather than risk contamination of the lipid extract with the aqueous layer. If layers are not visible, place liquid back in tube, vortex for 1 min and repeat Subheading 3.1, step 7.
8. Adding 100 μL of LC-MS grade water to the sample in Subheading 3.1, step 5 may help to visualize layers more easily.
9. If liquid is present after 90 min, dry at 15 min intervals until samples are completely dry. Remember to flush with argon gas.
10. Samples should not be stored in liquid at -80°C . Storing lipids in solution and freezing those increases lipid degradation.
11. Major problems with lipid standards derive from their instability. Store lipid standards at -20°C at all times and use only freshly prepared standards to obtain accurate results.
12. The chromatogram builder assumes that liquid chromatographic separation has preceded the mass spectrometric analysis and thus will analyze the data as a chromatogram (peak as a function of retention time). For data obtained in mass spectrometry with direct infusion a *pseudochromatogram* is produced. In this case, the retention time is the total analysis time and the peak intensity at any time point does not influence identification or quantitation of the spectra.
13. The mass spectrometer used for these analyses is of moderate resolution, meaning that the accuracy of the m/z is within $\pm 0.3 m/z$.
14. For accurate identification of peaks, the custom database needs to be altered to reflect mass changes in the species such as adducts.
15. A possible chain length dependency may be addressed by performing calibrations with a short-chain and a long-chain fatty acid external standards.

References

1. Piccinini M, Scandroglio F, Prioni S, Buccinna B, Loberto N, Aureli M, Chigorino V, Lupino E, DeMarco G, Lomartire A, Rinaudo MT, Sonnino S, Prinetti A (2010) Deregulated sphingolipid metabolism and membrane organization in neurodegenerative disorders. *Mol Neurobiol* 41 (2–3):314–340. <https://doi.org/10.1007/s12035-009-8096-6>
2. Spassieva SD, Ji X, Liu Y, Gable K, Bielawski J, Dunn TM, Bieberich E, Zhao L (2016) Ectopic expression of ceramide synthase 2 in neurons suppresses neurodegeneration induced by ceramide synthase 1 deficiency. *Proc Natl Acad Sci U S A* 113 (21):5928–5933. <https://doi.org/10.1073/pnas.1522071113>

3. Hannun YA, Obeid LM (2008) Principles of bioactive lipid signalling: lessons from sphingolipids. *Nat Rev Mol Cell Biol* 9(2):139–150
4. Haughey NJ (2010) Sphingolipids in neurodegeneration. *NeuroMolecular Med* 12(4):301–305. <https://doi.org/10.1007/s12017-010-8135-5>
5. Halmer R, Walter S, Faßbender K (2014) Sphingolipids: important players in multiple sclerosis. *Cell Physiol Biochem* 34(1):111–118
6. Guerra Y, Aljohani AJ, Edwards G, Bhattacharya SK (2014) A comparison of trabecular meshwork sphingolipids and ceramides of ocular normotensive and hypertensive states of DBA/2J mice. *J Ocul Pharmacol Ther* 30(2–3):283–290. <https://doi.org/10.1089/jop.2013.0168>
7. Aljohani AJ, Edwards G, Guerra Y, Dubovy S, Miller D, Lee RK, Bhattacharya SK (2014) Human trabecular meshwork sphingolipid and ceramide profiles and potential latent fungal commensalism. *Invest Ophthalmol Vis Sci* 55(6):3413–3422. <https://doi.org/10.1167/iovs.13-13570>
8. Simon MV, Prado Spalm FH, Politi LE, Rotstein NP (2015) Sphingosine-1-phosphate is a crucial signal for migration of retina Muller glial cells. *Invest Ophthalmol Vis Sci* 56(10):5808–5815. <https://doi.org/10.1167/iovs.14-16195>
9. Bruggen B, Kremser C, Bickert A, Ebel P, Vom Dorp K, Schultz K, Dormann P, Willecke K, Dedek K (2016) Defective ceramide synthases in mice cause reduced amplitudes in electroretinograms and altered sphingolipid composition in retina and cornea. *Eur J Neurosci* 44(1):1700–1713. <https://doi.org/10.1111/ejn.13260>
10. Rotstein NP, Miranda GE, Abraham CE, German OL (2010) Regulating survival and development in the retina: key roles for simple sphingolipids. *J Lipid Res* 51(6):1247–1262. <https://doi.org/10.1194/jlr.R003442>
11. Aljohani AJ, Munguba GC, Guerra Y, Lee RK, Bhattacharya SK (2013) Sphingolipids and ceramides in human aqueous humor. *Mol Vis* 19:1966–1984
12. Edwards G, Aribindi K, Guerra Y, Bhattacharya SK (2014) Sphingolipids and ceramides of mouse aqueous humor: comparative profiles from normotensive and hypertensive DBA/2J mice. *Biochimie* 105:99–109. <https://doi.org/10.1016/j.biochi.2014.06.019>
13. Han X, Yang K, Gross RW (2012) Multi-dimensional mass spectrometry-based shotgun lipidomics and novel strategies for lipidomic analyses. *Mass Spectrom Rev* 31(1):134–178. <https://doi.org/10.1002/mas.20342>
14. Jiang X, Han X (2006) Characterization and direct quantitation of sphingoid base-1-phosphates from lipid extracts: a shotgun lipidomics approach. *J Lipid Res* 47(8):1865–1873. <https://doi.org/10.1194/jlr.D600012-JLR200>
15. Houjou T, Yamatani K, Nakanishi H, Imagawa M, Shimizu T, Taguchi R (2004) Rapid and selective identification of molecular species in phosphatidylcholine and sphingomyelin by conditional neutral loss scanning and MS3. *Rapid Commun Mass Spectrom* 18(24):3123–3130. <https://doi.org/10.1002/rcm.1737>
16. Han X (2002) Characterization and direct quantitation of ceramide molecular species from lipid extracts of biological samples by electrospray ionization tandem mass spectrometry. *Anal Biochem* 302(2):199–212. <https://doi.org/10.1006/abio.2001.5536>
17. Smith PK, Krohn RI, Hermanson GT, Mallia AK, Gartner FH, Provenzano MD, Fujimoto EK, Goeke NM, Olson BJ, Klenk DC (1985) Measurement of protein using bicinchoninic acid. *Anal Biochem* 150(1):76–85
18. Bradford MM (1976) A rapid and sensitive method for the quantitation of microgram quantities of protein utilizing the principle of protein-dye binding. *Anal Biochem* 72:248–254
19. Vincent SG, Cunningham PR, Stephens NL, Halayko AJ, Fisher JT (1997) Quantitative densitometry of proteins stained with coomassie blue using a Hewlett Packard Scanjet scanner and Scanplot software. *Electrophoresis* 18(1):67–71. <https://doi.org/10.1002/elps.1150180114>
20. van Eijk HG, van Noort WL (1992) The analysis of human serum transferrins with the PhastSystem: quantitation of microheterogeneity. *Electrophoresis* 13(6):354–358
21. Amelinckx A, Castello M, Arrieta-Quintero E, Lee T, Salas N, Hernandez E, Lee RK, Bhattacharya SK, Parel JMA (2009) Laser trabeculoplasty induces changes in the trabecular meshwork glycoproteome: a pilot study. *J Proteome Res* 8(7):3727–3736. <https://doi.org/10.1021/pr900294g>

Chapter 11

Assessment of Aqueous Humor Dynamics in the Rodent by Constant Flow Infusion

J. Cameron Millar, Tien N. Phan, and Iok-Hou Pang

Abstract

Mice and rats are being increasingly used in glaucoma research and much useful data have been generated from them. One aspect of using these animals for this purpose involves assessment of aqueous humor dynamics. Several techniques have been described in the literature for the determination of one or more of these parameters in rodents, in both living animals and eyes perfused *ex vivo*. Here, we describe the practical details for a technique for the determination of all principal parameters of aqueous humor dynamics (intraocular pressure (IOP), aqueous humor formation rate (F_{in}), uveoscleral outflow rate (F_u), aqueous outflow facility (C), and episcleral venous pressure (P_e)) in the living rat and mouse eye, in a single experimental session.

Key words Rat, Mouse, Aqueous humor dynamics, Aqueous outflow facility, Uveoscleral outflow, Aqueous humor formation, Episcleral venous pressure, Intraocular pressure

1 Introduction

Primary open-angle glaucoma (POAG) is a leading cause of vision loss and blindness worldwide. The disease occurs mainly in the middle aged to elderly; it is estimated that there will be approximately 58.6 million cases globally by 2020 [1]. POAG is a neurodegenerative disorder characterized by injury to axons of the retinal ganglion cells (RGCs), and apoptosis of the cell soma. Resistance to outflow of aqueous humor is often increased, and in consequence in $\geq 2/3$ of glaucomas there is an elevation of intraocular pressure (IOP) above its normal value of 10–15 mmHg, to values in excess of 21 mmHg. The only clinically proven treatment is to reduce IOP toward normal values, either pharmacologically, surgically, or with laser technology. Lowering IOP however does not cure the condition. Therefore, many research efforts have targeted this disease, and numerous animal models have been devised in an attempt to further elucidate POAG pathophysiology.

Since the beginning of the twenty-first century, rodents have lent themselves well to glaucoma research. There are several reasons for this. Advances in the ability to measure IOP in the conscious rodent eye by tonometry using the TonoLab™ rebound tonometer have rendered such once-challenging measurements in these animals now routine [2]. The structural anatomy, and also the physiology, pharmacology, and arrangement of blood vessels and nerves of the anterior portion of the rodent eye are very similar to that of the human eye, much more so in fact than any other species with the exception of the non-human primate [3]. Rodents are also inexpensive to purchase and house, and as of the time of writing there are >20,000 transgenic strains of mouse commercially available. The brief maximal lifespan of these animals (~27 months or less, depending on strain) renders a mature phenotype achievable within a matter of 2–3 months from conception.

Because all current and many experimental therapies for the treatment of POAG are designed to lower IOP, an ability to measure IOP accurately and reproducibly in rodent models is important. But it is equally important to be able to determine the mechanism(s) of action of agents which lower IOP via their action on individual components of aqueous humor dynamics. IOP in the living eye is described mathematically by the modified Goldmann equation [4], which states that

$$\text{IOP} = [(\text{Fin} - \text{Fu}) / \text{C}] + \text{Pe}$$

where:

Fin = aqueous humor formation rate (units: $\mu\text{L}/\text{min}$).

Fu = uveoscleral outflow rate (units: $\mu\text{L}/\text{min}$).

C = outflow conductance or outflow facility (= reciprocal of resistance to aqueous outflow) (units: $\mu\text{L}/\text{min}/\text{mmHg}$).

Pe = episcleral venous pressure (units: mmHg).

IOP = intraocular pressure (units: mmHg).

Thus, in a mouse eye with a value for Fin of $0.14 \mu\text{L}/\text{min}$, a value for Fu of $0.042 \mu\text{L}/\text{min}$, a value for C of $0.018 \mu\text{L}/\text{min}/\text{mmHg}$, and a value of Pe of 9.5 mmHg , IOP theoretically = 14.9 mmHg . An agent that reduces IOP may do so by: reducing Fin , increasing Fu , increasing C , or reducing Pe , or by some combination of effects on two or more of these parameters. Hence, an ability to determine the effect of such an agent on each of these parameters is important. Using one methodology for such determinations, known as constant flow infusion [5], it is possible to measure IOP, C , and Pe , and derive estimates for Fu and Fin .

Here, we describe the technique of Millar et al. [5, 6]. This technique is applicable equally to both rats and mice.

2 Materials

2.1 Perfusate

We have used Balanced Salt Solution (BSS™) or Balanced Salt Solution plus Oxidized Glutathione (BSS-Plus™), or Phosphate-Buffered Saline (PBS™). All of these solutions may be purchased ready-made and sterile. Detailed components are shown in Tables 1, 2, and 3.

Immediately before use the perfusate should be filtered through a 0.2 µm HT Tuffryn® (polysulfone) membrane Low Protein Binding Non-Pyrogenic Syringe Filter.

As an alternative perfusate, Bárány's Mock Aqueous Humor (MAH) solution (Bárány's) may be utilized. MAH must be made up immediately before use, either fresh, or from pre-prepared 10 × stock. Detailed components are shown in Table 4. Since there is no commercial outlet for MAH, all components must be purchased separately from a chemical supplier.

Table 1
Balanced salt solution (BSS)

Compound	Molecular weight	g/L for 10× stock	g/L	Concentration (mM)
NaCl	58.4	71.4	7.14	122.0
KCl	74.6	3.8	0.38	5.1
MgCl ₂	95.2	2	0.2	2.1
CaCl ₂	111.0	1.54	0.154	1.4
NaH ₂ PO ₄	120.0	4.2	0.42	3.5

Table 2
Balanced salt solution plus oxidized glutathione (BSS-PLUS)

Compound	Molecular weight	g/L for 10× stock	g/L	Concentration (mM)
NaCl	58.4	71.4	7.14	122.0
KCl	74.6	3.8	0.38	5.1
MgCl ₂	95.2	2	0.2	2.1
CaCl ₂	111.0	1.5	0.154	1.4
NaH ₂ PO ₄	120.0	4.2	0.42	3.5
NaHCO ₃	84.0	21	2.1	25.0
D-glucose (dextrose)	180.2	9.2	0.92	5.1
Glutathione disulfide (oxidized glutathione)	612.6	1.84	0.184	0.3

Table 3
Phosphate buffered saline solution (PBS)

Compound	Molecular weight	g/L for 10× stock	g/L	Concentration (mM)
NaCl	58.4	80.1	8.01	137
KCl	74.6	2.0	0.20	2.7
Na ₂ HPO ₄	142.0	14.2	1.42	10
KH ₂ PO ₄	136.1	2.4	0.24	1.8

Table 4
Bárány's Mock Aqueous Humor (MAH) solution

Compound	Molecular weight	g/L for 10× stock	g/L	Concentration (mM)
NaCl	58.4	80	8	137
KCl	74.5	3.5	0.35	4.7
MgCl ₂	95.2	0.64	0.064 = 64 mg	0.67
CaCl ₂	111.0		0.17 ^a	1.53
Na ₂ HPO ₄	142.0	0.69	0.069 = 69 mg	0.49
NaH ₂ PO ₄	120.0	0.137	0.0137 = 13.7 mg	0.11
D-glucose (dextrose)	180.2	10	1	5.55
Ascorbic acid ^b	176.1	88.1 mg	0.00881 = 8.81 mg	50

^aAdd 1.53 mL from 1 M Stock solution *drop-wise* after adding all other components for final solution. Do *not* add CaCl₂ to 10× stock

^bAscorbic acid is optional. pH should be adjusted to 7.4 with 1 M HCl and/or 1 M NaOH added dropwise, as required

2.2 Apparatus

The components listed in Table 5 are sufficient to build an apparatus that can be used to perfuse four eyes (two animals) simultaneously. If more animals are to be perfused simultaneously, multiples of this apparatus will be needed. A schematic diagram illustrating the assembled apparatus has been previously published [5].

In addition to the components listed in Table 5, the following will also be required:

Syringe Needles (Luer type) 30G or finer, down to 36G, ½" or 1", or glass micro-needles may be used, retort stands, 30 mL or 20 mL syringes, 10 mL syringes, 1 mL glass syringes, 100 µL or 50 µL glass microsyringes, 3-way stopcocks, modeling clay.

Table 5
Components required to build constant flow infusion aqueous humor dynamics apparatus

Item	Number required	Model/catalog #	Supplier	Comment
Blood pressure transducer	4	BLPR2	World Precision Instruments (WPI), Sarasota, FL, USA	Supplied with 3-way valve equipped with Luer fittings
Microdialysis infusion pump	2	SP101i	WPI	
Amplifier/ balance box	1	Transbridge TBM4M	WPI	
Analog-to-digital converter	1	Lab-TRAX-4	WPI	
Data collection software	1	LabScribe2	WPI	Supplied as CD-ROM with LAB-TRAX-4 unit
Warming pad	1	CAT94B E12107 or similar	VWR	
High intensity illuminator	1	83365; 31804443434	Nikon instruments, Inc	
Dissecting microscope	1 or 2		Nikon or Bausch & Lomb or similar	
Cables	4		WPI	
Cables	4		WPI	
USB cable	1		WPI	
Tubing	10 m (~33 ft)	PE60	VWR	
Desktop or notebook computer	1			

3 Methods

Carry out all the procedures at room temperature unless otherwise specified.

3.1 Perfusate and Line-Filling

Make up ~250 mL of perfusate (BSS, BSS-Plus, PBS, or MAH). Filter the perfusate through a 0.2 μm filter and then store in another clean beaker or conical flask covered with a piece of ParaFilm™ or similar to keep freshly filtered perfusate free from airborne particulates (*see* **Note 1**).

Fill a 10 mL syringe with filtered perfusate. Attach to one end of perfusate tubing line running from one of the four syringes held in the two infusion pumps. After insuring that the 3-way stopcock is closed to the attached manometer line, and insuring that no needle is attached to the distal end of the infusion tubing line, fill the line with perfusate, taking care that no bubbles form in the tubing or transducer body. Remove a ½" or 1" 30G (or finer) needle from its sterile packaging (or use glass microneedle), and attach to the distal end of the infusion line.

Fill the manometers and all lines running from them with perfusate also.

Fill a 1 mL plastic or glass syringe (or 100 µL glass microsyringe or 50 µL glass microsyringe) with perfusate. Connect the 1 mL plastic or glass syringe (or 100 µL glass microsyringe or 50 µL glass microsyringe) to a side port formed by an additional 3-way stopcock included in the infusion line. Be careful when making this connection to eliminate any bubbles that may form.

As an alternative, if the additional 3-way stopcock is not used, carefully hold the proximal end of the tubing at the same height above the bench as the distal end. Remove the 10 mL syringe and replace rapidly with the filled 1 mL plastic or glass syringe (or 100 µL glass microsyringe or 50 µL glass microsyringe). Ensure drop-to-drop contact between syringe and tubing to prevent any bubbles from forming. Syringes may also be filled directly from their respective manometers.

Repeat the process for the additional infusion lines.

When all infusion lines are filled, place filled plastic or glass 1 mL syringes (or 100 µL or 50 µL glass syringes) in the infusion pumps, switch on the infusion pumps, and set to run at a flow rate of 0.1 µL/min. Switch on the TBM4M transbridge, and boot up the computer. Then click on the LabScribe2 Desktop Icon and open LabScribe2.

At this point it is advisable to leave the energized apparatus (in particular, the transducers) to settle for a period of 30 min (*see Note 2*).

3.2 Anesthesia

Following the 30 min settling-in period, weigh and anesthetize each animal to be utilized using a suitable injectable cocktail.

For mice we have used a sterile mixture of ketamine 10 mg/mL and xylazine 1 mg/mL, injected intraperitoneally (I.P.) as 100 µL/10 g body weight (*see Note 3*).

For rats we have used a sterile mixture of ketamine 33.33 mg/mL, xylazine 6.67 mg/mL, and acepromazine 3.33 mg/mL, injected intramuscularly (I.M.) as 100 µL/100 g body weight.

Allow animals 15 min following induction to develop anesthesia. At this point, if required (as evidenced by the presence of a flexor withdrawal response to a painful toe-pinch, a response to a painful tail-pinch, and the presence of a blink reflex in response to

lightly brushing the cornea with the tip of a Weck Sponge™ or similar), administer an additional maintenance dose of anesthetic ($\frac{1}{2} \times$ induction dose). Allow animals an additional 10 min to develop a surgical plane of anesthesia.

When surgical anesthesia has been achieved, measure IOP in both eyes using a TonoLab™ rebound tonometer, following the methodology of Wang et al. [2] or a suitable variant thereof. If desired, IOP may additionally be measured in conscious animals prior to administration of anesthesia, but this is not necessary.

Following this, place animals on the thermal pad set to maintain body temperature at 37 °C. Apply 1–2 drops of proparacaine HCl 0.5% to the corneas of each animal. Remove excess with the tip of a Weck Sponge™ or similar, or a piece of tissue paper.

3.3 Cannulation of Eyes

Insure once again that each infusion pump is set to a flow rate of 0.1 $\mu\text{L}/\text{min}$. Insure that the transducers (which are electronic and thus temperature-sensitive) are away from the thermal pad, and that their chambers are set at the same height on the bench as the eye to which they pertain. Insure that the baseline readings from each transducer are adjusted on the virtual chart recorder to read zero.

Under 10 \times to 30 \times magnification (dissection microscope), cannulate each eye by inserting a needle through the cornea 1 mm anterior to the limbus and carefully pushing to the opposite area of the anterior chamber from the point of cannulation (Fig. 1a). As an alternative, the posterior chamber may be

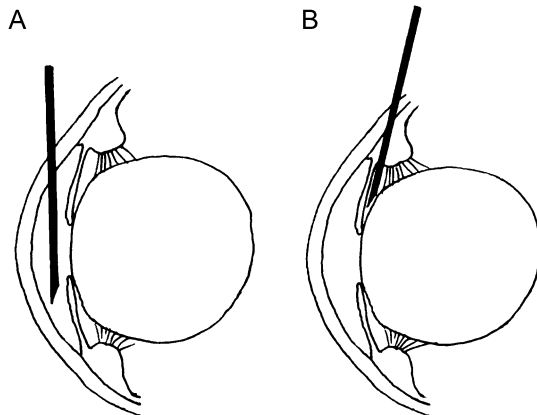


Fig. 1 Cannulation of the Aqueous Chamber. (a) In anterior chamber (AC) cannulation, the needle is inserted through the cornea 1–2 mm anterior to the limbus and pushed across the anterior chamber internally, taking care to avoid striking the corneal endothelium, anterior lens capsule, or iris. (b) In posterior chamber (PC) cannulation, the needle is inserted through the sclera 1–2 mm posterior to the limbus and pushed through the pars plicata of the ciliary body into the posterior chamber, behind the iris. In either case, we place the needle with the bevel opening facing posteriorly

cannulated by insertion through the anterior sclera 1–2 mm posterior to the limbus, and then carefully pushing through the sclera and underlying pars plicata of the ciliary body until the tip is seen to emerge from underneath the iris (Fig. 1b). At this point, the needle should be carefully and gently withdrawn until the tip just disappears once again beneath the iris (*see Note 4*).

3.4 Estimation of Episcleral Venous Pressure (Pe)

Because of their small size, at present, there is only one practical methodology for the measurement of Pe in rodent eyes, first described by Aihara et al. [7] in the mouse. This methodology is described here. After cannulation is complete, starting with one eye, adjust the 3-way stopcock connected to the manometer to open the manometer to the perfusion line, and adjust the pressure in the eye to equal the pre-cannulation anesthetized IOP. Allow 5 min for stabilization. Then, view the anterior segment of the eye through the dissection microscope under 10× to 30× magnification. Lower the manometer by 1.36 cm to manometrically reduce the pressure inside the eye by 1 mmHg. Wait for 1 min. View the eye through the microscope once again. Then repeat. In this way, reduce the pressure in the eye in 1 mmHg increments (at a rate *not to exceed* 1 mmHg/min), and view each time, until the episcleral veins/aqueous veins/scleral collector channels and Schlemm's canal are seen to be clearly injected/distended with blood (*see Note 5*). Record the pressure at which this occurs as the episcleral venous pressure (Pe). Then return the eye to a pressure equal to its pre-cannulation anesthetized IOP and close off the manometer from the perfusion line using the 3-way stopcock. This should also insure adequate chamber refilling prior to infusion. Allow to stabilize while being perfused at 0.1 μL/min for 15–30 min.

Repeat for all remaining eyes.

3.5 Perfusion of Live Animals

After 15–30 min of perfusion at 0.1 μL/min and pressure in each eye has stabilized (defined as the initial sharp rate of increase in pressure at any new flow rate has tailed off to <15% of the initial rate of increase, with inclusion of a certain amount of decrease also, alternating with increase, neither of which is >2 mmHg/min), record the pressure every 5 min over a 10–15 min period. Then increase the flow rate to 0.2 μL/min, wait 5 min, and then record the stabilized pressure every 5 min over a 10–15 min period once again. Repeat at flow rates of 0.3 μL/min, 0.4 μL/min, and 0.5 μL/min (*see Notes 6 and 7*).

3.6 Perfusion of Euthanized Animals

When complete, adjust the infusion pump flow rates to 0.1 μL/min once again. Euthanize the animals (anesthetic overdose) *without moving them or disturbing the needles cannulating their eyes*. When death is confirmed (absence of respiration, and absence of heartbeat as evidenced by retinal blanching (ophthalmoscopy), *see Note 8*), open the manometers once again to the perfusion lines using the

3-way stopcocks. Using the manometers, adjust the pressure in each eye to zero (corresponding to zero IOP that exists when IOP equals air pressure when aqueous humor formation has stopped and episcleral venous pressure has reduced to zero). Close the manometers to the circuit and allow the eyes to be perfused at 0.1 $\mu\text{L}/\text{min}$ for 10–15 min. Once pressure has stabilized (as defined above), record the pressure every 5 min over a 10–15 min period. Then increase the flow rate to 0.2 $\mu\text{L}/\text{min}$, wait 5 min, and then record the stabilized pressure every 5 min over a 10–15 min period once again. Repeat at flow rates of 0.3 $\mu\text{L}/\text{min}$, 0.4 $\mu\text{L}/\text{min}$, and 0.5 $\mu\text{L}/\text{min}$.

Remove the needles from the eyes and insure that pressure indicated by the transducers returns to zero. If it fails to do so, the respective needle(s) is/are blocked, and data from the affected eye(s) should be discarded. As a further test of needle patency, open the needles to the manometers and confirm steady dripping of fluid from the needle tips.

At this point the experiment is over. Dispose of the carcasses. Flush the system and manometers through with clean water, and switch off and disconnect all electrical apparatuses.

3.7 Calculations

3.7.1 Outflow Facility (C)

A graph of Mean Pressure (mmHg) at each flow rate as an ordinate against Flow Rate ($\mu\text{L}/\text{min}$) as abscissa is plotted. The slope (S) is determined by Simple Linear Regression (assuming intersection through the origin). Outflow Facility (C) ($\mu\text{L}/\text{min}/\text{mmHg}$) is then calculated as the reciprocal of S. This is performed for each eye under both live and euthanized (dead) conditions, to obtain values for $C_{(\text{live})}$ and $C_{(\text{dead})}$. According to our experience, $C_{(\text{live})}$ and $C_{(\text{dead})}$ are typically equal. The slope of the pressure versus Flow Rate plot should approximate to linearity; if not, then chamber refilling prior to commencement of infusion may not have been fully achieved. In that case, a curvilinear appearance may be evident, with a significantly lower slope at the lower (0.1–0.2 $\mu\text{L}/\text{min}$) as compared with the higher (0.3–0.5 $\mu\text{L}/\text{min}$) flow rates.

3.7.2 Uveoscleral Outflow (F_u)

Since F_{in} and P_e both equal zero following euthanasia, estimates for F_u at each flow rate can be derived from the expression:

$$F_u = \text{Flow Rate} - (\text{Mean Pressure at that Flow Rate} \times C_{(\text{dead})})$$

The mean value for F_u is then computed by averaging each individual value of F_u at each flow rate (*see Note 9*).

3.7.3 Aqueous Humor Formation Rate (F_{in})

An estimate for F_{in} while live is derived from the expression:

$$F_{in} = [C_{(\text{live})}(\text{IOP} - P_e)] + F_u$$

(where IOP = pre-infusion IOP as measured by rebound tonometry).

For further explanation of these calculations, *see* Millar et al. [5, 6] and also **Note 9**.

4 Notes

1. If desired, fluorescein or a derivative (e.g., fluorescein isothiocyanate dextran (FITC-dextran)) may be added to the perfusate at a concentration of 0.5–1% (we have used 0.7% FITC-dextran) to facilitate visualization of possible leaking from the eye upon perfusion.
2. However, if using a 50 μL microsyringe one should bear in mind that in 30 min at a flow rate of 0.1 $\mu\text{L}/\text{min}$, 3 μL of perfusate will be gone from the syringe. The remaining 47 μL will be sufficient to perfuse a single eye, but it may be desirable to reduce the flow rate during this 30 min settling-in period.
3. As an alternative anesthetic regimen in mice we have used a sterile mixture of: (1) ketamine 10 mg/mL, xylazine 1 mg/mL, and acepromazine 0.3 mg/mL, injected I.P. as 100 $\mu\text{L}/10$ g body weight, and (2) ketamine 72.73 mg/mL, xylazine 1.82 mg/mL, and acepromazine 1.82 mg/mL, injected I.P. as 10 $\mu\text{L}/10$ g body weight. But with these mixtures we have found that there is a small but significant probability of sudden death during an experiment, even when adhering strictly to all dosages.
4. Care should be taken not to snag any items of clothing or jewelry on the animal during cannulation, as this may cause the needle to be pulled out, which will ruin the chance of obtaining meaningful data from eye(s) so affected. To this end, when cannulating we routinely roll up our sleeves, and remove wristwatches, rings, bracelets, and neckties.
5. When intracameral pressure is artificially lowered until reaching the point at which the episcleral veins/aqueous veins/scleral collector channels and Schlemm's canal fill with blood, the assumption is made that P_e is at the same value throughout the entire episcleral venous plexus, which may or may not be the case [8]. Further, as intracameral pressure is slowly lowered, initially the aqueous veins/scleral collector channels fill with blood refluxed from the episcleral venous plexus, but Schlemm's canal itself remains blood-free. Lowering of intracameral pressure by an additional 1–1.5 mmHg will result in Schlemm's canal itself filling with blood. This is the point at which we routinely assume that intracameral pressure is equal to P_e . We choose this point because the aqueous veins and scleral collector channels are more difficult to visualize, even when filled with blood and under illumination and $30\times$

magnification, especially in pigmented animals. Schlemm's canal by contrast is very much easier to see when filled with blood in either albino or pigmented animals. But obviously measurement of P_e by this method is to an extent dependent on definition [6, 7].

6. At a flow rate of 0.5 $\mu\text{L}/\text{min}$, in a small proportion of animals we have observed a sharp rise in pressure where the pressure-flow rate curve deviates positively from linearity. We suspect that this may be related to a collapse of Schlemm's canal at this flow rate, which is more than $3 \times$ the normal physiological flow rate for mouse eye. If desired, this flow rate may be omitted.
7. In living animals, an absolute flat plateau in the pressure-time curve in practice is very difficult to obtain, perhaps due to small but continuous variations in outflow facility secondary to continual changes in release of neurotransmitter from sympathetic or parasympathetic nerve terminals, or small but continuous changes in P_e . This may continue for a time following euthanasia, although likely to a reduced extent.
8. Confirmation of death typically takes between 15 and 30 min.
9. A 10% error in the measurement of C can lead to as much as a 50–100% error in the estimation of F_u [9], although our data in mice would suggest a figure of approximately 36% [6]. As an alternative, F_u in living rodents can be measured directly via perfusion of tracer (e.g., fluorescein isothiocyanate-dextran (FITC-dextran)) followed by euthanasia, enucleation, ocular dissection, and recovery/quantification of tracer in uveoscleral pathway [6]. Agreement between the two techniques in mice has been of a similar order of magnitude but less than ideal (differing by a factor of ≤ 2) [6]. Both the approaches have produced equally large variation about the mean. However, to the best of our knowledge, there is no better method to date for achieving such measurements in rodents.

References

1. Quigley HA, Broman AT (2006) The number of people with glaucoma worldwide in 2010 and 2020. *Br J Ophthalmol* 90(3):262–267. <https://doi.org/10.1136/bjo.2005.081224>
2. Wang WH, Millar JC, Pang IH, Wax MB, Clark AF (2005) Noninvasive measurement of rodent intraocular pressure with a rebound tonometer. *Invest Ophthalmol Vis Sci* 46(12):4617–4621. <https://doi.org/10.1167/iovs.05-0781>
3. Overby DR, Bertrand J, Schicht M, Paulsen F, Stamer WD, Lutjen-Drecoll E (2014) The structure of the trabecular meshwork, its connections to the ciliary muscle, and the effect of pilocarpine on outflow facility in mice. *Invest Ophthalmol Vis Sci* 55(6):3727–3736. <https://doi.org/10.1167/iovs.13-13699>
4. Kaufman PL (1996) Pressure-dependent outflow. In: Ritch R, Shields MB, Krupin T (eds) *The glaucomas*. CV Mosby Yearbook, St Louis, p P307
5. Millar JC, Clark AF, Pang IH (2011) Assessment of aqueous humor dynamics in the mouse by a novel method of constant-flow infusion. *Invest Ophthalmol Vis Sci* 52(2):685–694. <https://doi.org/10.1167/iovs.10-6069>
6. Millar JC, Phan TN, Pang IH, Clark AF (2015) Strain and age effects on aqueous humor dynamics in the mouse. *Invest Ophthalmol Vis Sci* 56

- (10):5764–5776. <https://doi.org/10.1167/iops.15-16720>
7. Aihara M, Lindsey JD, Weinreb RN (2003) Episcleral venous pressure of mouse eye and effect of body position. *Curr Eye Res* 27 (6):355–362
8. Sit AJ, McLaren JW (2011) Measurement of episcleral venous pressure. *Exp Eye Res* 93 (3):291–298. <https://doi.org/10.1016/j.exer.2011.05.003>
9. Johnson M, McLaren JW, Overby DR (2016) Unconventional aqueous humor outflow: a review. *Exp Eye Res*. <https://doi.org/10.1016/j.exer.2016.01.017>

Methods for Analyzing Endoplasmic Reticulum Stress in the Trabecular Meshwork of Glaucoma Models

Prabhavathi Maddineni, Ramesh B. Kasetti, and Gulab S. Zode

Abstract

The pathological mechanisms underlying increased outflow resistance at the trabecular meshwork (TM) that is responsible for elevating intraocular pressure (IOP) have not been fully delineated. Recent studies have shown that progressive accumulation of misfolded proteins and induction of endoplasmic reticulum (ER) stress is associated with the pathophysiology of glaucomatous TM damage and IOP elevation. We have shown that known causes of human glaucoma, including expression of mutant myocilin or dexamethasone treatment induce abnormal protein accumulation and ER stress in the TM in vitro and in vivo models. To cope up with abnormal protein accumulation, TM cells activate a cytoprotective pathway of unfolded protein response (UPR). However, chronic ER stress can lead to TM dysfunction and IOP elevation. Using cell culture, mouse models, and human postmortem tissues as well as genetic and pharmacological manipulations, we have analyzed ER stress and UPR mediators in the glaucomatous TM damage and IOP elevation. In this chapter, we have described a detailed protocol for the analysis of protein misfolding and ER stress in TM cells and tissues and its association with glaucomatous TM damage and IOP elevation.

Key words ER stress in glaucomatous TM, Chemical induction of ER stress in TM, Unfolded protein response (UPR) target genes, XBP-1 splicing, Myocilin induced ER stress, Glucocorticoid-induced ocular hypertension, Genetic manipulation of ER stress

1 Introduction

1.1 Endoplasmic Reticulum (ER) Stress

Physiologic stresses such as increased secretory load or pathological stresses such as unfolded proteins can disrupt normal homeostasis of the endoplasmic reticulum (ER) causing ER stress [1–3]. To alleviate such cellular stress, eukaryotic cells activate a cytoprotective response known as the unfolded protein response (UPR). The activation of UPR involves four different mechanisms (Fig. 1). First, UPR inhibits protein synthesis, which prevents further accumulation of unfolded proteins. Second, UPR induces ER chaperones (GRP78 and GRP94), which aid in protein folding. Third, UPR induces the ER-associated protein degradation (ERAD) pathway, which targets unfolded protein degradation via proteasomes.

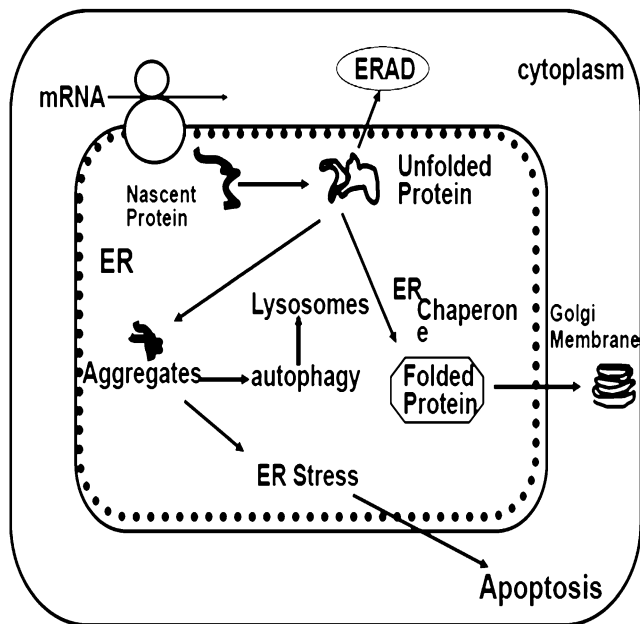


Fig. 1 Schematic showing induction of ER stress and activation of UPR pathway. UPR consists of (1) translational inhibition; (2) induction of ER chaperones; (3) enhanced ERAD; (4) apoptosis

Finally, sustained UPR leads to induction of apoptosis leading to cell death [1, 2]. Activation of the UPR involves sensing of ER stress via PERK, ATF6 α , and IRE1, which then controls the ER stress response. Activation of PERK phosphorylates eIF2 α , which inhibits protein translation. Activated IRE1 converts XBP-1 pre-mRNA to mature mRNA via an unconventional splicing mechanism [4, 5]. Processed XBP-1 acts as a transcriptional activator of genes involved in protein folding, quality control, and regulation of ER/Golgi biogenesis [4, 6–9]. Another ER stress sensor, ATF6 α , is a type II transmembrane protein located on the ER membrane, and is responsible for sensing ER stress. Upon ER stress induction, ATF6 α is activated, increasing the expression of some ER chaperones and ERAD proteins [1–3, 5, 7, 10–14]. Chronic ER stress can lead to ER dysfunction and apoptotic cell death [15, 16] via induction of CHOP, ER-specific caspase 12, and several other factors [17].

1.2 ER Stress in Glaucoma

Recent studies have shown the pathological role of protein misfolding and ER stress in glaucoma [18–21]. Mutations in the myocilin gene (MYOC) are the most common known genetic cause of glaucoma. We and others have demonstrated that disease-causing MYOC mutants are secretion incompetent and accumulate in the ER, inducing ER stress [19, 22–29]. Using *Tg-MYOC*^{Y437H} mice,

we determined that ER stress is associated with IOP elevation in MYOC-associated glaucoma [19]. In our study, loss of TM cells in older *Tg-MYOC^{Y437H}* mice was associated with increased CHOP expression [19]. Increasing MYOC secretion via chemical chaperone sodium 4-phenylbutyrate (PBA) rescues glaucoma phenotypes in *Tg-MYOC^{Y437H}* mice [18, 19]. In addition, we have demonstrated that ER stress plays an important role in ocular hypertension induced by glucocorticoid (GC) therapy [20]. Recently, we have also demonstrated the presence of ER stress in postmortem glaucomatous human TM tissues and cells [21].

2 Materials

The exact recipe for buffers made in our laboratory and sources for commercial reagents or kits are listed below. For commercial reagents and kits, follow the guidelines given by company. In addition, commonly used antibodies and primers sequences for ER stress analysis are listed in Tables 1 and 2 respectively.

2.1 Western Blot Analysis

1. Lysis Buffer: HEPES (50 mM), KCl (200 mM), EDTA (2 mM), MgCl₂ (1 mM), Triton X-100 (0.5%), and Glycerol (10%). Protease inhibitor cocktail tablets and 0.5 mM DTT were added to lysis buffer.
2. SDS-Polyacrylamide gels: NuPAGE 4–12% Bis-Tris Gels.
3. Resolving Gel Buffer: NuPAGE MES SDS Running Buffer (20×) or NuPAGE MOPS SDS Running Buffer (20×).

Table 1
List of primers for QPCR analysis of UPR genes

Gene	Primer sequence
GAPDH	Fw: 5'-GGATGATGTTCTGGAGAGCC-3' Rev.: 5'-CATCACCATCTTCCAGGAGC-3'
CHOP	Fw: 5'-CTGCCTTTCACCTTGGAGAC-3' Rev.: 5'-CGTTTTCTGGGGATGAGATA-3'
BiP	Fw: 5'-CGAGGAGGAGGACAAGAAGG-3' Rev.: 5'-CACCTTGAACGGCAAGAAGT-3'
Myocilin	Fw: 5'-AGACACCGGATATGGAGAAC-3' Rev.: 5'-CTCGCATCCACACACCATAC-3'
GRP 78	Fw: 5'-AAGGAGACTGCTGAGGCGTA-3' Rev.: 5'-CTCATGACATTCAGTCCAGCA-3'
GRP 94	Fw: 5'-GCCGCAACATGTCTCTGAT-3' Rev.: 5'-TTGTGGCCAGTCAAGTATGGA-3'

Table 2
List of antibodies used for Western blotting

	Antibody	Dilutions	Catalogue	Company
Primary antibody	Mouse monoclonal KDEL	1 in 1000	ab12223	Abcam
	Rabbit CHOP	1 in 1000	NBP2-13172	Novus Biologicals
	Rabbit ERO-1 α	1 in 1000	3264	Cell Signaling Technology
	Rabbit phosphor-eIF-2 α (Ser51)	1 in 1000	9721	Cell Signaling Technology
	Goat Myocilin (N-15)	1 in 1000	sc-21243	Santa Cruz Biotechnology
	Rabbit ATF-4	1 in 1000	11815	Cell Signaling Technology
Secondary antibody	Goat anti rabbit IgG-HRP	1 in 5000	sc-2004	Santa Cruz Biotechnology
	Donkey anti-goat IgG-HRP	1 in 5000	sc-2020	Santa Cruz Biotechnology

4. Sample preparation: NuPAGE LDS Sample Buffer (4 \times) and NuPAGE Sample Reducing Agent (10 \times).
5. Transfer was performed using semidry blotting (e.g., iBlot 2 from Invitrogen using PVDF regular/mini stacks).
6. PBST = 100 mL of 10 \times phosphate buffered saline (PBS) + 1 mL of Tween 20 + 900 mL of distilled water.
7. Blocking Buffer: 10% Nonfat dry milk in 1 \times PBST—30 min.
8. Antibody Buffer: 10% Nonfat dry milk in 1 \times PBST—overnight.
9. Blot development: Super signal West Femto Maximum Sensitivity Substrate from Thermo Scientific Inc.

2.2 PCR

1. Total RNA isolation kit.
2. cDNA synthesis kit.
3. Taq DNA Polymerase.
4. QPCR reagents: SYBR Green reaction mix.

2.3 Immunostaining

1. Blocking buffer: 10% Normal goat serum in PBS.
2. Washing buffer: 1 \times PBS.
3. Citrate Buffer (antigen retrieval buffer): 10 mM sodium citrate buffer pH 6: 2.91 g of trisodium citrate (anhydrous) dissolve in approximately 900 mL of distilled water. Adjust the pH to 6 with 1 N HCl. Bring up the volume to 1 L with water. Store at 4 $^{\circ}$ C.

3 Methods

3.1 ER Stress Inducers in Cultured TM Cells and Mice

We have utilized several chemical and physiological inducers of ER stress in the TM. Although less preferred due to considerable cell death, chemical induction of ER stress can cause a robust protein accumulation and ER stress in the TM. Most preferred approach is to express mutant myocilin or dexamethasone treatment that can induce abnormal protein accumulation and chronic ER stress without causing any significant TM cell death. A detailed protocol to create these models is described below.

3.1.1 Chemical Induction of ER Stress in TM Cells and Mice

Several commercial chemicals have been used to induce ER stress and activate UPR in cell culture and tissues including tunicamycin, thapsigargin, Brefeldin A, dithiothreitol, and MG132 [1]. We have used tunicamycin and thapsigargin to induce ER stress in human TM cells and mice (*see Note 1*). As shown in Fig. 2, human primary TM cells were treated with various concentrations of tunicamycin (Tu) or thapsigargin (Tg) along with vehicle control for 24 h. Western blot analysis of CHOP was performed to examine induction of ER stress. As evident, both tunicamycin and thapsigargin-induced CHOP in primary TM cells. Since higher concentration of these chemicals can lead to TM cell death, it is advisable to use minimum concentration. Although 1 μM is most commonly used concentration for these chemicals, we choose to use 0.5 μM for tunicamycin and 0.1 μM for thapsigargin as these concentrations had minimum cell toxicity 24 h posttreatment.

In our laboratory, we have also examined whether chemical induction of ER stress alone is sufficient to elevate IOP. Anterior chamber injections of tunicamycin (0.03, 0.3, and 3 $\mu\text{g}/\text{eye}$) or periocular injections of tunicamycin (2 μL , 0.2 $\mu\text{g}/\text{eye}$) resulted in IOP elevation in WT C57 mice. We have observed that anterior chamber injections of these chemicals can cause inflammation to eye structures. Interestingly, minimum toxicity was observed with periocular injections. Therefore, periocular injection of tunicamycin is a preferred approach to study chemical induction of ER stress

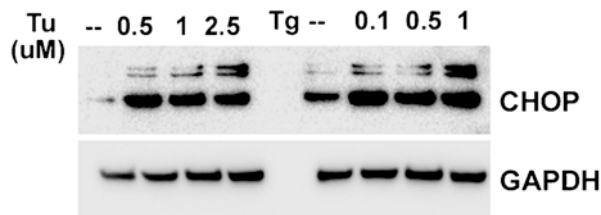


Fig. 2 Induction of CHOP by tunicamycin and thapsigargin. Human primary TM cells were treated with various concentrations of tunicamycin or thapsigargin for 24 h and CHOP levels were examined Western blot analysis

and its role in IOP elevation. ER stress markers including Grp78, Grp94, Chop, and phosphorylated eIF-2 α were found increased 24 h post injection prior to IOP elevation.

3.1.2 Expression of Mutant Myocilin in TM

We generated a transgenic mouse model (*Tg-MYOC^{Y437H}*), which expresses human Y437HMYOC under the control of the CMV promoter within relevant eye tissues including TM [19]. Using *Tg-MYOC^{Y437H}* mice, we determined that ER stress plays a key role in the elevation of IOP [19]. Starting at 3-months of age, *Tg-MYOC^{Y437H}* mice display glaucoma phenotypes including IOP elevation similar to human POAG patients with myocilin mutation. We have shown that ER stress occurs prior to the IOP elevation in *Tg-MYOC^{Y437H}* mice. Specifically, inhibition of secretion into the aqueous humor, increased accumulation of mutant myocilin, and increased ER stress markers in the TM were observed at 2-month old *Tg-MYOC^{Y437H}* mice prior to IOP elevation. We have also observed increased CHOP and cleaved caspase 12 as well as loss of TM cells in older *Tg-MYOC^{Y437H}* mice.

3.1.3 Cell Culture

To examine mutant myocilin-induced ER stress, we have generated IMCD3 or cells stably expressing DsRed tagged WT or mutant myocilin. IMCD3 cells were transfected with plasmid (pDSRed2-N1) containing DsRed tagged WT or Y437H mutant myocilin and G418 antibiotic resistance. Cells stably expressing WT or mutant myocilin were selected using 0.6 $\mu\text{g}/\text{mL}$ G418 antibiotic in the media. As shown in Fig. 3, IMCD3 cells expressing WT myocilin show punctate intracellular myocilin localization, which is transiently associated with ER marker KDEL. Mutant myocilin accumulates intracellularly in the ER as evident from colocalization with KDEL antibody. Similarly, transformed TM-5 or TM-3 cells stably expressing WT or mutant myocilin were generated to further analyze ER stress in TM cells. In addition, ER stress induction by mutant myocilin can be further analyzed in primary human TM cells. Since primary TM cells are hard to transfect with plasmid, we have utilized adenovirus 5 to express WT or mutant myocilin. Human primary TM cells are transduced with adenovirus 5 expressing WT or mutant myocilin for 48 h and ER stress markers are analyzed using immunostaining for myocilin and KDEL (recognizes GRP78 and GRP94). Since several ER stress antibodies do not work well with immunostaining, Western blot analysis of cellular proteins can be used to determine levels of other ER stress markers as described later in this chapter (*see Note 2*).

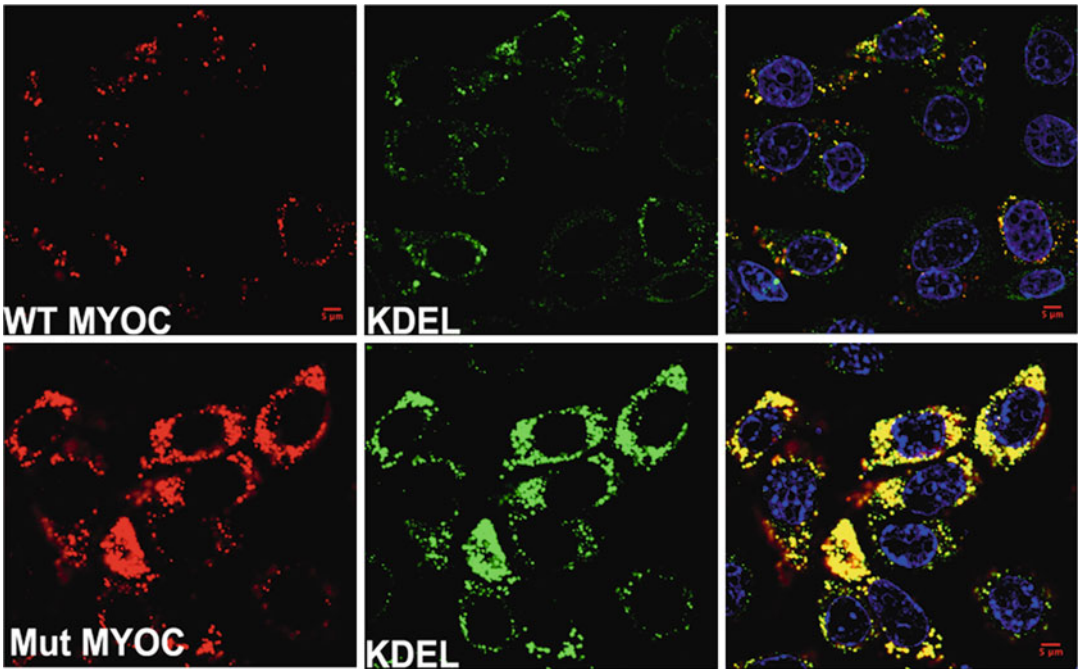


Fig. 3 Stable IMCD3 cells expressing DsRed tagged WT or mutant myocilin. IMCD3 cells expressing WT or mutant myocilin were stained with KDEL (*green*) and its colocalization was imaged via confocal microscopy. As shown in top panel, cells expressing WT myocilin transiently associate with ER while cells expressing mutant myocilin accumulate in ER as evident from its colocalization with KDEL antibody

3.2 Dexamethasone (Dex)-Induced ER Stress in TM Cells and Mice

3.2.1 Mouse Model of Dex-Induced Ocular Hypertension

Ocular hypertension is a serious side effect of glucocorticoid (GC) therapy that can lead to secondary iatrogenic open-angle glaucoma [30–32]. GC-induced ocular hypertension has been utilized to study glaucomatous TM damage in vitro and in vivo because it mimics many features of the TM in POAG including increased aqueous humor outflow resistance and similar morphological and biochemical changes in the TM. Recently, we demonstrated that topical ocular Dex (0.1%) treatment induced ocular hypertension and resulted in open-angle glaucoma in otherwise healthy C57BL/6 mice, similar to steroid glaucoma patients [20]. Topical 0.1% Dex phosphate or sterile PBS (phosphate-buffered saline) eye drops were applied to 3-month-old C57BL/6J mice three times daily for up to 20 weeks. A small eye drop (10 μ L) was applied to both eyes. Since mice often lick eye drops, mice were lightly held for 30–40 s after drop administration, then released in their cages to ensure the effective penetration of the eye drops into the anterior chamber. ER stress induction in the TM was examined using Western blot and immunostaining analysis of anterior segment tissue. Dex treatment also induced ER stress and activated UPR in the TM in vitro and in vivo.

3.2.2 *Dex-Induced ER Stress in Primary Human TM Cells*

TM cells were incubated with fresh medium with or without 100 nM Dex for 10 days. Media was changed every alternate day and fresh medium containing vehicle or Dex was added to cells. Alternatively, Dex induction of ER stress can be assessed in TM cells, treated with 500 nM Dex for 48 h. Total RNA was subjected to RT-PCR of XBP1. Total cell lysates were collected and subjected to Western blot analysis, as described later in this chapter.

3.3 **Experimental Approaches for Analysis of ER Stress**

3.3.1 *Analysis of XBP-1 Splicing*

Accumulation of unfolded proteins in the ER activates IRE1 α , which catalyzes splicing of XBP-1 by removing a 26 base pair intron from XBP-1 mRNA [8]. Spliced XBP-1 mRNA is more stable and acts as a transcriptional activator of UPR genes. Spliced XBP-1 is considered as a classical marker for ER stress induction and activation of UPR. In order to analyze the ER stress-associated unconventional splicing of XBP-1, total RNA was isolated from TM cells and reverse transcribed using commercially available kits as described in Materials. Total cDNA was subjected to PCR using XBP-1-specific primers (5' AACTCCAGCTAGAAAATCAGC 3' and 5' CCATGGGAA GATGTTCTGGG 3'). The PCR reaction contained 2 μ L cDNA, 4.1 μ L of water, 2 μ L of Taq buffer, 0.9 μ L MgCl₂, 0.25 μ L of each primers at 20 μ M concentration, 0.2 μ L of dNTPs mix (10 mM each) and 0.3 μ L Taq polymerase. The following PCR conditions were used. Initial denaturation step at 94 °C for 3 min, amplification step for 25 cycles at 94 °C for 30 s (denaturation), 55 °C for 30 s (annealing), 72 °C 30 s (extension), and 2 min final extension at 72 °C were used for analyzing XBP-1 splicing. Using 2% agarose gel, we had analyzed both spliced (257 base pairs) and unspliced (283 base pairs) PCR products of XBP-1. We further confirmed the unconventional splicing of XBP-1 by excising and sequencing both spliced and unspliced bands of XBP-1. As shown in Fig. 4, primary human TM cells were transduced with adenovirus 5 expressing either WT or mutant myocilin (100 MOI) for 72 h. Total DNA was subjected to XBP-1 PCR as described above and ran on 2% agarose gel. Mutant myocilin induces XBP-1 slicing as evident from presence of band at 257 base pairs compared to unspliced product at 283 base pairs (*see Note 3*).

3.3.2 *Analysis of UPR Genes*

Induction of ER stress activates gene expression of several UPR genes, which can be analyzed to examine ER stress in primary TM cells or mouse tissues. In our laboratory, we have utilized real-time PCR analysis of UPR target genes including GRP78, GRP94, and CHOP. These particular genes were selected because we have observed that protein levels of these genes increased dramatically when ER stress is induced by expression of mutant myocilin or Dex treatment. It is likely that other UPR target genes are also altered. The mouse eyes were enucleated from age-matched WT and *Tg-MYOC^{T437H}* littermates ($n = 5$). The TM rings were carefully

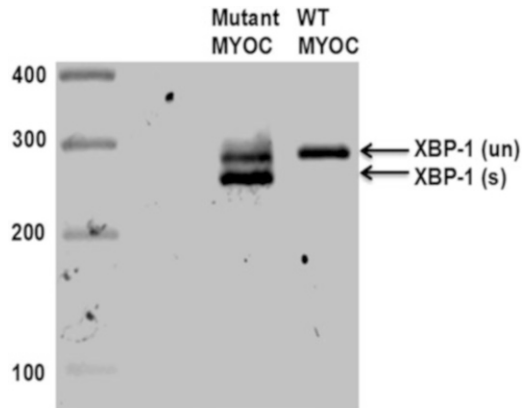


Fig. 4 Splicing of XBP-1. RT-PCR analysis of XBP-1 in primary TM cells transduced with adenovirus expressing WT or mutant myocilin. Spliced product was observed at 257 bp, while unspliced products were observed at 283 bp. Spliced XBP-1 was only observed in TM cells expressing mutant myocilin

dissected in such a way that the TM rings contained mainly TM tissue (*see Note 4*). Tissues were homogenized and total RNA was extracted using total RNA isolation Kit as described in Materials. First strand cDNA synthesis was carried out using Bio-Rad iScript cDNA synthesis Kit (Bio-Rad, Hercules, CA, USA). Each PCR reaction contained: 10 μL 2 \times SYBR Green Supermix, 0.25 μL forward primer (100 μM), 0.25 μL reverse primer (100 μM), 8.5 μL dH₂O, and 1.0 μL cDNA template (25 ng/ μL). The primers sequences used of QPCR of selected ER stress markers are listed in Table 1.

3.3.3 Analysis of ER Stress Markers by Western Blotting

The expression of UPR markers including GRP78, GRP94, ATF-6 α , caspase 12, ATF-4, ERO-1, and CHOP as well as phosphorylation of eIF2 α , IRE, and PERK was analyzed in TM cells and tissues by using western blotting. For mouse TM tissue, TM ring tissue was harvested from each eye and homogenized in 1 \times lysis buffer (200 μL) supplemented with complete protease inhibitor cocktail. Total lysate was centrifuged at 16,000 $\times g$ for 15 min and the supernatant was subjected to protein concentration measurement using DCTM Protein Assay from Bio-Rad (*see Note 4*). For the analysis of myocilin secretion in the aqueous humor, eyes were first wiped with Kim wipe and incision was made on cornea using a pointed forcep. A glass capillary was placed on eye at the incision site so that aqueous humor is collected using capillary action. The capillary was next placed in 1.5 mL tube containing 20 μL of 1 \times LDS-PAGE buffer and reducing agent. Approximately 2 μL of aqueous humor was collected from each eye and ran individually on SDS-PAGE gels. It should be noted that aqueous

humor from one eye is enough to detect target protein by Western blot analysis. We have also performed coomassie stain to detect total protein loading.

Approximately 30 µg of total protein lysates were subjected to SDS-PAGE gel electrophoresis under denaturing conditions and then the resolved proteins were transferred electrically to polyvinylidene difluoride (PVDF) membranes using commercial kits as detailed in Materials. Each blot was blocked with 10 mL of blocking buffer (10% nonfat dry milk) for 1 h at room temperature and then incubated overnight with specific primary antibodies at 4 °C. Later, the blots were washed with 1× PBST for three times and further incubated at room temperature for 2 h with corresponding secondary antibody, conjugated with horseradish peroxidase. Using electrochemiluminescence detection reagents, blots were visualized by Odyssey Fc Imager and quantified by Image J software. To ensure the equal protein loading, the same blot was probed with GAPDH antibody.

3.3.4 Immunostaining of ER Stress Markers in Mouse Tissues

Mouse eyes were enucleated and fixed with 4% formaldehyde and thoroughly washed with PBS. Eyes were then incubated in gradient concentration of sucrose solution (10% to 30%) overnight at 4 °C in a rotating shaker and embedded in OCT. Ten micron thick sections were cut using the Leica CM3050S cryostat. Using 5% normal serum, the sections were blocked and then incubated overnight with specific primary antibody (1:100 dilutions) at 4 °C in a humidified chamber. The sections were washed with 1× PBS for three times and further incubated with corresponding Alexa Fluor secondary antibodies (1:500 dilutions) at room temperature for 2 h. To stain the nuclei, we had subsequently incubated the sections with 4', 6'-diamino-2-phenylindole (DAPI) for 30 min. Followed by the incubation, the slides were washed with 1× PBS for three times and then mounted. Images were captured using a Leica TCS SP8 confocal imaging system.

3.3.5 Immunohistochemistry of ER Stress Markers in Human Tissue

Age-matched normal and open-angle glaucoma donor eyes were obtained from regional eye banks within 6 h of death and fixed in 10% formalin. Fixed tissues were dehydrated, embedded in paraffin, and stored until the usage. The paraffin-embedded tissues were cut in ten micron sagittal sections that were placed on microscope slides. Tissue sections were deparaffinized in xylene and rehydrated twice each with 100%, 95%, 70%, 50% ethanol for 5 min. For antigen retrieval, the tissue sections were incubated in citrate buffer (pH 6.0) at 100 °C for 13 min and cooled down slowly to room temperature. In order to avoid the nonspecific staining of tissues, we had incubated the tissue sections in blocking buffer for 30 min in a dark humidified chamber. Tissue sections were washed briefly and incubated overnight at 4 °C with either rabbit CHOP antibody

(1: 100 in blocking buffer, catalogue no. SC-575; Santa Cruz Biotechnology, TX, USA) or mouse KDEL antibody (1: 100 in blocking buffer), or nonimmune serum (negative controls) diluted 1:100 in 1.5% normal goat serum in PBS. After the three washes in $1 \times$ PBS, the tissue sections were incubated for 2 h at room temperature with appropriate secondary antibodies (Alexa donkey anti-mouse 568 and Alexa donkey anti-rabbit 488, 1:500 in PBS). Tissue sections were washed with $1 \times$ PBS and mounted with mounting media containing DAPI nuclear stain. Z-stacks were acquired in a confocal microscope and processed in ImageJ (<http://imagej.nih.gov/ij/>; provided in the public domain by the National Institutes of Health, Bethesda, MD, USA). Tissue sections incubated without primary antibody served as negative control and the relative signal intensities per square TM areas were subtracted with averaged background intensity.

3.3.6 Pharmacological or Genetic Manipulation of ER Stress in TM

To further analyze the role of ER stress in the pathophysiology of glaucomatous TM, we have utilized both pharmacological and genetic manipulations of UPR pathway. Chemical chaperone, sodium 4-phenylbutyrate (PBA), was used to reduce myocilin misfolding and reduce ER stress in the TM. Mice were given with either 20 mM PBA in drinking water or topical ocular 1% PBA eye drops three times daily (*see Note 5*). For cell culture treatments, TM cells were treated with 5 mM PBA for 48 h. Since PBA is highly water soluble, 5 mM PBA can be directly diluted in cell culture media. In addition, we routinely knock down GRP78, ATF-4, and CHOP using CRISPR-Cas9 genome editing methods in TM cells expressing mutant myocilin to further analyze the role ER stress on myocilin misfolding. In our laboratory, we have utilized *Atf6* and *Chop* knock-out mice which are available at the Jackson laboratories. These mice were crossed with *Tg-MYOC^{Y437H}* mice and IOPs were monitored.

4 Notes

1. For treatment of primary TM cells with tunicamycin or thapsigargin, optimum concentration of these chemicals without considerable cell death should be determined. In our laboratory, we utilized various doses of tunicamycin ranging from 0.5 μ M to 5 μ M that should be used. Since tunicamycin is nonspecific to the TM and may cause severe cell death of other ocular cells, IOP elevation and ER stress induction by tunicamycin is a less preferred approach compared to known physiological causes of glaucoma including expression of mutant myocilin or Dex treatment of mice.

2. It should be noted that mutant myocilin induced loss of TM cells in primary TM cells and in *Tg-MYOC^{Y437H}* mice but we failed to detect cell death via TUNEL stain. It is possible that TM cells die via non-apoptotic pathways. Also note that phosphorylation of eIF2- α can be detected in primary TM cells and mouse TM lysates. However, we failed to detect phosphorylation of PERK or IRE-1 in these samples. It is possible to detect phosphorylation of these proteins using a large number of cells such as growing TM cells in 10 cm dish.
3. For XBP-1 PCR, only 25 cycles were used because we have observed presence of another band at 300 bases when 35 cycles were used. It is assumed that spliced product anneal with unspliced product, which migrated at slightly higher size. We were able to get strong XBP-1 spliced product using three times higher polymerase and 25 cycles.
4. It should be noted that isolated mouse TM ring contains other tissues including ciliary body and sclera. Since mouse TM tissue is very small, it is very difficult to isolate pure TM tissue. We have observed that TM ring from one eye is enough for RNA or protein analysis. Normally, we obtain approximately 1–2 μ g of total RNA or around 150 μ g of total protein from one TM ring.
5. For topical ocular PBA treatment of mice, both eyes were applied with PBA eye drops because of concern about its potential systemic effect and high tissue penetration in the fellow eye. We have observed that there is no effect in fellow eye when PBA eye drops were given in the contralateral eye upto 1-week of treatment. However, we observed PBA presence in the fellow untreated eye after 1-week of treatment. Therefore, fellow eye should not be used as a control after 1 week of treatment.

Acknowledgments

This work was supported by funding from the following grants and organizations: National Eye Institute, EY022077 (R00) and EY026177 (R01) to G. S. Zode and funding from the North Texas Eye Research Institute.

References

1. Yoshida H (2007) ER stress and diseases. *FEBS J* 274(3):630–658. <https://doi.org/10.1111/j.1742-4658.2007.05639.x>
2. Schroder M, Kaufman RJ (2005) The mammalian unfolded protein response. *Annu Rev Biochem* 74:739–789. <https://doi.org/10.1146/annurev.biochem.73.011303.074134>
3. Ron D, Walter P (2007) Signal integration in the endoplasmic reticulum unfolded protein response. *Nat Rev Mol Cell Biol* 8

- (7):519–529. <https://doi.org/10.1038/nrm2199>
4. Calfon M, Zeng H, Urano F, Till JH, Hubbard SR, Harding HP, Clark SG, Ron D (2002) IRE1 couples endoplasmic reticulum load to secretory capacity by processing the XBP-1 mRNA. *Nature* 415(6867):92–96. <https://doi.org/10.1038/415092a>
 5. Schroder M, Kaufman RJ (2006) Divergent roles of IRE1alpha and PERK in the unfolded protein response. *Curr Mol Med* 6(1):5–36
 6. Yoshida H, Matsui T, Yamamoto A, Okada T, Mori K (2001) XBP1 mRNA is induced by ATF6 and spliced by IRE1 in response to ER stress to produce a highly active transcription factor. *Cell* 107(7):881–891
 7. Yoshida H (2004) Molecular biology of the ER stress response. *Seikagaku* 76(7):617–630
 8. Yoshida H (2007) Unconventional splicing of XBP-1 mRNA in the unfolded protein response. *Antioxid Redox Signal* 9(12):2323–2333. <https://doi.org/10.1089/ars.2007.1800>
 9. Acosta-Alvear D, Zhou Y, Blais A, Tsikitis M, Lents NH, Arias C, Lennon CJ, Kluger Y, Dynlacht BD (2007) XBP1 controls diverse cell type- and condition-specific transcriptional regulatory networks. *Mol Cell* 27(1):53–66. <https://doi.org/10.1016/j.molcel.2007.06.011>
 10. Wu J, Rutkowski DT, Dubois M, Swathirajan J, Saunders T, Wang J, Song B, Yau GD, Kaufman RJ (2007) ATF6alpha optimizes long-term endoplasmic reticulum function to protect cells from chronic stress. *Dev Cell* 13(3):351–364. <https://doi.org/10.1016/j.devcel.2007.07.005>
 11. Shen J, Chen X, Hendershot L, Prywes R (2002) ER stress regulation of ATF6 localization by dissociation of BiP/GRP78 binding and unmasking of Golgi localization signals. *Dev Cell* 3(1):99–111
 12. Wang Y, Shen J, Arenzana N, Tirasophon W, Kaufman RJ, Prywes R (2000) Activation of ATF6 and an ATF6 DNA binding site by the endoplasmic reticulum stress response. *J Biol Chem* 275(35):27013–27020. <https://doi.org/10.1074/jbc.M003322200>
 13. Haze K, Yoshida H, Yanagi H, Yura T, Mori K (1999) Mammalian transcription factor ATF6 is synthesized as a transmembrane protein and activated by proteolysis in response to endoplasmic reticulum stress. *Mol Biol Cell* 10(11):3787–3799
 14. Adachi Y, Yamamoto K, Okada T, Yoshida H, Harada A, Mori K (2008) ATF6 is a transcription factor specializing in the regulation of quality control proteins in the endoplasmic reticulum. *Cell Struct Funct* 33(1):75–89
 15. Rutkowski DT, Arnold SM, Miller CN, Wu J, Li J, Gunnison KM, Mori K, Sadighi Akha AA, Raden D, Kaufman RJ (2006) Adaptation to ER stress is mediated by differential stabilities of pro-survival and pro-apoptotic mRNAs and proteins. *PLoS Biol* 4(11):e374. <https://doi.org/10.1371/journal.pbio.0040374>
 16. Rutkowski DT, Wu J, Back SH, Callaghan MU, Ferris SP, Iqbal J, Clark R, Miao H, Hassler JR, Fornek J, Katze MG, Hussain MM, Song B, Swathirajan J, Wang J, Yau GD, Kaufman RJ (2008) UPR pathways combine to prevent hepatic steatosis caused by ER stress-mediated suppression of transcriptional master regulators. *Dev Cell* 15(6):829–840. <https://doi.org/10.1016/j.devcel.2008.10.015>
 17. Oyadomari S, Mori M (2004) Roles of CHOP/GADD153 in endoplasmic reticulum stress. *Cell Death Differ* 11(4):381–389. <https://doi.org/10.1038/sj.cdd.4401373>
 18. Zode GS, Bugge KE, Mohan K, Grozdanic SD, Peters JC, Koehn DR, Anderson MG, Kardon RH, Stone EM, Sheffield VC (2012) Topical ocular sodium 4-phenylbutyrate rescues glaucoma in a myocilin mouse model of primary open-angle glaucoma. *Invest Ophthalmol Vis Sci* 53(3):1557–1565. <https://doi.org/10.1167/iovs.11-8837>
 19. Zode GS, Kuehn MH, Nishimura DY, Searby CC, Mohan K, Grozdanic SD, Bugge K, Anderson MG, Clark AF, Stone EM, Sheffield VC (2011) Reduction of ER stress via a chemical chaperone prevents disease phenotypes in a mouse model of primary open angle glaucoma. *J Clin Invest* 121(9):3542–3553. <https://doi.org/10.1172/JCI58183>
 20. Zode GS, Sharma AB, Lin X, Searby CC, Bugge K, Kim GH, Clark AF, Sheffield VC (2014) Ocular-specific ER stress reduction rescues glaucoma in murine glucocorticoid-induced glaucoma. *J Clin Invest* 124(5):1956–1965. <https://doi.org/10.1172/JCI69774>
 21. Peters JC, Bhattacharya S, Clark AF, Zode GS (2015) Increased endoplasmic reticulum stress in human glaucomatous trabecular meshwork cells and tissues. *Invest Ophthalmol Vis Sci* 56(6):3860–3868. <https://doi.org/10.1167/iovs.14-16220>
 22. Sohn S, Joe MK, Kim TE, Im JE, Choi YR, Park H, Kee C (2009) Dual localization of wild-type myocilin in the endoplasmic reticulum and extracellular compartment likely occurs due to its incomplete secretion. *Mol Vis* 15:545–556

23. Tamm ER (2002) Myocilin and glaucoma: facts and ideas. *Prog Retin Eye Res* 21 (4):395–428
24. Liu Y, Vollrath D (2004) Reversal of mutant myocilin non-secretion and cell killing: implications for glaucoma. *Hum Mol Genet* 13 (11):1193–1204. <https://doi.org/10.1093/hmg/ddh128>
25. Jacobson N, Andrews M, Shepard AR, Nishimura D, Searby C, Fingert JH, Hageman G, Mullins R, Davidson BL, Kwon YH, Alward WL, Stone EM, Clark AF, Sheffield VC (2001) Non-secretion of mutant proteins of the glaucoma gene myocilin in cultured trabecular meshwork cells and in aqueous humor. *Hum Mol Genet* 10(2):117–125
26. Gobeil S, Rodrigue MA, Moisan S, Nguyen TD, Polansky JR, Morissette J, Raymond V (2004) Intracellular sequestration of hetero-oligomers formed by wild-type and glaucoma-causing myocilin mutants. *Invest Ophthalmol Vis Sci* 45(10):3560–3567. <https://doi.org/10.1167/iovs.04-0300>
27. Joe MK, Sohn S, Hur W, Moon Y, Choi YR, Kee C (2003) Accumulation of mutant myocilins in ER leads to ER stress and potential cytotoxicity in human trabecular meshwork cells. *Biochem Biophys Res Commun* 312 (3):592–600. <https://doi.org/10.1016/j.bbrc.2003.10.162>
28. Anholt RR, Carbone MA (2013) A molecular mechanism for glaucoma: endoplasmic reticulum stress and the unfolded protein response. *Trends Mol Med* 19(10):586–593. <https://doi.org/10.1016/j.molmed.2013.06.005>
29. Yam GH, Gaplovska-Kysela K, Zuber C, Roth J (2007) Aggregated myocilin induces russell bodies and causes apoptosis: implications for the pathogenesis of myocilin-caused primary open-angle glaucoma. *Am J Pathol* 170 (1):100–109. <https://doi.org/10.2353/ajpath.2007.060806>
30. Jones R 3rd, Rhee DJ (2006) Corticosteroid-induced ocular hypertension and glaucoma: a brief review and update of the literature. *Curr Opin Ophthalmol* 17(2):163–167. <https://doi.org/10.1097/01.icu.0000193079.55240.18>
31. Clark AF, Wordinger RJ (2009) The role of steroids in outflow resistance. *Exp Eye Res* 88 (4):752–759. <https://doi.org/10.1016/j.exer.2008.10.004>
32. Armaly MF, Becker B (1965) Intraocular pressure response to topical corticosteroids. *Fed Proc* 24(6):1274–1278

Quantification of Scleral Biomechanics and Collagen Fiber Alignment

Ian C. Campbell, Joseph M. Sherwood, Darryl R. Overby, Bailey G. Hannon, A. Thomas Read, Julia Raykin, and C. Ross Ethier

Abstract

The stiffness of the sclera is important in several ocular disorders, and there is hence a need to quantify the biomechanical properties of this tissue. Here, we present two methods for measuring the stiffness of scleral ocular tissues: ocular compliance testing and digital image correlation strain mapping. In tandem with these approaches, we provide two methods to spatially quantify the anisotropic alignment of collagen fibers making up the sclera, using second harmonic generation microscopy and small-angle light scattering. Together, these approaches allow specimen-specific measurement of tissue stiffness and collagen alignment, which are key factors in determining how the eye responds to mechanical loads.

Key words Biomechanics, Sclera, Ocular compliance, Digital image correlation, Second harmonic generation microscopy, Small-angle light scattering

1 Introduction

The posterior eye, principally containing the choroid, retina, vitreous humor, and optic nerve, is primarily supported by the surrounding sclera. The sclera is a stiff, collagenous tissue that provides structure and support to the eye and balances the outward push of intraocular pressure [1]. The relative stiffness of the sclera has been hypothesized to play an important role in a variety of conditions, such as glaucoma [2], myopia [3], and ocular trauma [4]. Therefore, there is an important need to measure quantitative biomechanical properties of this tissue when studying and developing treatments for such conditions.

“Stiffness” is an imprecise term with multiple possible definitions in a biomechanical context; it is generally used to describe the relative ability of a tissue to resist deformation from an applied load. Scleral stiffness can be quantified by measuring the compliance of the eye, i.e., the change in volume resulting from a change in intraocular pressure (IOP), or by directly measuring scleral

mechanical strain resulting from an applied IOP. In an engineering context, strain is a metric of how much a tissue has elongated or contracted relative to a reference state, and it is of particular note that the strain response of most biological tissues is not spatially uniform throughout the tissue. Further, tissue strain response usually depends on the direction in which the force is applied. For example, a strand of hair deforms considerably when pulled normal to its length, whereas it deforms much less when pulled tangent to its length. This property of direction-dependent mechanical response is called anisotropy, and is a characteristic of the sclera, primarily due to the distribution and alignment of collagen fibrils [1]. For example, a ring of highly aligned circumferential collagen fibers known as the “annulus” surrounds the optic nerve head, whereas closer to the equator of the eye, collagen fibers have a “basket-weave” structure and are not as uniformly aligned [5].

When interrogating the biomechanics of the sclera, it is therefore important to understand both the relative stiffness of the tissue and the degree of collagen anisotropy of various regions. We have thus divided this chapter into four sections:

1. Quantification of total ocular compliance.
2. Quantification of scleral strains during inflation testing using digital image correlation.
3. Quantification of scleral collagen orientation using second harmonic generation microscopy.
4. Quantification of scleral collagen orientation using small-angle light scattering.

The techniques described below are for the measurement of scleral properties in a laboratory, rather than a clinical, setting. Accordingly, we describe protocols for measurements on eyes from commonly used laboratory species.

1.1 Quantification of Total Ocular Compliance

1.1.1 General Remarks

Ocular compliance characterizes the pressure-volume relationship of the entire globe. It thus incorporates the mechanical behavior of the cornea and sclera, as well as potential changes in blood volume and viscoelastic effects (deformation dependent on how rapidly a load is applied). By capturing the behavior arising from many different components of the eye, ocular compliance is useful for characterizing the ocular response to transient changes in pressure and is a critical component in dynamic models of the whole eye. The ocular compliance, typically denoted as ϕ , is defined as the slope of the volume-pressure relationship, and has units of volume per unit pressure,

$$\phi(P) = \frac{dV}{dP} \quad (1)$$

where V is the volume of the eye and P is the intraocular pressure. An alternative parameter for characterizing the pressure-volume

relationship of the whole globe is Friedenwald's coefficient of ocular rigidity [6], K , defined based on

$$\frac{dP}{P} = k \frac{dV}{V} = K dV \quad (2)$$

where k is a dimensionless coefficient representing the rigidity of the eye, and it is assumed that relative changes in ocular volume are small, such that $K = k/V$ is approximately constant. K is defined in units of reciprocal volume and is related to ocular compliance according to $\phi = 1/KP$.

In order to measure ocular compliance, an eye must be interfaced with a measurement system, which will introduce its own additional compliances and resistances that will influence the overall quantification of ocular compliance. The interaction between the characteristics of the system and eye must both be considered in order to accurately measure ocular compliance. The accuracy and efficacy of such measurements are thereby subject to a number of potentially confounding factors that must be considered.

In this text, we first provide a description of a common experimental setup that can be used to measure ϕ . We then briefly describe the mathematical formulation that establishes the basic relationships between the ocular compliance and resistance with those of the measurement system and demonstrate the system dynamics for a mouse eye. Finally, we provide an experimental protocol for carrying out these measurements. With minor modifications, the described technique can be applied to other species or to in vivo measurements.

1.1.2 Measurement Approach

An enucleated eye is mounted on a platform in a temperature-regulated bath and fully immersed in isotonic saline. The eye is cannulated in the anterior chamber with a needle or pulled glass capillary, allowing fluid exchange between the system and the eye. The system comprises a syringe pump with a glass syringe (*see Note 1*), a pressure sensor, and associated tubing and valves (Fig. 1). A pressure-control reservoir is included for sensor calibration. In the basic procedure, an initial flow rate Q_0 into the eye is applied using the syringe pump until the pressure is approximately stable. Subsequently, a bolus of fluid of volume ΔV_p is delivered to the eye using the syringe pump, and the change in pressure ΔP_s , is measured over a short interval. Alternatively, it is possible to measure ocular compliance in response to a step change in pressure (e.g., using the iPerfusion system [7]). The latter approach will be the topic of a future publication.

The values ΔV_p and ΔP_s must then be related to the fluid volume change of the eye itself ΔV_ϕ (as some portion of ΔV_p will go toward changing the fluid volume of the system by ΔV_s) and the change in pressure in the eye ΔP_i , which can then be used to

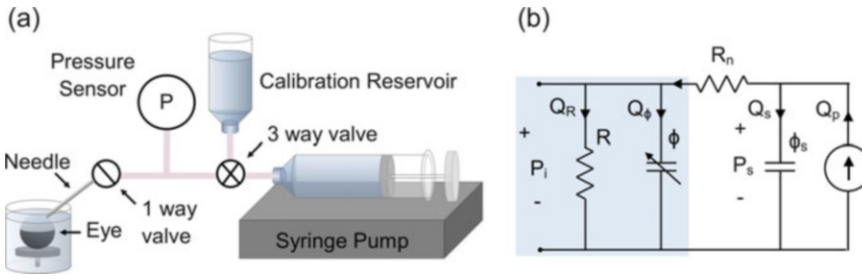


Fig. 1 (a) Schematic of the experimental setup. The eye is mounted on a small platform and fully immersed. The eye is then cannulated via the anterior chamber using a needle, and a fixed volume of fluid is delivered by a syringe pump while the change in pressure is measured. A pressure reservoir is used for pressure sensor calibration. (b) Lumped parameter model using electrical circuit analogies for the system, in which the shaded blue areas represent the eye. Parameter definitions are provided in the text

estimate ϕ based on $\Delta V_\phi/\Delta P_i$. Hence, it is important to account for the influence of the system itself, which can be demonstrated using a simple lumped parameter model, shown in Fig. 1b. ϕ_s is the system compliance, R_n is the needle resistance, R is the total resistance of the aqueous humor outflow pathways, P_s is the pressure sensor reading, and P_i is the intraocular pressure. Different flow rates are indicated by appropriate subscripts. Note that the ocular compliance ϕ depends on pressure.

1.1.3 System Response

In order to demonstrate the data analysis approach, a Simulink (Mathworks, Natick, USA) analysis of the lumped parameter model (Fig. 1b) was used to generate representative traces based on typical parameters for a mouse eye, as shown in Fig. 2.

Figure 2a shows the pressure response prior to the bolus injection and over the subsequent minute. Immediately before the injection, the system is at steady state, and the pressure in the eye is very slightly lower than the pressure measured by the pressure sensor, due to the pressure drop across the needle resistance at flow rate Q_0 . Immediately after the bolus is applied, both measured and intraocular pressures are elevated rapidly, but the measured pressure reaches a value 8.5 mmHg higher than the intraocular pressure at the time that the fluid bolus has been fully delivered (second solid gray vertical line). Figure 2b shows this dynamic in more detail. It can be seen that after around 5–6 s, the two pressures have equilibrated to approximately the same offset observed before the bolus injection. The cause of this response can be discerned by evaluating the flow rates in Fig. 2c. When the syringe pump is initially turned to the higher flow rate at $t = 0$ s, the delivered fluid first enters the system compliance (*green*). As time goes on, an increasing proportion of the perfused flow enters the eye (*red*). When the bolus is fully delivered ($t = 2.5$ s), the pressure difference across the needle drives flow from the system compliance into the eye, until the pressure gradient decays (negative Q_s between 2.5 and ≈ 4 s,

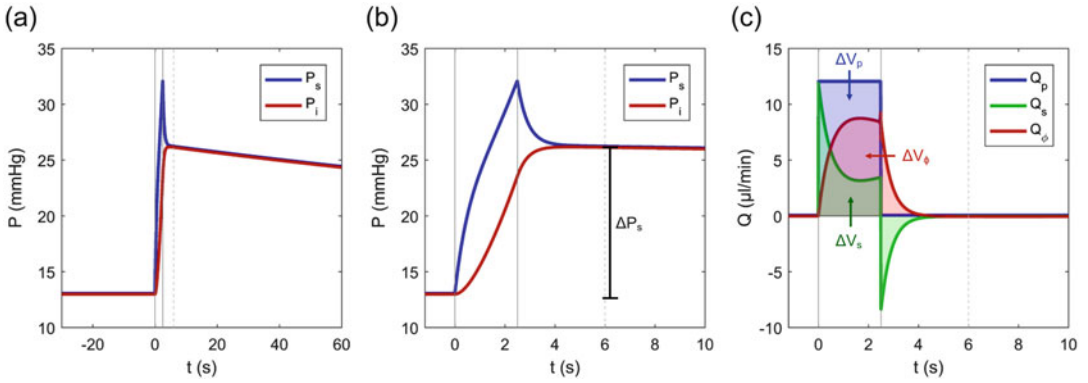


Fig. 2 Representative dynamic response of the system and eye to a bolus of injected volume ΔV_p . Pressure measured by the sensor (P_s) and the intraocular pressure (P_i) for the first minute (a) and over the first 10 s (b) after the bolus injection. Key flow rates in the model (c) flow into the measurement system (Q_s), flow into the eye (Q_ϕ), and total flow from the pump (Q_p). Shaded areas under the curves show the volume change in each part of the system. *Solid gray vertical lines* indicate the start and end of the syringe pump infusion, *dashed gray vertical lines* indicate time T

indicating flow out from the system compliance to the eye). The shaded areas under the curves represent ΔV_ϕ , ΔV_p , and ΔV_s . These dynamics are important to consider because it informs us that the measurement of ΔP_s should be taken at some time after the bolus has been delivered, at time T , indicated by the dashed vertical lines in Fig. 2.

At time T , both P_s and P_i are elevated relative to their respective values immediately prior to the injection. Some of the injected volume ΔV_p will therefore remain in the system compliance, which can be estimated by integrating Eq. 1 for the system

$$\Delta V_s = \phi_s \Delta P_s \quad (3)$$

The volume delivered to the eye is then

$$\Delta V_\phi = \Delta V_p - \Delta V_s \quad (4)$$

At T , the change in pressure in the system is effectively the same as that in the eye, $\Delta P_i \approx \Delta P_s$. Hence, we can estimate the ocular compliance by combining Eqs. 1, 3 and 4

$$\phi(P_\phi) = \frac{\Delta V_\phi}{\Delta P_i} \approx \frac{\Delta V_p}{\Delta P_s} - \frac{\Delta V_s}{\Delta P_s} = \frac{\Delta V_p}{\Delta P_s} - \phi_s \quad (5)$$

Note that the value of ϕ is defined at a particular pressure P_ϕ that represents the pressure that corresponds to the measured value of ocular compliance. Inclusion of P_ϕ is necessary because, as the ocular compliance is pressure-dependent, it changes over the measurement period. In order to calculate P_ϕ , we use the mean value theorem and an assumed model for the compliance-pressure

relationship, in this case the Friedenwald model (Eq. 2) [6]. The full derivation is beyond the scope of the present text, but P_ϕ can be calculated according to

$$P_\phi = \frac{\Delta P_s}{\ln\left(\frac{P_s(T)}{P_s(0)}\right)} \quad (6)$$

where $P_s(0)$ is evaluated just before the bolus infusion and $P_s(T)$ is evaluated at time T after the bolus infusion. Equations 5 and 6 can now be applied to measure ocular compliance. Note that Eq. 5 is based on the assumption that the volume of fluid that leaves the eye through outflow is very small compared to the volume of the fluid bolus, and it is hence necessary to make the bolus volume large, particularly at higher pressures (where the outflow rate increases).

1.1.4 Comparing Eyes

P_ϕ itself depends on the ocular compliance and will thus differ between eyes. However, in order to compare the ocular compliance between eyes, it is necessary that the compliances be compared at the same pressure. For this purpose, we introduce the reference pressure, P_r , and redefine Friedenwald's model in terms of ocular compliance:

$$\phi(P) = \phi_r \left(\frac{P_r}{P} \right) \quad (7)$$

such that at $P = P_r$, the compliance is equal to the reference compliance, $\phi(P_r) = \phi_r$. P_r is generally defined to be physiological IOP for the species. Although it is possible to calculate ϕ_r from a single measurement of ocular compliance, a more robust approach is to measure ocular compliance at several pressures, then fit Eq. 7 to the ϕ — P_ϕ data. The experimental protocol in Subheading 3.1.5 outlines this process.

1.2 Quantification of Scleral Strains During Inflation Testing Using Digital Image Correlation

The ocular compliance measurements described above provide a single integrated measure of corneoscleral stiffness. However, as the sclera is a heterogeneous tissue, one may want to determine spatially resolved stiffness, for example to compare the stiffness of the sclera in different quadrants of the posterior eye or locally around the optic nerve head. Such effects can be quantified by measuring the magnitude of mechanical strain in the sclera using a 3D imaging-based strain measurement system such as electronic speckle pattern interferometry (ESPI) [8] or digital image correlation (DIC) [9]. Such systems typically cost tens to hundreds of thousands of dollars but are nonetheless available at many institutions. Here, we will describe 3D-DIC measurement of scleral displacement. This approach measures the displacement of the surface of the eye by tracking the motion of a speckle pattern using a calibrated pair of stereo cameras. By measuring how the speckles move when the eye is inflated, we can quantify the mechanical strain of the ocular surface. Although this technique can only measure

deformation of the outer surface of the eye, it is useful for comparing the relative stiffness of various regions if one assumes the scleral thickness and biomechanical properties are relatively uniform in the direction normal to the scleral surface. Softer scleral regions should displace more and thus exhibit higher strains than equally thick regions that are stiff. We describe this technique for measurement of rat scleral properties.

1.3 Quantification of Scleral Collagen Orientation Using Second Harmonic Generation (SHG) Non-Linear Microscopy

The orientation of collagen and elastin fibers in the extracellular matrix has a major influence on the biomechanical behavior of tissues, and therefore this fiber distribution is of interest when characterizing the sclera. There are several methods for measuring such orientation; here, we focus on second harmonic generation (SHG) microscopy. SHG is a nonlinear imaging modality used to visualize collagen microstructure and alignment [10]. SHG signals are generated via short laser pulses, which result in emission of light at half the incident laser wavelength. Therefore, excitation of collagen with an 800 nm wavelength will generate incident light at 400 nm. SHG offers several advantages over other imaging modalities as it allows for label-free imaging at various tissue depths without the need for fixation or sectioning. In addition, collagen fiber re-orientation and uncrimping can be observed as a mechanical load is applied.

1.4 Quantification of Scleral Collagen Orientation Using Small-Angle Light Scattering

An alternate method to quantify fiber orientation in tissue is small-angle light scattering (SALS). SALS, similar to small-angle X-ray scattering, is based on the principle that incident radiation is anisotropically scattered by fibers. Visualization and analysis of the scattering pattern as light interacts with tissue therefore provides quantitative information about fiber distribution patterns. The theory and use of SALS for non-ocular tissues are presented elsewhere [11–16], as are experimental measurements on human [17] and rat [18] sclera.

2 Materials

2.1 Materials for Quantification of Total Ocular Compliance

1. Mouse eye, freshly harvested.
2. Phosphate-buffered saline without divalent cations for the eye bath.
3. Phosphate-buffered saline with divalent cations, supplemented with 5.5 mM glucose, sterile filtered.
4. Cyanoacrylate glue.
5. 33G needle.
6. Stereomicroscope.
7. Micromanipulator (e.g., Marzhauser MM33).

8. Perfusion system, setup as indicated in Fig. 1a, which includes a syringe pump (e.g., Harvard Apparatus PhD Ultra), pressure transducer (Honeywell 142PC01G), and associated tubing and valves.
9. Small glass syringe (25–50 μ l).
10. Computer and data acquisition system (e.g., LabVIEW) for the pressure sensor.

2.2 Materials for Quantification of Scleral Strains During Inflation Testing Using Digital Image Correlation

2.2.1 Mount for Rat Eye Inflation Test

2.2.2 Construction of Inflation Chamber

1. Acrylic sheet, 11/16" thick.
 2. 1/4" ball end mill bit.
 3. 1/16" drill bit.
 4. 1/8" flat end mill bit.
 5. 3/16" drill bit.
1. 7" \times 4" \times 5" or similar-sized rectangular plastic container with no top.
 2. 8" \times 8" sheet borosilicate glass, 1/8" thick.
 3. Bulkhead luer fitting, female to 1/4" barb.
 4. Silicone caulk.
 5. Drill.
 6. 10 ml syringe.
 7. Silicone tubing, 1/4" inner diameter.
 8. Ring heater with ID greater than eye (e.g., McMaster Carr 3682K25).
 9. PID controller for ring heater.

2.2.3 Preparation and Mounting of Rat Eye

1. Rat eye, freshly harvested.
2. Fine dissecting scissors and forceps.
3. PBS prepared with ultrapure water.
4. Q-tips and wooden applicator sticks.
5. Gel-style cyanoacrylate glue (e.g., Loctite[®] Super Glue Ultra-gel[®] Control).
6. Custom built mounting blocks (*see* Subheading 3.2.1 for manufacturing details).
7. Male luer to 10–32 tapered thread adapter.
8. Syringe fitted with large bore (e.g., 18G) blunt needle.
9. DIC software.

2.2.4 Speckling of Rat Eye

1. Airbrush.
2. Pure Powdered Graphite.
3. Fine Mesh (#60) Sieve.
4. 1 mm Biopsy Punch.

2.3 Materials for Quantification of Scleral Collagen Orientation Using SHG Nonlinear Microscopy

1. Freshly harvested eye, or histological section (fresh or fixed).
2. Coverslip (No. 1.5).
3. Multi-well cell culture plate with well diameter similar to that of eye.
4. Sylgard[®] silicone elastomer kit.
5. Multi-photon confocal microscope (e.g., Zeiss LSM 710 META inverted confocal microscope with a Chameleon Ultra Ti:Sapphire femtosecond laser (Coherent) and 40×/1.3 NA oil immersion objective).

2.4 Materials for Quantification of Scleral Collagen Orientation Using Small-Angle Light Scattering

1. A SALS system (Fig. 3). A description of the construction and testing of such a system is beyond the scope of this article, and readers are referred to other references [16, 18]. In brief, a laser beam, suitably conditioned to have a thin waist, is allowed to pass through the tissue sample of interest, and the resulting forward scattering pattern is visualized on a semi-transparent screen. A micropositioning system allows for relative motion between the beam and sample so that tissue regions, rather than a single point, can be interrogated. A camera captures the scattering patterns from the screen for later analysis.
2. Two 75 mm × 25 mm glass microscope slides.
3. 40% glycerol solution.
4. Double-sided adhesive tape, thickness c. 1 mm.
5. Quick drying silicone.
6. A scleral sample (*see* Notes 2 and 3) for specifics of an optimal specimen.

3 Methods

3.1 Methods for Quantification of Total Ocular Compliance

Methods to measure ocular compliance in mice are developed based on the protocol originally described by Lei et al. [19]. Several stages are necessary in the calculation of ocular compliance:

1. Calibrate the pressure sensor.
2. Measure the system compliance.
3. Prepare the eye.
4. Perfuse the eye.
5. Process data.

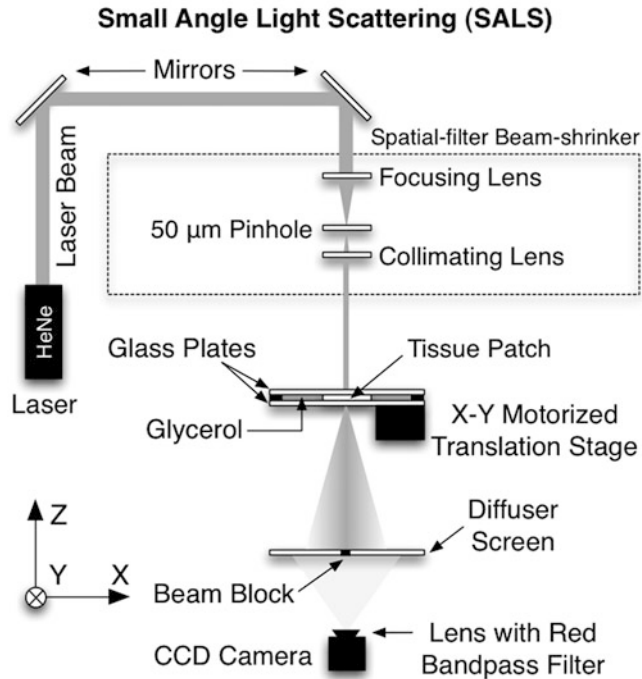


Fig. 3 Small-angle light scattering (SALS) apparatus schematic [18]. Light from a Helium-Neon (HeNe) laser is shined on a patch of tissue mounted between glass slides and then scattered as it passes through protein fibers (primarily collagen in the sclera). The laser is routed by aligned mirrors and collimated after passing through a beam shrinker and spatial filter. After passing through the tissue, it is projected onto a diffuser screen. The center of this screen is blacked out with a beam block to avoid saturating the camera with direct laser light. The scattered light pattern on the screen is then imaged by a CCD camera equipped with a red bandpass filter and saved for further processing

3.1.1 Calibrate the Pressure Sensor

1. Fill the eye bath to 1 cm above the eye platform.
2. Close the one-way valve upstream of the needle and open the pressure sensor to the calibration reservoir.
3. Set the height of the reservoir to the fluid level in the eye bath. This is the height corresponding to zero pressure. Note the recorded voltage (pressure transducer output), averaged over 5 s.
4. Increase the reservoir pressure in regular intervals of 100 mm and note the recorded voltage (averaged over 5 s) for each height (*see Note 4* for ideal setup).
5. Convert the heights in mmH₂O to mmHg and fit a straight line to the pressure vs. voltage data, to extract

$$P = mv + c \quad (8)$$

where m and c can be used to calculate the pressure from the voltage during the compliance measurement, and v is the voltage output of the pressure transducer.

- Return the reservoir to the level of the fluid in the eye bath (*see Note 5*).

3.1.2 Measure the System Compliance

- Close the one-way valve upstream of the needle.
- Close the three-way valve to block the reservoir only.
- At this point, the pressure will spike. Wait until the pressure reaches a stable value on the voltage readout.
- With the syringe pump, infuse $\Delta V_s = 25$ nl at a rate of 300 nl/min (requiring 2.5 s) (*see Note 6*).
- Extract the pressures from the pressure sensor 1 s prior to the infusion and a short time T after. The value of T should be based on the dynamics shown in Fig. 2, by evaluating the pressure trace when the initial spike has subsided. The difference between these pressures yields ΔP_s .
- Use Eq. 3 to calculate ϕ_s based on ΔV_s and ΔP_s .

3.1.3 Prepare the Eye

- Mount the needle on the micromanipulator and fill the perfusion tubing and needle with perfusate, making sure that there are no bubbles.
- Having enucleated the mouse eye, wash in PBS for use within 30 min of enucleation.
- Carefully dissect away excess tissue around the eye such as extraocular muscles.
- Remove fluid in the eye bath using a Pasteur pipette to a level below the eye platform.
- Place a very small amount of cyanoacrylate glue on the eye-mounting platform.
- Using forceps, place the eye, optic nerve down, onto the platform, and fill the eye bath with PBS to 1 cm above the platform. This will cause the glue to set almost instantaneously.
- Set the reservoir to a height corresponding to 100 mm above the level of the fluid in the eye bath.
- Open the one-way and three-way valves fully, ensuring that fluid is leaving the needle tip. This minimizes the risk of bubble formation at the needle tip.
- Cannulate the eye in the anterior chamber, making sure not to pierce the lens or iris.
- Heat the eye bath to 35 °C.

3.1.4 Perfuse the Eye

The following protocol allows for a four-level pressure measurement of ocular compliance in mouse eyes. This simplified procedure uses manual syringe pump control, obviating the need to interface the syringe pump with a computer. Figures 4a and b show the

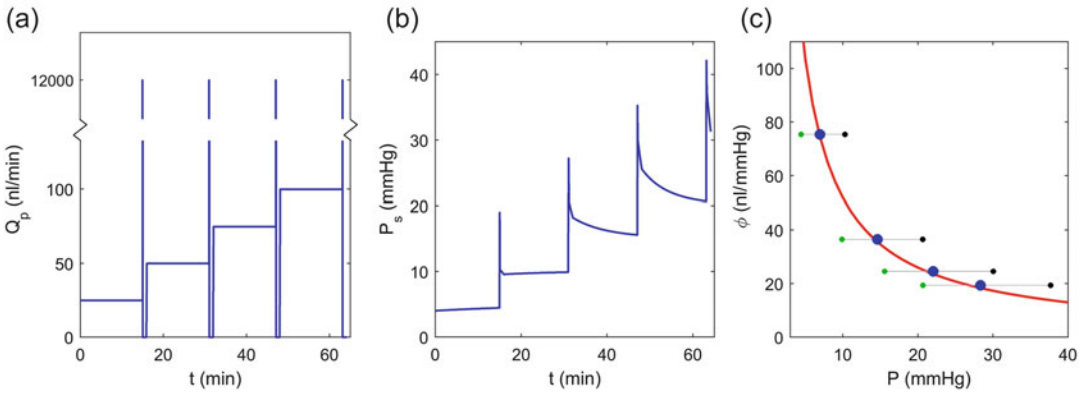


Fig. 4 Sample perfusion protocol: (a) perfused flow rate; (b) measured pressure; (c) fitting a model to the measured data. The *blue* data points in (c) indicate the value of $\phi(P_\phi)$ for each pressure step. *Green* markers indicate $P_s(0)$ and *black* markers indicate $P_s(T)$, in order to demonstrate the importance of calculating P_ϕ . The *red* curve shows the form of Eq. 7, which can be fit to the data to extract ϕ_r

pump flow rate and the expected pressure response determined using Simulink.

1. Set the pump infusion rate to 25 nl/min and perfuse continuously for 15 min.
2. When ready, set the infusion rate to 12 μ l/min and infuse a volume of 500 nl (requiring 2.5 s). The syringe pump will stop pumping after the bolus (*see* **Note 7**).
3. Record the pressure data for a further minute to allow enough of a pressure trace to identify the initial spike, as depicted in Fig. 2a, b.
4. Repeat for the remaining pressure steps, increasing the starting flow rate by 25 nl/min at each step.

3.1.5 Process the Data

1. For each step, extract the pressure from the pressure sensor 1 s prior to the infusion, yielding $P_s(0)$, and the pressure a short time T after the infusion $P_s(T)$, where the value of T should be based on the time when the initial pressure spike has subsided.
2. ΔV_p , $P_s(T)$, $P_s(0)$, and the predetermined value of ϕ_s can then be used with Eqs. 5 and 6 to calculate ϕ and P_ϕ for each step.
3. Plot ϕ against P_ϕ (*see* Fig. 4c, large blue circles).
4. Fit Eq. 7 to the data using nonlinear regression.
5. Extract ϕ_r and its confidence interval for further analysis.

3.2 Methods for Quantification of Scleral Strains During Inflation Testing Using Digital Image Correlation

3.2.1 Mounting Block Manufacturing

Following enucleation, the eyes should be stored in PBS, on wet ice, between procedures.

In order to attach the eye to the pressure reservoir, custom-machined acrylic mounting blocks are fabricated (Fig. 5). These mounting blocks can be made individually or in large batches using a CNC (Computer Numerical Control) device:

1. Drill a hemisphere into acrylic sheet with 1/4" ball end mill, 1/8" deep.
2. If fabricating multiple holders via CNC, repeat drilling of hemispheres evenly spaced approximately 0.625" apart in both the x and y directions.
3. Use a 1/16" drill bit to drill at least halfway through the thickness of the sheet, centered on each hemisphere.
4. Cut 0.625" × 0.625" slits around each hemisphere with a 1/8" flat end mill in CNC or other saw blade if preparing manually. The cuts should be 9/16" deep, leaving 1/8" of acrylic at the bottom so the mounting blocks are still attached to one another (*see Note 8*).
5. Flip the acrylic sheet over so that the hemisphere cut in **step 1** is now facing down.
6. Use a 3/16" drill bit and drill 1/2" deep directly over the center of each 1/16" hole using a drill press or hand drill.

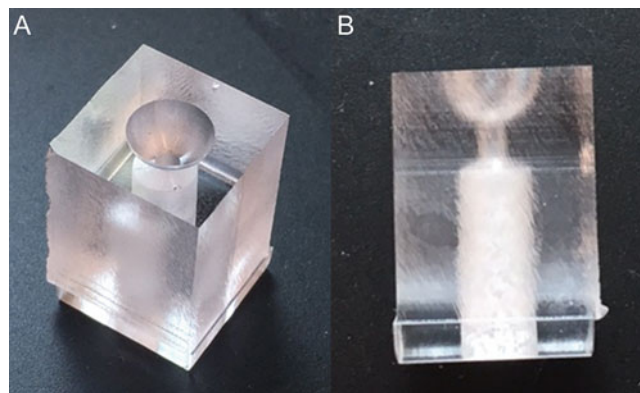


Fig. 5 Mounting block viewed from: (a) Top isometric view; (b) Side view. Hemisphere is at top, 1/16" channel connects hemisphere to 3/16" channel at bottom

7. Separate each square from the sheet using a band saw or laser cutter.
8. Clean holes in each block with a needle or piece of wire to make sure no burrs of acrylic remain in the drilled holes.

3.2.2 Inflation Chamber Construction

During inflation tests, the eye is submerged in a PBS-filled chamber, mounted via luer fitting, and connected to an adjustable-height hydrostatic pressure reservoir.

1. Drill a small hole in the bottom of the chamber and insert a bulkhead luer coupler with a female luer on the inside of the chamber. This will mate with the mounting blocks from Sub-heading 3.2.1 when eyes are mounted for inflation.
2. Seal bulkhead with silicone caulk on inside and outside. Allow to dry before proceeding.
3. Attach silicone tubing to barb fitting penetrating the bottom of the chamber. Connect to a second barb-to-luer connector and attach to the bottom of a syringe. The syringe can be elevated to act as a hydrostatic pressure reservoir to change the pressure within eyes mounted in the chamber. Fill with PBS and ensure there are no bubbles in the tubing.
4. Fill the immersion chamber with PBS.
5. If needed, elevate the chamber by adding feet made from rubber stoppers to avoid pinching the tubing coming out the bottom.
6. If desired, connect a peristaltic pump feeding PBS through a PID-controlled Peltier heater in order to maintain eyes at physiological temperatures. Attach two more luer fittings 1" from the bottom of the chamber on the opposite sides of the narrow walls of the chamber. Seal with silicone, allow to dry, and connect each end to peristaltic pump.
7. Place glass on chamber as a lid to minimize evaporation during extended testing.
8. Place ring heater on top of glass to prevent fogging from evaporation. Set PID controller to a temperature greater than water temperature.

3.2.3 Preparation and Application of Speckle Pattern

1. Under a dissecting scope, remove all excess fat, muscle, and connective tissue from the eye using fine scissors and forceps. It is critical that the sclera be clean and completely free of extraneous tissue, prior to applying the speckle pattern (Fig. 6, *see Note 9*).
2. Apply a small continuous bead of superglue around hemispherical rim of an acrylic eye mounting block. Label the block with a waterproof marker (*see Note 10*).



Fig. 6 Preparation of Brown Norway rat eye with sclera cleaned of extraorbital muscles, episclera, and other superficial tissues. Scale bar: 1 mm

3. Remove the eye from the PBS and gently blot dry with a Kimwipe. Suspending it from the optic nerve, lower the eye onto the mounting block hemisphere and press down lightly, to ensure good contact with the glue.
4. Using a wooden applicator stick with its end carved to a smooth, spatula shape, remove all excess glue from the mounting block/eye bonding region, then dip the unit into PBS to cure any remaining exposed glue. With a clean Q-tip, gently wipe the scleral surface and then flush PBS into the open $3/16''$ hole with the syringe.
5. Re-wet the sclera with PBS, move the eye into the ventilated speckling chamber (*see Note 11*), and rest it on a flat surface such as a culture dish. Load the 60 mesh sieve with a shallow layer of graphite powder, position it above the eye, and with short bursts from the air brush aimed at the sieve, generate a cloud of graphite which will settle upon the sclera to create the random speckle pattern. Rotate the eye and repeat, as necessary, to obtain a uniform pattern around the sclera.
6. Lightly tap the mounting block to dislodge any excess graphite and allow the sclera to dry slightly, so that the powder adheres to the sclera; this will take approximately 5–10 min and should be monitored closely under a dissecting microscope to prevent desiccation of the tissue, indicated by a darkening discoloration.
7. Gently rinse the sclera with PBS and assess the speckle pattern to confirm adherence of graphite (Fig. 7). **Steps 5 and 6** may be repeated as necessary (*see Note 12*).

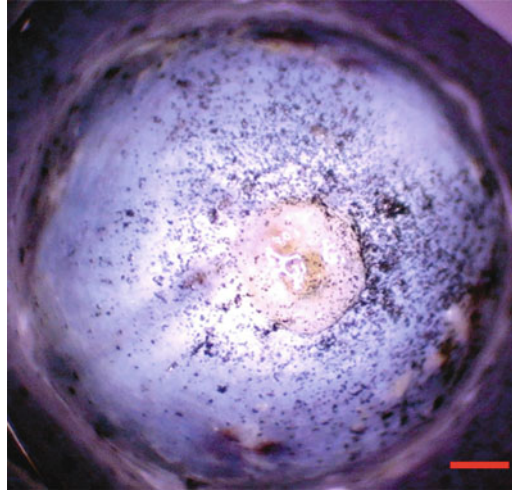


Fig. 7 Speckle pattern on sclera of Brown Norway rat. Scale bar: 1 mm

8. Carefully insert the biopsy punch into the 3/16" hole in the mounting block and gently push and twist the punch to puncture a hole in the cornea. Success will be indicated by a sudden deflation of the sclera.
9. Apply a generous bead of glue around the threads of a 10–32 thread to male luer fitting, then push this into the open end of the eye-mounting block, and twist slightly to ensure a good contact. Although the luer fitting has threads, these will not screw into any part of the acrylic. A solid fit is achieved by forcing the threads into the acrylic, sealed with glue.
10. Using a syringe and blunt needle, flush out all air bubbles between the tip of the luer fitting and the channel connecting to the eye.
11. The eye is now ready to be installed onto the PBS chamber for DIC testing (Fig. 8).

3.2.4 Inflation Testing and DIC

Stereo Camera Calibration

The stereo cameras of the DIC system should be calibrated daily (intrinsic parameters) in order to quantify the relative positions of the cameras. A calibration of extrinsic parameters should be performed for each eye to account for refraction from immersing the eye in PBS.

1. Using a standardized checkerboard calibration target, acquire intrinsic calibration parameters by imaging the target at nine or more positions.
2. Adjust the height of the pressure reservoir to be equal to the height of the eye.
3. Connect the eye mounted on its acrylic holder to the luer connection in the immersion chamber (Fig. 9). Make sure

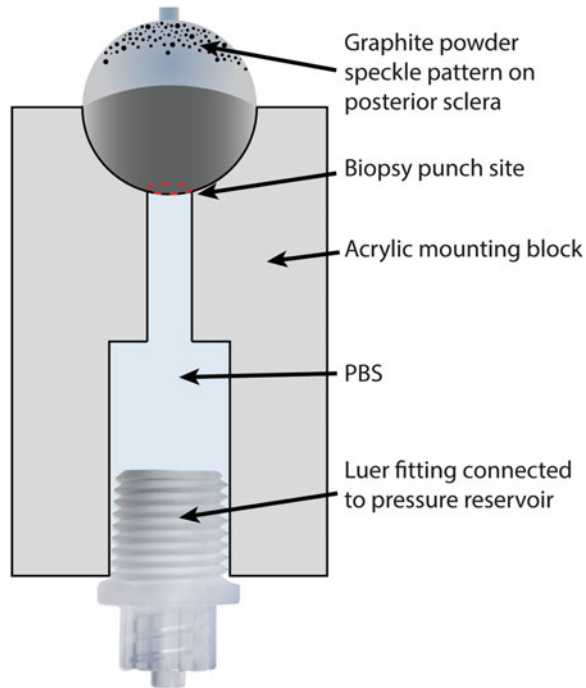


Fig. 8 Eye mounted onto block, ready for DIC testing

there are no bubbles caught in the mount, and open the valve to the reservoir *before* mating the luer connections to ensure there is no pressure spike when connecting the eye to a column of (nearly) incompressible PBS.

4. Focus the cameras on the eye.
5. Immerse the calibration target in the chamber and place at a height equal to the eye.
6. Translate the reservoir so that the calibration target is under the cameras, but do not adjust the focus. Adjust the calibration target height if focus is needed.
7. Acquire a single image of the target and compute extrinsic calibration parameters using it.
8. Translate the immersion chamber so the cameras are centered above the eye.

Inflation Testing

A hydrostatic pressure reservoir is used to inflate the eye for testing.

1. Acquire images of the eye at its baseline pressure. Wait at least 15 min for eye to equilibrate.
2. Move the reservoir vertically to a height equivalent to 15 mmHg above the eye, much as in **Note 4**.
3. Acquire additional images. Wait at least 15 more min.

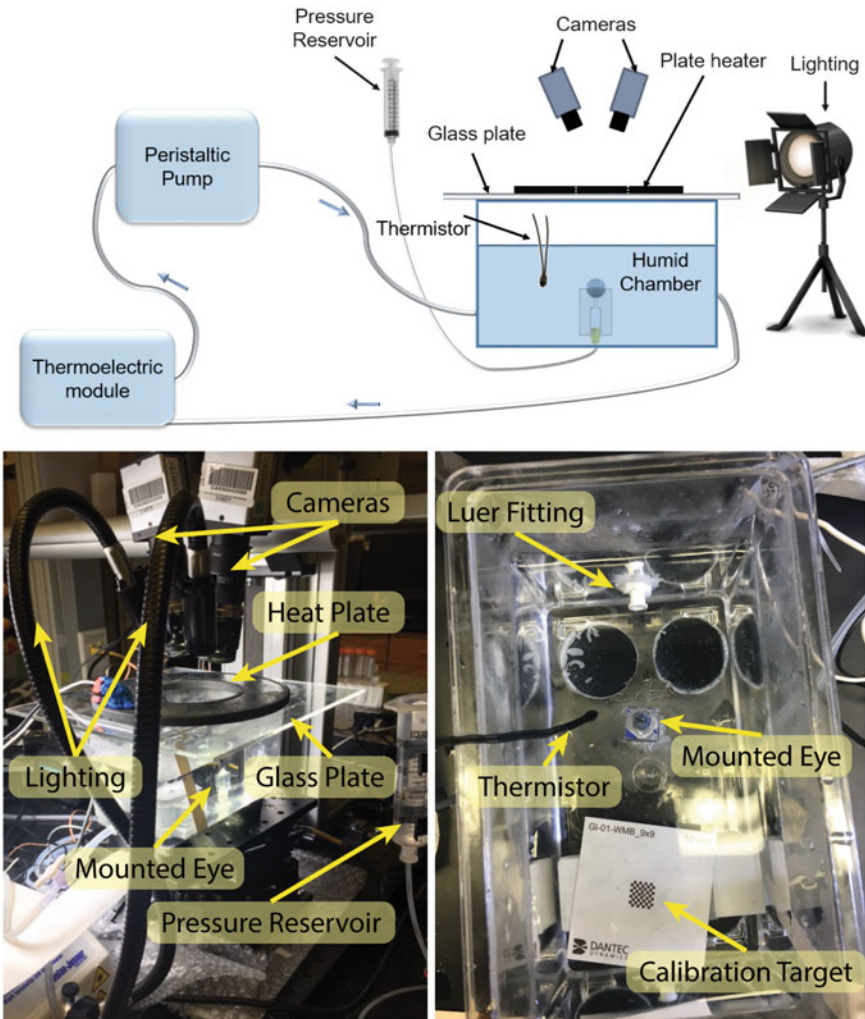


Fig. 9 Schematic of DIC setup (*top*) and photos of inflation chamber from side (*bottom left*) and top (*bottom right*)

4. Move the reservoir vertically to 30 mmHg and acquire additional images.
5. Using the DIC software [20], process the images to compute displacement and strain. Displacements should be smoothed within the DIC software before computing strain. Input parameters for DIC speckle tracking vary considerably between software packages; consult the documentation for your software for recommendations.
6. Export displacement and strain metrics from the DIC software into a data analysis package such as MATLAB.
7. Compare stiffness metrics among in regions of interest. Typically, the spatial average of 1st Principal Strain is used to

compare among eyes, but other metrics like 2nd Principal Strain or total displacement may be used as well.

**3.3 Methods
for Quantification
of Scleral Collagen
Orientation Using SHG
Nonlinear Microscopy**

1. Prepare whole mount sample, if relevant. Skip this step if imaging histological sections.
 - (a) Create a circle of silicone approximately the size of the well on a coverslip using a syringe, ensuring there is no silicone in the location of the specimen.
 - (b) Place the eye, posterior side down, into the well. Position the optic nerve head in the center of the circle.
 - (c) Cover the sample with PBS.
 - (d) Seal the well with the silicone-ringed coverslip.
2. Place the coverslip or histology slide on the microscope stage, add oil to objective.
3. Tune the laser to an excitation wavelength of 800 nm (*see Note 13*).
4. Configure the META module to use a bandpass filter of 380–420 nm in order to detect the backward scattering SHG signal from collagen.
5. Locate the optic nerve head to position the center of the sample in the field of view.
6. Adjust the laser power and detector gain to obtain optimal image quality.
7. To maximize the size of the sample imaged, 3D z-stacking and tile scanning functionality are utilized.
 - (a) To create a 3D stack, locate the top and bottom edges of the sample by adjusting the focus and enter these bounds into the Z-stack control (*see Note 14*).
 - (b) To create a tile scan and acquire a larger field of view in the x-y directions, select the desired number of tiles to encompass the sample. Each sub-image within the tile will cover a $225\ \mu\text{m} \times 225\ \mu\text{m}$ area with this objective.
8. Acquire image stack.
9. Create a maximum intensity projection of the 3D image.
10. Analyze collagen fiber orientation using the directionality plugin of FIJI (<https://fiji.sc/>), which generates a histogram of fiber orientation. For example, one can determine the predominant fiber angle and alignment index [21], which is defined by the fraction of the fibers that are aligned within $\pm 20^\circ$ of the predominant fiber angle normalized to the fraction of a random distribution of fibers (equal to $40^\circ/180^\circ$; Figs. 10 and 11).

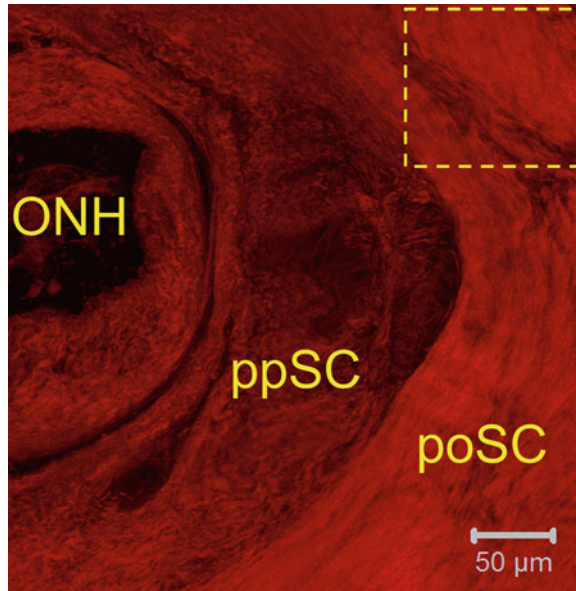


Fig. 10 Representative SHG image showing collagen orientation in the mouse sclera. Note the visual differences in collagen density and alignment in the various regions. *ONH* optic nerve head, *ppSC* peripapillary sclera, *poSC* posterior sclera

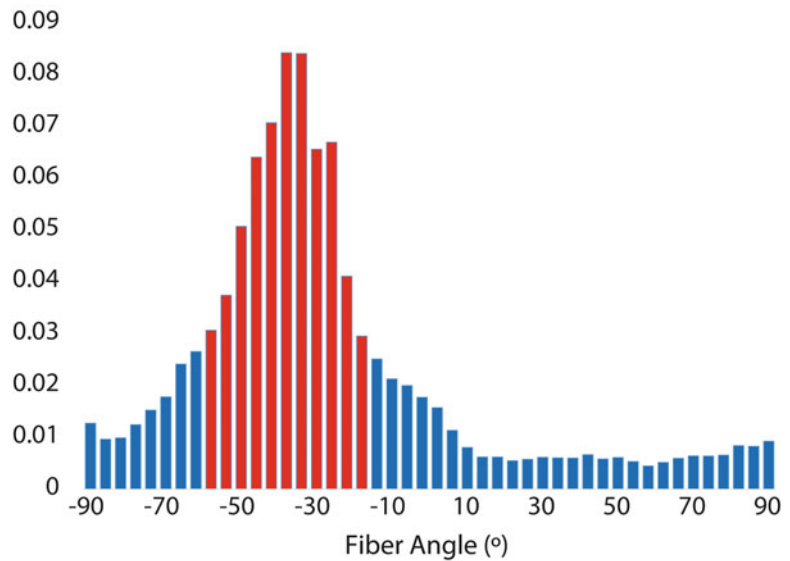


Fig. 11 Frequency histogram of the SHG image outlined by the *yellow* box in Fig. 10, generated using the directionality plugin of FIJI. 0° and 90° correspond to the East and North directions, respectively. In this case, the predominant fiber angle is -38° , and the alignment index is 3.04. The *red* bars indicate fibers within $\pm 20^\circ$ of the predominant fiber angle

3.4 Methods for Quantification of Scleral Collagen Orientation Using Small-Angle Light Scattering

1. Clear scleras of extraocular orbital tissues by careful dissection (similar to Subheading 3.2.3.).
2. Cut sclera into suitable “patches” (*see* Notes 2, 3, and 15) using sharp dissection.
3. For rat and mouse scleras, dip each patch in glycerol solution for several seconds to slightly enhance transparency.
4. Lay sample flat with a drop of glycerol solution between two microscope glass slides separated by double-sided adhesive tape at ends of slides.
5. Seal edges of glass plate assembly with quick drying silicone and store at 4 °C for 1 h to cure silicone.
6. Mount slides in SALS system (Fig. 3) and acquire images by shining laser at specimen.
7. Use micropositioning system to shift the point on the sclera being interrogated and thus build up a fiber distribution map over the desired scleral region.
8. *See* Notes 16 and 17 for specifics of image quantification and analysis, as in Fig. 12.

4 Notes

1. Using plastic syringes makes the system less repeatable and adds additional compliance to the system. Glass syringes are thus recommended.
2. The scleral specimen must be semi-transparent, since the measurement relies on the scattering pattern of light that has passed through the tissue. Rat and mouse sclera are sufficiently thin that they meet this requirement (*see* below); however, thicker scleral samples from larger eyes do not. In such cases, the sample can be cryosectioned in the plane of the sclera to create a thinner sample [17] or cleared using glycerol or other agents [22].
3. As SALS systems are presently configured, the tissue sample is clamped between glass slides, which implies that it must be flattened. There is therefore a tradeoff in sample size: larger scleral samples suffer more deformation when they are flattened, yet smaller samples suffer from proportionately more edge artifacts. (The scattering pattern is highly distorted, and therefore unusable, when the laser beam intersects any part of the edge of tissue sample.) Judicious choices about sample size and location must therefore be made, depending on the research questions being asked. Samples of edge length 3–5 mm have been successfully used in the past [18]. Early

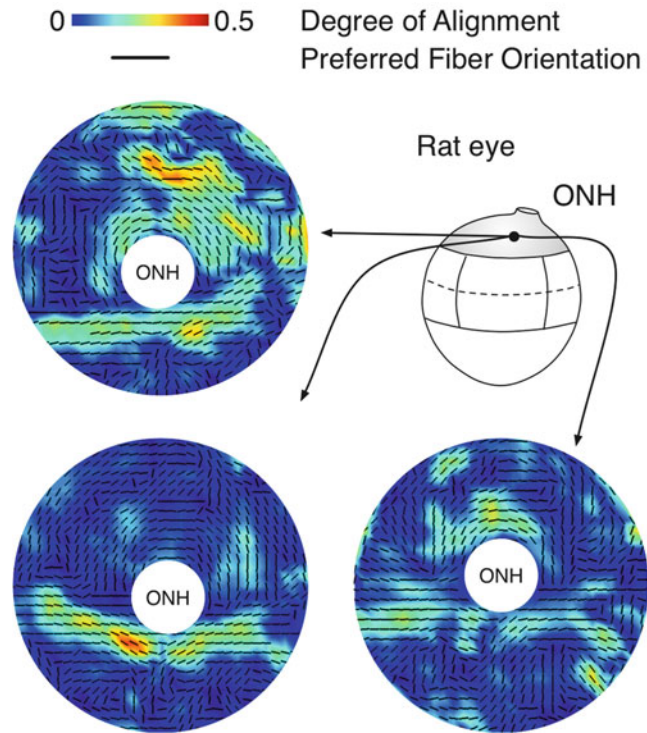


Fig. 12 Three representative fiber orientation maps from rat eyes. These maps comprise the peripapillary sclera around the optic nerve head (ONH). The color map indicates how locally aligned collagen fibers are, and *black lines* represent the primary fiber orientation at each measurement location. Image courtesy of [18]

efforts to allow investigation of curved samples are also promising [23].

4. The reservoir pressure is ideally controlled using a vertically mounted linear actuator but could be carried out with a stand with holes drilled at the desired locations. This technique could also be carried using a retort stand and visually measuring the meniscus height against a meter stick, but this is the least accurate method and can lead to decreased accuracy of ocular compliance.
5. Note that if the height of fluid in the eye bath changes, the measured pressure will no longer be accurate. However, as the current technique uses only pressure differences, this will not adversely affect the compliance measurement.
6. Note that ΔV_r should be kept small so as to avoid damaging the pressure sensor, hence our choice of 25 nl.
7. Note that reducing the volume of the bolus (e.g., to get higher pressure resolution) will tend to introduce errors into the

measurement of ocular compliance due to a larger relative contribution of outflow.

8. If making multiple acrylic holders simultaneously, this cut should make your sheet of acrylic look somewhat like a bar of chocolate so that each section can be snapped or cut off once both sides are drilled.
9. Do not allow the sclera to dry out while cleaning. Place the eye in a Petri dish and immerse in or apply PBS regularly.
10. Ensure the bead of glue is continuous. Any gaps will allow fluid to flow around the side of the eye rather than inflating it.
11. Application of the graphite powder should be carried out within an enclosed chamber equipped with a vacuum extraction device (e.g., Alsident[®] system “snorkel”) to limit spread of the graphite. A breathing mask and other PPE should be worn during the procedure.
12. If an unsatisfactory pattern is produced, for example by applying too much graphite, the sclera may be wiped with a PBS-moistened Q-tip to remove existing speckles and then retried. An ideal speckle pattern will be highly random and roughly 30–50% density.
13. We stimulate with 800 nm to avoid elastin absorption and thus selectively image collagen.
14. The number of slices or the optical section interval between stacks needs to be adjusted to avoid gaps between optical slices and minimize oversampling. Auto Z-brightness correction is used to compensate for signal intensity reduction deep inside the tissue by continuously adjusting laser power and detector gain during Z-stack acquisition.
15. Avoid cutting ragged edges as much as possible to minimize edge artifacts during measurements.
16. At each measurement location, the resulting scattering pattern must be analyzed to extract quantitative fiber orientation information. Approaches for such an analysis are described elsewhere [18].
17. At each measurement location, a histogram (distribution) of fiber orientations is obtained. It may be convenient to present this information in terms of the local (preferred) fiber orientation and a degree of alignment index. The latter quantity lies between 0 and 1 and characterizes the degree of fiber anisotropy: when it equals zero, fibers are randomly aligned in the plane perpendicular to the beam direction (planar isotropic material), while when it equals one, all fibers are perfectly aligned within this perpendicular plane (transversely isotropic material). This allows rapid visual understanding of the fiber orientation within the sample.

References

- Campbell IC, Coudrillier B, Ethier CR (2014) Biomechanics of the posterior eye: a critical role in health and disease. *J Biomech Eng* 136 (2):021005. <https://doi.org/10.1115/1.4026286>
- Sigal IA, Flanagan JG, Ethier CR (2005) Factors influencing optic nerve head biomechanics. *Invest Ophthalmol Vis Sci* 46 (11):4189–4199. <https://doi.org/10.1167/iovs.05-0541>
- Norton TT, Siegwart JT Jr (2013) Light levels, refractive development, and myopia—a speculative review. *Exp Eye Res* 114:48–57. <https://doi.org/10.1016/j.exer.2013.05.004>
- Bhardwaj R, Ziegler K, Seo JH, Ramesh KT, Nguyen TD (2014) A computational model of blast loading on the human eye. *Biomech Model Mechanobiol* 13(1):123–140. <https://doi.org/10.1007/s10237-013-0490-3>
- Komai Y, Ushiki T (1991) The three-dimensional organization of collagen fibrils in the human cornea and sclera. *Invest Ophthalmol Vis Sci* 32(8):2244–2258
- Friedenwald JS (1949) Clinical significance of ocular rigidity in relation to the tonometric measurement. *Trans Am Acad Ophthalmol Otolaryngol* 53:262–264
- Sherwood JM, Reina-Torres E, Bertrand JA, Rowe B, Overby DR (2016) Measurement of outflow facility using iPerfusion. *PLoS One* 11 (3):e0150694. <https://doi.org/10.1371/journal.pone.0150694>
- Fazio MA, Grytz R, Bruno L, Girard MJ, Gardiner S, Girkin CA, Downs JC (2012) Regional variations in mechanical strain in the posterior human sclera. *Invest Ophthalmol Vis Sci* 53(9):5326–5333. <https://doi.org/10.1167/iovs.12-9668>
- Coudrillier B, Tian J, Alexander S, Myers KM, Quigley HA, Nguyen TD (2012) Biomechanics of the human posterior sclera: age- and glaucoma-related changes measured using inflation testing. *Invest Ophthalmol Vis Sci* 53(4):1714–1728. <https://doi.org/10.1167/iovs.11-8009>
- Zoumi A, Yeh A, Tromberg BJ (2002) Imaging cells and extracellular matrix in vivo by using second-harmonic generation and two-photon excited fluorescence. *Proc Natl Acad Sci U S A* 99(17):11014–11019. <https://doi.org/10.1073/pnas.172368799>
- Chien JCW, Chang EP (1972) Small-angle light scattering of reconstituted collagen. *Macromolecules* 5:610–617
- Ferdman AG, Yannas IV (1993) Scattering of light from histologic sections: a new method for the analysis of connective tissue. *J Invest Dermatol* 100(5):710–716
- Garton A, Carlsson DJ, Stepaniak RF, Wiles DM (1979) The use of small-angle light-scattering (SALS) to examine the structure of fibers. *Text Res J* 49:335–342
- Joyce EM, Liao J, Schoen FJ, Mayer JE Jr, Sacks MS (2009) Functional collagen fiber architecture of the pulmonary heart valve cusp. *Ann Thorac Surg* 87(4):1240–1249. <https://doi.org/10.1016/j.athoracsur.2008.12.049>
- Kronick PL, Sacks MS (1991) Quantification of vertical-fiber defect in cattle hide by small-angle light scattering. *Connect Tissue Res* 27 (1):1–13
- Sacks MS, Smith DB, Hiester ED (1997) A small angle light scattering device for planar connective tissue microstructural analysis. *Ann Biomed Eng* 25(4):678–689
- Yan D, McPheeters S, Johnson G, Utzinger U, Vande Geest JP (2011) Microstructural differences in the human posterior sclera as a function of age and race. *Invest Ophthalmol Vis Sci* 52(2):821–829. <https://doi.org/10.1167/iovs.09-4651>
- Girard MJ, Dahlmann-Noor A, Rayapureddi S, Bechara JA, Bertin BM, Jones H, Albon J, Khaw PT, Ethier CR (2011) Quantitative mapping of scleral fiber orientation in normal rat eyes. *Invest Ophthalmol Vis Sci* 52 (13):9684–9693. <https://doi.org/10.1167/iovs.11-7894>
- Lei Y, Overby DR, Boussoimmier-Calleja A, Stamer WD, Ethier CR (2011) Outflow physiology of the mouse eye: pressure dependence and washout. *Invest Ophthalmol Vis Sci* 52 (3):1865–1871. <https://doi.org/10.1167/iovs.10-6019>
- Sutton MA (2008) Digital image correlation for shape and deformation measurements. In: Sharpe NW (ed) *Springer handbook of experimental solid mechanics*. Springer US, Boston, MA, pp 565–600. https://doi.org/10.1007/978-0-387-30877-7_20

21. Ng CP, Swartz MA (2006) Mechanisms of interstitial flow-induced remodeling of fibroblast-collagen cultures. *Ann Biomed Eng* 34(3):446–454. <https://doi.org/10.1007/s10439-005-9067-3>
22. Guo X, Guo Z, Wei H, Yang H, He Y, Xie S, Wu G, Deng X, Zhao Q, Li L (2011) In vivo comparison of the optical clearing efficacy of optical clearing agents in human skin by quantifying permeability using optical coherence tomography. *Photochem Photobiol* 87(3):734–740. <https://doi.org/10.1111/j.1751-1097.2011.00908.x>
23. Goh YK (2014) Quantitative mapping of collagen fibre organization in porcine corneas using small angle light scattering (SALS) technique. National University of Singapore, Singapore

Chapter 14

Biolistic Labeling of Retinal Ganglion Cells

Luca Della Santina and Yvonne Ou

Abstract

Labeling of cellular structures is of fundamental importance in the investigation of diseases of the central nervous system. Biolistic labeling of retinal ganglion cells (RGCs) allows visualization of dendritic and synaptic structures of RGCs in retinal explants from animal models of experimental glaucoma. This technique sparsely labels RGCs, and, due to the stochastic nature of the particle delivery, all RGC types can be potentially observed in the labeled tissue. Quantification of dendritic and synaptic properties permits examination of the specific alterations to RGC morphology at different stages of degeneration, such as dendritic shrinkage and excitatory synapse loss.

Key words Glaucoma, Biolistic labeling, Retinal ganglion cells, Dendrites, Excitatory synapses, PSD95, Degeneration

1 Introduction

Accurate quantification of morphological properties of RGCs in retinal disease, such as soma size, dendritic complexity, and synapse density along dendritic arbors, is powerful metrics with which disease progression can be followed and functional alterations to specific retinal circuits can be predicted. Pioneer studies in primates and cats allowed identification of such cellular properties following dye injection into individual RGCs [1, 2] or into the lateral geniculate nucleus (LGN) [3]. Moreover, dye injection into individual RGCs from transgenic mice in which specific RGC populations express fluorescent protein (FP) permits the identification of RGC type-specific dendritic alterations [4]. Although fine cellular morphology can be evaluated using this method, the relative low yield of this labeling technique limits the amount of RGCs that can be analyzed in each sample and limits the analysis to cellular and dendritic morphology without providing insights on the distribution of synaptic inputs.

The DiOlistic labeling technique is an unbiased approach to labeling across RGC types, animal species, and disease models

[5, 6]. Extension of this technique to deliver DNA plasmids permits exogenous expression of FP in target neurons, thus allowing biolistic labeling of dendritic structure. Co-expression of FP-tagged synaptic proteins results in targeted expression of FP in synapses within the same cell [7, 8]. In this chapter, we will describe the procedure required to label RGCs in the retina of mice and the quantification of morphological and synaptic properties of the dendritic arbor of individual RGCs [9].

2 Materials

1. Helios gene gun system (Biorad).
2. DNA plasmids: 1 $\mu\text{g}/\mu\text{l}$ or higher for optimal nucleic acid concentration.
 CMV-FP for cytoplasm filling: 25 μg .
 CMV-PSD95-FP for excitatory synapse labeling: 12 μg .
3. Spermidine: 50 μl of a 0.05 M solution.
4. Gold particles 1.6 μm average diameter (Biorad).
5. CaCl_2 : prepare a 1 M solution in water.
6. ETFE tubing (0.125" outer diameter \times 0.093" inner diameter, Saint Gobain).
7. 100% EtOH.
8. Benchtop centrifuge and vortex mixer.
9. Artificial mouse cerebro-spinal fluid (mACSF) for retinal explantation and culturing. Composition in mM: 119 mM NaCl, 2.5 mM KCl, 2.5 mM CaCl_2 , 1.3 mM MgCl_2 , 1 mM NaH_2PO_4 , 11 mM glucose, and 20 mM HEPES at room temperature; pH 7.4 adjusted with 5 M NaOH.
10. Vectashield mounting medium (Vector).
11. Analysis software packages: MATLAB (Mathworks), Imaris (Bitplane), ImageJ.
12. Custom Imaris functions for synaptic puncta analysis, available at: <https://github.com/lucadellasantina/imarisxt>.
13. Custom MATLAB functions for synaptic puncta analysis, available at: <https://github.com/lucadellasantina/dotfinder>.

3 Methods

3.1 Biolistic Labeling of Retinal Ganglion Cells

The labeling procedure consists of four fundamental steps (schematized in Fig. 1): Preparation of DNA-coated gold particles; delivery of gold particles to RGCs using the gene gun; incubation of transfected retinal explants to allow optimal expression of

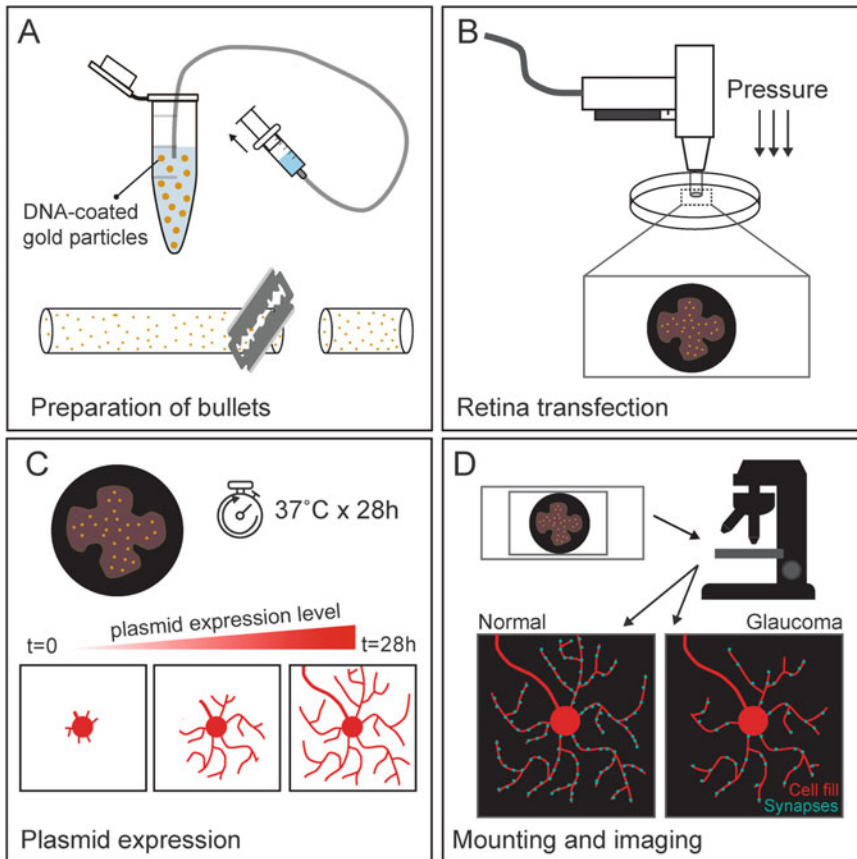


Fig. 1 Biolistic labeling of RGCs. **(a)** Preparation of a suspension of DNA-coated gold particles in ethanol and creation of plastic bullets for transfection using the gene gun. **(b)** Biolistic transfection of RGCs using the gene gun on flat-mounted retinas. **(c)** Incubation of transfected retinas to allow optimal expression of exogenous DNA. **(d)** Mounting and confocal imaging of transfected RGCs to acquire labeling of cell morphology (*red*) and excitatory synapses (*cyan*)

exogenous DNA; and finally, imaging of biolistically labeled RGC dendritic architecture and their synapses. Expression of FP in the cytoplasm will enable visualization of cell morphology under the epifluorescent microscope while co-expression of FP-tagged PSD95 will allow visualization of excitatory synapses, as the protein accumulates at RGC excitatory postsynaptic sites.

3.1.1 Preparation of DNA-Coated Gold Particles

1. Weigh 12.5 mg gold particles and add 50 μ l spermidine solution to the particles in a 1.5 ml plastic Eppendorf tube.
2. Sonicate for 15 s, add plasmids to the suspension, and spin three times in the vortex mixer.
3. Add 50 μ l of 1 M CaCl_2 solution drop by drop while agitating at low speed (setting 5–6) on the vortex mixer.

4. Wait 15 min at room temperature to let the DNA precipitate onto the gold particles.
5. Spin the suspension for 5 s in the benchtop centrifuge.
6. Remove the supernatant and add 1.4 ml of 100% ethanol to the pellet of DNA-coated gold particles, then vortex twice to recreate a homogeneous brown suspension. Spin 6 s in the benchtop centrifuge at lowest speed.
7. Remove the supernatant and repeat ethanol washes followed by vortex and spinning three times to completely remove water residue from the ethanol suspension of gold particles.
8. The final ethanol suspension should appear uniform to the eye without any visible coarse particles or agglomerates.

3.1.2 Preparation of Tubing for Bullets

1. Cut 33 cm of ETFE plastic tubing with a razor blade.
2. Dry the inside of tubing with nitrogen gas at 3.5 psi for 10 min in the rotating device provided with the Helios gene gun system.
3. Trim the endings of the ETFE tube with a razor blade if deformed from the previous step.
4. Connect a 20 ml plastic syringe to the ETFE tube using a flexible plastic tubing adaptor.
5. Slowly load the suspension into the ETFE tube by aspirating the contents of the Eppendorf tube containing the suspension of gold particles.
6. Lay the ETFE tubing horizontally on the benchtop with the syringe still connected.
7. Let the gold precipitate onto the ETFE tube for 5 min.
8. Slowly remove the ethanol using the connected syringe. The gold particles will remain attached to the tube in a string. Optimal suction speed will leave a continuous trail of gold particles within the ETFE tube.
9. Disconnect the syringe and cover both the ends of the ETFE tube with parafilm.
10. Flick with your fingers on the tube in order to spread the gold particles inside the ETFE tube.
11. Use the cutter provided with the Helios gene gun system to create individual bullets. Collect them into a glass jar with desiccating silica gel to prevent rehydration.
12. Store bullets in the refrigerator, sheltered from light and humidity. Use within 21 days from preparation.

3.1.3 Gene Gun Preparation

1. Remove a spacer and a barrel for the gene gun from ethanol storage.
2. Dry both items of ethanol using compressed air.
3. Load the revolver into the gene gun and connect the gene gun to the gas tank.
4. Shoot several blanks to adjust the gas pressure to 40 psi.
5. Load bullets containing DNA-coated gold particles into the gene gun's barrel.

3.1.4 Particle Delivery to Tissue

1. Dissect the mouse retinas in oxygenated mACSF and place retinal whole mounts ganglion cell side up onto nitrocellulose filter paper for optimal flattening of tissue.
2. Transfer the retina attached to filter paper into an empty plastic petri dish.
3. Center the loaded gene gun over the retina.
4. Trigger the gun to project gold particles onto the tissue.
5. Transfer the retina back into oxygenated mACSF solution.
6. Incubate retinas at 37 °C degrees for ~28 h in mACSF for optimal protein expression *see* **Notes 1–4**.

3.2 Image Acquisition and Processing

Once RGCs have reached optimal expression of the exogenous proteins, samples can be fixed and confocal image stacks acquired for further processing (Fig. 2).

Quantification of RGC dendritic arbor's properties and excitatory synapses requires processing of confocal image stacks in three dimensions with the provided custom-written MATLAB routines.

3.2.1 Image Acquisition

1. Fix the whole mount retina in 4% paraformaldehyde for 30 min and mount the fixed tissue onto glass slides using Vectashield mounting medium.
2. Under epifluorescent illumination of the confocal microscope, locate desired RGCs using a low magnification objective (usually 10×). Then switch to a higher magnification objective for the acquisition of the confocal image stack.
3. For optimal quantification of dendritic labeling, acquire the entire dendritic arbor at a voxel size of at least $0.3 \times 0.3 \times 0.5 \mu\text{m}$ (usually achieved using 40× or 60× objectives, depending on the RGC arbor size).
4. For optimal quantification of synaptic labeling, acquire synapses on the dendritic arbor at a voxel size of at least $0.1 \times 0.1 \times 0.3 \mu\text{m}$ (usually achieved using a 60× objective).
5. When acquiring signal from synaptic labeling, particular attention must be paid to amplify fluorescence signal (using laser power level and photomultiplier gain) within the dynamic

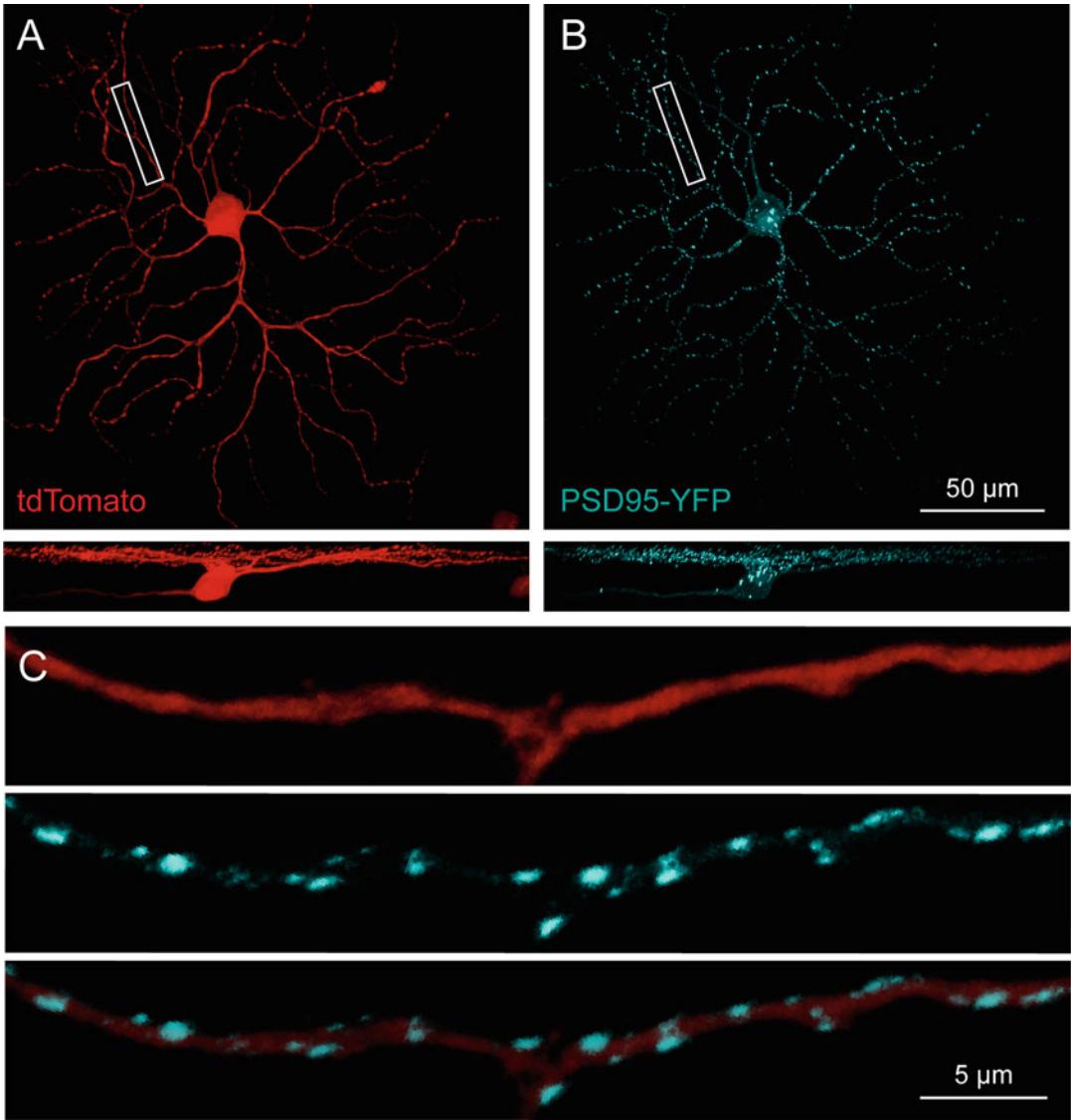


Fig. 2 Example of a biolistically labeled RGC. **(a)** Maximum intensity projection of a biolistically labeled RGC in which cell morphology is visible by cytosolic expression of the fluorescent protein tdTomato. *Bottom panel:* side-view of the same cell. **(b)** Co-expression of the synaptic protein PSD95-YFP enables the visualization of excitatory synapses in the same RGC. *Bottom panel:* side-view of the same cell. **(c)** Magnification of the boxed area in **(a)** and **(b)** reveals complete labeling of a RGC dendritic segment (*top panel, red*) and excitatory synapses (*bottom panels, cyan*)

range of your confocal microscope acquisition system. Acquisition of oversaturated images can lead to overestimation of synaptic puncta in the following steps. We prefer acquiring image stacks at 12-bit or 16-bit sampling depth if available in your confocal acquisition system.

6. Median filter acquired image stacks using ImageJ (kernel size = 3×3 pixels) to minimize acquired thermal noise from confocal microscope photomultipliers.
7. Downsample acquired image stacks to 8-bit in case your original image stacks have higher sampling resolution. This operation will speed up further processing steps.
8. Save each color channel of the confocal image stack into an individual .TIF file for further processing.

3.2.2 Quantification of RGC Dendritic Morphology

Following the acquisition of an image stack containing the cytoplasmic FP filling and PSD95-FP synaptic labeling, skeletonization of RGC dendrites with the image analysis software Imaris will allow for quantification of dendritic arbor properties such as dendritic area and Sholl analysis of dendritic complexity.

1. Open the cell fill labeling image stack using Imaris software.
2. Using the filament function, follow the guided procedure to obtain a digital skeleton of dendrites originating from the location of the cell body (Fig. 3b).
3. Calculate accurate volume of the dendritic skeleton using the “Filament edit” tab, “process filament, diameter” function. Typical settings for mouse RGCs are: small diameter = $0.5 \mu\text{m}$, large diameter = $20 \mu\text{m}$, contrast = 3.
4. Retrieve Sholl analysis information using the filament properties tab, “Filament No. Sholl Intersections” and save these data for further plotting as in Fig. 3d bottom-right panel.
5. Calculate dendritic area by first calculating the polygon encompassing distal dendritic tips using Imaris function “Filament processing, Filament Convex Hull” function. Then record the area of the convex hull polygon calculated in the “Detailed statistics” tab of the polygon object.

3.2.3 Quantification of RGC Synaptic Density

The following method illustrates how to use custom Imaris and MATLAB routines to obtain a semi-automatic quantification of PSD95-FP-tagged synapses of the target RGC. The identification of synaptic puncta is first calculated based on local contrast of PSD95-FP-tagged puncta in the image stack, following the procedure described by Morgan and colleagues [7]. Then the user performs thresholding and a final visual inspection of detected synaptic puncta candidates in the RGC-rendered volume by Imaris software.

The following puncta analysis method is sufficiently robust to be extended also to the quantification of synaptic puncta in transgenic mouse lines expressing FP-tagged synaptic proteins [10, 11] and to immunohistochemical labeling of synaptic proteins [9].

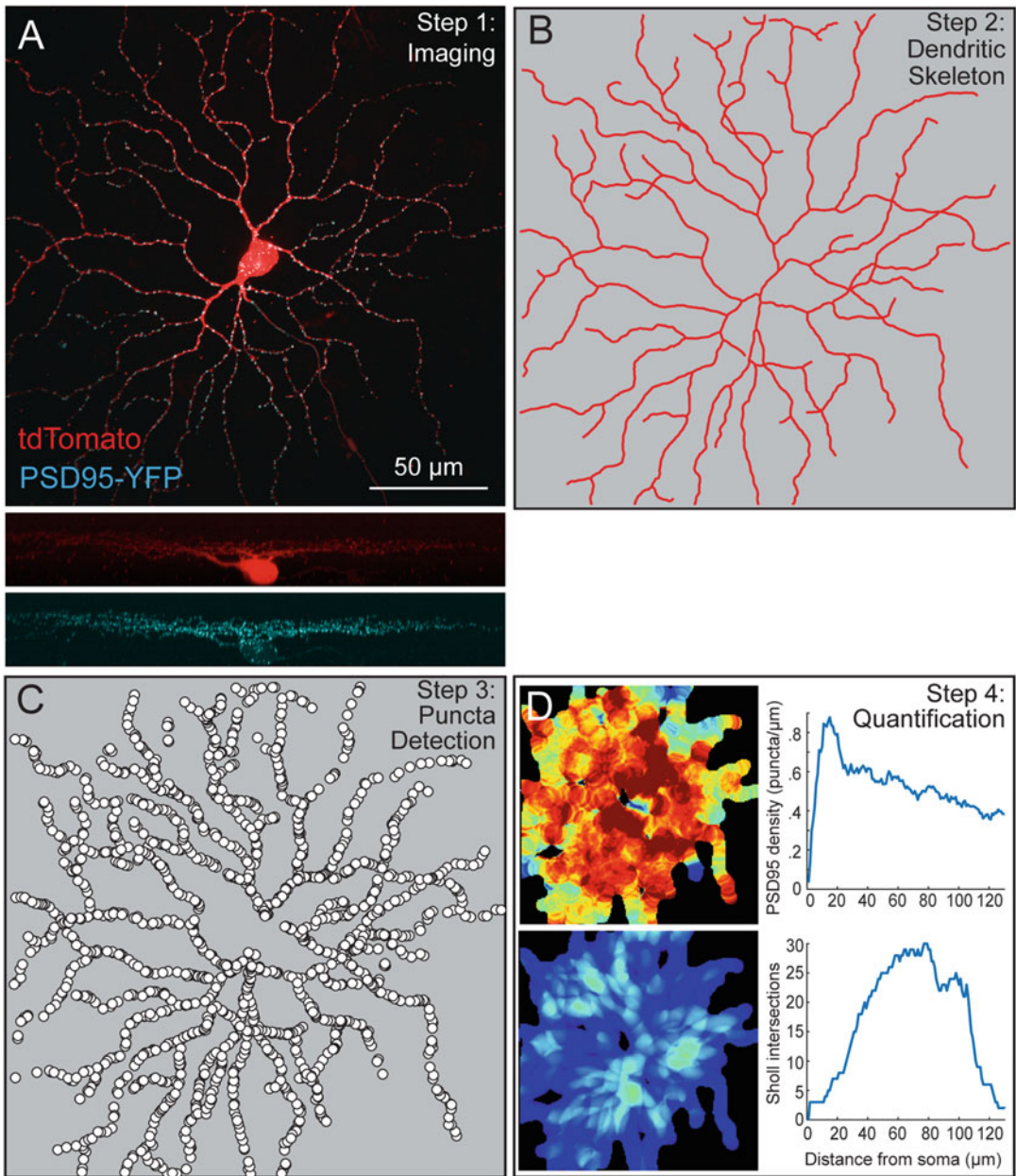


Fig. 3 Quantification of dendritic morphology and synaptic density. (a) Maximum intensity projection (*en face view*) of an ON α RGC biolistically labeled to express the cytosolic fluorescent protein tdTomato and the YFP-tagged postsynaptic protein PSD95. *Bottom panels*: side view of the tdTomato and PSD95-YFP fluorescence. (b) Skeleton of the dendritic arbor of the RGC in (a) obtained by semi-automated recognition of the dendritic trajectory. (c) Spatial distribution of PSD95-YFP fluorescent puncta of the RGC in (a) obtained by semi-automated recognition of fluorescent puncta. PSD95-YFP puncta are rendered as enlarged disks in the figure for easy visual recognition. (d) Quantification of synaptic and dendritic properties for the RGC in (a). *Top-left*: Spatial representation of postsynaptic density obtained by convolving a 20 μm disk representing local PSD95-YFP puncta density with image pixels. Hotter colors represent higher postsynaptic density. *Top-right*: Quantification of PSD95 density as a function of distance from the cell soma. *Bottom-left*: Spatial representation of dendritic density obtained by convolving a 20 μm disk representing local dendritic density with image pixels. *Bottom-right*: Sholl analysis of dendritic complexity as a function of concentric distance from the cell soma

1. Install provided MATLAB functions by copying the files into your local hard drive and add the folder to your MATLAB path settings.
2. Install provided Imaris extensions by copying the files into your local Imaris extensions folder.
3. Prepare a folder structure on your computer's hard drive, encompassing a main folder called "experiment_name" containing a subfolder named "I".
4. Copy the cell fill image stack and the synaptic image stack .TIF files into "experiment_name/I" folder.
5. Open Imaris and load the dataset of the analyzed RGC obtained in Subheading 3.2.2.
6. Add PSD95 image stack to the dataset using "add channel" function present in the Imaris edit menu.
7. Export the dendritic skeleton using the custom Imaris routine "Filament, save filament as .mat" choosing "experiment_name" folder as the target destination.
8. Export an expanded mask of RGC dendrites using the custom Imaris routine "Save filament mask," choosing "experiment_name" folder as the target destination.
9. Open MATLAB and run the custom routines from "RunAnalysis.m" to obtain a semi-automated quantification of synaptic puncta.
10. Synaptic locations identified in the image volume, as represented in a bidimensional image projection in Fig. 3c.
11. Synaptic density will be computed and represented as bidimensional heat-maps and as linear synaptic density as a function of distance from cell soma as in Fig. 3d.
12. Plots resulting from the semi-automated analysis are available inside the "experiment_name/images" folder generated by the processing pipeline.

4 Notes

1. If labeling of RGCs is too dense, use bullets loaded with a lower density of gold particles or cut each bullet in half before repeating the experiment.
2. If labeling of RGCs is too sparse, use bullets with a higher density of gold particles.
3. If there is no labeling after incubation, confirm under a dissection microscope that the bullets were targeted correctly onto the retina. This is confirmed by the presence of shiny dots on

the retinal surface observed under stereomicroscopy by direct illumination.

4. If the retina was successfully targeted by gold particles but still no fluorescent signal is present, confirm the integrity of DNA plasmids by standard transfection in cell culture (i.e., HEK-293 cells).

Acknowledgments

This work was supported in part by NIH Grant KEY022676A, Research to Prevent Blindness Career Development Award, Ron and Anita Wornick and That Man May See, E. Matilda Ziegler Foundation for the Blind award, BrighFocus Foundation National Glaucoma Research award, NIH-NEI EY002162 Core Grant for Vision Research, and a Research to Prevent Blindness Unrestricted Grant to the University of California, San Francisco to YO and University of Pisa, Fondi di Ateneo 2014-16 to LDS.

References

1. Weber AJ, Kaufman PL, Hubbard WC (1998) Morphology of single ganglion cells in the glaucomatous primate retina. *Invest Ophthalmol Vis Sci* 39:2304–2320
2. Glovinsky Y, Quigley HA, Pease ME (1993) Foveal ganglion cell loss is size dependent in experimental glaucoma. *Invest Ophthalmol Vis Sci* 34:395–400
3. Shou T, Liu J, Wang W et al (2003) Differential dendritic shrinkage of alpha and beta retinal ganglion cells in cats with chronic glaucoma. *Invest Ophthalmol Vis Sci* 44:3005–3010
4. El-Danaf RN, Huberman AD (2015) Characteristic patterns of dendritic remodeling in early-stage glaucoma: evidence from genetically identified retinal ganglion cell types. *J Neurosci* 35:2329–2343. <https://doi.org/10.1523/JNEUROSCI.1419-14.2015>
5. Gan WB, Grutzendler J, Wong WT et al (2000) Multicolor “DiOlistic” labeling of the nervous system using lipophilic dye combinations. *Neuron* 27:219–225
6. Morgan JL, Wong ROL (2008) Ballistic labeling with fluorescent dyes and indicators. *Curr Protoc Neurosci* Chapter 2:Unit 2.11–2.11.10. doi: <https://doi.org/10.1002/0471142301.ns0211s43>
7. Morgan JL, Schubert T, Wong ROL (2008) Developmental patterning of glutamatergic synapses onto retinal ganglion cells. *Neural Dev* 3:8. <https://doi.org/10.1186/1749-8104-3-8>
8. Okawa H, Santina Della L, Schwartz GW et al (2014) Interplay of cell-autonomous and non-autonomous mechanisms tailors synaptic connectivity of converging axons in vivo. *Neuron* 82:125–137. <https://doi.org/10.1016/j.neuron.2014.02.016>
9. Della Santina L, Inman DM, Lupien CB et al (2013) Differential progression of structural and functional alterations in distinct retinal ganglion cell types in a mouse model of glaucoma. *J Neurosci* 33:17444–17457. <https://doi.org/10.1523/JNEUROSCI.5461-12.2013>
10. Bleckert A, Parker ED, Kang Y et al (2013) Spatial relationships between GABAergic and glutamatergic synapses on the dendrites of distinct types of mouse retinal ganglion cells across development. *PLoS One* 8:e69612. <https://doi.org/10.1371/journal.pone.0069612>
11. Soto F, Bleckert A, Lewis R et al (2011) Coordinated increase in inhibitory and excitatory synapses onto retinal ganglion cells during development. *Neural Dev* 6:31. <https://doi.org/10.1186/1749-8104-6-31>

Anterograde Tract Tracing for Assaying Axonopathy and Transport Deficits in Glaucoma

Samuel D. Crish and Brett R. Schofield

Abstract

Whether to stage degeneration or investigate early pathology in glaucoma, examination of axonal structure and function is essential. There are a wide variety of methods available to investigators using animal models of glaucoma, with varying utilities depending on the questions asked. Here, we describe the use of anterograde neuronal tract tracing using cholera toxin B (CTB) for the determination of axon transport integrity of the retinofugal projection. This method reveals the structure of the retinal axons as well as the functional integrity of anterograde transport systems.

Key words Axonopathy, Axonal transport, Neuronal tracing, Optic nerve, Superior colliculus

1 Introduction

Glaucoma blinds through the dysfunction and degeneration of the projection cells of the eye, the retinal ganglion cells (RGCs). Information from the retina is transmitted to brain targets along RGC axons that comprise the optic nerve (prechiasm) and optic tract (postchiasm). As in other parts of the nervous system, axons are uniquely susceptible to stressors and disease processes [1]. Examining pathological changes in axon structure and function is important for identifying new targets for intervention as well as useful as an outcome measure for the determination of the amount of progression of pathology. Use of exogenously applied dyes for neuronal tract tracing has been a valuable tool for investigating the nervous system in health and disease for over half a century [2]. As such, there are a wide variety of techniques and analyses available to the investigator interested in using tract tracing in glaucoma. The retinofugal pathway is an ideal projection for using tract tracing, lacking many of the common hurdles intrinsic to neuronal tracing such as fibers-of-passage taking up tracer, injection site determination, etc. Most of the techniques take advantage of axonal transport: an active, tightly regulated process that shuttles

cargo along the axon. Axonal transport is an early dysfunction in glaucoma that likely drives the eventual axonal and somatic degeneration [3, 4]. Axonal transport occurs in both the anterograde and retrograde directions. Moreover, different molecular mechanisms are involved, and previous studies have shown that anterograde and retrograde transport becomes deficient at different stages of glaucoma [4]. This chapter will focus on using a common tracer, cholera toxin B (CTB), to assay anterograde transport from the eye to the superior colliculus (SC) in mice. This method is easily modified for other specific uses *see* also **Note 1**.

The superior colliculus is the most common target for tracing analysis in glaucoma [3–7] and other visual system pathologies [8–10]. It is a multilayered structure in the brainstem that receives sensory information from multiple modalities. For our purposes, we will be focusing on the “superficial” SC, the three most dorsal layers that receive a direct retinal projection. Neurons in the deeper layers respond to visual stimuli but receive their input from extraretinal sources [11]. There are two commonly used naming systems for the layers of the SC. The first uses the Latin (or its anglicized versions) nomenclature with the three superficial layers being (going dorsal to ventral) stratum zonale (SZ), stratum griseum superficiale (SGS), and stratum opticum (SO). We will use the numbered nomenclature of Wiener [12] of layers I (SZ), II (SGS), and III (SO). Layers I and II are gray matter, containing the retinorecipient neurons and interneurons. In most rodents, layer I is very thin, only a cell layer or two in depth, and often ignored. Layer III is white matter and consists almost entirely of RGC axons. The contralateral retina sends a dense projection through layer III to layers I and II across their entire breadth and length, with the exception of a small area representing the optic disc [5]. The sparse ipsilateral projection is located in patches at the deepest locations of layer II and in layer III, distinguishing this input from the contralateral projection. There are several advantages to assaying the SC in glaucoma. First, in mouse and rat, nearly all (>95%) retinal ganglion cells (RGC) project here [13–18], the projection is nearly entirely contralateral, and the projection forms a well-defined retinotopic map [19, 20], *see* also **Note 2**. Hence, each collicular lobe can be thought of as a map of contralateral retina; this is especially useful in sectorial degenerations such as glaucoma. Furthermore, unlike other retinotopic maps in the brain, the SC of rats and mice exhibits only mild anisotropy or magnification of different retinal subregions [19–21], making quantification of the extent of functional/structural loss and correlation between “gaps” in the tracer label and location of the source RGCs in the eye relatively straightforward. Finally, the SC is the farthest target from the eye, particularly relevant given the recent interest in distal axonopathy [3, 22]; note that these two manuscripts use opposite

terminology, Schlamp's proximal and distal are with respect to the brain, ours is with respect to the cell body.

We use CTB almost exclusively because of its sensitivity, versatility, and presence of label in RGC somata and along their entire axon to their terminals in the brain [3, 23]. Our use of intrinsically fluorescent conjugates of CTB allows us to confidently determine presence or absence of tracer with minimal staining artifacts and background fluorescence. We also are able to combine fluoro-CTB tracing in four- and five-color immunofluorescence assays for determination of other aspects of RGC structure, signaling, gliosis, and interaction with postsynaptic targets [3–6] *see also Note 3*.

2 Materials

2.1 Tracer

Cholera toxin B (CTB) is commercially available alone or with various conjugates, including horseradish peroxidase, gold particles for electron microscopy, and a variety of fluorophores. In our labs, we use it conjugated to one of the Alexa Fluor dyes due to their brightness and photostability (ThermoFisher Scientific). It typically comes as a lyophilized powder and is reconstituted using sterile physiological saline to a concentration of 1 $\mu\text{g}/\mu\text{l}$ (0.1%). We recommend aliquotting and freezing this solution until needed; we typically make up 10 μl aliquots in 0.2 ml microcentrifuge tubes. Factors for choosing a particular conjugate include availability of imaging options (filter cubes and necessary light source). We typically use CTB-AlexaFluor-488 or CTB-AlexaFluor-647; these are readily viewed in the most common green or far-red channels of widefield or confocal microscopes.

2.2 Injection Materials

Injections may be made with either stainless steel needles on a Hamilton syringe or glass micropipettes attached to a micro- or nanosyringe pump. For mice and rats, we use steel needles almost exclusively due to the ease, speed, and slightly greater injection success rate but glass pipettes may be considered for specialized experiments requiring multiple intravitreal injections, etc.

CTB should be prepared with sterile saline. All injection instruments should be sterilized via autoclave before use.

1. Small hub removable stainless steel needles: 33 ga, 0.375" length, point style 2.
2. Hamilton syringe 802 RN 25 μl with reinforced plunger.
3. Curved forceps for proptosing the eye.

Drugs

1. Proparacaine drops (a topical local anesthetic used for the eye): proparacaine hydrochloride ophthalmic solution 0.5%.

2. Isoflurane (if using inhalation anesthesia).
3. Ophthalmic antibiotic (Neomycin 5 mg/g, Polymyxin B 10,000 U/g, or Bacitracin 400 U/g).

2.3 Tissue Harvesting, Processing, and Visualization

1. Perfusion apparatus [24] (*see* Gerfen [24] for details).
2. 1× Phosphate-Buffered Saline (0.01 M PBS, pH 7.4).
3. 10% Formalin in PBS.
4. Sucrose.
5. Small spatula.
6. Small rongeurs or small surgical scissors.
7. Fine forceps (#5 or similar).
8. Sliding microtome or cryostat.
9. Microscope slides, coverslips, mounting media.
10. Freezing storage buffer (need recipe).

3 Methods

The following description focuses on details specific to the eye injections and related processing. These basic protocols allow for two analytical options: microscopic assessment of transport or whole tissue assay of protein or RNA based on transport integrity.

3.1 Tracer Injection

1. Anesthetize the mouse with 2.5% isoflurane in the induction chamber and then transfer to nose cone. Use tail or toe pinch to assess depth of anesthesia. Apply a drop of proparacaine to the eye.
2. Using sterile technique, remove metal ferrule from the needle and attach the needle to the syringe, rinse thoroughly with sterile saline to remove any debris. Load 1.5 μ l of the CTB solution into the syringe (2 μ l for rats).
3. With one hand, use the forceps to proptose the eye until the sclera is visible. Hold the syringe with the other hand and insert the needle just below the margin (corneal limbus; junction between cornea and sclera) and angled slightly toward the posterior pole of the eye (Fig. 1).
4. Depress the plunger. We find it best to have another individual do this rather than trying to manipulate the syringe with one hand while the needle is in the eye.
5. Remove the needle and apply antibiotic ointment to the eye. Refill the syringe to inject the other eye if desired, then remove the mouse from anesthesia and allow it to recover. If different color tracers are being used we recommend using dedicated syringes for each. Depending on your needs, you may want to

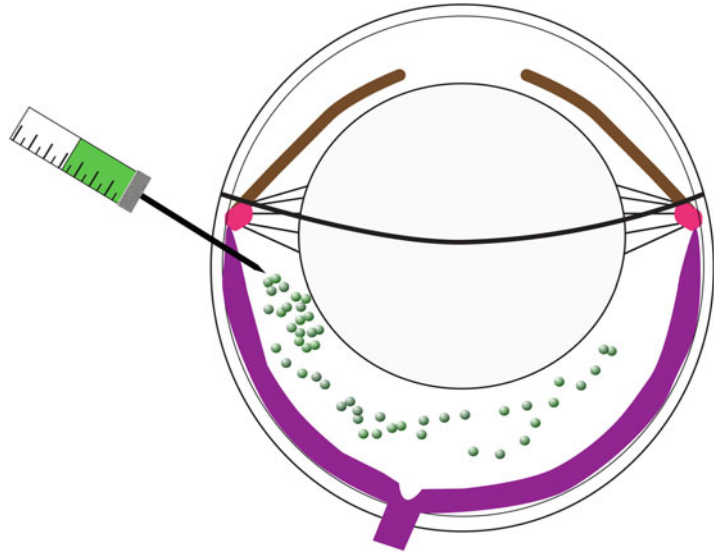


Fig. 1 Schematic section through the eye viewed from above showing the location of intravitreal injection of tracer

inject the same or different tracers in each eye. As the small ipsilateral retinal projection to the SC is distinguishable in rats and mice, we typically inject the same color tracer in each eye to free up an additional channel for immunofluorescence. Injections of a different color fluorophore in each eye can be used to easily distinguish output from each eye [25].

3.2 Tissue Harvesting

For retinofugal tracing, survival periods are typically 48–72 h. After this time period the mouse may undergo cervical dislocation or decapitation for visualization of axonal transport in fresh, unfixed tissue (*see* Fig. 2) or transcardially perfused for histology (*see* [24] for transcardial perfusion and brain removal).

1. Depending on the study, you may want to enucleate the eyes before or after brain removal. Enucleation with scissors before brain removal will leave the optic nerves (ON) attached to the brain with no fat or connective tissue attached; they may then be separated and prepared as desired. If preservation of the entire optic nerve head (ONH) is of interest, the brain should be dissected before the eyes. Before the removal of the brain from the cranial cavity the optic nerves may be cut near the chiasm, the entire optic nerve and eyes may then be removed together (careful enucleation before brain removal can result in an intact ONH, but we feel that there is too tight a margin for error if the entire ONH is desired. Here, we remove the brain first). To remove the brain for the preservation of the eye/-ONH/ON complex, work forward from the foramen magnum using rongeurs or surgical scissors and forceps to remove the

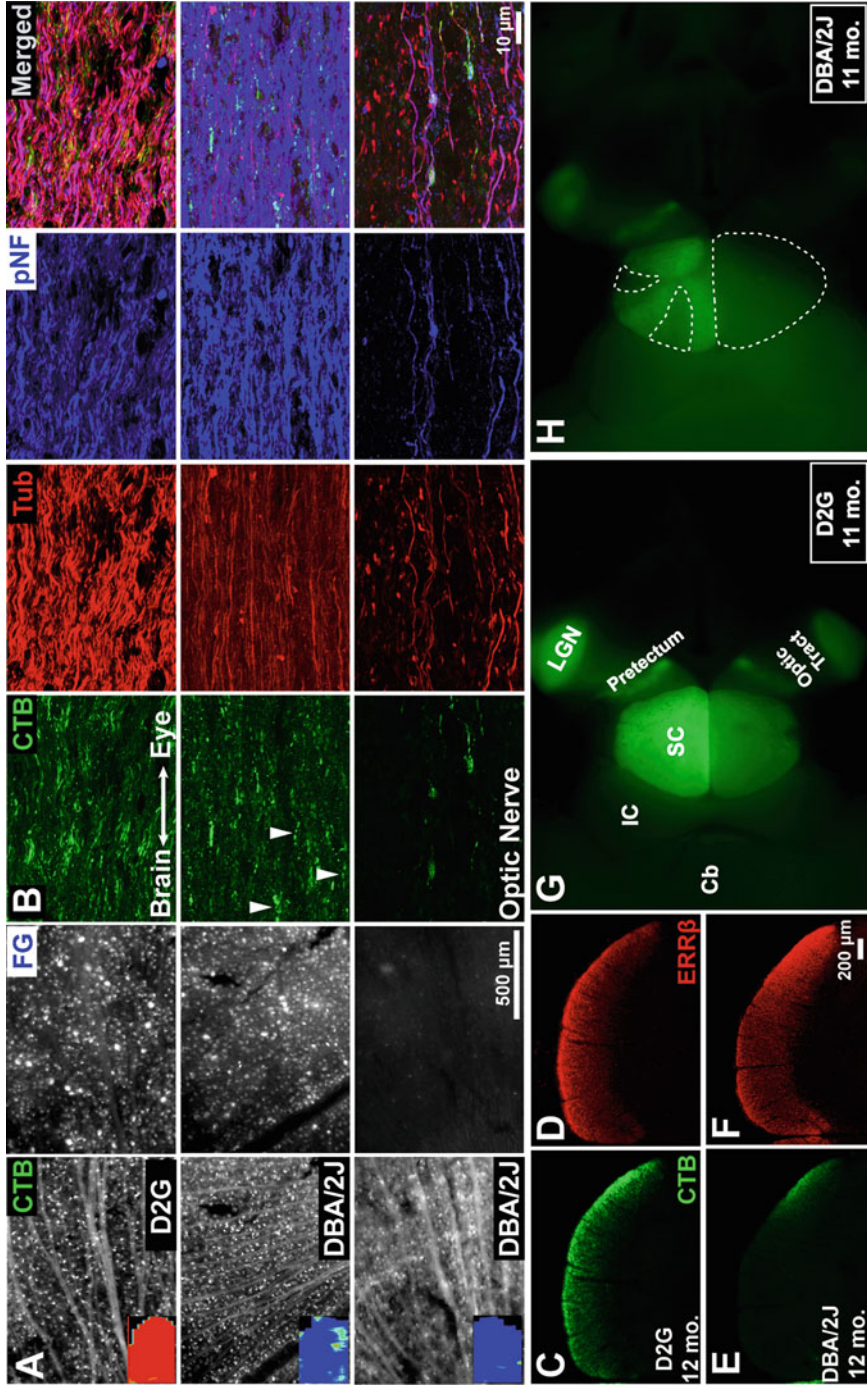


Fig. 2 Anterogradely transported fluoro-CTB in the retina and its projection (we used CTB conjugated to Alexa Fluor 488; ThermoFisher). **(A)** CTB + RGCs and axons are easily visualized in whole mount preparations and can be compared to retrograde tracing with fluorogold (FG) in the same projection. **(B)** Longitudinal sections of optic nerve show CTB colocalization with axoskeletal proteins β -tubulin and neurofilament-heavy in control nerves (*top row*). Glaucomatous optic nerves in this particular study showed reductions in CTB and β -tubulin and increased neurofilament (*second row*) before eventual degeneration (*third row*). **(C and D)** are fluorescent micrographs of coronal sections through midbrain showing anterogradely transported CTB and the RGC projection marker estrogen-related receptor-beta in control **(C and D)** and glaucomatous **(E and F)** superior colliculi. In these examples, we reported axonal transport integrity decreases before the RGC projection marker, suggesting a functional deficit. **(G and H)** shows whole mount preparations of brain with cerebrum removed to visualize retinal targets. **(H)** shows normal CTB label in the lateral geniculate nucleus (LGN), optic tract, pretectum, and superior colliculus (SC). **(G)** shows sectorial loss in the *left* SC (*top lobe*) and complete loss in the *right* lobe (*bottom lobe*) following injections of CTB-AF488 into both eyes. Inferior colliculus (IC) and cerebellum (Cb) are labeled for orientation. **A-F** are adapted from [4]; **G and H** are adapted from [7]

dorsal and lateral skull, gently lift the brain using forceps or a spatula to expose the cranial nerves on the ventral surface of the brain. Cut the large trigeminal nerves and optic nerves (if eyes are still in place) and lift the brain out of the skull. The eye and ON may then be dissected out whole from the skull.

2. If fluorescent tracers are used (as we are using here), transport to the brain may be visualized in a whole mount preparation after dissection (either fresh or perfusion-fixed methods are used). Carefully remove the overlying cortex with a spatula, then visualize the superior colliculus under an epifluorescence microscope (Fig. 2). We use an Axiozoom V16 microscope (Zeiss, Jena, Germany) because of the long working distance, but in the past we have used low power objectives on a standard compound fluorescence microscope by carefully removing the ventral portions of the brain [5, 26]. At this point tissue (typically the superior colliculus) may be microdissected into “transport-intact” or “transport-deficient” regions for further analysis (e.g., RNA/protein assays in fresh tissue [5, 6] or for the preparation for specialized histological preparation in fixed tissue, such as electron microscopy [7]).
3. In these cases, the retinas should also be removed for the determination of injection success as even experienced investigators have the occasional failed injection. Retinas should be prepared as whole mounts [27]. They may be briefly visualized or imaged for fluoro-CTB before any desired immunochemical or other processing techniques.
4. For standard light microscopy studies, postfix the brain in 10% formalin overnight, then overnight in 20% sucrose/PBS. The following day block the brain (with or without cortex, there is no direct retinal projection to these areas) through the cerebellum and rostral to the optic chiasm. Freeze on the microtome stage and take 50 μm coronal sections, removing them from the blade with a paintbrush into PBS if using them within a week or into freezing storage buffer if not (*see* http://www.ihcworld.com/_protocols/histology/cryoprotectant.htm). Periodically make a hole in the tegmentum on one side with a needle to keep track of sides. A lab should always mark the same side to prevent confusion across lab members.
5. Because CTB is readily visible in neuronal somata and along the axon, optic nerves and retinas may be analyzed. Retinas may be prepared as whole mounts or sectioned. We have found Alexa Fluor-conjugated CTB retains its fluorescence after paraffin embedding but, for combining with immunofluorescence, we prefer frozen sectioning to preserve antigenicity. Cross- or longitudinal sections may be taken of optic nerves on a sliding microtome or cryostat. For longitudinal sections, a frozen

sucrose/PBS platform is prepared on the freezing stage by freezing some of the sucrose/PBS solution on the stage and then cutting it down to a flat surface with the microtome blade. This ensures a cutting plane in line with blade travel. Whole optic nerve is then placed on a slide and deposited on this ice platform using slight pressure on the slide to keep the ON flat. 10–20 μm sections are taken and removed from the blade using fine forceps or a paintbrush. Mouse ON cross-sections are able to be taken on a sliding microtome [28] but handling is more difficult than using a cryostat or paraffin histology.

3.3 Analysis of the Retinocollicular Projection

1. Sections through the midbrain may be stained using standard immunofluorescence techniques [3–5] (Fig. 2). Sections are then mounted on microscope slides and coverslipped with Fluoromount-G. We typically mount every other section in a series for a high-resolution representation of the collicular retinotopic map but fewer sections may be used depending on the study. Sections containing SC are then imaged with an epifluorescence microscope (a 4 or 5 \times objective typically can contain an entire side of the SC in the field of view on a typical compound microscope and camera).
2. Sections are then analyzed. Depending on the question, several programs are able to perform analysis. We use a custom macro in ImageJ [4] *see* **Note 4** for the full macro. Copy into a text file and place in the Macros subfolder in the ImageJ Program File Folder.
3. Running and using the ImageJ macro
 - (a) Open the image. Launch the macro (either press “c” or select it under “Plugins”). Follow the prompted commands.
 - (b) Select an area of non-retinorecipient brain for thresholding.
 - (c) Outline the superficial superior colliculus (you can use the shape of the structure and the slight autofluorescence of layer III for guidance). Do not connect the starting and end points of your polygon.
 - (d) Select bin size (how detailed of a representation is needed); this is based on your individual needs. The program will then assign each pixel a binary value; either above (1) or at/below (0) background. Figure 3 represents the major steps of the process.
 - (e) The data are then exported to Excel, listing bin, number of labeled pixels in each bin, total pixels in each bin, and the ratio between them (i.e., percentage of pixels that were above threshold). Typically, for disorders of the visual system, a percent area fraction (the ratio of labeled pixels over total number of pixels) is quantified and/or plotted (retinal ischemia: [8]; experimental glaucoma:

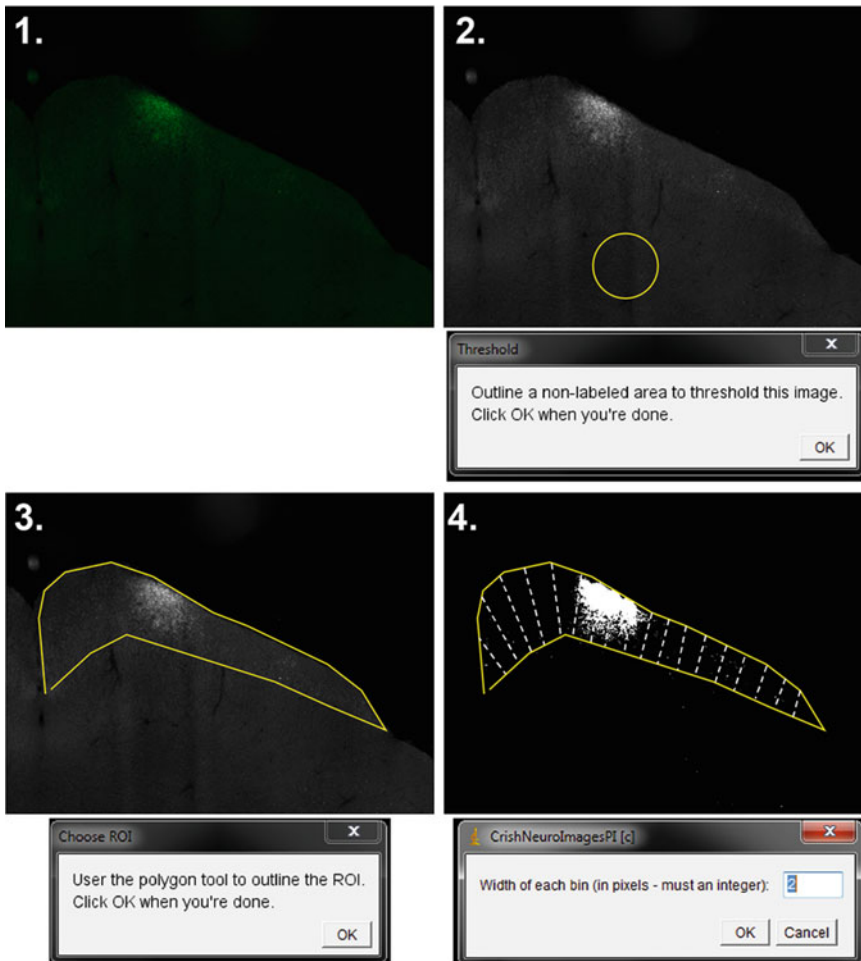


Fig. 3 Schematic of the initial steps of topographical percent area fraction plotting. (1) Original image of coronal section through the midbrain of a DBA/2 J mouse with extensive loss of retinofugal tracing (*Green* fluorescence is CTB label from the corresponding retina). (2) Thresholding based on non-retinorecipient brain areas. (3) Outline of superficial SC. (4) The macro creates bins along the medial-lateral extent of the section. These bins are only representative for illustration in the figure. They would typically be much narrower

[3, 4]; diabetic retinopathy: [9, 10]). Sections may be graphed individually or a number of sections may be aligned in a colorimetric representation for retinotopic map analysis [3, 4]. We use Origin for heat map creation. For models with classic sectorial loss, we have found good agreement between the ratio totals for the entire collicular lobe vs. sectorial loss measured as a percentage using the colorimetric maps (see notes for a discussion on magnification of the retinotopic map).

4 Notes

1. *Why assess anterograde transport?* While many experiments use retrograde tracing from the SC to examine the RGC population, this method is unsuitable for studying many axonopathy or axon transport questions. Among other reasons, it is difficult to assay how much of any tracing deficit is due to dysfunctional transport, axon loss, the extent of any axon loss, etc. Furthermore, most collicular injections of tracers such as fluorogold (FG—the most commonly used tracer for these experiments) can result in extensive damage to the SC. While this does not seem to affect RGC tracing, it does preclude collicular analysis for retinal ganglion cell structures, although we recently were able to successfully combine both types of tracing in a mouse model of glaucoma by performing multiple injections into the overlying cortex and allowing FG to diffuse into the SC [4].

Using anterograde tracing with CTB allows easy determination of uptake and transport in the retina. In fact, when transport issues do occur, one may visualize the point of blockage in the optic nerve, optic tract, or brain targets themselves [3]. There is no apparent damage to either the retina or its brain targets. The full projection, from cell body to axon terminals, is able to be visualized. These characteristics allow detailed correlation of structures for combination with other histological techniques or microdissection for protein and RNA determination [6].

A major caveat is that *in vivo* neuronal tracing is not simply an axon marker. While uptake may be active or passive, *in vivo* tracing requires functional active anterograde transport. Even the so-called passive tracers such as the carbocyanines (DiI, DiA, etc.) incorporate into vesicles and are actively transported *in vivo*; passive diffusion along the membrane only occurs across short distances [29]. While we have taken advantage of tracers' requiring active processes for tracing to determine functional deficits in axonal transport, investigators desirous of examining axon structure in neurodegeneration should combine tracing with immunochemical methodologies (*see* [3] for example) or transgenic mice that exhibit fluorescent reporters along the projection [30–33].

2. *Why the superior colliculus?* There are multiple advantages to using the SC as the structure of interest for analyzing axonopathy and axonal transport deficits in the retinal projection.

First is that nearly all RGCs project to this structure. A common percentage cited for RGCs projecting to the SC in mice is 70%. This is based on Hofbauer and Dräger's [34] manuscript using HRP injections into the mouse superior colliculus [34]. The authors state in the abstract and later in the

discussion that they are very likely underestimating this percentage, but this point is often overlooked. Other work by Linden and Perry [13] found over 90% of RGCs projected to the SC in the rat [13] and recent work by Vidal-Sanz's group that specifically investigated this question using various tracing methodologies put the percentage at 95% or more in mouse and rat [14–18]. Our results with retrograde tracers support the conclusion that 95% or more of the RGCs in mice project to the SC. Thus, assessment of retinal projections to the SC is unlikely to miss a significant population of RGCs.

In addition, the SC has a highly ordered retinotopic map with most of the axons decussating at the optic chiasm. As such, each SC projection can be thought of as a map of contralateral retina, allowing simple and direct assessment of axonal transport in relation to retinal sector (and corresponding visual field). As stated above, the small ipsilateral projection in mouse and rat is easily distinguished.

3. *Why use CTB?* While tracers are thought of as interchangeable to many investigators, they actually have different uptake and transport characteristics important when considering their utility for glaucoma research.

CTB is a sensitive bidirectional tracer that has been used for retinofugal tracing since the mid-1990s [23]. Except in advanced pathology, it is selectively taken up by retinal ganglion cells. As it requires active uptake and packaging mechanisms, it can be used as a rough indicator of the presence of semifunctional RGCs. Its selectivity also allows for easy determination of injection success—even the best hands have the occasional “miss.” Even if only the brain and/or optic nerve is being investigated it is imperative to examine the retina to exclude defective injections. These are evident by either complete absence of CTB in the retina, vasculature-only label, or diffuse, non-cellular label due to an errant intra-retinal injection. When using a fluorescent tracer, whole mount retinas may be examined under epifluorescence—cell bodies and axons are typically visible with CTB+ astrocytes becoming evident after extensive RGC loss (at least in the DBA/2 J mouse model of glaucoma).

CTB is anterogradely transported down all or nearly all axons. Other common anterograde tracers may not label all axons (or all their branches) and may only label terminals. For example, we were unable to detect label in the retinal projection to the suprachiasmatic nucleus in naked mole-rats using peroxidase-labeled wheat germ agglutinin (WGA-HRP) but CTB tracing labeled a dense retinal projection to that structure [35]. Others have reported that other tracers, such as dextrans, only label a small subset of RGC axons [23]. Given the subtle

axon modifications that occur in glaucoma, this is not to be taken lightly; one could easily attribute a loss of transport to pathology when in fact it could result from limitations of the tracer employed.

Finally, CTB is strictly monosynaptic. While we have used tracers with transynaptic properties, they have very limited use for assaying the primary retinal projection; following the interconnections of the retinal targets would be very difficult.

4. *Full text for the ImageJ SC Analysis Macro*

```
macro "CrishNeuroImagesPI [c]" {
  title=getTitle();
  rename(title + "_annotated");
  title=getTitle();
  // Change mode to 16 bit gray scale
  selectWindow(title);
  run('16-bit');
  // Ask user to outline a black area for thresholding
  setTool("oval");
  waitForUser("Threshold",
  "Outline a non-labeled area to threshold this image.\n\nClick
  OK when you're done.");
  getStatistics(foo1,foo2,foo3,ThresholdMax);
  // Ask user to delineate the ROI
  setTool("polygon");
  waitForUser("Choose ROI",
  "User the polygon tool to outline the ROI."+
  "\n\nClick OK when you're done.");
  // Get the selection bounds and then create a clipping mask
  getSelectionBounds(xmin,ymin,selWdth,selHght);
  run("Create Mask");
  // Use the mask to clip the image to just the ROI
  selectWindow("Mask");
  run("Create Selection");
  if (getInfo('os.name')!='Mac OS X') {
  run("Make Inverse");
  }
  run("Copy"); close();
  run("Paste");
  // Query the user for the number of bins
  BinSpan=getNumber('Width of each bin (in pixels - must an
  integer):',2);
  nBins=round(selWdth/BinSpan);
  // For loop to divide the image into bins and get the mean
  pixel value out of them
  hght=getHeight(); setColor(255,255,255);
  for (i=1; i<=nBins; i++) {
```

```

xLeft=round(xmin+BinSpan*(i-1));
xRight=round(xmin+BinSpan*i);
// drawLine(xRight,0,xRight,hght);
nLabelled=0; nPixels=0;
for (x=xLeft; x&lt;=xRight; x++) {
for (y=0; y&lt;=hght; y++) {
Pixel=getPixel(x,y);
if (Pixel&gt;0) nPixels=nPixels+1;
if (Pixel&gt;ThresholdMax) nLabelled=nLabelled+1;
}
}
RelativeDensity=nLabelled/nPixels;
setResult("Bin",i-1,i);
setResult("Norm. Int.",i-1,RelativeDensity);
setResult("xLeft",i-1,xLeft);
setResult("xRight",i-1,xRight);
setResult("nLabelled",i-1,nLabelled);
setResult("nPixels",i-1,nPixels);
}
// Save results as tab-delimited text
saveAs("Results");
}

```

References

1. Crish SD, Calkins DJ (2011) Neurodegeneration in glaucoma: progression and calcium-dependent intracellular mechanisms. *Neuroscience* 176:1–11. <https://doi.org/10.1016/j.neuroscience.2010.12.036>
2. Lanciego JL, Wouterlood FG (2011) A half century of experimental neuroanatomical tracing. *J Chem Neuroanat* 42(3):157–183. <https://doi.org/10.1016/j.jchemneu.2011.07.001>
3. Crish SD, Sappington RM, Inman DM, Horner PJ, Calkins DJ (2010) Distal axonopathy with structural persistence in glaucomatous neurodegeneration. *Proc Natl Acad Sci U S A* 107(11):5196–5201. <https://doi.org/10.1073/pnas.0913141107>
4. Dengler-Crish CM, Smith MA, Inman DM, Wilson GN, Young JW, Crish SD (2014) Anterograde transport blockade precedes deficits in retrograde transport in the visual projection of the DBA/2J mouse model of glaucoma. *Front Neurosci* 8:290. <https://doi.org/10.3389/fnins.2014.00290>
5. Crish SD, Dapper JD, MacNamee SE, Balaram P, Sidorova TN, Lambert WS, Calkins DJ (2013) Failure of axonal transport induces a spatially coincident increase in astrocyte BDNF prior to synapse loss in a central target. *Neuroscience* 229:55–70. <https://doi.org/10.1016/j.neuroscience.2012.10.069>
6. Wilson GN, Inman DM, Dengler Crish CM, Smith MA, Crish SD (2015) Early pro-inflammatory cytokine elevations in the DBA/2J mouse model of glaucoma. *J Neuroinflammation* 12:176. <https://doi.org/10.1186/s12974-015-0399-0>
7. Smith MA, Xia CZ, Dengler-Crish CM, Fening KM, Inman DM, Schofield BR, Crish SD (2016) Persistence of intact retinal ganglion cell terminals after axonal transport loss in the DBA/2J mouse model of glaucoma. *J Comp Neurol* 524(17):3503–3517. <https://doi.org/10.1002/cne.24012>
8. Aviles-Trigueros M, Mayor-Torroglosa S, Garcia-Aviles A, Lafuente MP, Rodriguez ME, Miralles de Imperial J, Villegas-Perez MP, Vidal-Sanz M (2003) Transient ischemia of the retina results in massive degeneration of the retinotectal projection: long-term neuroprotection with brimonidine. *Exp Neurol* 184(2):767–777. [https://doi.org/10.1016/S0014-4886\(03\)00298-X](https://doi.org/10.1016/S0014-4886(03)00298-X)

9. Fernandez DC, Pasquini LA, Dorfman D, Aldana Marcos HJ, Rosenstein RE (2012) Ischemic conditioning protects from axoglial alterations of the optic pathway induced by experimental diabetes in rats. *PLoS One* 7 (12):e51966. <https://doi.org/10.1371/journal.pone.0051966>
10. Fernandez DC, Pasquini LA, Dorfman D, Aldana Marcos HJ, Rosenstein RE (2012) Early distal axonopathy of the visual pathway in experimental diabetes. *Am J Pathol* 180 (1):303–313. <https://doi.org/10.1016/j.ajpath.2011.09.018>
11. May PJ (2006) The mammalian superior colliculus: laminar structure and connections. *Prog Brain Res* 151:321–378. [https://doi.org/10.1016/S0079-6123\(05\)51011-2](https://doi.org/10.1016/S0079-6123(05)51011-2)
12. Wiener SI (1986) Laminar distribution and patchiness of cytochrome oxidase in mouse superior colliculus. *J Comp Neurol* 244(2):137–148. PubMed PMID: 3005379
13. Linden R, Perry VH (1983) Massive retinotectal projection in rats. *Brain Res* 272 (1):145–149
14. Salinas-Navarro M, Mayor-Torroglosa S, Jimenez-Lopez M, Aviles-Trigueros M, Holmes TM, Lund RD, Villegas-Perez MP, Vidal-Sanz M (2009) A computerized analysis of the entire retinal ganglion cell population and its spatial distribution in adult rats. *Vision Res* 49(1):115–126. <https://doi.org/10.1016/j.visres.2008.09.029>
15. Salinas-Navarro M, Jimenez-Lopez M, Valiente-Soriano FJ, Alarcon-Martinez L, Aviles-Trigueros M, Mayor S, Holmes T, Lund RD, Villegas-Perez MP, Vidal-Sanz M (2009) Retinal ganglion cell population in adult albino and pigmented mice: a computerized analysis of the entire population and its spatial distribution. *Vision Res* 49 (6):637–647. <https://doi.org/10.1016/j.visres.2009.01.010>
16. Nadal-Nicolas FM, Jimenez-Lopez M, Sobrado-Calvo P, Nieto-Lopez L, Canovas-Martinez I, Salinas-Navarro M, Vidal-Sanz M, Agudo M (2009) Brn3a as a marker of retinal ganglion cells: qualitative and quantitative time course studies in naive and optic nerve-injured retinas. *Invest Ophthalmol Vis Sci* 50 (8):3860–3868. <https://doi.org/10.1167/iovs.08-3267>
17. Nadal-Nicolas FM, Jimenez-Lopez M, Salinas-Navarro M, Sobrado-Calvo P, Albuquerque-Bejar JJ, Vidal-Sanz M, Agudo-Barriuso M (2012) Whole number, distribution and co-expression of brn3 transcription factors in retinal ganglion cells of adult albino and pigmented rats. *PLoS One* 7(11):e49830. <https://doi.org/10.1371/journal.pone.0049830>
18. Galindo-Romero C, Aviles-Trigueros M, Jimenez-Lopez M, Valiente-Soriano FJ, Salinas-Navarro M, Nadal-Nicolas F, Villegas-Perez MP, Vidal-Sanz M, Agudo-Barriuso M (2011) Axotomy-induced retinal ganglion cell death in adult mice: quantitative and topographic time course analyses. *Exp Eye Res* 92 (5):377–387. <https://doi.org/10.1016/j.exer.2011.02.008>
19. Siminoff R, Schwassmann HO, Kruger L (1966) An electrophysiological study of the visual projection to the superior colliculus of the rat. *J Comp Neurol* 127(4):435–444. <https://doi.org/10.1002/cne.901270402>
20. Dräger UC, Hubel DH (1976) Topography of visual and somatosensory projections to mouse superior colliculus. *J Neurophysiol* 39 (1):91–101
21. Stein BE, Meredith MA (1993) *The merging of the senses*. MIT Press, Cambridge, MA
22. Schlamp CL, Li Y, Dietz JA, Janssen KT, Nickells RW (2006) Progressive ganglion cell loss and optic nerve degeneration in DBA/2J mice is variable and asymmetric. *BMC Neurosci* 7:66. <https://doi.org/10.1186/1471-2202-7-66>
23. Angelucci A, Clasca F, Sur M (1996) Anterograde axonal tracing with the subunit B of cholera toxin: a highly sensitive immunohistochemical protocol for revealing fine axonal morphology in adult and neonatal brains. *J Neurosci Methods* 65(1):101–112
24. Gerfen CR (1997) Neuroanatomical methods. In: Gerfen CR, Rogawski MA, Sibley DR, Skolnick P, Wray S (eds) *Current protocols in neuroscience*. John Wiley & Sons, Hoboken, NJ, pp Unit 1.1.1–Unit 1.1.11
25. Hunt DL, King B, Kahn DM, Yamoah EN, Shull GE, Krubitzer L (2005) Aberrant retinal projections in congenitally deaf mice: how are phenotypic characteristics specified in development and evolution? *Anat Rec A Discov Mol Cell Evol Biol* 287(1):1051–1066. <https://doi.org/10.1002/ar.a.20251>
26. Crish SD, Comer CM, Marasco PD, Catania KC (2003) Somatosensation in the superior colliculus of the star-nosed mole. *J Comp Neurol* 464(4):415–425. <https://doi.org/10.1002/cne.10791>
27. Ullmann JF, Moore BA, Temple SE, Fernandez-Juricic E, Collin SP (2012) The retinal wholemount technique: a window to understanding the brain and behaviour. *Brain*

- Behav Evol 79(1):26–44. <https://doi.org/10.1159/000332802>
28. Cooper ML, Crish SD, Inman DM, Horner PJ, Calkins DJ (2016) Early astrocyte redistribution in the optic nerve precedes axonopathy in the DBA/2J mouse model of glaucoma. *Exp Eye Res* 150:22–33. <https://doi.org/10.1016/j.exer.2015.11.016>
 29. Kobbert C, Apps R, Bechmann I, Lanciego JL, Mey J, Thanos S (2000) Current concepts in neuroanatomical tracing. *Prog Neurobiol* 62(4):327–351
 30. Raymond ID, Vila A, Huynh UC, Brecha NC (2008) Cyan fluorescent protein expression in ganglion and amacrine cells in a thy1-CFP transgenic mouse retina. *Mol Vis* 14:1559–1574
 31. Dratviman-Storobinsky O, Hasanreisoglu M, Offen D, Barhum Y, Weinberger D, Goldenberg-Cohen N (2008) Progressive damage along the optic nerve following induction of crush injury or rodent anterior ischemic optic neuropathy in transgenic mice. *Mol Vis* 14:2171–2179
 32. Huberman AD, Wei W, Elstrott J, Stafford BK, Feller MB, Barres BA (2009) Genetic identification of an On-Off direction-selective retinal ganglion cell subtype reveals a layer-specific subcortical map of posterior motion. *Neuron* 62(3):327–334. <https://doi.org/10.1016/j.neuron.2009.04.014>
 33. Kim IJ, Zhang Y, Meister M, Sanes JR (2010) Laminar restriction of retinal ganglion cell dendrites and axons: subtype-specific developmental patterns revealed with transgenic markers. *J Neurosci* 30(4):1452–1462. <https://doi.org/10.1523/JNEUROSCI.4779-09.2010>
 34. Hofbauer A, Dräger UC (1985) Depth segregation of retinal ganglion cells projecting to mouse superior colliculus. *J Comp Neurol* 234(4):465–474. <https://doi.org/10.1002/cne.902340405>
 35. Crish SD, Dengler-Crish CM, Catania KC (2006) Central visual system of the naked mole-rat (*Heterocephalus Glaber*). *Anat Rec A Discov Mol Cell Evol Biol* 288(2):205–212. <https://doi.org/10.1002/ar.a.20288>

In Vitro and In Vivo Methods for Studying Retinal Ganglion Cell Survival and Optic Nerve Regeneration

Yuqin Yin and Larry I. Benowitz

Abstract

Glaucoma is marked by a progressive degeneration of the optic nerve and delayed loss of retinal ganglion cells (RGCs), the projection neurons of the eye. Because RGCs are not replaced and because surviving RGCs cannot regenerate their axons, the visual loss in glaucoma is largely irreversible. Here, we describe methods to evaluate treatments that may be beneficial for treating glaucoma using in vitro cell culture models (immunopanning to isolate neonatal RGCs, dissociated mature retinal neurons, retinal explants) and in vivo models that test potential treatments or investigate underlying molecular mechanisms in an intact system. Potentially, use of these models can help investigators continue to improve treatments to preserve RGCs and restore visual function in patients with glaucoma.

Key words Retina, Retinal ganglion cells, Optic nerve, Glaucoma, Cell culture, Explants, Trophic factors, Axon regeneration, Cell signaling mechanisms, Quantitative methods

1 Introduction

Like most pathways in the mature central nervous system (CNS), the optic nerve cannot regenerate if injured [1]. Consequently, victims of traumatic, ischemic, or degenerative optic nerve damage suffer lifelong visual losses. Retinal ganglion cells (RGCs), the projection neurons of the eye, show little ability to extend axons distal to the site of nerve damage and begin to die after a few days [2]. Over the past few decades, many studies have identified factors that suppress or promote RGC survival and optic nerve regeneration. These studies have been motivated by the centrality of vision in our lives, the high prevalence of disorders that affect vision, and the likelihood that factors and pathways discovered using the optic nerve as a model system will afford insights into mechanisms to enhance regeneration in other parts of the CNS. Of particular relevance here is the significance of this research to glaucoma. Visual loss in glaucoma is most commonly associated with elevated intraocular pressure (IOP) which, in current thinking, leads to

changes in astrocytes and inflammatory cells at the lamina cribrosa/optic nerve head that impair axonal function and ultimately lead to RGC death [3–5]. Whereas glaucoma therapy primarily aims at decreasing intraocular pressure, this approach fails to slow disease progression in many patients and does not protect RGCs that have begun to die nor does it restore axonal function. Consequently, glaucomatous loss of vision remains irreversible, and early detection and treatment are of great importance. The methods described below enable the investigator to evaluate agents that are neuroprotective for RGCs and/or that promote axon regeneration in cases in which the cell bodies are still viable. Hopefully, these methods will enable us to discover better ways to reverse optic nerve damage and restore the transmission of information from the eye to the brain.

1.1 *In Vitro Methods*

Many studies aimed at identifying factors that promote RGC survival and axon regeneration, or investigating the mechanisms that underlie the effects of such factors, begin with in vitro experiments. Three in vitro methods have been used to study RGC survival and axon outgrowth: purified neonatal RGC cultures, mixed adult retinal cell cultures, and retinal explants.

Purified RGC cultures: This method uses young postnatal RGCs (prior to P12) and enables one to investigate the direct effects of various factors on RGCs in the absence of other cell types. However, this method is not suitable for studying adult RGCs due to the low survival of mature RGCs after purification.

RGCs are purified from a whole retina cell suspension through “immunopanning,” a two-step method that utilizes antibody-mediated plate adhesion. This procedure yields a highly pure population of RGCs (>99%), with a recovery rate ranging from 25% to 50% depending on the vigor used in the washing step and other factors. This technique was first used in rat RGC purification and has been modified for mouse RGCs as well. Immunopanning RGCs was developed by Barres [6] and modified by others.

Mixed RGC cultures: Although purified adult RGCs do not survive well in culture, they survive well in mixed retinal cultures, enabling one to investigate factors and signaling pathways that promote RGC survival and/or axon regeneration [7, 8]. In order to distinguish RGCs from other retinal cells, RGCs are pre-labeled by retrograde transport of a dye (usually Fluorogold) injected into the superior colliculus 1 week prior to preparing the culture. Mixed retinal cultures are mostly derived from rats, although some groups have recently begun to use mouse retinas. In this case, one can use mice in which RGCs are labeled genetically [9].

Retinal explant culture: Retinal explant cultures can be viewed as a model that is intermediate between dissociated retinal cell cultures and the in vivo model. Retinal explants have been used to study processes such as retinal differentiation [10], neurodegeneration

[11], and neurite outgrowth [12]. The major advantage of explant cultures is that cells are maintained within a semi-normal environment, with preservation of cell-cell interactions, while maintaining a higher level of experimental control than in animal models [13]. Thus, retinal explant cultures provide a good platform for the identification and validation of novel neuroprotective or pro-regenerative factors. In general, however, they do not allow one to conclude that any observed effects are due to the direct action of agents on RGCs.

Neurite outgrowth from the explants is commonly visualized by phase microscopy or fluorescent immunostaining. A disadvantage of the former is that no objective distinction can be made between the glial and neuronal processes, which can lead to inaccurate assessments of neurite outgrowth. This distinction can be made using antibodies to neuron-specific markers such as β 3-tubulin or neurofilament proteins, although there can still be a question as to the identity of the neurons from which the neurites originate. Use of transgenic animals that express a fluorescent protein in RGCs, such as Thy1-YFP mice [9], may allow for better identification of RGC axons provided that levels of Thy1 promoter activity, and thus of YFP expression, do not decline appreciably as a result of retinal dissection and the inevitable transection of RGC axons [14, 15].

1.2 In Vivo Methods

Although in vitro cell cultures have been invaluable for mechanistic studies, for screening growth factors, evaluating effects of inhibitory substrates, and other purposes, in vivo studies provide the clearest evidence that a given treatment may be clinically relevant to promoting RGC survival and/or optic nerve regeneration. In addition, current methods allow for precise, quantitative evaluation of the effect size. In recent years, numerous labs have explored ways to promote RGC survival and to stimulate optic nerve regeneration using the in vivo model. The methods for an in vivo study include: establishing a nerve injury model, delivering the treatment via intraocular injection, and appropriate methods to evaluate RGC survival and axon regeneration. Many earlier studies had used a peripheral nerve graft model that has been described in detail [16], but this model is seldom used since the discovery that, with suitable stimulation, RGCs can be induced to extend lengthy axons through the optic nerve itself [17, 18].

1.3 Evaluation of Optic Nerve Regeneration

Following optic nerve injury and treatment, animals usually survive from 2 weeks up to a few months for the study of short-term or long-term treatment effects on RGC survival and axon regeneration. There are several ways to evaluate axon regeneration: GAP-43 immunostaining in longitudinal sections through the optic nerve and manual counting of axons; anterograde tracing of regenerating axons with cholera toxin B fragment (CTB), in some cases combined with immunostaining; a tissue-clearing technique to visualize

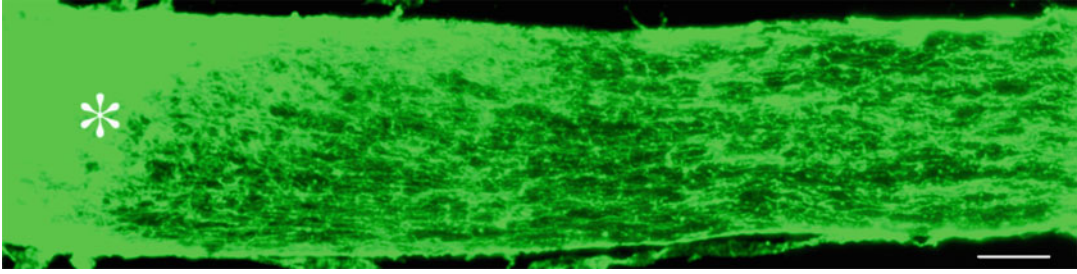


Fig. 1 GAP-43-positive axons in mouse optic nerve. Three weeks after optic nerve crush and intraocular injection of an AAV2-shPten virus plus oncomodulin and CPT-cAMP, many GAP-43-positive axons (green) extend past the crush injury site (*asterisk*) into the distal optic nerve. Scale bar: 60 μm . (Y. Yin, H.-Y. Gilbert, L.I. Benowitz, unpublished)

axons in unsectioned nerves; or genetically labeling RGCs with an axonally transported protein linked to a fluorescent dye. Each of these methods has its advantages and can be combined to use in the studies.

GAP-43 immunostaining: GAP-43 is a prototypical Growth-Associated Protein with an apparent molecular mass ~ 43 kDa (true size ~ 24 kDa). It is dramatically upregulated in RGCs and their axons when the cells are in a growth state, and downregulated in normal uninjured or non-growing nerve fibers [19, 20]. Therefore, GAP-43 is a reliable indicator for RGC axons that have been damaged and are actively regenerating (Fig. 1).

CTB anterograde tracing: Cholera Toxin B subunit (CTB) is a sensitive neuronal tracer with unique features. It stains axons and terminals in great detail, so that single axons can be followed over long distances and their arbors reconstructed in their entirety. As an anterograde tracer, two types of CTB are often used to visualize regenerating axons: fluorescence-conjugated CTB or un-conjugated CTB [21–23]. Usually, CTB is injected intravitreally 2–4 days before the animal is perfused to allow for transport from the cell body to the terminals. If injecting the fluorescent-conjugated CTB, the regenerating axons can be visualized under the fluorescent microscope right after the nerve sectioning. Therefore, the latter method is popular in many labs though the cost is relatively high if used in a large number of samples. In cases in which unconjugated CTB is used, the label can be visualized by immunostaining as in the sample shown below in which numerous CTB-positive axons regenerate along the entire length of optic nerve and enter the optic chiasm (Fig. 2).

Tissue clearing and light sheet fluorescence microscopy in unsectioned optic nerves: Longitudinal sectioning of the optic nerve can result in sections showing axon fragments that disappear out of the plane of section and a loss of 3D information, especially when studying axon turning or branching in the nerve or the trajectory of axons that enter the brain. Several methods for optical clearing of

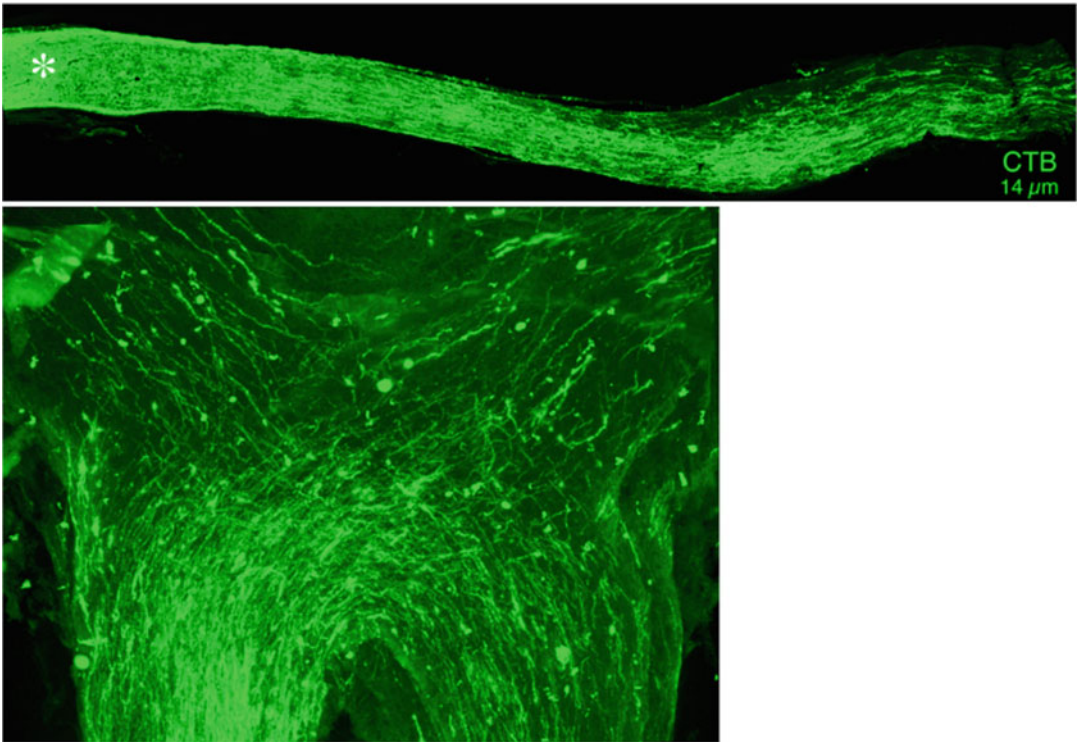


Fig. 2 CTB-positive axons regenerating through the optic nerve and into the optic chiasm. *Top:* Axons are visualized in a longitudinal section through the optic nerve (14 μm thick) 6 weeks after nerve crush followed by intraocular injection of an adeno-associated virus expressing an shRNA to knock down expression of the *pten* gene (AAV2-shPten), a shH10-oncomodulin virus, AAV2-c/a-Adenylate Cyclase, and the chemokine stromal cell-derived factor 1 (SDF1). *Bottom:* Regenerating axons entering the optic chiasm. Axons were labeled with unconjugated CTB and were visualized by anti-CTB immunostaining. Note clear morphology and high resolution (Composite of five 14 μm chiasm sections: Y. Yin, H.-Y. Gilbert, L.I. Benowitz, unpublished)

tissue have been developed that overcome some of these problems. One study [24] has described a method involving an organic solvent-based clearing protocol that allows for 3-D visualization the axon regeneration patterns after optic nerve injury in mice. This method consists of axon labeling with conjugated CTB *in vivo*, whole-tissue dehydration after tissue fixation, tissue clearing, and imaging with light-sheet fluorescent microscopy (LSFM) to visualize the pattern of optic nerve regeneration in adult tissues. This method is able to provide better understanding of 3D axon growth pattern but requires special microscopy techniques. It may also underestimate the numbers of weakly labeled regenerating axons.

1.4 Quantification of Axon Growth

Axon growth can be quantified by counting the number of GAP-43-positive (or CTB-positive) axons extending 0.5 and 1 mm (or other pre-specified distances) from the end of the nerve injury site in at least four longitudinal sections per case. Using a calibrated ocular to measure distance, the cross-sectional width of

the nerve is measured at the point at which the counts are taken and is used to calculate the number of axons per millimeter of nerve width (axons/mm). The number of axons per millimeter will be then averaged over the four sections. Σa_d , the total number of axons extending distance d in a nerve having a radius of r (determined empirically as half the greatest cross-section width), is estimated by summing over all sections having a thickness t (14 μm) [18]:

$$\Sigma a_d = \pi r^2 \times [\text{average axons/mm width}]/t$$

Note that many published papers appear to have erroneously used the full nerve diameter instead of the radius r in this formula, which leads to a fourfold higher number of regenerating axons. This can be seen by comparing the images of regenerating axons vs. the numbers of axons reported in graphs from different labs. After calculating the total axon number in each case, the group means and SEMs can be obtained and the appropriate statistical tests applied to determine the significance of inter-group differences.

2 Materials

2.1 *Materials for In Vitro Methods*

2.1.1 *For Purification of Postnatal RGCs via Immunopanning*

Materials for Retrograde Labeling Before Immunopanning (Optional)

1. Fast blue (1% in H₂O).
2. 10 μl Hamilton syringe.

Materials for Preparing Retinal Cell Suspensions

1. Earle's Balanced Salts Solution (EBSS containing Ca²⁺ and Mg²⁺, pH 7.4).
2. Ovomucoid solution (egg white inhibitor, 13 mg/3 ml).
3. Papain (about 40–45 mg protein/ml, 30 U/mg).
4. Rabbit anti-rat macrophage antiserum (Cedarlane, CLAD51240).
5. Minimum Essential Medium Eagle (MEM) with 0.05% bovine serum albumin (BSA).
6. Nitex mesh.

Materials for Preparing Plastic Petri Dishes for Panning

1. Two 150 \times 15 mm petri dishes (Falcon 1058).
2. Two 100 \times 15 mm petri dishes (Falcon 1029).

3. Affinity-purified goat anti-mouse IgM, μ -chain-specific (1 mg/ml).
4. Affinity-purified goat anti-rabbit IgG H + L (1 mg/ml).
5. T11D7 supernatant (monoclonal supernatant containing IgM antibodies directed against Thy1.1, and the cell line is available from ATCC, no. TIB 103, name T11D7e2).
6. IgM Thy1.2 antibody for panning of mouse cells (Accurate Chemical Co., Cat No. MAS 731; or MCA01, Serotec).
7. Tris-HCl (50 mM, pH 9.5).
8. Dulbecco's phosphate-buffered saline (DPBS).

Materials for Panning

1. Nitex mesh.
2. MEM.
3. Trypsin in EBSS (0.125%).
4. Fetal Calf Serum (FCS).

Materials for the Evaluation of Neurite Outgrowth in Purified RGC Cultures

1. Calcein (a fluorescent dye to stain live cell bodies and processes).
2. Hoechst 33342 (a fluorescent dye to stain nuclei).
3. Paraformaldehyde (4%).
4. Appropriate antibodies.
5. Cellomics Kinetiscan.

2.1.2 For Mixed Adult RGC Cultures

Materials for Mixed RGC Cultures

1. Fluorogold (FG, 2% in saline solution).
2. 10 μ l Nanofil syringe.
3. Stereotaxic frame.
4. L₁₅ medium.
5. NaHCO₃.
6. 24-well plates.
7. HEPES (1 M).
8. Transferrin (stock: 2 mg/ml in H₂O).
9. Superoxide Dismutase (stock: 30,000 U/ml in H₂O).
10. Catalase (stock: 1 mg/ml in H₂O).
11. Gentamicin (stock: 10 mg/ml).
12. Insulin (stock: 5 mg/ml in H₂O).
13. Bovine serum albumin (BSA).
14. HKPPST: every 12 ml of 25 \times HKPPST consists of Hydrocortisone (60 μ l of stock at 500 nM), Kynurenic acid (56.8 mg), Putrescine dihydrochloride (968 μ l of stock at 2.5 mM), Progesterone (60 μ l of stock at 500 nM), Sodium selenite (90 μ l of stock at 750 nM), and 6. 3, 3', 5-triiodo-L-thyronine (T3) (60 μ l of stock at 7.5 nM).

15. Papain suspension.
16. L-cysteine (stock: 3 mg/10 μ l H₂O).
17. DNase (stock: 1 mg/ml in H₂O).
18. Paraformaldehyde (4%).
19. Poly-L-lysine solution.

2.2 Materials for In Vivo Methods

2.2.1 Optic Nerve Crush and Intraocular Injection

1. Ketamine (75 mg/kg for rats; 100 mg/kg for mice) & Xylazine (10 mg/kg for rats or mice).
2. Microsurgical tools.
3. Jewelers' forceps #5.
4. Sutures 10-0.
5. Needle 30G 1/2' or fine tip glass catheters.
6. Polysporin ointment.
7. Isoflurane.

2.2.2 Materials for Animal Perfusion, Tissue Preparation, and GAP43 Immunostaining

1. Isoflurane.
2. Heparinized saline (10 unit/ml).
3. Paraformaldehyde (4%).
4. Sucrose (30%).
5. Superfrost Plus glass slides.
6. Polyclonal anti-GAP-43 antibody made in sheep.
7. Tris-buffered saline (TBS).
8. Methanol.
9. Donkey serum.
10. TBS₂T (TBS containing 2 \times NaCl and 0.1% Tween-20).
11. Solution A (5% donkey serum, 2% BSA in TBS₂T).
12. AlexaFluor 488 donkey anti-sheep IgG.

2.2.3 Materials for Whole Mount Retina Staining and Quantification of RGC Survival after Optic Nerve Regeneration

1. Paraformaldehyde (4%).
2. Phosphate-buffered saline (PBS).
3. Goat serum.
4. Triton X-100.
5. Rabbit anti- β III-tubulin antibody.
6. TUJ1 (a monoclonal antibody to β III-tubulin, Covance, MMS-435p).
7. Fluorescent secondary antibody goat anti-rabbit or goat anti-mouse IgG.
8. ImageJ software.

3 Methods

3.1 *In Vitro* Methods

3.1.1 For Purified Postnatal RGC Cultures

Retrograde Labeling of RGCs in Postnatal Rats (Optional)

To check the purity of isolated cells, retrograde labeling of RGCs is a reliable indicator. Postnatal animals are anesthetized and, under visual guidance, 4 μ l of Fast Blue solution is injected through a 10 μ l Hamilton syringe into the brachium of the superior colliculus bilaterally (*see Note 1*). Injections are performed through the skull, which is exposed on the dorsal surface by making a small longitudinal incision in the skin midline. It is not necessary to use a stereotactic device. In P6-P8 animals, the needle can be accurately positioned 2 mm lateral to the midsagittal sinus just anterior to its intersection with the transverse sinus at a depth of 4 mm. With these coordinates, the injection site lies at the intersection of the dorsal midbrain and diencephalon [25].

Preparing the Retinal Cell Suspension

1. One to ten rats (P8-P10) from a Sprague/Dawley or Long/Evans natural litter are used.
2. After removing the lens and vitreous humor, the dissected retinas are stored at room temperature in EBSS until the retinas are dissected from all animals.
3. After incubation with papain for 30 min, retinas are rinsed once and then triturated in an ovomucoid solution containing anti-rat-macrophage antiserum (1:100).
4. After allowing the cell suspension to incubate with the antiserum for 20 min, cells are centrifuged, resuspended in 10 ml MEM/BSA, filtered through Nitex mesh, and MEM/BSA is added to a final volume to about 15 ml.

Preparing Plastic Petri Panning Dishes

1. One day before panning, prepare two 150 mm Petri dishes for anti-macrophage panning. To each dish, add 20 ml Tris-HCl with 60 μ l of the secondary antibody, affinity-purified goat anti-rabbit IgG, and store overnight at 4 °C.
2. One day before panning, prepare two 100 mm Thy1/T11D7 panning dishes for RGC adhesion. To each dish, add 10 ml Tris-HCl with 30 μ l of Goat anti-mouse IgM, keep at 4 °C overnight (*see Note 2*).
3. On the day of panning, rinse 150 mm Petri dishes 3 \times with DPBS, then add 10 ml DPBS to each, and set aside at RT until use.
4. Rinse 100 mm Petri dishes 3 \times with DPBS, add 8–10 ml of T11D7 supernatant, incubate at RT for at least 2 h. Before panning, rinse the dishes 3 \times with DPBS.

Panning

1. Incubate the retinal cell suspension on the first anti-macrophage dish for 45 min. Gently agitate the dish every 15–20 min or so to ensure access of all the cells to the bottom of the dish. Transfer the cell suspension to the second anti-macrophage dish for 45 min (agitate gently every 15 min).
2. Collect the cell suspension, filter through Nitex mesh to remove small clumps that formed on the anti-macrophage dishes, incubate half of the cell suspension on each of the two T11D7-dishes for 45–60 min (agitate gently every 15 min) at RT or for 30 min in a 37 °C incubator.
3. Gently wash off non-adherent cells on the T11D7 dishes with 5–8 washes of MEM. Check under a microscope to make sure all of the non-adherent cells are gone; if not, wash a few more times. Do not wash too vigorously or you will wash off the RGCs.
4. To release the purified RGCs, add Trypsin-EBSS solution, incubate 8 min in a 37 °C incubator or 10 min at RT. Transfer the trypsin/cell suspension to a 15 ml tube containing 30% FCS in DMEM to stop the digestion. Spin cells 15 min at $200 \times g$ to rinse out the traces of FCS and resuspend cells in pre-equilibrated RGC growth media. An average yield for P6 animals is 50–60 K cells per animal; about 40 K cells per P8 rat (*see Note 3*).

Evaluation of Neurite
Outgrowth in Purified RGC
Cultures

Purified RGCs can be grown in Neurobasal A plus B27 media for 3 days (10,000 cells per 96-well). Cells can be stained with Calcein (Fig. 3) and Hoechst 33342, and imaged in 25 fields per well using a Cellomics Kinetiscan (or equivalent), and neurite outgrowth can be calculated using the Cellomics Image Analysis Algorithm (or equivalent). Cultured cells can also be fixed 10 min with 4% paraformaldehyde at room temperature and immunostained with appropriate antibodies as required.

3.1.2 *Mixed Adult RGC
Culture*

Retrograde Labeling
in Adult Rats

1. Adult rats (>200 g) are anaesthetized, immobilized in a stereotaxic frame, and the skin is incised to expose the top of the skull.
2. Drill two holes bilaterally 1.2 mm lateral to the midline 6.5 mm posterior to Bregma.
3. Slowly inject FG solution (8 μ l) at a depth of 4.0 mm into the superior colliculi. Leave the needle in situ for a few minutes and then withdraw slowly.
4. One week after the surgery, the animal is sacrificed and the two FG-labeled retinas are removed to prepare cell cultures.

Preparing the Culture
Medium and Plates

1. Selection of medium: Instead of Neurobasal A plus B27, this culture uses a defined serum-free medium called Medium E. The reason of this selection is that Neurobasal A with B27

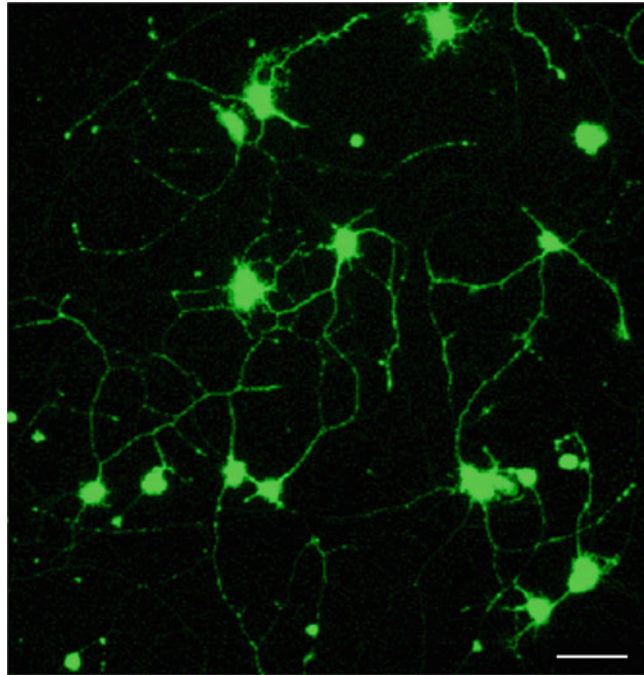


Fig. 3 Neurite outgrowth in purified postnatal day 6 mouse RGCs. With exposure to the growth factor oncomodulin combined with forskolin (to elevate cAMP) and mannose, many mouse RGCs isolated by immunopanning extend long processes in culture (Calcein staining). Scale bar: 40 μm [7]

increases background growth levels, which could occlude the axon-promoting effects of factors being tested. L_{15} medium is the base medium in this culture. Since it does not contain HCO_3^- , the pH will change when placed in a CO_2 incubator, and therefore, the medium must be supplemented with NaHCO_3 (22 mg per 10 ml), *see Note 4*.

2. Plates: Since RGCs represent only $\sim 0.5\%$ of the total cells in the retina, we typically use plates with larger wells (24- instead of 96-well plate) to enable us to obtain enough RGCs in each well for analysis. The plate is precoated with Poly-L-lysine for 30 min, then washed with dd H_2O once. The total volume of medium in each well of a 24-well plate is 400 μl and includes three parts: 100 μl of Medium E (4 \times), 250 μl of the experimental sample, and 50 μl of retinal cell suspension. L_{15} : NaHCO_3 is the basic medium for all three parts.

3. Medium E (4×):

3 ml	L ₁₅ :NaHCO ₃
960 μl	HKPPST
360 μl	HEPES
120 μl	Transferrin
48 μl	Superoxide dismutase
24 μl	Catalase
24 μl	Gentamicin
24 μl	Insulin
240 mg	BSA
Adjust pH to 7.4,	Bring the volume up to 6 ml with L ₁₅ :NaHCO ₃

4. Digestion solution:

L ₁₅ :NaHCO ₃	6 ml
Papain	200 μl
1% BSA	28 μl
L-cysteine	10 μl
DNase	100 μl
Adjust pH to 7.4,	Bring the volume up to 10 ml with L ₁₅ :NaHCO ₃

5. Washing solution

L ₁₅	25 ml
BSA	30 mg
DNase	200 μl
Adjust pH to 7.4,	Bring the volume up to 30 ml with L ₁₅

6. Testing samples: The retinal cells from one rat are enough to test ten different samples (factors) in quadruplicate ($10 \times 4 = 40$ wells). The samples are made with L₁₅:NaHCO₃.

Preparing the Dissociated Retinal Cell Suspension

Pre-labeled rat retinas are dissected from the eyes and incubated in the digestion solution in a CO₂ incubator for 30 min. Gently wash retinas two times with 10 ml washing solution and use the last 10 ml washing solution for the gentle trituration until all of the cells are dissociated. Centrifuge the cell suspension at $130 \times g$ for 10 min, use L₁₅:NaHCO₃ to resuspend (2 ml medium for two retinas), *see* **Note 5**.

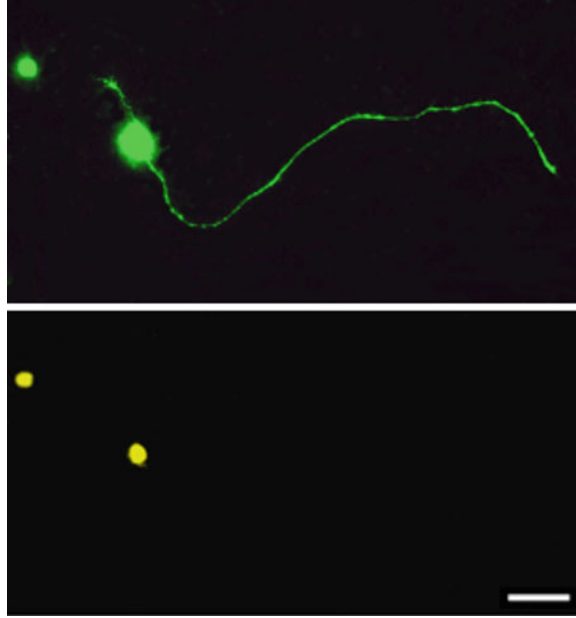


Fig. 4 Axon outgrowth in Fluorogold-labeled RGCs in a mixed retinal culture. Fluorogold was injected into the superior colliculus 1 week prior to sacrifice, retinal dissection, and dissociation. After a 3-day exposure in culture to oncomodulin, forskolin, and mannose, cells were fixed with 4% paraformaldehyde and stained with an antibody against GAP-43, a marker of axon outgrowth. Here, retrogradely-labeled RGCs (*bottom*) are seen growing lengthy axons (*upper image*). Scale bar: 25 μm [8]

Plating Cells and Evaluation of Axon Growth

Plate 50 μl of cell suspension in each well together with 100 μl of 4 \times Medium E and 250 μl of test samples to make 400 μl in each well. After 3 days cell growth in a CO_2 incubator, axon growth and cell survival can be quantified under fluorescent and phase microscopy. RGCs are first recognized by Fluorogold labeling, then their axons are visualized under the phase contrast. Axon outgrowth is quantified as the percentage of FG-positive RGCs extending axons $>30 \mu\text{m}$ (twice the average diameter of cultured RGCs). Based on prior experience, we do not count axons shorter than 30 μm in order to exclude spontaneous sprouting. Cells can be fixed with 4% paraformaldehyde 10 min at RT and stained with suitable antibodies as required by the experiment (Fig. 4).

3.2 In Vivo Methods

3.2.1 Optic Nerve Crush Model

The surgical approaches for rat and mouse optic nerve crushes are slightly different. The access to the rat optic nerve is through a skin incision on the top of the orbit and the Harderian gland around the optic nerve; whereas access to the mouse optic nerve is through the conjunctival sac that provides an easier surgical operation but a small, narrow exposure to the optic nerve.

Rat Optic Nerve Crush

1. Surgery is carried out under aseptic conditions.
2. Adult rats (>200 g body weight) are anesthetized using ketamine and xylazine injected intraperitoneally (IP).
3. The optic nerve is surgically exposed by retracting the overlying Harderian gland and resecting a minimal amount of muscle and connective tissue around the nerve, with extreme care taken not to damage the ophthalmic artery.
4. The epineurium surrounding the optic nerve is carefully slit and the nerve is crushed 2 mm from the optic nerve head for 10 s using #5 jewelers' forceps.

Rat Optic Nerve Microcrush

To minimize overall tissue damage, a limited injury model called a microcrush has been developed [26]. Instead of using forceps, a microcrush lesion is made using a 10-0 suture to completely constrict the optic nerve by making a tight knot for 60 s and then releasing the suture. The microcrush causes much less of a cavity to form adjacent to the lesion site compared to conventional use of forceps while at the same time transecting all axons completely. In addition, the lesion site is sharply defined, which allows for accurate measurements of the distance of axon growth past the lesion site.

Intraocular Injection in Rat

After nerve crush or microcrush, depending on the experimental design, animals may receive an intraocular injection of growth factors, viruses, or other agents. A typical injection volume in rat is 5–10 μ l per eye, with the same volume of aqueous withdrawn beforehand, or after making a small puncture on the cornea, to release excess pressure. The injection is delivered into the posterior chamber of the eye through a sterile 30 1/2G or thinner needle or a fine tip of glass catheter. The needle is left in situ for about 10 s for better distribution of the agent being injected, then withdrawn very slowly to avoid back-leakage. It is essential to avoid damaging the lens during the injections, since lens injury causes considerable inflammation that itself has massive effects in promoting RGC survival and axon regeneration [18, 27]. It is not necessary to dilate the pupil during the injection since the injection is made from the back of the eye. The surgical wound is sutured shut and swabbed with Polysporin ointment. The fundus is examined under a dissecting microscope for signs of ischemic damage or lens injury. Animals showing such damage are removed and sacrificed with an overdose of isoflurane. Animals are allowed to recover from anesthesia and returned to their cages. In some experiments, agents are introduced prior to optic nerve injury. This occurs, for example, when attempting to affect changes that occur quickly after optic nerve injury or, in gene therapy studies, a lead time is required to allow a virally encoded gene to be expressed at sufficient levels.

Mouse Optic Nerve Crush and Intraocular Injection

1. Adult mice (8 weeks or older) are anesthetized with a combination of ketamine and xylazine given i.p.
2. Surgery is done under sterile conditions using a stereomicroscope.
3. A conjunctival incision is made over the dorsal aspect of the eye, then gently rotated the eye downward in the orbit.
4. The orbital muscles are slightly separated to expose the optic nerve at its exit from the eyeball, which is then crushed for 5 s with #5 jewelers' forceps near the back of the eye (within 0.5 mm) [21]. Care is taken not to damage the ophthalmic artery and retrobulbar sinus.
5. After the nerve crush, no suture is needed since the incision is very small and closes by itself after releasing all instruments from the eye.
6. Intraocular injections in mouse eyes are similar to those in rats except that the maximum volume is ~3 μ l [21].

3.2.2 Animal Perfusion, Tissue Preparation, and Immunostaining for GAP-43 in Optic Nerve Sections

Animals are given an overdose of isoflurane and perfused intracardially with heparin-saline (50 ml for rat and 20 ml for mouse) followed by 4% paraformaldehyde (100 ml for rat and 20 ml for mouse). The optic nerve is dissected out and placed in 4% paraformaldehyde again for post-fixation (2 h RT or 4 °C overnight). After immersion for several hours to overnight in 30% sucrose at 4 °C, the optic nerve is frozen in O.C.T., sectioned longitudinally on a Cryostat (14 μ m thickness), mounted on Superfrost Plus glass slides, dried, and is then ready to use for GAP-43 immunostaining. Unstained slides can be stored in -20 °C for many months. The detailed procedure is as follows:

1. Five minutes in TBS pH 7.4.
2. Ten minutes in methanol (*see Note 6*).
3. One hour in blocking solution (10% donkey serum in TBS).
4. Overnight in primary antibody (4 °C): sheep anti-GAP-43 in solution A (*see Note 7*).
5. Washing: on the second day, wash slides 1 h in TBS₂T, 4 °C; 1 h in solution A, RT; 1 h in TBS₂T, RT. Gently shake continuously (*see Note 8*).
6. Two hour in secondary antibody, RT: AlexaFluor 488 donkey anti-sheep IgG 1:500 in solution A.
7. 2 \times 5 min wash in TBS₂T.
8. Five minutes wash in TBS.

3.2.3 Evaluating RGC Survival

While using optic nerve to evaluate nerve regeneration, the retinas are used to determine RGC survival. After animal perfusion, the whole retinas are dissected out, and four partial cuts are made from

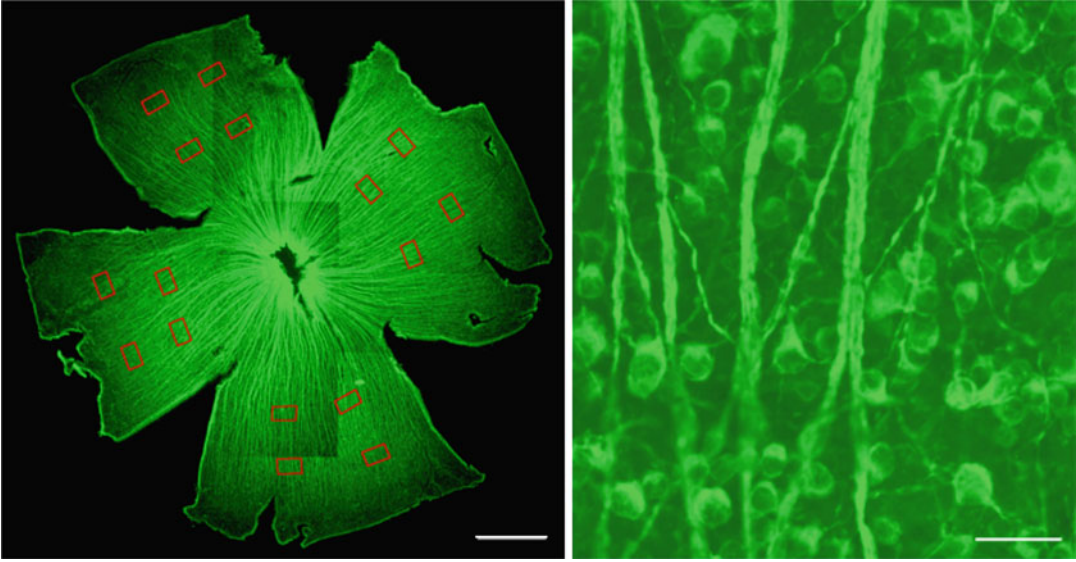


Fig. 5 Whole mount rat retina immunostained for β III-tubulin. The normal whole retina was dissected out from the eye and cut as following to open the cup. The red-rectangles indicate the areas selected for RGC quantification (*left*). Immunostaining to β III-tubulin shows strongly positive staining for RGC fiber bundles, cell bodies, and their fine processes (*left and right*). Scale bar: *left*: 500 μ m; *right*: 40 μ m. (Y. Yin, H.-Y. Gilbert, L.I. Benowitz, unpublished)

the peripheral edge in order to open the retinal cup for flat-mounting (Fig. 5). Retinas are post-fixed in 4% paraformaldehyde 2 h at RT, then rinsed with PBS and stored at 4 °C until immunostaining. Staining includes:

1. Three washes in PBS, 5 min. For each.
2. Blocking and permeabilization with 10% goat serum plus 0.2% Triton X-100, 1 h, RT; Incubation with a rabbit anti- β III-tubulin antibody (1:500) in PBS with 5% goat serum and 0.2% Triton X-100 overnight at 4 °C (*see Note 9*).
3. Three washes in PBS with 2% goat serum and 0.2% Triton X-100, 30 min. For each, RT; One wash in PBS, 10 min.
4. Fluorescent-conjugated antibody to rabbit IgG made in goat, 2 h at RT.
5. Three washes in PBS.

Within the ganglion cell layer, β III tubulin is expressed selectively in RGCs [27–29]. Immuno-positive cells are counted using ImageJ software in 16 fields per retina in rats or eight fields per retina in mice distributed in four quadrants of the eye at pre-specified distances from the optic disc (red rectangles in Fig. 5). Cell survival is reported as the number of β III-tubulin⁺ cells per mm² averaged over all the fields sampled in each retina, and then averaged across all cases within each experimental group.

Following optic nerve injury and regeneration, the expression level of β III-tubulin can change, which can affect cell counting. The transcription factor Brn3a is a specific marker for RGCs in naive or optic nerve-injured retinas [30]. It stains RGC nuclei and cell numbers are easy to quantify with appropriate software. However, Brn3a does not exist in all of RGCs (about 80% RGCs express Brn3a) and levels of Brn3a decline sharply after optic nerve injury [31]. Therefore, detection of Brn3a (and/or 3b) may be combined with another marker to get a more accurate count for RGC survival. We have been using TUJ1 plus Brn3a co-staining and count cells that express either marker or both as RGCs. This could become a routine way to accurately represent RGC survival after nerve injury and treatment. Other studies have used antibodies to a recently discovered RNA-binding protein that is expressed selectively in RGCs [32], though in our experience, its distribution becomes diffuse after nerve injury.

3.3 Conclusions

Preservation of injured retinal ganglion cells and regeneration of the optic nerve could benefit millions of patients with glaucoma as well as victims of traumatic or ischemic damage to the retina or optic nerve. The methods for testing potential therapeutics described here include *in vitro* and *in vivo* approaches. Whereas the former include the use of purified RGC cultures (derived from neonatal animals), mixed retinal cultures, and retinal tissue explant cultures, the latter include the optic nerve injury models and methods to quantify the results of these studies. Application of these methods may someday lead to the development of treatments that can restore sight, arguably the most important of all our sensory faculties.

4 Notes

1. The injection should take place over a period of 1 min or so to allow for good spreading and uptake of the dye.
2. If purified RGCs are derived from mouse, the procedures are modified slightly. Usually, P8-P10 CD1 mice or other Thy1.2-positive strains are used. Instead of IgM Thy1.1 antibody, an IgM Thy1.2 antibody is used for the panning dish (1:500).
3. During this procedure, cells should never be exposed to glutamate, aspartate, or glutamine since these are toxic to RGCs.
4. This is only necessary when the medium is to be used in the CO₂ incubator. Otherwise, as with the washing buffer used in the hood and exposing to air, no NaHCO₃ is added.
5. It is important to carry out the retinal dissection as quickly as possible, preferably within 5 min. During the trituration, it is

better to add a small volume (e.g., 1 ml) of buffer at a time, gently triturate, allow the cell clusters to settle down, transfer the dissociated cell suspension to another tube, then add another small volume of buffer to triturate the remaining cell clusters until all cells are completely dissociated.

6. Methanol helps penetration and strengthens the staining intensity.
7. Our lab uses a custom-made polyclonal anti-GAP-43 antibody prepared in sheep [33].
8. The sheep anti-GAP-43 antibody requires extra-long washing to avoid background staining.
9. At times, TUJ1 (1:500), a monoclonal antibody to β III-tubulin, gives a cleaner background.

References

1. Ramon Y, Cajal S (1991) Degeneration and regeneration in of the nervous system (trans: May RM). Oxford University Press, New York
2. Bray GM, Vidal-Sanz M, Aguayo AJ (1987) Regeneration of axons from the central nervous system of adult rats. *Prog Brain Res* 71:373–379
3. Lye-Barthel M, Sun D, Jakobs TC (2013) Morphology of astrocytes in a glaucomatous optic nerve. *Invest Ophthalmol Vis Sci* 54 (2):909–917. <https://doi.org/10.1167/iovs.12-10109>
4. Matsumoto H, Murakami Y, Kataoka K, Notomi S, Mantopoulos D, Trichonas G, Miller JW, Gregory MS, Ksander BR, Marshak-Rothstein A, Vavvas DG (2015) Membrane-bound and soluble Fas ligands have opposite functions in photoreceptor cell death following separation from the retinal pigment epithelium. *Cell Death Dis* 6:e1986. <https://doi.org/10.1038/cddis.2015.334>
5. Roh M, Zhang Y, Murakami Y, Thanos A, Lee SC, Vavvas DG, Benowitz LI, Miller JW (2012) Etanercept, a widely used inhibitor of tumor necrosis factor- α (TNF- α), prevents retinal ganglion cell loss in a rat model of glaucoma. *PLoS One* 7(7):e40065. <https://doi.org/10.1371/journal.pone.0040065>
6. Barres BA, Silverstein BE, Corey DP, Chun LL (1988) Immunological, morphological, and electrophysiological variation among retinal ganglion cells purified by panning. *Neuron* 1 (9):791–803
7. Yin Y, Cui Q, Gilbert HY, Yang Y, Yang Z, Berlinicke C, Li Z, Zaverucha-do-Valle C, He H, Petkova V, Zack DJ, Benowitz LI (2009) Oncomodulin links inflammation to optic nerve regeneration. *Proc Natl Acad Sci U S A* 106(46):19587–19592. <https://doi.org/10.1073/pnas.0907085106>
8. Yin Y, Henzl MT, Lorber B, Nakazawa T, Thomas TT, Jiang F, Langer R, Benowitz LI (2006) Oncomodulin is a macrophage-derived signal for axon regeneration in retinal ganglion cells. *Nat Neurosci* 9(6):843–852. <https://doi.org/10.1038/nn1701>
9. Feng G, Mellor RH, Bernstein M, Keller-Peck C, Nguyen QT, Wallace M, Nerbonne JM, Lichtman JW, Sanes JR (2000) Imaging neuronal subsets in transgenic mice expressing multiple spectral variants of GFP. *Neuron* 28 (1):41–51
10. Wang SW, Mu X, Bowers WJ, Klein WH (2002) Retinal ganglion cell differentiation in cultured mouse retinal explants. *Methods* 28 (4):448–456
11. Manabe S, Kashii S, Honda Y, Yamamoto R, Katsuki H, Akaike A (2002) Quantification of axotomized ganglion cell death by explant culture of the rat retina. *Neurosci Lett* 334 (1):33–36
12. Lagreze WA, Pielen A, Steingart R, Schlunck G, Hofmann HD, Gozes I, Kirsch M (2005) The peptides ADNF-9 and NAP increase survival and neurite outgrowth of rat retinal ganglion cells in vitro. *Invest Ophthalmol Vis Sci* 46(3):933–938. <https://doi.org/10.1167/iovs.04-0766>
13. Toops KA, Berlinicke C, Zack DJ, Nickells RW (2012) Hydrocortisone stimulates neurite outgrowth from mouse retinal explants by modulating macroglial activity. *Invest Ophthalmol Vis Sci* 53(4):2046–2061. <https://doi.org/10.1167/iovs.11-8646>

14. Gasparini L, Crowther RA, Martin KR, Berg N, Coleman M, Goedert M, Spillantini MG (2011) Tau inclusions in retinal ganglion cells of human P301S tau transgenic mice: effects on axonal viability. *Neurobiol Aging* 32(3):419–433. <https://doi.org/10.1016/j.neurobiolaging.2009.03.002>
15. Bull ND, Johnson TV, Welsapar G, DeKorver NW, Tomarev SI, Martin KR (2011) Use of an adult rat retinal explant model for screening of potential retinal ganglion cell neuroprotective therapies. *Invest Ophthalmol Vis Sci* 52(6):3309–3320. <https://doi.org/10.1167/iovs.10-6873>
16. So KF, Aguayo AJ (1985) Lengthy regrowth of cut axons from ganglion cells after peripheral nerve transplantation into the retina of adult rats. *Brain Res* 328(2):349–354
17. Berry M, Carlile J, Hunter A (1996) Peripheral nerve explants grafted into the vitreous body of the eye promote the regeneration of retinal ganglion cell axons severed in the optic nerve. *J Neurocytol* 25(2):147–170
18. Leon S, Yin Y, Nguyen J, Irwin N, Benowitz LI (2000) Lens injury stimulates axon regeneration in the mature rat optic nerve. *J Neurosci* 20(12):4615–4626
19. Benowitz LI, Routtenberg A (1997) GAP-43: an intrinsic determinant of neuronal development and plasticity. *Trends Neurosci* 20(2):84–91
20. Skene JH (1989) Axonal growth-associated proteins. *Annu Rev Neurosci* 12:127–156. <https://doi.org/10.1146/annurev.ne.12.030189.001015>
21. Kurimoto T, Yin Y, Omura K, Gilbert HY, Kim D, Cen LP, Moko L, Kugler S, Benowitz LI (2010) Long-distance axon regeneration in the mature optic nerve: contributions of oncomodulin, cAMP, and pten gene deletion. *J Neurosci* 30(46):15654–15663. <https://doi.org/10.1523/JNEUROSCI.4340-10.2010>
22. de Lima S, Koriyama Y, Kurimoto T, Oliveira JT, Yin Y, Li Y, Gilbert HY, Fagiolini M, Martinez AM, Benowitz L (2012) Full-length axon regeneration in the adult mouse optic nerve and partial recovery of simple visual behaviors. *Proc Natl Acad Sci U S A* 109(23):9149–9154. <https://doi.org/10.1073/pnas.1119449109>
23. Moore DL, Blackmore MG, Hu Y, Kaestner KH, Bixby JL, Lemmon VP, Goldberg JL (2009) KLF family members regulate intrinsic axon regeneration ability. *Science* 326(5950):298–301. <https://doi.org/10.1126/science.1175737>
24. Luo X, Yungher B, Park KK (2014) Application of tissue clearing and light sheet fluorescence microscopy to assess optic nerve regeneration in unsectioned tissues. *Methods Mol Biol* 1162:209–217. https://doi.org/10.1007/978-1-4939-0777-9_17
25. Potts RA, Dreher B, Bennett MR (1982) The loss of ganglion cells in the developing retina of the rat. *Brain Res* 255(3):481–486
26. Selles-Navarro I, Ellezam B, Fajardo R, Latour M, McKerracher L (2001) Retinal ganglion cell and nonneuronal cell responses to a microcrush lesion of adult rat optic nerve. *Exp Neurol* 167(2):282–289. <https://doi.org/10.1006/exnr.2000.7573>
27. Yin Y, Cui Q, Li Y, Irwin N, Fischer D, Harvey AR, Benowitz LI (2003) Macrophage-derived factors stimulate optic nerve regeneration. *J Neurosci* 23(6):2284–2293
28. Park K, Luo JM, Hisheh S, Harvey AR, Cui Q (2004) Cellular mechanisms associated with spontaneous and ciliary neurotrophic factor-cAMP-induced survival and axonal regeneration of adult retinal ganglion cells. *J Neurosci* 24(48):10806–10815. <https://doi.org/10.1523/JNEUROSCI.3532-04.2004>
29. Cui Q, Yip HK, Zhao RC, So KF, Harvey AR (2003) Intraocular elevation of cyclic AMP potentiates ciliary neurotrophic factor-induced regeneration of adult rat retinal ganglion cell axons. *Mol Cell Neurosci* 22(1):49–61
30. Nadal-Nicolas FM, Jimenez-Lopez M, Sobrado-Calvo P, Nieto-Lopez L, Canovas-Martinez I, Salinas-Navarro M, Vidal-Sanz M, Agudo M (2009) Brn3a as a marker of retinal ganglion cells: qualitative and quantitative time course studies in naive and optic nerve-injured retinas. *Invest Ophthalmol Vis Sci* 50(8):3860–3868. <https://doi.org/10.1167/iovs.08-3267>
31. Yukita M, Machida S, Nishiguchi KM, Tsuda S, Yokoyama Y, Yasuda M, Maruyama K, Nakazawa T (2015) Molecular, anatomical and functional changes in the retinal ganglion cells after optic nerve crush in mice. *Doc Ophthalmol* 130(2):149–156. <https://doi.org/10.1007/s10633-014-9478-2>
32. Rodriguez AR, de Sevilla Muller LP, Brecha NC (2014) The RNA binding protein RBPMS is a selective marker of ganglion cells in the mammalian retina. *J Comp Neurol* 522(6):1411–1443. <https://doi.org/10.1002/cnc.23521>
33. Benowitz LI, Apostolides PJ, Perrone-Bizzozero N, Finklestein SP, Zwiers H (1988) Anatomical distribution of the growth-associated protein GAP-43/B-50 in the adult rat brain. *J Neurosci* 8(1):339–352

Chapter 17

3D Histomorphometric Reconstruction and Quantification of the Optic Nerve Head Connective Tissues

Hongli Yang, Juan Reynaud, Howard Lockwood, Galen Williams, Christy Hardin, Luke Reyes, Stuart K. Gardiner, and Claude F. Burgoyne

Abstract

Accurately characterizing the 3D geometry of the optic nerve head neural and connective tissues has been the goal of a large and important body of scientific work. In the present report, we summarize our methods for the high-resolution, digital, 3D histomorphometric reconstruction of the optic nerve head tissues, including their visualization, parameterization, and quantification. In addition, we present our methods for between-eye comparisons of this anatomy, and their use to determine animal-specific and experiment-wide experimental glaucoma versus Control eye differences in the unilateral, monkey experimental glaucoma model. Finally, we demonstrate its application to finite element modeling, 3D optic nerve head reconstruction of other species, and 3D optic nerve head reconstructions using other imaging modalities.

Key words Three dimensional, Glaucoma, Histomorphometry, 3D reconstruction, Optic nerve head, Lamina cribrosa, Sclera, Monkey, Glaucoma, Rat

1 Introduction

The purpose of this chapter is to summarize our methodology for high-resolution, digital 3D reconstruction (3D HMRN) and quantification of the neural and connective tissues of the monkey optic nerve head (ONH). To demonstrate how this methodology can be useful in a more generic sense, we further describe its application to other species, other imaging modalities, finite element modeling, and other problems of anatomic visualization, delineation, parameterization, and quantification [1–9]. Table 1 provides a list of the most commonly used abbreviations and acronyms with their definitions. Subheading 2 provides a list of materials and instructions for tissue Fixation, paraffin embedding, and stains. Subheadings 3.1–3.3 provide a detailed description of Methods and include sections on tissue processing, block face staining and imaging, 3D reconstruction and radial digital sagittal section image generation. Subheadings 3.4–3.10 describe the general application and post 3D

Table 1
Common acronyms and terms with their descriptions. All parameters are italicized so as to distinguish them from the anatomic landmark, structure or phenomena they measure

Terms	Full name/Description
ALI	Anterior LC insertion
<i>ALIP</i>	<i>Anterior laminar insertion position</i>
ASAS	Anterior-most subarachnoid space—the anterior most extension of the CSF space
ASCO	Anterior scleral canal opening
<i>BD</i>	<i>Beam diameter</i>
BM	Bruch's membrane
BMO	Bruch's membrane opening
Control	Contralateral control eye of each animal with a unilateral intervention such as EG or ONT
<i>CTV</i>	<i>Connective tissue volume</i> —the sum of all connective tissue voxels
<i>CTVF</i>	<i>Connective tissue volume fraction</i> —the ratio of <i>CTV/LV</i>
CRV	Central retinal vessel
EG	Experimental glaucoma
FoBMO Axis	Axis between the Foveal center and the BMO_{centroid}
3D HMRN	3 Dimensional histomorphometric reconstruction
ILM	Internal limiting membrane
LE	Left eye
LC	Lamina cribrosa
<i>LIL</i>	<i>Laminar insertion length</i>
LMA	Lamina cribrosa microarchitecture—as characterized by <i>BD</i> , <i>PD</i> , <i>LV</i> and <i>CTVF</i>
<i>LV</i>	<i>Laminar volume</i> —the sum of all beam and pore voxels
MV	Multiview software
NB	Neural boundary—the boundary that contains the RGC axons as they pass through the wall of the eye
OCT	Optical coherence tomography
ON	Optic nerve
ONH	Optic nerve head—defined to include the tissues within and adjacent to BMO and the scleral canal
ONT	Optic nerve transection
<i>PBMOTPV</i>	<i>Post-BMO total prelaminar volume</i>
<i>PD</i>	<i>Pore diameter</i>
<i>PID</i>	<i>Physiologic inter-eye difference</i>

(continued)

Table 1
(continued)

Terms	Full name/Description
<i>PID_{max}</i>	<i>PID_{max}</i> = Maximum PID, the maximum PID among the 6 bilaterally normal animals for a given parameter and depth
<i>PIPD</i>	<i>Physiologic inter-eye percent difference</i>
<i>PIPD_{max}</i>	<i>PIPD_{max}</i> = Maximum PIPD, the maximum PIPD among the 6 bilaterally normal animals for a given parameter and depth
PLI	Posterior LC insertion
<i>PLIP</i>	<i>Posterior laminar insertion position</i>
PSCO	Posterior scleral canal opening
RE	Right eye
RE configuration	Right eye configuration—all LE data is converted to RE configuration as demonstrated in Fig. 6

reconstruction processing including 3D delineation of ONH landmarks, establishing the Foveal to Bruch's membrane opening (BMO) axis (FoBMO), converting all left eye data to right eye configuration, ONH macroarchitecture parameterization, and laminar microarchitecture parameterization. In addition, there are Subheadings 3.10–3.13 explaining our methodology's application to finite element modeling [9], the reconstruction of the rat ONH [7, 10], colocalization of 3D histomorphometry to Optical Coherence Tomography (OCT), and ONH 3D HMRN versus orbital optic nerve (ON) axon loss colocalization. Subheading 4 includes Notes regarding method fine points and suggestions. Throughout this chapter, all parameters are italicized so as to distinguish them from the anatomic landmark or structure they measure.

2 Materials

2.1 Tissue Fixation

2.1.1 4%

Paraformaldehyde 1000 ml

1. Weigh out 40 g of paraformaldehyde prills.
2. Add 700 ml of double distilled H₂O (ddH₂O) to a 1000 ml beaker.
3. Heat to 60 degrees while stirring with stir bar. Once at desired temp, remove from heat and place on a non-heated plate and continue to stir.
4. Add prills slowly.

5. Add 3 ml of 1 N NaOH solution, then add in a dropwise fashion until the solution turns from a milky white to nearly colorless.
6. Filter the solution by using a 0.45 μm cellulose acetate filter.
7. Fill the filtered solution into a 1000 ml beaker.
8. Add 200 ml of 0.5 M Stock Sorenson's solution.
9. Add 1 ml of 1% CaCl_2 .
10. Add drops of 1 N HCl to pH 7.4 while stirring.
11. Transfer solution to a 1000 ml graduated cylinder.
12. Bring up to 1000 ml by adding ddH₂O to remaining solution.
13. Transfer to a 1000 ml bottle and store at 4 °C.

**2.1.2 5% Glutaraldehyde
1000 ml**

1. Mix the components below in a 1000 ml beaker.
2. 200 ml 0.5 M Stock Sorenson's.
3. 100 ml 50% EM Grade Glutaraldehyde.
4. 1 ml of 1% CaCl_2 .
5. Adjust pH to 7.4.
6. Transfer the solution to a 1000 ml graduated cylinder and add ddH₂O to remaining up to 1000 ml.

**2.1.3 0.5 M Stock
Sorenson's 1000 ml**

1. Add 800 ml ddH₂O to a 1000 ml beaker.
2. Use a stir plate and stir bar to mix solution.
3. Add 10.21 g KH_2PO_4 . Always add this first.
4. Once the KH_2PO_4 has dissolved add 60.33 g Na_2HPO_4 .
5. Once the Na_2HPO_4 has dissolved adjust pH using 1 N NaOH or HCl to reach pH 7.4.

**2.2 Paraffin
Embedding**

All ONH trephines are prepared for serial sectioning with a Sakura Tissue-Tek[®] VIP[®] automated tissue processor (Sakura Finetek USA, Torrance, CA) using the protocol in Table 2. Each ONH is placed in a labeled embedding cassette for processing. Cassettes are placed in the retort of the Tissue-Tek[®] VIP[®] in a stainless-steel cage to ensure cassettes remain beneath the processing solutions at all times. The agitation setting as well as the vacuum infiltration processing settings should be set to “on.”

After the infiltration steps are complete, a stainless-steel base mold is fitted with a polystyrene embedding ring. This is placed on the hot plate of the Sakura Tissue-Tek[®] TEC[®] (Sakura Finetek USA, Torrance, CA). Each ONH is removed from its cassette and placed retina side down in a base mold. The base mold is then filled to the top of the embedding ring with liquid Paraplast[™] paraffin and placed on a cold plate at 0 °C. After 2–3 h at 0 °C, the embedding ring with ONH is removed from the base mold for serial sectioning.

Table 2
Preparation of ONH trephines

Step	Solution	Time (h)	Temperature (°C)
Dehydrate	80% EtOH	6	35°
	95% EtOH	1	35°
	95% EtOH	1	35°
	95% EtOH	1	35°
	100% EtOH	1	35°
	100% EtOH	1	35°
	100% EtOH	1	35°
Clear	Chloroform, HPLC	1	35°
	Chloroform, HPLC	1	35°
	Chloroform, HPLC	1	35°
Infiltrate	Paraplast™ paraffin	2	60°
	Paraplast™ paraffin	2	60°

2.3 Stain

1. To make 100 ml of stain solution, 0.5 g Acid Fuchsin, 0.5 g Ponceau S, 8.3 ml 2.0 N of Acetic Acid, and ddH₂O are required.
2. Weigh out and place the first three components into a 200 ml beaker with about 80 ml of ddH₂O.
3. Add a stir bar and mix on a stir plate until Acid Fuchsin and Ponceau S are dissolved, around 10 min.
4. Transfer to a 100 ml graduated cylinder and then wash the beaker into the cylinder with approximately 10 ml ddH₂O.
5. Fill graduated cylinder up to 100 ml with ddH₂O.
6. Filter the solution with Whatman #1 (Whatman plc, Maidstone, United Kingdom) filter paper.

3 Methods

3.1 Animal Sacrifice and Tissue Processing

1. Animals are sacrificed by perfusion fixation via the descending aorta or direct left ventricle cannulation [11]. Immersion fixation of tissues can also be performed.
2. After perfusion fixation, maintain IOP for 1 h, then enucleate each eye and remove all extra orbital tissues. Remove the anterior chamber 2–3 mm posterior to the limbus. Document the thoroughness of the perfusion and comment on any remaining blood in the tissues.
3. Place the posterior scleral shells with intact ONH, choroid, and retina in the 5% glutaraldehyde solution for 1 week, then process the tissue or transfer to 4% paraformaldehyde for long-term storage.

4. At the time of tissue processing take careful photographs and make careful drawings of the subsequent steps to document the process for future reference.
5. After 1 week, remove all extraocular muscles and orbital fat from the globe and orbital optic nerve. Carefully dissect the dural sheath away from the optic nerve and pial sheath down to its insertion into the sclera. Take care to avoid damaging the posterior ciliary artery insertions and the scleral flange and peripapillary sclera.
6. From inside the globe, pass a 10-0 prolene suture on a straight needle (Ethicon, Somerville, NJ) through the fovea, choroid, and sclera to mark the location of the fovea on the outer surface of the posterior scleral shell. With a tissue marking pen project the location of the fovea on the posterior scleral surface to the midpoint of the temporal optic nerve and mark the FoBMO axis projection on the temporal nerve pial sheath (the dural sheath having been removed). Photograph each aspect of this anatomy.
7. Place a second mark (the FoBMO axis superior projection mark) on the superior nerve pial sheath, 90 degrees from the temporal FoBMO axis projection mark with the tissue marking pen.
8. Using a caliper, place a third mark, 3 mm from the back of the globe, along the distal projection of the superior optic nerve with the marking pen—this will be the posterior extent of the 3D HMRN optic nerve stump, after the optic nerve cut (**step 9**, below) is made. Be prepared to make this cut 3.5–4.0 mm behind the globe (in both the EG and Control eyes) if the depth of EG eye cupping is profound, as the posteriorly deformed lamina may be in the optic nerve cut otherwise.
9. For future regionalization of axon counts, use a 15° super sharp blade to make three incisions along the length of the nerve that will be continuous between the 3 mm 3D HMRN optic nerve stump and the distal orbital optic nerve. For each incision, begin roughly 2 mm behind the globe and continue for 1–1.5 mm distally (in the direction away from the globe). Start with a single temporal cut that extends the FoBMO axis projection point distally along the nerve. Then add two superior cuts one on each side of the 3 mm superior FoBMO axis projection.
10. Next, make a perpendicular cut completely through the optic nerve with a fresh razorblade 3 mm from the globe. Use the superior FoBMO axis projection mark made previously as a guide.
11. Identify each cut in the cut face of the optic nerve stump. Document by drawing and photographing the location of

these cuts, relative to the central retinal vein and artery—which will also be visible.

12. Store the distal orbital optic nerve piece in 4% paraformaldehyde for axon counting.
13. Trepine the ONH and surrounding peripapillary sclera (6 mm diameter).
14. Store the ONH trephine and posterior scleral shells in separate vials in 4% paraformaldehyde.
15. Process the ONH trephine tissue for paraffin embedding (see Subheading 2.2 above).

3.2 Block-Face Staining and Imaging (Fig. 1)

1. Mount the embedded ONH trephine on a microtome (RM2165; Leica, Wetzlar, Germany) so that the vitreous side of the ONH surface is visible in the block. Adjust the block to achieve proper clinical orientation (Fig. 1).
2. Insert a Leica® 819 low profile disposable microtome blade (Leica Microsystems, Buffalo Grove, IL) in the blade holder.
3. Adjust the vertical and horizontal tilt of the embedded block so that it is parallel with the plane of the microtome blade.
4. Begin to face the block by cutting 10–20 μm sections until the cutting plane is close to the retinal surface. Readjust the vertical and horizontal tilts of the embedded block such that the plane of the peripapillary retina is approximately parallel to the plane of the microtome blade.
5. Continue to face the block and adjust until the blade is just superficial to the internal limiting membrane of the retina and the entire trephine has been faced.
6. Change the cutting depth to 1.5 μm and cut five sections.
7. Open the acquisition software (CutterMaster, custom application) and proceed through the prescribed set-up steps.
8. Initiate the first cut.
9. Start the image acquisition process. Our current imaging system consists of a 14-bit, 4096×4096 pixel monochrome digital camera (Alta U16 M, Andor Technology Ltd., Belfast, UK) outfitted with a $2\times$ apochromatic lens (AZ Plan Fluor, 0.2NA, Nikon Instruments Inc., Melville, NY) and a 3-color (RGB) filter (AI-FW50, Andor Technology Ltd., Belfast, UK). The camera is mounted on a custom-built, computer-controlled Y-Z stage (AVS125/ATS02015, Aerotech Inc., Pittsburgh, PA) and calibrated to produce images with a $1.5 \times 1.5 \mu\text{m}$ resolution. Because of the size of the chip, the $6.1 \times 6.1 \text{ mm}$ field of view allows us to cover the entire 6 mm ONH trephine with a single image. The system also includes a laser displacement sensor (Keyence Corp. Woodcliff Lake, NJ) to measure the

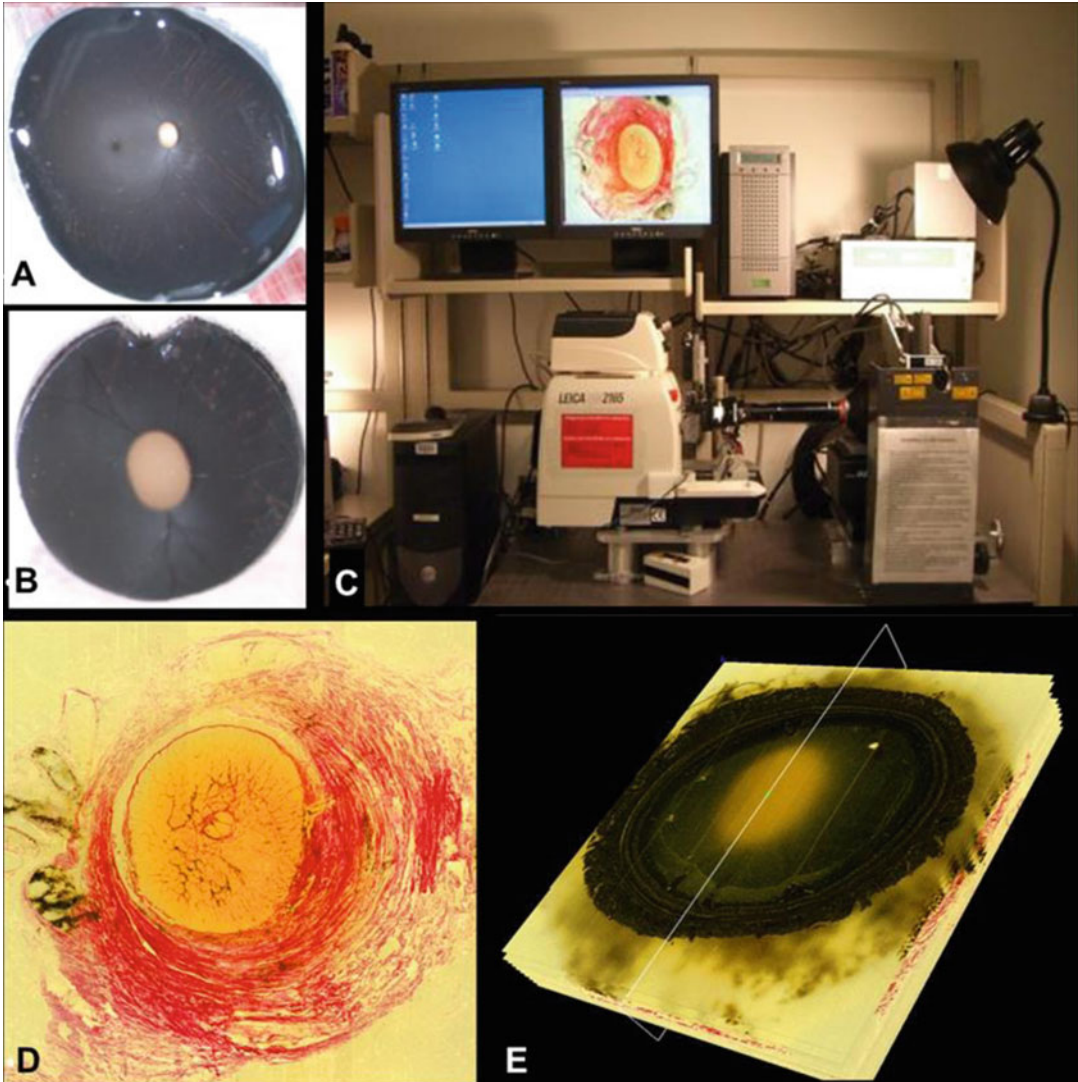


Fig. 1 Fixation, tissue processing, block face staining and serial sectioning, 3D reconstruction and radial digital section image generation. (a) Immersion or perfusion fixed ocular tissues are trimmed of extraocular muscles and orbital fat and the dural sheath is carefully dissected away from the orbital optic nerve and removed just distal to its insertion into the outer layers of the sclera. Care is taken to avoid disruption of the anterior most subarachnoid space and the posterior ciliary artery insertions. The orbital optic nerve is cut 3 mm behind the globe. (b) A 6 mm trephine, centered on the ONH, is passed through the retina and peripapillary sclera, isolating the optic nerve head tissues which thus contain the peripapillary sclera, choroid and retina as well as the retrolaminar orbital optic nerve stump (not shown). (c) The trephine is embedded face down in paraffin and mounted on a microtome with the vitreous surface of the trephine facing out. The fresh block surface is stained with a 1:1 (v/v) mixture of Ponceau S and acid fuchsin stains, imaged at a transverse resolution of $1.5 \times 1.5 \mu\text{m}$ per pixel and serial-sectioned at $1.5 \mu\text{m}$ increments. (d) Imaging of the stained embedded tissue block surface starts at the vitreoretinal interface and ends approximately 1 mm into the retrolaminar orbital optic nerve. The position of the tissue block and camera are recorded by laser displacement sensors (Keyence Corporation, Woodcliff Lake, NJ) at each serial section. (e) All acquired digital section images are then stacked and aligned using the laser position data into a digital 3-D reconstruction

location of the microtome head prior to imaging. The current system is an upgrade to our previous one that utilized a smaller camera that captured images at $2.5 \times 2.5 \mu\text{m}$ resolution [1].

10. The image acquisition process involves seven scripted steps:
 - (a) Stain the surface of the block with a 1:1 (v/v) mixture of Ponceau S and acid fuchsin stains (which only adheres to the exposed connective tissues).
 - (b) Allow the stain to penetrate for a fixed length of time (10–15 s, depending on the tissue).
 - (c) Wipe the surface of the block with a ddH₂O wetted MiraSwab[®] (Foamtec International WCC, Oceanside, CA) oval tipped cleaning swab.
 - (d) Disperse any residual stain by gently blowing the surface of the block with compressed air.
 - (e) Image the surface of the block. Use the first laser displacement measurement as reference and then shift all subsequent images along the Y-axis by an amount proportional to the difference of the current laser displacement measurement to reference. This ensures the correct alignment of the images so that they can be stacked in the Z direction to form a volume. Save the image to disk. This step may need to be repeated if the stain penetration is not deemed to be satisfactory (in which case, the process starts again at step (a), *see Note 1*).
 - (f) Cut the block at $1.5 \mu\text{m}$ thickness and repeat the process again until the cut section is approximately $200 \mu\text{m}$ past the outer-most point of the posterior (outer) lamina boundary.
 - (g) Change the section thickness to $20 \mu\text{m}$ and section through the remaining nerve to view the nerve cuts made prior to removing the optic nerve from the globe.

Additional details on how to incorporate room temperature and the need to cut through the lamina in a single cutting session (due to block face tissue swelling overnight) are discussed in **Notes 1** and **2**.

Fig. 1 (continued) consisting of approximately 3400 (width) \times 3200 (height) \times 500 – 1000 (depth) voxels, each $1.5 \times 1.5 \times 1.5 \mu\text{m}$ in size. The completed 3D reconstruction can then be digitally sectioned in any manner. Our current protocols generate 40 radial digital section images (the location of a single radial section is schematically depicted as a faint *white box*, above). The ONH anatomy within each digital section image thus samples the nerve in 4.5° increments. Pertinent ONH landmarks and surfaces are manually delineated as outlined in Figs. **2** and **3**

3.3 3D Reconstruction and Radial Digital Section Image Creation (Fig. 1)

1. All acquired images must be color-mapped and stacked to form a 3D HMRN volume. To perform the color mapping, custom software is utilized that quantifies all colors present in all images into 256 bins. The value of every pixel in the image stack is then replaced with the bin number that holds the color that's closest to the original. This reduces the memory footprint of the volume while preserving the original color information.
2. Once images are color-mapped, they are combined using custom software into a single stack (volume file). The volume file consists of a 2048-byte header (containing information such as the volume's dimensions, origin, and pixel sizes) followed by the stack of images organized in the same order as they are acquired (i.e., first acquired image frame is first in the stack). The volume is complemented with the color map file obtained in **step 1**.
3. Radial section images are produced using Multiview (MV), a custom-developed software application based on the Visualization Toolkit (VTK, Clifton Park, NY). Once a 3D HMRN volume is loaded, a center of rotation must be selected using MV's secondary (transverse) view. This point in space is generally located at the center of the ONH. To generate the radial section images, MV cuts the volume about the center of rotation perpendicularly to the X-Y plane. The resulting sagittal slice is presented to the user so that the ONH landmarks and surfaces can be delineated. The volume is cut at 4.5° creating a total of 80 radial sagittal section images. See **Note 3** for more details on the functionality of MV.

3.4 3D Delineation of ONH Landmarks and Surfaces (Figs. 2 and 3)

Delineation is an interactive process. While landmark points are placed on the sagittal view, the user continuously consults the transverse view where a cursor shows the linked transverse location (Fig. 2c). Thus, each landmark or surface point is selected with full awareness of the point's location within both the sagittal and transverse planes. If the landmark or structure is not readily visible in the sagittal section image, the delineator has the ability to scroll through six adjacent sections (three in front and three behind) to locate a section in which the landmark can be clearly identified and marked. For continuous landmarks, MV automatically generates and displays a real-time Bézier curve based on the landmark's discrete points. A separate window also shows the 3D point cloud (colorized according to landmark category). This view is particularly useful for checking mark placement. The delineated mark categories are listed below:

1. For each sagittal slice, seven landmark surfaces are delineated (Figs. 2b and 3a):

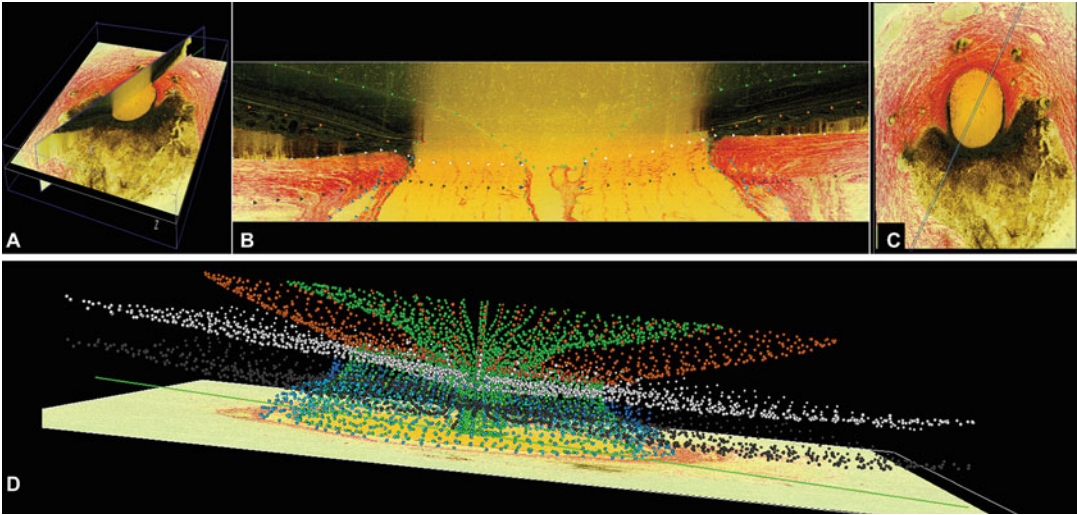


Fig. 2 3D delineation of ONH landmarks and surfaces. (a) A total of 40 serial digital radial sagittal slices, each 7 voxels thick, are served to the delineator at 4.5° intervals. (b) The representative digital sagittal section image seen in (a), in which each ONH landmark and surface (Fig. 3) has been 3D-delineated using linked, simultaneous, colocalization of the sagittal slice (shown) and the transverse section image through each delineated point (c). (d) Representative 3D point cloud showing all the delineated points from all 40 delineated radial section images for a normal monkey ONH, relative to the posterior-most transverse section image (vitreous top, orbital optic nerve bottom). *Reproduced from Investigative Ophthalmology & Visual Science, 2011, with permission from the Association for Research in Vision and Ophthalmology [5]*

- (a) Internal limiting membrane (ILM) (vitreo-retinal interface).
 - (b) Anterior and posterior surfaces of the peripapillary sclera.
 - (c) Anterior and posterior surfaces of the lamina cribrosa.
 - (d) External surfaces of the central retinal vessels (CRV).
 - (e) Bruch's membrane (BM).
 - (f) Neural canal wall (boundary between the neural and connective tissues starting at BMO, proceeding posteriorly along the border tissues of Elschnig, through the scleral canal, and along the pia matter boundary to the posterior edge of the reconstruction).
 - (g) Subarachnoid space (internal surface of the dural sheath and external surface of the pia matter).
2. For each sagittal slice, six pairs of neural canal landmark points (one point on each side of the canal) are delineated (Fig. 3a, b):
 - (a) Bruch's membrane opening (BMO).
 - (b) Anterior scleral canal opening (ASCO).
 - (c) Anterior laminar insertion (ALI).
 - (d) Posterior laminar insertion (PLI).

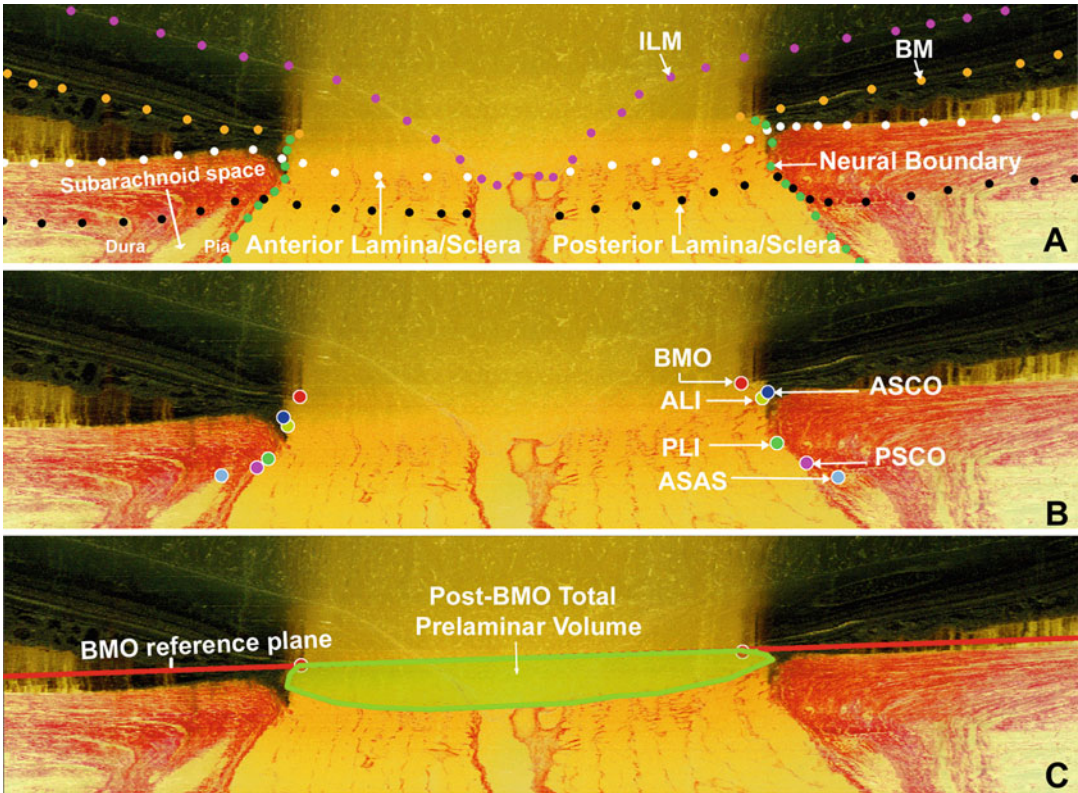


Fig. 3 ONH landmark and surface definitions. (a) A representative digital sagittal slice showing the internal limiting membrane (ILM, pink dots), Bruch’s membrane (BM, orange dots), anterior LC/scleral surface (white dots), posterior LC/scleral surface (black dots), and neural boundary (green dots). Subarachnoid space is the space between pial and dural sheaths in which the cerebrospinal fluid is contained. (b) A representative digital sagittal slice showing neural canal architecture. The neural canal includes Bruch’s membrane opening (BMO, the opening in the Bruch’s Membrane/Retinal Pigment Epithelial complex, red), the anterior scleral canal opening (ASCO, dark blue), the anterior LC insertion (ALI, dark yellow, partly hidden behind the ASCO in dark blue), the posterior LC insertion (PLI, green), and the posterior scleral canal opening (PSCO, pink). The anterior-most aspect of the subarachnoid space (ASAS, light blue) was also delineated. The portion of the 3D histomorphometric reconstruction that was defined to be “lamina cribrosa” for laminar beam segmentation purposes was contained within the anterior and posterior LC surfaces and the neural boundary. (c) *Post-BMO total prelaminar volume* (light green: a measure of the LC or connective tissue component of cupping) is the volume beneath the BMO zero reference plane (in red), above the lamina cribrosa and within the neural canal wall. *Reproduced from Investigative Ophthalmology & Visual Science, 2011, with permission from the Association for Research in Vision and Ophthalmology [5]*

- (e) Posterior scleral canal opening (PSCO).
 - (f) Anterior-most aspect of the subarachnoid space (ASAS).
3. The marks are saved to a disk.

3.5 Clinical Colocalization to ONH Stereophotos (Figs. 4 and 5)

To establish the clinical orientation of each 3D HMRN, the central retinal vessels (CRV) are delineated in MV (in the transverse view) starting at the top of the volume where the CRV branches are visible and continuing until all branches converge to the central retinal vessel trunk. In addition, the BMO is delineated in the sagittal view as described in Subheading 3.4. Once the vessels and BMO delineations are complete, the BMO centroid is computed and a plane is fit to the BMO marks and rotated so that it rests parallel to the X-Y plane. The same rotation is then applied to the CRV marks. A 2D projection of the rotated BMO and CRV marks (as well as the location of the BMO centroid) is then generated and saved as an image to be used in the colocalization step below (Fig. 5b). A clinical stereophoto showing the ONH as well as the CRV and the fovea of the same eye is then obtained (Fig. 5a). Using custom software, the 2D projection image is matched to the clinical photo using the vessels and BMO as landmarks (Fig. 5c). Next the center of the fovea in the clinical image is marked (Fig. 5d). The transformation (translation, rotation, and scaling) that is applied to the BMO and CRV projection image, and the location of the fovea and BMO centroid, are then saved as a colocalization (.col) file. The colocalized clinical image superimposed with the BMO and CRV projected delineations is also saved.

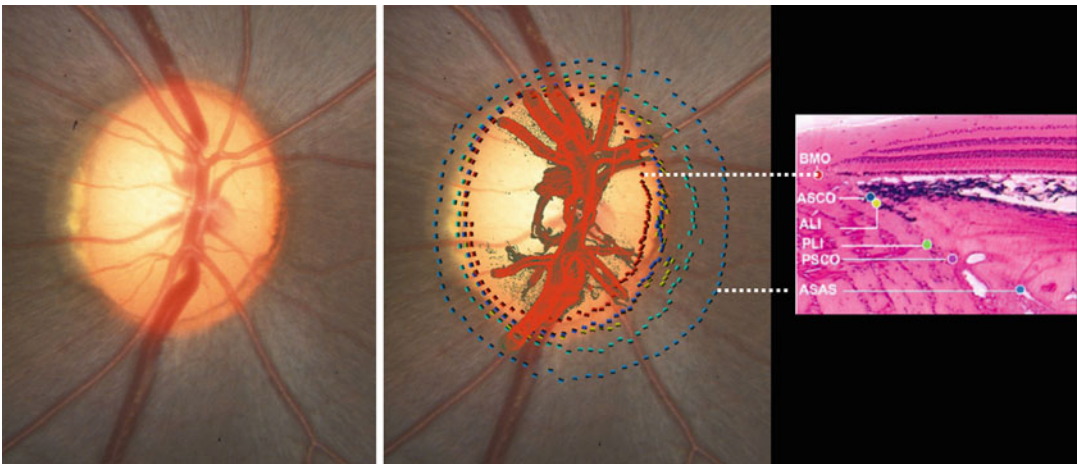


Fig. 4 Colocalization of the 3D histomorphometric reconstruction to a 2D clinical photo using Bruchs Membrane Opening (BMO—red dots) and the central retinal vessels. (Left) Color photo of the optic nerve head (ONH) of a control monkey eye. (Middle) Within the 3D histomorphometric reconstruction (3D HMRN) point cloud (Fig. 2d, above), the central retinal vessel (in red) and neural canal landmarks have been isolated. (Right) BMO is Bruch's Membrane Opening, ASCO is anterior scleral canal opening, ALI is anterior laminar insertion, PLI is posterior laminar insertion, PSCO is posterior scleral canal opening and ASAS is the anterior most sub-arachnoid space. The vessel and neural canal point clouds can be zoomed, rotated, and tilted, relative to the flat plane of the photograph to achieve the best match between the vessels, the clinical disc margin, and BMO (which usually colocalize in the monkey eye) [4, 12]

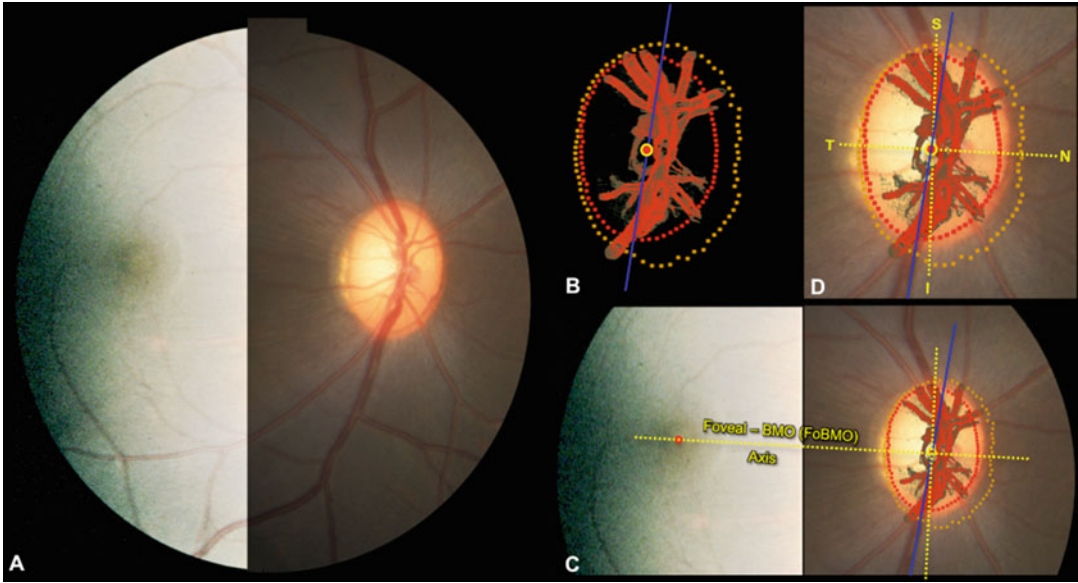


Fig. 5 Projecting the Foveal-BMO (FoBMO) Axis onto the 3D HMRN BMO reference plane of each ONH. (a) A fundus photo (here with brightness enhanced temporarily to better see the fovea), confocal scanning laser reflectance image (not shown) [6], or postmortem fundus photo (not shown) can be used to establish the axis between the fovea and the centroid of BMO for each eye as follows. (b) Delineated neural canal point clouds (BMO—red; anterior laminar insertion (ALI)—Dark Yellow) and central retinal vessels (red) accompanied by the BMO centroid (red circle with yellow outline) and the embedded tissue block vertical (blue line) orientation are colocalized to the clinical fundus photo (c) using the vascular tree and BMO points (Fig. 4, above). In this image BMO reference plane is slightly rotated out of the plane of the image to enhance visualization. The center of the fovea (red dot, (c)) is assigned to be the center of the dark foveal reflex or the center of the foveal capillaries. The axis connecting the center of the fovea to the BMO centroid (yellow with red center) is the FoBMO axis (c). Using the FoBMO axis as the nasal temporal (horizontal) midline, a FoBMO vertical axis is established perpendicular to it (c) allowing anatomically consistent, FoBMO superior, inferior, nasal, and temporal landmarks (d) within the BMO reference plane of each studied eye to be established. *Reproduced from Investigative Ophthalmology & Visual Science, 2015, with permission from the Association for Research in Vision and Ophthalmology* [6]

3.6 Establishing the Foveal-BMO Axis (Fig. 5)

The importance of the FoBMO axis to the organization of retinal and ONH anatomy has been described in a series of previous reports [13–19]. In our recent work [6] we estimated the location of the FoBMO axis relative to the vertical and horizontal axes of the embedded 3D HMRN so as to impose a consistent regionalization of ONH anatomy of each eye. Figure 5 describes the process for establishing the axis between the BMO centroid and the center of the fovea as the FoBMO nasal-temporal axis. The FoBMO vertical axis also passes through the BMO centroid, perpendicular to the nasal-temporal axis (Fig. 5c). Then, anatomically consistent, FoBMO superior, inferior, nasal, and temporal landmarks (Fig. 5d) within the BMO reference plane can be consistently established for each eye.

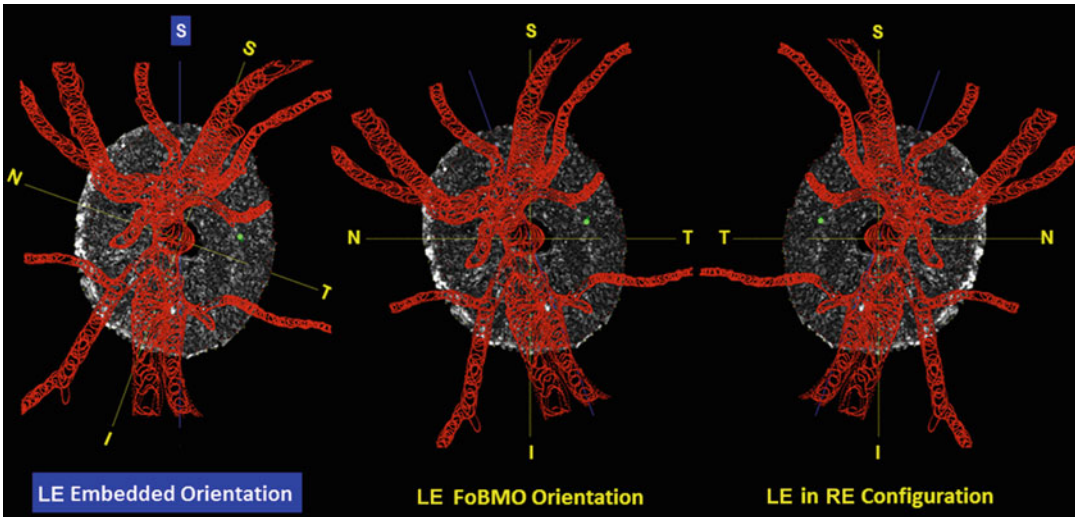


Fig. 6 Converting the 3D HMRN reconstruction from “embedded” to “FoBMO” orientation and from “left” to “right” eye configuration. (*Left*) Each ONH is embedded in a slightly different orientation, knowing that a Foveal-BMO (FoBMO) orientation can be imposed following ONH landmark delineation. The FoBMO vertical axis is established relative to the embedded tissue vertical as depicted for a right eye (RE) in Fig. 5, above. (*Middle*) The embedded data set is rotated (in this eye, counterclockwise 19.8°) to bring the FoBMO vertical optic nerve head anatomy into the vertical coordinate position. (*Right*) FoBMO oriented left eye (LE) data is translated to FoBMO right eye configuration, by shifting the x axis location of each voxel to a position that is equal in distance but opposite in direction from the y (FoBMO vertical) axis while holding the y and z axis positions (not shown) constant. The position of a representative group of surface voxels is shown through each step of the process by a green dot. *Reproduced from Investigative Ophthalmology & Visual Science, 2015, with permission from the Association for Research in Vision and Ophthalmology [6]*

3.7 Converting All Eyes to Right Eye (RE) Configuration (Fig. 6)

To most fairly compare the retinal and ONH anatomy of the left and right eyes, the anatomy of both the eyes must share the same coordinate system. In order to achieve this, we rotate all left eye (LE) data about the FoBMO vertical axis so that the nasal and temporal quadrants for both RE and LE agree. The example in Fig. 6 depicts the process used to transform LE data into RE eye orientation for laminar microarchitecture data [6]. First, the embedded LE data set is rotated (Fig. 6 left, in this eye, counterclockwise 19.8°) to bring the FoBMO vertical axis into the y-axis of the vertical coordinate position (Fig. 6 middle). FoBMO-oriented LE data are then translated to match the origin of its coordinate system with that of the RE (Fig. 6 right).

3.8 ONH Macroarchitecture Parameterization

3.8.1 Neural Canal (Fig. 7)

Quantification of the neural canal was done using custom-developed MATLAB (The Mathworks, Natick, MA) routines [20]. For each 3D HMRN, a least-squares ellipse is fitted to the 80 marks defining BMO, creating a BMO zero reference plane (Fig. 71). The centroid of the BMO ellipse establishes the center point and origin for all measurements. From the BMO fitted

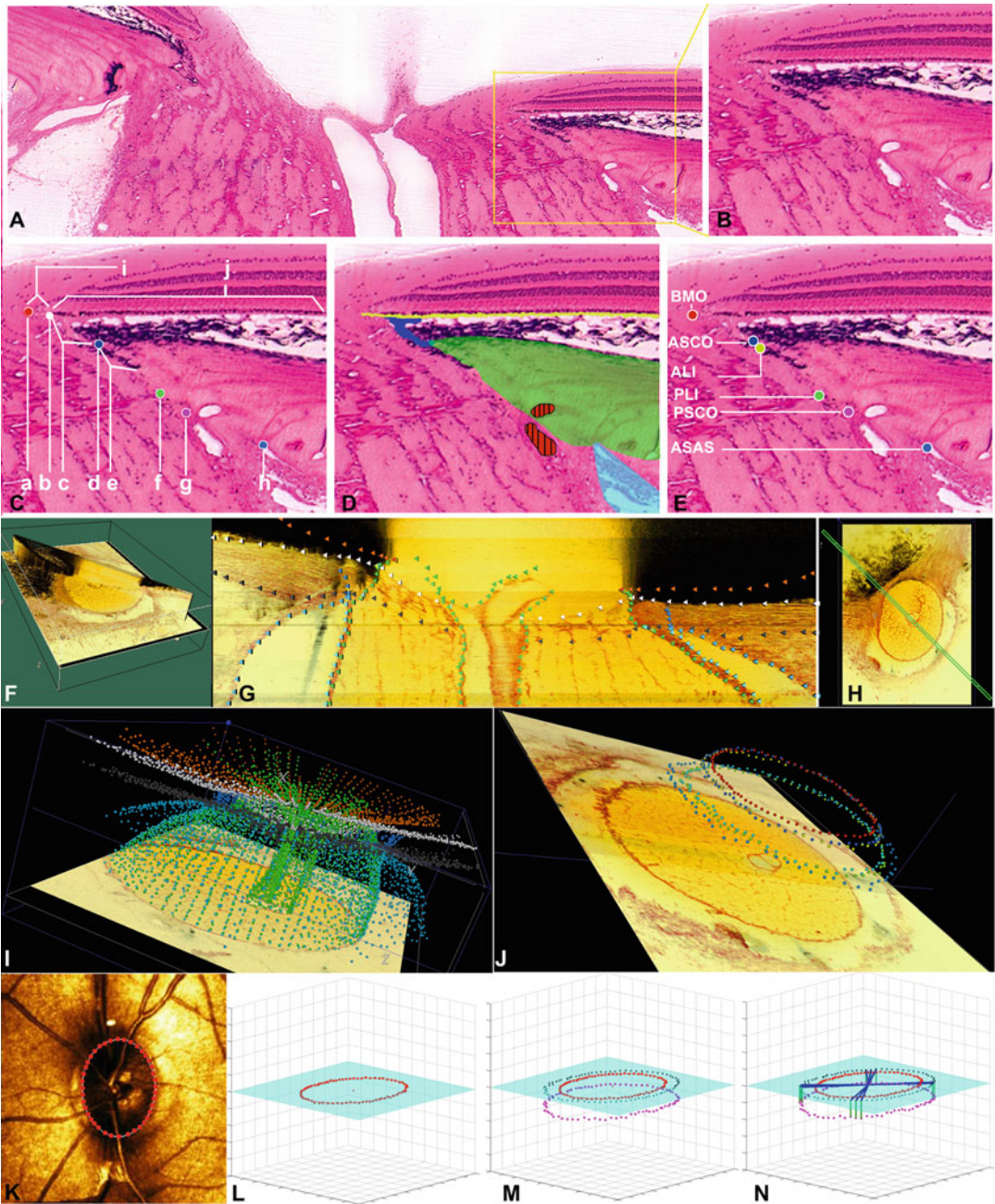


Fig. 7 3D delineation of ONH and peripapillary scleral landmark points within colorized, stacked-section, 3D ONH reconstructions. (a) Digital image of a representative central horizontal histologic section from a normal monkey eye perfusion fixed at an IOP of 10 mm Hg with the nasal side of the canal magnified in (b). (c) Histologic landmarks within (b) are labeled as follows: (a) Bruch's Membrane opening (BMO) margin; (b) insertion of the Border Tissues of Elschnig into Bruch's Membrane; (c) Border Tissues of Elschnig; (d) anterior scleral canal opening (ASCO); (e) Border Tissues of Jacoby, which in this region are heavily pigmented; (f) posterior lamellar insertion (PLI); (g) posterior scleral canal opening (PSCO); (h) anterior-most aspect of the subarachnoid space (ASAS); (i) BM flange, extending centrally beyond the Border Tissues and in

ellipse, the ellipse area and major and minor diameters as well as the BMO plane error (defined as the average of the shortest distance of each BMO point to the fitted BMO plane) are also recorded (*see Note 4*). Each neural canal landmark point collection (80 points, 2 for each of the 40 radial sagittal slices) (*see Subheading 3.4, step 2*) is projected onto the BMO zero reference plane (Fig. 7m). Two parameters are defined and calculated for each landmark point and structure (Fig. 7n): (1) *depth*—the anterior-to-posterior distance of each marked point to the BMO zero reference plane; and (2) *offset*—the radial distance (within the BMO zero reference plane) of each projected mark to the BMO centroid. These parameters can be regionalized using four (90°), eight (four 30° and four 60°) [2, 3, 20], twelve (30°) [6, 21], or Garway-Heath [19] sectors relative to FoBMO axis.

The following parameters are generated in this process:

1. BMO parameters
 - (a) *BMO fitted ellipse area.*
 - (b) *BMO Major and Minor diameters.*
 - (c) *BMO plane error.*
2. *Depth* parameters in 80 radials
 - (a) *ASCO depth.*
 - (b) *ALI depth.*
 - (c) *PLI depth.*
 - (d) *PSCO depth.*
 - (e) *ASAS depth.*

Fig. 7 (continued) this case without pigmentation and not covered by Retinal Pigment Epithelium (RPE); (j) RPE sitting on BM; (d) Principle tissues colored as follows: *yellow*—BM; *dark blue*—Border Tissues of Elschnig; *green*—sclera; *red hatched*—branches of posterior ciliary arteries; *light blue*—subarachnoid space; (e) Neural canal landmark points analyzed in this report; (f–j) 3D delineation methodology—note that generation of 3D ONH reconstructions from aligned serial section images is explained in Figs. 1 and 2 of our previous publication [1]. (f) A total of 40 serial digital, radial, sagittal slices (each 7 voxels thick) are served to the delineator at 4.5° intervals. (g) A representative digital sagittal slice, showing the marks for 7 landmark surfaces and 6 pairs of landmark points, which are 3D-delineated using linked, simultaneous, colocalization of the sagittal slice (shown) and the transverse section image (h). (i) Representative 3D point cloud showing all delineated points for a normal monkey ONH relative to the last section image of the reconstruction. (j) The subset of the 3D point cloud showing the neural canal landmarks reported in this study. (k) The 80 delineated BMO points are fit to an ellipse (l) that defines the BMO zero reference plane and the BMO centroid. All other neural canal landmark points are projected onto the BMO zero reference plane (m) shown here for the PSCO, only, then the distance from the BMO centroid (offset—*blue lines*) and distance from the BMO zero reference plane (depth—*green lines*) are noted for each marked point (n). *Reproduced from Investigative Ophthalmology & Visual Science, 2007, with permission from the Association for Research in Vision and Ophthalmology [20]*

3. *Offset* parameters in 80 radials

- (a) *BMO offset*.
- (b) *ASCO offset*.
- (c) *ALI offset*.
- (d) *PLI offset*.
- (e) *PSCO offset*.
- (f) *ASAS offset*.

Final results are saved in a text file for further statistical data analysis. See **Notes 5** and **6** for comments regarding these measurements.

3.8.2 *Clinical Disc Margin Anatomy (Fig. 8)*

In most monkey eyes, the connective tissues of the choroidal border zone (the Border Tissues of Elschnig [23, 24]) are robust and rise up to fuse with Bruch's Membrane which continues as a cantilevered connective tissue flange of variable length beyond this junction. The end of Bruch's Membrane is referred to as Bruch's Membrane Opening (BMO) (Figs. 7–9). Figure 8 demonstrates an example in which Bruch's Membrane extends beyond the Border Tissues of Elschnig, and is covered by mottled pigment. In this eye, BMO also colocalizes to the clinically visible optic disc margin.

In order to generate the diagrams shown in Fig. 8, the 3D reconstruction of the central retinal vessels and BMO (red) and ASCO points (blue) are first overlaid onto the clinical photo to obtain the best qualitative alignment of the vessel branch points using custom software, as explained in detail in Subheading 3.5 and Figs. 4 and 5. In Fig. 8d, the green line shows the approximate location of the digital sagittal section that is loaded into MV software in which the operator has delineated BMO on the nasal side of the canal (red dot) by positioning the cursor on this image (Fig. 8e) while simultaneously noting its position (red dot in green cross-hairs) within the slaved transverse section image (Fig. 8f). By referencing the colocalized image in Fig. 8b, the location of the digital section in 3D reconstruction is estimated in the clinical photo shown in Fig. 8g. Comparisons between the digital section image and the clinical photo can be made at the same radial section to correlate structures between these two modalities. It should also be noted that BMO can extend “inside” of or “beyond” the clinically visible optic disc margin, in monkeys [20] and more commonly humans [22]. This mismatch of BMO and the clinical disc margin can have important implications [21, 25].

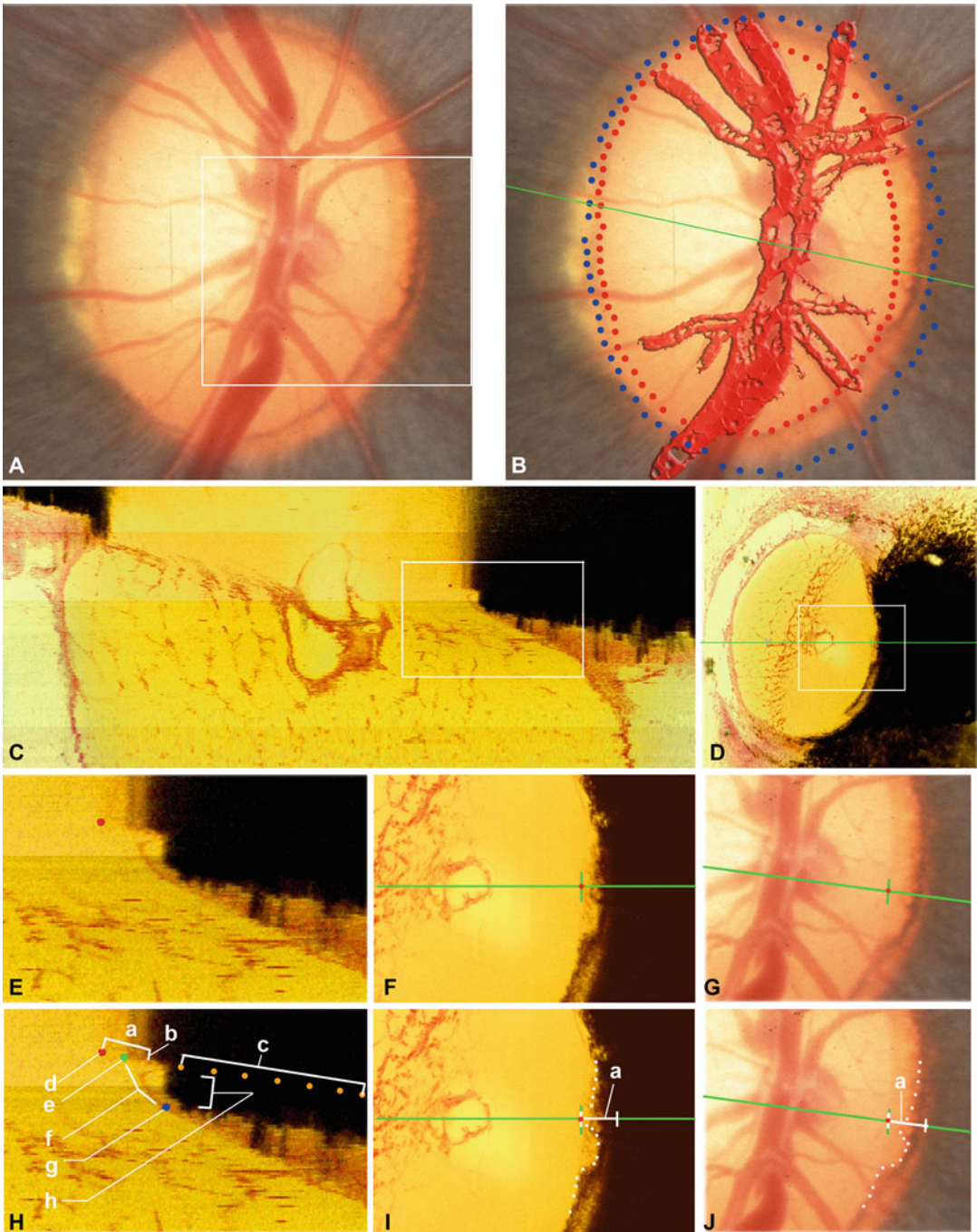


Fig. 8 Bruch's membrane opening is the clinically visible optic disc margin within clinical photos of Monkey 3. (a) Clinical photo of the control eye of Monkey 3 from previous publication [20]. The *white box* is shown in panels (g) and (j), (lower right). (b) 3D reconstruction of the central retinal vessels and BMO (*red*) and ASCO points (*blue*) for this eye are overlaid onto the clinical photo to achieve the best qualitative alignment of the vessel branch points. Note the alignment of BMO points with the optic disc margin in the clinical photo. The *green line* is the approximate location of the digital sagittal section shown in (c). (c) Digital sagittal section in

3.8.3 *Anterior Lamina Cribrosa and Peripapillary Scleral Position Relative to BMO Zero Reference Plane (Fig. 9)*

Laminar and peripapillary scleral position quantification utilizes custom MATLAB routines [3]. *The anterior lamina cribrosa position* is calculated at each anterior lamina point as the distance from the BMO zero reference plane (Fig. 9c) along a vector normal to that plane through the lamina point. *Peripapillary scleral position* is measured from each anterior peripapillary scleral surface point as the distance from the BMO zero reference plane along a vector normal to that plane (not shown). Position data can have both positive and negative values indicating its anterior or posterior position relative to the BMO zero reference plane. Lamina cribrosa and peripapillary scleral position data can also be regionalized by four, twelve [6, 21], seventeen [3], or Garway-Heath sectors [19] relative to the FoBMO axis and within central and peripheral locations relative to the center of BMO. See Notes 5 and 6 for comments regarding these measurements.

3.8.4 *Laminar and Peripapillary Scleral Thickness (Fig. 9)*

Laminar and peripapillary scleral thickness quantification utilizes custom MATLAB routines [3] in which the anterior and posterior lamina surface points are fit to continuous anterior and posterior surfaces using thin-plate B-splines. The anterior lamina B-spline surface is used to generate a normal vector at each delineated point (Fig. 9d, e). *The thickness of the lamina cribrosa* is calculated along the normal vector of each point at the vectors intersection with the posterior laminar surface (Fig. 9f) in 3D space. *Scleral thickness* is determined in a similar manner. Peripapillary scleral thickness is calculated at each delineated anterior scleral surface

Fig. 8 (continued) which the operator has delineated BMO on the nasal side of the canal (*red dot*) by positioning the cursor in this image, while simultaneously noting its position (*red dot within green cross-hairs*) within the slaved transverse section image through that point (*red dot within the green cross-hairs*) shown in (d). The *white boxes* in (c) and (d) are shown in magnified view in (e) and (f) along with an estimate of their location superimposed onto the clinical photo shown in (g). Labeling of panels (e), (f), and (g) that occurs in panels (h), (i), and (j) is as follows: (a) Bruch's Membrane extending over and beyond the Border Tissues of Elschnig, covered by variably mottled pigment; (b) probable start of viable RPE with a greater density of pigment; (c) BM points that are not clearly seen in this section image but are present when the brightness and contrast are adjusted (part of the normal delineation sequence); (d) BMO point (*red*) which is marked by the delineator by colocalizing the cursor in image (e) with the *green cross-hairs* of the cursor in the slaved transverse view (f); (e) the junction of the Border tissues of Elschnig (f) with Bruch's Membrane; (f) the Border Tissues of Elschnig; (g) the anterior scleral canal opening (ASCO); (h) heavy pigmentation within the choroid. The *white dotted line* in panels (i) and (j) outlines the border of more densely mottled pigment on BM which that is visible within the clinical photos and serial transverse section images of the 3D reconstruction. *Summary.* Taken together, the images within this figure demonstrate that for this region of this eye, lightly pigmented BM extends beyond the Border Tissues of Elschnig and BMO is the clinically visible optic disc margin in this eye. However, it should also be noted that BMO commonly extends inside of or beyond the anatomy that underlies the clinical disc margin in monkey eyes [20], and this is even more common in human eyes [22]. *Reproduced from Investigative Ophthalmology & Visual Science, 2007, with permission from the Association for Research in Vision and Ophthalmology [20]*

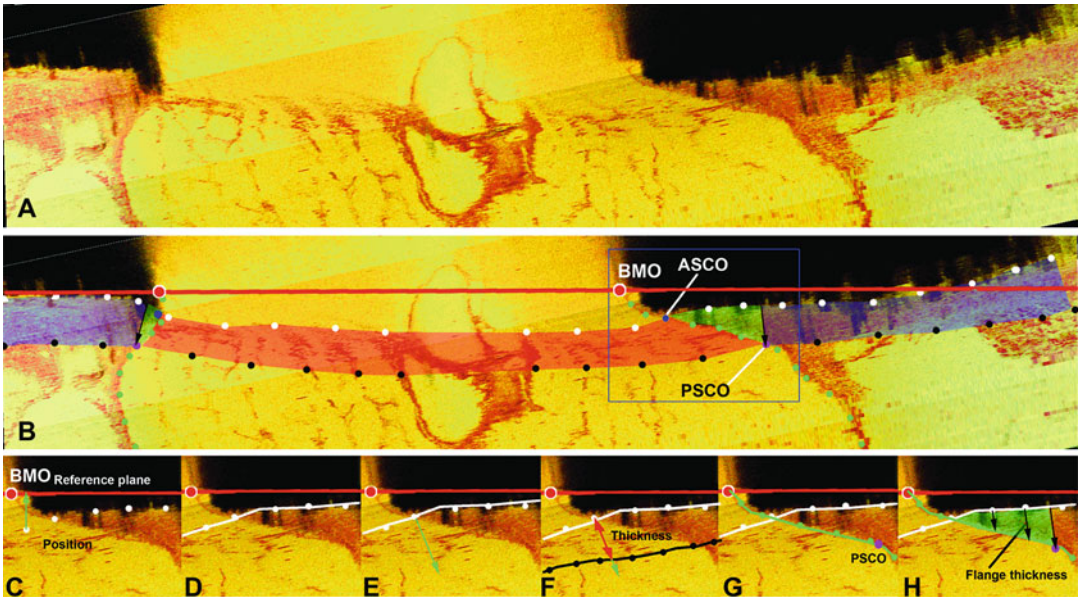


Fig. 9 ONH and peripapillary scleral anatomy and parameters. (a) Representative horizontal, digital sagittal section image from the 3D reconstruction of the left eye of Monkey 3 from previous publication [3] (temporal on left, nasal on right). (b) The definition and extent of the major structures quantified in the paper: lamina cribrosa (red) inserts into the scleral flange (green), which transitions into the peripapillary sclera (purple) at the posterior scleral canal opening (PSCO). The delineated points marking the anterior (white dots) and posterior (black dots) surfaces of the lamina cribrosa and sclera, the neural canal boundary (green dots), and neural canal landmark points are shown. The scleral flange is defined as the peripapillary sclera that extends from the anterior scleral canal opening (ASCO) to the normal from the anterior surface through the posterior scleral canal opening (PSCO normal vector—black arrow). The Bruch’s Membrane opening (BMO) zero reference plane is also shown (red line). (c) Laminar and scleral position (green arrow) at each delineated anterior laminal surface point (white dot) is defined as the shortest distance from the delineated point to BMO zero reference plane. (d) LC and peripapillary sclera thickness at each delineated anterior surface point is determined by fitting a continuous surface (white line) to all of the delineated anterior surface points (d). (e, f) Thickness is defined as the distance along a normal vector to the anterior surface (green arrow in e) from each anterior delineated point to the posterior surface (black line in f). (g) Thickness of the scleral flange at each delineated anterior surface point (white dots) is defined as the distance between the neural canal boundary points (green line in g and h), along a vector parallel to the PSCO normal vector. Reproduced from *Investigative Ophthalmology & Visual Science*, 2007, with permission from the Association for Research in Vision and Ophthalmology [3]

point along its normal vector at the point of intersection with the posterior scleral surface in 3D space. *Lamina cribrosa and peripapillary scleral thickness* are regionalized as outlined for their respective positions in Subheading 3.8.3, above. See Notes 5 and 6 for additional comments regarding these measurements.

3.8.5 Scleral Flange Thickness (Figs. 9 and 10)

We use the term “scleral flange” to refer to the sclera immediately adjacent to the neural canal. The scleral flange represents the transition between the lamina cribrosa, the oblique sclera canal wall,

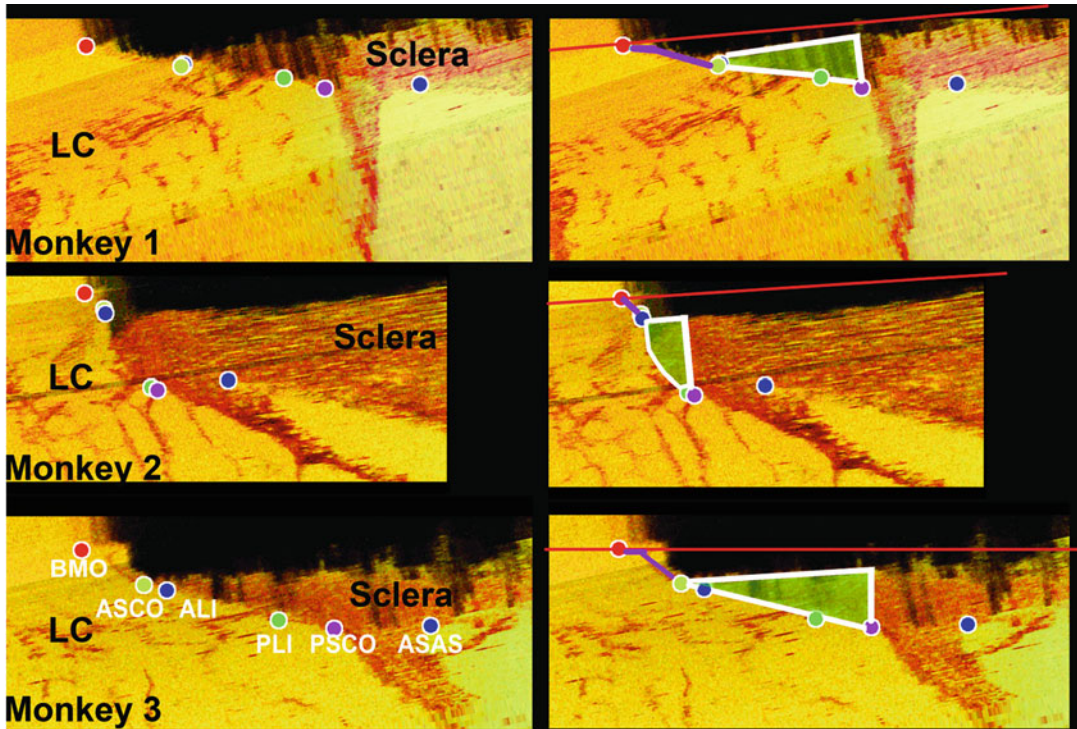


Fig. 10 Neural canal landmarks and scleral flange architecture within the nasal region of the control eye of three monkeys (*Left*) Neural canal landmarks within a digital sagittal section of the nasal ONH for each Control eye [20]. (*Right*) Border Tissues of Elschnig (*purple*) and scleral flange (*green*); note the relationship between regional neural canal obliqueness and scleral flange obliqueness in each eye. In general, a more oblique neural canal results in a more oblique scleral flange. While regional neural canal and scleral flange obliqueness are related, they may have separate clinical implications. *Reproduced from Investigative Ophthalmology & Visual Science, 2007, with permission from the Association for Research in Vision and Ophthalmology* [20]

and the peripapillary sclera. We define the peripapillary sclera to start at that portion of the peripapillary sclera that has obtained its full thickness. Because in most eyes, the scleral canal is both oblique to the plane of the inner and outer scleral surfaces and smaller at its inner (anterior) opening than at its outer (posterior) opening, (i.e., it expands within the sclera), the scleral flange is commonly triangular, with its tip underlying the ASCO and its base forming the start of the full-thickness peripapillary sclera [3].

We treat the scleral flange as a unique structure because it contains the penetrating branches of the Circle of Zinn-Haller and likely underlies scleral involvement in the neuropathy of monkey and human glaucoma. Figure 10 illustrates scleral flange architecture and demonstrates the fundamental relationship between scleral canal and scleral flange obliqueness at a given radial location. *Scleral flange* thickness is defined as the distance from the anterior scleral flange surface to the scleral canal wall surface and its

quantification is performed within custom MATLAB routines [3]. Anterior scleral flange surface and scleral canal wall surface points are fitted to continuous anterior and posterior surfaces of the scleral flange using thin-plate B-splines. *Scleral flange thickness* is calculated along a normal vector from each scleral flange surface point to its intersection with the scleral canal wall surface (Fig. 9g, h). Scleral flange thickness can be regionalized as outlined for other parameters above, relative to the FoBMO axis and within central and peripheral locations relative to the center of BMO. See **Notes 5** and **6** for additional comments regarding these measurements.

3.8.6 Prelaminar and Lamellar Cupping (Figs. 11, 12, and 13)

Figure 11 demonstrates our four ONH cupping parameters: *Post-BMO Cup Volume*, *Post-BMO Total Prelaminar Volume*, *Prelaminar Neural Tissue Volume*, and *Prelaminar Tissue Thickness* [2]. *Post-BMO Cup Volume* is a measure of the clinical cup, which we define to be the volume of empty space beneath the BMO zero reference plane but above the ILM surface. *Post-BMO Total Prelaminar Volume* is defined to be the total volume (tissue and non-tissue) beneath the BMO zero reference plane, above the lamina cribrosa, and within the neural canal wall. It is designed to detect three forms of scleral canal wall and lamina cribrosa connective tissue deformation and remodeling including scleral canal expansion, lamina cribrosa posterior deformation, and anterior lamellar insertion posterior migration. *Prelaminar Tissue Volume* is intended to detect increases or decreases in the volume of the prelaminar tissues. It is defined to be the total volume of tissues (including vascular and neural) above the lamina cribrosa, below the internal limiting membrane, and within the anterior projection of BMO.

A combination of commercial (Geomagic, Geomagic Research, Triangle Park, NC) and custom software is used to generate the volumetric parameters described above. Briefly, delineated marks are separated by category after transforming them to the BMO reference plane coordinate system (BMO centroid is the origin, BMO plane is the x-y plane) and loaded into Geomagic software. Smooth surfaces are fit to ILM, neural boundary, and the anterior lamina cribrosa surface points. Geomagic “Boolean,” “Cross-section,” and “Extrude” tools are used to generate the following closed, isolated surfaces: *Post-BMO Cup Volume* (Fig. 11d), *Prelaminar Tissue Volume* (Fig. 11e), and *Post-BMO Total Prelaminar Volume* (Fig. 11c). These surfaces are then loaded into custom applications to generate regional values, which are used to project 15° radial regional maps onto fundus photographs or Confocal Scanning Laser Tomography images as shown in Figs. 12 and 13. Between-eye regional difference maps are generated for each animal (Figs. 12 and 13) to depict EG versus Control eye differences of an

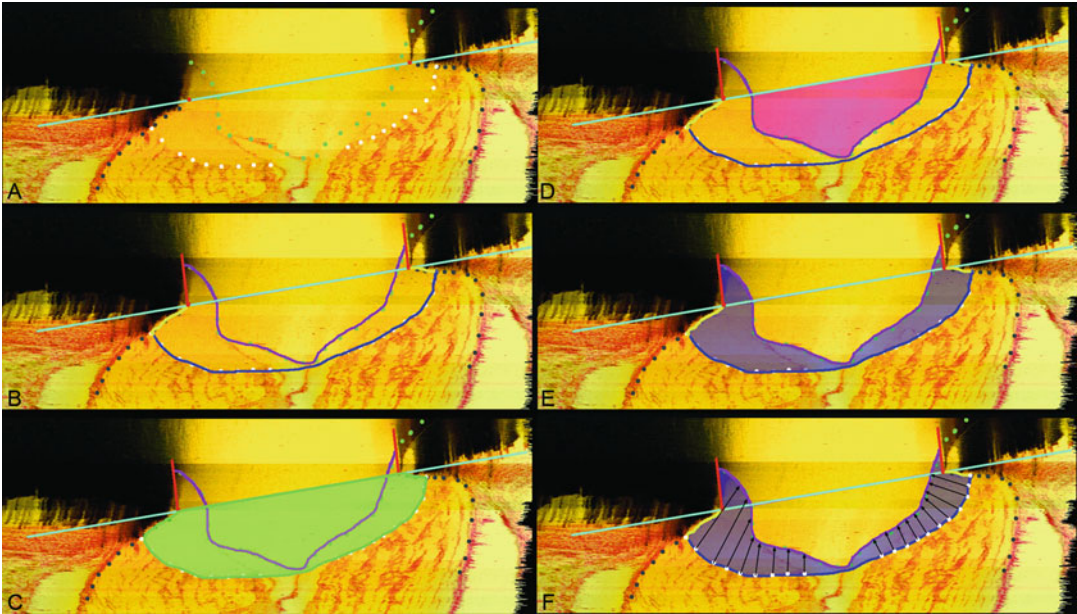
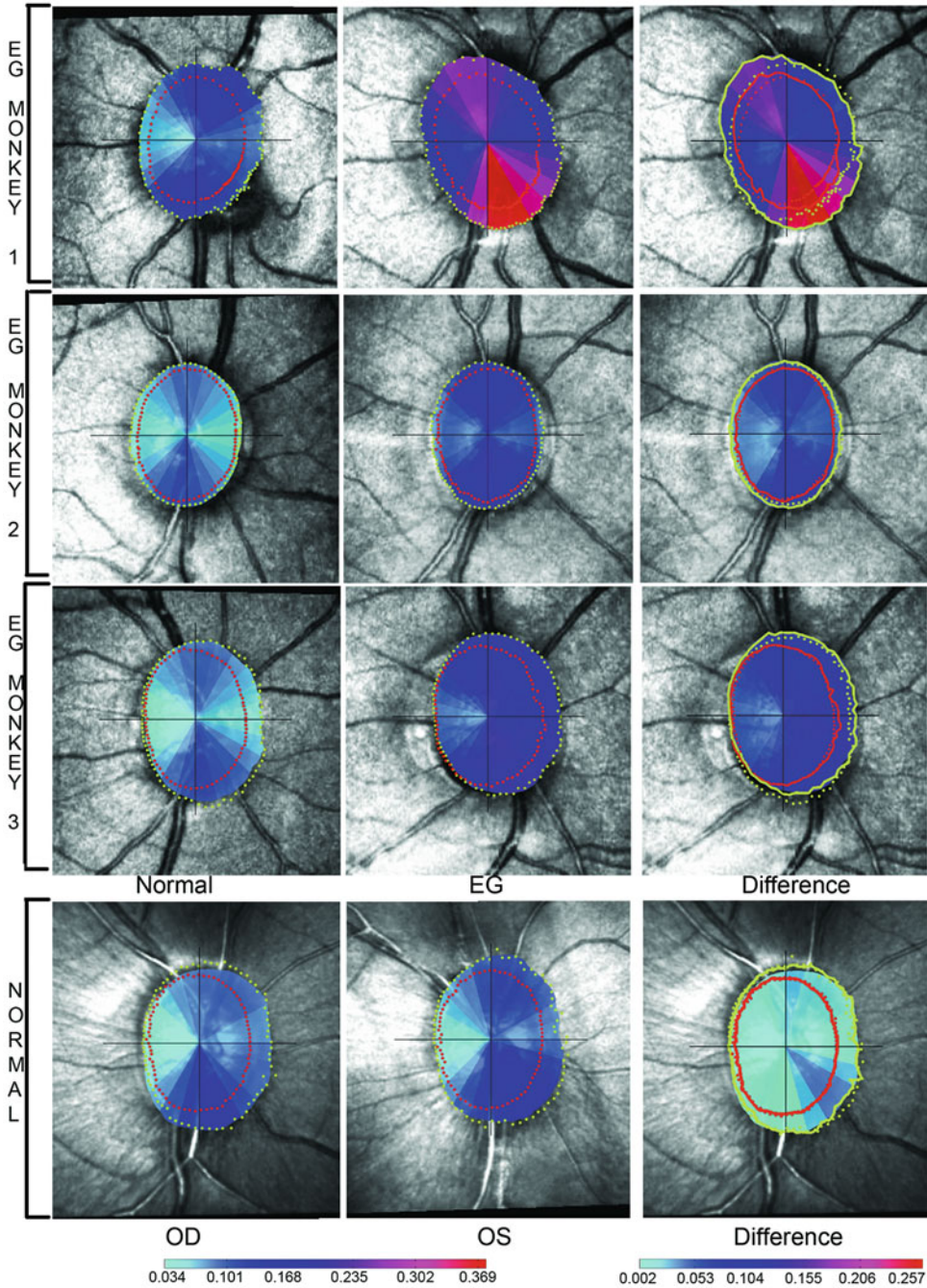


Fig. 11 Prelaminar tissue landmarks and cupping parameters. (a) Representative horizontal, digital, sagittal section image from the 3D reconstruction of the experimental glaucoma (EG) eye of Monkey 1 from previous publication [2] (temporal on right, nasal on left) with the following prelaminar tissue landmarks delineated: Internal limiting membrane (ILM—green dot); anterior lamellar surface (white dot); neural canal wall (dark gray dot); Bruch’s membrane opening (BMO—red dot). BMO-zero reference plane (cyan line). (b) Continuous surfaces are fit to internal limiting membrane (pink line), neural canal wall (yellow line), and anterior lamellar surface (dark blue). A cylindrical surface generated by projecting the BMO points up to the internal limiting membrane surface (red line) defines the outer border of the prelaminar tissue volume above BMO reference plane. (c) *Post-BMO Total Prelaminar Volume* (light green shading—a measure of the “lamellar” or connective tissue component of cupping) is the volume beneath BMO zero reference plane, above the lamina cribrosa and within the neural canal wall; (d) *Post-BMO Cup Volume* (pink shading—a measure of the clinical cup) is the volume (of the clinical cup) beneath BMO zero reference plane but above the internal limiting membrane; (e) *Prelaminar Tissue Volume* (purple shading) is the volume above the lamina, inside the neural canal and below the internal limiting membrane within the cylinder defined by the BMO projection; and (f) *Prelaminar Tissue Thickness* (purple with arrows) is defined as the distance along a normal vector from each delineated anterior lamellar surface point (white dots), to the internal limiting membrane surface (pink line). *Reproduced from Investigative Ophthalmology & Visual Science, 2007, with permission from the Association for Research in Vision and Ophthalmology* [2]

individual EG monkey or the between eye differences of a bilaterally normal monkey.

Continuous plots of *Prelaminar Tissue Thickness* are generated for each eye by interpolating between the values measured at each delineated anterior lamellar surface point (Delaunay-based cubic interpolation; Matlab, The Mathworks, Natick, MA). *Prelaminar Tissue Thickness* regional and between eye difference maps are plotted for each eye and each animal, respectively, as outlined above. See **Notes 5** and **6** for additional comments regarding these measurements.



Post-BMO Total Prelaminar Volume

Fig. 12 Regional *Post-BMO Total Prelaminar Volume* and Difference Maps for three representative early experimental glaucoma (EG) and one bilateral normal monkey [2]. Fifteen degree radial region maps for the control (*left column*) and EG eye (*middle column*) of three EG monkeys (Top three rows) —all presented in right eye (RE) configuration. Data for the right and left eyes (LE) of the bilateral normal monkey (both in RE configuration) are mapped below, for context. Difference maps (EG—control eye for the three EG monkeys;

3.8.7 Laminar Insertion and Migration (Figs. 14, 15, and 16)

To precisely quantify laminar insertion position within the scleral canal so as to test hypotheses regarding EG versus control eye laminar insertion migration in early EG, we developed the four laminar insertion and migration parameters depicted in Fig. 15 [5] and defined below:

1. *Anterior Laminar Insertion Position (ALIP)*, defined to be the position of the ALI measured as a direct line distance from the ASCO.
2. *Posterior Laminar Insertion Position (PLIP)*, defined to be the position of the PLI measured as a direct line distance from the PSCO.
3. *Laminar Insertion Length (LIL)*, defined as the distance from the ALI to the PLI.
4. *Scleral Thickness at ASAS*, defined as the minimum distance between anterior scleral surface and the posterior scleral surface at the ASAS.

Because the most consistent and statistically robust characterization of this anatomy (within and between eyes) would be based on equally-spaced measurements within radial sections that are perpendicular to the BMO reference plane, the initial delineations described above are digitally resampled to produce 40 “*resampled*” radial section images as explained in Fig. 15. For each ONH 3D HMRN, ASCO, ALI, PSCO, and PLI landmarks (2 points in each of the 40 original, radial digital section images or 80 total points for each landmark) are fitted with B-spline curves as shown in Fig. 15b. The BMO reference plane is obtained (*see* Subheading 3.8.1) and used to generate a second set of 40 *resampled* radial digital sections centered on the BMO centroid and perpendicular to the BMO reference plane (Fig. 15d). The cut surface of a representative *resampled* radial section image is shown in Fig. 15d. The isolated neural boundary from the edge of the cut surface is illustrated in Fig. 15f. *ALIP*, *PLIP*, and *LIL* calculations are performed on the isolated neural boundary from both sides of each radial section as the straight distance between points along the curved boundary (Figs. 14 and 15).

←

Fig. 12 (continued) LE—RE eye for the bilateral normal monkey) are plotted in RE configuration on the EG (EG monkeys) or RE (normal monkey) eye in the right column. Colocalized Bruch’s Membrane Opening (BMO—*red points*) and anterior laminar insertion (ALI—*yellow points*) are present in each eye-specific figure (left and middle columns) and are overlaid onto the difference maps on the right (solid line for EG eyes of EG monkey or RE eye of normal monkey and dotted for control eyes of EG monkey or LE eye of normal monkey). Color-coded volume unit is mm^3 (*see* scale below). Note that volume expansion in all three EG monkey difference maps exceeds physiologic intra-animal difference as quantified (requiring lighter colors) in the normal monkey difference map (*bottom right*). *Reproduced from Investigative Ophthalmology & Visual Science, 2007, with permission from the Association for Research in Vision and Ophthalmology [2]*

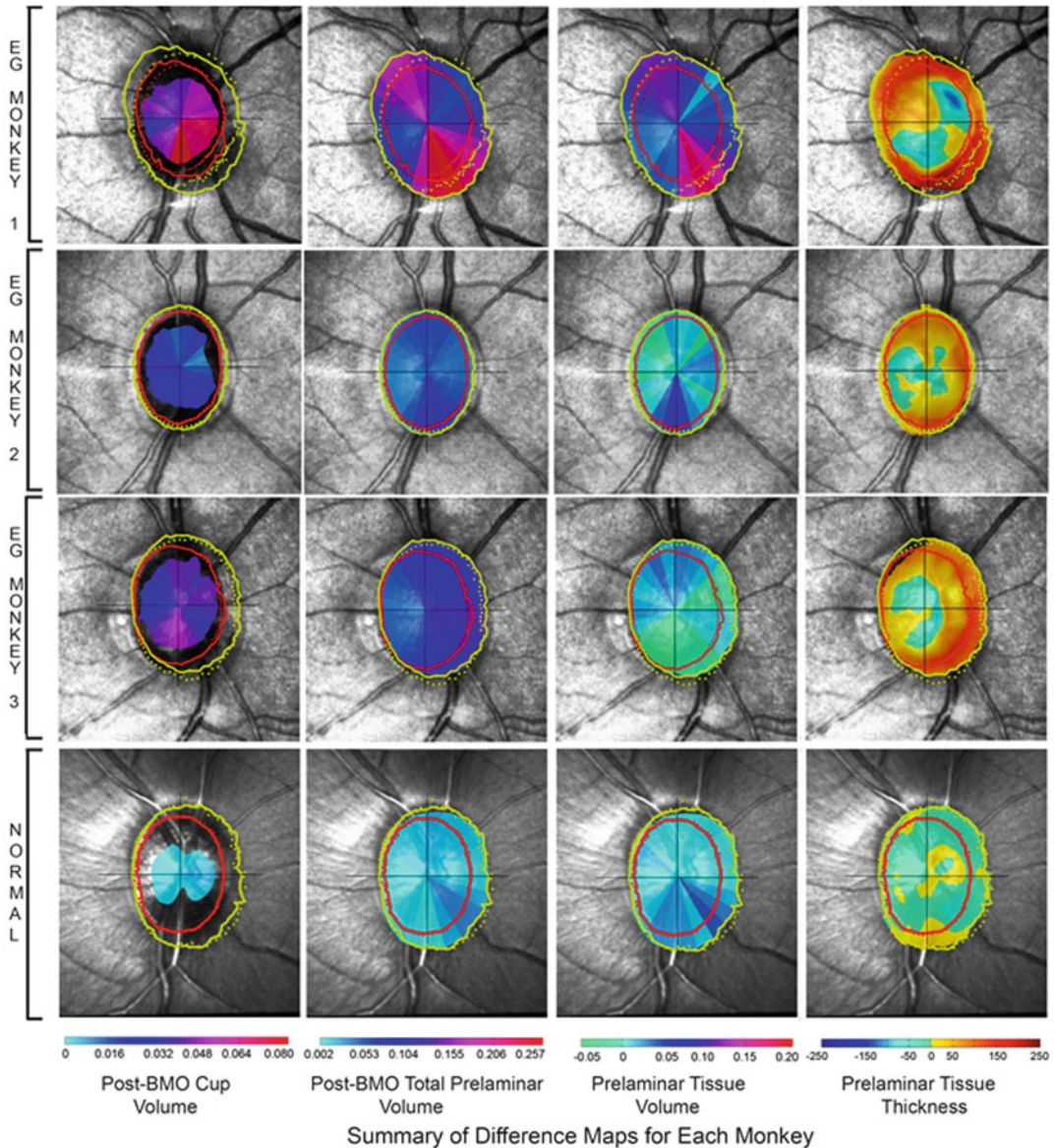


Fig. 13 Summary of cupping parameter difference maps for three representative early experimental glaucoma (EG) monkeys and one bilateral normal monkey. EG versus control eye difference maps of *Post-BMO Cup Volume*, *Post-BMO Total Prelaminar Volume*, and *Prelaminar Tissue Volume* (1st, 2nd, and 3rd columns in mm^3) and *Prelaminar Tissue Thickness* (4th column in μm) for three representative EG monkeys (above) and a bilateral normal monkey (below) are presented in columns 1–4. A scale for each parameter is shown below its column. *Reproduced from Investigative Ophthalmology & Visual Science, 2007, with permission from the Association for Research in Vision and Ophthalmology [2]*

To calculate *scleral thickness at the ASAS*, B-Spline surfaces are fit to the anterior scleral and posterior scleral points. The ASAS is then projected to the posterior scleral surface and the minimum distance from the anterior scleral surface to the posterior scleral

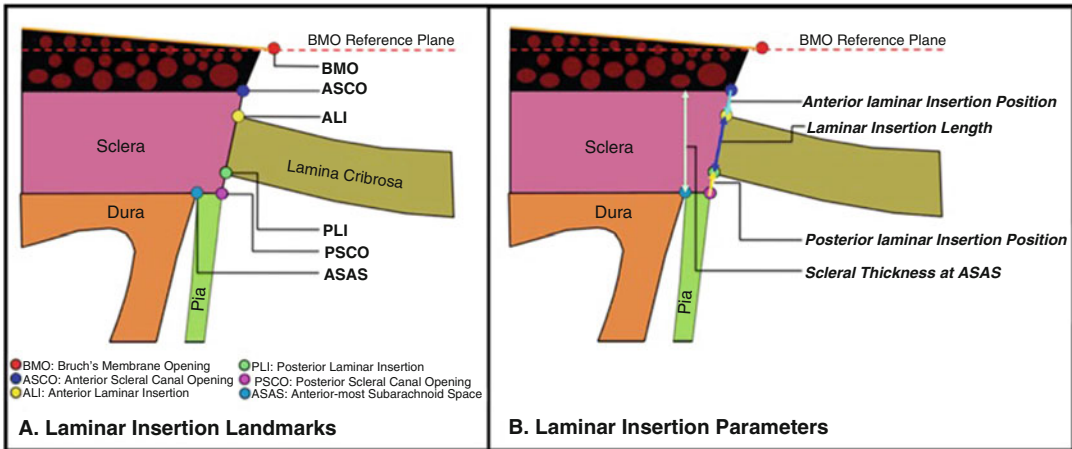


Fig. 14 Lamellar insertion landmarks (A) and parameters (B). (a) Schematic depiction of the six lamellar insertion landmarks. (b) Four lamellar insertion parameters are depicted in (B). *Anterior Lamellar Insertion Position (ALIP)* is the position of the anterior lamellar insertion (ALI) relative to the anterior scleral canal opening (ASCO). ALIP is positive (not shown) when the anterior lamina inserts into the Border Tissues of Elshnig and negative (*cyan arrow*) when the anterior lamina inserts into the sclera. *Posterior Lamellar Insertion Position (PLIP)* is the position of the posterior lamellar insertion (PLI) relative to the PSCO. PLIP is positive (*red arrow*) when the posterior lamina inserts to the sclera and negative when the posterior lamina inserts to the pia (shown in Fig. 16b). *Lamellar Insertion Length (LIL)* is the distance between the anterior and posterior lamellar insertions (*blue arrow*). *Scleral Thickness at ASAS (light green arrow)* is the minimum scleral thickness measured from the anterior most aspect of the subarachnoid space. Reproduced from *Investigative Ophthalmology & Visual Science*, 2011, with permission from the Association for Research in Vision and Ophthalmology [5]

surface passing through the projected ASAS point is obtained. Lamellar insertion parameters can also be regionalized as outlined for their respective positions in Subheading 3.8.3. These measurements are done using custom software that incorporates VTK (VTK Visualization Toolkit, Kitware Inc., New York).

3.8.8 Physiologic Inter-Eye Difference Characterization

We characterized the upper range of *physiologic inter-eye differences (PIDs)* and *percent differences (PIPDs)* in ONH neural and connective tissue parameters within six bilaterally normal monkeys so as to be able to require that EG versus control eye differences in each individual EG animal exceed these differences to be meaningful [4, 26, 27]. For each animal, it is calculated for each parameter (both overall and regionally) by converting all LE data to RE configuration, subtracting the LE from the RE parameter value and taking the absolute value (*see Note 7*). *PIPD* for each parameter is calculated as the *PID* divided by the minimum of the absolute measurement values of the two eyes. *PID* range is the range of *PID* values among the six bilateral normal animals. *PID_{Max}* is the largest *PID* value (the upper range of *PID*) among the six bilateral normal animals. *PIPD* range is the range of *PIPD* values among the six bilateral normal animals and the *PIPD_{Max}* value is the largest *PIPD* (the upper range of *PIPD*) among the six bilateral normal animals.

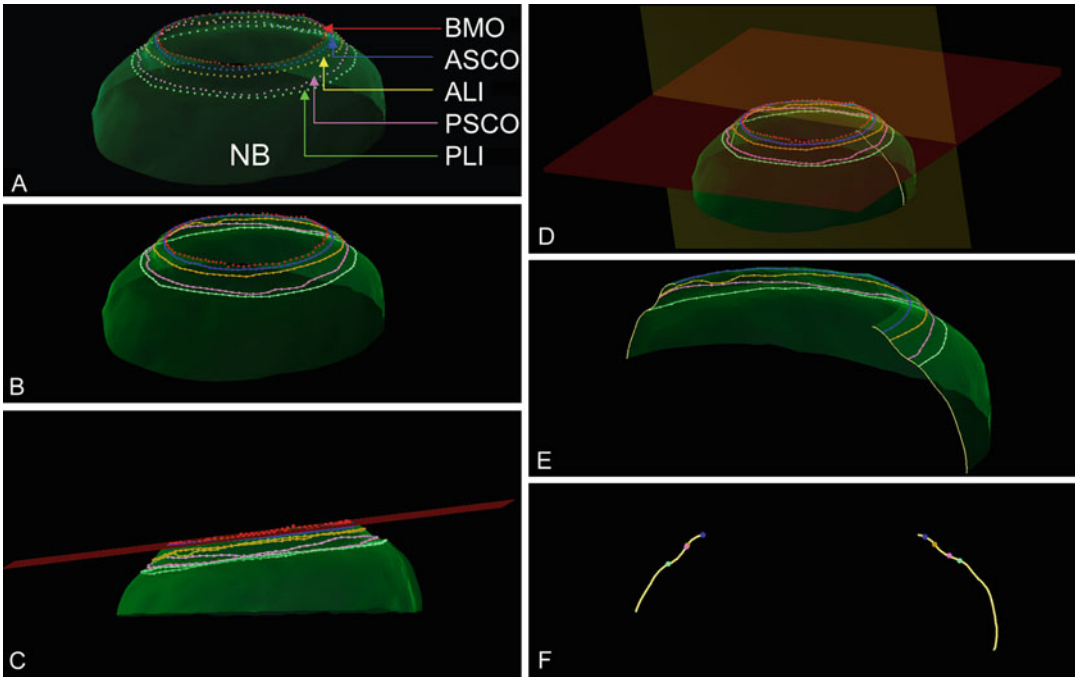


Fig. 15 Laminar migration and pialization parameters are measured within a separate set of 40 digital radial sections of the neural boundary surface and neural canal landmark B-splines acquired relative to the BMO centroid and perpendicular to the BMO reference plane. The most consistent and statistically robust characterization of this anatomy (within and between eyes) is based on equally spaced measurements within true perpendicular sections. Therefore, initial laminar insertion landmark delineations of each eye (described in Fig. 14a) are digitally resampled as follows: (a) 3D delineated neural canal landmark points (Fig. 14a) are shown as colored dots on the fitted neural boundary surface. (b) Each set of neural canal landmark points is fit with a smoothed B-spline curve. (c) A BMO reference plane (*red*) is fit to the 80 BMO landmark points satisfying a least mean square error as previously described [3, 20]. (d) To generate the laminar migration and pialization parameters explained in Fig. 14b, the neural canal landmark B-splines are then sampled using 40 radial digital sagittal sections that are centered at the BMO centroid and acquired perpendicular to the BMO reference plane. (e) The cut surface of the radial section in (d) is shown in the nasal-temporal region of the ONH. (f) The isolated neural boundary from the edge of the cut surface is illustrated. *Reproduced from Investigative Ophthalmology & Visual Science, 2011, with permission from the Association for Research in Vision and Ophthalmology* [5]

3.8.9 Experiment-Wide and Animal-Specific EG Versus Control Eye Difference Determination

To evaluate experiment-wide (all EG animals considered together) EG versus control eye differences for parameters with multiple values per eye or region, (like *scleral* or *laminar thickness*) a general estimating equation is commonly used in which significance is achieved at $p < 0.05$. However, to establish the most conservative criteria required to account for multiple comparisons, the required p value is $p < 0.05/N$, where (N) is the number of comparisons. All steps are performed within Microsoft Excel (Microsoft, Redmond, WA, USA) or in R statistical Software (R Foundation for Statistical Computing, Vienna, Austria). To evaluate experiment-wide EG versus Control eye differences in parameters with a single value

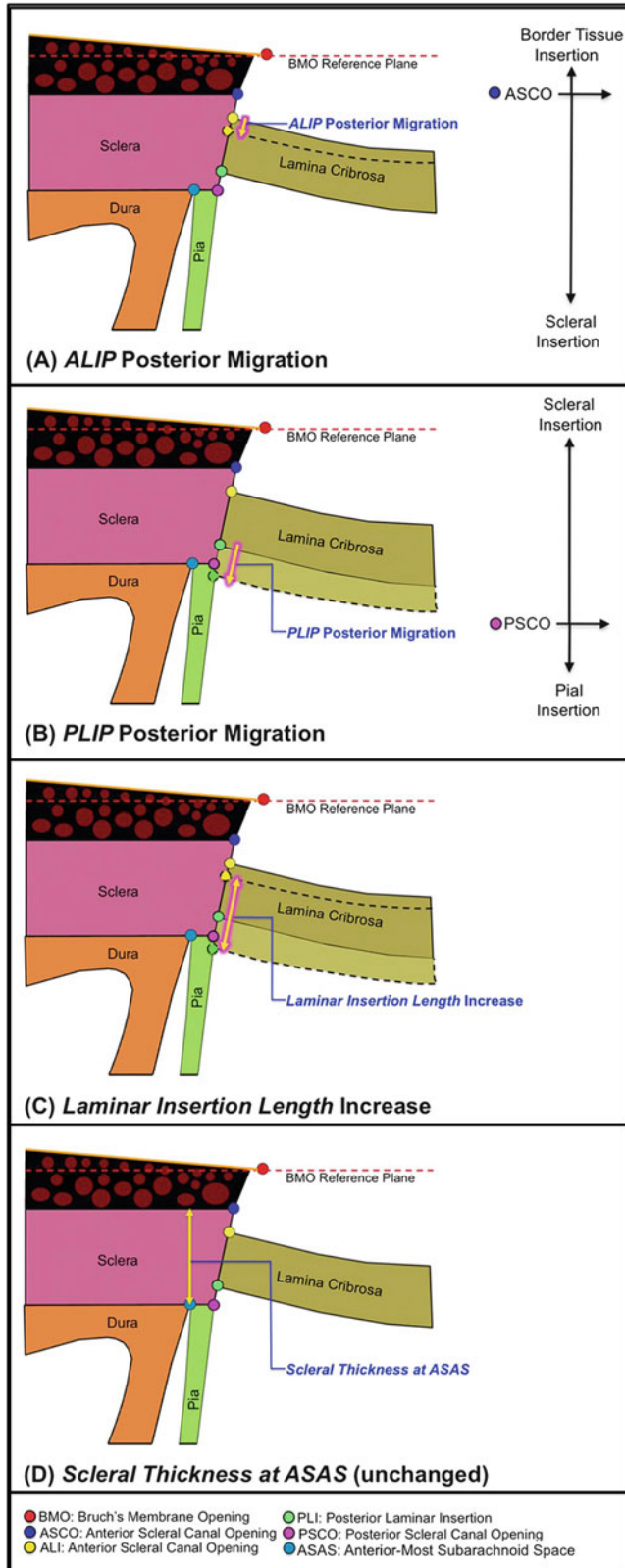


Fig. 16 Definitions of lamina insertion migration. (a) *Anterior Lamina Insertion Position (ALIP)* is plotted relative to the Anterior Scleral Canal Opening (ASCO) and becomes more negative as the ALI migrates away

per eye (such as global *Post-BMO Total Prelaminar Volume*), a paired T-test is applied with the same p value required for significance, and the same adjustment in the p value is made to establish the most conservative criteria for accounting for multiple comparisons. Animal-specific EG versus control eye differences for each parameter are required to achieve statistical significance (for those parameters with multiple measurements per eye) and/or exceed global and/or regional PID_{max} or $PIPD_{max}$ values for that parameter (*see* Subheading 3.8.8, above) [2–4, 20, 26, 27].

3.9 Laminar Microarchitecture Parameterization (Figs. 17, 18, 19, 20, 21, 22, 23, 24, 25, 26, and 27)

An overview of the method is depicted in Fig. 17 [6]. Details of each step are outlined in Figs. 18–27. Within these Figures, scaling for *beam diameter* (BD), *pore diameter* (PD), *connective tissue volume fraction* ($CTVF$), and *connective tissue volume* (CTV) has been adjusted so that “white” suggests “more” and “black” suggests “less” connective tissue. *Lamina volume* (LV) is depicted in green because it is not intended to convey connective tissue magnitude or density. All data are reported in 12 FoBMO 30° sectors within 12 central and 12 peripheral *subsectors* (Fig. 17); and also within inner ($1/3$), middle ($1/3$), and outer ($1/3$) lamina cribrosa (LC) layers (Fig. 21). We use “global” to refer to LMA data for a single ONH that includes all sectors, subsectors, and depths. We use “overall” or “experiment-wide” to refer to LMA data for all study eyes considered together.

3.9.1 Laminar Beam Segmentation (Fig. 18)

To isolate the laminar portion of the 3D HMRN (i.e., the *laminar volume*), the delineated points for the anterior and posterior sclera and LC are fit with B-spline surfaces using custom-developed software incorporating VTK and re-sampled at a higher point density for additional processing. A Boolean intersection between the anterior and posterior scleral/LC surfaces and the scleral canal wall surface is performed to define the boundaries of a volume enclosing the LC space [9]. This volume definition is then used as a mask to identify all voxels within each 3D ONH reconstruction corresponding to the LC (parameterized as LV).

The connective tissue voxels within the laminar volume are segmented using a custom 3D segmentation algorithm specifically designed to classify each voxel as either connective tissue (beam) or non-connective tissue (pore) voxels [28]. After our transition from

Fig. 16 (continued) from the ASCO (*glowing yellow arrow*). **(b)** *Posterior Laminar Insertion Position (PLIP)* is plotted relative to the Posterior Scleral Canal Opening (PSCO) and becomes less positive as the PLI migrates toward the PSCO (*glowing yellow arrow*). “Pialization” is present within this diagram by the fact that the *glowing yellow arrow* extends beyond the PSCO and into the pia. **(c)** An increase in *Laminar Insertion Length* (*glowing yellow arrow*—left) suggests that posterior *PLIP* migration exceeds posterior *ALIP* migration in an EG eye. **(d)** *Scleral Thickness at ASAS* measures the thickness of the sclera over the ASAS. A decrease in scleral thickness may suggest ASAS anterior extension and/or scleral splitting. *Reproduced from Investigative Ophthalmology & Visual Science, 2011, with permission from the Association for Research in Vision and Ophthalmology* [5]

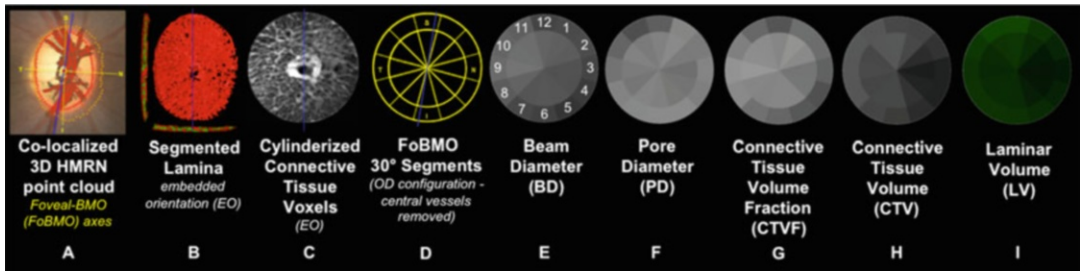


Fig. 17 Laminar Microarchitecture (LMA) method overview using data from a representative control eye. (a) The Foveal-BMO (FoBMO) axis (Fig. 5) is determined and defined to be the nasal temporal axis of the ONH 3D histomorphometric reconstruction (3D HMRN) (relative to the embedded orientation (EO) of the tissues (embedded vertical axis depicted by blue line)) by colocalizing the reconstructed vessels to a fundus photo (fovea not shown—see Fig. 5). Lamina is isolated, the beams are segmented (b) (Fig. 18) and each beam voxel and pore voxel have the associated diameter values assigned (Fig. 19). (c) Each voxel is then translated to a common cylinderized space (Figs. 21 and 22). (d) The cylinder is rotated to establish FoBMO-oriented 30 degree (centered on the clinical clock-hours) sectors which straddle the FoBMO nasal-temporal and superior-inferior axes. All left eye data are converted into right eye orientation (Fig. 6). The three principal laminar microarchitecture outcome parameters are (e) *Beam diameter (BD)* (with right eye, clock-hour, 30° sector designations) (f) *Pore diameter (PD)*, and (g) *Connective Tissue Volume Fraction (CTVF)*. Secondary volumetric outcome parameters include (h) *Connective Tissue Volume (CTV)* and (i) *Laminar Volume (LV)*. For all connective tissue and pore parameters, scaling is adjusted so that white suggests more and black suggests less connective tissue. *Laminar volume* is depicted in green because it is not related to connective tissue. All parameters are reported within 12 central and 12 peripheral FoBMO oriented 30 degree sectors (d). A separate analysis considers inner (1/3), middle (1/3), and outer (1/3) laminar layers (Fig. 23). *Reproduced from Investigative Ophthalmology & Visual Science, 2015, with permission from the Association for Research in Vision and Ophthalmology* [6]

a $2.5 \times 2.5 \times 3.0 \mu\text{m}$ voxel resolution to $1.5 \times 1.5 \times 1.5 \mu\text{m}$ voxel resolution within our 3D HMRNs, the segmentation algorithm was adjusted to consistently segment LC beams in both low and high-resolution data sets, by requiring that LC beam capillaries be consistently segmented within the beams (*see* Fig. 18 for additional details). Note that once segmented, the algorithm fills in the capillary space within the LC beams by classifying each capillary lumen as connective tissue. The final segmented 3D binary volumes form the basis for the visualization and quantification procedures that follow. *See Note 8* for additional information.

3.9.2 Laminar Beam and Pore Diameter (Fig. 19)

Each beam or pore voxel is assigned a beam or pore diameter defined to be the diameter of the largest sphere that contains that voxel and also fits into either the beam or pore in which it sits (Fig. 19) [29–31]. *BD* for a given beam or 30° sector is therefore defined by the population of *BDs* of the constituent voxels of that beam or sector. Likewise, *PD* for a given pore or 30° sector is defined by the population of *PDs* of the constituent voxels of that pore or sector. We use a modified version of the ImageJ (Rasband, W.S., ImageJ), U. S. National Institutes of Health, Bethesda, Maryland, USA,

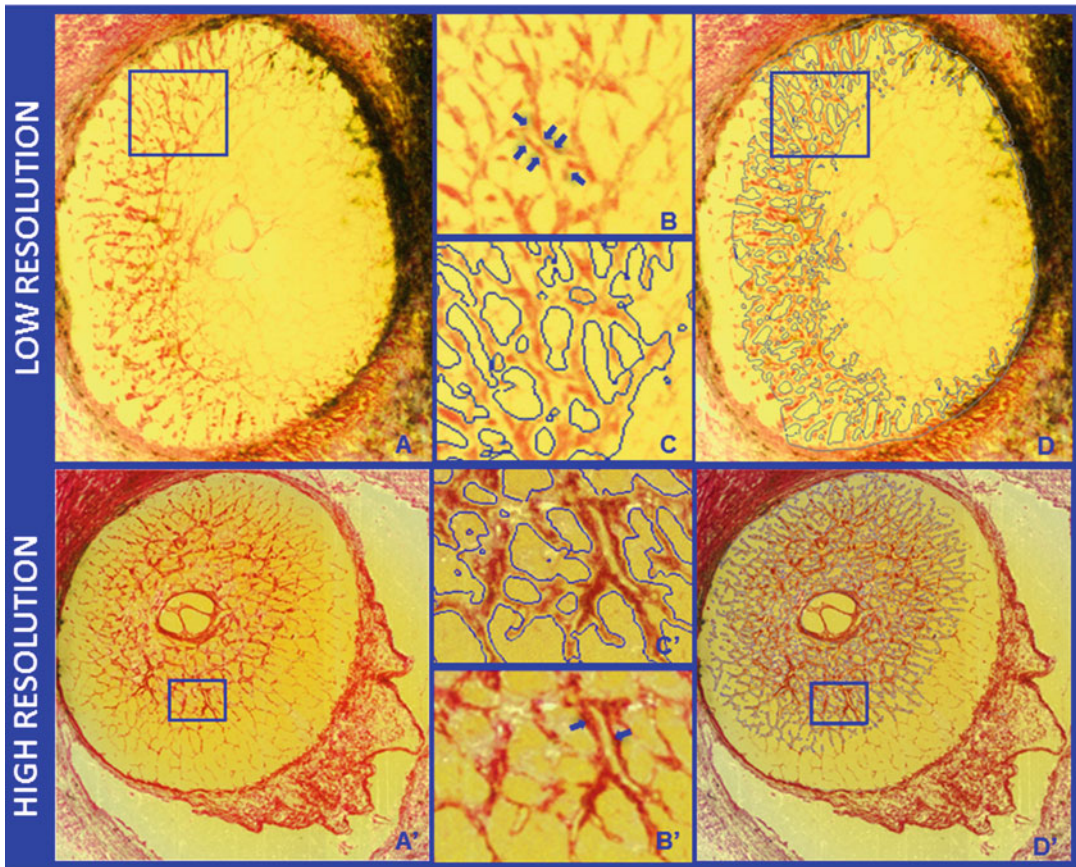


Fig. 18 Representative segmentation endpoints for low and high-resolution 3D HMRN data sets. Representative digital section images from a low (**a-upper**, $3 \times 3 \times 2.5$ micron voxel) and high (**a'-lower**, $1.5 \times 1.5 \times 1.5$ micron voxel) resolution 3D HMRNM are shown. Magnified regions of unsegmented LC beams are shown in **b** and **b'**, respectively. An LC beam with its central capillary is shown by *blue arrows* in both **b** and **b'**. Note that an algorithm may easily segment this single beam as two (smaller) beams if the capillary space is considered an LC pore. Because they contain more detail, this is more likely to occur within high-resolution HMRNs. After an initial report [9] we adjusted the segmentation algorithm to achieve consistent inclusion of the capillary within the LC beam in both low and high-resolution HMRNs by visual inspection (**c** and **c'**, respectively). Note that LC beam segmentation is a 3D process in that data from 7 section images on either side of a given section image are included in the assignment of beam borders (**d** and **d'**). Once segmented, the algorithm fills in the LC beam capillary space by classifying each capillary lumen as connective tissue. *Reproduced from Investigative Ophthalmology & Visual Science, 2015, with permission from the Association for Research in Vision and Ophthalmology [6]*

<http://imagej.nih.gov/ij/>, 1997–2016.) “Local Thickness” module to input our final segmented 3D binary volumes, and save the LC *BD* and *PD* values in VTK file format for further processing.

3.9.3 BD and PD Frequency Data (Fig. 20)

Beam voxel and pore voxel diameter distributions are frequency mapped by the percentage of total voxels falling into $3 \mu\text{m}$ wide “diameter bins” [$(0 < \text{Bin1} < 3 \mu\text{m})$, $(3 \leq \text{Bin2} < 6.0 \mu\text{m})$, etc.],

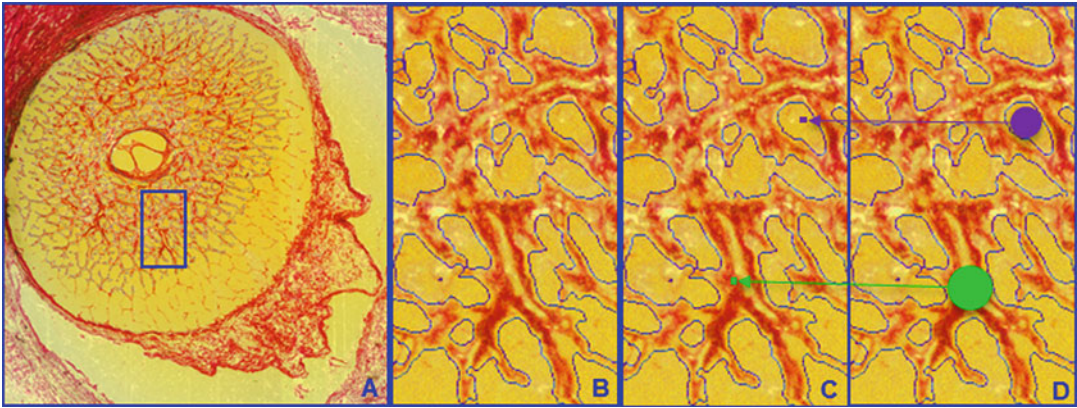


Fig. 19 Laminar beam and pore diameter. Within each laminar 3D HMRN reconstruction, beam voxels are segmented (shown within a single-section image in (a)—and magnified in (b)). All beam voxels are identified as connective tissue (one representative beam voxel is represented by a *green dot* in (c)). All remaining voxels are “pore” voxels (one representative pore voxel is represented by a *purple dot* in (c)). Each beam or pore voxel is assigned a beam or pore diameter which is the diameter of the largest sphere that contains that voxel and fits into either the beam or pore in which it sits (d). Beam or pore diameter for a given beam or region is defined by the population of beam or pore diameters of the constituent voxels. *Reproduced from Investigative Ophthalmology & Visual Science, 2015, with permission from the Association for Research in Vision and Ophthalmology [6]*

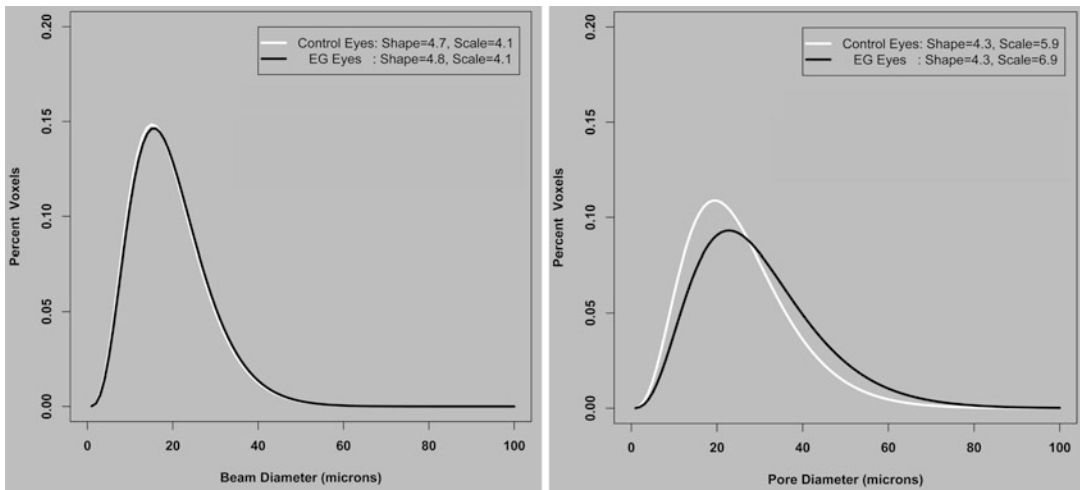


Fig. 20 The frequency distribution of *Beam Diameter (BD)* and *Pore diameter (PD)* among 14 EG animals fit to a Gamma distribution. The two fitted parameters that describe the Gamma distribution are in the corner of each plot. For *BD*, neither *Shape* nor *Scale* change significantly. For *PD*, there is no difference in *Shape*, but *Scale* has increased, equivalent to all pores being $(6.9-5.9)/5.9$ times larger (i.e., 17% larger) in the EG eyes. *Reproduced from Investigative Ophthalmology & Visual Science, 2016, under the CC BY-NC-ND 4.0 license [8]*

and fit using a Gamma distribution [32]. Whereas a normal distribution is defined by its mean and standard deviation, a Gamma distribution is defined by its *Shape* and *Scale* parameters. If (and

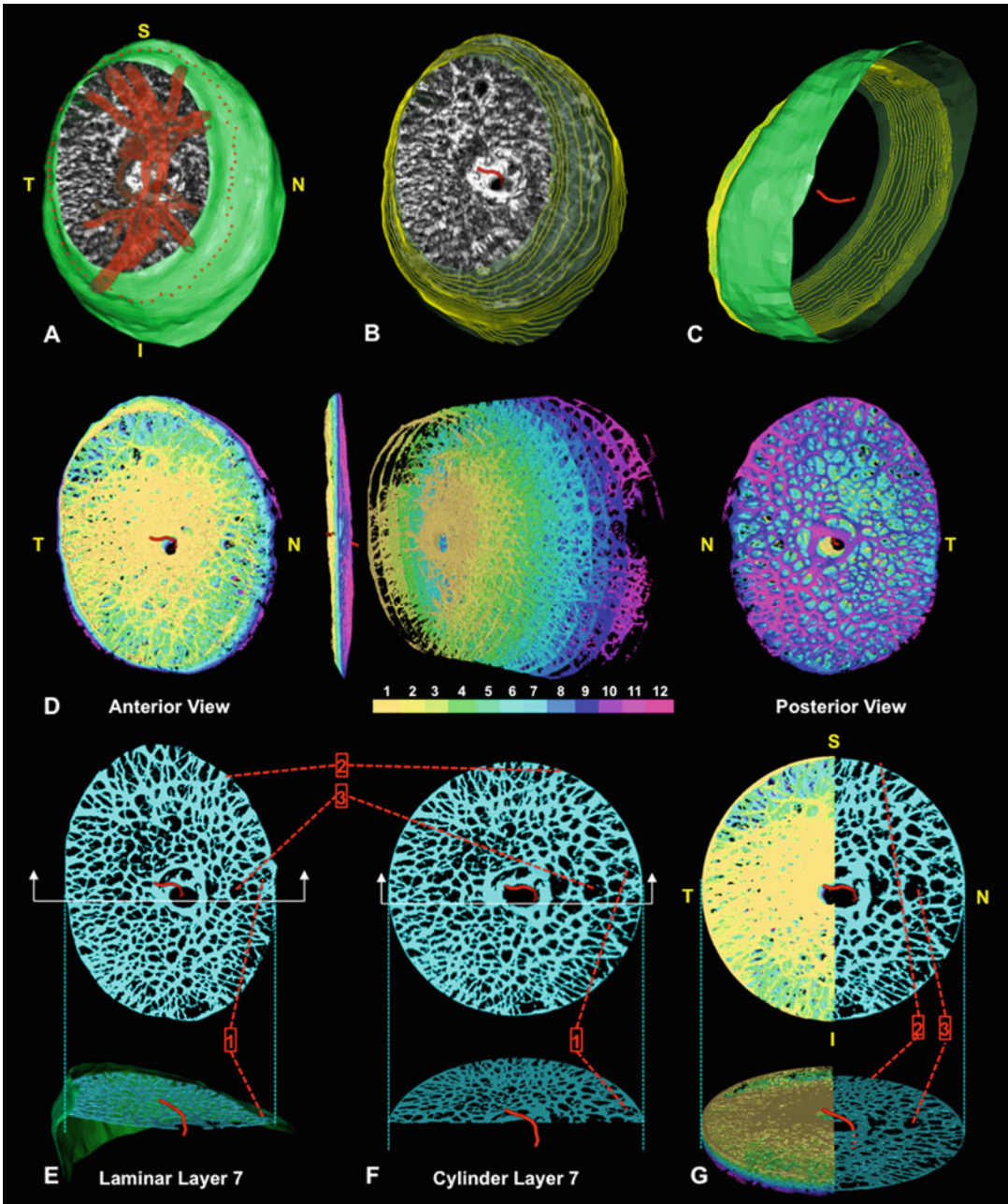


Fig. 21 Transformation of each lamina cribrosa beam and pore voxel to a common cylinder. Panels **a–g** are screen captures of live data from a representative monkey Control Eye during cylinderization. **(a)** Isolated LC segmentation and vessel tree with its neural boundary surface (*green*) in FoBMO right eye orientation (Figs. 4, 5, and 6). The delineated anterior LC insertion (ALI) points are shown in *red* along the neural boundary surface. **(b)** Vessel tree removed to reveal the anterior neural boundary centroid spline (*red*) and neural boundary contours projected as faint *yellow* lines through the neural boundary surface. **(c)** View from the underside with the LC removed to reveal the posterior extent of the neural boundary centroid spline relative to the inner neural boundary surface (contours again shown in *yellow*). The centroid spline passes through the center of mass of

only if) *Shape* remains constant between two populations, then the values in one population have the same distribution as the values in the second population multiplied by *Scale*. Both *Shape* and *Scale* for *BD* and *PD* are generated from their respective Gamma distributions using a maximum likelihood estimation method. The Estimated Mean of a distribution equals $Shape \times Scale$. The Estimated SD (standard deviation) equals $\sqrt{Shape} \times Scale$.

To robustly characterize *BD* and *PD* distributions within normal and control monkey eyes, the pooled *BD* and *PD* distributions of 49 normal and control eyes have been used to create five pooled *BD* and *PD* bins as follows: 1) for *BD*: smallest ($BD \leq 5 \mu\text{m}$), small ($BD \leq 13 \mu\text{m}$), mid-sized ($13 \mu\text{m} < BD \leq 26 \mu\text{m}$), large ($26 \mu\text{m} < BD \leq 39 \mu\text{m}$), and largest ($39 \mu\text{m} < BD$); and 2) for *PD*: smallest: ($PD \leq 5 \mu\text{m}$), small ($PD \leq 18 \mu\text{m}$), mid-sized ($18 \mu\text{m} < PD \leq 36 \mu\text{m}$), large ($36 \mu\text{m} < PD \leq 54 \mu\text{m}$), and largest ($54 \mu\text{m} < PD$), respectively. The dimensions of these bins were determined as follows. First, the upper limit of the “large” *BD* and *PD* bins was defined to be the maximum value of all 90th percentile *BD* and *PD* values from the 49 pooled eyes ($40 \mu\text{m}$ for *BD* and $55 \mu\text{m}$ for *PD*). Once the upper limit of the “large” bin was established, the “small,” “mid-sized,” and “large” bins were defined by equally dividing the maximum value of the “large” bin. Finally, the “largest” and the “smallest” bins were defined by the observation of the histogram such that they defined the extremes of the distribution.

3.9.4 Cylinderization and Regionalization (Figs. 21, 22, and 23)

Cylinderization and regionalization steps are implemented using custom software incorporating VTK. A plane is fit to the delineated ALI points (ALI reference plane) and all 3D HMRN data are re-oriented relative to the ALI centroid (which becomes the origin). The x, y, and z-axes are aligned with the ALI plane normal vectors, and pass through the ALI centroid. Polar coordinates ($p(r,$

Fig. 21 (continued) each neural boundary contour. **(d)** To cylinderize the data, each LC voxel is assigned to one of 12 layers. Anterior (left), side (middle left), exploded (middle right), and posterior (right) views are shown. **(e)** Layer 7 voxels in pre-cylinder orientation depicting specific voxel locations within the LC structure using pointers 1, 2, and 3. Below the corresponding side cutout view is shown with pointer 1 identifying three pores along the border of the nasal neural boundary. **(f and g)** Layer 7 voxels after cylinderization. Figure 22 explains the voxel-specific calculations that underlie this transformation. Note the location of three corresponding individual voxel locations shown with pointers in **(e)**, **(f)**, and **(g)**. Note that the central and peripheral locations of voxels pre-cylinderization remain after they are cylinderized. **(g)** All 12 layers of cylinderized LC voxels are shown to the left of the superior/inferior axis. Layer 7 is isolated to the right. Below is a side view of the same rendering. Note that every beam or pore voxel has a diameter assigned (Fig. 19) prior to cylinderization that is retained throughout the cylinderization process. Voxel size is not modified. Only voxel locations are modified during cylinderization. In polar coordinates (r, θ), θ is held constant while r is adjusted as depicted in Fig. 22. Reproduced from *Investigative Ophthalmology & Visual Science*, 2015, with permission from the Association for Research in Vision and Ophthalmology [6]

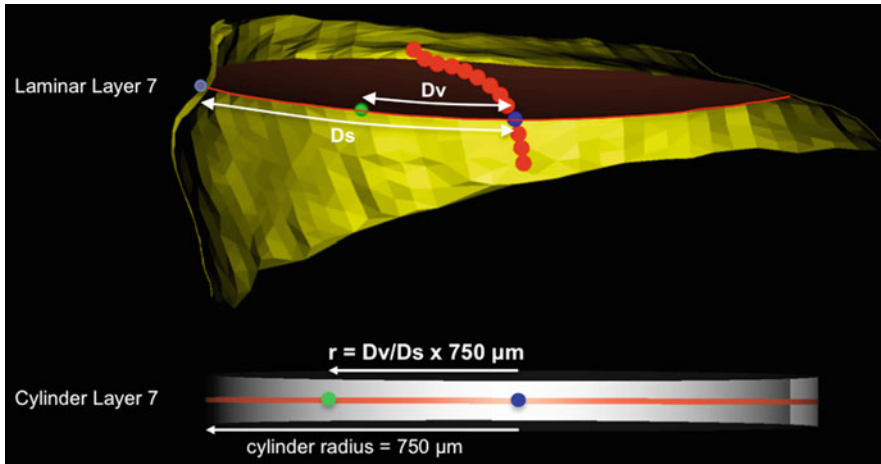


Fig. 22 Cylinderization of a representative lamina voxel assigned to layer 7 of representative monkey control eye. (*Upper*) All lamina voxels within lamina layer 7 of the pre-cylinderized lamina are assigned a polar coordinate (D_v , θ) where D_v is the distance along the mid-layer reference surface (*red*) from the neural boundary centroid spline (*red dots*) centroid (*blue dot*) and D_s is the radial distance along the surface of the mid-layer reference surface from the centroid to the neural boundary (*yellow*). (*Lower*) Within cylinder layer 7, θ is held constant, but r is proportionally adjusted using the precylinder ratio of D_v/D_s and the cylinder radius of 750 μm . Distances D_v and D_s are calculated along a pre-cylinderized reference layer surface contour (curve) that is obtained for every LC voxel. It is not a straight-line measurement in a plane. *Reproduced from Investigative Ophthalmology & Visual Science, 2015, with permission from the Association for Research in Vision and Ophthalmology* [6]

θ)) are then assigned to each LC voxel relative to the ALI centroid. A scleral canal centroid spline (Figs. 21a–c and 22) is generated from the centers of mass of a series of scleral canal wall contour lines sampled at 3.0 μm (low resolution 3D HMRN) or 1.5 μm (high resolution 3D HMRN) intervals parallel to the ALI reference plane. The LC is divided into 12 layers by projecting normal vectors from a uniform 20 μm anterior LC surface grid to the posterior LC surface. The distance between the anterior and posterior LC surfaces on each vector is divided into 12 equal segments and sub-surfaces are fit to each group of vector segments to create LC layers 1–12, (1—anterior (inner) to 12, posterior (outer) respectively). Each LC voxel is then assigned to its closest layer (*see Note 9*). The position of each voxel within each LC layer is expressed relative to the layer centroid and the scleral canal wall (Fig. 22—upper). The voxel position within the equivalent cylinder layer is then proportionally assigned (Fig. 22—lower).

We impose FoBMO 30° Sectoral, Central and Peripheral Sub-sectoral, and Inner, Middle and Outer Regions on the Cylinderized Data (Figs. 5, 6, 17, and 21). All LC segmentation as well as beam and pore voxel quantification are performed on “raw” LC data in embedded tissue orientation. After each voxel has been cylinderized, the data is rotated such that the FoBMO vertical and

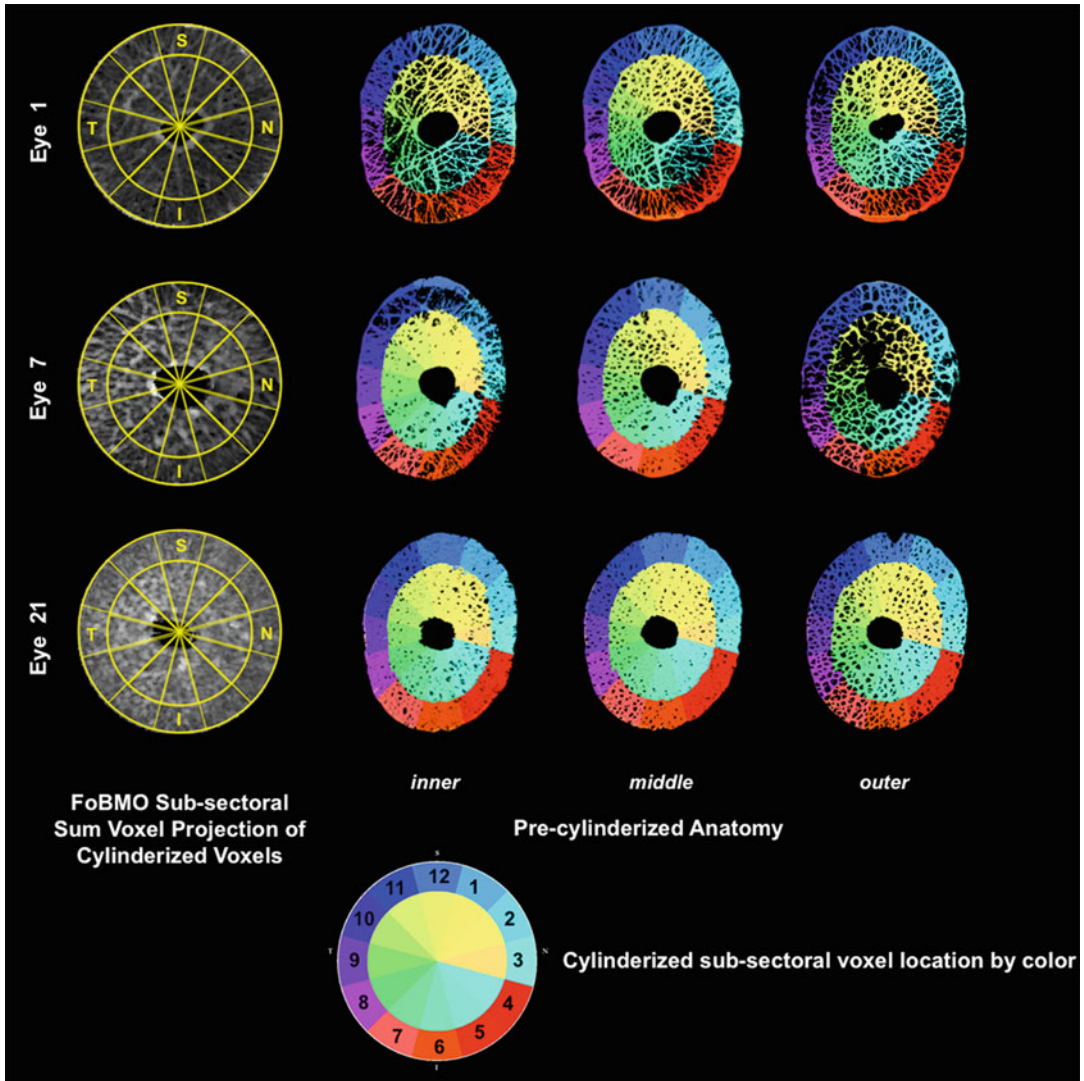


Fig. 23 Voxel-specific cylinderized subsectoral assignments projected to pre-cylinderized laminar anatomy in representative low, moderate, and high *CTVF* control eyes. For all eyes processed through laminar micro-architecture (LMA) analysis, the cylinderized, subsectoral assignment of each voxel is qualitatively compared to its location within the pre-cylinderized laminar anatomy by coloring each voxel based on its cylinderized subsectoral location (see color chart lower middle). Comparisons are shown for representative low (Eye 1), moderate (Eye 7), and high (Eye 21) *CTVF* eyes, within inner, middle, and outer laminar layers. Low (Eye 7) and high-resolution (Eyes 1 and 21) 3D HMRNs are also represented. Note the lack of transverse connectivity within the outer layer of Study Eye 7. Contributing causes for this finding are considered in the Methods section on LMA. *Reproduced from Investigative Ophthalmology & Visual Science, 2015, with permission from the Association for Research in Vision and Ophthalmology* [6]

horizontal axes are in the 12 to 6 and 3 to 9 clock-hour locations, respectively (Fig. 17c). Data for left eyes are transformed to right eye configuration as demonstrated in Fig. 6. Data is presented in

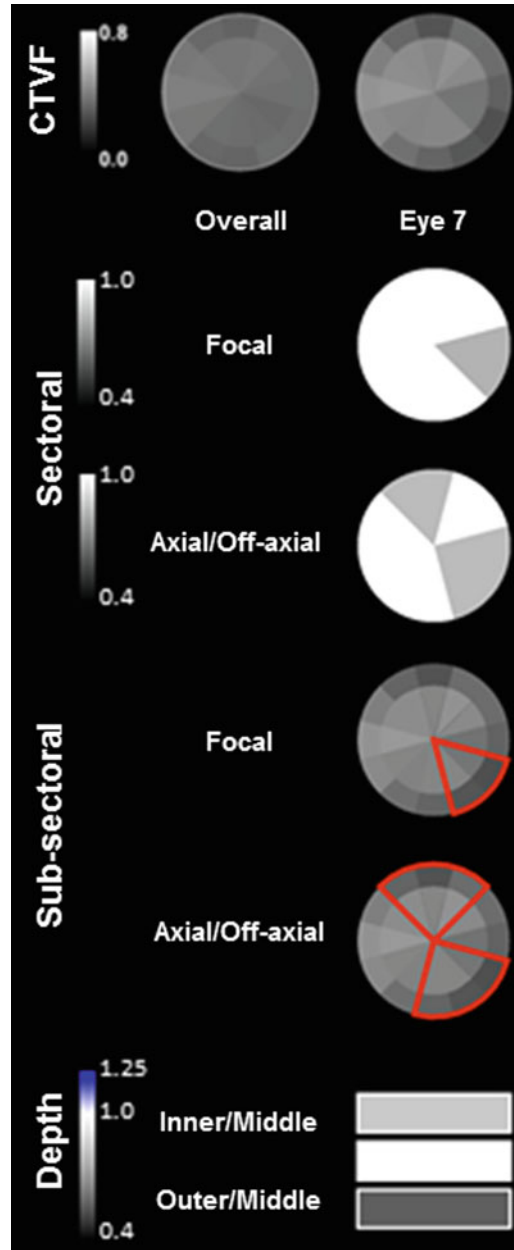


Fig. 24 Eye-specific LMA connective tissue density mapping in a representative control eye. Overall (left—a summary of 21 normal and control eyes) and eye-specific (a single control eye—right) FoBMO subsectoral *CTVF* data are shown for Study Eye 7 in the top row. For *CTVF*, we define LMA discordance to be present in those sectors in which *CTVF* is lowest compared to all other sectors of the ONH. Focal (all combinations of 2, 3, or 4 adjacent sectors) and axial sectoral discordance (all possible combinations of 4, 5, or 6 sectors on either side of BMO centroid—2 or 3 adjacent sectors on one side and 2, 3, or 4 adjacent sectors on the other side) are shown in rows 2 and 3. These plots

two ways: (1) Data by sector, subsector, and depth in which each 30 degree sector is divided into equal volume central and peripheral subsectors and inner (layers 1–4, Fig. 21), middle (layers 5–8, Fig. 21), and outer (layers 9–12, Fig. 21) depth ranges. (2) Full thickness data without depth. Voxels lying on sectoral or subsectoral boundaries are assigned to the least numbered sector and the central subsector. See **Notes 10** and **11** for additional information.

3.9.5 Connective Tissue Density Discordance Mapping (Figs. 24 and 25, Table 3)

A large literature has suggested that the classic pattern of inferior and superior temporal axon loss in glaucoma is related to the underlying architecture of the lamina cribrosa beams and pores [33–38]. Our strategy to identify eye-specific, LMA connective tissue density *sectoral*, *subsectoral*, and *depth discordance* (Figs. 24 and 25; Table 3) builds upon previous attempts to quantify LC pore size and connective tissue density within four quadrants (S, I, N, and T) and their central versus peripheral sub-quadrants [6]. For our purposes, LMA discordance analysis attempts to identify LC sectors, subsectors, or layers that demonstrate a relative decrease in LC connective tissue density compared to the rest of the ONH. Connective tissue density is only one determinant of connective tissue structural stiffness. Other components such as material properties, anisotropy, and fiber orientation are not currently assessed. The process to generate eye-specific connective tissue density discordance maps is described in the sections that follow. See **Note 12** for additional information.

1. We define LMA connective tissue density *sectoral discordance* to be present in those sectors in which *BD* and *CTVF* are lowest and *PD* is highest compared to all other sectors of the ONH (Fig. 24). Sectors of low connective tissue density can occur focally (all possible combinations of 2, 3, or 4 adjacent sectors on one side of BMO centroid) or axially (all possible combinations of 4, 5, or 6 sectors on either side of the BMO centroid

←

Fig. 24 (continued) identify the sectoral location and magnitude (gray scale, left) of the greatest discordance from all other sectors (depicted in *white*). The location of focal and axial *subsectoral discordance* is depicted in red in rows 4 and 5. These plots identify those sectors in which the ratio of the peripheral versus central subsectoral *CTVF* is lowest compared to all other sectors. The magnitude of that ratio is not depicted. The magnitude of inner versus middle and outer versus middle *CTVF depth discordance* (scale to the left) is depicted in the bottom row. Note that while the superior temporal (11 and 12) and inferior temporal (6 and 7) sectors are qualitatively lowest in *CTVF* in the overall data for all 21 eyes, the nasal, inferior nasal, and superior sectors are most commonly involved in sectoral and subsectoral discordance in Study Eye 7. *Reproduced from Investigative Ophthalmology & Visual Science, 2015, with permission from the Association for Research in Vision and Ophthalmology [6]*

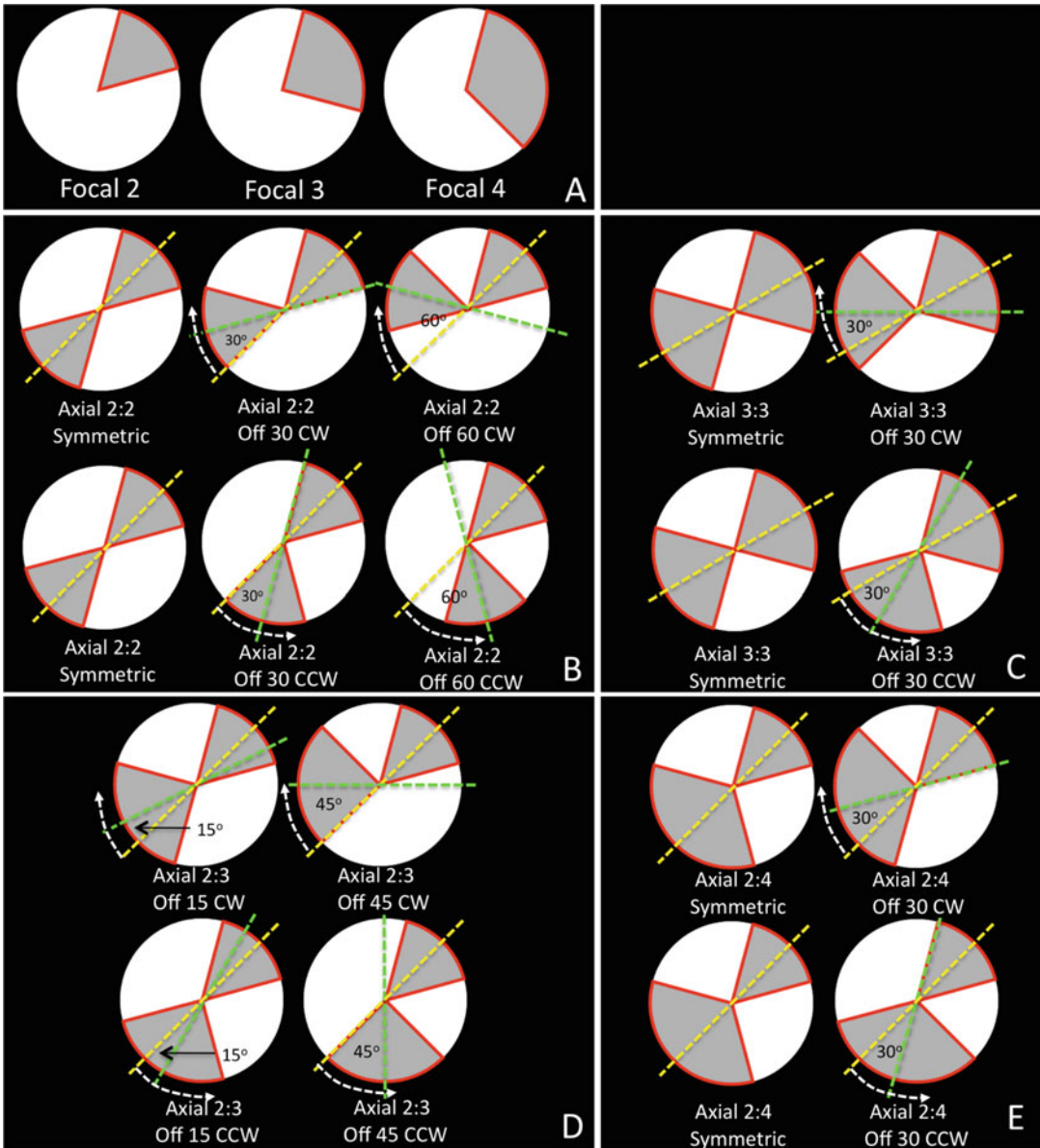


Fig. 25 Representative examples of focal and axial sectoral and subsectoral LMA discordance. (a) Focal discordance is defined to be the combination of 2, 3, or 4 adjacent sectors in which *BD* and *CTVF* are lowest and *PD* is highest compared to all other sectors of the ONH. For a given eye, focal discordance may occur within any 2, 3, or 4 sectors—i.e., at any adjacent clock-hour locations, with only sectors 1–4 demonstrated here. There are 36 unique focal configurations in which the ratio of each parameter relative to its value in all the remaining sectors can be assessed. The lowest ratio (*BD* and *CTVF*) or highest ratio (*PD*) among all 36 configurations is sought as the discordance value. (b–e) Axial Discordance attempts to quantify relationships that are within the plane of the LC and occur along (or just off) an axis that includes both the sides of the BMO centroid. Axial discordance attempts to quantify phenomena such as the classic superior and inferior pattern of large pores in human and monkey eyes. For a given eye, axial discordance may occur within any combination of 4, 5, or 6 sectors on either side of the BMO centroid (2 or 3 adjacent sectors on one side and

(2 or 3 adjacent sectors on one side and 2, 3, or 4 adjacent sectors on the other side)). Axial discordance does not refer to discordance along the z-axis (this is *depth discordance* or discordance between inner, middle, and outer LC layers). Axial discordance attempts to quantify relationships that are within the plane of the LC and occur along (or just off) an axis that includes both sides of the BMO centroid—such as the classic superior and inferior pattern of large pores in human and monkey eyes. All steps outlined in this Subheading (3.9.5) are implemented in Excel and/or R programs unless separately noted.

2. A table of *sectoral*, *subsectoral*, and *depth discordance* combinations is created in Excel for all possible focal and axial discordance configurations (Fig. 25). There are in total 36 unique focal configurations in which the ratio of each parameter relative to its value in all the remaining sectors can be assessed (30 possible 2:2 discordance configurations; 18 possible 3:3 configurations; 48 possible 2:3 configurations; and 36 possible 2:4 configurations).
3. For each possible combination, discordance for the parameter of interest is calculated as the ratio of the pooled value from the specific region of interest versus the pooled value of the rest of the regions (*see* Table 3 for the detailed algorithm).
4. Maps of the focal or axial sectors with the greatest discordance (lowest *BD* and *CTVF* or largest *PD*) (Fig. 24) are generated using custom software depicting the magnitude of discordance via the intensity of gray.
5. Focal and axial forms of *subsectoral discordance* can also be identified in which the ratio of peripheral to central subsectoral connective tissue density can be determined (smallest for *BD* and *CTVF* and largest for *PD*) using strategies that are identical to those listed above.
6. Eye-specific discordance between the inner/middle, outer/middle, and inner/outer LC layers can also be assessed.

Fig. 25 (continued) 2, 3 or 4 adjacent sectors on the other side). Representative combinations of 2:2, 3:3, 2:3, and 2:4 axial and off axial discordance combinations are shown in (b), (c), (d), and (e), respectively. The *yellow dotted line* is the principal axis of the discordance (when axial). The *green dotted line* is the magnitude by which the two focal regions on either side of BMO_{centroid} are off-axis. CW or CCW describe the relative location of the *green* relative to the *yellow axis line*. By our definitions, there are a total of 30 possible 2:2 discordance configurations; 18 possible 3:3 configurations; 48 possible 2:3 configurations; and 36 possible 2:4 configurations. Thus, a total of 168 Sectoral and Subsectoral LMA discordance configurations are considered for each parameter, for each eye. Depth discordance is not illustrated here but its quantification is explained in Table 3. *Reproduced from Investigative Ophthalmology & Visual Science, 2015, with permission from the Association for Research in Vision and Ophthalmology [6]*

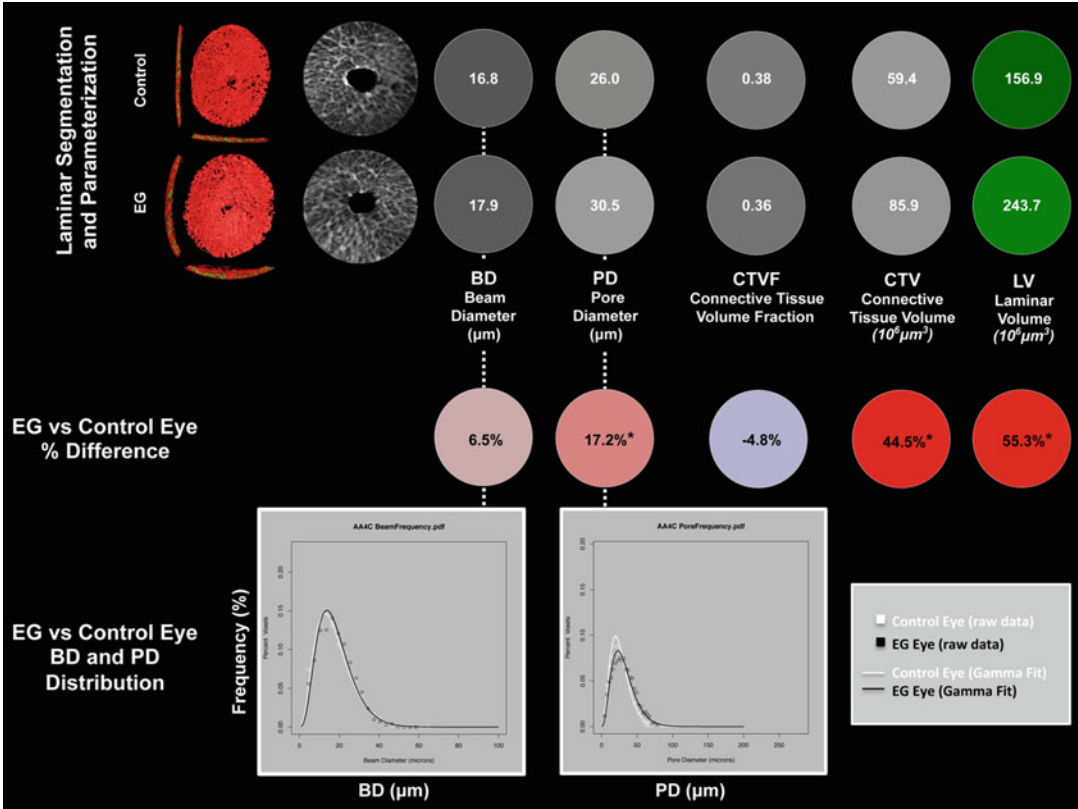


Fig. 26 Method overview for determining animal-specific, Global Experimental Glaucoma (EG) versus Control eye Lamina Microarchitecture (LMA) differences. (Upper two rows). For both the control and experimental glaucoma (EG) eye of one representative early EG animal, segmented lamina cribrosa (LC) (Figs. 18 and 19) with beam and pore diameters (Fig. 19) assigned to each beam and pore voxel are cylinderized (Figs. 21–23) in right eye orientation (Fig. 6). The global mean beam diameter (BD), mean pore diameter (PD), Connective Tissue Volume Fraction (CTVF), Connective Tissue Volume (CTV), and Lamina Cribrosa Volume (LV) are reported in white font for each eye on a gray or green scale background (gray and green scales not shown). For all connective tissue and pore parameters, scaling is adjusted so that white suggests more and black suggests less connective tissue. LC volume is depicted in green because it is not solely related to connective tissue. Middle Row. Global EG versus Control eye differences in each parameter are reported in black font on a red (increased) or blue (decreased) background (color scales not shown). Asterisks (*) denote that the EG versus Control eye difference for this parameter exceeds the maximum Physiologic Inter-eye Percent Difference Value (PIPD_{max}) for that parameter as determined by six bilateral normal animals (as previously reported) [8]. An additional analysis considers EG versus Control eye comparisons that are confined to the inner (1/3), middle (1/3), and outer (1/3) LC layers (not shown). Bottom Row. BD and PD frequency data are fitted with Gamma distribution to more robustly assess if there is a shape or scale change in the distribution of beam and pore diameters within the EG compared to the Control eye of each animal. See the appropriate method sections for detailed explanations of each step. Reproduced from *Investigative Ophthalmology & Visual Science*, 2016, under the [CC BY-NC-ND 4.0 license](https://creativecommons.org/licenses/by-nc-nd/4.0/) [8]

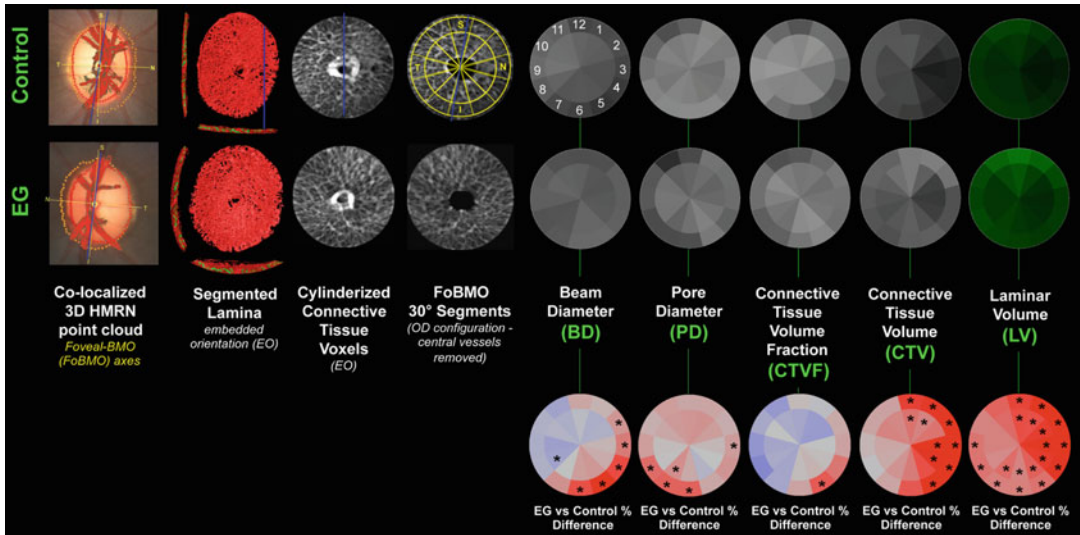


Fig. 27 Method overview for determining animal-specific, sectoral and subsectoral Experimental Glaucoma (EG) versus Control eye Lamina Microarchitecture (LMA) differences. Upper two rows. For both the control and experimental glaucoma (EG) eye of a representative early EG animal, the Foveal-BMO (FoBMO) axis (Fig. 5) is determined and defined to be the nasal temporal axis of the ONH 3D histomorphometric reconstruction (3D HMRN) (relative to the embedded orientation (EO) of the tissues (embedded vertical axis depicted by blue line)) by colocalizing the reconstructed vessels to a fundus photo (Fig. 5). Lamina is isolated (not shown), the beams are segmented (2nd column and Fig. 18), and each beam voxel and pore voxel have the associated diameter values assigned (Fig. 19). Each voxel is then translated to a common cylinderized space (3rd column, detail in Figs. 21 and 22). The cylinder is rotated to establish FoBMO-oriented 30 degree (centered on the clinical clock-hours) sectors which straddle the FoBMO nasal-temporal and superior-inferior axes. All left eye data are converted into right eye orientation (4th column, detail in Fig. 6). The three principal lamina microarchitecture outcome parameters are (5th column) beam diameter (BD) (with right eye, clock-hour, 30° sector designations) (6th column); pore diameter (PD) and (7th column) Connective Tissue Volume Fraction (CTVF). Secondary volumetric outcome parameters include (8th column) Connective Tissue Volume (CTV) and (9th column) Laminar Volume (LV). For all connective tissue and pore parameters, scaling is adjusted so that white suggests more and black suggests less connective tissue. Laminar volume is depicted in green because it is not related to connective tissue. All parameters are reported within 12 central and 12 peripheral FoBMO oriented 30 degree sectors. Bottom Row. EG versus Control eye differences in each parameter and each subsector are reported on a red (increased) or blue (decreased) color-coded background (color scales not shown). Asterisks (*) denote that the EG versus Control eye difference for this parameter exceeds the maximum Physiologic Inter-eye Percent Difference Value (PIPD_{max}) for that parameter in this subsector as determined by 6 bilateral normal animals (previously reported [8]). Two separate analyses are not shown here, the first one considers inner (1/3), middle (1/3), and outer (1/3) lamina layers and the second one only consider 12 sectors (sector analysis)

3.9.6 Physiologic Inter-Eye Difference Characterization

Using a similar approach to that established for ONH macroarchitecture parameters above (Subheading 3.8.8), PIPD_{max} and PIPD_{max} for LMA parameters (BD, PD, CTVF, CTV, and LV) have also been generated [4]. First, PID and PIPD range and maximum for six bilateral normal monkeys were calculated. For each eye, global, sectoral, subsectoral, and depth average values are calculated for

each parameter using R software. For each animal, *PID* and *PIPD* were calculated for each parameter (global, sector, subsector, and depth) as described in Subheading 3.8.8. The *PID* range is the range of *PID* values among the six bilateral normal animals and the *PID_{max}* is the largest *PID* (the upper range) among the six animals. The *PIPD* range is the range of *PIPD* values among the six bilateral normal animals and the *PIPD_{max}* as the largest *PIPD* (the upper range) among the six animals.

3.9.7 Experiment-Wide and Animal-Specific EG Versus Control Eye Difference Determination (Figs. 26 and 27)

An overview of our LC segmentation, parameterization, quantification, and EG vs. Control eye significance strategies is depicted in Fig. 26 for global and distribution data [8], and in Fig. 27 for sector and subsector data. To evaluate experiment-wide EG versus control eye differences by sector, subsector, and depth, a linear mix-effects model is applied in which significance is achieved at $p < 0.05$. However, to establish the most conservative criteria required to account for multiple comparisons, the required p value is $p < 0.05/N$, where (N) is the number of comparisons. Animal-specific EG versus Control eye differences (EG–C) and percent differences ((EG–C)/C %) are generated for each parameter for each animal. Animal-specific EG versus Control eye differences are required to exceed the *PID_{max}* and *PIPD_{max}* values for each parameter (Subheading 3.9.6, above) to achieve significance [4]. Sector, subsector, and depth maps are plotted for each control and treated eye and are color-coded as a function of the magnitude of the parameter value using custom software. Between-eye, color-coded, difference maps (labeled with “*” to represent significant change) for each parameter by sector, subsector, and depth are also generated (Figs. 26 and 27). Finally, experiment-wide EG versus Control eye *scale* and *shape* distribution parameter change for *BD* and *PD* are separately assessed using paired T-tests. Animal-specific EG eye *scale* and *shape* distribution parameter change can be separately assessed for *BD* and *PD* by comparison to the $n = 49$ normal and control eye distribution data outlined in Subheading 3.9.3, above. All calculations and statistical data analyses outlined above are implemented in R and excel programs unless noted otherwise.

3.10 Finite Element Modeling

Finite Element Modeling (FEM) [9, 39–45] is an engineering technique used for studying the distribution of stress and strain within complicated load-bearing structures. Our digital 3D HMRNs of the ONH connective tissues have been constructed, in part, to provide digital 3D neural and connective tissue architecture for FEM. Our engineering collaborators apply material property assignments to each voxel as well as boundary and loading conditions so as to model IOP-related stress and strain within the neural and connective tissues of the ONH. To date, continuum and micro finite element models of the EG and control eye monkey

Table 3
Eye-specific LMA discordance calculations

Sectoral discordance	
Focal	Sectoral location and magnitude of the minimum (<i>BD</i> , <i>CTVF</i>) or maximum (<i>PD</i>) value of the following ratio: $M_{(2,3,4adj)}/M_{(8,9,10)}$ where: $M_{(2,3,4adj)} = \text{Mean of all possible combinations of 2, 3 or 4 adjacent sector combinations}$ $M_{(8,9,10)} = \text{Mean of the remaining 8, 9 or 10 sectors}$
Axial or off-axial	Sectoral locations and magnitude of the 2 and 3 sector hourglass (axial) or bent hourglass (off-axial) minimum or maximum as determined by the following ratio: $M_{(2,3adjOppBMO)}/M_{(all)}$ where: $M_{(2,3adjOppBMO)} = \text{Mean of all possible combinations of 2 or 3 adjacent sectors on opposite sides of } BMO_{centroid}$ $M_{(all)} = \text{Mean of all remaining sectors}$
Subsectoral discordance	
Focal	Sectoral location and magnitude of the minimum and/or maximum value of the following ratio: $M_{(c/p\ 2,3adj)}/M_{(c/p\ 9,10)}$ where: $M_{(c/p\ 2,3adj)} = \text{Mean of central/peripheral subsector ratios for all possible 2 or 3 adjacent sector combinations}$ $M_{(c/p\ 9,10)} = \text{Mean of central/peripheral subsector ratios of the remaining 9 or 10 sectors}$
Axial or off-axial	Sectoral locations and magnitude of the 2 and 3 sector hourglass (axial) or bent hourglass (off-axial) minimum or maximum as determined by the following ratio: $M_{(c/p\ 2,3adjOppBMO)}/M_{(c/p\ all)}$ where: $M_{(c/p\ 2,3adjOppBMO)} = \text{Mean of central/peripheral subsector ratios for all possible 2 or 3 adjacent sector combinations on opposite sides of } BMO_{centroid}$ $M_{(c/p\ all)} = \text{Mean of central/peripheral subsector ratios of all remaining sectors}$
Depth discordance	
Inner vs middle	$M_{(Inner\ all)}/M_{(Middle\ all)}$ where: $M_{(Inner\ all)} = \text{Mean of all inner sectors}$ $M_{(Middle\ all)} = \text{Mean of all middle sectors}$
Outer vs middle	$M_{(Outer\ all)}/M_{(Middle\ all)}$ where: $M_{(Outer\ all)} = \text{Mean of all outer sectors}$ $M_{(Middle\ all)} = \text{Mean of all middle sectors}$

Reproduced from *Investigative Ophthalmology & Visual Science*, 2015, with permission from the Association for Research in Vision and Ophthalmology [6]

ONH have been constructed and efforts are underway to correlate their outputs to EG eye connective tissue deformation and remodeling as well as axonal injury [9].

3.11 3D HMRN of the Rat ONH (Figs. 28 and 29)

We recently extended our 3D reconstruction techniques to the Brown Norway rat ONH [7, 10]. The ONH and peripapillary sclera of the Control and EG eyes of 8 Brown Norway rats were trephined (3 mm diameter), embedded in paraffin, mounted to a microtome (RM2165; Leica, Wetzlar, Germany), and serial

sectioned at 1.5 μm thickness from the vitreous surface through the optic nerve head and into the orbital optic nerve. After each section was cut, the block surface was stained with a 1:1 (v/v) mixture of Ponceau S and acid fuchsin stains, and then imaged at a resolution of $1.5 \times 1.5 \mu\text{m}$ per pixel as outlined in Subheading 3.2. For each ONH, 275 to 501 serial digital transverse section images were captured, aligned, and stacked into a digital 3D HMRN volume. Because of the dense pigmentation within the rat ONH, volumes were built using the green channel images only as visualization of BM, BMO, and other deep ONH landmarks were most consistent in this channel. Please *see* Figs. 28 and 29 as well as the original publications [7, 10] for details of the methods and findings that are unique to the rat ONH.

3.12 Eye-Specific Colocalization of ONH OCT and 3D HMRN Data Sets (Fig. 30)

The ability of current OCT imaging to visualize deep ONH anatomy such as the posterior LC surface, the anterior and posterior scleral surfaces, and the scleral canal wall remains controversial [46–48]. We are currently colocalizing ONH OCT data sets obtained just prior to sacrifice to postmortem 3D HMRNs of the same eyes, so as to utilize 3D HMRN anatomy to support OCT visualization of the deep ONH. Once shared anatomic landmarks in both data sets are identified they can be used to maximize the colocalization of both data sets in 3D space. Once colocalized, the 3D HMRN volume can be “digitally” sliced in a manner that most precisely matches the location of each, pre-sacrifice OCT B-scan. Our method for achieving the digital colocalization of OCT and 3D HMRN data sets is depicted in Fig. 30 and explained as follows.

1. A high density (768×768) 15° A-scan grid or standard 24 radial B-scan OCT scan data set is acquired as close to the day of sacrifice as possible, 30 min after IOP has been set to 10 mmHg using an anterior chamber needle and manometer. (*see* **Note 13** for additional details).
2. The animal is sacrificed by perfusion fixation 30 min after IOP has been set to 10 mmHg, using an anterior chamber needle connected to a manometer as outlined in Subheading 2.1.
3. 3D HMRN reconstruction of the ONH tissues is carried out as per Subheading 3.
4. 3D HMRN BMO is delineated within 40 digital radial section images (*see* Subheading 3.4, **step 2**).
5. An ellipse is fit to the 3D HMRN BMO landmarks and its centroid and major and minor axes are obtained. The area of the ellipse is calculated.

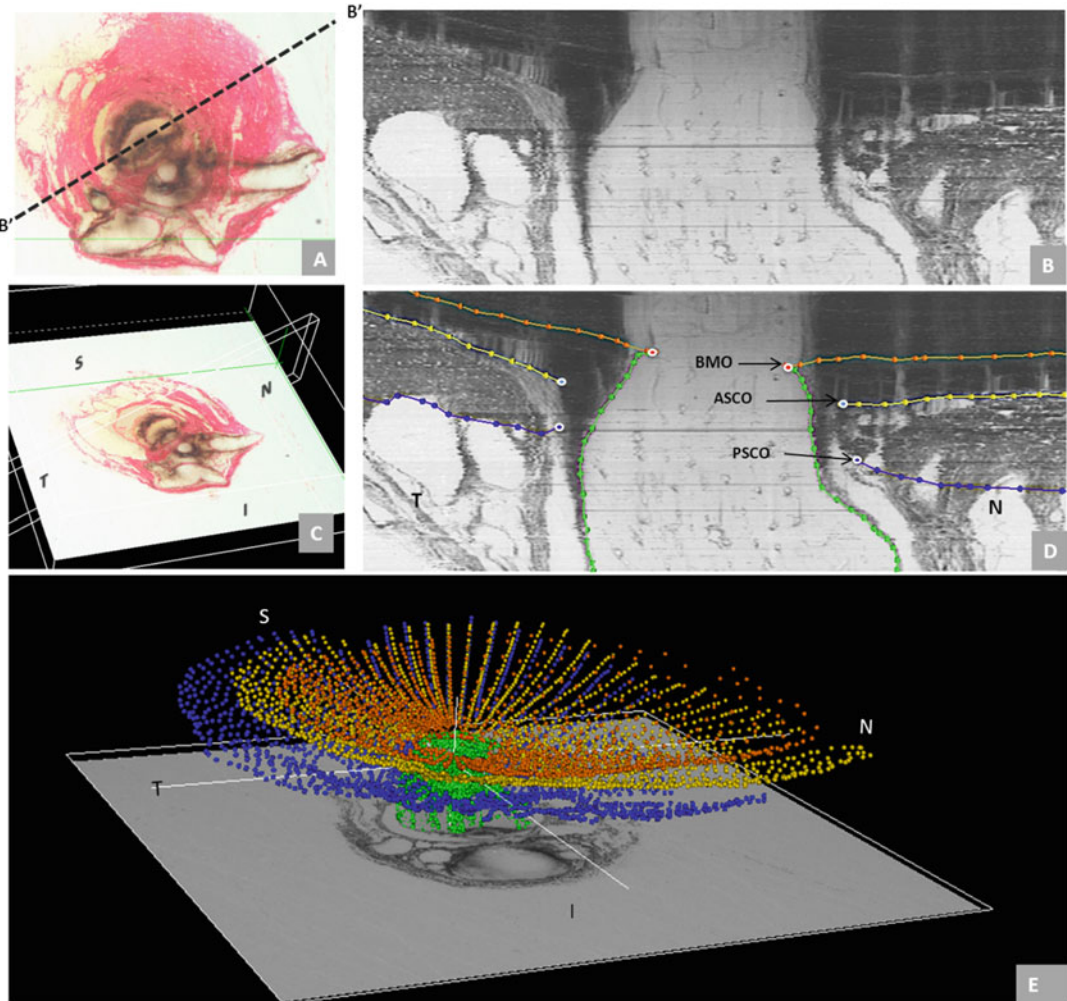


Fig. 28 3D Delineation of the ONH and peripapillary scleral landmarks. Delineated landmark points within 40 digital radial sagittal section images of a representative rat ONH. The delineator first assigned the center of the scleral portion of the optic nerve (a) to be the center of rotation through which, forty, 7-voxel thick, digital radial sagittal section images (b) of the digital 3D reconstruction (c) were serially served at 4.5° intervals. The Nasal-Temporal location of (b) is shown here two dimensionally (dotted line marked B'-B') within the transverse section image in (a) and three-dimensionally (7 μm thick white-edged rectangle) within the 3D reconstruction in (c). Within each digital sagittal section image (b) the delineator marked four landmark surfaces and three pairs of neurovascular canal landmarks (one point on each side of the canal). The landmark surfaces were: (1) Bruch's membrane (*orange*); (2) the anterior (*yellow*) and (3) posterior (*blue*) surfaces of peripapillary sclera; and (4) the optic nerve boundary extending from Bruch's membrane opening, through the scleral canal and along the pia mater to the posterior edge of the reconstruction (*green*). The landmark points were Bruch's Membrane Opening (BMO—*red*), the anterior scleral canal opening (ASCO—*light blue*), and the posterior scleral canal opening (PSCO—*purple*). A representative point cloud that contains all delineated landmark types for all 40 radial sections of an individual reconstruction is viewed from its superior surface three dimensionally in (d) (nasal is to the left and temporal is to the right). Three dimensional reconstructions of the landmark point clouds (d) of each eye were 3D visualized together and separately (turning each landmark category on and off) so as to qualitatively determine their principal macroscopic relationships. In

6. The OCT data set is loaded into MV delineation software and BMO landmarks are delineated in all pertinent B-Scans.
7. An ellipse is fit to the OCT BMO points and its centroid and major and minor axes are obtained. The area of the ellipse is calculated.
8. The scale factor between the two data sets is computed as
$$\sqrt{\frac{3D \text{ HMRN ellipse area}}{OCT \text{ ellipse area}}}.$$
9. The OCT ellipse centroid and major and minor axes are then aligned to the 3D HMRN centroid and major and minor axes. The 3D transformation matrix required for this alignment is recorded.
10. For each OCT B-Scan of interest, the coordinates of the B-Scan corners are scaled by the factor obtained in (step 8), above, and rotated and translated using the 3D matrix calculated in (step 9). This effectively places the B-Scan into its best-matched position with the 3D HMRN space.
11. Using the transformed B-Scan coordinates found in (step 10), a plane is constructed and used to section the 3D HMRN volume. The resulting 3D HMRN section image is then the best-matched 3D HMRN section image to the in-vivo OCT B-Scan.
12. The process (steps 10 and 11) is repeated for all OCT B-Scans of interest.

3.13 Eye-Specific Colocalization of EG Versus Control Eye Orbital ON Axon Count Differences to EG Versus Control Eye 3D HMRN Subsectoral Parameter Differences (Fig. 31)

We have previously reported our method for performing 100% monkey optic nerve axon counting using an automated technique [49]. A central goal of our 3D HMRN technique is to correlate or make comparisons between EG eye regional patterns of 3D HMRN LMA and FEM stress and strain and the regional patterns of EG eye optic nerve axon loss. To achieve meaningful comparisons, each data set needs to possess a common, clinically oriented, coordinate system and must be commonly aligned to the FoBMO axis.

Establishing the clinical orientation of a given 3D HMRN and FoBMO axis based sectoral and subsectoral regionalization has been described in detail in Subheadings 3.5 and 3.6. However, since axon counting is performed using an ON cross-section that is separate from (and distal to) the 3D HMRN optic nerve stump, establishing FoBMO sectoral and subsectoral regionalization within the orbital ON section requires that it undergo several colocalization and alignment steps as described below:



Fig. 28 (continued) Panel (e) the superior course of the optic nerve (outlined by *green dots*) as it passes through the sclera and its sharper bend into the orbit can be appreciated. N—Nasal; T—Temporal; I—Inferior; S—Superior. *Reproduced from Experimental Eye Research, 2015, with permission from Elsevier*

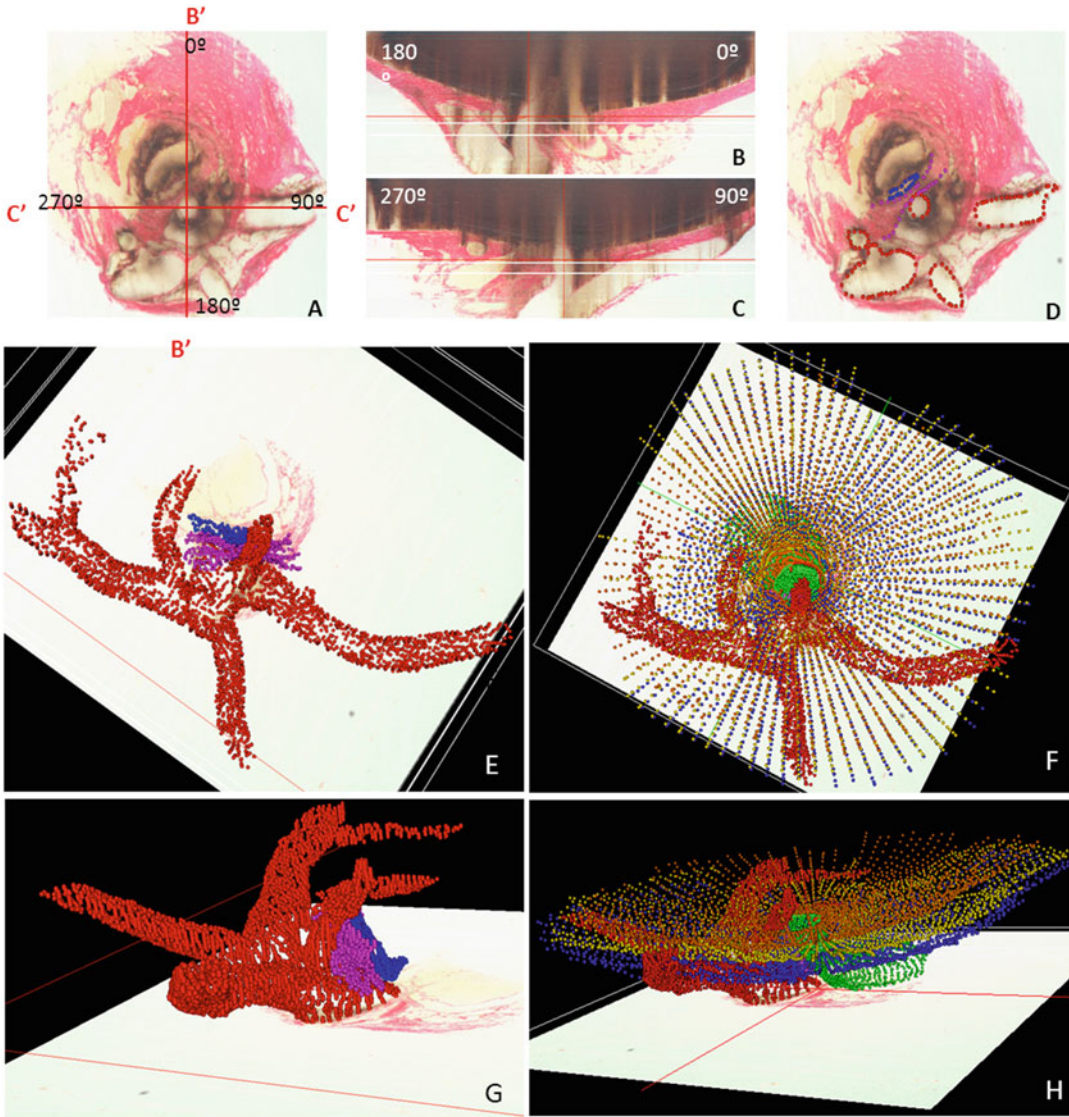


Fig. 29 3D delineation of the ONH and peripapillary scleral vasculature and scleral sling within digital transverse section images. Vessel and scleral sling delineation were performed within every fourth digital transverse section image (a) while simultaneously viewing one linked window which displayed either embedded vertical (b) or embedded horizontal (c) digital sagittal sections through the point being delineated. The lines marked B'-B' and C'-C' in panel (a) mark the location of the embedded vertical and embedded horizontal digital sagittal section images depicted in panels (b) and (c), respectively. Note that these are vertical and horizontal sections through the 3D reconstruction, but because the tissues are not embedded in perfect clinical orientation, they are not "anatomic" vertical and horizontal sections through the ONH. The following landmark categories were individually marked and catalogued within each delineated transverse section image (d): Ophthalmic artery (OA—red); Central retinal artery (CRA—red); Long posterior ciliary arteries (LPCA—red); Short posterior ciliary arteries (SPCA—reds—and branches of the LPCAs in rats); Central retinal vein (CRV—blue); and (6) the vascular or neural boundary of the scleral sling (magenta). Three dimensional reconstructions of the landmark point clouds (panels e-h) were then 3D visualized together and

1. The 3D HMRN volume is colocalized to a fundus image and FoBMO axis-based, 30° sectors and subsectors are imposed as described in Subheadings 3.5 and 3.6.
2. If necessary, 3D HMRN data are converted to right eye orientation (Subheading 3.7). This and the previous step (**step 1**) produce a colocalization (.col) file that is saved for later use.
3. The last image from the 3D HMRN volume (of the ON stump containing the ON cuts) is retrieved and ON stump cuts made at the time of postmortem tissue processing (Subheading 3.1, **step 9**, above) are identified relative to the position of the central retinal artery and vein.
4. The ON axon count cross-section is imaged using an inverted microscope (DM-IRBE, Leica, Wetzlar, Germany) with a 100x oil-immersion lens (FL FLUOTAR, 1.3NA, Leica, Wetzlar, Germany). The microscope is outfitted with a monochrome, 2758 × 2202 pixel digital camera (Retiga 6000, QImaging, Surrey, BC) and a computer-controlled X-Y-Z stage (MS-2000, Applied Scientific Instrumentation, Eugene, OR). A custom software application controls the motorized stage and camera allowing for a fully automated imaging system. Due to the high magnification used, covering the entire ON cross-section requires anywhere from 300 to 500 primary axon images.
5. Using the primary axon images acquired in previous step (**step 4**), a single ON cross-section composite (ON composite) image is built and the temporal and superior cuts made during tissue processing (Subheading 3.1, **step 9**) are identified. Because the optic nerve cross-section can be flipped and inverted in tissue processing the position of the cuts, relative to the central retinal vein and artery are carefully compared to the position of the cuts and central retinal vein and artery in the optic nerve stump photos described in Subheading 3.1, **step 11**, above.
6. Every normal axon is identified in each primary axon image using custom software [49].
7. Following compositing, the x and y locations of all identified axons are noted and axons within the overlapping areas of adjacent primary axon images are identified and counted once.
8. To obtain final RE clinical orientation and FoBMO sectoral and subsectoral regionalization, the ON composite image is first colocalized to the last 3D HMRN section image (**step 3**)

Fig. 29 (continued) separately (turning each landmark category on and off) so as to determine their principal macroscopic relationships. *Reproduced from Experimental Eye Research, 2015, with permission from Elsevier*

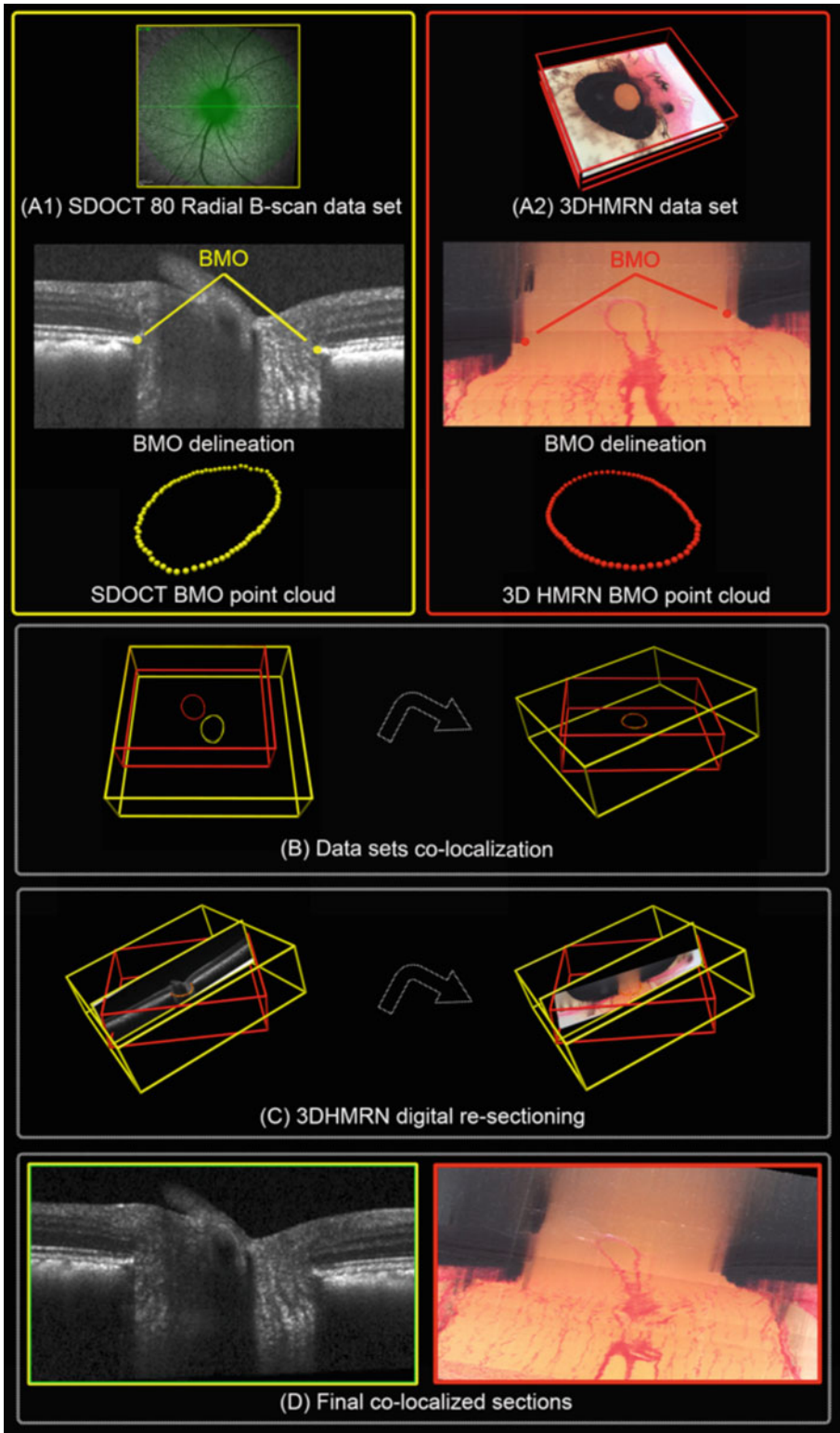


Fig. 30 Colocalization of a 3D HMRN to the sacrifice-day Optical Coherence Tomography (OCT) data set. (a1) OCT image acquisition and BMO generation (*Yellow outline*). Eighty ONH radial OCT B-scans were obtained

and then transformed into RE FoBMO clinical orientation using the colocalization file obtained in (**step 2**).

Figure 31 shows an example of animal-specific comparisons between clinically colocalized LMA and ON Axon Density Maps. Control eye data is shown across the top and EG eye data across the bottom of the figure. EG versus Control eye difference maps for individual parameters are shown in the middle. This figure illustrates how these methodologies allow us to make regional comparisons between the location and magnitude of EG versus Control eye LMA parameter differences and the regional location and magnitude of EG versus Control eye ON axon count differences.

4 Notes

1. **Monitoring the consistency of staining within the 3D HMRN.** After each image capture, the operator checks the current and previous images as well as the real-time horizontal and vertical sagittal views of the image stack to ensure that connective tissue is stained evenly and that it is consistent with the previous image. The ability to see the previous image and image stack helps the operator decide if re-staining is needed.
2. **Overnight 3D HMRN block-face expansion and shrinkage.** To minimize the overnight temperature effects (expansion or shrinkage) on the paraffin tissue block, we place a 1" × 1" piece of cellophane on the cut surface of the block at the end of a cutting session. We also try to make each cutting session at least 8 h long, and ensure that we cut through the lamina cribrosa within one session so that overnight shrinkage and expansion do not affect the LC portion of the reconstruction.
3. **Multiview (MV) custom 3D delineation software.** MV is a custom software application developed in our lab to load and visualize 3D HMRN volumes and to allow users to interactively

Fig. 30 (continued) 30 min after manometric IOP lowering to 10 mmHg (*Top*). BMO was delineated in a subset of 40 radial B-scans of each data set (*yellow points, middle*) and a 3D BMO point cloud was then generated (*bottom*). (**a2**) 3D HMRN data set and BMO generation (*Red outline*). The 3D reconstruction of the ONH was digitally sectioned in 40 radial sagittal sections (*Top*). Within each section, BMO was delineated (*red points, middle*) and a 3D BMO point cloud was generated (*bottom*). An ellipse satisfying a mean least square error constraint was then fitted to the BMO points for both data sets. (**b**) OCT (*yellow cube*) and 3DHMRN (*red cube*) data sets in the same 3D space. Note that the OCT and 3D HMRN BMO ellipses are in different spatial positions (*left*). The OCT data set was re-arranged in space and the BMO ellipses were aligned (*right*) in both direction and size. (**c**) Once the data sets were colocalized, the coordinates of the OCT B-scans planes (*yellow*) were used to digitally re-slice the 3DHMRN volume (*red cube, right*). (**d**) The original OCT B-scan (*left*) and the matching (re-sliced) 3D HMRN section image (*right*) are shown

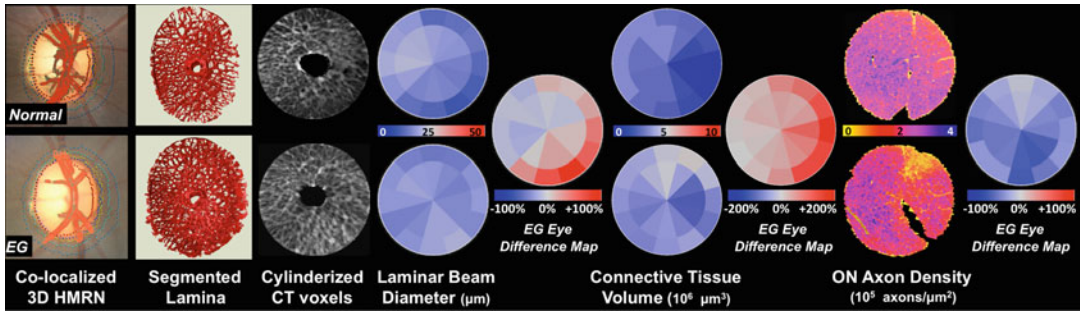


Fig. 31 Clinically Colocalized Laminar Microarchitecture (LMA) and Optic Nerve (ON) axon density maps. Control eye data is across the top, EG eye data on the bottom and EG versus Control eye difference maps for individual parameters are in the middle. 3D Histomorphometric Reconstruction (3D HMRN) data sets (all in RE configuration) can be colocalized to photos (shown) or infrared images taken at the time of OCT data set acquisition (not shown) using the reconstructed vessels. Within the 3D HMRN, laminar beam connective tissue (CT) voxels are segmented (Fig. 18) then transformed into a common 1.5 mm diameter \times 120 micron thick “cylinder” (Figs. 21–23) for between-eye and between-animal comparison [8]. Each laminar beam (and pore—not shown) voxel is assigned a value corresponding to the largest sphere containing it (Fig. 19). Data can be summarized in clock hour regions as shown. EG eye difference maps are reported in percentages (EG-control/control) as shown or actual values (not shown). *Connective Tissue Volume (CTV)* is the number of CT voxels within a region. *CTV fraction (CTVF—*not shown) is the percentage of CT voxels within a region. Our automated method for clinically aligned ON axon density map generation has been published [49]. Our method for regional between-eye difference map generation is in preparation for publication. The accomplishment of these methodologies allows us to make comparisons between the regional location and magnitude of 3D HMRN/LMA deformation and remodeling parameter change and the regional location and magnitude of ON axon loss. In this animal, control eye regions of thinnest *beam diameter* and low *CTV* qualitatively predict the regions of increased *CTV* and highest axon loss in the EG eye

delineate the principal structures of the ONH and other tissues. The principal (sagittal) and alternate (transverse) views are connected allowing users to delineate in one window while simultaneously checking the other views. All delineations are color-coded and displayed as a point cloud in a separate window, allowing the study of the anatomy in 3D space by individual structure or any combination of structures. All delineations can be saved to disk and later loaded back into MV for further assessment and checking. MV includes basic editing tools that allow the user to add points or to modify and delete existing ones.

4. **Stability of the BMO reference plane relative to more peripheral structures.** A few parameter measurements within the reconstructions are made relative to the BMO reference plane. Any posterior bending of BMO relative to the ASCO, collapse of the Border Tissue of Elshnig, or compression of the choroid [50], could alter these points leading to a posterior shift or tilt of the reference plane in the EG eye. In a recent publication [27], however, we detected a significant decrease in the distance between BMO and the ASCO in only 4 of 21 EG

eyes [27]. When we re-calculated both *Laminar Position* and *Post-BMO Total prelaminar Volume* using a reference plane based on the anterior scleral canal opening rather than BMO, none of the important results changed. In addition, in our work in rat ONH 3D reconstructions [7, 10] and OCT [51–53] we have developed peripheral sclera and BM reference planes which attempt to capture peri-papillary scleral deformation and avoid the potential problems associated with a BMO reference plane.

5. **3D HMRN shrinkage effects.** The parameter measurements are not the actual physiologic dimensions of the living monkey prior to sacrifice due to uncharacterized tissue shrinkage effects (from both fixation and embedding) associated with our 3D HMRN technique. However, since both eyes of each animal are treated identically (i.e., at the same time and within the same dehydration solutions), comparisons between the two eyes of each monkey should still be valid. However, it is possible that the character of differential shrinkage is itself, altered in the experimental glaucoma, compared to the control eye. This possibility is currently under study.
6. **Recent automation of 3D HMRN and LMA parameter generation.** In an effort to automate the ONH Macroarchitecture parameter measurement techniques described in this section, custom software has been written. This software replicates the steps described in this section and eliminates the use of Matlab, Geomagic, and Amira. Automated non-subjective creation of all required anatomical surfaces is also performed using custom written software. The software reads the delineated marks files, makes the parameter measurements, provides 3D visualization of the parameter measurements/structures, and outputs the resulting parameter data.
7. **Physiologic Inter-eye Difference.** The true range of physiologic inter-eye variation would be best characterized within hundreds of pairs of normal eyes and include groups designed to assess the effects of species, age, and asymmetries in ocular dimensions and refractive errors. While we did not pre-select these animals, we may have studied monkeys in which the two eyes of each animal were very similar. Using only six animals may over or under estimate true Physiologic Inter-eye Difference estimates.
8. **Custom Software has been built to run laminar segmentation within high resolution 3D HMRN data sets.** Custom software is now used to produce all required surfaces including the Laminar Volume surface. In addition, the LC segmentation algorithm was initially implemented in Matlab. Our transition to higher resolution imaging (Fig. 18) introduced memory and

image processing time challenges for this implementation. To overcome these challenges, custom software that incorporates ITK (Insight Toolkit, Kitware Inc., New York) was developed and is used for LC segmentation.

9. **Voxel layer assignment during cylinderization.** To determine which surface an LC voxel is closest to, a sphere is placed on each voxel and its size is incrementally increased until it intersects with its closest LC surface layer. If the voxel is equidistant from two layers it is assigned to the layer that was first intersected.
10. **Limitations of FoBMO 30° sectoral regionalization.** Even though a common strategy of FoBMO orientation is employed, within 3D HMRN, LMA, FEM, ON axon count and longitudinal and cross-sectional OCT ONH and Retinal Nerve Fiber Layer data sets, there are inherent theoretical and practical weaknesses in this approach which should be considered. First, there is no proper way to consistently and accurately project FoBMO 30° subsectoral boundaries from the flat BMO reference plane through the morphologically complex architecture of the pre-laminar, laminar and retrolaminar ONH tissues. These tissues expand [20] as they pass obliquely through the scleral canal, then turn sharply downward (in most eyes) as they exit the sclera, before resuming a path toward the midline optic nerve chiasm. Second, this 3D morphologic problem becomes even more challenging as the EG ONH is profoundly altered by glaucomatous deformation and remodeling.

Our LMA cylinderization strategy is intended to address this complex 3D problem, but may introduce artifacts that we have not yet recognized. Our exploration of the subsectoral location of cylinderized voxels projected back into position within the uncylinderized LC anatomy (Fig. 23) is reassuring. Within these projections, the voxel positions appear regionally accurate and the mid-LC layer demonstrates the greatest transverse continuity of LC beam architecture, with variable levels of transverse discontinuity evident within the inner and outer layers of each eye. However, while we believe this finding represents actual connective tissue discontinuity within the inner and outer LC layers, its regional extent may be under or over-estimated by delineation, surface curve fitting, and segmentation inaccuracies. Delineation inaccuracy can occur if the LC surfaces are delineated “above” or “below” actual biological transverse connectivity. Surface curve fitting inaccuracy can occur because the parametric quadric surfaces that are fit to the anterior LC surface and posterior LC surface point clouds do not necessarily follow the anatomical shape of the anterior and posterior borders of the LC, creating patches of

LC that lack transverse continuity. Segmentation inaccuracy can occur if our segmentation algorithm fails to make transverse connective tissue connections where they are biologically present and visible using our 3D delineation techniques. Because all three forms of inaccuracy are likely present within our data, distinctions between inner, middle, and outer LC layers should be conservatively interpreted with these limitations in mind.

Attempting to compare regions of 3D HMRN, LMA, FEM, and OCT data (Control, EG or EG versus Control eye differences) to orbital optic nerve axon counts raises additional issues [49]. First, our FoBMO axis landmarks can only be estimated and apart from the position of the fovea on the posterior sclera cannot be anatomically assigned. Second, substantial migration of at least a subset of axons likely occurs within the first 3 mm of the orbital ON stump (i.e., the ONH trephine ON stump). Axons may be in one FoBMO subsector as they pass through the BMO reference plane, a different one as they pass through the lamina and in yet another within the orbital ON cross-section in which they are counted. In the short term, we will interpret these data and their analyses carefully and employ statistical strategies to account for these uncertainties. In the long term, axon transport studies designed to characterize the magnitude of these effects will be necessary to ultimately resolve these issues.

11. **LMA regionalization is performed using the polar coordinates of each voxel.** Regionalizing the LC Microarchitecture parameter data into sectors and subsectors is determined by using the polar coordinates of each LC Voxel, and the LC surface layers they belong to.

12. **LMA Discordance Mapping can also be used to identify sectors of high connective tissue density.**

Identifying those sectors in which connective tissue density is greatest may also be an important form of LMA discordance mapping. Our method for discordance mapping can provide this information as well, and this will be explored in future analyses.

13. **Colocalizing pre-sacrifice OCT and post-mortem 3D HMRN data sets.** OCT imaging both the EG and control eyes of a monkey immediately preceding perfusion fixation and subsequent 3D HMRN would be the best way of performing these comparisons, as disease-related changes in the tissue that occurred between OCT imaging and sacrifice would be minimized. Obtaining OCT images in this fashion would be possible if the animal's ONH could be imaged with the animal lying flat on the sacrifice table—such as currently is done using intraoperative OCT instruments. At present we do not have

these capabilities and so manometer controlled OCT imaging must be performed within 2–3 days prior to sacrifice, and not immediately prior.

Acknowledgment

Supported in part by USPHS grants R01EY011610 (CFB) from the National Eye Institute, National Institutes of Health, Bethesda, Maryland; a grant from the American Health Assistance Foundation (now known as Bright Focus), Rockville, Maryland (CFB); a grant from The Whitaker Foundation, Arlington, Virginia (CFB); a Research to Prevent Blindness Career Development Award (CFB); The Alcon Research Institute; The Legacy Good Samaritan Foundation, Portland, Oregon; and the Sears Trust for Biomedical Research, Mexico, Missouri.

References

- Burgoyne CF, Downs JC, Bellezza AJ, Hart RT (2004) Three-dimensional reconstruction of normal and early glaucoma monkey optic nerve head connective tissues. *Invest Ophthalmol Vis Sci* 45(12):4388–4399. <https://doi.org/10.1167/iovs.04-0022>
- Yang H, Downs JC, Bellezza A, Thompson H, Burgoyne CF (2007) 3-D histomorphometry of the normal and early glaucomatous monkey optic nerve head: prelaminar neural tissues and cupping. *Invest Ophthalmol Vis Sci* 48(11):5068–5084. <https://doi.org/10.1167/iovs.07-0790>
- Yang H, Downs JC, Girkin C, Sakata L, Bellezza A, Thompson H, Burgoyne CF (2007) 3-D histomorphometry of the normal and early glaucomatous monkey optic nerve head: lamina cribrosa and peripapillary scleral position and thickness. *Invest Ophthalmol Vis Sci* 48(10):4597–4607. <https://doi.org/10.1167/iovs.07-0349>
- Yang H, Downs JC, Burgoyne CF (2009) Physiologic intereye differences in monkey optic nerve head architecture and their relation to changes in early experimental glaucoma. *Invest Ophthalmol Vis Sci* 50(1):224–234. <https://doi.org/10.1167/iovs.08-2464>
- Yang H, Williams G, Downs JC, Sigal IA, Roberts MD, Thompson H, Burgoyne CF (2011) Posterior (outward) migration of the lamina cribrosa and early cupping in monkey experimental glaucoma. *Invest Ophthalmol Vis Sci* 52(10):7109–7121. <https://doi.org/10.1167/iovs.11-7448>
- Lockwood H, Reynaud J, Gardiner S, Grimm J, Libertaux V, Downs JC, Yang H, Burgoyne CF (2015) Lamina cribrosa microarchitecture in normal monkey eyes part 1: methods and initial results. *Invest Ophthalmol Vis Sci* 56(3):1618–1637. <https://doi.org/10.1167/iovs.14-15967>
- Pazos M, Yang H, Gardiner SK, Cepurna WO, Johnson EC, Morrison JC, Burgoyne CF (2016) Expansions of the neurovascular scleral canal and contained optic nerve occur early in the hypertonic saline rat experimental glaucoma model. *Exp Eye Res* 145:173–186. <https://doi.org/10.1016/j.exer.2015.10.014>
- Reynaud J, Lockwood H, Gardiner SK, Williams G, Yang H, Burgoyne CF (2016) Lamina cribrosa microarchitecture in monkey early experimental glaucoma: global change. *Invest Ophthalmol Vis Sci* 57(7):3451–3469. <https://doi.org/10.1167/iovs.16-19474>
- Roberts MD, Grau V, Grimm J, Reynaud J, Bellezza AJ, Burgoyne CF, Downs JC (2009) Remodeling of the connective tissue microarchitecture of the lamina cribrosa in early experimental glaucoma. *Invest Ophthalmol Vis Sci* 50(2):681–690. <https://doi.org/10.1167/iovs.08-1792>
- Pazos M, Yang H, Gardiner SK, Cepurna WO, Johnson EC, Morrison JC, Burgoyne CF (2015) Rat optic nerve head anatomy within 3D histomorphometric reconstructions of normal control eyes. *Exp Eye Res* 139:1–12. <https://doi.org/10.1016/j.exer.2015.05.011>
- Burgoyne CF (2015) The non-human primate experimental glaucoma model. *Exp Eye Res*

- 141:57–73. <https://doi.org/10.1016/j.exer.2015.06.005>
12. Strouthidis NG, Yang H, Fortune B, Downs JC, Burgoyne CF (2009) Detection of optic nerve head neural canal opening within histomorphometric and spectral domain optical coherence tomography data sets. *Invest Ophthalmol Vis Sci* 50(1):214–223. <https://doi.org/10.1167/iovs.08-2302>
 13. Jansonius NM, Nevalainen J, Selig B, Zangwill LM, Sample PA, Budde WM, Jonas JB, Lagreze WA, Airaksinen PJ, Vonthein R, Levin LA, Paetzold J, Schiefer U (2009) A mathematical description of nerve fiber bundle trajectories and their variability in the human retina. *Vis Res* 49(17):2157–2163. <https://doi.org/10.1016/j.visres.2009.04.029>
 14. Hood DC, Kardon RH (2007) A framework for comparing structural and functional measures of glaucomatous damage. *Prog Retin Eye Res* 26(6):688–710. <https://doi.org/10.1016/j.preteyeres.2007.08.001>
 15. Turpin A, Sampson GP, McKendrick AM (2009) Combining ganglion cell topology and data of patients with glaucoma to determine a structure-function map. *Invest Ophthalmol Vis Sci* 50(7):3249–3256. <https://doi.org/10.1167/iovs.08-2492>
 16. Harwerth RS, Wheat JL, Fredette MJ, Anderson DR (2010) Linking structure and function in glaucoma. *Prog Retin Eye Res* 29(4):249–271. <https://doi.org/10.1016/j.preteyeres.2010.02.001>
 17. Jonas JB, Nguyen NX, Naumann GO (1989) The retinal nerve fiber layer in normal eyes. *Ophthalmology* 96(5):627–632
 18. Patel NB, Wheat JL, Rodriguez A, Tran V, Harwerth RS (2012) Agreement between retinal nerve fiber layer measures from Spectralis and cirrus spectral domain OCT. *Optom Vis Sci* 89(5):E652–E666. <https://doi.org/10.1097/OPX.0b013e318238c34c>
 19. Garway-Heath DF, Poinoosawmy D, Fitzke FW, Hitchings RA (2000) Mapping the visual field to the optic disc in normal tension glaucoma eyes. *Ophthalmology* 107(10):1809–1815
 20. Downs JC, Yang H, Girkin C, Sakata L, Bellezza A, Thompson H, Burgoyne CF (2007) Three-dimensional histomorphometry of the normal and early glaucomatous monkey optic nerve head: neural canal and subarachnoid space architecture. *Invest Ophthalmol Vis Sci* 48(7):3195–3208. <https://doi.org/10.1167/iovs.07-0021>
 21. He L, Ren R, Yang H, Hardin C, Reyes L, Reynaud J, Gardiner SK, Fortune B, Demirel S, Burgoyne CF (2014) Anatomic vs. acquired image frame discordance in spectral domain optical coherence tomography minimum rim measurements. *PLoS One* 9(3):e92225. <https://doi.org/10.1371/journal.pone.0092225>
 22. Reis AS, Sharpe GP, Yang H, Nicoleta MT, Burgoyne CF, Chauhan BC (2012) Optic disc margin anatomy in patients with glaucoma and normal controls with spectral domain optical coherence tomography. *Ophthalmology* 119(4):738–747. <https://doi.org/10.1016/j.ophtha.2011.09.054>
 23. Anderson DR, Hoyt WF (1969) Ultrastructure of intraorbital portion of human and monkey optic nerve. *Arch Ophthalmol* 82(4):506–530
 24. Elschnig A (1928) Über Glaukom. *Albrecht von Graefes Archiv für Ophthalmologie* 120(1–2):94–116. <https://doi.org/10.1007/bf01852791>
 25. Reis AS, O’Leary N, Yang H, Sharpe GP, Nicoleta MT, Burgoyne CF, Chauhan BC (2012) Influence of clinically invisible, but optical coherence tomography detected, optic disc margin anatomy on neuroretinal rim evaluation. *Invest Ophthalmol Vis Sci* 53(4):1852–1860. <https://doi.org/10.1167/iovs.11-9309>
 26. Yang H, Thompson H, Roberts MD, Sigal IA, Downs JC, Burgoyne CF (2011) Deformation of the early glaucomatous monkey optic nerve head connective tissue after acute IOP elevation in 3-D histomorphometric reconstructions. *Invest Ophthalmol Vis Sci* 52(1):345–363. <https://doi.org/10.1167/iovs.09-5122>
 27. Yang H, Ren R, Lockwood H, Williams G, Libertiaux V, Downs C, Gardiner SK, Burgoyne CF (2015) The connective tissue components of optic nerve head cupping in monkey experimental glaucoma part I: global change. *Invest Ophthalmol Vis Sci* 56(13):7661–7678. <https://doi.org/10.1167/iovs.15-17624>
 28. Grau V, Downs JC, Burgoyne CF (2006) Segmentation of trabeculated structures using an anisotropic Markov random field: application to the study of the optic nerve head in glaucoma. *IEEE Trans Med Imaging* 25(3):245–255. <https://doi.org/10.1109/TMI.2005.862743>
 29. Dougherty RP, Kunzelmann K-H 2007 Computing local thickness of 3D structures with ImageJ. In: *Microscopy & microanalysis meeting*, Fort. Lauderdale, FL, 5–9 August 2007
 30. Saito T, Toriwaki J-I (1994) New algorithms for euclidean distance transformation of an

- n-dimensional digitized picture with applications. *Pattern Recogn* 27(11):1551–1565. [https://doi.org/10.1016/0031-3203\(94\)90133-3](https://doi.org/10.1016/0031-3203(94)90133-3)
31. Hildebrand T, Rügsegger P (1997) A new method for the model-independent assessment of thickness in three-dimensional images. *J Microsc* 185(1):67–75. <https://doi.org/10.1046/j.1365-2818.1997.1340694.x>
 32. Carolynne AK (2014) Chapter III: two parameter gamma distribution. In: Carolynne AK (ed) *Gamma and related distributions*. Books on Demand, Norderstedt, Germany, pp 6–27
 33. Quigley HA, Hohman RM, Addicks EM, Massof RW, Green WR (1983) Morphologic changes in the lamina cribrosa correlated with neural loss in open-angle glaucoma. *Am J Ophthalmol* 95(5):673–691
 34. Minckler DS, Spaeth GL (1981) Optic nerve damage in glaucoma. *Surv Ophthalmol* 26(3):128–148
 35. Quigley H, Anderson DR (1976) The dynamics and location of axonal transport blockade by acute intraocular pressure elevation in primate optic nerve. *Investig Ophthalmol* 15(8):606–616
 36. Minckler DS (1986) Correlations between anatomic features and axonal transport in primate optic nerve head. *Trans Am Ophthalmol Soc* 84:429–452
 37. Quigley HA, Addicks EM (1981) Regional differences in the structure of the lamina cribrosa and their relation to glaucomatous optic nerve damage. *Arch Ophthalmol* 99(1):137–143
 38. Radius RL, Gonzales M (1981) Anatomy of the lamina cribrosa in human eyes. *Arch Ophthalmol* 99(12):2159–2162
 39. Bellezza AJ, Hart RT, Burgoyne CF (2000) The optic nerve head as a biomechanical structure: initial finite element modeling. *Invest Ophthalmol Vis Sci* 41(10):2991–3000
 40. Sigal IA, Yang H, Roberts MD, Downs JC (2010) Morphing methods to parameterize specimen-specific finite element model geometries. *J Biomech* 43(2):254–262. <https://doi.org/10.1016/j.jbiomech.2009.08.036>
 41. Sigal IA, Yang H, Roberts MD, Grimm JL, Burgoyne CF, Demirel S, Downs JC (2011) IOP-induced lamina cribrosa deformation and scleral canal expansion: independent or related? *Invest Ophthalmol Vis Sci* 52(12):9023–9032. <https://doi.org/10.1167/iovs.11-8183>
 42. Girard MJ, Suh JK, Bottlang M, Burgoyne CF, Downs JC (2009) Scleral biomechanics in the aging monkey eye. *Invest Ophthalmol Vis Sci* 50(11):5226–5237. <https://doi.org/10.1167/iovs.08-3363>
 43. Fazio MA, Grytz R, Bruno L, Girard MJ, Gardiner S, Girkin CA, Downs JC (2012) Regional variations in mechanical strain in the posterior human sclera. *Invest Ophthalmol Vis Sci* 53(9):5326–5333. <https://doi.org/10.1167/iovs.12-9668>
 44. Grytz R, Meschke G (2010) A computational remodeling approach to predict the physiological architecture of the collagen fibril network in corneo-scleral shells. *Biomech Model Mechanobiol* 9(2):225–235. <https://doi.org/10.1007/s10237-009-0173-2>
 45. Coudrillier B, Pijanka JK, Jefferys JL, Goel A, Quigley HA, Boote C, Nguyen TD (2015) Glaucoma-related changes in the mechanical properties and collagen micro-architecture of the human sclera. *PLoS One* 10(7):e0131396. <https://doi.org/10.1371/journal.pone.0131396>
 46. Srinivasan VJ, Adler DC, Chen Y, Gorczyńska I, Huber R, Duker J, Schuman JS, Fujimoto JG (2008) Ultrahigh-speed optical coherence tomography for three-dimensional and en face imaging of the retina and optic nerve head. *Invest Ophthalmol Vis Sci* 49(11):5103–5110. <https://doi.org/10.1167/iovs.08-2127>
 47. Lee EJ, Kim TW, Weinreb RN, Park KH, Kim SH, Kim DM (2011) Visualization of the lamina cribrosa using enhanced depth imaging spectral-domain optical coherence tomography. *Am J Ophthalmol* 152(1):87–95. e81. <https://doi.org/10.1016/j.ajo.2011.01.024>
 48. Girard MJ, Tun TA, Husain R, Acharyya S, Haaland BA, Wei X, Mari JM, Perera SA, Baskaran M, Aung T, Strouthidis NG (2015) Lamina cribrosa visibility using optical coherence tomography: comparison of devices and effects of image enhancement techniques. *Invest Ophthalmol Vis Sci* 56(2):865–874. <https://doi.org/10.1167/iovs.14-14903>
 49. Reynaud J, Cull G, Wang L, Fortune B, Gardiner S, Burgoyne CF, Cioffi GA (2012) Automated quantification of optic nerve axons in primate glaucomatous and normal eyes—method and comparison to semi-automated manual quantification. *Invest Ophthalmol Vis Sci* 53(6):2951–2959. <https://doi.org/10.1167/iovs.11-9274>
 50. Johnstone J, Fazio M, Rojananuangnit K, Smith B, Clark M, Downs C, Owsley C, Girard MJ, Mari JM, Girkin CA (2014) Variation of the axial location of Bruch’s membrane opening with age, choroidal thickness, and race. *Invest Ophthalmol Vis Sci* 55(3):2004–2009. <https://doi.org/10.1167/iovs.13-12937>

51. He L, Yang H, Gardiner SK, Williams G, Hardin C, Strouthidis NG, Fortune B, Burgoyne CF (2014) Longitudinal detection of optic nerve head changes by spectral domain optical coherence tomography in early experimental glaucoma. *Invest Ophthalmol Vis Sci* 55(1):574–586. <https://doi.org/10.1167/iovs.13-13245>
52. Yang H, He L, Gardiner SK, Reynaud J, Williams G, Hardin C, Strouthidis NG, Downs JC, Fortune B, Burgoyne CF (2014) Age-related differences in longitudinal structural change by spectral-domain optical coherence tomography in early experimental glaucoma. *Invest Ophthalmol Vis Sci* 55(10):6409–6420. <https://doi.org/10.1167/iovs.14-14156>
53. Ivers KM, Yang H, Gardiner SK, Qin L, Reyes L, Fortune B, Burgoyne CF (2016) In vivo detection of laminar and peripapillary scleral hypercompliance in early monkey experimental glaucoma. *Invest Ophthalmol Vis Sci* 57(9):OCT388–OCT403. <https://doi.org/10.1167/iovs.15-18666>

Visualizing Astrocytes of the Optic Nerve

Daniel Sun

Abstract

Astrocytes make up approximately 30% of all the cells in the mammalian central nervous system. They are not passive, as once thought, but are integral to brain physiology and perform many functions that are important for normal neuronal development and metabolism, synapse formation, synaptic transmission, and in repair following injury/disease. Astrocytes also communicate with neurons, blood vessels, and other types of glial cells. Astrocytes within the optic nerve head region play a key role in glaucomatous axon degeneration. In this chapter, we describe ways in which astrocytes of the optic nerve head can be visualized, beginning with basic immunohistochemical staining methods, to single-cell dye injections and then to transgenic animals. We will also discuss the pros and cons of each method. Many of the methods were initially developed to visualize brain astrocytes; in some cases, the method has translated well to astrocytes of the optic nerve, and in others, it remains unclear.

Key words Astrocytes, Optic nerve, Glaucoma, Glia, Transgenic mice

1 Introduction

Astrocytes constitute the most abundant glial cell type in the central nervous system. There is growing interest in understanding these cells as it has become clear that they are not simply elements that fill space not occupied by neurons, nor are they entirely passive. Astrocytes are responsible for a wide variety of essential and complex functions in the normal healthy tissue, interacting with other glial cell types, neurons, and blood vessels [1]. For example, astrocytes have primary roles in synaptic transmission and information processing, neurotransmitter clearance, ion homeostasis; they participate in maintaining the blood-brain barrier, regulating blood flow, and providing neurotrophic support for neurons [2–7]. Astrocytes express K^+ and Na^+ channels and can exhibit evoked inward currents, but unlike neurons, astrocytes do not propagate action potentials. Rather, astrocytes exhibit regulated increases in intracellular Ca^{2+} that represent a form of astrocyte excitability. These Ca^{2+} waves can spread and are of functional significance in astrocyte-astrocyte as well as astrocyte-neuron communications [8, 9].

Astrocytes respond to virtually all injuries and diseases by becoming reactive [1, 10]. This process was originally described over 100 years ago and identified by a change in morphology and an upregulation in the expression of GFAP. Perhaps the most well-known aspect of this reactive process is the formation of a glial scar that prevents axon regeneration, leading to the notion that reactivity is harmful and should be prevented [11]. We now know that this is not necessarily true [12]. Reactivity is not a single all-or-none response as a first thought, but it is a complex process that can involve a continuum of changes ranging from subtle and reversible alterations in morphology and gene expression to the pronounced and long lasting changes associated with scar formation. Moreover, the reactive response can differ depending on the type of astrocyte involved, the type of injury, the location of the astrocyte in relation to the site of injury, and the time post-injury [1, 10, 13]. Reactive astrocytes and scar formation can have beneficial effects, and preventing these functions has the potential to contribute to, or to be primary causes of CNS disease mechanisms and eventually clinical signs [14–18]. Ultimately, astrocytes show immense heterogeneity, in morphology, development, physiology, functionally, and in response to injury and diseases [19].

The earliest glaucomatous damage to retinal ganglion cells is hypothesized to occur to their axons within the optic nerve head. In many species, including rats, mice, monkeys, and humans, this region is densely populated by astrocytes, hence the special interest in studying these cells within this region [20–23]. In this chapter, we will review the different ways in which astrocytes within the optic nerve can be visualized, beginning with basic immunohistochemical staining methods, to single-cell dye injections and then to transgenic animals. We will also discuss the pros and cons of each method.

1.1 Immunohistochemical Staining

Astrocytes have traditionally been labeled by antibodies against their intermediate filaments or cytoplasmic/membrane bound proteins. GFAP has been the prototypical astrocyte marker and labels a cell's intermediate filaments. Antibodies against GFAP are readily available and are very reliable. The expression pattern for GFAP differs across the CNS and it undoubtedly labels more than a single type of astrocyte. In the cortex and hippocampus, GFAP labeling of protoplasmic astrocytes reveals the typical star shaped appearance of astrocytes, and in the cerebellum, a radial appearance. In the optic nerve, astrocytes are organized in such a dense manner that labeling for GFAP simply shows a meshwork of processes, making it impossible to discern the extent and boundaries of each astrocyte (Fig. 1a and b) [23]. However, in the corpus callosum, another white matter tract of the brain, this is not the case. Here, GFAP labeled astrocytes appear stellate and are clearly separated from one another [25]. Similar to the optic nerve, retinal astrocytes labeled with

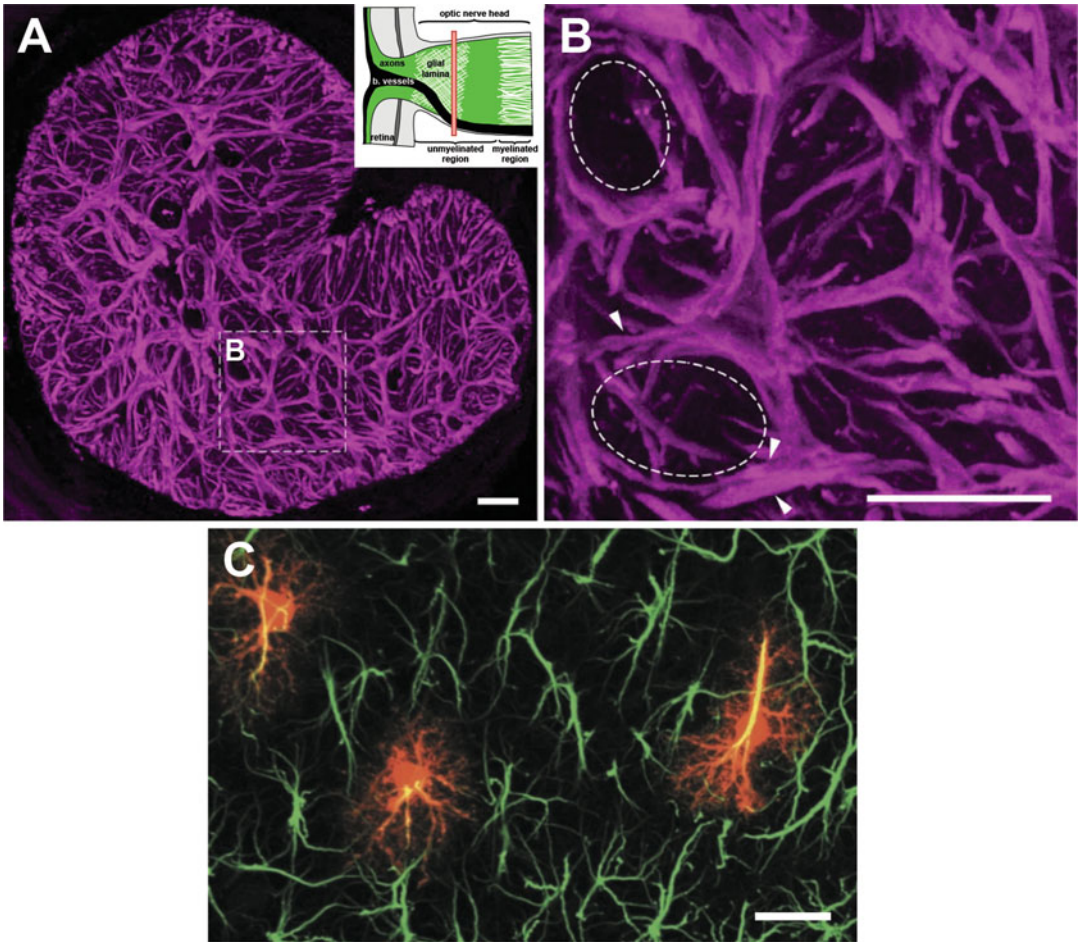


Fig. 1 (a, b) A transverse cross-section of the optic nerve head labeled with GFAP. GFAP labels the intermediate filaments of the astrocytes, producing a dense labeling pattern where one cannot see the entire extent of a single astrocyte. (b) The thick astrocyte processes (*arrowheads*) form what we call glial tubes, through which the ganglion cell axons go through (*dashed ellipse*). (c) GFAP labeling of Lucifer yellow filled protoplasmic astrocytes from the CA1 stratum radiatum. Dye filled astrocytes (*red*) consistently display a GFAP cytoskeleton (*green*). This maximum intensity projection demonstrates how GFAP labeling under-represents the full morphology of an astrocyte. Scale bars = 20 μm . Panels A and B adapted from Sun et al. [23], C from Bushong et al. [24]

GFAP show no separation. In the cortex of humans and chimpanzees GFAP labels at least four distinct morphological types of astrocytes (interlaminar, varicose projecting, protoplasmic, and fibrous), compared with two in the rodent (protoplasmic, fibrous), and three within lower order primates such as rhesus macaques and squirrel monkeys [26]. Several other antibodies against intermediate filaments are also commonly used to label astrocytes, such as vimentin and nestin.

There are limitations to using antibodies against intermediate filaments. In most cases, the labeling is restricted to only those

processes that contain intermediate filaments. Therefore, neither the shape of the cell body, the full length of the processes, or the fine processes are revealed. For example, GFAP delineates only 15% of the total volume of an astrocyte, underestimating its complete branching pattern and territory, and leaving much of it unseen (Fig. 1c) [24, 27, 28]. Another limitation is that GFAP does not label all normal astrocytes, its expression shows both local and regional variability. In the optic nerve head and proper, it is most certain that GFAP labels all astrocytes, but this is not the case in the corpus callosum. GFAP has a preference for protoplasmic astrocytes, fibrous astrocytes, Bergmann glia, and subependymal astrocytes adjacent to the cerebral ventricles. Furthermore, GFAP is expressed by virtually all Bergmann glial cells in the cerebellum, whereas only 15–20% of the astrocytes in the cortex and hippocampus express GFAP. Moreover, GFAP mRNA is predominantly expressed in white matter [29].

Cytoplasmic or membrane protein markers such as S100 calcium-binding protein β (S100 β), glutamine synthetase (GS), glutamate transporter 1 (GLT-1), or glutamate/aspartate transporter (GLAST) can reveal the full body and fine processes of an astrocyte but may produce a labeling pattern with little separation between neighboring astrocytes. In the optic nerve, these markers produce a very dense labeling pattern, similar to what you see when staining with GFAP. Moreover, some of these markers are not exclusive to astrocytes. Although GLAST is specific for astrocytes [30–32], antibodies against S100 β also label some oligodendrocytes, NG2 glial cells, and even neurons [33–36].

A problem with the current set of immunohistochemical markers is that there are none that label all astrocytes, and there are none that are specific for different types. As an example, there is yet to be a marker that can segregate the two broadest types of astrocytes; protoplasmic astrocytes that reside in the gray matter and fibrous astrocytes that reside in the white matter. In general, location and morphology remain the best way to identify different types of astrocytes, although it does not always hold true. In the optic nerve proper, several morphologically distinct astrocytes exist and yet they all stain equally well with GFAP, vimentin, nestin, and S100 β [23]. Do they represent different subtypes of fibrous astrocytes? Fundamentally, we do not really know how many different types of astrocytes there are. This poses a problem because then it is unclear whether the behavior of an astrocyte is a general property of all astrocytes or only of a particular type.

In a study to identify new immunohistochemical markers of astrocytes, Cahoy et al. [29] analyzed the transcriptome of purified cortical astrocytes and identified the aldehyde dehydrogenase 1 family, member L1 (Aldh1L1) gene to be specific and highly expressed in astrocytes. Staining with an Aldh1L1 specific polyclonal antibody revealed the highly branched astrocyte morphology, including the

astrocyte cell body and its extensive processes. This is in contrast to antibodies against GFAP which only label the main thick processes. Furthermore, Aldh1L1 mRNA is more widely expressed throughout the brain compared to GFAP and many more astrocytes were immunolabeled with Aldh1L1 than GFAP. Aldh1L1 may be a better pan astrocyte marker than GFAP.

Immunostaining gives an incomplete view of an astrocyte. With the introduction of single-cell dye injections, particle mediated dye transfer, and transgenic mice (*see* below), the complete morphology of individual astrocytes and their spatial organization can be better studied. These techniques reveal immense diversity in the morphology of astrocytes that was not apparent with simple GFAP labeling. For example, protoplasmic and fibrous astrocytes may appear rather similar upon GFAP labeling but are distinctly different when their full morphology is visualized.

1.2 Single-Cell Dye Injections

Fluorescent indicators can be injected via iontophoresis into individual astrocytes using either sharp microelectrodes or patch pipettes. This approach is technically demanding, time consuming and only a small number of astrocytes can be injected at any one time. There are several advantages: (1) neighboring astrocytes can be injected to study their overlap, in isolation of other astrocytes (Fig. 2a), (2) the entire morphology of the astrocyte can be visualized, even the finest of processes (Fig. 2b–d), and (3) gap junctional coupling between astrocytes can be studied when an appropriate tracer dye is chosen. Either live or lightly fixed tissues can be used. Compounds used to fill the astrocytes either fill the cytoplasm or stain the lipophilic plasma membrane, these include lucifer yellow, carbocyanine dyes such as DiI or DiO, biocytin, neurobiotin and dextran coupled fluorescein or rhodamine isothiocyanate. Using various combinations of these dyes, neighboring astrocytes can be labeled in different colors. Tissues such as the retina are far easier to inject than the optic nerve, where the density of the tissue makes it difficult to maneuver the microelectrode. Astrocytes in the gray matter (Fig. 2a) [24, 37] and white matter (fibrous astrocytes of the optic nerve, Fig. 2b–d, [38, 39]) have been dye injected successfully.

1.3 Particle Mediated Dye Transfer

Populations of astrocytes can be labeled in slice preparations of nervous tissue by particle-mediated ballistic delivery of lipophilic dyes such as DiI, DiO, and DiD. This is an adaptation of the original gene transfection techniques by Lo et al. [40]. This “DiO-lytic” technique uses high pressure helium to shoot gold or tungsten particles coated with the lipophilic dye into the tissue, which then penetrates into the cells. Using carbocyanine dyes, the labeling involves passive dye transfer and diffusion along the cell membrane, revealing the entire morphology of the astrocyte. Living or fixed tissue can be labeled rapidly by many different colors at low or very

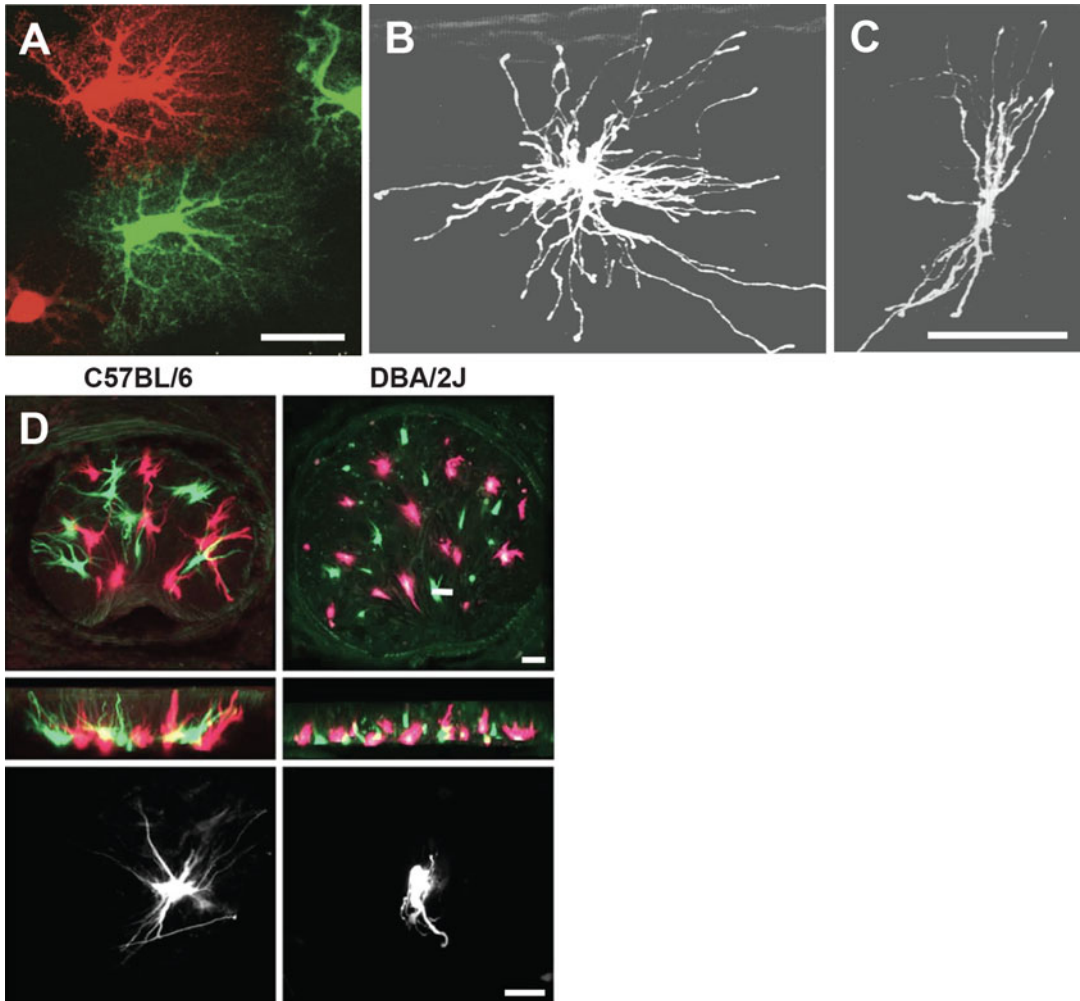


Fig. 2 (a) Overlap of astrocyte territories assessed by dye-filling of neighboring cells (Lucifer yellow and Alexa Fluor 568). Maximum intensity projections of protoplasmic astrocytes from the molecular layer of the normal dentate gyrus. Scale bar = 25 μm . (b, c) Fibrous astrocytes from the rat optic nerve following dye injection, showing two very different morphologies. Scale bar = 50 μm . (d) Single-cell dye injected astrocytes from the optic nerve head of C57BL/6 mice and DBA/2J glaucomatous mice in which the astrocytes are reactive. Astrocytes were filled with Lucifer yellow or Alexa Fluor 568. Scale bar = 20 μm . Panel A adapted from Wilhelmsson et al. [37], B and C from Butt and Colquhoun [38], D from Ju et al. [39]

high densities. With this method, it is difficult to control how many and which astrocytes are labeled. We have previously used this method on fixed vibratome sections of the optic nerve (Fig. 3) [25]. In general, there are now better methods of visualizing astrocytes.

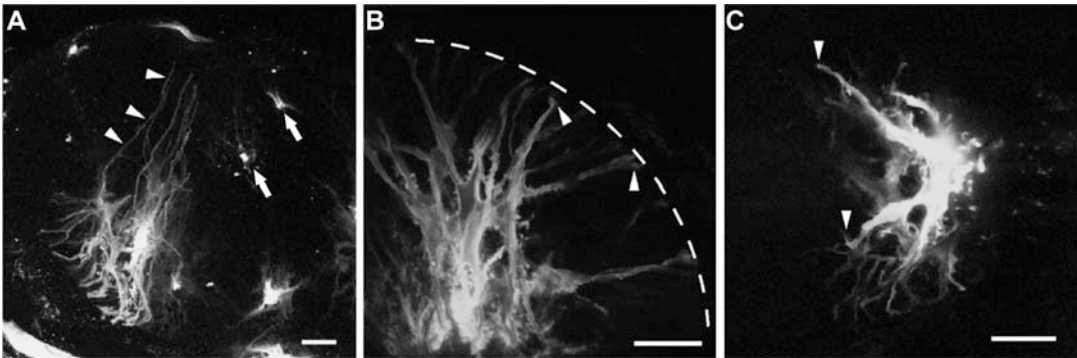


Fig. 3 (a, b) Particle-mediated dye labeling of normal and (c) reactive (3 days post-nerve crush) astrocytes within the optic nerve head of C57Bl/6 mice. With this method there is no control over how many and which astrocytes are targeted. Some of the dye particles may randomly hit areas where there are no cellular compartments, thus the dye does not diffuse anywhere (*arrows*), or hit distal processes and not diffuse enough to label the entire cell. When labeled properly though, the full morphology of the astrocyte can be seen. Before mounting the tissue, one typically waits long enough for the dye to pass through the long processes of the astrocytes (a, *arrowheads*) and fill the endfeet (b, c, *arrows*). (c) This method can be used to visualize reactive astrocytes, revealing the characteristic hypertrophy and shortening of processes. Scale bars = 20 μm . Adapted from Sun et al. [25]

1.4 Transgenic Mice

1.4.1 Single-Color Labeling of Astrocytes

Transgenic mice have been developed in which astrocyte specific proteins (e.g., GFAP, GLT-1, Aldh1L1) are used to target reporter molecules (e.g., EGFP, tdTomato). These mice offer several advantages over traditional labeling techniques: (1) the complete morphology of the astrocyte is revealed. As the reporter molecules typically distribute throughout the entire cytoplasm, even the fine processes can be discerned by confocal microscopy; (2) Astrocytes can be easily visualized in situ and in vivo without additional labeling steps; (3) large populations of astrocytes can be isolated using FACS, and (4) the spatial arrangement of a population of astrocytes can be studied, although with some caveats (*see* below). Table 1 shows some of the transgenic mouse strains available for visualizing astrocytes. As a note, many of these strains were developed for visualizing brain astrocytes, whether astrocytes in the optic nerve also express the reporter molecule is not clear. Here, we highlight two strains that are particularly useful for visualizing optic nerve astrocytes.

The hGFAPpr-EGFP mouse strain was developed by Nolte et al. [41] and remains the best transgenic strain with which to visualize astrocytes in the optic nerve. It was developed by injecting a 2.2 kb fragment of the human GFAP promoter fused to the EGFP gene into oocytes of FVB/N mice. The resulting strain displays green fluorescent labeling of subsets of astrocytes in the central (brain, spinal cord, optic nerve) and peripheral nervous system (Fig. 4a–c) [23]. Neither neurons, microglia, or oligodendrocytes are labeled. A peculiarity of this mouse strain is that the

Table 1
Transgenic mouse strains with fluorescently labeled astrocytes

Reference	Promoter	Reporter
Nolte et al. [41]	Human GFAP	EGFP
Zhuo et al. [42]	Human GFAP	hGFP-S65 T
Suzuki et al. [43]	Mouse GFAP	EGFP
Livet et al. [44]	Stochastic	Various
Yamaguchi et al. [45]	Rat nestin	EGFP
Vives et al. [33]	Mouse S100 β	EGFP
Yang et al. [46]	EAAT2	tdTomato
Regan et al. [47]	BAC-GLT1	EGFP
Heintz [48]; Doyle et al. [49]	BAC-Aldh1L1	EGFP

distribution and expression of EGFP is heterogenous. There are areas of the brain where EGFP expression does not completely overlap with GFAP immunostaining, (e.g., there are GFAP-positive astrocytes that do not express EGFP), and individual astrocytes can display variable levels of EGFP expression, ranging from almost undetectable levels to high brightness. Mice in which there are very many EGFP expressing astrocytes can be used to study spatial organization, while mice that have very few isolated EGFP expressing astrocytes can be used to study individual morphologies. An example of this for the optic nerve is shown in Fig. 4a and c [23]. Interestingly, in the retina EGFP is expressed exclusively in Müller cells and not in the astrocytes located within the inner limiting membrane, although astrocytes express abundant GFAP and Müller cells do not. This mouse strain is also useful in studying reactive astrocytes. We have used this mouse strain to address the question of what individual reactive fibrous astrocytes look like within an injured white matter tract and how a population of these cells organize to form a glial scar (Fig. 4d and e; [25]).

A second very useful transgenic strain is the BAC Aldh1L1 EGFP mouse which was generated by the GENSAT project (Heintz [48]). These mice overexpress EGFP driven by a cell-specific promoter, usually with the use of a bacterial artificial chromosome (BAC). At least in the cortex, EGFP expression overlaps well with Aldh1L1 and GFAP immunostaining (~90% for each; [46]). This transgenic strain has not been extensively used in studies of optic nerve astrocytes, but one study by Ju et al. [39] showed that the EGFP expression pattern in a transverse section of the nerve head looks very similar to what is observed in the hGFAPpr-EGFP mouse, and colocalizes well with GFAP (Fig. 5).

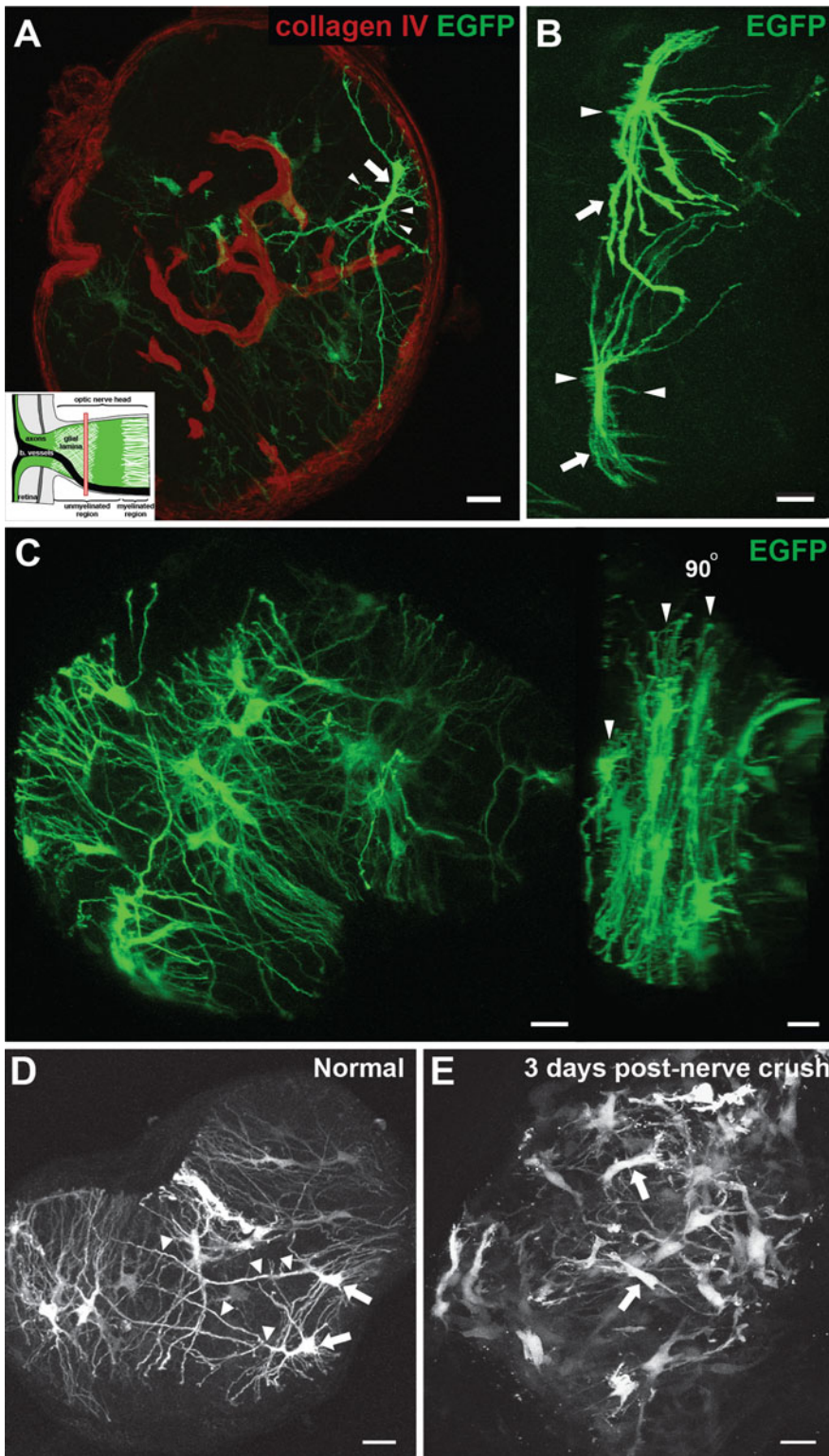


Fig. 4 (a) Transverse cross-section of hGFAPpr-EGFP optic nerve colabeled with collagen IV. This mouse strain is able to display the exquisite morphology of astrocytes. This is an example of a transversely oriented

1.4.2 Multi-Color Labeling of Astrocytes

A major limitation in transgenic labeling studies has been that cells belonging to one cell type are typically labeled by the same color (e.g., one promoter to drive one color expression for all members of that cell type, as described above). Since like cells are often in close proximity to one another, it is difficult to resolve morphology, neuronal connections, spatial organization/tiling, and movement of individual cells. This is particularly challenging in complex tissue such as the CNS. One solution to this is the Brainbow transgenic strategy [44, 50]. Although developed with neurons in mind, some of these transgenic lines do have labeling of brain astrocytes. Very few studies have used these lines to visualize astrocytes in the retina or optic nerve; nevertheless, we have included this section to allow readers to explore the technology.

Brainbow is a transgenic system for stochastic expression of multiple genes coding spectral variants of green fluorescent protein (GFP) based on Cre-*lox* recombination. In mice expressing *Brainbow* constructs under the control of the neuronal promoter Thy1, cells express random combinations of three or more spectrally distinct fluorescent proteins, such as tdTomato, mCerulean (CFP), and enhanced yellow fluorescent protein (YFP). In animals expressing several *Brainbow* transgene copies, multiple hues are created by mixing these three primary colors, providing a spectrum of colors allowing one to distinguish multiple neighboring cells and their processes in a single-tissue sample. The color combinations are unique to each cell and can therefore serve as cellular identification tags that can be visualized by the light microscope [44, 50]. Since the initial Brainbow strategy was developed (Brainbow 1.0, 1.1, 2.0, 2.1; [44]), several other Brainbow versions (Brainbow 3.1, 3.2) and Brainbow-like strategies have been developed, including those that use different recombinase/recognition sites (e.g., Flybow and Flpbow; [51]). Strength of the Brainbow strategy is its broad applicability. A variety of adaptations have been developed for different tissues and model organisms such as mouse, rat, chick, zebrafish, fruit fly, and plants. It has also been used in both germline transgenic approaches and somatic labeling

Fig. 4 (continued) astrocyte with a thick elongated cell body and primary processes extending long distances. Many small branches emanate from the cell body (*arrowheads*). **(b)** A longitudinal cross-section of the hGFAPPr-EGFP optic nerve in which only two astrocytes express EGFP. The long processes (*arrows*) and small branches emanating from the cell body are shown (*arrowheads*). **(c)** A transverse cross-section of the hGFAPPr-EGFP optic nerve in which very many astrocytes express EGFP. Although the individual morphologies cannot be discerned, one can see the spatial organization of a population of astrocytes and how it forms the structure seen on GFAP labeling (*see Fig. 1*). A 90 degree rotation shows the layering of astrocytes (*arrowheads*). **(d, e)** The hGFAPPr-EGFP mouse strain can also be used to study reactive astrocytes. Three days post optic nerve crush, astrocytes show significant morphological remodeling. The cell bodies hypertrophy and processes retract compared to normal (**d**, *arrowheads*). Scale bar = 20 μm . Panels A-C adapted from Sun et al. [23], D-E from Sun et al. [25]

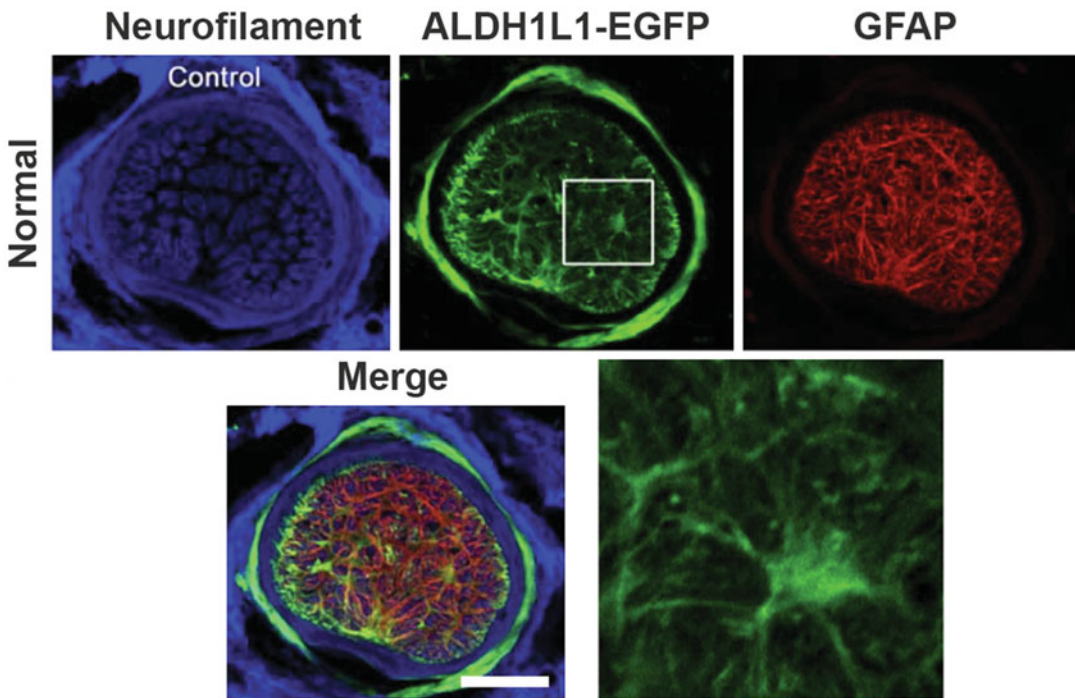


Fig. 5 Astrocytes of the optic nerve head from normal BAC *Aldh1L1* EGFP mice. EGFP expressing astrocytes colocalize well with GFAP labeling. Scale bar = 50 μm . Adapted from Ju et al. [39]

approaches, where Brainbow can be delivered to somatic cells via DNA injection, electroporation, or viral transduction.

A few of the early *Thy1-Brainbow* transgenic lines label entire glial cells. Large populations of astrocytes, cerebellar Bergmann glia, and non-myelinating Schwann cells have been labeled, allowing observation of the anatomical interactions between juxtaposed glial cells [44]. Wang et al. [52] used the Brainbow strategy to assess the complete morphology of retinal Muller glia and how neighboring cells tile in the tangential plane to form a network. Dumas et al. [53] used the strategy to study neighboring oligodendrocyte-oligodendrocyte and oligodendrocyte-axon interactions within the optic nerve.

2 Materials

2.1 Materials for Sectioning the Optic Nerve

1. Fine dissection forceps and scissors.
2. 0.1 M phosphate-buffered saline (PBS, pH 7.4).
3. Large petri dish (approx. 100 \times 15 mm).
4. Cryostat.
5. Dissecting microscope.

6. Tissue freezing medium.
7. Disposable plastic base molds (15 × 15 × 5 mm).
8. Ponseau Red.
9. 4% agarose.

2.2 Materials for Single-Cell Dye Injection of Astrocytes

1. Function generator or recording amplifier.
2. 3-axis micromanipulator with an electrode holder.
3. Microelectrode puller.
4. Borosilicate glass capillaries for the preparation of the sharp microelectrodes, 1.5 mm outer diameter, 0.84 mm inner diameter, thin wall, with filament. The filament is required to allow the dye to travel by capillary action.
5. Vibratome.
6. 4% agarose.
7. 0.1 M phosphate-buffered saline (PBS, pH 7.4).
8. 4% paraformaldehyde in 0.1 M PBS (pH 7.4).
9. 200 mM potassium chloride (KCl).
10. 100% ethanol.
11. Dyes that can be used to fill the cell:
 - (a) Alex Fluor 488 or 568.
 - (b) Rhodamine-dextran.
 - (c) Lucifer yellow.
 - (d) DiI or DiO.
12. Glass slides and coverslip.
13. Mounting medium.

3 Methods

3.1 Transverse/ Longitudinal Sectioning of the Optic Nerve

1. Sacrifice the mouse according to approved animal procedures of your institution.
2. The optic nerve needs to be removed without causing mechanical damage. Decapitate the head using large scissors. Open the skull to expose the brain and carefully separate it from the optic nerve and chiasm. Fix the head by immersing in 4% paraformaldehyde for 2 h at room temperature.
3. Wash in 0.1 M PBS (pH 7.4) for 3 × 10 min.
4. From here on, do all dissections in a PBS filled petri dish placed under a dissecting microscope. Do not let the tissue dry.
5. Remove the orbital bones, retrobulbar tissue, and ocular muscles surrounding each globe and optic nerve. Cut the optic

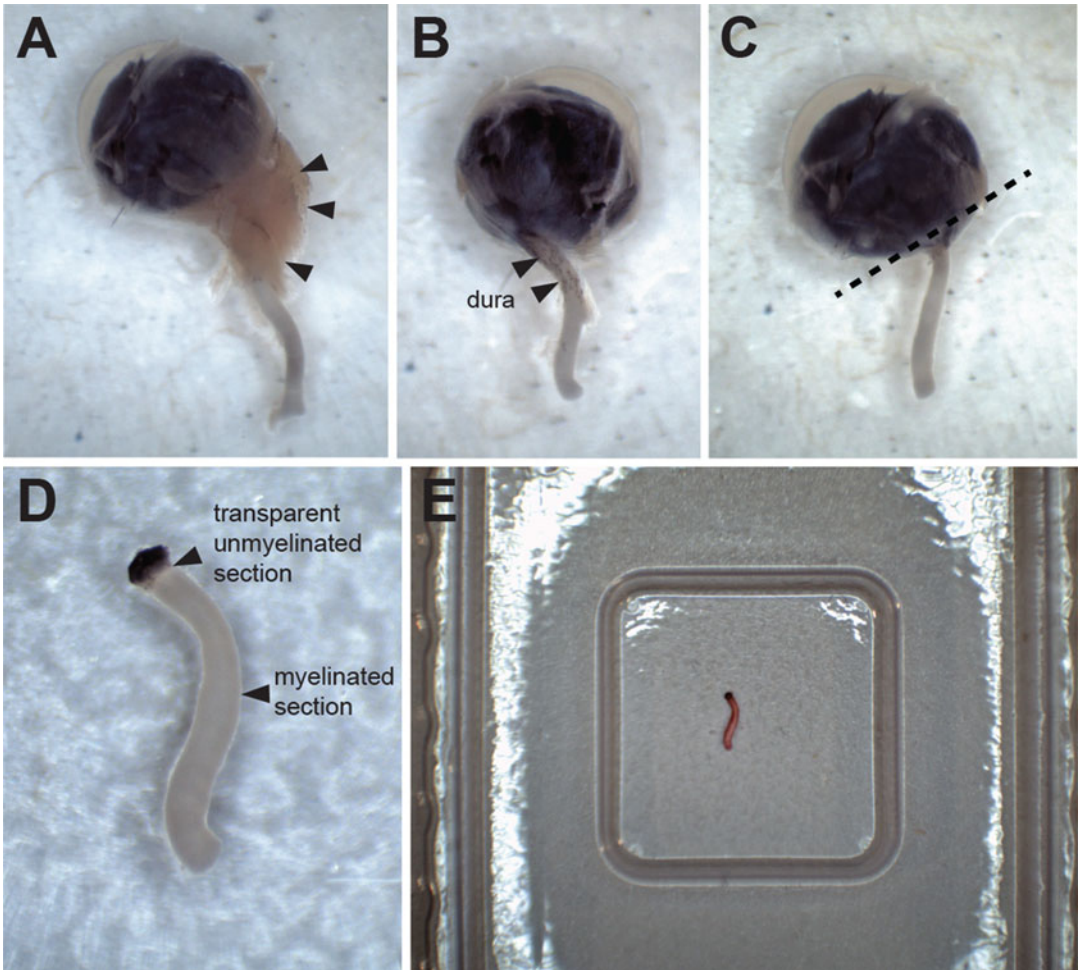


Fig. 6 Steps demonstrating how the optic nerve can be dissected cleanly from the globe, then mounted in plastic molds in preparation for freezing and sectioning

nerve near the chiasm. At this point you should be able to remove the globe with attached optic nerve from the head of the animal (Fig. 6a).

6. Delicately remove the dura surrounding the optic nerve using fine dissection scissors and use a razor blade to cut away the globe from the optic nerve (Fig. 6b-d).
7. Very lightly dip the optic nerve in Ponceau Red. Both the optic nerve and the freezing medium are white when frozen so it is very difficult to locate without using this dye. Ponceau Red will wash off when doing the PBS washes and does not affect the immunostaining.
8. For longitudinal sections, place the optic nerve at the very bottom of a plastic base mold. The optic nerve is often curved, so rotate the nerve around until you can get the nerve as flat as

possible along the bottom of the mold. Using the base of mold to lay down the optic nerve is extremely helpful, preventing the nerve from tilting and subsequently not being able to maximize the length of the longitudinal sections (Fig. 6c).

9. Fill the mold with freezing medium then freeze.
10. When sectioning on the cryostat, begin sectioning on the side of the block which the optic nerve is on.
11. For transverse sections, it is not necessary to lay the optic nerve down flat on the bottom of the mold. Fill the mold with freezing medium first, then place the optic nerve in the middle of the medium.
12. Freeze then section.

3.2 Single-Cell Dye Injection of Astrocytes

1. Prepare the sharp microelectrodes by pulling the borosilicate glass using an electrode puller. This can be done before the day of injection and stored.
2. Sacrifice the mouse according to approved animal procedures of your institution.
3. See Subheading 3.1 on how to remove the optic nerve without causing mechanical damage.
4. Mount the optic nerve in a slab of 4% agarose and section transversely at 200 μm on a vibratome.
5. Place the optic nerve/agarose slice in a PBS filled dish under a microscope that has dual epifluorescence/differential interference contrast capabilities.
6. Fill the sharp microelectrode with any of the following dyes (*see Note 1*):
 - (a) 10 mM Alexa Fluor 568 in 200 mM KCl.
 - (b) 10 mM Alexa Fluor 488 in 200 mM KCl.
 - (c) 5% aqueous dilithium Lucifer Yellow CH.
 - (d) 0.5–1% DiI in 100% ethanol.
 - (e) 0.5–1% DiO in methylene chloride.
 - (f) 2–5% lysinated tetramethylrhodamine-dextran (*see Note 2*).
7. Using the micromanipulator, maneuver the sharp microelectrode and impale an astrocyte soma, which can typically be identified by the distinct shape and size of their soma.
8. Inject the dye by applying a 0.5–1 s current pulse (1 Hz) at 0.5–3 nA, until the processes are completely filled (*see Notes 3 and 4*). After you remove the electrode from the soma, let the preparation sit for another 30 min to allow diffusion and/or transport of the dye.

9. Inject as many cells as required, then place the slice in 4% paraformaldehyde for 1 h at room temperature, in the dark or covered up.
10. Wash in 0.1 M PBS (pH 7.4) for 3×10 min.
11. Mount on a glass slide with mounting medium.
12. The tissue is now ready for imaging on a confocal microscope.

4 Notes

1. Transfer a small volume of your dye into an Eppendorf tube. Pull your microelectrodes. The most important thing is to use borosilicate glass with filament to allow the dye to travel by capillary action and to provide electrical contact. Place a microelectrode upside down into the tube and wait several minutes for the tip to fill (this won't work without a filament in the glass microelectrode). For dye injections, it is sometimes not necessary to fill the shank of the microelectrode with an electrolyte. A long silver wire in the electrode holder that contacts the wet filament should be sufficient. If this does not work, you can always fill the shank of the microelectrode the appropriate electrolyte. Make sure to leave an air gap between the dye in the tip and the electrolyte, so as not to dilute the dye too much. An alternative method of filling the microelectrode is to backfill it. A small amount of the dye solution, about 0.25–0.5 μl , is drawn into a secondary filling pipette and is then deposited inside the primary microelectrode at the taper, as close to the tip as possible. Allow a minute for capillary action to carry the dye into the tip and for any air bubbles to be displaced. Immediately before the pipette is to be mounted on the manipulator, a second filling pipette is used to backfill the shank of the pipette with electrolyte solution. Remember to leave an air gap.
2. Dextrans come in all kinds of carbon chain length and conjugated with all kinds of different fluorophores. We recommend Tetramethylrhodamine, 3000 MW, anionic lysine fixable. 3000 MW means it is the smallest molecule (other options are 10,000 and 30,000). It is designed to be fixable in paraformaldehyde by lysine-cross linking. Use at 2–5% in distilled water.
3. Alexa hydrazides, dextrans, Lucifer yellow, and DiI/DiO are anions, so you should inject negative current. Only for neurobiotin you need positive current.
4. The duration of dye iontophoresis varies with a number of factors, including the size of the dye molecule (smaller = faster), the size of the injection current (larger = faster), and the size of the cells (smaller = faster).

References

1. Sofroniew MV, Vinters HV (2010) Astrocytes: biology and pathology. *Acta Neuropathol* 119:7–35. <https://doi.org/10.1007/s00401-009-0619-8>
2. Chung W-S, Allen NJ, Eroglu C (2015) Astrocytes control synapse formation, function, and elimination. *Cold Spring Harb Perspect Biol* 7:a020370. <https://doi.org/10.1101/cshperspect.a020370>
3. Iadecola C, Nedergaard M (2007) Glial regulation of the cerebral microvasculature. *Nat Neurosci* 10:1369–1376. <https://doi.org/10.1038/nn2003>
4. Simard M, Nedergaard M (2004) The neurobiology of glia in the context of water and ion homeostasis. *Neuroscience* 129:877–896. <https://doi.org/10.1016/j.neuroscience.2004.09.053>
5. Pellerin L, Bouzier-Sore A-K, Aubert A, Serres S, Merle M, Costalat R, Magistretti PJ (2007) Activity-dependent regulation of energy metabolism by astrocytes: an update. *Glia* 55:1251–1262. <https://doi.org/10.1002/glia.20528>
6. Rouach N, Koulakoff A, Abudara V, Willecke K, Giaume C (2008) Astroglial metabolic networks sustain hippocampal synaptic transmission. *Science* 322:1–5. <https://doi.org/10.1126/science.1164022>
7. Robel S, Berninger B, Götz M (2011) The stem cell potential of glia: lessons from reactive gliosis. *Nat Rev Neurosci* 12:88–104. <https://doi.org/10.1038/nrn2978>
8. Khakh BS, McCarthy KD (2015) Astrocyte calcium signaling: from observations to functions and the challenges therein. *Cold Spring Harb Perspect Biol* 7:a020404. <https://doi.org/10.1101/cshperspect.a020404>
9. Bazargani N, Attwell D (2016) Astrocyte calcium signaling: the third wave. *Nat Neurosci* 19:182–189. <https://doi.org/10.1038/nn.4201>
10. Sofroniew MV (2009) Molecular dissection of reactive astrogliosis and glial scar formation. *Trends Neurosci* 32:638–647. <https://doi.org/10.1016/j.tins.2009.08.002>
11. Silver J, Miller JH (2004) Regeneration beyond the glial scar. *Nat Rev Neurosci* 5:146–156. <https://doi.org/10.1038/nrn1326>
12. Anderson MA, Burda JE, Ren Y, Ao Y, O’Shea TM, Kawaguchi R, Coppola G, Khakh BS, Deming TJ, Sofroniew MV (2016) Astrocyte scar formation aids central nervous system axon regeneration. *Nature* 532(7598):195–200. <https://doi.org/10.1038/nature17623>
13. Anderson MA, Ao Y, Sofroniew MV (2014) Heterogeneity of reactive astrocytes. *Neurosci Lett* 565:23–29. <https://doi.org/10.1016/j.neulet.2013.12.030>
14. Okada S, Nakamura M, Katoh H, Miyao T, Shimazaki T, Ishii K, Yamane J, Yoshimura A, Iwamoto Y, Toyama Y, Okano H (2006) Conditional ablation of Stat3 or Socs3 discloses a dual role for reactive astrocytes after spinal cord injury. *Nat Med* 12:829–834. <https://doi.org/10.1038/nm1425>
15. Wanner IB, Anderson MA, Song B, Levine J, Fernandez A, Gray-Thompson Z, Ao Y, Sofroniew MV (2013) Glial scar borders are formed by newly proliferated, elongated astrocytes that interact to corral inflammatory and fibrotic cells via STAT3-dependent mechanisms after spinal cord injury. *J Neurosci* 33:12870–12886. <https://doi.org/10.1523/JNEUROSCI.2121-13.2013>
16. Voskuhl RR, Peterson RS, Song B, Ao Y, Morales LBJ, Tiwari-Woodruff S, Sofroniew MV (2009) Reactive astrocytes form scar-like perivascular barriers to leukocytes during adaptive immune inflammation of the CNS. *J Neurosci* 29:11511–11522. <https://doi.org/10.1523/JNEUROSCI.1514-09.2009>
17. Herrmann JE, Imura T, Song B, Qi J, Ao Y, Nguyen TK, Korsak RA, Takeda K, Akira S, Sofroniew MV (2008) STAT3 is a critical regulator of astrogliosis and scar formation after spinal cord injury. *J Neurosci* 28:7231–7243. <https://doi.org/10.1523/JNEUROSCI.1709-08.2008>
18. Faulkner JR, Herrmann JE, Woo MJ, Tansey KE, Doan NB, Sofroniew MV (2004) Reactive astrocytes protect tissue and preserve function after spinal cord injury. *J Neurosci* 24:2143–2155. <https://doi.org/10.1523/JNEUROSCI.3547-03.2004>
19. Zhang Y, Barres BA (2010) Astrocyte heterogeneity: an underappreciated topic in neurobiology. *Curr Opin Neurobiol* 20:588–594. <https://doi.org/10.1016/j.conb.2010.06.005>
20. Howell GR, Libby RT, Jakobs TC, Smith RS, Phalan FC, Barter JW, Barbay JM, Marchant JK, Mahesh N, Porciatti V, Whitmore AV, Masland RH, John SWM (2007) Axons of retinal ganglion cells are insulted in the optic nerve early in DBA/2J glaucoma. *J Cell Biol* 179:1523–1537. <https://doi.org/10.1083/jcb.200706181>

21. Buckingham BP, Inman DM, Lambert W, Oglesby E, Calkins DJ, Steele MR, Vetter ML, Marsh-Armstrong N, Horner PJ (2008) Progressive ganglion cell degeneration precedes neuronal loss in a mouse model of glaucoma. *J Neurosci* 28:2735–2744. <https://doi.org/10.1523/JNEUROSCI.4443-07.2008>
22. Soto I, Oglesby E, Buckingham BP, Son JL, Roberson EDO, Steele MR, Inman DM, Vetter ML, Horner PJ, Marsh-Armstrong N (2008) Retinal ganglion cells downregulate gene expression and lose their axons within the optic nerve head in a mouse glaucoma model. *J Neurosci* 28:548–561. <https://doi.org/10.1523/JNEUROSCI.3714-07.2008>
23. Sun D, Lye-Barthel M, Masland RH, Jakobs TC (2009) The morphology and spatial arrangement of astrocytes in the optic nerve head of the mouse. *J Comp Neurol* 516:1–19. <https://doi.org/10.1002/cne.22058>
24. Bushong EA, Martone ME, Jones YZ, Ellisman MH (2002) Protoplasmic astrocytes in CA1 stratum radiatum occupy separate anatomical domains. *J Neurosci* 22:183–192
25. Sun D, Lye-Barthel M, Masland RH, Jakobs TC (2010) Structural remodeling of fibrous astrocytes after axonal injury. *J Neurosci* 30:14008–14019. <https://doi.org/10.1523/JNEUROSCI.3605-10.2010>
26. Oberheim NA, Wang X, Goldman S, Nedergaard M (2006) Astrocytic complexity distinguishes the human brain. *Trends Neurosci* 29:547–553. <https://doi.org/10.1016/j.tins.2006.08.004>
27. Connor JR, Berkowitz EM (1985) A demonstration of glial filament distribution in astrocytes isolated from rat cerebral cortex. *Neuroscience* 16:33–44
28. Maxwell DS, Kruger L (1965) The fine structure of astrocytes in the cerebral cortex and their response to focal injury produced by heavy ionizing particles. *J Cell Biol* 25:141–157
29. Cahoy JD, Emery B, Kaushal A, Foo LC, Zamanian JL, Christopherson KS, Xing Y, Lubischer JL, Krieg PA, Krupenko SA, Thompson WJ, Barres BA (2008) A transcriptome database for astrocytes, neurons, and oligodendrocytes: a new resource for understanding brain development and function. *J Neurosci* 28:264–278. <https://doi.org/10.1523/JNEUROSCI.4178-07.2008>
30. Chaudhry FA, Lehre KP, van Lookeren CM, Ottersen OP, Danbolt NC, Storm-Mathisen J (1995) Glutamate transporters in glial plasma membranes: highly differentiated localizations revealed by quantitative ultrastructural immunocytochemistry. *Neuron* 15:711–720
31. Lehre KP, Levy LM, Ottersen OP, Storm-Mathisen J, Danbolt NC (1995) Differential expression of two glial glutamate transporters in the rat brain: quantitative and immunocytochemical observations. *J Neurosci* 15:1835–1853
32. Schmitt A, Asan E, Püschel B, Kugler P (1997) Cellular and regional distribution of the glutamate transporter GLAST in the CNS of rats: nonradioactive in situ hybridization and comparative immunocytochemistry. *J Neurosci* 17:1–10
33. Vives V, Alonso G, Solal AC, Joubert D, Legraverend C (2003) Visualization of S100B-positive neurons and glia in the central nervous system of EGFP transgenic mice. *J Comp Neurol* 457:404–419. <https://doi.org/10.1002/cne.10552>
34. Deloulme JC, Raponi E, Gentil BJ, Bertacchi N, Marks A, Labourdette G, Baudier J (2004) Nuclear expression of S100B in oligodendrocyte progenitor cells correlates with differentiation toward the oligodendroglial lineage and modulates oligodendrocytes maturation. *Mol Cell Neurosci* 27:453–465. <https://doi.org/10.1016/j.mcn.2004.07.008>
35. Hachem S, Aguirre A, Vives V, Marks A, Gallo V, Legraverend C (2005) Spatial and temporal expression of S100B in cells of oligodendrocyte lineage. *Glia* 51:81–97. <https://doi.org/10.1002/glia.20184>
36. Steiner J, Bernstein H-G, Biellau H, Berndt A, Brisch R, Mawrin C, Keilhoff G, Bogerts B (2007) 1471-2202-8-2.fm. *BMC Neurosci* 8:2–10. <https://doi.org/10.1186/1471-2202-8-2>
37. Wilhelmsson U, Bushong EA, Price DL, Smarr BL, Phung V, Terada M, Ellisman MH, Pekny M (2006) Redefining the concept of reactive astrocytes as cells that remain within their unique domains upon reaction to injury. *Proc Natl Acad Sci U S A* 103:17513–17518. <https://doi.org/10.1073/pnas.0602841103>
38. Butt A, Colquhoun K (1996) Glial cells in transected optic nerves of immature rats. I. An analysis of individual cells by intracellular dye-injection. *J Neurocytol* 25(1):365–380
39. Ju W-K, Kim K-Y, Noh YH, Hoshijima M, Lukas TJ, Ellisman MH, Weinreb RN, Perkins GA (2015) Increased mitochondrial fission and volume density by blocking glutamate excitotoxicity protect glaucomatous optic nerve head astrocytes. *Glia* 63:736–753. <https://doi.org/10.1002/glia.22781>
40. Lo DC, McAllister AK, Katz LC (1994) Neuronal transfection in brain slices using particle-mediated gene transfer. *Neuron* 13(6):1263–1268

41. Nolte C, Matyash M, Pivneva T, Schipke CG, Ohlemeyer C, Hanisch UK, Kirchhoff F, Kettenmann H (2001) GFAP promoter-controlled EGFP-expressing transgenic mice: a tool to visualize astrocytes and astrogliosis in living brain tissue. *Glia* 33:72–86
42. Zhuo L, Sun B, Zhang CL, Fine A, Chiu SY, Messing A (1997) Live astrocytes visualized by green fluorescent protein in transgenic mice. *Dev Biol* 187(1):36–42
43. Suzuki R, Watanabe J, Arata S, Funahashi H, Kikuyama S, Shioda S (2003) A transgenic mouse model for the detailed morphological study of astrocytes. *Neurosci Res* 47(4):451–454
44. Livet J, Weissman TA, Kang H, Draft RW, Lu J, Bennis RA, Sanes JR, Lichtman JW (2007) Transgenic strategies for combinatorial expression of fluorescent proteins in the nervous system. *Nature* 450:56–62. <https://doi.org/10.1038/nature06293>
45. Yamaguchi M, Saito H, Suzuki M, Mori K (2000) Visualization of neurogenesis in the central nervous system using nestin promoter-GFP transgenic mice. *Neuroreport* 11(9):1991–1996
46. Yang Y, Vidensky S, Jin L, Jie C, Lorenzini I, Frankl M, Rothstein JD (2011) Molecular comparison of GLT1+ and ALDH1L1+ astrocytes in vivo in astroglial reporter mice. *Glia* 59:200–207. <https://doi.org/10.1002/glia.21089>
47. Regan MR, Huang YH, Kim YS, Dykes-Hoberg MI, Jin L, Watkins AM et al (2007) Variations in promoter activity reveal a differential expression and physiology of glutamate transporters by glia in the developing and mature CNS. *J Neurosci* 27(25):6607–6619
48. Heintz N (2004) Nat neurosci 2004 heintz. *Nat Neurosci* 7:1–1. <https://doi.org/10.1038/nn0504-483>
49. Doyle JP, Dougherty JD, Heiman M, Schmidt EF, Stevens TR, Ma G et al (2008) Application of a translational profiling approach for the comparative analysis of CNS cell types. *Cell* 135(4):749–762
50. Lichtman JW, Livet J, Sanes JR (2008) A technicolour approach to the connectome. *Nat Rev Neurosci* 9:417–422. <https://doi.org/10.1038/nrn2391>
51. Cai D, Cohen KB, Luo T, Lichtman JW, Sanes JR (2013) Improved tools for the Brainbow toolbox. *Nat Methods* 10:540–547. <https://doi.org/10.1038/nmeth.2450>
52. Wang J, O’Sullivan ML, Mukherjee D, Puñal VM, Farsiu S, Kay JN (2016) Anatomy and spatial organization of Müller glia in mouse retina. *J Comp Neurol* 525(8):1759–1777. <https://doi.org/10.1002/cne.24153>
53. Dumas L, Heitz-Marchaland C, Fouquet S, Suter U, Livet J, Moreau-Fauvarque C, Chédotal A (2015) Multicolor analysis of oligodendrocyte morphology, interactions, and development with Brainbow. *Glia* 63:699–717. <https://doi.org/10.1002/glia.22779>

Investigation of MicroRNA Expression in Experimental Glaucoma

Hari Jayaram, Diana C. Lozano, Elaine C. Johnson, and John C. Morrison

Abstract

MicroRNAs are small, endogenous noncoding RNAs that modulate post-transcriptional gene expression. Recent evidence suggests that they may have a potential role in the regulation of the complex biological responses that develop in response to elevated intraocular pressure. However, contemporary microRNA assay techniques (e.g., microarrays and next-generation sequencing) typically require large amounts of RNA template that are often times difficult to obtain from glaucomatous tissue. We describe in detail an experimental protocol utilizing targeted pre-amplification and low-density polymerase chain reaction arrays to circumvent this hurdle. This approach optimizes the simultaneous high-throughput screening of small tissue samples, such as the rodent optic nerve head, for up to 754 microRNA probes while also providing an opportunity for subsequent confirmatory reactions of technical or biological replicates.

Key words MicroRNA, Optic nerve head, Gene expression, Post-transcriptional silencing, MicroRNA array card, PCR, Taqman, Quantitative PCR

1 Introduction

1.1 *MicroRNA Biology and Glaucoma Research*

Glaucoma is a leading cause of irreversible worldwide blindness, characterized by progressive retinal ganglion cell loss and optic nerve degeneration often due to elevated intraocular pressure [1–3]. Although the cellular mechanisms of glaucomatous damage are still poorly understood, it is widely accepted that the primary insult occurs at the optic nerve head (ONH), and may involve several processes, including obstruction of axoplasmic transport [4, 5], ischemia [6], events secondary to retinal ganglion cell axonal loss [7], and events related to the biomechanical stresses upon axons [8, 9].

MicroRNAs are small, highly conserved endogenous noncoding oligoribonucleotides that modulate the post-transcriptional silencing of gene expression [10]. They act through the recognition of specific motifs in target messenger RNAs and predominantly act to reduce expression of their gene targets [11]. Several microRNAs

have been implicated in trabecular meshwork physiology [12] and have also been identified within aqueous humor in preliminary reports [13–15]. Differential expression of microRNAs has also been identified within the retina in experimental paradigms of both retinal degenerations [16] and glaucoma [17].

The purpose of this article is to describe a reliable and cost-effective approach to studying microRNA expression within the ONH and retina. Enhancing our understanding of how microRNAs may influence the mechanisms associated with glaucomatous damage in both these tissues will be critical to developing novel therapies in the future that may seek to harness microRNA biology as an approach to attenuate glaucomatous injury.

1.2 Choice of Methodology

The analysis of microRNA expression in experimental glaucoma using high-throughput screening techniques is limited by the relatively large amount of starting template required. Microarrays will typically require upward of 30 ng total RNA. This initial requirement increases tenfold in order to perform the “gold-standard” traditional next-generation microRNA sequencing. Therefore, in the context of rodent glaucoma models, the choice of microRNA assay technique will depend upon the anticipated RNA yield of the tissue under investigation. Microarray analysis and small RNA sequencing are possible when using ocular tissues with higher RNA yields (e.g., rodent retina will generate several micrograms of total RNA), but are more challenging with those tissues that yield small amounts of RNA (e.g., the rodent optic nerve head typically yields 20–30 ng).

Taqman[®] Low Density microRNA Array cards (Applied Biosystems, Thermo Fisher Scientific, Grand Island, NY), which utilize Polymerase Chain Reaction (PCR) chemistry, provide a cost-effective approach that permits high-throughput screening of samples with low RNA yield (*see Note 1*). Each array card can detect 384 probes, which include 377 individual microRNAs, endogenous small RNA controls, and a negative control. The two array cards (A & B Cards v3.0) in the set can together detect 754 mature microRNAs present in miRBase v20. The use of targeted and proportional pre-amplification also enables analysis of starting RNA template upward of 1 ng, which may even permit analysis at a single-cell level. This additional step has been shown to be sensitive and reliable without introducing bias in the analysis of very small amounts of starting template [18]. This efficient use of input template will leave sufficient residual RNA to also perform high-throughput analysis of gene expression on the same samples, using either microarrays or RNA-Sequencing. This will enable further downstream integration of data to generate functional microRNA-gene networks. This process will ultimately advance our understanding of how specific microRNAs may influence the biological pathways associated with glaucomatous injury.

Verification of experimental findings typically requires performing two separate assays on the same sample, or independent confirmation using biological replicates. The pre-amplification product generated for each sample can be probed for specific microRNA targets using both array cards and individual confirmatory PCR reactions, for which technical replicates may also be readily utilized.

2 Materials

1. Compatible Real-Time PCR System, e.g., Thermo Fisher QuantStudio™ 12K Flex Real-Time PCR System with Array Card Block, Applied Biosystems 7900HT.
2. Centrifuge with buckets and metal adapters specific to the Array Cards.
3. Low Density Array Sealer.
4. Dry Ice.
5. Wet Ice.
6. RNaseZAP™.
7. Qiagen miRNEasy Micro Kit (#17084, www.qiagen.com).
8. Qiagen RNase-Free DNase Kit (#79254, www.qiagen.com).
9. Molecular Biology Grade 2-Propanol.
10. Molecular Biology Grade Ethanol.
11. Molecular Biology Grade Chloroform.
12. Molecular Biology Grade Water.
13. Molecular Biology Grade Tris-EDTA Buffer.
14. Motorized Pestle (e.g., #749540-0000, www.kimble-chase.com).
15. RNase-Free Disposable Pellet Pestle & Microcentrifuge tubes (e.g., #749520-0090, www.kimble-chase.com) (*see Note 2*).
16. Megaplex™ Primer Pools, Rodent Pools Set v3.0 (#44444766, www.thermofisher.com).
17. Taqman® MicroRNA RT Kit (#4366596, www.thermofisher.com).
18. Taqman® PreAmp Master Mix (#4391128, www.thermofisher.com).
19. Taqman® Universal PCR Master Mix, no AmpErase® UNG (#4324018, www.thermofisher.com).
20. Taqman® Array Rodent MicroRNA A + B Cards Set v3.0 (#44444909, www.thermofisher.com).

3 Methods

The protocols described in this section detail the optimized steps following the sourcing of tissue to acquisition of microRNA expression data. These include isolation of microRNA from rodent ONHs, reverse transcription and pre-amplification and the running of MicroRNA Taqman[®] Low Density Array Cards. The pre-amplification products can also be used for subsequent individual quantitative PCR reactions, the protocol for which is also described.

3.1 Isolation of MicroRNA from Rodent Optic Nerve Heads

1. Following decapitation under anesthesia and rapid cool dissection, the anterior 400 μm of the optic nerve head is removed and immediately placed in individual precooled 1.5 ml microcentrifuge tubes on dry ice (*see Note 3*). Samples are stored at -80°C until needed for the subsequent steps.
2. Thoroughly clean all laboratory surfaces and pipettes with RNaseZAP prior to all experimental work to eliminate RNAses.
3. Cool Qiazol[®] Lysis Reagent on wet ice (350 μl per ONH).
4. Precool packaged pestle tips in wet ice.
5. Precool microcentrifuge to 4°C .
6. Prepare reagents from Qiagen MiRNEasy kit:
 - (a) Add 44 ml ethanol to Buffer RPE (proprietary wash buffer within isolation kit) concentrate.
 - (b) Add 30 ml 2-propanol to Buffer RWT (proprietary wash buffer within isolation kit) concentrate (necessary for enriched microRNA isolation).
7. Remove microcentrifuge tubes containing frozen ONHs from -80°C storage and place on dry ice.
8. Add 350 μl Qiazol[®] Lysis Reagent to each 1.5 ml microcentrifuge tube and homogenize immediately on wet ice for 30 s using the motorized pestle.
9. In order to maximize yield, wash the pestle with a further 350 μl Qiazol[®] Lysis Reagent collecting this fluid in the same microcentrifuge tube (*see Note 4*).
10. Allow samples to rest at room temperature for 5 min.
11. Add 140 μl chloroform to each sample in a fume hood and vortex vigorously for 15 s.
12. Allow samples to rest at room temperature for 3 min.
13. Centrifuge samples for 15 min at $12,000 \times g$ at 4°C .
14. Carefully collect the clear upper aqueous phase (approximately 350 μl). Avoid drawing up any material from the interface (*see Note 5*), and then add 525 μl 100% ethanol.

15. Mix thoroughly and immediately place up to 700 μl of the sample onto an RNeasy[®] MinElute[®] spin column set in a 2 ml microcentrifuge tube. Centrifuge at $\geq 8000 \times g$ for 15 s at room temperature and discard flow-through.
16. Repeat **step 13** with the remainder of sample.
17. Add 350 μl Buffer RWT to the column and centrifuge at $\geq 8000 \times g$ for 15 s to wash and discard flow-through.
18. Place column in a new 2 ml collection tube.
19. Prepare sufficient DNase incubation mix for all samples, (10 μl DNase 1 stock solution added to 70 μl Buffer RDD per sample) and mix by gentle inversion.
20. Add 80 μl DNase incubation mix directly onto the center of the column membrane and allow it to rest at room temperature for 30 min.
21. Add 500 μl Buffer RWT to the column and centrifuge at $\geq 8000 \times g$ for 15 s and keep the flow-through.
22. Add the flow-through from **step 19** to the column and centrifuge at $\geq 8000 \times g$ for 15 s and discard the flow-through.
23. Add 500 μl Buffer RPE to the column and centrifuge at $\geq 8000 \times g$ for 15 s and discard the flow-through.
24. Add 500 μl 80% Ethanol to column and centrifuge at $\geq 8000 \times g$ for 2 min and discard the flow-through.
25. Place column in a new 2 ml collection tube.
26. Centrifuge columns with open lids at $12,000 \times g$ for 5 min at room temperature to dry membrane and then discard the flow-through.
27. Place column in a new 1.5 ml collection tube.
28. Apply 14 μl of molecular biology grade water to center of membrane and centrifuge at $12,000 \times g$ for 1 min at room temperature to elute total RNA.

**3.2 Reverse
Transcription and Pre-
Amplification of ONH
MicroRNA**

1. Assess the quality and concentration of isolated total RNA (including microRNA) from each sample with the Agilent Bioanalyzer Pico Chip and ensure a RNA Integrity Number (RIN) score >8.0 . RIN scores of samples enriched for small RNAs are generally lower than for mRNA alone. This occurs because the standard RIN algorithm considers the small RNA fraction part of the degraded mRNA.
2. Prepare and label PCR strip tubes for the subsequent reverse transcription and pre-amplification reactions. Strips must be prepared in duplicate for each individual sample, corresponding to the subsequent parallel “A” and “B” card workflows that follow.

3. Normalization to the lowest concentration of RNA should be performed such that all individual reactions have the same starting amount of RNA template in a final volume of 3.2 μl (made up with molecular biology grade water). The RNA/-water mix must be prepared in duplicate for each sample for the parallel “A” and “B” card workflows from **step 4** onward.
4. Prepare the reverse transcription master mix as required using the following components for one sample:
 - (a) 0.8 μl Megaplex™ RT Primers (either “A” or “B” depending on workflow).
 - (b) 0.2 μl dNTPs with dTTP.
 - (c) 1.5 μl Multiscribe RT Enzyme.
 - (d) 0.8 μl 10 \times RT Buffer.
 - (e) 0.9 μl 25 mM MgCl₂.
 - (f) 0.1 μl RNAse inhibitor.
5. Add 4.3 μl of the above master mix to the individual PCR strip tubes containing 3.2 μl of RNA/water mix, resulting in a total reaction volume of 7.5 μl , and incubate on wet ice for 5 min.
6. Perform the reverse transcription reactions in a thermal cycler programmed for 40 cycles of 16 °C for 2 min, 42 °C for 2 min, and 50 °C for 1 s, a single step of 85 °C for 5 min and a final hold at 4 °C. The cDNA can be stored at –80 °C at this stage if required.
7. Prepare the pre-amplification reaction mix as required using the following components for one sample, and then invert several times to mix and centrifuge briefly:
 - (a) 2.5 μl Megaplex™ PreAmp Primers (either “A” or “B” depending on workflow).
 - (b) 12.5 μl Taqman® PreAmp Master Mix.
 - (c) 7.5 μl Molecular Biology Grade Water.
8. Add 2.5 μl of the reverse transcription product for each sample to a new PCR strip tube.
9. Add 22.5 μl of the pre-amplification reaction mix to each tube, resulting in a total reaction volume of 25 μl . Invert several times to mix and centrifuge briefly.
10. Perform the pre-amplification reactions in a thermal cycler programmed for 95 °C for 10 min, 55 °C for 2 min, 72 °C for 2 min, followed by 14 cycles (*see Note 6*) of 95 °C for 15 s, 60 °C for 4 min, and 50 °C for 1 s, followed by an enzyme inactivation step of 99.9 °C for 10 min and a final hold at 4 °C.
11. Add 75 μl of 0.1 \times Tris-EDTA Buffer to each sample, resulting in a final volume of 100 μl . The pre-amplification product can be stored at –80 °C until required.
12. Repeat **steps 4–11** for the “B” card workflow.

3.3 Setting Up and Running MicroRNA Taqman Low-Density Array Cards

1. Each sample will have a separate pre-amplification product to be run on the “A” and “B” array cards respectively. Each array card will take around 2 h to run so typically four cards can be run during a normal working day.
2. Thaw the required diluted pre-amplification product on wet ice.
3. For each array card, combine the following in a 1.5 ml microcentrifuge tube, invert several times to mix and centrifuge briefly:
 - (a) 432 μ l molecular biology grade water.
 - (b) 450 μ l Taqman[®] Universal PCR Master Mix.
 - (c) 18 μ l diluted pre-amplification product.
4. Gently mix the contents of the microcentrifuge tube by slowly pipetting up and down. Slowly dispense 100 μ l of reaction mix into each of the eight fill reservoirs of the specific array card, without pushing the pipette down to the hard stop.
5. Repeat **step 3** for the required number of cards to be run.
6. Place the array cards in the custom metal rack with wells facing outward and place this in the bucket within the centrifuge.
7. Centrifuge twice for 1 min at $250 \times g$.
8. Remove the array cards from the centrifuge and visually inspect each card to confirm uniform filling by comparing residual fluid within the fill reservoirs. Make note of any wells containing air bubbles as data from these wells may be unreliable.
9. Seal each array card with a slow, steady motion using the Low-Density Array Sealer.
10. Using sharp scissors, cut off the fill reservoirs and refrigerate array cards at 4 °C until required. Array cards should be run within 64 h of preparation (*see Note 7*).
11. Create a data file for each array card using the QuantStudio[™] software by importing the template file specific to either the “A” or “B” card provided by the manufacturer. The template file has details of the specific microRNA probes in each well including endogenous controls. Data files can be customized to include sample details and to allow for subsequent analysis of biological replicates.
12. If refrigerated, allow array card to acclimate at room temperature for 10 min before use.
13. Load the array card into the real-time PCR system (*see Note 8*).
14. The experiment can be initiated using the standard array card protocol from within the QuantStudio[™] software, which will also save the data once complete.
15. Repeat **steps 11–13** for all “A” and “B” cards for each sample.

3.4 Individual Quantitative Polymerase Chain Reaction Protocol

Individual quantitative PCR reactions can be performed using the pre-amplification product obtained in Subheading 3.2 as the input template. This will facilitate confirmation of significant findings generated by the analysis of array cards.

1. In advance of the experiment, single-tube Taqman[®] MicroRNA Assays specific to the targets of interest should be ordered from www.thermofisher.com
2. Thaw the required diluted pre-amplification product and single-tube Taqman[®] MicroRNA Assays on wet ice.
3. Prepare a sample-specific master mix (e.g., Two microRNA assays per sample, performed in triplicate will require six individual reactions) combining the following for a single reaction:
 - (a) 8.6 μ l molecular biology grade water.
 - (b) 10 μ l Taqman[®] Universal PCR Master Mix.
 - (c) 0.4 μ l diluted pre-amplification product.
4. Add 1 μ l of the specific Taqman[®] MicroRNA Assay to wells in a PCR tube strips or compatible 96-well plate.
5. Add 19 μ l of sample-specific master mix to each well, resulting in a final volume of 20 μ l.
6. Seal tubes/plate and briefly centrifuge.
7. Perform the quantitative PCR reactions in a thermal cycler programmed for 95 °C for 10 min, followed by 40 cycles of 95 °C for 15 s, and 60 °C for 1 min, followed by a final hold at 4 °C.

3.5 Approaches to Data Analysis

Preprocessing of the data from each array card can be performed using the QuantStudio[™] software or can be performed remotely using the Thermo Fisher Cloud (<https://www.thermofisher.com/us/en/home/cloud.html>) which is free to access. The profiles of the amplification curves should be verified to confirm exponential amplification. The software can also be customized to highlight wells with potential errors, e.g., no amplification, inconsistencies with the passive reference dye, or failure of the automatic baseline and thresholding algorithms. Cycle threshold (C_t) values above 36 should also be regarded with caution when performing data analysis.

The analysis pipeline provides several options for data normalization. Global normalization [19] is often preferred, or alternatively a selection of endogenous controls and/or other microRNAs that demonstrate stable expression across both experimental groups may be chosen. Comparison between experimental groups and controls is performed using the $\Delta\Delta C_t$ method. Lists of differentially expressed microRNAs, fold change values, and significance levels can be generated following the analysis of the pre-processed and normalized data. If required, the output of relative quantification can include a Benjamini-Hochberg corrected false discovery rate for p -values.

4 Notes

1. The experimental approach described in this chapter is optimized for the Taqman chemistry to quantify microRNA expression. Certain reagents for this protocol therefore need to be ordered from a specific supplier (Applied Biosystems, Thermo Fisher Scientific, Grand Island, NY).
2. Thorough homogenization of small amounts of tissue is important to sufficiently disrupt tissues to maximize subsequent RNA yield. It is important to use a pestle that does not leave any dead space within the microcentrifuge tube, as this may lead to inadequate disruption. The product listed has pestles that are designed to fit the supplied microcentrifuge tubes.
3. The integrity of data obtained is dependent upon the generation of high-quality RNA. In tissues with a high level of metabolic activity such as the ONH, it is crucial to minimize the time taken from sacrifice to freezing tissue to minimize RNA degradation. All the steps of the eye dissection should therefore be performed at 4 °C by cooling instruments and petri dishes in advance and working on frozen packs that have been stored at –20 °C. It is also vital not to allow the frozen ONHs to thaw prior to the addition of the lysis reagent. This is a common error that leads to significantly reduced RNA yields with poor quality.
4. Washing the pestle can be performed in two steps, first by slow expulsion of half the volume on the anterior side of the pestle. Careful rotation of the motor/pestle complex through 180° is necessary before using the remaining volume to wash the posterior side of the pestle. It is important to maintain some contact between the pestle and the open microcentrifuge tube during this transition to prevent inadvertent spillage.
5. If any interface material is accidentally drawn up (the appearance will seem more viscous at the opening of the pipette tip), it is advisable to expel all fluid back into the original microcentrifuge tube and repeat the centrifugation in **step 12**. Proceeding with interface material and/or organic solvent will result in lower RIN scores and inaccurate quantitation.
6. The number of cycles for the pre-amplification reaction can vary from 12 to 16. The impact of increasing the number of cycles is a left shift in the C_t values obtained when running the MicroRNA Taqman Low Density Array Cards. The number of cycles in the pre-amplification step can be optimized for your own samples to ensure that good exponential amplification is observed with the majority of C_t values ranging from 16 to 32. For rodent optic nerve heads with approximately 15 ng total

RNA per reverse transcription reaction, 14 cycles are a good starting point.

7. In order to efficiently use booking time of shared equipment during the working day, it may be practical to carefully prepare the array cards in the afternoon prior to the scheduled experiment with overnight storage at 4 °C.
8. Ensure that the array card is correctly orientated when placed in the real time PCR machine. Check that well A1 corresponds to the marker on the array card holder. However if it is noted retrospectively that the array card has been incorrectly inserted, manual relabeling of the wells within the software will enable the data to still be used.

Acknowledgments

The US-UK Fulbright Commission in conjunction with Fight for Sight; The Special Trustees of Moorfields Eye Hospital (in conjunction with the National Institute for Health Research award to Moorfields Eye Hospital NHS Foundation Trust and UCL Institute of Ophthalmology for a Biomedical Research Centre for Ophthalmology) (HJ). The National Institutes of Health Grants: R01EY010145 (JCM), P30EY010572 (OHSU Core Grant) and an unrestricted grant from Research to Prevent Blindness (RPB), Inc. JCM is a past RPB Senior Investigator.

References

1. Quigley HA (1999) Neuronal death in glaucoma. *Prog Retin Eye Res* 18(1):39–57
2. Weinreb RN, Khaw PT (2004) Primary open-angle glaucoma. *Lancet* 363 (9422):1711–1720. [https://doi.org/10.1016/S0140-6736\(04\)16257-0](https://doi.org/10.1016/S0140-6736(04)16257-0)
3. Tham YC, Li X, Wong TY, Quigley HA, Aung T, Cheng CY (2014) Global prevalence of glaucoma and projections of glaucoma burden through 2040: a systematic review and meta-analysis. *Ophthalmology* 121 (11):2081–2090. <https://doi.org/10.1016/j.ophtha.2014.05.013>
4. Quigley HA, Addicks EM (1980) Chronic experimental glaucoma in primates. II. Effect of extended intraocular pressure elevation on optic nerve head and axonal transport. *Invest Ophthalmol Vis Sci* 19(2):137–152
5. Quigley HA, Addicks EM, Green WR, Mautner AE (1981) Optic nerve damage in human glaucoma. II. The site of injury and susceptibility to damage. *Arch Ophthalmol* 99 (4):635–649
6. Cherecheanu AP, Garhofer G, Schmidl D, Werkmeister R, Schmetterer L (2013) Ocular perfusion pressure and ocular blood flow in glaucoma. *Curr Opin Pharmacol* 13 (1):36–42. <https://doi.org/10.1016/j.coph.2012.09.003>
7. Morrison JC, Johnson EC, Cepurna W, Jia L (2005) Understanding mechanisms of pressure-induced optic nerve damage. *Prog Retin Eye Res* 24(2):217–240. <https://doi.org/10.1016/j.preteyeres.2004.08.003>
8. Burgoyne CF, Downs JC, Bellezza AJ, Suh JK, Hart RT (2005) The optic nerve head as a biomechanical structure: a new paradigm for understanding the role of IOP-related stress and strain in the pathophysiology of glaucomatous optic nerve head damage. *Prog Retin Eye Res* 24(1):39–73. <https://doi.org/10.1016/j.preteyeres.2004.06.001>
9. Downs JC, Roberts MD, Burgoyne CF (2008) Mechanical environment of the optic nerve head in glaucoma. *Optom Vis Sci* 85

- (6):425–435. <https://doi.org/10.1097/OPX.0b013e31817841cb>
10. Bartel DP (2004) MicroRNAs: genomics, biogenesis, mechanism, and function. *Cell* 116(2):281–297
 11. Guo H, Ingolia NT, Weissman JS, Bartel DP (2010) Mammalian microRNAs predominantly act to decrease target mRNA levels. *Nature* 466(7308):835–840. <https://doi.org/10.1038/nature09267>
 12. Gonzalez P, Li G, Qiu J, Wu J, Luna C (2014) Role of microRNAs in the trabecular meshwork. *J Ocul Pharmacol Ther* 30(2–3):128–137. <https://doi.org/10.1089/jop.2013.0191>
 13. Dunmire JJ, Lagouros E, Bouhenni RA, Jones M, Edward DP (2013) MicroRNA in aqueous humor from patients with cataract. *Exp Eye Res* 108:68–71. <https://doi.org/10.1016/j.exer.2012.10.016>
 14. Wecker T, Hoffmeier K, Plotner A, Gruning BA, Horres R, Backofen R, Reinhard T, Schlunck G (2016) MicroRNA profiling in aqueous humor of individual human eyes by next-generation sequencing. *Invest Ophthalmol Vis Sci* 57(4):1706–1713. <https://doi.org/10.1167/iovs.15-17828>
 15. Dismuke WM, Challa P, Navarro I, Stamer WD, Liu Y (2015) Human aqueous humor exosomes. *Exp Eye Res* 132:73–77. <https://doi.org/10.1016/j.exer.2015.01.019>
 16. Saxena K, Rutar MV, Provis JM, Natoli RC (2015) Identification of miRNAs in a model of retinal degenerations. *Invest Ophthalmol Vis Sci* 56(3):1820–1829. <https://doi.org/10.1167/iovs.14-15449>
 17. Jayaram H, Cepurna WO, Johnson EC, Morrison JC (2015) MicroRNA expression in the glaucomatous retina. *Invest Ophthalmol Vis Sci* 56(13):7971–7982. <https://doi.org/10.1167/iovs.15-18088>
 18. Mestdagh P, Feys T, Bernard N, Guenther S, Chen C, Speleman F, Vandesompele J (2008) High-throughput stem-loop RT-qPCR miRNA expression profiling using minute amounts of input RNA. *Nucleic Acids Res* 36(21):e143. <https://doi.org/10.1093/nar/gkn725>
 19. Mestdagh P, Van Vlierberghe P, De Weer A, Muth D, Westermann F, Speleman F, Vandesompele J (2009) A novel and universal method for microRNA RT-qPCR data normalization. *Genome Biol* 10(6):R64. <https://doi.org/10.1186/gb-2009-10-6-r64>

Utilizing RNA-Seq to Identify Differentially Expressed Genes in Glaucoma Model Tissues, Such as the Rodent Optic Nerve Head

Diana C. Lozano, Dongseok Choi, Hari Jayaram, John C. Morrison, and Elaine C. Johnson

Abstract

Understanding the cellular pathways activated by elevated intraocular pressure (IOP) is crucial for the development of more effective glaucoma treatments. Microarray studies have previously been used to identify several key gene expression changes in early and extensively injured ONH, as well as in the retina. Limitations of microarrays include that they can only be used to detect transcripts that correspond to existing genomic sequencing information and their narrower dynamic range. However, RNA sequencing (RNA-seq) is a powerful tool for investigating known transcripts, as well as for exploring new ones (including noncoding RNAs and small RNAs), is more quantitative, and has the added benefit that the data can be re-analyzed as new sequencing information becomes available. Here, we describe an RNA-seq method specifically developed for identifying differentially expressed genes in optic nerve heads of eyes exposed to elevated intraocular pressure. The methods described here could also be applied to small tissue samples (less than 100 ng in total RNA yield) from retina, optic nerve, or other regions of the central nervous system.

Key words RNA-seq, Glaucoma, Rodent, Optic nerve head, Central nervous system, Retina

1 Introduction

Microarray studies have greatly increased our knowledge about the cellular pathways accompanying axonal damage in glaucoma. Previous studies have shown that elevated intraocular pressure is associated with alterations in optic nerve head gene expression levels that pertain to cell proliferation, immune responses, and extracellular matrix processes [1–3]. Also, there are time-dependent gene expression changes that suggest axonal damage is associated with sequences of metabolic changes, inflammatory and immune responses, and delayed retinal ganglion cell death [4–8]. While these studies have shed light on the process of glaucomatous axonal damage, the technology used (microarrays) has a limited dynamic

range (restricting the detection of gene expression changes) and can only be used to detect transcripts corresponding to existing genomic sequencing information. RNA-seq is a method for identifying and determining the abundance of RNA sequences in biological samples. These experiments can be designed to answer a variety of scientific questions and, as such, there is no “gold-standard” method for running a successful experiment. Here, we present the major steps required for a RNA-seq analysis to identify and determine the biological significance of differentially expressed genes in a small piece of tissue, such as the rat ONH. We will walk the reader through important topics to consider before starting an experiment, the RNA-extraction steps, library preparation, data analysis, and biological interpretation. While this protocol was developed to analyze the small rodent optic nerve head, it can readily be applied to study other central nervous tissues with small RNA yields. Furthermore, two different analysis methods are introduced to guide an experienced programmer (described in Subheadings 2.3, 2.4, and 3.3, **step 1**) or a beginner analyst (Subheadings 2.5 and 3.3, **step 2**) in exploring their RNA-seq data.

Here, we present the protocol we meticulously planned and evaluated that led to comparable results from our previous studies and other published work. We highly recommend consulting your RNA-seq facility manager before starting an experiment to ensure your experimental design meets your research goals. An important topic to discuss with the facility manager is how to enrich messenger RNA (mRNA) in your samples, as the majority of total RNA is ribosomal (rRNA). Removal of rRNA is accomplished by either enriching mRNA using polyadenylation selection or by depleting rRNA. Next, you should discuss whether to do single-end reads (sufficient for gene expression characterization) or paired-end reads (generally used for de novo transcript discovery). Lastly, it is important to discuss the sequencing depth (the number of sequenced reads for a sample) needed to detect and quantify transcripts from your specific samples. A recent review by Conesa et al. provides more details about these and other topics to be considered before starting an RNA-seq experiment [9]. We also recommend meeting with a biostatistician to assist with experimental design and calculating an adequate number of biological and/or technical replicates needed to answer your specific scientific question. Furthermore, the book by Korpelainen et al. provides a comprehensive general introduction to RNA-seq data analysis [10]. Lastly, RNA-seq data analysis is an evolving field and we highly recommend that readers keep up to date with analysis methodologies to determine the best techniques to use with their RNA-seq data.

2 Materials

2.1 RNA Extraction

See the “Investigation of MicroRNA Expression in Experimental Glaucoma” chapter by Jayaram and colleagues in this volume for a list of materials needed to extract RNA from the rodent optic nerve head and other small biological tissues. This is the exact method we used to extract total RNA, including miRNA, from the rodent optic nerve head.

2.2 Library Preparation and Quality Check

1. The Agilent Bioanalyzer Pico Chip will be used to assess quality and concentration of isolated total RNA.
2. Library preparation is done with the NuGEN Ovation V2 kit and the Illumina TruSeq DNA-seq kit.
3. Sequencing is done on an Illumina HiSeq sequencer.

2.3 Computer Hardware Requirement for Data Analysis

1. Considerable computing power is required for RNA-seq analysis. Even for a moderately sized experiment, a cluster computing environment is highly recommended, in particular for aligning raw sequencing data to a reference genome. It is possible that your RNA-seq service facility provides mapped counts data as package service. Here, we present a list of computer hardware and software requirements that will be adequate for analyzing less than 100 samples. A LINUX workstation with multi-core CPU(s) with at least 32GB, a SSD primary drive for the operating system, and a secondary drive for data storage should be used. The size of the drive will depend on the number of samples in your study and the sequencing depth (larger files for deeper sequenced samples). For example, in our study, a single file (representing one sample) was 3–5 GB in size.
2. An external back-up hard-drive.

2.4 Computer Software, Reference Genome, and Genome Annotation Files

1. *Bowtie2* (*see Note 1*).
2. *Tophat2* (*see Note 2*).
3. R for Statistical Computing (<http://www.r-project.org>) with the following add-on packages from Bioconductor (<http://www.bioconductor.org>).
 - (a) *EdgeR* (*see Note 3*).
 - (b) *Limma* (*see Note 4*).
 - (c) *Rsubread* (*see Note 5*).
4. Download reference genome and annotation files from iGenomes (http://support.illumina.com/sequencing/sequencing_software/igenome.html).

2.5 An Alternative Method for Analyzing RNA-seq Data Is Through the User-Friendly Galaxy Web Interface (<https://www.Galaxyproject.Org>; See Subheading 3.3.2)

1. Galaxy runs on both Windows and MAC OSX (*see Note 6*).
2. Run Galaxy on either FireFox or Google Chrome.
3. Generate a Galaxy account (Click “User” on the top horizontal tab then click “Register”).

3 Methods

3.1 RNA Extraction

See the “Investigation of MicroRNA Expression in Experimental Glaucoma” chapter by Hari Jayaram in this volume for a description of how to extract RNA from the rodent optic nerve head and other small biological tissues.

3.2 Library Preparation and Quality Check

1. Library Preparation—RNA is checked for integrity on the Bioanalyzer (Agilent). Total RNA is then used as a template for library preparation using the Nugen Ovation protocol. First-strand cDNA is generated from mRNA using Nugen’s DNA/RNA chimeric primer mix, which is designed to avoid priming from ribosomal RNA. Fragmentation of the cDNA/mRNA hybrid creates second-strand priming sites for DNA polymerase. The resulting cDNA, with a terminal RNA/DNA heteroduplex, then undergoes single-primer isothermal amplification (SPIA) to generate a double-stranded cDNA. The cDNA is used to make a library with the TruSeq DNA-seq kit (Illumina). Basically, the cDNA is blunted ended, then a single “A” nucleotide is added to the 3’ end of each strand. Illumina adaptors are ligated to the cDNAs and the resulting ligation products undergo a limited number of cycles of polymerase chain reaction (PCR). Libraries are quantified using real-time PCR (Kapa Biosystems), mixed, and diluted as needed to reach appropriate cluster densities.
2. Samples are run on a HiSeq 2000 in RapidRun mode. Eight libraries were sequenced per lane. Each lane generates about 155 million clusters that were sequenced using a single-read 100-cycle protocol.
3. Fastq files are generated using base call files (.bcl) using the CASAVA package (Illumina).

3.3 Data Analysis (See Note 7)

Overview: Data analysis begins once the millions of raw reads are obtained. Here, we present an analysis pipeline with some of the most commonly used techniques for RNA-seq data analysis. The first step in this analysis pipeline is to assess the overall quality of the raw reads and determine if there are low-quality bases that need to

be filtered out. As of this article, there is no clear consensus whether such a filtering method is actually helpful to downstream analysis. The filtered or raw data are aligned to a reference genome with the goal of finding the origin of each read. This is a computationally intensive step that requires some command line tools (tophat2) and, oftentimes, is performed in a Linux workstation or a cluster computer system (*see* Subheading 3.3, **step 1** for more details). Alternatively, you can use a user-friendly web graphical interface called Galaxy (*see* Subheading 3.3, **step 2**). Further statistical analysis is performed for differential gene expression between experimental groups using a statistical package (for example, R for Statistical Computing). With this information, you can evaluate the biological significance of your differentially expressed genes using open-source gene annotation analytical tools such as the NIH Database for Annotation, Visualization, Integrated Discovery (DAVID; <https://david.ncifcrf.gov/>).

1. Analysis pipeline for using a command line interface (Using *TopHat2*, *Rsubread*, and *EdgeR*):
 - (a) All raw read files (fastq.gz) are collected.
 - (b) Check quality of reads using *FastQC* (*see* **Note 8**).
 - (c) Align raw reads to reference genome using *TopHat2*.
 - (d) Count how many reads map to each gene using *featureCounts* from the *Rsubread* package. The *featureCounts* function takes as an input the aligned reads and an annotation file (a gtf/gff format file) that can also be exported from iGenome (*see* **Note 9**).
 - (e) Identify differentially expressed genes using *EdgeR*.
 - Use the “calcNormFactors” functions to normalize counts per gene (*see* **Note 10**).
 - Exploratory plots are useful for identifying similarities between biological replicates and/or identifying possible outliers. For example, the “boxplot” function can be used to visualize the distribution of mapped reads to known genes. Furthermore, the “plotMDS” function can generate multi-dimensional scaling plot to detect similarities/differences between samples (*see* **Note 11**).
 - Set up a design matrix per study design.
 - A negative binomial regression model is fitted to the counts data. There are other R packages that can fit a negative binomial regression model, for example *DESeq2* (*see* **Note 12**).
 - Summarize proper coefficients to determine genes that are significantly differentially expressed between experimental conditions.

- (f) From here, proceed to annotation and biological significance determination using tools such as NIH DAVID Bioinformatics Resources (<https://david.ncifcrf.gov/>). See Subheading 3.4 for further discussion of how to interpret the results.
2. Alternative analysis using Galaxy web interface: The Galaxy web interface is divided into three regions. The left hand region lists all the various “Tools” available to process your RNA-seq reads. The middle region will activate once you select a tool. Also, this is where you will be able to specify which files you want to process. The right-hand side has the “History” tab and will show the progress of each “Tool” being processed. A new line is added to the “History” tab every time a new tool is being executed. These lines will turn yellow when they are being processed, green once the program has been executed, or red if an error occurred. Below are the steps used to quantify the number of reads per gene:
- (a) Upload raw reads (.fastq files): Under the “Tools” tab click “Get Data,” click “Upload File,” and click “Choose local File.” Select the Fastq file to upload. Then, under “Type” select “fastqsanger,” select the sample genome, and click “Start” to begin uploading your file into the History tab (*see Note 13*).
 - (b) Check quality of reads: Under “Tools,” select “NGS: QC and Manipulation,” select “FastQC,” select the raw read file, and click “Execute.” Analyze results to determine if the raw data needs to be filtered or trimmed (*see Note 8*).
 - (c) Align raw reads to reference genome: Under “Tools,” select “NGS: RNA Analysis,” click on “TopHat.” Select the raw read file and make the appropriate selection from the “Select a reference genome” drop menu and click “Execute.”
 - (d) Upload reference genome annotation file: Under “Tools,” select “Get Data,” click on “UCSC Main.” This will take you to the University of California Santa Cruz (UCSC) table browser. Select the appropriate genome and assembly parameters to export the desired reference annotation file. Make sure to select “GTF—gene transfer format” under the “Output format” drop menu. Also, make sure that “Galaxy” is clicked under the “Send output to “Galaxy” tab. Push “get output” and then click on “Send query to Galaxy.” This will put a “gtf” file in the History tab.
 - (e) Count aligned reads per gene: Under “Tools,” select “NGS: RNA Analysis,” select “htseq-count,” select the “TopHat” generated file, and under “GFF File,” select

the gtf file exported from the previous step. Click execute. Once this is done, click on “htseq-count” from the History tab and click on the floppy-disk image to export a tab-delimited text file containing the gene IDs and the number of counts for each of these genes.

- (f) All other statistical analyses were performed with the counts per gene in R language as described above. Alternatively, “DESeq2” under the “NGS: RNA Analysis” section can be used to determine differentially expressed genes.
- (g) Normalized counts per gene: Alternatively, normalized counts per gene can be obtained by selecting “NGS: RNA Analysis,” and clicking “Cufflinks” to obtain RPKM (Reads per Kilobase per Million mapped reads) values. Inspect the “Status” column on the processed data and make sure all the rows say “OK” (*see Note 14*). Differentially expressed genes can then be determined by using “cuffdiff” under the “NGS: RNA Analysis” section.

3.4 Biological Interpretation

1. As a first step, we recommend looking at the variability in total counts between samples to determine the uniformity in your RNA-seq samples. Compare the actual counts in your samples to what you expected. For example, we expected 15 million counts per sample, but obtained 14–17.5 million counts per sample. These total counts should be normalized to counts per million (cpm) to account for the variability in library size between samples. Compare cpm with previously published results and determine if your counts make sense for your tissue source (*see Note 15*).
2. Differential gene expression analysis. A negative binomial regression model, like those found in the Bioconductor and *EdgeR* functions, is widely used for differential gene expression analysis. The negative binomial model takes raw counts or normalized counts as input. Due to high dimensionality of data, multiple test correction is often employed. The most popular one is false discovery rate adjustment to raw (or marginal) p-values. In addition to statistical significance, a threshold of fold changes is often considered to rule out tiny fold changes that may not be biologically meaningful.
3. Interpretation: There are many tools available for exploring the biological implications of gene expression changes. A number of commercial programs may be useful, but can require expensive licenses. We recommend first exploring the free tools listed below. These are linked to the largest, most frequently updated databases including NCBI (National Center for Biotechnology Information, www.ncbi.nlm.nih.gov/) and Ensembl genome

browser 85 (www.ensembl.org/). These will give you a good start and help you evaluate potential benefits of the commercial programs.

- (a) To obtain a brief functional description of each gene on your list, you can use the BioMart tool at Ensembl (<http://www.ensembl.org/index.html>) or SOURCE search (<http://source-search.princeton.edu/>). Both will efficiently handle uploading and annotation of relatively long lists of genes based on a number of identifiers of which Ensembl gene id and Entrez gene id are especially useful. These sources will provide you with related gene identifiers and gene ontology information regarding molecular function, cellular component, and biological process for each gene based on the Gene Ontology Consortium (<http://geneontology.org>). By reviewing this information and using PUBMED resources (<http://www.ncbi.nlm.nih.gov/pubmed>), you can easily find the most recent information about the function of genes that catch your attention or those with dramatic expression changes. We find using MESH (<http://www.ncbi.nlm.nih.gov/mesh/>) and Gene (<http://www.ncbi.nlm.nih.gov/gene/>) databases and combining basic PUBMED searches using the Advanced tool helpful additions to a basic PUBMED search.
- (b) Another user-friendly and free tool is DAVID Bioinformatics Resources at <https://david.ncifcrf.gov/> [11, 12]. Using the DAVID tools, you can functionally annotate genes, use the functional annotation charts to discover the genes associated with the most statistically significant Gene Ontology terms, Kyoto Encyclopedia of Genes and Genomes (KEGG) signaling pathways (<http://www.genome.jp/kegg/>) and other gene-associated annotation databases that are directly linked to DAVID. The same annotation terms can be used to cluster functionally related terms and statistically evaluate using the EASE score, a modified Fisher Exact P value. Clusters are assigned an Enrichment Score, which is based on the EASE scores of cluster members. We typically accept an enrichment score greater than 1.3 as statistically significant. However, the exact enrichment score to be used for biological significance may vary between studies. All of these tools allow separate analysis of up and downregulated genes; however, none of these tools takes into account the magnitude of the change in gene expression. The DAVID 6.8 version (now in Beta version) will use Entrez gene ID as the central identifier, allowing for more timely updates. An additional source of free analysis tools

that you may find useful is the Broad Institute's Gene Set Enrichment Analysis tools found at <http://software.broadinstitute.org/gsea/index.jsp>.

4 Notes

1. *Bowtie2* manual is located here: <http://bowtie-bio.sourceforge.net/bowtie2/manual.shtml>.
2. See <https://ccb.jhu.edu/software/tophat/manual.shtml> for instructions on how to run *TopHat2*. You will also need *bowtie2* and *samtools* (<http://www.htslib.org/doc/samtools.html>) to align data to a reference genome. Also, *HISAT2* (<https://ccb.jhu.edu/software/hisat2/index.shtml>), *STAR* (<https://github.com/alexdobin/STAR>), or *GSNAP* (<http://research-pub.gene.com/gmap/>) are all great programs to consider using for RNA-seq data alignment to the reference genome.
3. See <https://www.bioconductor.org/packages/devel/bioc/vignettes/edgeR/inst/doc/edgeRUsersGuide.pdf> for more information about using *EdgeR* to identify differentially expressed genes.
4. Read *limma* manual here: <https://bioconductor.org/packages/release/bioc/html/limma.html>.
5. See <https://bioconductor.org/packages/release/bioc/html/Rsubread.html> for the *Rsubread* package manual.
6. Some caveats of using the Galaxy Web-Interface are: (1) that the storage space is limited and may hinder its usage with large datasets, (2) processes (like alignment of raw files to a reference genome) will take a long time to run with large data files, (3) the website may occasionally be down due to technical problems, and (4) you are limited to using the tools that are pre-installed in the Galaxy Web-instance you are using. It is possible to install Galaxy locally in your computer to avoid some of these issues and to take full advantage of all available tools. See the Galaxy website for more information on how to install this program in your local computer.
7. We recommend doing a trial small RNA-seq study or downloading data from studies similar to the one planned and using this published data for practice data analysis. Follow the steps in this method on these data files to confirm that you are running the programs correctly.
8. See <http://www.bioinformatics.babraham.ac.uk/projects/fastqc/> for instructions and information about *FastQC*. Check that the base quality does not decrease in the late sequencing cycles. Inspect the "Per Base Sequence quality" section on the

FastQC file. Make sure that the mean base quality for the reads is higher than 25. Reads containing low-quality reads should be filtered out.

9. Read the *featureCounts* manual here: <http://bioinf.wehi.edu.au/featureCounts/>.
10. Normalize read counts per gene to compare expression levels between genes or between experimental groups. Read counts alone cannot be used to compare expression levels because they do not take into consideration differences in library size, transcript length, or RNA composition. Instead, it is recommended to normalize the read counts per gene to either FPKMs (Fragments per Kilobase per Million mapped reads) or RPKM (Reads per Kilobase per Million mapped reads) for abundance reporting purposes. RPKM/FPKM values can then be used to rank gene expression levels within samples. Another method of normalizing read counts per gene is TMM (trimmed mean values) that takes into consideration variability between sample RNA content and other experimental/technical variations that may skew the distribution of counts between all given genes [13].
11. Biological and/or technical replicates should cluster in MDS plots. Therefore, MDS plots can be helpful in identifying outliers or possible batch effects that will need to be considered in any downstream analysis.
12. See <https://bioconductor.org/packages/release/bioc/html/DESeq2.html> for the *DESeq2* manual and examples on how to use this function.
13. Use an FTP service if the compressed sequencing files are larger than 2GB. To connect to the Galaxy FTP server, install FileZilla (<https://filezilla-project.org/>). In the top panel, enter usegalaxy.org as the “Host,” enter your Galaxy credentials (email and password), and click the “Quick Connect” button. You will get a message stating that you are connected to the Galaxy FTP server. Next, locate the necessary files from your local computer (left panel on the FileZilla program) and drag them to the Galaxy FTP server (right panel on the FileZilla program). Monitor the bottom panel of the FileZilla program to ensure the files are being transferred. Once the transfer is complete you will need to go back to the Galaxy website, click “Get Data,” “Upload File,” and “Choose FTP File.” This will place your file into the Galaxy “History” tab.
14. Increase the “max-bundle-frags” option to a large enough number (try 10^9) if you get the “HIDATA” error. Also, cufflinks can only test for differential expression between two groups (e.g., control vs. treatment) and other methods, like

EdgeR or *DESeq2*, should be implemented for datasets with more than two comparisons.

15. Look at gene abundance within your samples to make sure expected transcripts are present and abundant. Consider differential expression data that have been published. Do your results overall agree with what is known, in this case, about the ONH and its responses to elevated IOP exposure? We recommend aligning your raw reads to a different genome if you have detected problems at this step. For example, if you first aligned your reads to the Ensembl genome, re-align your reads to the UCSC genome and re-run your analysis. We obtain results comparable to our previous Microarray results and other previously published results when we aligned our raw reads to the UCSC genome (rn6) as opposed to the Ensembl genome (Rnor6).

Acknowledgments

The National Institutes of Health Grants: 3 R01EY010145-17S1 (DCL); The US-UK Fulbright Commission in conjunction with Fight for Sight; The Special Trustees of Moorfields Eye Hospital (in conjunction with the National Institute for Health Research award to Moorfields Eye Hospital NHS Foundation Trust and UCL Institute of Ophthalmology for a Biomedical Research Centre for Ophthalmology) (HJ); R01EY010145 (JCM); P30EY010572 (OHSU Core Grant); and an unrestricted grant from Research to Prevent Blindness (RPB), Inc. JCM is a past RPB Senior Investigator. Short read sequencing assays were performed by the Oregon Health & Science University Massively Parallel Sequencing Shared Resource.

References

1. Howell GR, Macalinao DG, Sousa GL, Walden M, Soto I, Kneeland SC, Barbay JM, King BL, Marchant JK, Hibbs M, Stevens B, Barres BA, Clark AF, Libby RT, John SW (2011) Molecular clustering identifies complement and endothelin induction as early events in a mouse model of glaucoma. *J Clin Invest* 121(4):1429–1444. <https://doi.org/10.1172/JCI44646>
2. Johnson EC, Doser TA, Cepurna WO, Dyck JA, Jia L, Guo Y, Lambert WS, Morrison JC (2011) Cell proliferation and interleukin-6-type cytokine signaling are implicated by gene expression responses in early optic nerve head injury in rat glaucoma. *Invest Ophthalmol Vis Sci* 52(1):504–518. <https://doi.org/10.1167/iops.10-5317>
3. Johnson EC, Jia L, Cepurna WO, Doser TA, Morrison JC (2007) Global changes in optic nerve head gene expression after exposure to elevated intraocular pressure in a rat glaucoma model. *Invest Ophthalmol Vis Sci* 48(7):3161–3177. <https://doi.org/10.1167/iops.06-1282>
4. Ahmed F, Brown KM, Stephan DA, Morrison JC, Johnson EC, Tomarev SI (2004) Microarray analysis of changes in mRNA levels in the rat retina after experimental elevation of intraocular pressure. *Invest Ophthalmol Vis Sci* 45(4):1247–1258

5. Andreeva K, Zhang M, Fan W, Li X, Chen Y, Rebolledo-Mendez JD, Cooper NG (2014) Time-dependent gene profiling indicates the presence of different phases for ischemia/reperfusion injury in retina. *Ophthalmol Eye Dis* 6:43–54. <https://doi.org/10.4137/OED.S17671>
6. Guo Y, Cepurna WO, Dyck JA, Doser TA, Johnson EC, Morrison JC (2010) Retinal cell responses to elevated intraocular pressure: a gene array comparison between the whole retina and retinal ganglion cell layer. *Invest Ophthalmol Vis Sci* 51(6):3003–3018. <https://doi.org/10.1167/iovs.09-4663>
7. Panagis L, Zhao X, Ge Y, Ren L, Mittag TW, Danias J (2011) Retinal gene expression changes related to IOP exposure and axonal loss in DBA/2J mice. *Invest Ophthalmol Vis Sci* 52(11):7807–7816. <https://doi.org/10.1167/iovs.10-7063>
8. Steele MR, Inman DM, Calkins DJ, Horner PJ, Vetter ML (2006) Microarray analysis of retinal gene expression in the DBA/2J model of glaucoma. *Invest Ophthalmol Vis Sci* 47(3):977–985. <https://doi.org/10.1167/iovs.05-0865>
9. Conesa A, Madrigal P, Tarazona S, Gomez-Cabrero D, Cervera A, McPherson A, Szczesniak MW, Gaffney DJ, Elo LL, Zhang X, Mortazavi A (2016) A survey of best practices for RNA-seq data analysis. *Genome Biol* 17:13. <https://doi.org/10.1186/s13059-016-0881-8>
10. Korpelainen E, Tuimala J, Somervuo P, Huss M, Wong G (2015) RNA-seq data analysis: a practical approach. Chapman & Hall/CRC mathematical and computational biology. CRC Press, Boca Raton
11. Huang da W, Sherman BT, Lempicki RA (2009) Systematic and integrative analysis of large gene lists using DAVID bioinformatics resources. *Nat Protoc* 4(1):44–57. <https://doi.org/10.1038/nprot.2008.211>
12. Huang da W, Sherman BT, Lempicki RA (2009) Bioinformatics enrichment tools: paths toward the comprehensive functional analysis of large gene lists. *Nucleic Acids Res* 37(1):1–13. <https://doi.org/10.1093/nar/gkn923>
13. Robinson MD, Oshlack A (2010) A scaling normalization method for differential expression analysis of RNA-seq data. *Genome Biol* 11(3):R25. <https://doi.org/10.1186/gb-2010-11-3-r25>

Single-Cell Dissociation and Characterization in the Murine Retina and Optic Nerve

Hee Joo Choi, Rui Wang, and Tatjana C. Jakobs

Abstract

Recent technological advances have extended the range of analytic tools to very small samples. It is now possible to assay the transcriptome, and in some cases even the proteome, of single cells reliably. This allows addressing novel questions, such as the genotype/phenotype relationships of single neurons, heterogeneity within individual cells of the same type, or the basis of differential vulnerability to injury. An important prerequisite for these kinds of studies is the ability to isolate well-defined individual cells without contamination by adjacent tissue. In the retina and optic nerve, cells of different types and functions are closely intermingled, limiting the use of standard methods such as laser capture microdissection. Here, we describe a simple method to isolate morphologically intact cells from the retina and the optic nerve and discuss considerations in recognizing and isolating different cell types after dissociation.

Key words Dissociation, Cell types, Retinal ganglion cells, Muller cells, Bipolar cells, Amacrine cells, Optic nerve head, Glia, Astrocytes, Microglia, Single-cell PCR

1 Introduction

1.1 *Single-Cell Isolation*

Anatomical and biochemical changes in glaucoma have been described for many tissues and cell types in the eye, though in many cases the functional consequences are poorly understood. In vivo, pathological changes in any one ocular tissue are likely to affect other structures as well, but in order to understand the contributions of individual cell types it is often desirable to isolate cells for analysis. Several technological advances of the last decade have made it possible to perform extended analyses on very few cells, in some cases even on single cells. Examples include gene expression profiling [1–5], single-cell RT-PCR [6–8], immunohistochemistry on isolated cells [9, 10], metabolic analysis [11], and electrophysiological recording [12].

There are several techniques available to isolate cells of a single type. Perhaps the most widely used is fluorescence activated cell sorting (FACS), and this method has been used for ocular cell

types successfully. However, FACS requires the expression of a characteristic surface epitope that is recognized by an antibody or the expression of a genetically encoded fluorescent marker in the cell type of interest. Another requirement is that the cells are reasonably abundant and constitute a homogeneous population. This is not the case for several of the cell types in the retina. There are about 20 different types of ganglion cells [13–16], more than 20 types of amacrine cells [17], and 10 types of bipolar cells [18, 19]. To complicate matters further, even within a narrowly defined cell type, considerable heterogeneity in terms of gene expression can be found [8]. An alternative technique for the isolation of small tissue samples is laser microdissection (LMD). The main advantage is the speed and ease of use so that samples from multiple sites in the eye can be collected in a short time. Of course, LMD is not compatible with any downstream use that requires live cells. It is also fairly difficult to isolate individual cells without contamination from neighboring cells that may be of different types. This is of particular concern in the retina where the cells are closely packed. Even after labeling ganglion cells by retrograde axonal transport of fluorogold and targeting labeled cells with LMD, a recent study found evidence of contamination by retinal surface astrocytes in the gene expression profile of their sample [20]. Thus, LMD is more suitable to the isolation of whole anatomical structures or samples that are enriched in a particular cell type than to the isolation of individual cells. Finally, it is possible to culture various cell types from the eye and the optic nerve [21–24]. This has the advantage of making the cells amenable to biochemical or physical manipulation and cell culture has been used to study the influence of stretch on optic nerve astrocytes, the responses of conjunctival goblet cells to inflammatory mediators, the mutual influences of retinal ganglion cells and glia, and the gene expression profile of trabecular meshwork cells, to name only a few. However, not all ocular cell types have been successfully cultured, and cells in culture can change in phenotype and lose some of the characteristics they display *in vivo* [25].

All these techniques are powerful tools in glaucoma research. In this chapter, we describe an alternative method to isolate single cells after dissociation from the retina or the optic nerve. The strengths of this method are that (1) it is possible to isolate single cells without contamination from other cell types; (2) the cells can be kept alive, at least for hours; (3) cells of defined type can be isolated, especially if the method is used together with labeling techniques. On the downside, isolation of single cells is labor intensive and time consuming, and recognizing cell types after dissociation requires experience. We will provide protocols optimized for single-cell isolation from the retina and the optic nerve, a gallery of cell morphologies after dissociation, a list of transgenic mouse lines that express fluorescent proteins in well-characterized cell types, and some recommendations for downstream techniques.

1.2 Useful Transgenic Mouse Strains with Cell-Type Specific Expression of Fluorescent Markers

Mice have become one of the most common model organisms in glaucoma research even though their retinas and optic nerves differ in some respects from those of humans. In contrast to primates, small rodents do not contain a true, collagenous lamina cribrosa in their optic nerve [26, 27]. Mice also do not have a fovea centralis; and the density distribution of rod and cone photoreceptors is relatively flat, with rods dominating throughout [28]. On the other hand, the central retinal circulation is well developed, in contrast to other popular models in eye research such as guinea pigs and rabbits, whose retinas are avascular and are supplied by the choroid plexus. However, the main advantage of mice in glaucoma research is the availability of genetic tools and transgenic strains to manipulate individual genes or genetic pathways. Several recent advances in glaucoma research depended critically on the use of such transgenic strains and would have been impossible in any other species. Examples include the identification of microglial involvement early in the pathology of glaucoma [29], the discovery that optic nerve astrocytes contribute to the disposal of spent axonal mitochondria [30], or the elucidation of the role of Fas ligand in glaucomatous ganglion cell death [31].

The anatomical organization of the mouse retina is similar to that of other mammalian retinas (with the exception of the primate fovea), and all major cell classes are similar in morphology and function to their counterparts in human retinas (with the exception of horizontal cells, of which mice have only one type rather than two, as do most other mammals) [14, 19, 28, 32, 33]. Cell densities in the ganglion cell layer are higher in the central retina (9000–10,000 cells/mm²) and fall off to about 5500 cells/mm² in the periphery. However, only about 40% of the cells in the ganglion cell layer are actually retinal ganglion cells (RGCs), the others being “displaced” amacrine cells [28]. As the main cell type undergoing degeneration in glaucoma, RGCs are of particular interest. The ganglion cell layer contains displaced amacrine cells, Muller cell endfeet, and retinal surface astrocytes in close proximity, so isolating the ganglion cell layer using LMD yields a population that is enriched in RGCs, but certainly not pure. After dissociation of the retina, RGCs lose most of their dendrites and are not easily distinguishable from large amacrine cells or horizontal cells. If one wishes to isolate pure ganglion cells from a dissociate of the retina, the cells must be labeled beforehand. Fortunately, several transgenic mouse strains are available that express a fluorescent protein in all (or most) RGCs, and in some cases even specifically in a functionally characterized type of RGC. Very useful strains for this purpose were originally described by Feng and coworkers [34]. They express green fluorescent protein (GFP) or one of its relatives under the control of the Thy-1 promoter. In many of the strains, ganglion cells and sometimes other retinal neurons are labeled (*see* Table 1 in [34] for retinal expression patterns). Some

Table 1**Transgenic mouse strains expressing a fluorescent protein in retinal ganglion cells and other retinal neurons**

	Strain name, Repository strain # (if applicable)	Labeled cells	Physiological function	References
Ganglion cells (RGC)	Thy1-YFP (Jax, several #)	Depending on mouse line, RGC, other retinal neurons, other neuronal cells in the CNS		[34]
	D2.Cg-Tg(Thy1-CFP)23Jrs/SjJ (Jax #018671)	RGC, mouse strain develops glaucoma		[35]
	Brainbow (Jax, several #, <i>see</i> https://www.jax.org/search?q=Brainbow)	Depending on mouse line		[36–38]
	Jam-B-creER crossed with Thy1-STOP-YFP (Jax #005630)	Specific RGC type: Jam-B (“arrow cells”)	Upward motion sensitive GC	[39]
	Tg(Drd4-EGFP)W18Gsat/Mmnc (MMRRC #000231-UNC)	Specific RGC type: CB2, ON/OFF direction sensitive RGC	Directionally sensitive motion detection	[40, 41]
	Kcng4-cre crossed with Thy1-STOP-YFP	Alpha RGC, most cells also express osteopontin	Brisk transient RGC	[42]
	Opn4-EGFP	Melanopsin-containing RGC, intrinsically photosensitive RGC	Involved in circadian rhythm entrainment	[43]
Other neurons (AC, BPC, HC)	GAD65-tdTomato	GABAergic AC	Retinal image processing	[44]
	Tg(Pcp2-cre)1Amc/J (Jax #006207) crossed with B6.129S6-Gt(ROSA)26Sor ^{tm9(CAG-tdTomato)Hze} /J (Jax #007905)	Rod bipolar cells, 2 types of cone bipolar cells	Information transmission from PR to GC	[45]
	Tg(5-HTR2a-EGFP)DQ118Gsat/Mmucd (MMRRC #DQ118)	One type of OFF cone BPC (bright labeling), one type of ON cone BPC (dim)	Information transmission from PR to GC	[40, 46]
	Connexin57-iCre crossed with ROSA26-tdTomato	Horizontal cells	Integration of photoreceptor signaling	[47, 48]

RGC retinal ganglion cell, CB2 type2 cone bipolar cell, AC amacrine cell, BPC bipolar cell, HC horizontal cell

of the strains (e.g., YFP-12 or GFP-H) contain enough labeled RGCs that FACS would be feasible. The expression pattern of some of the strains in this series is specific for ganglion cells, but it does not distinguish between types of ganglion cells. Most of the lines are available from the Jackson Laboratory (Bar Harbor, ME). Some

lines in this series have been backcrossed onto the DBA/2J genetic background and develop glaucoma spontaneously with age, making them particularly valuable for research in this field [35, 49]. One of these mouse lines is also available through the Jackson Laboratory (D2.Cg-Tg(Thy1-CFP)23Jrs/SjJ, stock number 018671). An alternative method to express fluorescent markers—in this case, of many different spectral variants in the same animal—was described recently [36, 37]. It makes use of stochastic inversions or excisions mediated by cre recombinase, and the resulting lines can be used to identify specific cell types. The original “Brainbow” mice and several related strains [38] are available from the Jackson Laboratory (<https://www.jax.org/news-and-insights/2013/december/an-expanded-brainbow-tool-kit-for-fluorescent-labelling-cells-in-mice>).

There are about 20 different kinds of ganglion cells in the mammalian retina [13–16, 32, 50], and in many, but not all, the physiological function has been characterized [51–53]. There still is some controversy whether individual ganglion cell types are differentially vulnerable to glaucomatous degeneration [54–59], but changes with ocular hypertension become apparent in the dendritic arbor of OFF ganglion cells before those of other RGCs [58, 60], whereas some other cell types, for instance ON-OFF (bistratified) RGCs are relatively more resistant [61]. There are some transgenic mouse lines available that express GFP in one (or a few) ganglion cell types [39–41, 62]. Of particular interest may be mouse lines that express GFP under the control of the osteopontin (also known as SPP1) promoter because osteopontin-expressing ganglion cells constitute a type—morphologically similar to alpha ganglion cells—that is particularly resistant to optic nerve damage and shows regenerative capacity [42]. Such lines have been created, but as of today the retinal GFP expression pattern has not been ascertained [63, 64]. However, *Kcng4* promoter-driven expression of YFP was recently shown to label a cell population that largely overlaps with the osteopontin-positive cells [42]. In addition, other strains are available that show expression of GFP or its relatives in well-characterized ganglion cell types (Table 1).

Retinal neurons other than ganglion cells are not usually considered primary targets of glaucomatous degeneration, though there is evidence that some types of amacrine cells also die, especially if they are coupled to degenerating RGCs via gap junctions [65]. Similarly to RGCs, amacrine cells cannot be recognized with certainty after dissociation unless they are labeled beforehand. Several mouse strains that express GFP in some types of amacrine cells have been described in the literature, but very often the expression is not strictly limited to amacrine cells, and some of the ganglion cells also express the marker [66, 67]. A list of mouse lines with GFP or red fluorescent protein (RFP) expression in amacrine cell populations can be found in Table 1. In contrast to most other

retinal neurons, bipolar cell axons and dendrites are very resistant to dissociation, and the cells can be recognized easily (Fig. 2a, b). With practice, it is possible to distinguish rod bipolar cells from cone bipolar cells, but further subdivision of cone bipolar cells requires the use of transgenic strains (Table 1). Finally, horizontal cells are rare and also lose most of their processes during dissociation. Horizontal cells can be labeled by crossing a strain that expresses cre recombinase under the control of the connexin-57 promoter with a universal reporter strain, such as Gt(ROSA)26Sor^{tm9(CAG-tdTomato)Hze}/J [47].

In addition to neurons, there are three types of glial cells in the retina: Muller cells, astrocytes, and microglia/macrophages. The optic nerve head contains astrocytes and microglia/macrophages, NG2-positive glial cells, and posterior to the myelination transition zone, oligodendrocytes. Glial cells in the retina and the optic nerve have received considerable attention as major players in the pathology of glaucoma, though it is not yet clear whether their role is mostly beneficial or mostly detrimental [68–71]. Muller cells and astrocytes can be recognized by morphology alone (Figs. 2d, e and 3), and in addition several mouse lines expressing fluorescent markers in glial cells have been described (Table 2). Microglial cells tend to lose their processes after dissociation, so a GFP-expressing strain should be used (e.g., heterozygous B6.129P-Cx3cr1^{tm1litt}/J). It should be noted that with very few exceptions microglia and macrophages express very similar markers, and Cx3cr1 does not distinguish between these two cell types. Truly microglia-specific markers have become available only recently [76–78].

Table 2
Transgenic mouse strains expressing a fluorescent protein in glial cells

	Strain name, Repository strain # (if applicable)	Labeled cells	Physiological function	References
Glial cells	GFAP-GFP	Retinal Muller cells, retinal astrocytes	Various supportive functions	[72]
	hGFAPpr-EGFP	Individual optic nerve astrocytes, NG2 ⁺ cells, retinal Muller cells, retinal astrocytes not labeled	Various supportive functions	[27, 73]
	B6.Cg-Tg(GFAP-cre) 73.12Mvs/J (Jax #012886) crossed with B6.129S6-Gt (ROSA)26Sor ^{tm9} (CAG-tdTomato)Hze/J (Jax #007905)	Astrocytes, whole population	Various supportive functions	[74]
	B6.129P-Cx3cr1 ^{tm1litt} /J (Jax #005582)	Microglia/macrophages in retina and optic nerve	Immune cells	[75]

1.3 Labeling of Ganglion Cells by Retrograde Axonal Transport of Tracers

Sometimes, the use of a GFP-expressing reporter strain is not desirable. This may be the case when one wants to isolate ganglion cells from a transgenic mouse with a deletion of a gene of interest. It would, in principle, be possible to cross the knock-out strain with a GFP-expressing strain, but this is time consuming and may take more than one generation of breeding, especially if the knock-out produces a phenotype only in the homozygous state. Another potential problem may arise if the knock-out strain and the GFP-expressing strain are not on the same genetic background. Mixing genetic backgrounds may create unexpected phenotypes or add to the variability of gene expression [79, 80], and these problems can sometimes only be overcome by backcrossing the strains for several generations. In such cases, an alternative method for specifically labeling RGCs can be used. In mice, most ganglion cells project to the superior colliculus [81], and injections of tracer dyes into this structure lead to a very specific labeling of only the ganglion cells in the retina via retrograde axonal transport. After injection, the dye-coupled tracer molecules are transported back to the cell soma, where they appear as punctate inclusion bodies about 4–5 days later [57, 82]. A drawback of this method is that, especially in later stages of glaucoma, considerable blockage of axonal transport occurs [83–90], so that only very few ganglion cells were labeled when this method was used in aged DBA/2J mice [57]. This limits the use of retrograde ganglion cell labeling to early stages of glaucoma.

The murine superior colliculus is large enough that an injection does not strictly require the use of a stereotaxic frame, though it is certainly an advantage if such a device is available. A free hand injection using a Hamilton syringe to deliver the dye leads to satisfactory labeling of many ganglion cells, with a preference for the inferior half of the retina of the contralateral eye, and some labeling in the ipsilateral eye. If a more targeted injection is desired, a stereotaxic frame should be used (*see Note 1*). In this case, it is recommended to use a glass micropipette for injection.

A variety of retrograde axonal tracers are available, but the most useful ones for this application are rhodamine- or FITC-coupled dextrans. However, Fluorogold (hydroxystilbamidine bis-methanesulfonate) can also be used. The choice of the fluorescent label is mainly dictated by the filter sets of the microscope used for collecting the cells. We usually use either tetramethylrhodamine-conjugated dextran, MW 10,000 or fluorescein-conjugated dextran, MW 10,000 (*see Note 2*).

1.4 Dissociation of the Retina or the Optic Nerve into Single Cells

Several methods for the dissociation of the retina into single cells have been described in the literature for use with FACS, electrophysiological recording, cell culture, and cell characterization by PCR or profiling [7, 74, 91–95]. We present a streamlined protocol that combines ease of use with satisfactory preservation of cell morphology and that can be used for retina and (with small

modifications) optic nerve alike. Generally, young adult mice (1–2 months) are preferred. We have successfully isolated single cells from mice up to 8 months of age, though the yield of well-preserved cells is lower. Retinas or optic nerves are first treated with papain for enzymatic dissociation and then triturated using a series of heat-polished Pasteur pipettes for mechanical dissociation.

Rods and cones are not lost in primary open angle glaucoma [96], and there is little evidence for morphological or functional alterations other than a swelling of cone photoreceptors [97–99]. Isolation of photoreceptors is therefore probably less of a priority in glaucoma research. However, the isolation of rods and cones is even easier than that of other retinal neurons. Since the cells are extremely fragile and the outer segment breaks off easily, the enzymatic digestion step is omitted. Rather, one makes use of the fact that photoreceptors spontaneously separate as “rafts” from small pieces of undigested tissue soon dissociate into single cells [100]. Rods are recognizable by their morphology. Cones are much rarer in the murine retina. To target cones efficiently, it is recommended to add FITC-conjugated peanut agglutinin, which stains cone photoreceptors [101, 102]. After identifying the cone photoreceptors under fluorescent illumination, they can be found more easily (*see Note 3*).

The protocol for retina dissociation can be slightly modified for optic nerve head dissociation. Astrocytes are the major cell type in the optic nerve head, but it also contains cell types such as ganglion cell axons, endothelial cells, and microglia. Most other components, however, either show poor survival in single-cell suspension (such as axons) or have morphological features that are different from astrocytes (such as endothelial cells). The shape of microglia is somewhat similar to astrocytes, but their delicate processes are usually broken off during dissociation and the cells are smaller, making them easily distinguishable from astrocytes [74]. The optic nerve head is very small compared to the retina and there are only about 200 astrocytes per nerve head [27]. Microglial cells are even rarer.

1.5 Preservation of Cell Morphology After Dissociation

Some cell types can be recognized by their morphology. We will provide guidelines for recognizing several cell types from the retina and optic nerve. To obtain cells with well-preserved morphology, the amount of papain and the dissociation time should be kept to the necessary minimum. Using the protocols in this chapter we have consistently obtained cells with good morphology, but some optimization may be necessary. As a general rule, dissociated cells should be used immediately for single-cell collection. An experienced operator can collect >30 individual cells in an hour, but the single-cell suspensions should not be used for longer than 90 min after dissociation.

1.6 Downstream Applications

The expression of several (>20) genes of interest can be tested simultaneously in a single cell using two rounds of PCR amplification [7]. A convenient method is the use of one-tube reaction kits that allow performing the reverse transcription and the first round PCR in the same tube. In this case, the isolated cell is expelled into 5 μ L of reaction buffer in a reaction tube that contains primers for all target genes and controls. The number of cycles for the first round PCR should be kept low (18–20) to prevent the buildup of unspecific amplification products. After the first round, the reaction product can be diluted up to 60-fold and used as a template for the second round PCR. For the second round, each target gene is amplified separately with a nested primer pair. It is possible to use the reaction product from the first round amplification for quantitative PCR; however, the variability between individual single cells is high. For quantitative PCR it may therefore be better to pool 12–20 cells in a single PCR tube before proceeding to the RT-PCR. Alternatively, cDNA libraries can be prepared from single cells or a small number of cells. There are several options for the transcription and amplification of the cDNA, some which are compatible with most downstream applications, including RNAseq.

2 Materials

2.1 Materials for the Injection of Conjugated Dextran into the Superior Colliculus

1. Solutions of dye-conjugated dextrans in a sterile saline solution at 0.2 mg/ μ L.
2. Ketamine/xylazine (100 mg/kg and 20 mg/kg body weight) for anesthesia.
3. Razor for shaving the mouse head.
4. Betadine and alcohol swabs to clean the surgical incision site.
5. Artificial tear fluid.
6. Warming blanket (37 °C).
7. Optional: stereotaxic frame.
8. Surgical scalpel with blades (# 10), sterile forceps.
9. Sterile surgical gloves and drapes.
10. High-speed bone drill with drill bits (*see Note 4*).
11. Hamilton syringe (5 or 10 μ L) with a beveled needle.
12. Gelfoam and surgical clips for wound closure.
13. Buprenorphine (0.05–0.1 mg/kg) for post-surgical analgesia.

2.2 Materials for the Dissociation of Retinas and Optic Nerves into Single Cells

1. Calcium and magnesium-free Hank's balanced salt solution (HBSS).
2. Three heat-polished Pasteur pipettes with decreasing tip size for trituration: 300 μm lumen diameter (for the largest) to 100 μm (for the smallest), *see* **Note 5**.
3. Papain suspension (35 mg/mL), *see* **Note 6**.
4. L-cysteine stock solution (10 mg/mL in HBSS).
5. Small curved forceps.
6. Chilled Phosphate-buffered saline (PBS).
7. Dissecting microscope.
8. Microcentrifuge.
9. Normal horse serum (*see* **Note 7**).
10. DNase I stock solution (at least 600 U/mL).

2.3 Materials for Collection of Single Cells

1. Inverted microscope with 10 \times and 20 \times objectives (*see* **Note 8**).
2. 5 mL syringes with Luer locks.
3. Tubing.
4. 3-axis micromanipulator with an electrode holder (two micromanipulators are preferred).
5. Glass rods for the preparation of micropipettes, 1 mm outer diameter, 0.75 mm inner diameter, thin wall, no filament (*see* **Note 9**).
6. Microelectrode puller.
7. Microscope slides for immunocytochemistry with 2 wells (*see* **Note 10**).
8. PBS with 2% bovine serum albumin.
9. Thin-wall PCR tubes.
10. PBS.
11. Optional: reaction buffer for the intended downstream application.
12. Microcentrifuge.
13. Crushed dry ice.

3 Methods

3.1 Injection of Conjugated Dextran into the Superior Colliculus

1. Deeply anesthetize the mouse with a mixture of ketamine and xylazine according to approved animal procedures of your institution. After anesthesia the mouse should be kept on a warming blanket throughout the whole procedure. Artificial

tear fluid should be applied to the corneas to prevent drying of the eyes during anesthesia.

2. After shaving the fur on the head and scrub the surgery site with Betadine and alcohol wipes.
3. Optional: at this point, the animal can be put into a stereotaxic frame.
4. Make a midline incision on the mouse head with a scalpel blade.
5. Identify the bregma and lambda (intersection between the sagittal and lambdoid sutures) anatomical markers.
6. Observing a sterile technique and using a sterilized drill bit, a hole is drilled into the parietal bone just anterior to the lambdoid suture (*see* Fig. 1a).
7. Every few seconds, the drill should be stopped and the hole in the skull should be probed gently with a sterile needle until reaching the dura. The dura is recognized by the pink/red color of the underlying tissue and the absence of hard bony resistance to probing.
8. A Hamilton syringe with a beveled needle is inserted through the dura no more than 2 mm deep, at a slight angle (*see* Fig. 1b). About 0.5 μL of dye-coupled dextran is slowly injected into the superior colliculus.
9. Withdraw the needle and fill the hole in the bone with crushed gelfoam. Re-apposition the skin and close the surgical incision with two surgical clips.
10. Buprenorphine should be administered s.c. directly after the procedure (while the mouse is still under anesthesia), and afterward for 48 h in 8–12 h intervals.
11. About 5 days after the injection, enough dye-coupled dextran has accumulated in the ganglion cell somata to proceed to tissue dissociation.

3.2 Retina Dissociation

1. Prepare the dissociation solution by adding 36 μL papain suspension and 10 μL of L-cysteine stock solution to 2 mL $\text{Ca}^{2+}/\text{Mg}^{2+}$ free HBSS (*see* Note 6).
2. Incubate the HBSS/papain solution for 15 min at 37 °C to activate the papain.
3. In the meantime, euthanize the mouse as per your institution's guidelines for animal euthanasia and remove the eyes using a pair of curved forceps and place them in prechilled phosphate-buffered saline (PBS). Take out the retina and cut it into four to five pieces under a dissecting microscope.
4. Transfer the pieces into the HBSS/papain solution and incubate for 15–25 min at 37 °C depending on the age of the mouse (*see* Note 11).

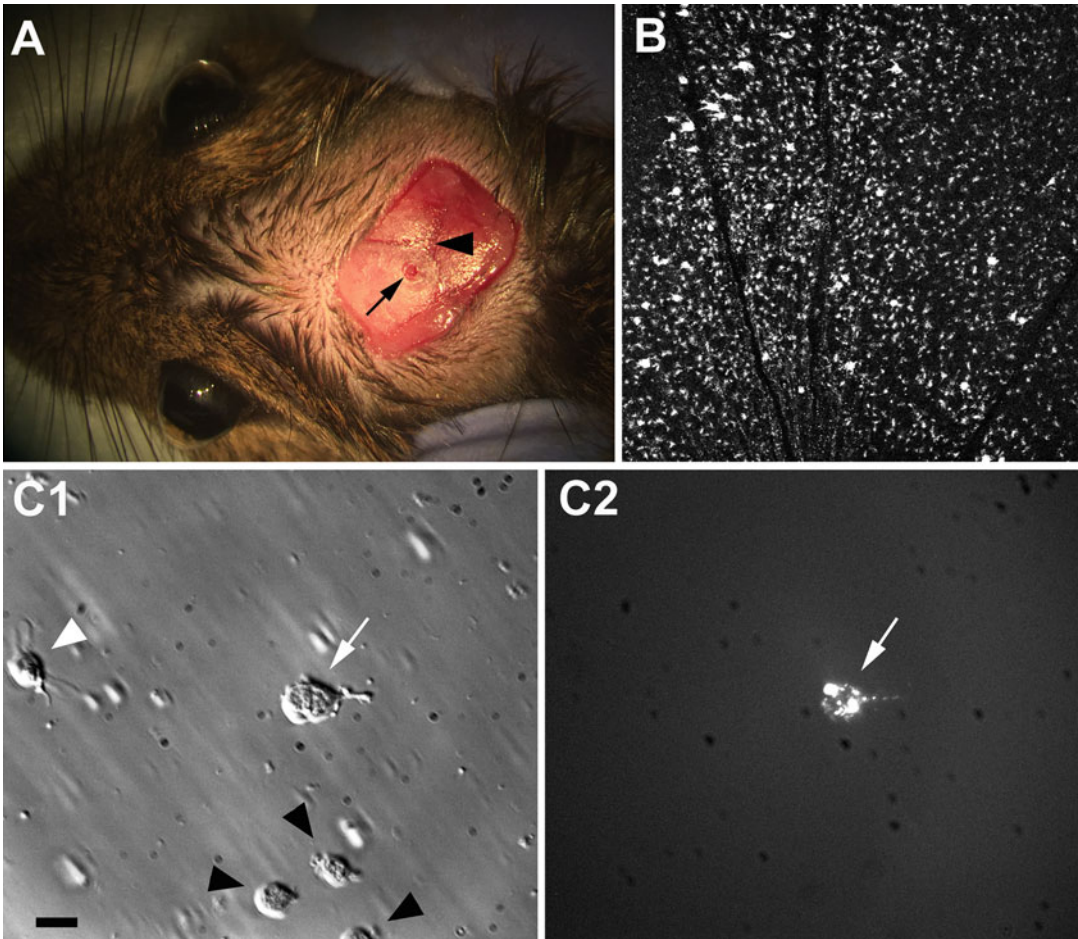


Fig. 1 Retrograde labeling of retinal ganglion cells. (a) Localization of the injection site (*arrow*). Lambda is indicated by an arrowhead. (b) Labeled ganglion cells in the mouse retina 5 days after injection of rhodamine-dextran into the superior colliculus. (c1) Isolated cells from the retina labeled with rhodamine-dextran as shown in (b). The largest cell (*white arrow*) is a ganglion cell and can be easily identified by its fluorescence (*white arrow*, c2) after dissociation. Note that other cells (bipolar cell: *white arrowhead*, unidentified cells: *black arrowheads*) did not show any fluorescence. Scale bar for (c1) and (c2): 20 μ m

5. After the incubation, centrifuge the digested retina at $400 \times g$ for 5 min at room temperature. Remove the HBSS/papain solution and resuspend the pellet in 1 mL HBSS with 10% normal horse serum to inactivate the papain.
6. Triturate the retina gently three times with a heat-polished Pasteur pipette (largest tip diameter).
7. Centrifuge the cell suspension and undissociated retina at $400 \times g$ for 5 min at room temperature and resuspend in 1 mL HBSS with 10% normal horse serum and 60 U/mL DNase to remove extracellular DNA.

8. Repeat trituration with a series of three heat-polished Pasteur pipettes until all visible chunks of tissue are completely dissociated (*see* **Note 12**).
9. Keep the resulting cell suspension on ice and use directly for single-cell collection.

3.3 Dissociation of Photoreceptors

1. Euthanize the mouse and dissect the retina as under Subheading 3.2.
2. Transfer the retina to HBSS and cut into small pieces.
3. Triturate gently with a heat-polished Pasteur pipette (lumen diameter about 300 μm).
4. Immediately proceed to single-cell collection.

3.4 Optic Nerve Head Dissociation

1. Prepare and activate the dissociation solution as under Subheading 3.2, **steps 1** and **2**. However, only 500 μL HBSS/papain solution should be used.
2. Euthanize the mouse and dissect the eyes with a curved forceps.
3. Remove the sclera and detach the optic nerves gently from the retina.
4. Under a dissection microscope, identify the unmyelinated segment of the optic nerve and cut it from the myelinated segment (*see* **Note 13**).
5. Transfer the nerve head into HBSS/papain solution. It is recommended to start with a minimum of two pooled optic nerve heads to obtain enough isolated astrocytes.
6. Incubate for 15–25 min at 37 °C.
7. Transfer the digested optic nerve heads from the HBSS/papain solution directly into 200 μL HBSS with 10% normal horse serum and 60 U/mL DNase using a Pasteur pipette (*see* **Note 14**).
8. Triturate the tissue with three Pasteur pipettes with descending size.
9. Keep the single-cell suspension on ice and directly proceed to cell collection.

3.5 Single-Cell Collection

1. On the day before cell collection, prepare glass micropipettes from the glass rods using an electrode puller. The mouth of the micropipette should be 10–20 μm in diameter (*see* **Note 15**). Figure 4c, d show suitable shapes of the tip. Store the micropipettes until further use (*see* **Note 16**).
2. Optional: silanize the micropipettes (*see* **Note 17**).
3. Prepare the cell collection rig (*see* Fig. 2 and **Note 18**).

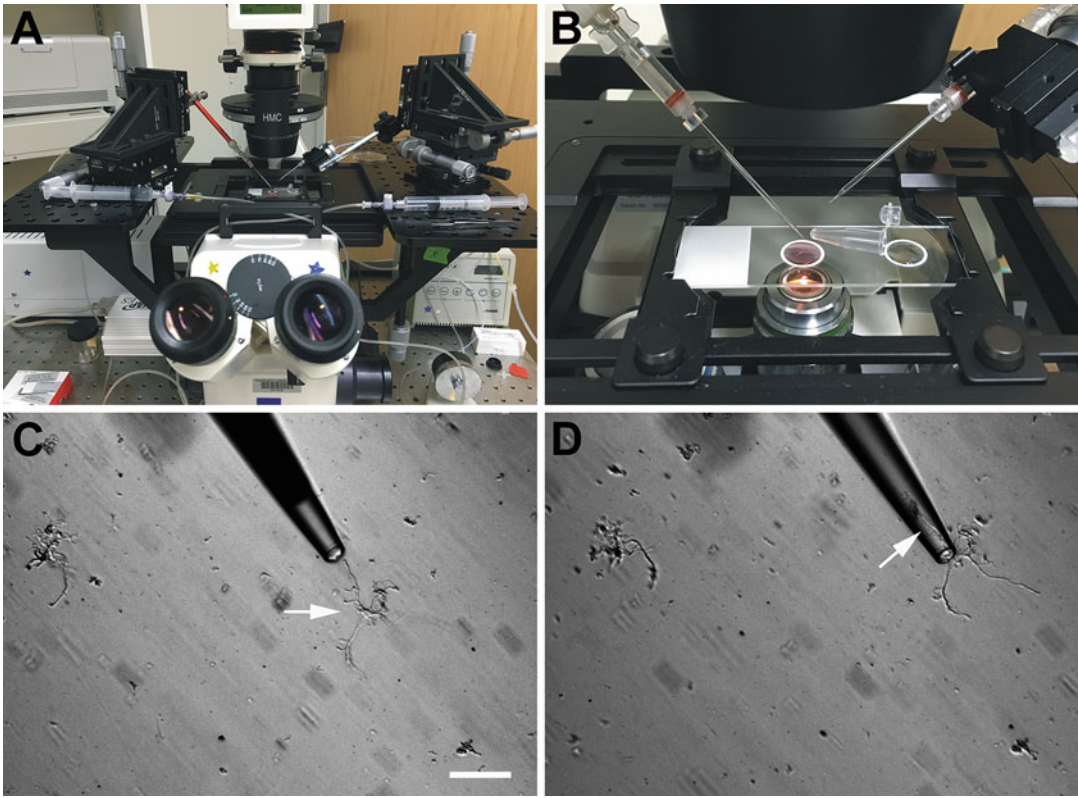


Fig. 2 Experimental setup for single-cell collection. (a) Two micromanipulators mounted on an inverted microscope are used to move micropipettes along three different axes. Pressures to aspirate and expel a single cell are adjusted using 5 mL Luer lock syringes. (b) Enlarged view of (a) A microscope slide with two rings is used to hold both cell suspension and the washing buffer. A thin-wall PCR tube containing 5 μ L PBS is placed between the rings to expel the collected cell from the washing buffer. (c, d) Collecting an optic nerve head astrocyte. The astrocyte aspirated into the pipette is indicated by an arrow. Scale bar: 40 μ m

4. Add 50 μ L PBS containing 2% bovine serum albumin into one ceramic ring of an immunocytochemistry slide and 50 μ L of the cell suspension into the other (Fig. 2b).
5. Allow the cells to settle down on the slide for 3–5 min.
6. Aspirate a cell from the suspension with a glass micropipette by applying negative pressure and transfer it to the PBS/BSA solution.
7. Expel the cell by applying positive pressure for washing (*see Note 19*).
8. Place a thin-wall PCR tube between the rings that contains 5 μ L PBS (Fig. 2b, *see Note 20*). The PBS should be placed close to the mouth of the tube (*see Note 21*).
9. Aspirate the cell again with a new micropipette and transfer to the PCR tube. A single cell is collected in the PCR tube under optical control.

10. Centrifuge the PCR tube briefly and keep it on dry ice until further use (*see Note 22*).
11. Do not use single-cell suspensions for more than about 90 min after dissociation (*see Note 23*).

3.6 Recognizing Cell Types After Dissociation

1. Refer to Fig. 3 for typical cell morphologies after retinal dissociation. Bipolar cells retain their shape well and even the difference between cone bipolar cells and rod bipolar cells is still obvious (Panels A and B). In rod bipolar cells, the dendrites emerge as a tuft from the cell body and the long axon ends in a bulb. Panel C shows a rod photoreceptor with cell body and outer segment still intact, though in this cell the axon was lost. Mueller cells (Panels D and E) also are very resistant to dissociation. In situ, the cells send multiple small processes into the inner and outer plexiform layers that ensheath synapses between retinal neurons [72, 103]. These processes give the cells the characteristic “hairy” appearance after dissociation.

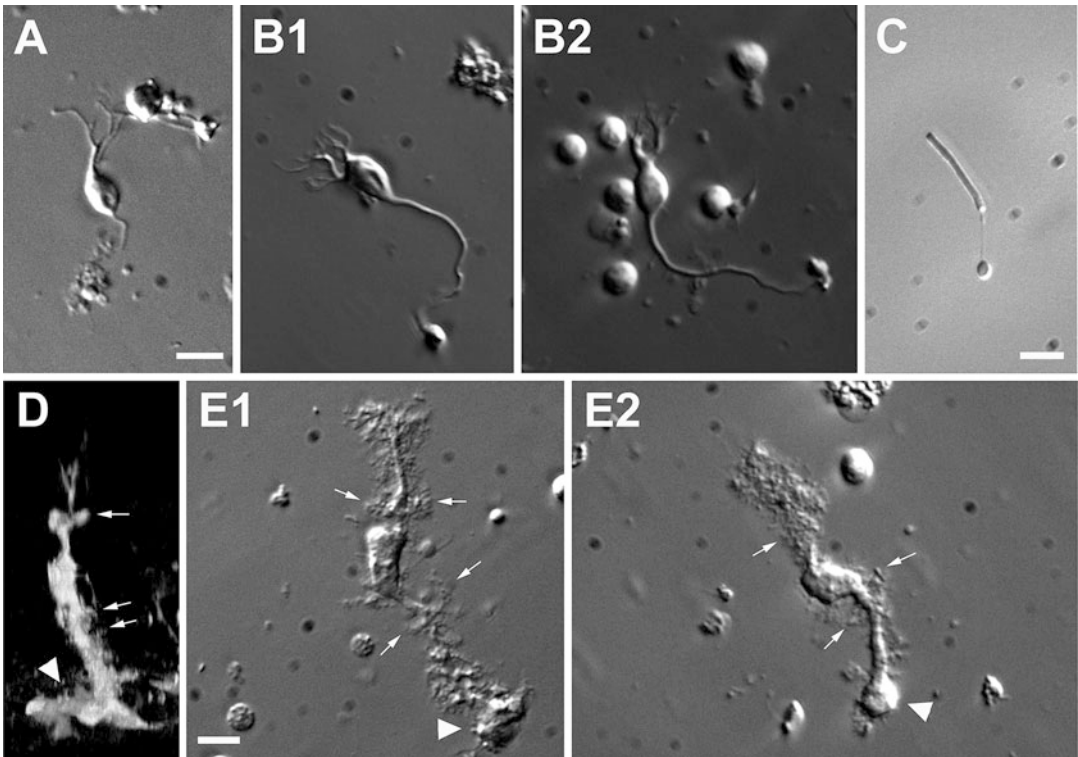


Fig. 3 Isolation of retinal neurons. (a) Cone bipolar cell. (b1, b2) Rod bipolar cells show their characteristic dendritic tufts and axons longer than those of cone bipolar cells. Scale bar for (a) and (b): 20 μm . (c) Rod photoreceptor with an intact outer segment. Scale bar: 10 μm . (d) Confocal image of a Muller cell in a transverse section of the retina. (e1, e2) The morphologic features of Muller cells were retained well after dissociation, showing their endfeet (arrowheads) and small processes (arrows). Two thick processes of Muller cells extend in opposite directions. Scale bar: 20 μm

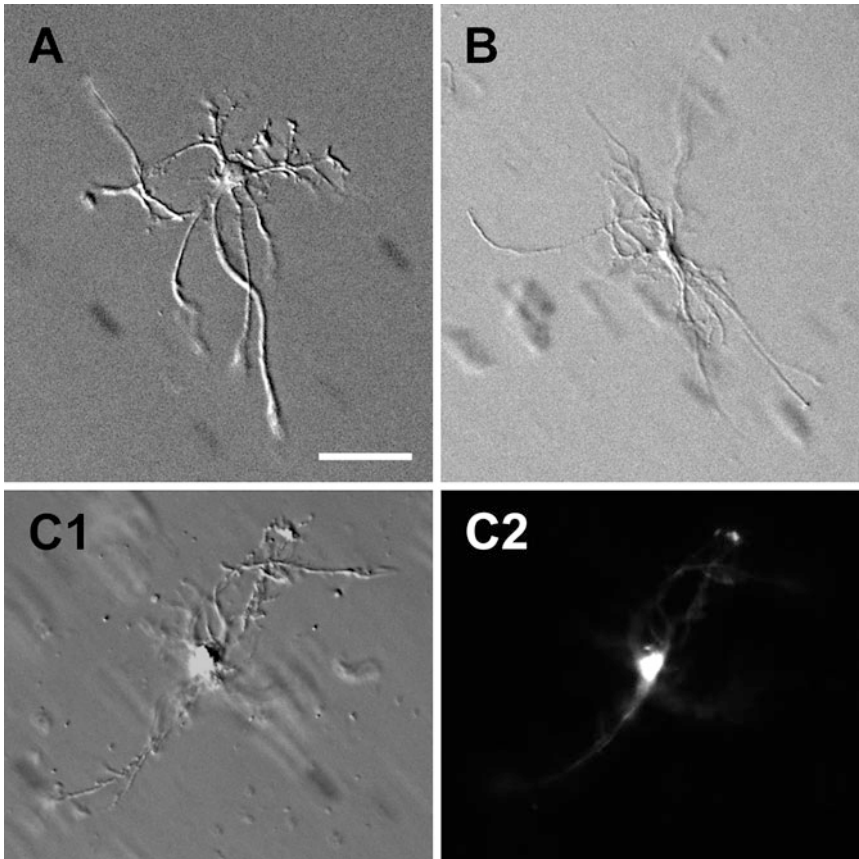


Fig. 4 Astrocytes dissociated from the optic nerve head. (a, b) Isolated astrocytes have thick cell bodies and extend 6–8, long primary processes in all directions. (c1) Optic nerve head astrocyte isolated from a B6.GFAP-cre/Rosa mouse. (c2) Fluorescence image of the same cell in (c1). Scale bar: 40 μ m

2. The astrocytes of the optic nerve head are a morphological type of white matter astrocytes and retain their processes exceptionally well after dissociation [8, 74]. As shown in Fig. 4, these cells are unmistakable even without labeling (Panels A and B). Panels C1 and C2 show the same astrocyte isolated from a B6.GFAP-cre/Rosa mouse to show the specific fluorescent labeling in this cross. Microglia/macrophages, which are present in the optic nerve head albeit in low numbers, are much smaller and their delicate processes do not survive dissociation and only the cell bodies can be isolated.

4 Notes

1. An excellent online resource for stereotaxic coordinates in mice can be found on the Allen Institute website under: <https://scalablebrainatlas.incf.org/mouse/ABA12>.

2. Different molecular size dextrans are available, but we found that the MW 10,000 dextrans are better retained in the ganglion cells than the smaller dextrans.
3. It should be noted that though all cones are labeled, PNA has a preference for short-wavelength cones and stains them more brightly than their middle/long wavelength counterparts [104, 105].
4. High-speed bone drills are available, e.g., from Fine Science Tools (Foster City, CA), who also sell drill bits of various shapes. Conical drill bits with a tip size of about 1 mm work well.
5. It is not necessary to silanize the Pasteur pipettes.
6. The source of the papain matters. We use 36 μ L papain suspension (~35 mg papain/mL; Worthington, catalog # 3126, Lakewood, NJ) in 2 mL HBSS. If the enzyme suspension from other suppliers is used, the concentration must be determined empirically.
7. Horse serum is used to quench the papain activity. Using horse serum rather than fetal bovine serum is mainly a matter of economy, but other types of serum could be substituted.
8. It is important to do every step of the single-cell collection under visual control. An inverted scope with long working-length objectives is the best choice.
9. Thin-wall capillaries allow for easier visualization of the aspirated cell. It is important that the glass capillaries do not have an interior filament, as the cells tend to stick to it.
10. The slides from Gold Seal Products, catalog # 3032, Portsmouth, NH, work well for this application.
11. The older the animal, the longer the dissociation time should be.
12. It is not necessary to check microscopically whether all small clumps of tissue are completely dissociated. Very small clumps of tissue are commonly found between dissociated cells and do not interfere with single-cell collection.
13. The unmyelinated segment of the nerve can be identified by its more “glassy” appearance.
14. At this stage, the optic nerve heads are still in one piece. Directly transferring them to HBSS/10% horse serum/DNAse avoids the need to collect dissociated cells by centrifugation. This minimizes cell loss.
15. Any microelectrode puller for electrophysiology can be used. The settings should be chosen for a pipet tip size larger than a normal patch pipette. The tip diameter should be varied according to the targeted cell type. Ideally, it should be about

the same size as the soma diameter of the target cells. Cells should deform slightly as they enter into the tip. If the tip size is too large, it is very easy to inadvertently aspirate more than one cell, or to lose the cell during the transfer. The tip should not taper too quickly.

16. A low-cost storage container for glass microelectrodes can be made from a petri dish and modeling clay.
17. Generally, it is unnecessary to silanize the micropipettes. However, some cells (especially bipolar cells) have a tendency to stick to the wall of the micropipette to an extent that it is difficult to expel them. In this case, the micropipettes should be silanized before use. For silane coating, glass micropipettes are prepared by pulling first and then the tips are dipped in a 5% silane/toluene solution. The excess of the silane/toluene solution is removed by applying positive pressure using a syringe. The micropipettes should be completely dried before use.
18. If using two micromanipulators for cell aspiration/washing and for transfer into the reaction tube, respectively, it is useful to connect the tubing to the syringes crosswise. In this way, one can manipulate the cells with one hand and control the pressure in the micropipette with the other.
19. The most common problem in single-cell RT-PCR is contamination of the target cell by a carryover of cell debris or RNA that has spilled from lysed cells into the medium. Though washing and re-picking dissociated cells before transfer into the PCR tube reduces the risk of contamination, positive (to verify the cells' identities) and negative (to exclude contaminated cells) should always be used. For retinal neurons other than rods, we use rod-opsin as a negative control. About half of the cells in the mouse retina are rod photoreceptors, and spurious detection of rod-opsin RNA is a sensitive marker for contamination [106]. For astrocytes and microglia/macrophages of the optic nerve, we use rod-opsin and myelin basic protein as negative controls.
20. If the downstream application requires another buffer than PBS, this buffer should be used to directly collect the cell into the appropriate buffer.
21. Ideally, one should see the cell going into the collection tube through the wall of the tube. The drop of PBS should be placed very close to the mouth of the PCR tube to make it easier to reach within the tube with the micropipette and expel the cell. Alternatively, one can break the collection pipette with the cell into the collection buffer. However, in our experience this leads to a higher failure rate of the downstream applications.
22. If the cells are not to be used immediately, they can be stored at -80°C for several weeks.

23. If the cells start sticking to the glass tube and become difficult to expel, or membrane blebbing is observed (even after less than 90 min), these are signs that the cells are starting to die, and the preparation should be discarded.

References

1. Saliba AE, Westermann AJ, Gorski SA, Vogel J (2014) Single-cell RNA-seq: advances and future challenges. *Nucleic Acids Res* 42 (14):8845–8860. <https://doi.org/10.1093/nar/gku555>. gku555 [pii]
2. Macosko EZ, Basu A, Satija R, Nemesh J, Shekhar K, Goldman M, Tirosh I, Bialas AR, Kamitaki N, Martersteck EM, Trombetta JJ, Weitz DA, Sanes JR, Shalek AK, Regev A, McCarroll SA (2015) Highly parallel genome-wide expression profiling of individual cells using nanoliter droplets. *Cell* 161 (5):1202–1214. <https://doi.org/10.1016/j.cell.2015.05.002>
3. Chintalapudi SR, Djenderedjian L, Stiemke AB, Steinle JJ, Jablonski MM, Morales-Tirado VM (2016) Isolation and molecular profiling of primary mouse retinal ganglion cells: comparison of phenotypes from healthy and glaucomatous retinas. *Front Aging Neurosci* 8:93. <https://doi.org/10.3389/fnagi.2016.00093>
4. Goetz JJ, Trimarchi JM (2012) Single-cell profiling of developing and mature retinal neurons. *J Vis Exp* 62. <https://doi.org/10.3791/3824>
5. Trimarchi JM, Stadler MB, Roska B, Billings N, Sun B, Bartch B, Cepko CL (2007) Molecular heterogeneity of developing retinal ganglion and amacrine cells revealed through single cell gene expression profiling. *J Comp Neurol* 502(6):1047–1065. <https://doi.org/10.1002/cne.21368>
6. Janssen-Bienhold U, Schultz K, Gellhaus A, Schmidt P, Ammermuller J, Weiler R (2001) Identification and localization of connexin26 within the photoreceptor-horizontal cell synaptic complex. *Vis Neurosci* 18(2):169–178. S0952523801182015 [pii]
7. Jakobs TC, Ben Y, Masland RH (2007) Expression of mRNA for glutamate receptor subunits distinguishes the major classes of retinal neurons, but is less specific for individual cell types. *Mol Vis* 13:933–948. v13/a99 [pii]
8. Choi HJ, Sun D, Jakobs TC (2015) Astrocytes in the optic nerve head express putative mechanosensitive channels. *Mol Vis* 21:749–766
9. Lin B, Jakobs TC, Masland RH (2005) Different functional types of bipolar cells use different gap-junctional proteins. *J Neurosci* 25 (28):6696–6701. 25/28/6696 [pii]. <https://doi.org/10.1523/JNEUROSCI.1894-05.2005>
10. Haseleu J, Anlauf E, Blaess S, Endl E, Derouiche A (2013) Studying subcellular detail in fixed astrocytes: dissociation of morphologically intact glial cells (DIMIGs). *Front Cell Neurosci* 7:54. <https://doi.org/10.3389/fncel.2013.00054>
11. Rubakhin SS, Romanova EV, Nemes P, Sweedler JV (2011) Profiling metabolites and peptides in single cells. *Nat Methods* 8(4 Suppl):S20–S29. <https://doi.org/10.1038/nmeth.1549>
12. Feigenspan A, Weiler R (2004) Electrophysiological properties of mouse horizontal cell GABAA receptors. *J Neurophysiol* 92 (5):2789–2801. <https://doi.org/10.1152/jn.00284.2004>
13. Rockhill RL, Daly FJ, MacNeil MA, Brown SP, Masland RH (2002) The diversity of ganglion cells in a mammalian retina. *J Neurosci* 22(9):3831–3843. 20026369. 22/9/3831 [pii]
14. Sun W, Li N, He S (2002) Large-scale morphological survey of mouse retinal ganglion cells. *J Comp Neurol* 451(2):115–126. <https://doi.org/10.1002/cne.10323>
15. Kong JH, Fish DR, Rockhill RL, Masland RH (2005) Diversity of ganglion cells in the mouse retina: unsupervised morphological classification and its limits. *J Comp Neurol* 489(3):293–310. <https://doi.org/10.1002/cne.20631>
16. Sumbul U, Song S, McCulloch K, Becker M, Lin B, Sanes JR, Masland RH, Seung HS (2014) A genetic and computational approach to structurally classify neuronal types. *Nat Commun* 5:3512. <https://doi.org/10.1038/ncomms4512>. ncomms4512 [pii]
17. MacNeil MA, Masland RH (1998) Extreme diversity among amacrine cells: implications for function. *Neuron* 20(5):971–982. S0896-6273(00)80478-X [pii]

18. MacNeil MA, Heussy JK, Dacheux RF, Raviola E, Masland RH (2004) The population of bipolar cells in the rabbit retina. *J Comp Neurol* 472(1):73–86. <https://doi.org/10.1002/cne.20063>
19. Wassle H, Puller C, Muller F, Haverkamp S (2009) Cone contacts, mosaics, and territories of bipolar cells in the mouse retina. *J Neurosci* 29(1):106–117. 29/1/106 [pii]. <https://doi.org/10.1523/JNEUROSCI.4442-08.2009>
20. Wang DY, Ray A, Rodgers K, Ergorul C, Hyman BT, Huang W, Grosskreutz CL (2010) Global gene expression changes in rat retinal ganglion cells in experimental glaucoma. *Invest Ophthalmol Vis Sci* 51(8):4084–4095. <https://doi.org/10.1167/iov.09-4864> [pii]
21. Shatos MA, Rios JD, Tepavcevic V, Kano H, Hodges R, Dartt DA (2001) Isolation, characterization, and propagation of rat conjunctival goblet cells in vitro. *Invest Ophthalmol Vis Sci* 42(7):1455–1464
22. Shatos MA, Rios JD, Horikawa Y, Hodges RR, Chang EL, Bernardino CR, Rubin PA, Dartt DA (2003) Isolation and characterization of cultured human conjunctival goblet cells. *Invest Ophthalmol Vis Sci* 44(6):2477–2486
23. Shen S, Wiemelt AP, McMorris FA, Barres BA (1999) Retinal ganglion cells lose trophic responsiveness after axotomy. *Neuron* 23(2):285–295. S0896-6273(00)80780-1 [pii]
24. Hernandez MR, Igoe F, Neufeld AH (1988) Cell culture of the human lamina cribrosa. *Invest Ophthalmol Vis Sci* 29(1):78–89
25. Foo LC, Allen NJ, Bushong EA, Ventura PB, Chung WS, Zhou L, Cahoy JD, Daneman R, Zong H, Ellisman MH, Barres BA (2011) Development of a method for the purification and culture of rodent astrocytes. *Neuron* 71(5):799–811. S0896-6273(11)00649-0 [pii]. <https://doi.org/10.1016/j.neuron.2011.07.022>
26. May CA, Lutjen-Drecoll E (2002) Morphology of the murine optic nerve. *Invest Ophthalmol Vis Sci* 43(7):2206–2212
27. Sun D, Lye-Barthel M, Masland RH, Jakobs TC (2009) The morphology and spatial arrangement of astrocytes in the optic nerve head of the mouse. *J Comp Neurol* 516(1):1–19. <https://doi.org/10.1002/cne.22058>
28. Jeon CJ, Strettoi E, Masland RH (1998) The major cell populations of the mouse retina. *J Neurosci* 18(21):8936–8946
29. Bosco A, Romero CO, Breen KT, Chagovetz AA, Steele MR, Ambati BK, Vetter ML (2015) Neurodegeneration severity can be predicted from early microglia alterations monitored in vivo in a mouse model of chronic glaucoma. *Dis Model Mech* 8(5):443–455. <https://doi.org/10.1242/dmm.018788> [pii]
30. Davis CH, Kim KY, Bushong EA, Mills EA, Boassa D, Shih T, Kinebuchi M, Phan S, Zhou Y, Bihlmeyer NA, Nguyen JV, Jin Y, Ellisman MH, Marsh-Armstrong N (2014) Transcellular degradation of axonal mitochondria. *Proc Natl Acad Sci U S A* 111(26):9633–9638. <https://doi.org/10.1073/pnas.1404651111> [pii]
31. Gregory MS, Hackett CG, Abernathy EF, Lee KS, Saff RR, Hohlbaum AM, Moody KS, Hobson MW, Jones A, Kolovou P, Karray S, Giani A, John SW, Chen DF, Marshak-Rothstein A, Ksander BR (2011) Opposing roles for membrane bound and soluble Fas ligand in glaucoma-associated retinal ganglion cell death. *PLoS One* 6(3):e17659. <https://doi.org/10.1371/journal.pone.0017659>
32. Coombs J, van der List D, Wang GY, Chalupa LM (2006) Morphological properties of mouse retinal ganglion cells. *Neuroscience* 140(1):123–136. S0306-4522(06)00204-1 [pii]. <https://doi.org/10.1016/j.neuroscience.2006.02.079>
33. Peichl L, Gonzalez-Soriano J (1994) Morphological types of horizontal cell in rodent retinae: a comparison of rat, mouse, gerbil, and guinea pig. *Vis Neurosci* 11(3):501–517
34. Feng G, Mellor RH, Bernstein M, Keller-Peck C, Nguyen QT, Wallace M, Nerbonne JM, Lichtman JW, Sanes JR (2000) Imaging neuronal subsets in transgenic mice expressing multiple spectral variants of GFP. *Neuron* 28(1):41–51. S0896-6273(00)00084-2 [pii]
35. Howell GR, Libby RT, Jakobs TC, Smith RS, Phalan FC, Barter JW, Barbay JM, Marchant JK, Mahesh N, Porciatti V, Whitmore AV, Masland RH, John SW (2007) Axons of retinal ganglion cells are insulted in the optic nerve early in DBA/2J glaucoma. *J Cell Biol* 179(7):1523–1537. jcb.200706181 [pii]. <https://doi.org/10.1083/jcb.200706181>
36. Livet J, Weissman TA, Kang H, Draft RW, Lu J, Bennis RA, Sanes JR, Lichtman JW (2007) Transgenic strategies for combinatorial expression of fluorescent proteins in the nervous system. *Nature* 450(7166):56–62. nature06293 [pii]. <https://doi.org/10.1038/nature06293>

37. Lichtman JW, Livet J, Sanes JR (2008) A technicolour approach to the connectome. *Nat Rev Neurosci* 9(6):417–422. <https://doi.org/10.1038/nrn2391>. nrn2391 [pii]
38. Snippert HJ, van der Flier LG, Sato T, van Es JH, van den Born M, Kroon-Veenboer C, Barker N, Klein AM, van Rheenen J, Simons BD, Clevers H (2010) Intestinal crypt homeostasis results from neutral competition between symmetrically dividing Lgr5 stem cells. *Cell* 143(1):134–144. <https://doi.org/10.1016/j.cell.2010.09.016>
39. Kim IJ, Zhang Y, Yamagata M, Meister M, Sanes JR (2008) Molecular identification of a retinal cell type that responds to upward motion. *Nature* 452(7186):478–482. nature06739 [pii]. <https://doi.org/10.1038/nature06739>
40. Gong S, Zheng C, Doughty ML, Losos K, Didkovsky N, Schambra UB, Nowak NJ, Joyner A, Leblanc G, Hatten ME, Heintz N (2003) A gene expression atlas of the central nervous system based on bacterial artificial chromosomes. *Nature* 425(6961):917–925. <https://doi.org/10.1038/nature02033>
41. Huberman AD, Wei W, Elstrott J, Stafford BK, Feller MB, Barres BA (2009) Genetic identification of an on-off direction-selective retinal ganglion cell subtype reveals a layer-specific subcortical map of posterior motion. *Neuron* 62(3):327–334. S0896-6273(09)00295-5 [pii]. <https://doi.org/10.1016/j.neuron.2009.04.014>
42. Duan X, Qiao M, Bei F, Kim IJ, He Z, Sanes JR (2015) Subtype-specific regeneration of retinal ganglion cells following axotomy: effects of osteopontin and mTOR signaling. *Neuron* 85(6):1244–1256. <https://doi.org/10.1016/j.neuron.2015.02.017>. S0896-6273(15)00132-4 [pii]
43. Schmidt TM, Taniguchi K, Kofuji P (2008) Intrinsic and extrinsic light responses in melanopsin-expressing ganglion cells during mouse development. *J Neurophysiol* 100(1):371–384. <https://doi.org/10.1152/jn.00062.2008>
44. Besser S, Sicker M, Marx G, Winkler U, Eulenburg V, Hulsmann S, Hirrlinger J (2015) A transgenic mouse line expressing the red fluorescent protein tdTomato in GABAergic neurons. *PLoS One* 10(6):e0129934. <https://doi.org/10.1371/journal.pone.0129934>
45. Lu Q, Ivanova E, Ganjawala TH, Pan ZH (2013) Cre-mediated recombination efficiency and transgene expression patterns of three retinal bipolar cell-expressing Cre transgenic mouse lines. *Mol Vis* 19:1310–1320
46. Lu Q, Ivanova E, Pan ZH (2009) Characterization of green fluorescent protein-expressing retinal cone bipolar cells in a 5-hydroxytryptamine receptor 2a transgenic mouse line. *Neuroscience* 163(2):662–668. <https://doi.org/10.1016/j.neuroscience.2009.07.002>
47. Liu X, Grove JC, Hirano AA, Brecha NC, Barnes S (2016) Dopamine D1 receptor modulation of calcium channel currents in horizontal cells of mouse retina. *J Neurophysiol* 116(2) 686–697. doi:<https://doi.org/10.1152/jn.00990.2015>. jn 00990 02015
48. Hoon M, Sinha R, Okawa H, Suzuki SC, Hirano AA, Brecha N, Rieke F, Wong RO (2015) Neurotransmission plays contrasting roles in the maturation of inhibitory synapses on axons and dendrites of retinal bipolar cells. *Proc Natl Acad Sci U S A* 112(41):12840–12845. <https://doi.org/10.1073/pnas.1510483112>
49. Raymond ID, Pool AL, Vila A, Brecha NC (2009) A Thy1-CFP DBA/2J mouse line with cyan fluorescent protein expression in retinal ganglion cells. *Vis Neurosci* 26(5–6):453–465. <https://doi.org/10.1017/S095252380999023X>
50. Badea TC, Nathans J (2011) Morphologies of mouse retinal ganglion cells expressing transcription factors Brn3a, Brn3b, and Brn3c: analysis of wild type and mutant cells using genetically-directed sparse labeling. *Vis Res* 51(2):269–279. S0042-6989(10)00434-7 [pii]. <https://doi.org/10.1016/j.visres.2010.08.039>
51. Roska B, Werblin F (2001) Vertical interactions across ten parallel, stacked representations in the mammalian retina. *Nature* 410(6828):583–587. <https://doi.org/10.1038/35069068>. 35069068 [pii]
52. Wässle H (2004) Parallel processing in the mammalian retina. *Nat Rev Neurosci* 5(10):747–757. <https://doi.org/10.1038/nrn1497>. nrn1497 [pii]
53. Sanes JR, Masland RH (2015) The types of retinal ganglion cells: current status and implications for neuronal classification. *Annu Rev Neurosci* 38:221–246. <https://doi.org/10.1146/annurev-neuro-071714-034120>
54. Quigley HA, Dunkelberger GR, Green WR (1988) Chronic human glaucoma causing selectively greater loss of large optic nerve fibers. *Ophthalmology* 95(3):357–363
55. Quigley HA, Sanchez RM, Dunkelberger GR, L'Hernault NL, Baginski TA (1987) Chronic glaucoma selectively damages large optic nerve fibers. *Invest Ophthalmol Vis Sci* 28(6):913–920

56. Glovinsky Y, Quigley HA, Dunkelberger GR (1991) Retinal ganglion cell loss is size dependent in experimental glaucoma. *Invest Ophthalmol Vis Sci* 32(3):484–491
57. Jakobs TC, Libby RT, Ben Y, John SW, Masland RH (2005) Retinal ganglion cell degeneration is topological but not cell type specific in DBA/2J mice. *J Cell Biol* 171(2):313–325. jcb.200506099 [pii]. <https://doi.org/10.1083/jcb.200506099>
58. Della Santina L, Inman DM, Lupien CB, Horner PJ, Wong RO (2013) Differential progression of structural and functional alterations in distinct retinal ganglion cell types in a mouse model of glaucoma. *J Neurosci* 33(44):17444–17457. <https://doi.org/10.1523/JNEUROSCI.5461-12.2013>. 33/44/17444 [pii]
59. Puyang Z, Chen H, Liu X (2015) Subtype-dependent morphological and functional degeneration of retinal ganglion cells in mouse models of experimental glaucoma. *J Nat Sci* 1(5):e103
60. El-Danaf RN, Huberman AD (2015) Characteristic patterns of dendritic remodeling in early-stage glaucoma: evidence from genetically identified retinal ganglion cell types. *J Neurosci* 35(6):2329–2343. <https://doi.org/10.1523/JNEUROSCI.1419-14.2015>. 35/6/2329 [pii]
61. Feng L, Zhao Y, Yoshida M, Chen H, Yang JF, Kim TS, Cang J, Troy JB, Liu X (2013) Sustained ocular hypertension induces dendritic degeneration of mouse retinal ganglion cells that depends on cell type and location. *Invest Ophthalmol Vis Sci* 54(2):1106–1117. <https://doi.org/10.1167/iovs.12-10791>. iovs.12-10791 [pii]
62. Kim IJ, Zhang Y, Meister M, Sanes JR (2010) Laminar restriction of retinal ganglion cell dendrites and axons: subtype-specific developmental patterns revealed with transgenic markers. *J Neurosci* 30(4):1452–1462. 30/4/1452 [pii]. <https://doi.org/10.1523/JNEUROSCI.4779-09.2010>
63. Fujihara S, Yokozeki M, Oba Y, Higashibata Y, Nomura S, Moriyama K (2006) Function and regulation of osteopontin in response to mechanical stress. *J Bone Miner Res* 21(6):956–964. <https://doi.org/10.1359/jbmr.060315>
64. Higashibata Y, Sakuma T, Kawahata H, Fujihara S, Moriyama K, Okada A, Yasui T, Kohri K, Kitamura Y, Nomura S (2004) Identification of promoter regions involved in cell- and developmental stage-specific osteopontin expression in bone, kidney, placenta, and mammary gland: an analysis of transgenic mice. *J Bone Miner Res* 19(1):78–88. <https://doi.org/10.1359/jbmr.2004.19.1.78>
65. Akopian A, Atlasz T, Pan F, Wong S, Zhang Y, Volgyi B, Paul DL, Bloomfield SA (2014) Gap junction-mediated death of retinal neurons is connexin and insult specific: a potential target for neuroprotection. *J Neurosci* 34(32):10582–10591. <https://doi.org/10.1523/JNEUROSCI.1912-14.2014>
66. Sarthy V, Hoshi H, Mills S, Dudley VJ (2007) Characterization of green fluorescent protein-expressing retinal cells in CD 44-transgenic mice. *Neuroscience* 144(3):1087–1093. <https://doi.org/10.1016/j.neuroscience.2006.09.061>
67. Haverkamp S, Inta D, Monyer H, Wässle H (2009) Expression analysis of green fluorescent protein in retinal neurons of four transgenic mouse lines. *Neuroscience* 160(1):126–139. S0306-4522(09)00099-2 [pii]. <https://doi.org/10.1016/j.neuroscience.2009.01.081>
68. Neufeld AH, Liu B (2003) Glaucomatous optic neuropathy: when glia misbehave. *Neuroscientist* 9(6):485–495. <https://doi.org/10.1177/1073858403253460>
69. Hernandez MR, Miao H, Lukas T (2008) Astrocytes in glaucomatous optic neuropathy. *Prog Brain Res* 173:353–373. S0079-6123(08)01125-4 [pii]. [https://doi.org/10.1016/S0079-6123\(08\)01125-4](https://doi.org/10.1016/S0079-6123(08)01125-4)
70. Johnson EC, Morrison JC (2009) Friend or foe? Resolving the impact of glial responses in glaucoma. *J Glaucoma* 18(5):341–353. <https://doi.org/10.1097/IJG.0b013e31818c6ef6>. 00061198-200906000-00001 [pii]
71. Sun D, Jakobs TC (2012) Structural remodeling of astrocytes in the injured CNS. *Neuroscientist* 18(6):567–588. <https://doi.org/10.1177/1073858411423441>. 1073858411423441 [pii]
72. Kuzmanovic M, Dudley VJ, Sarthy VP (2003) GFAP promoter drives Muller cell-specific expression in transgenic mice. *Invest Ophthalmol Vis Sci* 44(8):3606–3613
73. Nolte C, Matyash M, Pivneva T, Schipke CG, Ohlemeyer C, Hanisch UK, Kirchhoff F, Kettenmann H (2001) GFAP promoter-controlled EGFP-expressing transgenic mice: a tool to visualize astrocytes and astrogliosis in living brain tissue. *Glia* 33(1):72–86. [https://doi.org/10.1002/1098-1136\(20010101\)33:1<72::AID-GLIA1007>3.0.CO;2-A](https://doi.org/10.1002/1098-1136(20010101)33:1<72::AID-GLIA1007>3.0.CO;2-A)
74. Choi HJ, Sun D, Jakobs TC (2015) Isolation of intact astrocytes from the optic nerve head

- of adult mice. *Exp Eye Res* 137:103–110. <https://doi.org/10.1016/j.exer.2015.06.014>. S0014-4835(15)00202-X [pii]
75. Jung S, Aliberti J, Graemmel P, Sunshine MJ, Kreutzberg GW, Sher A, Littman DR (2000) Analysis of fractalkine receptor CX(3)CR1 function by targeted deletion and green fluorescent protein reporter gene insertion. *Mol Cell Biol* 20(11):4106–4114
 76. Butovsky O, Jedrychowski MP, Moore CS, Cialic R, Lanser AJ, Gabrieli G, Koeglsperger T, Dake B, Wu PM, Doykan CE, Fanek Z, Liu L, Chen Z, Rothstein JD, Ransohoff RM, Gygi SP, Antel JP, Weiner HL (2014) Identification of a unique TGF-beta-dependent molecular and functional signature in microglia. *Nat Neurosci* 17(1):131–143. <https://doi.org/10.1038/nn.3599>. nn.3599 [pii]
 77. Moore CS, Ase AR, Kinsara A, Rao VT, Michell-Robinson M, Leong SY, Butovsky O, Ludwin SK, Seguela P, Bar-Or A, Antel JP (2015) P2Y12 expression and function in alternatively activated human microglia. *Neurol Neuroimmunol Neuroinflamm* 2(2):e80. <https://doi.org/10.1212/NXI.0000000000000080>
 78. Bennett ML, Bennett FC, Liddelow SA, Ajami B, Zamarian JL, Fernhoff NB, Mulinnyaw SB, Bohlen CJ, Adil A, Tucker A, Weissman IL, Chang EF, Li G, Grant GA, Hayden Gephart MG, Barres BA (2016) New tools for studying microglia in the mouse and human CNS. *Proc Natl Acad Sci U S A* 113(12):E1738–E1746. <https://doi.org/10.1073/pnas.1525528113>
 79. Anderson MG, Libby RT, Mao M, Cosma IM, Wilson LA, Smith RS, John SW (2006) Genetic context determines susceptibility to intraocular pressure elevation in a mouse pigmented glaucoma. *BMC Biol* 4:20. 1741-7007-4-20 [pii]. <https://doi.org/10.1186/1741-7007-4-20>
 80. Sandberg R, Yasuda R, Pankratz DG, Carter TA, Del Rio JA, Wodicka L, Mayford M, Lockhart DJ, Barlow C (2000) Regional and strain-specific gene expression mapping in the adult mouse brain. *Proc Natl Acad Sci U S A* 97(20):11038–11043. 97/20/11038 [pii]
 81. Hofbauer A, Drager UC (1985) Depth segregation of retinal ganglion cells projecting to mouse superior colliculus. *J Comp Neurol* 234(4):465–474. <https://doi.org/10.1002/cne.902340405>
 82. Dacey DM, Peterson BB, Robinson FR, Gamlin PD (2003) Fireworks in the primate retina: in vitro photodynamics reveals diverse LGN-projecting ganglion cell types. *Neuron* 37(1):15–27. S0896627302011431 [pii]
 83. Quigley HA, Addicks EM (1980) Chronic experimental glaucoma in primates. II. Effect of extended intraocular pressure elevation on optic nerve head and axonal transport. *Invest Ophthalmol Vis Sci* 19(2):137–152
 84. Quigley HA, Anderson DR (1977) Distribution of axonal transport blockade by acute intraocular pressure elevation in the primate optic nerve head. *Invest Ophthalmol Vis Sci* 16(7):640–644
 85. Quigley HA, Guy J, Anderson DR (1979) Blockade of rapid axonal transport. Effect of intraocular pressure elevation in primate optic nerve. *Arch Ophthalmol* 97(3):525–531
 86. Quigley HA, McKinnon SJ, Zack DJ, Pease ME, Kerrigan-Baumrind LA, Kerrigan DF, Mitchell RS (2000) Retrograde axonal transport of BDNF in retinal ganglion cells is blocked by acute IOP elevation in rats. *Invest Ophthalmol Vis Sci* 41(11):3460–3466
 87. Crish SD, Sappington RM, Inman DM, Horner PJ, Calkins DJ (2010) Distal axonopathy with structural persistence in glaucomatous neurodegeneration. *Proc Natl Acad Sci U S A* 107(11):5196–5201. 0913141107 [pii]. <https://doi.org/10.1073/pnas.0913141107>
 88. Johansson JO (1988) Inhibition and recovery of retrograde axoplasmic transport in rat optic nerve during and after elevated IOP in vivo. *Exp Eye Res* 46(2):223–227
 89. Johansson JO (1986) Retrograde axoplasmic transport in rat optic nerve in vivo. What causes blockage at increased intraocular pressure? *Exp Eye Res* 43(4):653–660
 90. Johansson JO (1983) Inhibition of retrograde axoplasmic transport in rat optic nerve by increased IOP in vitro. *Invest Ophthalmol Vis Sci* 24(12):1552–1558
 91. Sarthy PV, Lam DM (1978) Biochemical studies of isolated glial (Muller) cells from the turtle retina. *J Cell Biol* 78(3):675–684
 92. Shimauchi-Matsukawa Y, Aman Y, Tachibanaki S, Kawamura S (2008) Identification of differentially expressed genes in carp rods and cones. *Mol Vis* 14:358–369
 93. Hirooka K, Kourennyi DE, Barnes S (2000) Calcium channel activation facilitated by nitric oxide in retinal ganglion cells. *J Neurophysiol* 83(1):198–206
 94. Bigiani A, Petrucci C, Ghiaroni V, Dal Monte M, Cozzi A, Kreienkamp HJ, Richter D, Bagnoli P (2004) Functional correlates of somatostatin receptor

- 2 overexpression in the retina of mice with genetic deletion of somatostatin receptor 1. *Brain Res* 1025(1–2):177–185. <https://doi.org/10.1016/j.brainres.2004.07.083>
95. Schubert T, Weiler R, Feigenspan A (2006) Intracellular calcium is regulated by different pathways in horizontal cells of the mouse retina. *J Neurophysiol* 96(3):1278–1292. <https://doi.org/10.1152/jn.00191.2006>
 96. Kendell KR, Quigley HA, Kerrigan LA, Pease ME, Quigley EN (1995) Primary open-angle glaucoma is not associated with photoreceptor loss. *Invest Ophthalmol Vis Sci* 36(1):200–205
 97. Nork TM, Ver Hoeve JN, Poulsen GL, Nickells RW, Davis MD, Weber AJ, Vaegan SSH, Lemley HL, Millicchia LL (2000) Swelling and loss of photoreceptors in chronic human and experimental glaucomas. *Arch Ophthalmol* 118(2):235–245
 98. Holopigian K, Greenstein VC, Seiple W, Hood DC, Ritch R (2000) Electrophysiologic assessment of photoreceptor function in patients with primary open-angle glaucoma. *J Glaucoma* 9(2):163–168
 99. Colotto A, Falsini B, Salgarello T, Iarossi G, Galan ME, Scullica L (2000) Photopic negative response of the human ERG: losses associated with glaucomatous damage. *Invest Ophthalmol Vis Sci* 41(8):2205–2211
 100. Hagstrom SA, Neitz M, Neitz J (2000) Cone pigment gene expression in individual photoreceptors and the chromatic topography of the retina. *J Opt Soc Am A Opt Image Sci Vis* 17(3):527–537
 101. Bridges CD (1981) Lectin receptors of rods and cones. Visualization by fluorescent label. *Invest Ophthalmol Vis Sci* 20(1):8–16
 102. Sarthy PV, Bridges CD, Kretzer FL, Lam DM (1981) Lectin receptors on cells isolated from the turtle retina. *J Comp Neurol* 202(4):561–569. <https://doi.org/10.1002/cne.902020408>
 103. Burris C, Klug K, Ngo IT, Sterling P, Schein S (2002) How Muller glial cells in macaque fovea coat and isolate the synaptic terminals of cone photoreceptors. *J Comp Neurol* 453(1):100–111. <https://doi.org/10.1002/cne.10397>
 104. Szel A, von Schantz M, Rohlich P, Farber DB, van Veen T (1993) Difference in PNA label intensity between short- and middle-wavelength sensitive cones in the ground squirrel retina. *Invest Ophthalmol Vis Sci* 34(13):3641–3645
 105. Daniele LL, Insinna C, Chance R, Wang J, Nikonov SS, Pugh EN Jr (2011) A mouse M-opsin monochromat: retinal cone photoreceptors have increased M-opsin expression when S-opsin is knocked out. *Vis Res* 51(4):447–458. <https://doi.org/10.1016/j.visres.2010.12.017>
 106. Jakobs TC, Ben Y, Masland RH (2003) CD15 immunoreactive amacrine cells in the mouse retina. *J Comp Neurol* 465(3):361–371. <https://doi.org/10.1002/cne.10845>

INDEX

A

- Amacrine cells..... 1, 6, 312, 314, 315
 Amplifiers..... 73, 75, 83, 84, 86, 113, 280
 Anesthesia
 isoflurane..... 17, 25–27, 30, 35, 37, 174, 200
 in minipigs..... 44
 in rodents..... 71, 73, 75, 116, 290
 Angle
 closure..... 1, 4
 iridocorneal..... 25
 Anterior chamber..... 2, 11, 12,
 15, 16, 23, 24, 33, 35–38, 42, 45, 46, 58, 89, 115,
 125, 127, 137, 138, 145, 211, 253
 Aqueous humor
 dynamics..... 109–119
 formation..... 11, 16, 110, 117
 outflow..... 2, 11, 41, 42, 109, 127, 138
 Astrocytes..... 3, 181, 188,
 269–283, 312, 316, 318, 322, 324, 326, 328
 Axon..... 1, 23, 82,
 109, 171, 187, 209, 270, 287, 299, 312
 Axonal transport
 anterograde..... 172, 176, 180
 retrograde..... 172, 176, 312, 314
 Axonopathy..... 171–183

B

- Biolistic labeling..... 161–170
 Biomarker..... 69
 Biomechanics..... 135, 141, 287
 Bipolar cells..... 312, 314, 316, 322, 324, 325, 328
 Bligh and Dyer..... 97
 Block face
 imaging..... 207, 212
 staining..... 207, 212–215
 Bruch's membrane..... 209, 217–219,
 222, 223, 225–227, 230, 232, 254

C

- Calibration curve..... 56
 Cannulation..... 49, 57, 115, 116, 118, 211
 Carbocyanine dye
 DiI..... 180, 271
 DiO..... 271

- Cell cultures..... 91, 125, 126, 131,
 143, 170, 188, 189, 196, 312, 314
 Ceramide..... 99
 Cholera toxin beta (CTB)..... 172–174,
 176, 177, 179, 181, 182, 189–191
 Collagen..... 135–157, 312
 Conjunctiva..... 14, 16, 17,
 42, 45, 199, 201, 312
 Connective tissues..... 2, 3, 15,
 148, 175, 200, 207–264
 Cornea..... 34–37, 46, 50, 51, 53, 54, 56,
 58, 59, 63, 115, 129, 136, 150, 174, 200, 321

D

- Data analysis..... 85, 91,
 92, 138, 152, 224, 251, 294, 300–306
 Dendrites..... 166, 169, 312, 316, 324
 Digital image correlation (DIC)..... 136,
 139, 141–143, 146–153
 3D reconstruction..... 207, 214–216,
 223, 225, 226, 230, 252, 254, 256, 259, 261

E

- Electrodes..... 28, 36, 63–66,
 68, 72, 73, 75, 82–86, 280, 281, 283, 320, 322
 Electroretinogram (ERG)..... 63, 65, 67, 68
 Electrospray ionization-tandem mass spectrometry
 (ESI-MS/MS)..... 97
 Endoplasmic reticulum (ER)..... 121–132
 Episcleral vein
 cannulation..... 116, 118
 episcleral venous pressure..... 110, 116, 117
 injection..... 11, 42
 Explant..... 162, 188, 189, 202
 Extracellular recording..... 72, 85
 Extraction
 lipid..... 98, 100
 microRNA..... 301, 302
 protein..... 98, 100
 RNA..... 300–302
 Ex vivo..... 82, 86

F

- Fluorogold..... 176, 180, 188, 193, 199, 312, 314

G

Gene gun 162–165
 Glia 41, 272, 279, 312
 Glial fibrillary acidic protein (GFAP) 270–274,
 276, 278, 279, 316, 326
 Glucocorticoid (GC) 123, 127, 314
 Green fluorescent protein (GFP) 276, 312, 314–316

H

Histomorphometry 207, 218, 219,
 238, 250, 260
 Human 1–8, 24, 41,
 42, 50, 51, 94, 110, 123, 125, 126, 128, 130,
 131, 141, 226, 228, 247, 248, 270, 271, 274,
 276, 312
 Hypertonic saline 3, 11–19, 24

I

ImageJ 131, 167, 177, 182, 194, 202, 238
 Immunohistochemistry 130, 131, 311
 Immunopanning 188, 192, 193, 197
 Injection
 anterior chamber 2, 11, 15,
 16, 37, 38, 42, 45, 46, 125
 episcleral vein 42
 superior colliculus 176, 195, 314, 319–322
 Intraocular pressure (IOP)
 elevation 2, 3, 5–7, 11,
 12, 16, 19, 24, 35–37, 41, 42, 45, 46, 49, 109,
 123, 125, 126, 131
 measurement 7, 12, 30,
 46, 47, 49–60, 76, 116, 139
 iTRAQ 4plex 89–94

L

Lamina cribrosa 2, 3, 188, 217,
 218, 226–228, 230, 237, 241, 243, 249, 257, 312
 Laminar beam 218, 237–240, 260
 Lateral geniculate nucleus (LGN) 70, 161, 176
 Limbus 14, 16, 115, 174, 211

M

Matrix effect 255, 299, 303
 Microbeads 3, 4, 23–38, 42, 44–47
 Microelectrodes 29, 72,
 73, 76, 81–86, 271, 280, 281, 283, 320, 327
 Microneedle 12, 14, 15, 17
 Micropipettes 12, 25,
 28–38, 72, 173, 314, 320, 322, 324, 328
 MicroRNA 287–296, 301, 302

Microsyringes 25, 27, 28,
 30, 32, 34, 36, 112, 114, 118
 Minipigs 41–47
 Monkeys ... 2–7, 42, 207, 217, 219, 222, 223, 225, 227,
 228, 230–233, 241–243, 247, 248, 251, 255,
 261, 263, 270, 271

Mouse

 brainbow 279, 314, 315
 DBA/2J 4, 71, 77, 86, 179, 181, 314, 315
 glaucoma model 3, 4, 6
 transgenic 24, 72,
 126, 161, 166, 180, 274–279, 312, 314–316
 Muller cells 276, 312, 316, 325
 Myocilin 122, 125–129, 131
 MZmine 2.21 100

N

Neurodegeneration 75, 180, 188

O

Ocular compliance 136–139,
 141–146, 156, 157
 Ocular hypertension 25, 27,
 30, 31, 33, 34, 38, 43, 45–47, 70, 71, 77, 123,
 127, 315
 Optic nerve (ON)
 crush 4, 194, 199–201
 degeneration 1, 70, 171, 176
 regeneration 187–191,
 194, 201, 203
 Optic nerve head (ONH) 1, 2,
 5, 12, 136, 139, 152, 154, 156, 175, 188, 200,
 207, 214, 219, 221, 270, 272, 275, 277, 279,
 287, 288, 290–292, 295, 299–309, 316, 318,
 322, 324, 326, 327

Outflow

 aqueous humor 2, 11,
 16, 41, 43, 109, 127, 138
 uveoscleral 110, 117

P

Pattern electroretinogram (PERG, P-ERG) 63–68
 Polymerase chain reaction (PCR)
 quantitative PCR 290, 294, 319
 RT-PCR 128, 129, 319, 328
 single-cell PCR 311, 328
 Taqman assay 290, 294
 Primary open angle glaucoma (POAG) 42,
 70, 109, 110, 126, 127, 318
 Proteomic 89–94
 PSD95 162, 163, 166, 168, 169

Q

Quantitation
 relative..... 90, 92, 94

R

Rat..... 3, 4, 6, 13, 14,
 16, 17, 53, 82, 90, 141–143, 149, 155, 156, 172,
 181, 188, 192, 196, 197, 199, 200, 202, 209,
 252–254, 261, 274, 276, 300

Retinal ganglion cell (RGC)
 axon..... 1–7, 23,
 82, 85, 109, 171, 173, 176, 180, 187–190, 270,
 287
 degeneration..... 1, 23, 70,
 171, 172, 176, 312, 315
 dendrite..... 167, 169, 313
 dissociation..... 199, 312, 315
 in glaucoma..... 1, 2, 4, 6,
 7, 171, 172, 182, 187, 312, 314
 labeling..... 6, 161
 marker..... 176, 189, 203, 315
 number..... 5, 6, 202, 203
 projection..... 172, 176, 181
 regeneration..... 187–189, 194, 200, 203
 synapses..... 162, 163, 165–169
 types..... 5, 86, 161, 312, 314

RNA sequencing (RNAseq)..... 288, 302, 319

S

Schlemm’s canal..... 13–15, 18, 116, 118, 119

Sclera..... 5, 6, 83,
 115, 116, 132, 135, 136, 139, 141, 144,
 148–150, 155–157, 174, 212, 214, 217, 223,
 227, 228, 234, 237, 255, 261, 263, 322

Second harmonic generation microscopy..... 136

Shotgun lipidomics..... 97

Small-angle light scattering (SALS)..... 136,
 141, 143, 144, 155

Sphingolipid..... 97–106

Sphingomyelin..... 99, 101

Sphingosine..... 99

Sphingosine 1-phosphate..... 98, 99

Standard
 external..... 72, 75, 217, 301
 internal..... 6, 24,
 78, 86, 115, 212, 217, 228, 230

Stereotaxic..... 71–73,
 76, 193, 196, 314, 319, 321, 326

Stiffness..... 135, 136,
 139, 141, 152, 243

Superior colliculus (SC)..... 2, 172,
 176, 177, 180, 181, 188, 195, 196, 199, 314,
 319–322

Synapse
 excitatory..... 162, 163, 165, 166
 labeling..... 162, 163, 165, 166

T

Tonometers..... 2, 3, 44,
 46, 51–54, 56, 57, 59, 71, 76, 110, 115

Tonometry
 applanation..... 50, 51, 53, 54
 electronic..... 50, 51, 53, 56
 pneumotonometry..... 50, 51, 53, 56, 59
 rebound..... 3, 44,
 46, 50–53, 57, 60, 110, 115, 117
 TonoLab..... 3, 44, 53, 71, 110, 115
 Tonopen..... 3, 51, 56

Trabecular meshwork (TM)..... 3,
 13, 15, 18, 23, 24, 36, 42, 43, 46, 121, 312

Tracing..... 56, 59,
 171, 176, 179, 189, 190

U

Ultra-high performance liquid chromatography-
 tandem mass spectrometry
 (UHPLC-MS/MS)..... 90

Unfolded protein response (UPR)..... 121

V

Visual evoked cortical potential (VEP)..... 69–79

Visual stimuli..... 73, 172

Vitreous..... 4, 83,
 86, 195, 212, 214, 217, 253

W

Western blotting..... 129, 130

X

XBP-1..... 128, 129, 132